Deformation processes along continental transform faults: the southern Dead Sea Fault System, Israel

EVANS, SIAN,HELENE

Durham University

Deformation processes along continental transform faults: the southern Dead Sea Fault System, Israel

Siân Hélène Evans

A thesis submitted in partial fulfilment of the requirements for the degree of Doctor of Philosophy at Durham University

Department of Earth Sciences
Durham University
October 2015

Abstract

The mechanical weakening processes involved in the development of major crustal fault systems have been widely documented, and it is recognised that clay-bearing fault rocks frequently have a significant influence on fault strength and slip behaviour in the upper crust. It is less well-understood how mechanical processes, such as cataclasis and the entrainment of shales along fault zones, interact with chemical processes, such as clay mineral transformations, during fault rock development. These processes can combine to form fault zones that may be both lithologically and mechanically heterogeneous, and which may also evolve over time, changing the nature of observed heterogeneities.

Data are presented here from a suite of exhumed fault sections of the southern Dead Sea Fault System (DSFS), Israel. The DSFS is an active continental transform fault that has accumulated approximately 105 km of sinistral displacement since the mid-Miocene; 60 km in an initial phase (20-18 Ma) and a further 45 km within the last 5 Ma. The studied faults lie immediately to the west of the active fault trace, west of the town of Elat, southern Israel, and are estimated to have been exhumed from shallow depths (<5 km, but potentially significantly less). Fieldwork has been carried out to document the architecture of the fault outcrops, recording comprehensive structural data, and to collect samples of a range of fault rocks. Samples have been analysed by optical and scanning electron microscopy to record microstructures and mineralogy of framework minerals, by X-ray diffraction (XRD) to record mineralogy of clay minerals, and by fusion inductively coupled plasma mass spectrometry (FUS-ICP/MS) to quantify elemental composition.

Results show the fault sections to be highly heterogeneous and comprise a range of fault rocks: variably fractured damage zones hosted in crystalline basement and sedimentary cover rocks; crushed crystalline basement rocks; mechanically entrained shale gouges; and fault gouges formed by a combination of cataclasis and neomineralisation of Mg-bearing smectite. Through operation of grain-size reduction and limited fluid-rock interactions, there is a bulk change from fault rocks dominated by frictionally strong phases, such as quartz, feldspars and calcite, displaying no obvious fabric, through to foliated phyllosilicate-rich fault gouges that likely have much lower frictional strengths. Elemental compositions across the fault zones suggest limit ingress of chemically reactive exotic fluids during neomineralisation. Mechanically entrained shale that has not undergone significant brittle deformation is also present in relatively large volumes in some instances and it is likely that the incorporation of this material inhibits further cataclastic deformation within the fault zones. Phyllosilicate-rich gouges contain microfolds on the centimetre to micron-scales, and preserve evidence of distributed deformation at shallow depth and low temperature conditions.

The heterogeneous nature of mechanically complex fault zones is influenced largely by the initial mineralogy of protolith rocks, but also by syn-tectonic processes, leading to the evolution of fault rock mineralogy with time. The development of layers of aligned phyllosilicate minerals have the potential to significantly alter the physical properties and mechanical strength of a fault zone, even if they are not present in large volumes (perhaps as little as 10-20%). The precipitation and/or entrainment of weak mineral phases may account for the evidence of both aseismic creep (microfolding) and coseismic slip (rock pulverisation) within these fault zones, recording different stages in their evolution.

Contents

List of Figures

List of Tables

Declaration and copyright

I declare that this thesis, which I submit for the degree of Doctor of Philosophy at Durham University, is my own work and not substantially the same as any which has previously been submitted at this or any other university.

Siân Hélène Evans
Durham University
October 2015

Acknowledgements

I would firstly like to thank my supervisors, Bob Holdsworth and Jonny Imber here in Durham, for giving me the opportunity to pursue a PhD; Shmulik Marco at Tel Aviv University for finding such a spectacular field area and together with Bob, setting up the project; and Rami Weinberger at the Geological Survey of Israel for provision of maps and somewhere to direct my queries about the specifics of local geology. I would like to thank you all for your guidance and useful discussions throughout. Fieldwork (and even getting home, on one occasion) would not have been possible without Shmulik and Rami's detailed local knowledge, and the assurances that stray rockets, though possible, were unlikely. I'd particularly like to thank Jonny for coming on board as a supervisor midway through proceedings, and for always accommodating the unexpected knock on your office door. Other people that provided invaluable support are those that helped in the field; Rachael, Eddie and Andy. I'd also like to acknowledge a NERC studentship and funding from the Geological Survey of Israel that enabled me not only to conduct the research, but also provided the opportunity to present my results at various conferences in the UK and abroad.

Much of this work would not have been possible without the support and assistance of many people in various labs, especially when I was venturing into unfamiliar territory: thank you to Fred Worrall and Darren Gröcke for the use of your labs, and João Trabucho-Alexandre for your time spent showing me how to prepare samples for XRD and interpret the results. Thanks to Gary Oswald for XRD training; to Leon Bowen for SEM training and quick responses when I thought I'd done something fatal; and to Ian Chaplin for your patience and expertise in sectioning some "challenging" materials. I'd also like to thank my personal government advisor, Simon Dixon, for your equation-checking and helpful input for the statistics.

There are many people that have made my time in Durham more enjoyable that it might otherwise have been, but I'd particularly like to thank Rachael, for your help in the field, for not panicking (on the outside at least) during the car vs. rock incident and for all of the general chat, geology and otherwise, over the last four years. I hope some of it was useful for you, too!; Fran, Sam, Cat, Dean and Alison, for Monday-bunday, Sunday film club and other fun times and positive thoughts; Loraine, for your almost never-ending positivity - I'm glad I've been able to repay some of that - and of course for the lunches this past week. I've eaten many more vegetables than if I'd been left to fend for myself!; Simon, Viv and Suzie, for your friendship at the very beginning and since; and Ben, for the honest conversations and encouraging words. Many thanks also to Mark Pearce and Cara Burberry for your much-needed feedback and comments at a very difficult time, they helped enormously.

Huge thanks to Deak, Lorraine, Tom, Kate, James, Mikey and Ste, for making the trips to the far north, for the fun and supportive conversations and general good times; it will be good to get back to some of that. Rosie, thanks for being a mother hen even from an ocean and a continent away, you're amazing. And the biggest thanks to Vic for your friendship and support, daily.

Andy, the ways you have helped and supported me are too numerous to include here and I think you know anyway, so I will limit it to saying thank you for the cooking, the wine and the chocolate. Mostly the chocolate.

To my family, Guillaume, Rhiannon for the emergency suppplies; Dad, I wish you could have been here to see this but I know you're in everything I do; Maman, merci pour tout ce que vous avez fait et ce que tu continues à faire. Ça n'aurait jamais été possible sans vous.

This thesis dedicated in loving memory to Pete Evans,
we miss you every day

1 Introduction

1.1 Scientific rationale

The mechanical processes involved in the development of both ancient and modern strike-slip fault systems have been widely documented (e.g Faulkner et al., 2003; Mitchell et al., 2011; Rutter et al., 1986; Jefferies et al., 2006a,b; Watts et al., 2007) and it is recognised that clay-bearing fault gouges frequently have a significant influence on fault strength (e.g. Collettini et al., 2009; Morrow et al., 1992; Wibberley, 2007; Solum and van der Pluijm, 2009; Smith et al., 2011c). However, it is less well-documented how these mechanical processes interact with others during gouge development, such as chemical alteration and smearing. Such processes may be significant in the understanding of the development and evolution of fault behaviours as they have the potential to both alter the mineralogy of fault zones and distribute fault rocks in ways that are distinct from those documented by mechanical processes. For example, the smearing of a clay mineral formed by alteration or other chemical processes may modify the frictional properties of a fault zone, by producing an interconnected network of frictionally weak material, which is not expected to occur by comminution of grains alone. We will consider these processes here and assess the influence of fault rock development on the strength and dynamic behaviour of faults. A better understanding of the controls on fault strength and behaviour are important factors in assessing, and mitigating, the seismic hazard associated with faults. Using data collected in studies such as this can help us predict which faults are more likely to fail seismogenically, even if we cannot yet predict when this may occur.

Although theoretical and experimental works (e.g. Byerlee, 1978; Scholz, 1998; Sibson, 1994) have produced predictable values of friction coefficients, and therefore strength, of a variety of minerals and rocks, many faults have been observed to be weak compared to these predicted values, for example the San Andreas Fault (e.g. Carpenter et al., 2011; Moore and Lockner, 2013), low-angle normal faults (e.g. Smith and Faulkner, 2010), the Median Tectonic Line (e.g. Holdsworth, 2004; Jefferies et al., 2006b) and the New Zealand Alpine Fault (e.g. Warr and Cox, 2001). The reasons for apparent fault weakening in the upper crust are well-established, namely: *(i)* the presence of weak minerals; *(ii)* fabric development; *(iii)* the development of high pore fluid pressures within fault zones; *(iv)* short-term dynamic weakening during seismogenic slip. What is less well-understood, however, is how the different properties of a fault zone may combine to produce weak minerals and fabrics. For example, the relative importance and contribution of wall rock mineralogy and structure, regional strain orientation and fluid flow, amongst others.

Whilst the formation of fault gouge has traditionally been viewed as a mechanical process (e.g. Engelder, 1974; Sammis et al., 1987), several studies over the last two decades have begun to assess the role of clay transformations as a chemically-driven process of fault weakening in a variety of structural and depth settings, in strike-slip faults (e.g. Carpenter et al., 2011; Chester et al., 1993,

amongst others); low-angle normal faults (e.g. Collettini and Holdsworth, 2004; Haines and van der Pluijm, 2012); thrust faults (e.g. Vrolijk and van der Pluijm, 1999) and mid-crustal shear zones (e.g. Stewart et al., 2000; Gueydan et al., 2003). It is recognised that clay transformations contribute to fault weakening by both increasing the volume of weak minerals and through fabric development. However, the role of clay transformations in overall gouge development is less well-documented and we seek to address this.

This study will consider a selection of faults from the southern Dead Sea Fault System, southern Israel, that all contain varying amounts of fault gouge within so-called fault "cores" (Chapter 2). The variation in wall rock mineralogy and geometry (including estimated displacements) will be used to identify the controls on fault gouge formation, testing the hypothesis that clay transformations are driven by mechanical as well as a geochemical processes, and that both have a significant role in fault development and strength.

1.2 The importance of continental transform faults and transtensional regions

Continental transform faults are plate boundary-forming, strike-slip faults and are usually continuous for several hundreds of kilometres. Notable examples of such faults are the North Anatolian Fault, Turkey; the Alpine Fault, New Zealand; the San Andreas Fault, USA and the Dead Sea Fault in the Middle East. Transform faults are also common in association with mid-ocean ridges such as the Mid-Atlantic Ridge. Although transform faults are dominated by transcurrent motion, they may also be associated with compressional or extensional elements and in such cases may be referred to as transpressional or transtensional, respectively. The presence and degree or transpression/transtension is often related to factors independent of the fault itself, such as regional stress field, and may therefore vary along the length of a fault. In addition, local changes in the structure of faults, such as bends and stepovers, may lead to localised zones of transpression, transtension or pull-apart basins.

Transform faults are associated with seismic activity, with many significant ($\geq$M 7) earthquake events occurring in these regions throughout the historic and modern eras, including, but not limited to:

- *North Anatolian Fault*: M 7.9, 1939, (Stein et al., 1997); M 7.7, 1943, (Stein et al., 1997); M 7.0, 1967, (Stein et al., 1997); M 7.4, 1999 (İzmit earthquake, Barka et al., 2002);
- *Alpine Fault*: $\sim$M 7.6, 1620, (Sutherland et al., 2007); $\sim$M 7.9, 1430, $\sim$M 8.0, (Sutherland et al., 2007); 1717, (Sutherland et al., 2007; Pascale and Langridge, 2012);
- *San Andreas Fault*: M 7.1, 1857, (Zielke et al., 2012, Fort Tejon earthquake,); M 7.7, 1906, (Lawson and Reid, 1908; Thatcher et al., 1997); M 7.1, 1989, (Loma Prieta earthquake, Oppenheimer, 1990); M 7.4, 1992 (Landers earthquake, Stein et al., 1992);
- *Dead Sea Fault*: M 7-7.5, A.D. 749, (Marco et al., 2003); $\sim$M 7.6 1202, (Ambraseys and Melville, 1988; Marco et al., 2005); $\sim$M 7.4, 1759, (Ambraseys and Barazangi, 1989; Marco et al., 2005); M 7.2, 1995, (`http://www.globalcmt.org`; Dziewonski et al., 1981; Ekström et al., 2012).

Large population centres are also found close to all of these faults (North Anatolian Fault: İzmit, Istanbul; Alpine Fault: Christchurch; San Andreas Fault: Los Angeles, San Francisco; Dead Sea Fault: Jerusalem, Beirut). As a result, continental transform faults have been the subject of numerous studies that aim to understand a range of properties, from structure and stress fields to rupture mechanisms and their evolution through time.

1.2.1 The Dead Sea Fault System

The Dead Sea Fault System is a sinistral transform system that extends for over 1000 km from southern Turkey in the north to northern Egypt (Sinai) in the south (see Section 2.6 and Fig. 2.1). The southern part of the fault system, in southern Israel, consists of a main, active fault trace (the Arava Fault) and several bounding normal faults in the Gulf of Elat-Aqaba. Although the active fault is largely buried in the region, in the area west of the town on Elat, at the northern tip of the Gulf of Elat-Aqaba, there is a suite of exhumed fault structures that are parallel/sub-parallel to the active fault. This area has been chosen for the present study as these faults are thought to form part of the palaeo-Dead Sea Fault System, and provide exhumed analogues for current deformation processes taking place within the active fault zone. The climate of the area is arid desert and there is very little weathering taking place, resulting in well-preserved fault rocks.

1.3 Structure of fault zones

Fault zones are rarely discrete, planar structures and typically consist of a network of deformation, whether this is in the form of brittle or ductile features. In the frictional regime of the upper crust, it is common to observe fault zones that comprise a fault core, usually in the centre of the zone and where deformation is most intense, bound on either side by damage zones, where deformation of the wall rocks is less intense than in the fault core. Fault cores are typically mm - m wide and associated damage zones cm - 100s of m wide; damage zones are not always of equal width on either side of a fault. Intensity of deformation within fault cores represent the zones that have accommodated the highest strains, and in large faults a principle slip zone (PSZ) and principle slip surface (PSS) may also be found within this part of the fault zone. A number of fault zone properties may vary across the different parts of the fault zone, such as permeability and frictional behaviour, and as such it is important to accurately describe these both as separate regions and as part of an overall fault system (Fig. 1.1). The conceptual fault core-damage zone model has been documented by numerous authors and may be described as a simple fault core

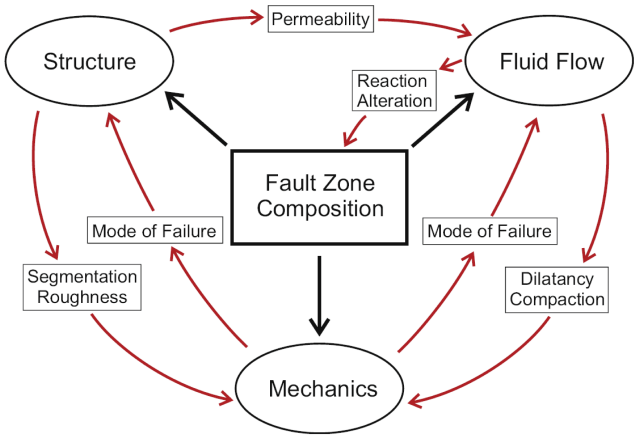

Figure 1.1: *Diagram showing relationships of various fault zone properties (Faulkner et al., 2010).*

bounded by damage zones on either side (e.g. Chester and Logan, 1986; Evans et al., 1997; Ben-Zion and Sammis, 2003; Sibson, 2003; Faulkner et al., 2008; Walker et al., 2013) or as a more complex arrangement of interconnected lenses of fault core and damage zone materials (e.g. Caine et al., 1996; Faulkner et al., 2003) and typical representations are shown in Figure 1.2. It is important to document fault zone architecture as the presence of and arrangement of various types of fault rocks is strongly linked to the fault zone properties shown in Figure 1.1, particularly with respect to fluid flow and mechanics (frictional behaviour).

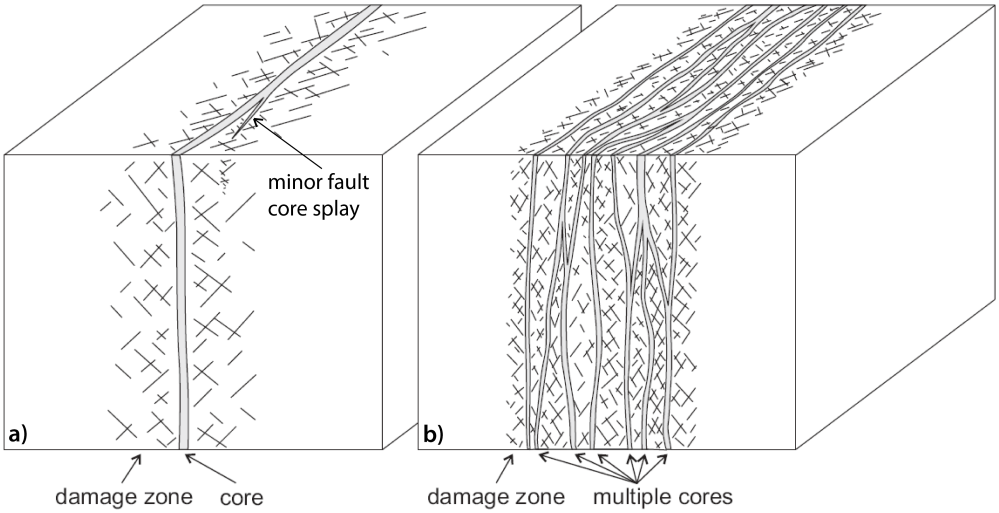

Figure 1.2: *Schematic diagrams showing typical fault core-damage zone structure in fault zones:* ***(a)*** *simple fault zone structure with a central fault core bounded by damage zones on either side, minor splays of the fault core may propagate into the damage zone but displacement is largely accommodated within the fault core;* ***(b)*** *complex fault zone structure with multiple, interconnected fault cores and lenses of damage zone in between. Displacement is likely to be spread across the multiple fault cores (after Faulkner et al., 2010).*

In the frictional regime, damages zones of the conceptual model (Fig. 1.2) are typically high permeability regions, due to the presence of brittle open fractures, in the early part of fault zone evolution. This may change over time according to the composition of circulating fluids and wall rocks, as precipitation of authigenic minerals within fractures (calcite or quartz, for example) or alteration of framework minerals in the wall rocks (such as feldspars to clay minerals) may lead to a reduction in both porosity and permeability.

The permeability of fault cores may also vary depending on grain size, composition, fabric and effective stresses. Whilst brittle deformation through cataclasis may initially lead to a fault core of relatively high permeability and a conduit to fluid flow, continued comminution and the formation of fault gouge is likely to result in a low permeability zone within the fault core, and such a fault is expected to act as a baffle to fluid flow (e.g. Caine et al., 1996). Changes in fault core composition, for example through the development of clay-bearing fault rocks (see Section 1.6.3 for more details), may also affect permeability. In particular, the development of foliated, clay-rich fault cores can result in fault zones with high permeability anisotropy (e.g. Faulkner and Rutter, 2001) as the alignment of platy minerals can create conduits for fluid flow in one direction (parallel to the foliation) and barriers in others (oblique and orthogonal to the foliation).

1.4 Terminology of fault rocks

Fault rocks are traditionally classified according to their fabric and cohesiveness (Fig. 1.3) and the main distinguishing features are the relative abundances of fragments and clasts to matrix. At depth, below the frictional-plastic transition, crystal plastic processes dominate and the mylonitic group of fault rocks are found to dominate within shear zones. At shallower levels within the crust and lithosphere, however, frictional (brittle) processes, such as microcracking and frictional sliding, are prevalent and the cataclastic group of fault rocks (including breccia, gouge and cataclasite) are produced and it is this range of fault rocks that we will consider here. In addition to the information provided in Fig. 1.3, Schmid and Handy (1991) provide further clarification to the Sibson (1977) terminology and state that cataclasites and gouges can be foliated, which is in agreement with observations made at both the meso- and microscales in this study (Chapters 2 and 3) and others (e.g Evans, 1988; Jefferies et al., 2006a; Collettini et al., 2009; Tesei et al., 2013). We have also observed "ductile" deformation but where this term is used it refers to continuous, bulk deformation such as folds, likely formed by the slow creep of a strongly foliated material and not to crystal plastic mechanisms.

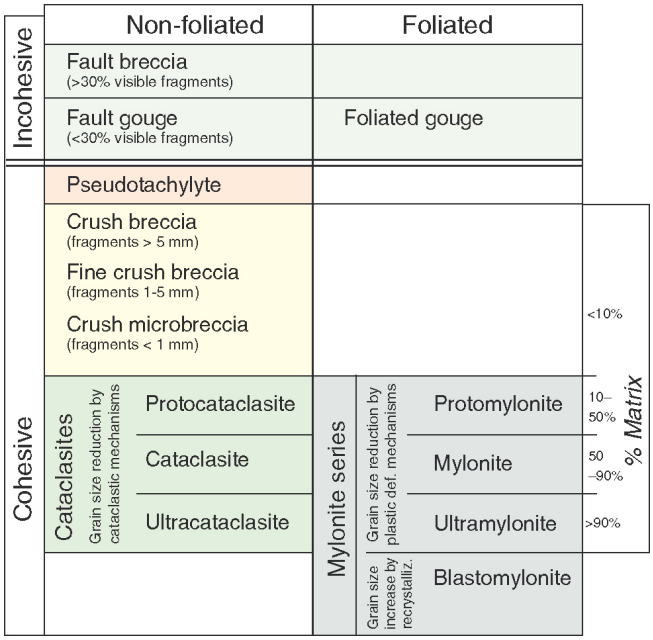

Figure 1.3: *Table of fault rock classifications, defined by cohesiveness and fabric (Fossen (2010), after Sibson, 1977).*

1.5 Properties of fault rocks

Fault zone properties are strongly linked to the physical characteristics of their constituent minerals, but are also affected by factors such the texture, fabric and grain size of these minerals. It is useful to look at weakening mechanisms of rocks and minerals as these can help broaden our understanding of the development and behaviour of fault zones.

1.5.1 Fault zone weakening mechanisms

Fault zone weakening mechanisms can be divided into long-term mechanisms, where changes in mineralogy or fabric potentially continue to affect the strength of a fault zone even after deformation has ceased, and transient mechanisms, such as elevated pore fluid pressure or thermal changes, that may only influence fault zone properties for relatively short periods, usually synchronous with deformation.

1.5.1.1 Long-term mechanisms

The two most significant long-term weakening mechanisms in faults in the frictional regime are mineralogical changes and fabric development. Mineralogical changes are significant when relatively strong framework silicate minerals, such as feldspars and quartz, are replaced by weaker phases such as phyllosilicates and clay minerals. Although these changes can happen by a variety of metamorphic processes, in the upper crust they are less likely to be the result of changing P-T conditions and instead are fluid-assisted processes; these include alteration, fluid-assisted diffusive mass transfer (DMT) and clay transformations. Changes in fabric are strongly associated with mineralogical changes in brittle faulting, since there is no development of crystal plastic fabrics and phyllosilicates and clay minerals are generally platy in shape and so are easily susceptible to alignment when sheared. The alignment of weak mineral phases within fault zones is of particular significance as several authors (e.g Handy et al., 1999; Rutter et al., 2013; Holdsworth et al., 2001) have observed that relatively low volumes of weak material are needed to have a significant effect on overall rock strength, provided they are present in continuous layers; Rutter et al. (2013) found that as little as 10 wt% of weak phase (graphite, in a quartz-kaolinite matrix) was sufficient to reduce the friction coefficient of the sample by almost 50%, from $\mu = 0.59$ to $\mu = 0.31$.

1.5.1.2 Transient mechanisms

The transient weakening mechanisms of fault zones are more difficult to predict than long-term mechanisms as they are often related to a combination of factors, such as internal structure of the fault zone, and external factors, such as the presence of fluids, rather than simply to the predictable behaviour of minerals under specific regional P-T conditions. The effect of an increase in pore fluid pressure within a fault zone can be to lower the effective stress, thereby reducing friction within the fault zone and overall fault strength (Sibson, 1977). Pore fluids themselves can also serve to lubricate the fault zone, promoting further sliding. An increase in pore fluid pressure can be very closely linked to fabrics within fault zones, since a strong fabric parallel/sub-parallel to the fault plane can drastically reduce cross-fault permeability (e.g. Faulkner and Rutter, 2001) and maintain overpressure by trapping fluids more effectively.

1.5.2 Coseismic slip vs. aseismic creep in shallow faults

Whilst many fault zones are observed in the field to comprise of centimetre - metre wide fault cores, and associated damage zones metres - 100s of metres wide (e.g. Chester and Logan, 1986; Chester et al., 1993; Billi et al., 2003), the nature of slip distribution across a fault zone has been recognised as an important factor to consider when assessing the potential of past seismic rupture of faults. Distributed slip (cm - m) is typically recognised as evidence of aseismic creep (e.g. Sibson, 2003; Faulkner et al., 2003; Rowe et al., 2013; Balsamo et al., 2014), whilst localised slip (mm - cm) is often associated with coseismic slip (e.g. Chester and Chester, 1998; Sibson, 2003; Ujiie et al., 2007; Rowe et al., 2013; Bullock et al., 2015; Ikari, 2015). Evidence of localised slip is typically preserved by the development principal slip zones (PSZs, typically mm - cm) and associated principal slip surface (PSS, typically a few µm or less) that have accommodated the majority of coseismic displacement,

and may be found either within fault cores or at fault core - damage zone boundaries (e.g. Chester and Chester, 1998; Sibson, 2003; Wibberley and Shimamoto, 2003; Smith et al., 2011a; Bullock et al., 2014). The presence (or lack) of PSZs in fault zone outcrops may therefore be significant in recognising the potential past seismogenic behaviour of these faults. It should also be noted that whilst the relationship between slip distribution and the seismogenic behaviour of upper crustal faults is well-established, there is some debate as to whether the presence of a preserved PSZ in exhumed faults is an indicator of previous coseismic slip (e.g. Chester and Chester, 1998; Sibson, 2003) or whether PSZs are precursors to coseismic slip and therefore not indicative that it has already taken place (Ikari, 2015).

1.6 Deformation mechanisms and products of shallow, upper crustal faults

Although shear zones can be found extending to substantial depths within the Earth's crust (Fig. 1.4), the present focus is on upper crustal faults and associated deformation mechanisms, found within the top ~5 km of the crust. Whilst brittle fracturing and grain abrasion are the principal deformation mechanisms within the frictional regime, the importance of frictional sliding without fracturing in shales, combined with the non-frictional process of clay transformations, will also be considered.

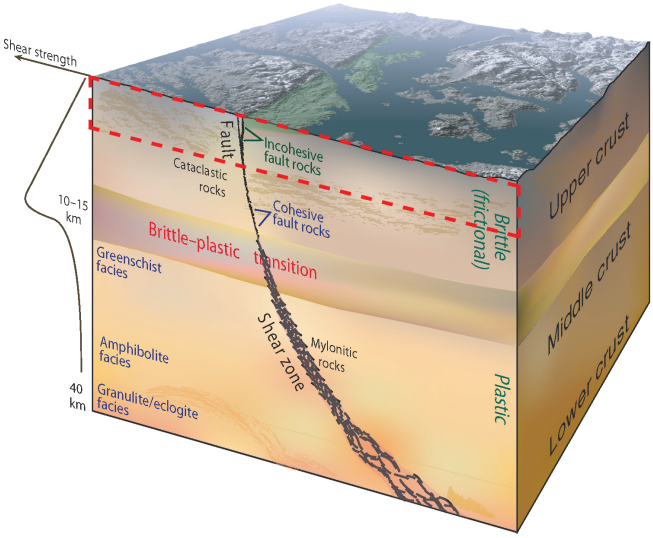

Figure 1.4: *Schematic block diagram showing relative shear strength of rocks with the crust, and position of frictional/plastic and cohesive/incohesive fault rocks within it (after Fossen, 2010).*

1.6.1 Fracturing and cataclasis

There are three principal mechanisms of frictional deformation: fracturing, grain boundary sliding, and grain rotation (Fossen, 2010). Whilst grain rotation and sliding are found in a range of shallow and surface materials, the presence of fracturing is largely dependant on the cohesiveness of the starting material. In poorly-consolidated materials (such as sands and soils), frictional deformation primarily takes occurs rotation of grains and sliding along grain boundaries to produce granular flow. In more cohesive, lithified materials, however, fracturing takes place and frictional sliding occurs along both original grain boundaries and along newly formed fractures. With a rotational component, these mechanisms combine to produce cataclasis. The continued comminution of grains during sustained cataclasis may result in the formation of a fine-grained fault gouge (Fig. 1.3, Engelder, 1974; Sammis et al., 1987), although gouges may not always form by solely frictional processes (see Section 1.6.3). Pervasive, in-situ tensile fracturing without rotation or sliding may also occur, known as pulverisation, and is thought to represent very high strain rates, commonly associated with seismic events (Fossen, 2010).

1.6.2 Shale entrainment

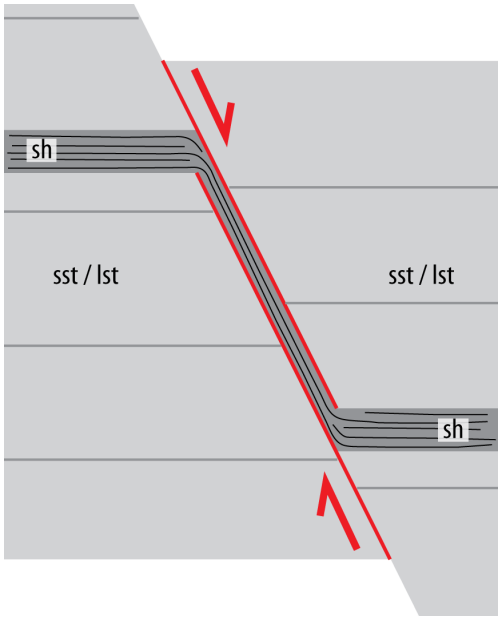

Figure 1.5: *Schematic diagram illustrating shale entrainment along a normal fault. Rigid sandstone or limestone blocks slide past each other but foliated shale is entrained and smeared along the fault; the thickness of the shale smear becomes progressively thinner as displacement increases.*

The entrainment (or 'smearing') of relatively weak and mobile material along faults is widely recognised as a fault-sealing processes in hydrocarbon settings but is relatively little-considered as a deformation process in a more general context. Mechanical entrainment of material along a fault is typically seen in shales, which are generally strongly foliated and are composed (at least in part) of clay minerals with low frictional strengths such as smectite and hydrous chlorite (e.g. Byerlee, 1978; Moore and Lockner, 2007; Bullock et al., 2015). It is defined by Lindsay et al. (1993) as "[w]here a shale layer is offset by a fault throw greater than the vertical thickness of the layer", and occurs by frictional sliding along aligned, platy clay minerals (shearing), abrasion and injection, though shearing is the only mechanism by which a relatively thick (> mm) layer of shale material becomes entrained along the principal fault plane.

In the case of abrasion, only very thin coatings (<1 mm) of shale are created on slip surfaces through cataclastic processes by the sliding of two blocks past one another; in the case of injection, shale is injected away from the main fault plane, typically as the result of overpressure within the fault zone (Lindsay et al., 1993). In stratigraphic sequences where shales are sandwiched between frictionally stronger and more massive lithologies such as sandstones and carbonates, shales may be smeared along a fault zone by normal drag (Fig. 1.5). The thickness and continuity of this shale layer depends on the amount of offset on the fault and the initial thickness of the shale layer, but if there is sufficient shale material in the stratigraphy the smeared layer may be continuous along the fault between the source layer in the foot- and hanging wall rocks (Lindsay et al., 1993). The entrained shale is derived ∼equally from the source layer in both the foot- and hanging wall sides. If a fault continues to be active after shales have been incorporated into the fault core, this material may appear to behave in a "ductile" manner and localised folds may be produced, though the mechanism can be entirely frictional (as described in Section 1.4). This mode of deformation may serve to rapidly incorporate relatively large volumes (relative to cataclastically-derived gouge) of connected, frictionally weak material into a fault zone and the potential effects on fault behaviour as a result are discussed in Section 1.5.1.

1.6.3 Clay transformations

Whilst the formation of fault gouges in the brittle domain is traditionally viewed as a wholly cataclastic processes (e.g. Engelder, 1974; Sammis et al., 1987; Blenkinsop, 1991), the role of so-called clay transformations is increasingly being recognised as a significant component in

the formation of clay-rich fault gouges (e.g. Vrolijk and van der Pluijm, 1999; Haines and van der Pluijm, 2012). Clay transformations can occur by a range of processes, usually by alteration (of framework silicate minerals, for example), by diagenetic processes (e.g. illitisation of smectite) or by precipitation of new authigenic clay minerals after dissolution of existing minerals. These processes are complex and the driving mechanisms are still poorly-understood, but it is expected that some degree of fracturing and cataclasis have occurred in the first instance, in order to provide the necessary conditions to allow the ingress of fluids and operation of pressure solution processes at grain boundaries that are required during neomineralisation.

1.7 Aims and objectives

The aim of this project is to document the deformation processes associated with the southern part of the Dead Sea Fault System and this will be done by:

- Documenting the geometry and architecture of a suite of exhumed faults along the western margins of the southern Dead Sea Fault system;
- Documenting the processes involved in the formation of fault gouges and assess the role of mechanical and chemical processes;
- Establishing the role of wall rock lithology and fluid-rock interactions and their likely influences over fault zone evolution.

Specific questions to be addressed are:

- What are the nature and ranges of fault displacement within the Dead Sea Fault System studied?
- Are these faults related to movement on the Dead Sea Fault?
- What is the role of clay transformations in the development of fault gouges?
- What are the implications for the frictional strength of these faults, and the potential affect on local seismicity, of the development of clay-rich fault gouges?
- What are the likely protoliths of fine-grained fault core gouges?
- To what degree have fluid-rock interactions influenced the development of clay-rich fault core gouges?

1.8 Methods of data collection and analysis

1.8.1 Fieldwork

Field data were collected from 326 localities in the desert area immediately to the west of the town of Elat in southern Israel. Comprehensive structural data were collected from seven N-S to NE-SW striking faults at nine localities (Fig. 2.4b). Oriented samples were collected from these fault sections, representing the full range of fault and wall rocks present; samples were also collected from representative protolith rocks across the area. Further structural measurements

were collected from transects through crystalline basement and sedimentary cover sequences. Due to the topography and terrain of the area, the majority of data were collected along dried river beds and marked footpaths that cross-cut the area. Many river beds are oriented perpendicular - oblique to the strike of major and minor faults, allowing for the collection of along-fault and off-fault data. It was not possible to access the western-most part of the field area because of its proximity to the border with Egypt due to security and military restrictions. In addition, it was not possible to re-visit two localities in the second field season due to them being destroyed by a new road being built and access to the border region being further restricted by the Israeli military.

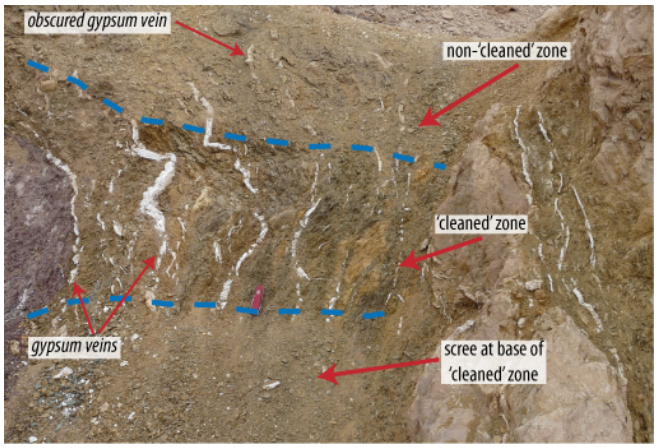

Figure 1.6: *Photograph illustrating 'cleaned' and non-'cleaned' clay-rich fault core. The top part of the photograph represents the outcrop as it was found; the overall appearance of the outcrop is of weathered material with little-no internal structure visible beneath the loose, friable surface. The central part of the photograph shows the outcrop, a clay-rich fault core, after cleaning with brushes; gypsum veins are obvious and a foliation can be observed in the clay-rich fault gouge.*

Although exposure of exhumed fault zones in the field area is very good due to the lack of vegetation resulting from the desert climate, many fault outcrops, particularly the clay-rich fault cores, were covered with a relatively thin (<1 - 10 cm) top layer of weathered material. In order to expose the detailed structure of the fault zone, fault cores were 'cleaned' with tools of varying delicacy, including a broom head, shoe brush, small decorating paintbrushes and a rubber air blower, of the sort used for cleaning the dust from cameras and other electronics (Fig. 1.6). The finer tools were used particularly in the case of fragile, friable fault gouges composed of soft clay material. This is viewed as a relatively non-destructive method of studying outcrops, since only the surface weathered layer was removed, and in the majority of cases this was < 1 cm.

Epoxy resin was used in the field for collection of the most incohesive fault rocks during the first field season (April - May 2012). A two component resin was mixed in the field and applied to prepared samples. Samples were prepared by excavating a small border to create a sample that protruded from the outcrop surface (Fig. 1.7a). In some cases, depending on the orientation of exposure of the outcrop, a shelf was made to prevent the resin from running away (Fig. 1.7) and the mixed resin was poured slowly onto the sample area (Fig. 1.7b). Ambient temperatures in excess of 30° C resulted in very quick drying time for the resin, between 30 and 60 minutes. Penetration of the highly viscous resin into the samples was largely dependent on the permeability of the sample; for low permeability rocks such as clay-rich gouges and crystalline rocks, penetration was only achieved along wider fractures and foliation planes, and for less permeable cataclasites only a coating of the sample was achieved. Samples were removed by gentle hammering around sample edges, slightly oblique inwards to prise the sample away from the outcrop. Any excess or spilled resin was easily removable from the outcrop/ground surface as its low viscosity resulted in it setting in thick clumps.

Figure 1.7: *Photographs highlighting use of resin in the field for collection of fragile samples:* ***(a)*** *prepared sample areas before application of resin; a small boarder has been excavated around each sample area and a cardboard shelf created to prevent run-off of excess resin;* ***(b)*** *after application of resin during drying period.*

Epoxy resin was not used during the second field season (November - December 2013) as it was found to make the lab impregnation process much more difficult due to the impermeable barrier it created along fractures and foliation planes (see Section 1.8.2, below). In this case, samples were instead held together with elastic bands, where possible, and wrapped tightly in cling film followed by duct tape; for shipping samples were tightly packed in boxes lined with polystyrene board and filled with tissue paper to ensure they moved as little as possible during transit.

1.8.2 Microstructural analysis

Microstructural analysis was carried out on thin sections made from samples collected during fieldwork. Samples collected during fieldwork were mostly cut perpendicular to fault strike and parallel to the principal measured striae for each fault zone. Those that were too fragile to reduce to the necessary size for thin sectioning using a rock saw were further impregnated with resin in the lab. This resin was much less viscous than that used in the field. In addition, samples were impregnated on a hot plate and under vacuum, to achieve maximum penetration. This process was repeated, where necessary, until resin had penetrated to sufficient depth within the sample to allow a billet to be cut and sectioned.

Thin sections were cut and polished in preparation for analysis by optical microscopy, and additionally carbon-coated in preparation for analysis by scanning electron microscopy. Optical microscopy

was used for initial microstructural analysis and field emission scanning electron microscopy (FE-SEM) was used for more detailed analysis. SEM images were taken in back-scattered electron (BSE) and secondary electron (SE) conditions. BSE images are grey-scaled according to the atomic mass of the material present (lighter colours represent materials of greater atomic mass) whilst SE images show the surface topography of a sample. Although paired images were always collected, in order to ensure topographic effects were not interpreted as compositional or textural features, BSE images have primarily been used here since both microstructural and mineralogical features are more obvious under these conditions.

1.8.3 Mineralogical analysis

1.8.3.1 Energy dispersive X-ray

Mineralogy was initially determined using optical techniques but for samples that are wholly or partially composed of fine grains, the use of energy dispersive X-ray (EDX) was necessary. EDX was also used to identify the specific minerals present when imaging under BSE conditions as the grey-scale colours produced are relative and cannot be used for mineral identification. EDX works by focussing a beam of charged electrons at a sample, in order to excite the atoms and eject them from the inner shells of the atom; upon subsequently returning to their shells they generate X-rays, which are recorded by a detector (Welton, 1984). Each element produces a specific X-ray pattern relating to its atomic structure and can therefore be identified from the resulting spectra (example shown in Fig. 1.8). Only the atoms at the surface of the media are excited by the electron beam, so EDX can only be used for surface analysis; geological speaking, it is useful for identifying framework minerals that have a regular crystal structure but not for clay minerals, which may be composed of interlayered minerals (e.g. illite-smectite) and may contain impurities. EDX also works best on samples with relatively flat topography so that the maximum number of X-rays reach the detector and are not refracted elsewhere (L. Bowen, pers. comm., October 2013).

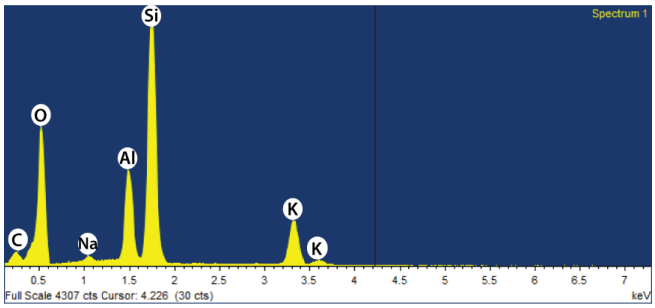

Figure 1.8: *Example EDX spectra of a mineral surface with elements identified (mineral is K-fsp); the presence of C is due to coating of the sample during preparation.*

1.8.3.2 X-ray diffraction

Although EDX can be used to satisfactorily identify highly crystalline minerals (such as quartz, feldspar, calcite) that have predictable forms and elemental composition, it is generally not possible to distinguish between clay minerals using this technique, due to both the variety composition and the fact that impurities are very frequently adsorbed onto clay minerals. As such, X-ray diffraction (XRD) is the preferred method for clay mineral identification. The techniques used for preparation of samples is described in detail in Section 3.2.

1.8.4 Geochemical analysis

Geochemical analyses were carried out in order to determine the elemental composition of a range of samples collected in the field. These were chosen to represent the full range of fault rocks present within the studied sections, along with their protoliths. Preparation and analyses were carried out by Actlabs Ltd., Ontario, Canada and involved major, trace and rare earth element concentration analysis by mass spectrometry. A more detailed description is provided in Sections 4.1 and 4.2.

1.9 Thesis outline

Following this introductory chapter, structure of the thesis is as follows:

Chapter 2: This chapter provides a regional scale introduction to the Dead Sea Fault System and a detailed mesoscale analysis of the suite of fault zones studied in the region of Elat, southern Israel. A description of the principal lithostratigraphic units is provided, along with an overview of pre-Dead Sea Fault structures and neo-tectonics of the region. Estimated displacements of the seven studied faults are provided, and the field-scale structures of each fault are presented.

Chapter 3: In Chapter 3 the results of a detailed microstructural and mineralogical analysis are provided in order to identify fault zone deformation mechanisms and processes. Microstructural analysis has been carried out using both optical and scanning electron microscopy. Mineralogical identification has been achieved using optical methods (in optical microscopy), energy dispersive X-ray (in scanning election microscopy) and by X-ray diffraction for the identification of clay minerals. Results are presented for each fault zone studied, as well as country rocks assumed to be protoliths, and from these we have proposed a model for fault zone evolution.

Chapter 4: Results of geochemical analysis are presented, giving detailed elemental concentrations of major element oxides, trace elements and REEs for the range of fault rocks analysed in Chapter 3. These data are used to further constrain the origin of fault core gouges, as well as assess the degree of mixing between hanging- and footwall rocks.

Chapter 5: This chapter includes a discussion combining the results of Chapters 2 to 4, along with conclusions and suggestions for future work.

2 Regional geology and field relationships of the southern Dead Sea Fault System

2.1 Introduction

Whilst the Dead Sea Fault System (DSFS) has been studied extensively over the last century, much of this work has focussed on mapping the subsurface structure of the fault (e.g. Ben-Avraham et al., 1979; Quennell, 1984; Ben-Avraham, 1985; Garfunkel and Ben-Avraham, 1996; Beyth et al., 2013; Shalev et al., 2013) , the plate-scale tectonics of the region (Quennell, 1958; Bartov et al., 1980; Chu and Gordon, 1998; Gomez et al., 2007; Smit et al., 2010; Mahmoud et al., 2013) and seismicity relating to the DSFS (Ben-Menahem, 1991; Marco and Agnon, 1995; Hamiel et al., 2009; Meghraoui et al., 2003; Hofstetter et al., 2003; Zilberman et al., 2005; Janssen et al., 2007; Salamon, 2008). Relatively little attention has been paid to specific modes of deformation within fault zones and the influence of lithological variations across fault strands.

We aim here to describe a suite of exhumed faults in the southern DSFS in order to characterise the fault zone architecture of each, describing macro- and mesoscale structures and kinematic indicators, in order to determine the style of faulting in the area and assess how this fits with previously published regional models. It also provides a framework for subsequent microstructural and geochemical analysis (Chapters 3 and 4).

2.2 The Dead Sea Fault: an overview

The Dead Sea Fault System (DSFS; also known as the Dead Sea Rift or Transform) is a NNE-SSW trending sinistral transform fault separating the Arabian plate and Sinai sub-plate of Africa (Fig. 2.1). It is over 1000 km long, connecting the Taurus and Zagros Mountain belts in the north to the Red Sea rift in the south. There are several associated pull-apart basins along its length, most notably those forming the Dead Sea, Sea of Galilee and the submerged Gulf of Elat-Aqaba. The fault has accumulated a total of 105 km of sinistral displacement since the mid-Miocene, evidence for which lies in the presence of displacement markers that are either adjacent when offsets are restored or part of the same structure (Quennell, 1958). These markers include: pairs of faults; metalliferous sandstone bodies; porphyritic igneous bodies; the southern edge of an upper Cretaceous marine transgressive sequence outcrop; and an offset of the Hauran basalt (amongst others). These structures are all known to be of pre-Miocene age (Quennell, 1959).

The Arabia-Eurasia collision began at approximately 35 Ma (Allen and Armstrong, 2008, and references therein), creating the Anatolian suture (and later, the Zagros suture). The rifting of Arabia began approximately 20 – 25 Ma (Garfunkel, 1988) and was first manifested along the

current Red Sea and Gulf of Suez. The Dead Sea Fault System is oriented oblique to this plate movement and accommodated the rifting in a predominantly strike-slip sense. This resulted in the formation of two new plate boundaries; the Gulf of Suez Rift and also the DSFS, forming the Sinai sub-plate (Fig. 2.1). These plate boundaries are connected through linkage of the DSFS to the Zagros and Taurus collisional mountain belt in the north. The southern segment of the Dead Sea Fault System is known as the Arava Fault and is variably exposed along the southern Israel-Jordan border, which it approximately follows. The DSFS system continues northwards, through Lebanon and into Syria. It runs through the Arava Valley (Fig. 2.1), a low-lying, N-S topographic feature filled with Quaternary and older strata (Bender, 1974; Garfunkel, 1981) and out into the Gulf of Elat-Aqaba. The Arava Valley is inferred to be the transform valley in this part of the fault system.

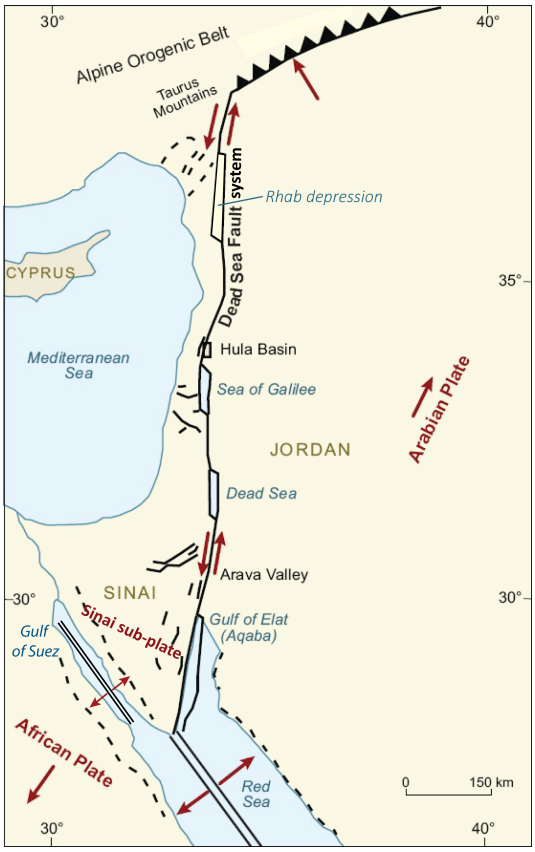

Figure 2.1: *Map showing regional relative plate motions, Dead Sea Fault System and its sinistral nature. (after Ben-Avraham et al., 2008).*

Movement on the fault system is estimated to have initiated in the early to mid-Miocene and is thought to be related to, but slightly later than, the opening of the Red Sea and Gulf of Suez (Courtillot et al., 1987; Eyal et al., 1981; Garfunkel, 1988). The age of rift initiation is well constrained due to the presence of associated (largely basaltic) igneous activity, both in the form of intrusive and extrusive bodies (Garfunkel, 1988). Since this time, the total displacement is thought to have been accumulated during two distinct phases of movement. The first resulted in approximately 60 km of left-lateral movement and is well-constrained to have occurred 20 – 18 Ma, based on offset markers of known ages such as dykes, sedimentary units and river valleys which can be traced from Sinai into Israel and across the fault zone into Jordan (Freund et al., 1968; Quennell, 1959). There is no compelling evidence of any pre-Miocene offsets of sedimentary rocks, structures or igneous bodies in this area of Sinai and Arabia (Marco, 2007). The second phase of movement is less well-constrained due to an absence of suitable markers, but it is generally agreed that the remaining 45 – 47 km of movement occurred within the last 5 Ma (e.g Freund, 1965; Le Pichon and Francheteau, 1978; Noy, 1978) based on the extent of upper Pleistocene Lisan sediments (Kaufman et al., 1992) which are confined within the Dead Sea basin and faulting of Neogene rocks in the Galilee region (Freund, 1965).

As with many regional transform faults, pull-apart basins and compression ridges have formed along the length of the fault system due to the presence of bends within, and overlapping of, fault segments (Fig. 2.1). The pull-apart basins of the DSFS are commonly referred to as "rhomb-shaped grabens" in the existing literature (e.g. Freund, 1965; Garfunkel, 1981, 1988; Quennell, 1959). It is also common for a system of normal faults to form surrounding the strike-slip system, bounding a transform valley (e.g. Garfunkel, 1981; MacDonald et al., 1979; Pollard and Aydin, 1984). As a result there may be a complex system of primary strike-slip movement with secondary

normal faults (relatively minor faults in the pull-aparts and more significant structures at the limit of the transform valley) and compressional features. This has significant implications for the development of the DSFS. For example, has the currently active segment always been contained within the transform valley we see today, or has it (and the transform valley) changed position over time? A related issue will be that changes in the active fault segment will be likely associated with changes in seismicity of the region.

2.3 Regional setting

The tectonic history of the Gulf of Elat-Aqaba region can be broadly divided into three stages, (as described by Garfunkel, 1988): "orogenic"; "platformal"; and "transtensional" (referred to as "rifting" by Garfunkel, 1988). Further north, in the Dead Sea Basin, local deformation related to salt movements has played an additional and important part in the tectonic development of the basin, but this salt is absent in the south.

2.3.1 The orogenic stage and its immediate aftermath

Southern Israel is located within the northern part of the Arabian-Nubian shield (ANS), which is believed to represent juvenile continental crust of Neoproterozoic age (ca. 800-600 Ma, Beyth et al., 2013, and references therein), extending approximately 3000 km N – S and more than 500 km either side of the Red Sea (Morag et al., 2011, and references therein). The igneous and metamorphic basement rocks of southern Israel were largely formed during this time, over a period of approximately 200 Ma. It is believed that this Pan-African Orogeny was associated with the collisional assembly of the Late Neoproterozoic supercontinent Pannotia following earlier breakup of the older Proterozoic supercontinent Rodinia (see Li et al., 2008).

The exposed Precambrian basement in the area surrounding Elat consists largely of metamorphic gneisses and schists, felsic – intermediate igneous plutons, basic – intermediate shallow intrusions and acid volcanics (Kröner et al., 1990). Several studies (Bielski, 1982; Bentor, 1985; Halpern and Tristan, 1981; Kröner et al., 1990) have used radiometric dating to determine the ages of these rocks and obtained similar results. The approximate chronology and related events are summarised by Kröner et al. (1990) as follows:

- 820 – 800 Ma: island-arc sedimentation;
- 810 – 780 Ma: regional metamorphism;
- 780 – 760 Ma and 745 Ma: two phases of plutonism (tonalitic followed by granitic) intruding into metamorphosed sedimentary rocks;
- 640 Ma: later igneous phase (gabbroic-dioritic);
- 705 Ma, 605 Ma (Morag et al., 2011), 585 Ma (Katzir et al., 2007) and 530 Ma (Beyth and Heimann, 1999): several episodes of dyke emplacement. Some of the dykes were intruded in multiple phases, indicated by their composite nature.

Gneisses and schists preserve evidence of high-temperature, low-pressure metamorphism with

peak temperatures and pressures estimated at 550 – 600 °C and 200 – 500 MPa respectively, representing burial depths of 7 – 15 km (Garfunkel, 1988). Whilst Kröner et al. (1990) estimate the youngest igneous activity to be approximately 640 Ma, both Halpern and Tristan (1981) and Bentor (1985) produce radiometric dating evidence for later emplacement of granitic plutons, in the region at ca. 600 – 590 Ma. Despite the differences in estimated ages, it is generally agreed in the literature that the basement rocks of Sinai-Arabia were all in existence by the end of the Proterozoic.

The final stage of the Precambrian orogenic sequence was a period of uplift, during which erosion of the exhumed basement provided source-material for a group of conglomeratic units, though their exact age is poorly constrained (Garfunkel, 1980). These Precambrian sedimentary rocks are faulted and form local graben structures, oriented N-S - NE-SW ((see Garfunkel, 1980, and) Beyth et al. (2014)). Tectonic activity in the region is believed to have ended by 550 – 540 Ma and there followed a period of significant erosion and an extensive peneplain was formed. This erosion was not thought to be associated with any further uplift (Garfunkel, 1980).

2.3.2 Post Pan-African events

2.3.2.1 The platformal stage: Late-Cambrian - Late-Oligocene (∼500-23 Ma)

The long-duration platformal stage of regional development is the least tectonically active stage. From Cambrian to Eocene times the region was subject to a number of transgressions, regressions and phases of regional subsidence and uplift. Sedimentation and erosion patterns varied accordingly during this time and Garfunkel (1988) has described these in detail. The main points of interest are that some minor folding occurred during this time, associated with the Alpine Orogeny in Europe, and that although Palaeozoic and early-Mesozoic rocks are present in other areas of the ANS, they are almost completely absent in southern Israel where the lithostratigraphic sequence jumps from Cambrian to Cretaceous. As they are present elsewhere, it is inferred that they have been eroded from the region of southern Israel rather than never having been present at all (Garfunkel, 1988). To the east in southern Jordan, for example, there is a sequence of Cambrian – Devonian sedimentary rocks amounting to some 1500 m thickness (Garfunkel, 1988). Significant periods of regional uplift and erosion occurred in the early Devonian, early Permian and late Jurassic – early Cretaceous. Other important plate-scale events during this period include the formation of the Mediterranean continental margin in the late Triassic and its subsequent

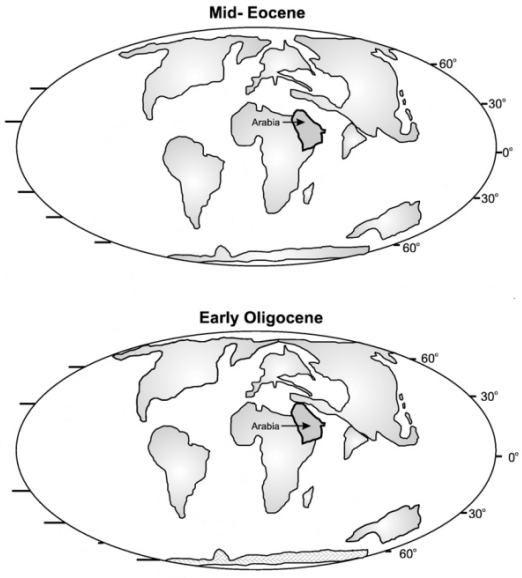

Figure 2.2: *Palaeogeographic reconstructions of continental positions in the mid-Eocene and early Oligocene, highlighting the position of Arabia in relation to Eurasia (after Allen and Armstrong, 2008).*

subsidence, forming the shallow marine platform onto which the Cretaceous carbonates seen in southern Israel were deposited (Garfunkel, 1988).

2.3.2.2 The transtensional stage: Miocene - Present (∼23-0.01 Ma)

The final so-called transtensional stage, and one which is continues to the present day, initiated with the continental break-up of Arabia-Africa and formation of new plate boundaries Fig. 2.2. As the new plate boundaries formed, uplift also occurred along their flanks which, together with the changing subsidence, greatly influence the pattern of sedimentation in the region as Sinai and Arabia were finally disconnected from the Mediterranean basin (Garfunkel, 1988). Structures formed during this stage are discussed in more much more detail in Section 2.6.

2.3.3 Neo-tectonics of the Dead Sea Fault System

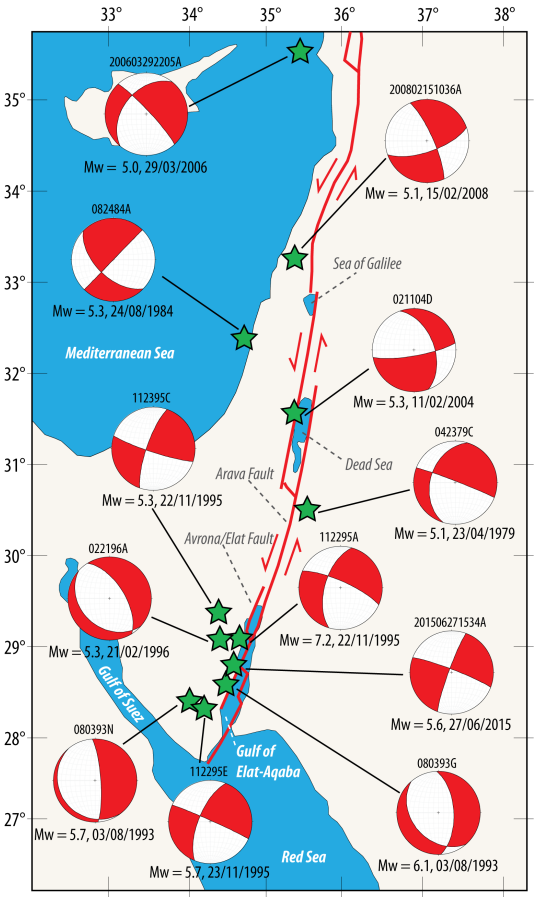

Figure 2.3: *Schematic map showing magnitude, location and focal mechanisms of earthquakes along the Dead Sea Fault System. Earthquake data (event identifier, magnitude, date, location and focal mechanism) are from the Global CMT catalog; fault structures are from Marco (2007) and Ben-Avraham et al. (2008).*

The Middle-Eastern region where the DSFS is located, from Iran to northern Egypt, is a tectonically active region; there is an historic record of large (M 6 – 7) earthquakes in AD 749, AD 1068 and AD 1202, based on written records (e.g Mayer, 1972; Ernoul et al., 1871) and palaeoseismic evidence (e.g. Marco et al., 2003; Zilberman et al., 2005; Amit et al., 1999; Haynes et al., 2006). Similar historical fault activity has also been recognised in northern Israel along the Jordan Gorge segment, north of the Sea of Galilee where combined archaeological and geological evidence has been used to date one such movement to 1759 (Marco et al., 2005).

In modern times, an earthquake of M7.2 occurred in the Gulf of Elat in 1995 (Amit et al., 2002), highlighting the continuing occurrence of seismic events along the DSFS. However, Zilberman et al. (2005) recently showed that whilst large, seismogenic events do occur, these are more likely to be isolated events and that the southern DSFS is, most of the time, seismically inactive. This proposal is supported by instrumental monitoring across the region since 1983 (Hamiel et al., 2009), and a record of events since 1979 is provided in the Global Centroid Moment Tensor (CMT) Catalog (`www.globalcmt.org`, Dziewonski et al., 1981; Ekström et al., 2012). A summary of the location and focal mechanisms of Mw > 4 for the period 1979-2015 is provided in Fig. 2.3.

Along the southern portion of the system, in Sinai, events close to the active fault strands are strongly strike slip whilst more marginal events are normal; in the north, close to the Dead Sea Basin, resolved focal mechanisms indicate more oblique movement (Fig. 2.3). Zilberman et al. (2005) also suggest that the frequency of large, seismic events has been reducing, though as the magnitude of the 1995 earthquake shows, their intensity has not. In the Arava Valley, along the southern portion of the DSFS, modern alluvial fans are locally offset, showing there has been some recent activity on fault strands within the valley; this is also supported by the very recent (June 2015) 5.6 magnitude event at the western edge of the Gulf of Elat-Aqaba (Fig. 2.3).

2.4 Lithostratigraphy of Elat

The stratigraphy of the southern DSFS, in the area around the town of Elat, can be subdivided into three broad rock groups (Fig. 2.4a): *(i)* Precambrian - Cambrian basement rocks (pink/orange/yellow horst blocks on Fig. 2.4b, Section 2.4.1); *(ii)* Cretaceous - Neogene cover rocks (green/brown grabens on Fig. 2.4b, Section 2.4.2) and *(iii)* Quaternary - Recent sediments (grey on Fig. 2.4b, Section 2.4.3). All age ranges provided are from Beyth et al. (2011), and references therein and larger versions of Figs. 2.4a and 2.4b are found in Appendix 1A.

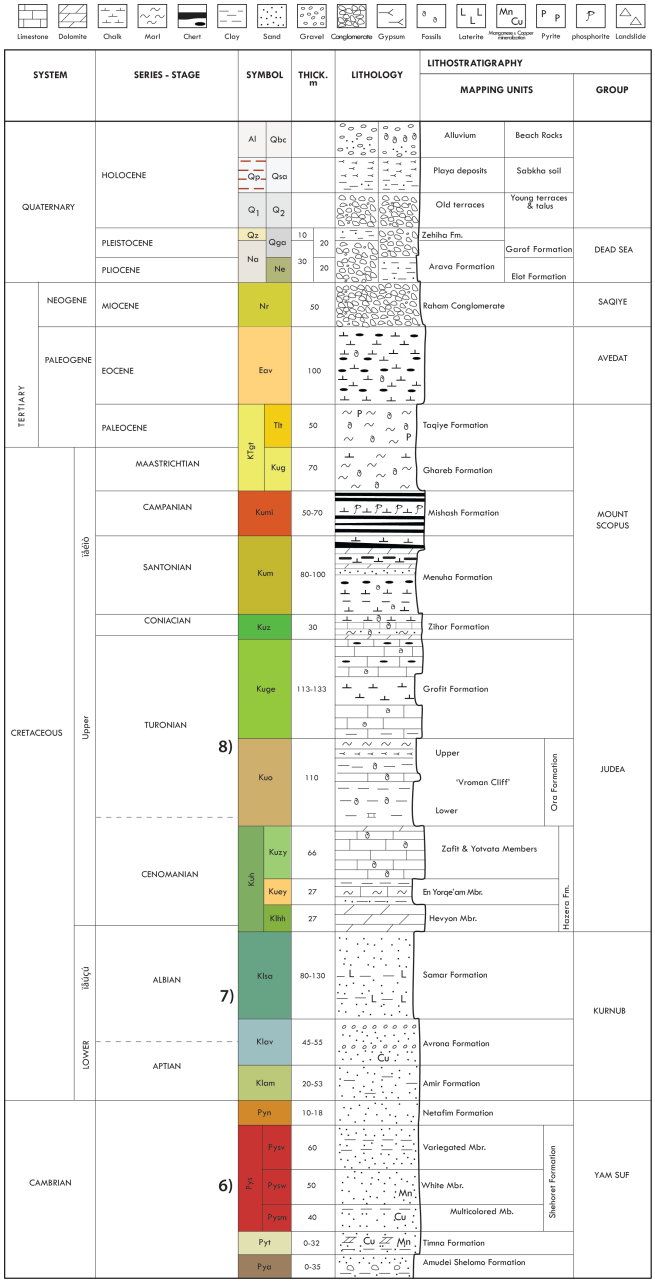

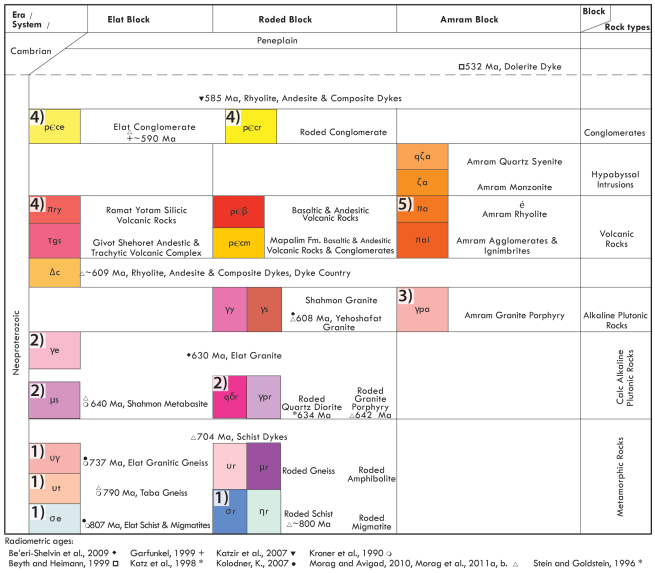

(a) *Detailed stratigraphic column for the area of Elat (Beyth et al. (2013), Geological Map of Israel, Sheet 26 Elat). Numbers 1-8 refer to stratigraphic groups highlighted on Fig. 2.4b.*

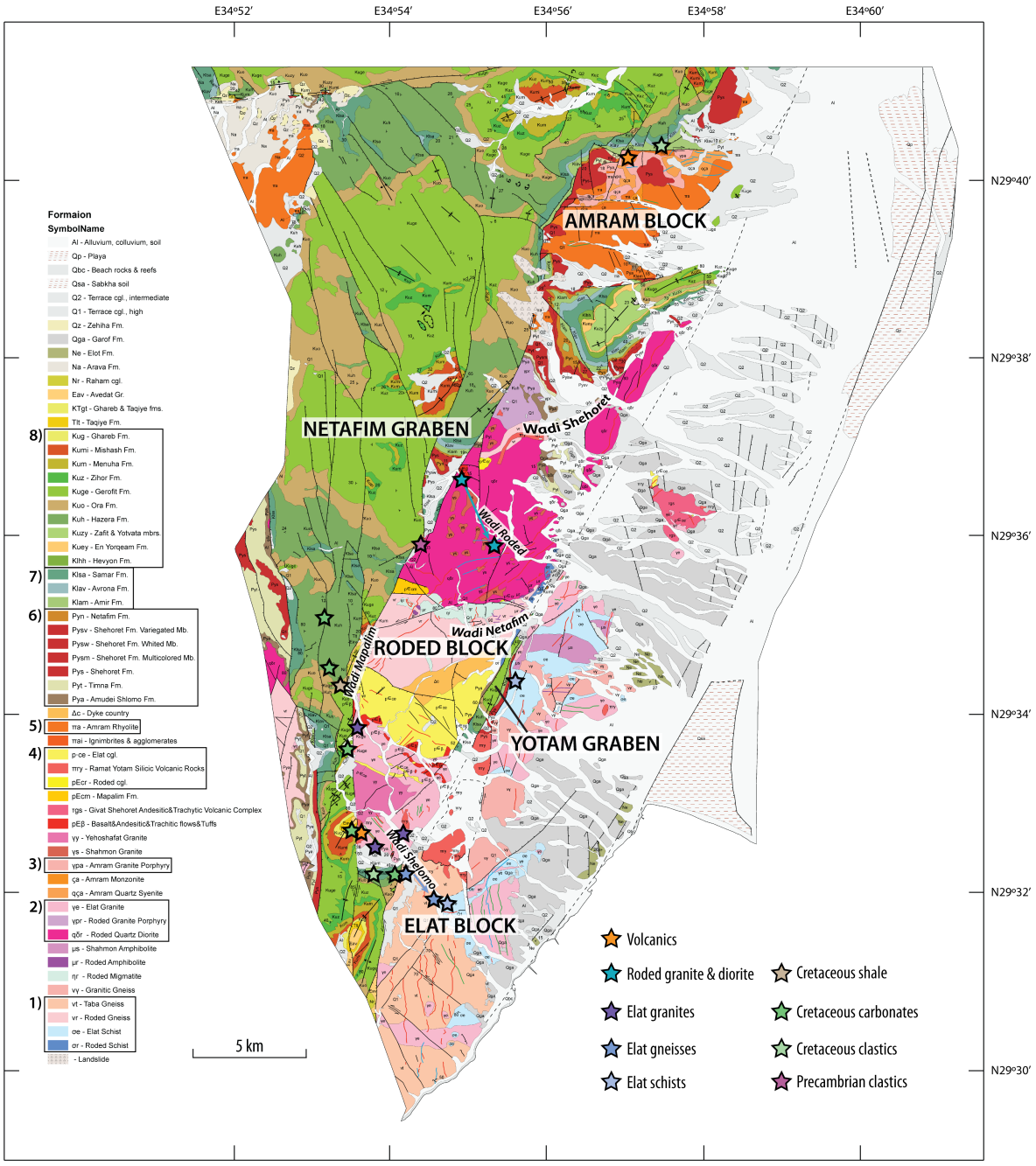

(b) *Geological map of Elat ((modified from Beyth et al., 2013), Geological Map of Israel, Sheet 26 Elat, scale 1:50,000). Significant lithologies are highlighted in the column to the left, and type localities for protolith rocks by stars.*

Figure 2.4: ***(a)*** *Detailed stratigraphic column;* ***(b)*** *and geological map of the southern DSFS around the town of Elat, southern Israel; enlarged versions of both can be found in Appendix 1A.*

2.4.1 Precambrian basement

There are a number of basement metamorphic and igneous rock types exposed in the Elat region, the most common being granite (Elat Granite; Shahmon Granite; Yehoshafat Granite) and gneiss (Roded Gneiss) within the Elat, Roded and Amram blocks (Fig. 2.4b). Minor exposures of silicic volcanics (Ramat Yotam Volcanics), schist (Roded Schist), diorite (Roded Quartz Diorite) and basaltic, rhyolitic and andesitic volcanics are also present (Beyth et al., 2013). There are also a number of dykes, rhyolitic, andesitic and composite in nature, cross-cutting many of the plutonic and metamorphic rocks but not the younger cover sequences.

2.4.1.1 Metamorphic rocks (~807-737 Ma)

Schists (~807-800 Ma) The oldest basement rocks exposed in the Elat area are amphibolite facies schists of the Elat and Roded blocks. The Elat Schist only outcrops in the south-east of the area (Fig. 2.4b) and is separated from the Roded igneous-metamorphic block and Mesozoic sedimentary rocks to the north-west by a series of NE-SW trending faults. There are only minor outcrops of the Roded Schists in the Elat area, nor are they well-exposed. The better exposed Elat Schists are metapelites and metasammites, typically containing biotite, staurolite, andalusite, sillimanite, cordierite and garnet (Beyth et al., 2011) and the source rocks are thought to be approximately 800 Ma in age (Kröner et al., 1990). They have been studied at two locations (29°31'53.79"N,34°54'38.13"E and 29°34'6.40"N,34°55'32.53"E) and here forms prominent outcrops up to 5 m high, with the face of the outcrop frequently determined by the orientation of the schistosity. Grain size varies but is generally fine-grained, though some porphyroblasts of garnet and staurolite to do occur. The schistosity is very well-defined at the mm-scale (Fig. 2.5a) and there is also a secondary compositional foliation spaced every 10-40 cm at the mesoscale (Fig. 2.5b). At the northern outcrop, garnet porphyroblasts are common and 2-5 mm in size (Fig. 2.5c). The Elat Schist is intruded by various pegmatite veins, generally 15-30 cm wide, that cross-cut the schistosity. These are usually continuous for >2 m with well-defined and angular edges and

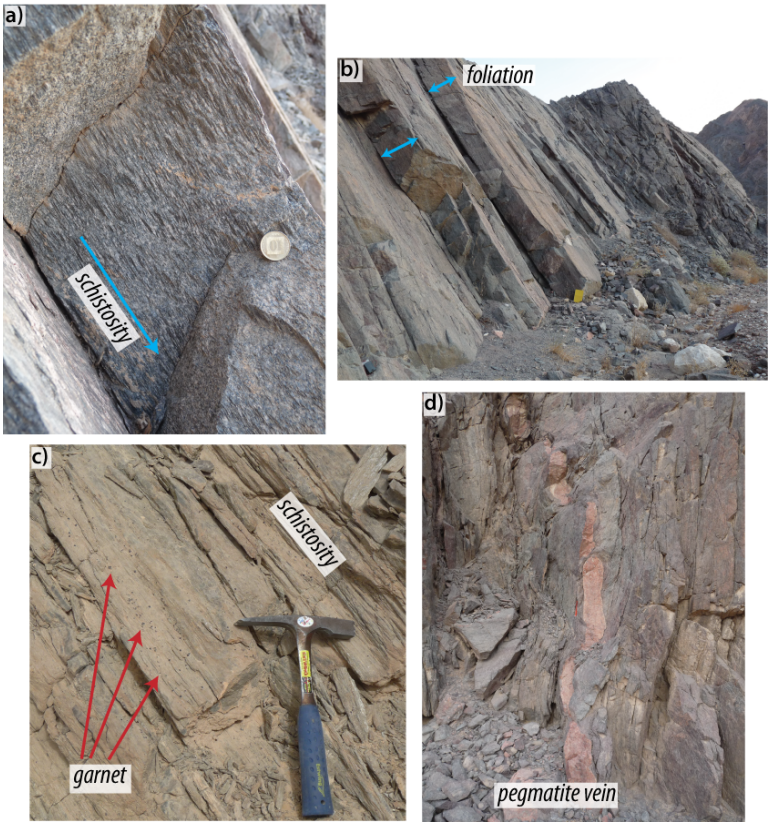

Figure 2.5: *Photographs showing typical appearance of the Elat Schist:* ***(a)*** *Schistose foliation (N29°32'9.63", E34°54'27.67");* ***(b)*** *Foliation (N29°32'9.63", E34°54'27.67");* ***(c)*** *garnet porphyroblasts (N29°34'8.38", E34°55'36.63");* ***(d)*** *boudinaged pegmatite vein (N29°31'56.86", E34°54'39.69").*

are inferred to post-date metamorphism, but there are also examples where the pegmatite vein appears laterally fragmented with rounded edges (Fig. 2.5d), suggesting in these instances they have been subjected to some degree of ductile deformation and boudinage.

Gneisses (∼790-737 Ma) The second significant type of metamorphic rocks in this area are gneisses, again divided between the Elat and Roded blocks. These are thought to be younger than the schists and metamorphism has been dated at between 790 ma (Taba Gneiss, Morag et al., 2011) and 737 Ma (Elat Granitic Gneiss, Kolodner, 2007). The Roded Gneiss has not been dated, but is assumed to fall within the same age range. The protoliths of these gneisses are believed to be felsic plutonic rocks (Garfunkel, 1988) and their mineral assemblages reflect this; they are dominated by quartz, feldspars and micas (largely biotite). The largest exposure of the Roded Gneiss is within the central portion of the Roded Block, but has not been studied in detail here.

The Taba Gneiss crops out in the very south of the area, in the region between the border with Egypt and the coastline, and has been studied along a transect between N29°32'18.93", E34°54'10.16" and N29°31'51.69", E34°54'35.69" (Fig. 2.4b). The Taba Gneiss here is consistently relatively coarse- grained with grains up to 2 mm in size. However, grain shapes are not consistent due to variations in the fabrics of the gneiss, which range from strongly linear (L-tectonites, Fig. 2.6a & b) to strongly planar (S-tectonites, Fig. 2.6c & d), and combinations of the two (LS-tectonites). Fabrics vary over relatively short distances, sometimes within just a few metres at a single outcrop, but in general the S-fabric becomes more prevalent moving south-eastwards.

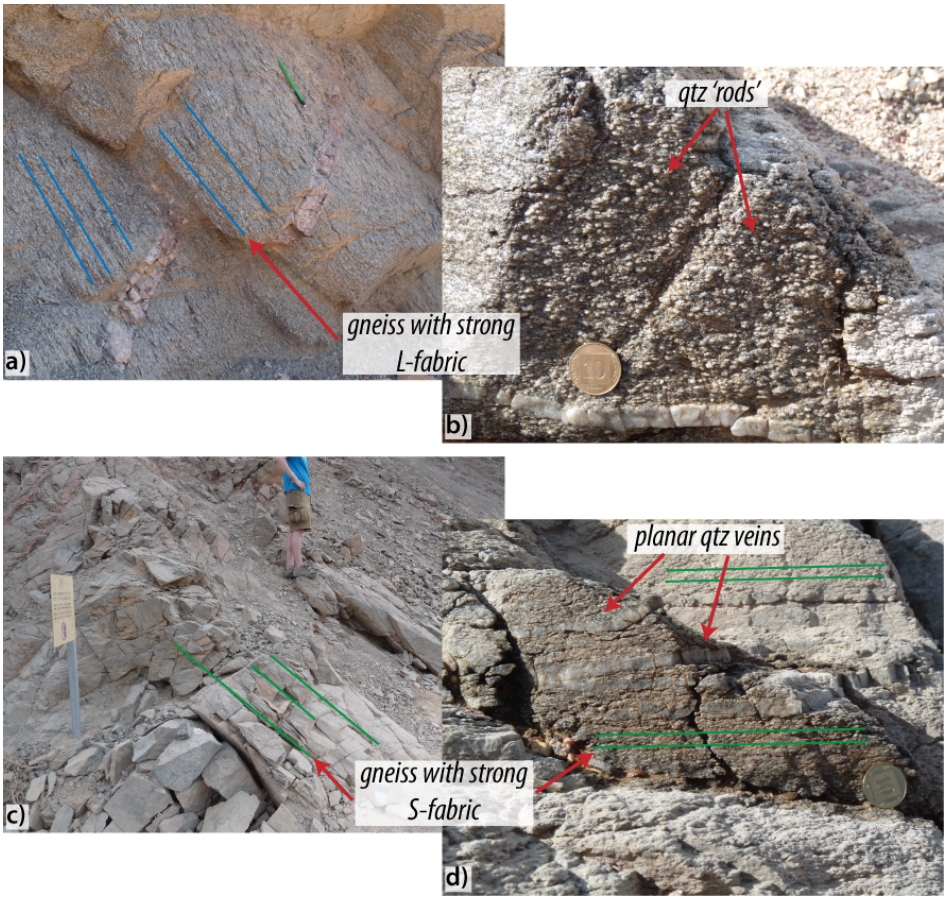

Figure 2.6: *Photographs showing typical appearance of the Taba Gneiss:* ***(a & b)*** *outcrops of gneiss with a strong L-fabric (N29°32'17.51", E34°54'17.62" and N29°32'10.40", E34°54'24.20", respectively);* ***(c & d)*** *outcrops of gneiss with a strong S-fabric (N29°32'18.52", E34°54'9.64" and N29°32'10.40", E34°54'24.20", respectively).*

2.4.1.2 Plutonic rocks (~642-608 Ma)

The plutonic rocks of the region can be divided into two groups according to their age. An older phase of plutonism occurred between approximately 642 and 630 Ma (Morag et al., 2011; Kröner et al., 1990; Katz et al., 1998; Be'eri-Shlevin et al., 2009), emplacing a range of rocks, including the Roded Granite Porphyry (642 Ma) and Shahmon Metabasite (640 Ma), but most significantly in this area the Elat Granite (630 Ma) and Roded Quartz Diorite (634 Ma). A younger phase of plutonism occurred at around 608 Ma (Be'eri-Shlevin et al., 2009; Morag et al., 2011), emplacing the Shahmon Granite, Yehoshafat Granite and Amram Granite Porphyry, but there are only very small outcrops in this region (Fig. 2.4b) and they have not been studied here.

Granites (~642-630 Ma) The Elat Granite predominantly crops out in the southern parts of the Elat and Roded blocks, generally in close association with metamorphic rocks of the Elat block (particularly the Elat Schist and Granitic Gneiss). There are minor outcrops of it further to the north of the area, suggesting it is also close to the surface in areas that are covered by Quaternary deposits (Fig. 2.4b). The Elat Granite is composed largely of quartz, feldspars (K-feldspar and plagioclase) and biotite (which has frequently been altered to chlorite). There is also minor apatite, Ti-oxide and zircon (Eyal et al., 2004).

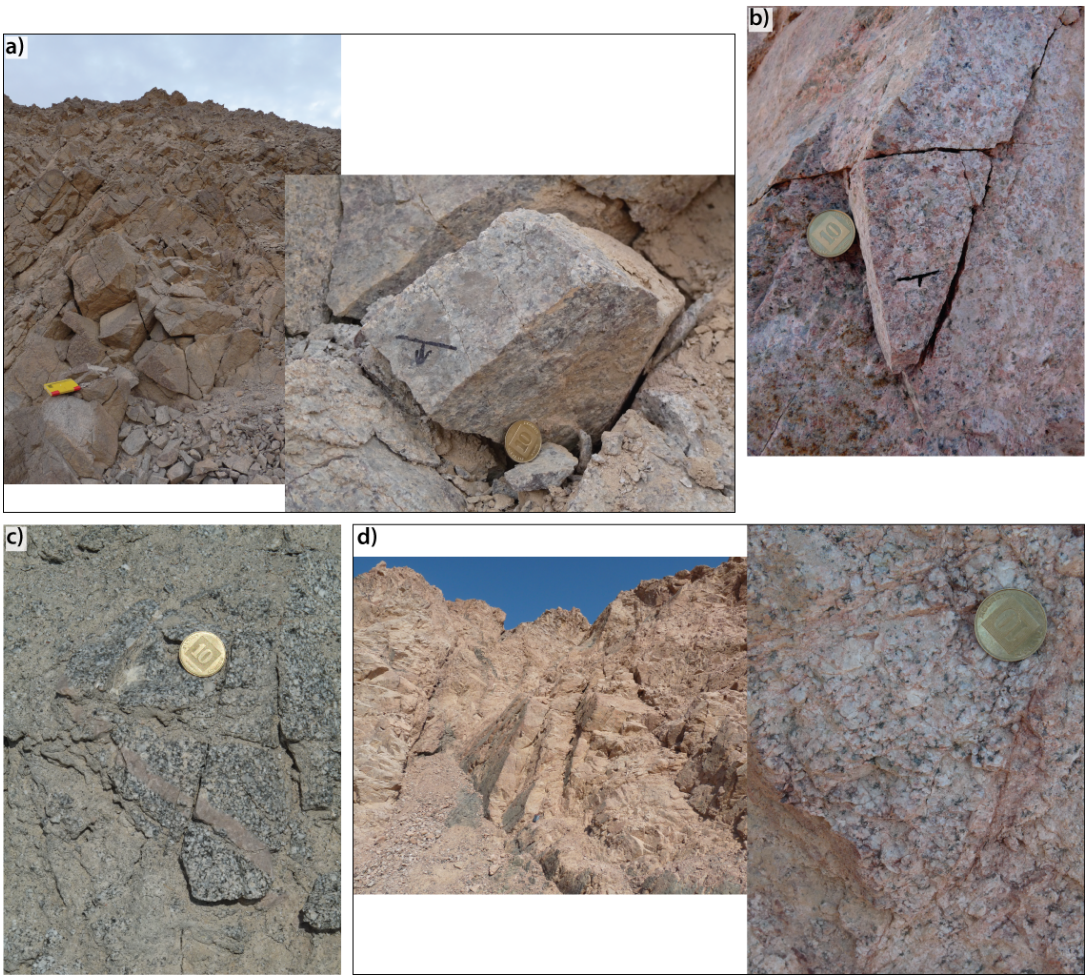

Figure 2.7: *Photographs showing typical and varied appearances of the Elat Granite:* ***(a)*** *pale-grey coloured, K-feldspar-poor example (N29°32'32.19", E34°53'34.54");* ***(b)*** *pink coloured, K-feldspar-rich example (N29°33'49.66", E34°53'29.99");* ***(c)*** *dark-grey, biotite-rich example (N29°32'37.84", E34°54'8.20");* ***(d)*** *pink-white, plagioclase-rich example (N29°32'33.42", E 34°54'9.67").*

The granites studied here (Fig. 2.4b) form part of the Rehavam pluton (Eyal et al., 2004) and vary in composition locally. They are all relatively coarse-grained (Fig. 2.7) but are distinguished by their varying amounts of feldspars (relative enrichment/depletion of K-feldspar) and micas (relative enrichment/depletion of biotite), examples of which are shown in Figure 2.7a-d. The Elat granite is variably fractured across the studied area (see Sections 2.5 and 2.6) and generally has a blocky weathering with many loose blocks.

Quartz diorite (∼634 Ma) The second significant plutonic igneous rock in the area is the Roded Quartz Diorite that is exposed within the northern part of the Roded Block (Fig. 2.4b). It has been studied here in a section following the Wadi Roded (from N29°36'0.77", E34°55'23.24" to N29°36'42.97", E34°54'51.83", Fig. 2.4b) that bisects the outcrop of this unit from ∼SE-NW. The quartz diorite is composed of quartz, biotite and feldspar and is typically very coarse-grained, with grains of quartz up to 3 mm common (fewer biotite crystals of this size are also present). There is some local variation in feldspar content (Fig. 2.8).

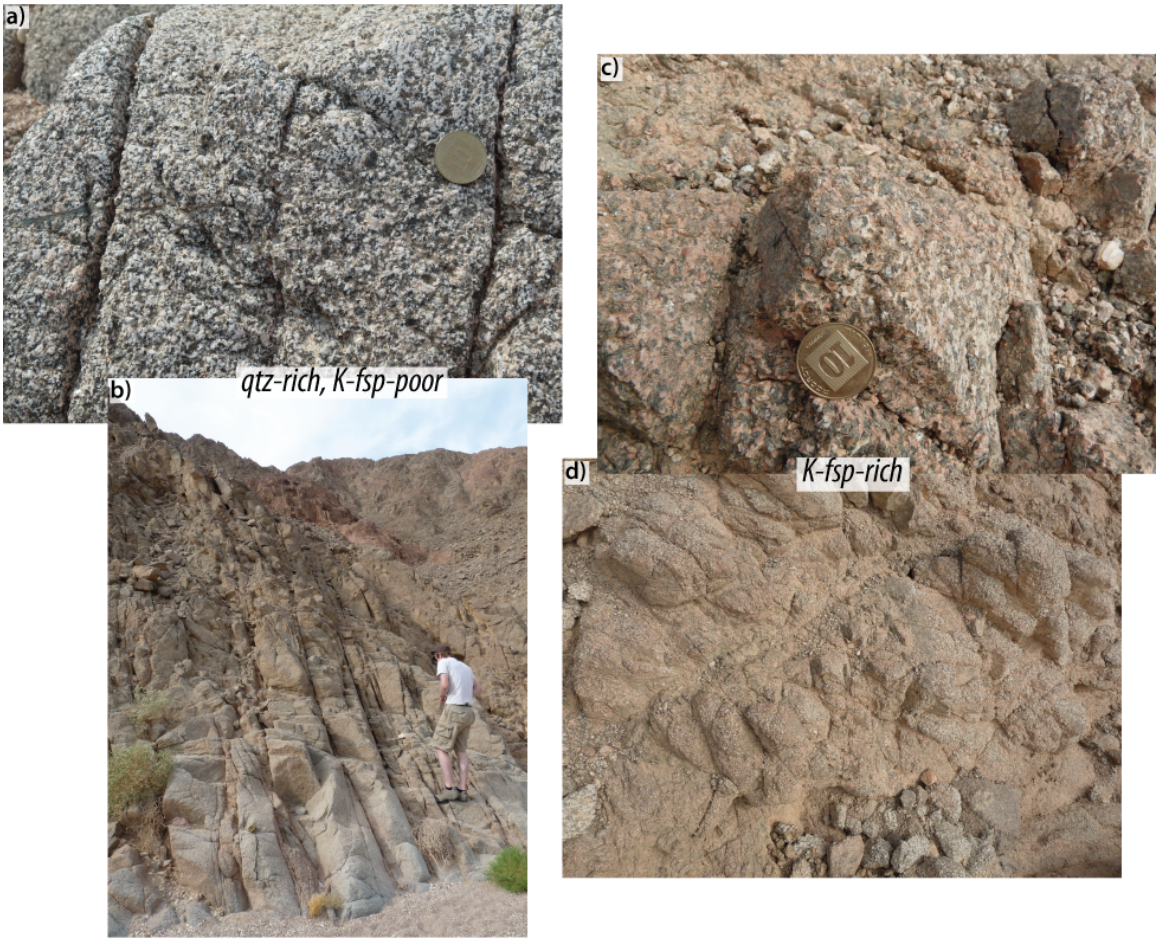

Figure 2.8: *Photographs showing typical appearances of the Roded Quartz Diorite:* ***(a & b)*** *Medium-grained, K-fsp-poor exposures (N29°36'0.77", E34°55'23.24" and N29°36'1.43", E34°55'14.60", respectively);* ***(c & d)*** *coarse-grained, K-fsp-rich exposure (N29°35'58.22", E34°54'25.98").*

2.4.1.3 Volcanic rocks and intrusions (∼609-532 Ma)

The third group of crystalline basement rocks that crop out in the area are dykes and extrusive volcanic rocks, both of which vary in composition. Dyke emplacement is known to have occurred

in four stages, between approximately 615 and 535 Ma (Katzir et al., 2006), with the composition of the earlier phases being rhyolitic, andesitic and composite (felsic cores with mafic margins) (Katzir et al., 2007), and the latest phase being doleritic (Beyth et al., 2011). The dykes intrude into almost all of the basement units, including the late-Precambrian conglomerates (Section 2.4.1.4). In the Elat Block gneiss and granite, the dykes have a general north-south trends and may be controlled by the strong ductile fabric of the gneiss. However, in the Roded Block there is no strong preferred orientation of dykes.

The most significant outcrop of volcanic rocks is the Amram Rhyolite, in the north of the area, otherwise exposures are limited. This group of rocks is varied in composition, being composed of basaltic, andesitic, trachytic and silicic members, as well as the main rhyolitic unit. The volcanic extrusions have not been directly dated, but due to their position within the Precambrian sequence are thought to have been emplaced c. 609-590 Ma, between the first phase of dyke emplacement and the deposition of the Elat and Roded conglomerates (Beyth et al., 2011). We have studied a silicic member here that is in close association to one of the studied faults (N29°32'32.19", E34°53'34.54").

2.4.1.4 Precambrian Clastic rocks (∼590 Ma)

Clastic basement rocks are present in the form of late-Precambrian conglomerates. Precambrian Elat and Roded conglomerates form an extensive peneplain (Fig. 2.9), dated at approximately 590 Ma (Morag et al., 2011; Garfunkel, 1999), suggesting there had been a period of major erosion prior to their deposition. Garfunkel (1999) suggests that up to as much as 12 km of the existing succession of Precambrian sedimentary rocks was removed. Clasts of a range of igneous and metamorphic basement units are evident within these conglomerates and are generally poorly-sorted but well-rounded.

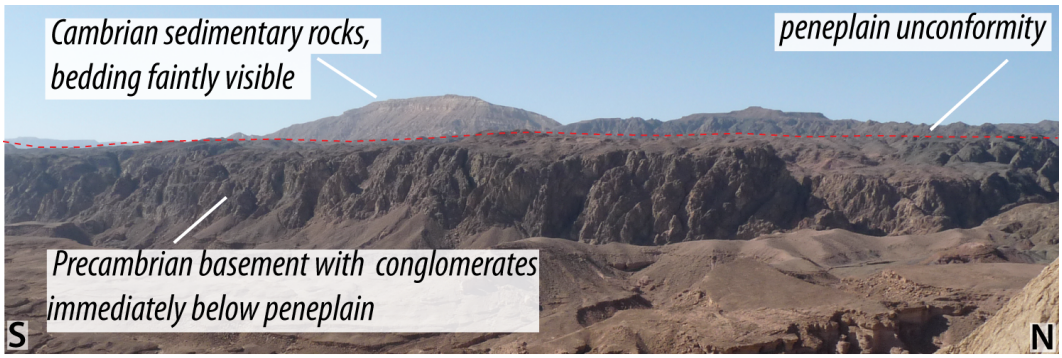

Figure 2.9: *Photograph showing sub-horizontal peneplain unconformity between the Precambrian crystalline basement and Cambrian sedimentary rocks.*

2.4.2 Cambrian - Neogene cover rocks (∼542-1.8 Ma)

The stratigraphy of Elat during the Palaeozoic - Neogene was deposited in three main phases: Cambrian clastic rocks; Cretaceous clastic and carbonate rocks; and Tertiary carbonates with clastics.

2.4.2.1 Cambrian Clastic rocks (∼542-488 Ma)

The oldest sedimentary rocks above the Precambrian peneplain are seen in exposures of the sands and clay-sands of the Amudei Shelomo, Timna and Shehoret Formations (Fig. 2.4; Beyth et al., 2014). These little-deformed, unmetamorphosed sedimentary rocks have been dated using marker fossils (Garfunkel, 1980) and are up to 300 m thick (Beyth et al., 2011). They comprise medium-grained sub-arkosic sandstones with an upward transition into deeper marine shales and carbonates towards the end of this period. The latest Cambrian sequence is defined by a return to shallow marine and fluvial sandstones (Garfunkel, 1988). In the field, these sedimentary rocks vary in appearance; they are sometimes dark-red to brown and difficult to distinguish from the crystalline basement at distance. There is also a variegated member (Fig. 2.4a, Fig. 2.10) that outcrops most frequently.

Figure 2.10: *Photograph showing typical appearance of Cambrian sandstone variegated member (N29°35'58.22", E 34°54'25.98").*

2.4.2.2 Cretaceous sedimentary rocks (∼145.5-65.5 Ma)

In the mid-Cretaceous, southern Israel formed part of an extensive carbonate platform, leading to the deposition of the thick, up to 1500 m, sequences of predominantly carbonate rocks seen (Garfunkel, 1988), though there are also significant thicknesses of clastic rocks in the Lower Cretaceous (Fig. 2.4). They are essentially unmetamorphosed, little deformed and unconformably overlie the basement and Cambrian rocks (Garfunkel, 1988). The entire stratigraphic sequence between the Cambrian and Cretaceous is absent, suggesting that some 1.5 km of sedimentary cover are missing due to the effects of post-Cambrian, pre-Cretaceous uplift and erosion (Marco, 2007).

Cretaceous clastic rocks (∼145.5-99.6 Ma) The sandstones that form the lower part of the Cretaceous stratigraphy (up to 250 m thick, Beyth et al., 2011) in this region (the Amir, Avrona and Samar formations, Figs. 2.4a and 2.11) are all similar in appearance and composition; they are pale pink in colour and are quartz-rich, sub-arkosic sandstones. These rocks are variably lithified, with the younger Avrona and Samar formations being more cemented than the less cohesive Amir Formation. The Amir sandstone is also coarser grained than the other unit, with medium-coarse grains of quartz (approximately 500 µm). By contrast, the younger rocks are variably fine-medium grained (approximately 150-300 µm). Honeycomb weathering is common in the Avrona sandstone (Fig. 2.11a).

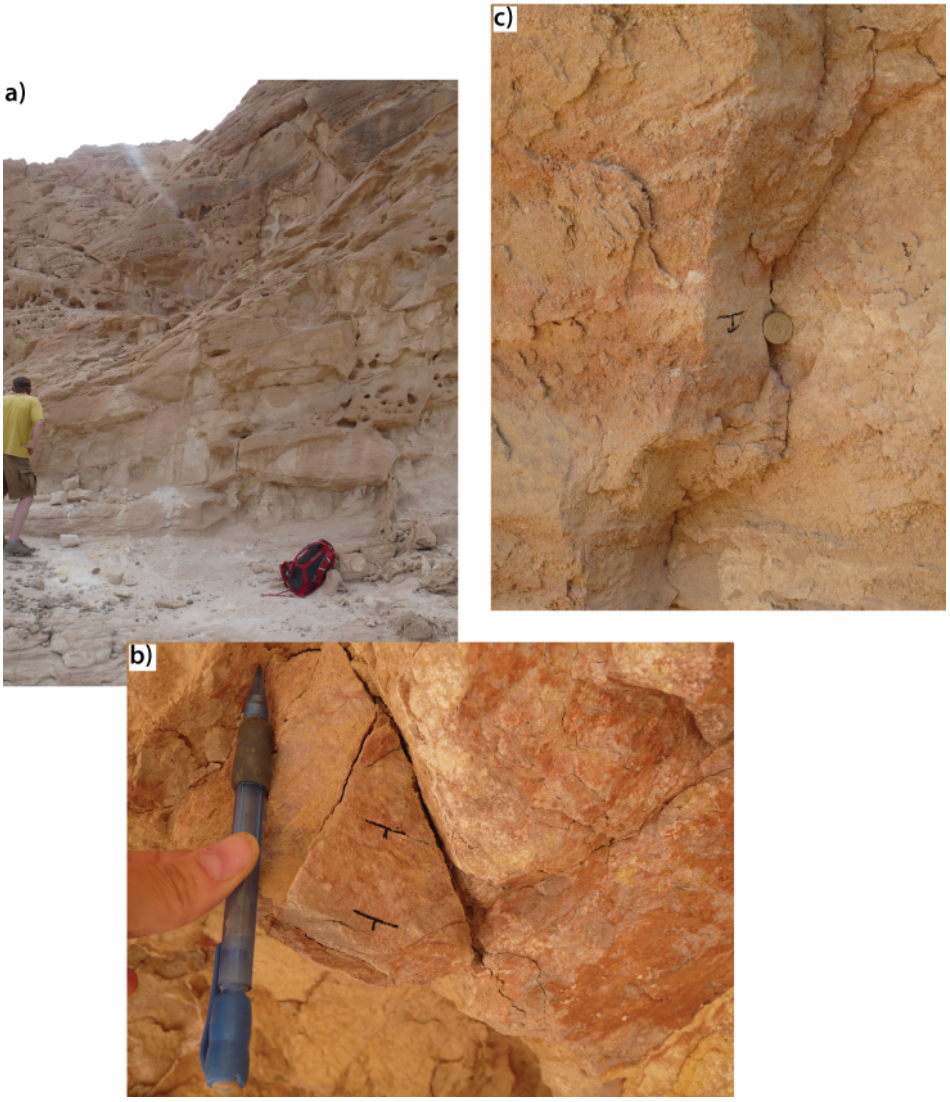

Figure 2.11: *Photograph showing typical appearance of Cretaceous sandstones:* ***(a)*** *Avrona Formation; pink on weathered surfaces and white on fresh surfaces, with honeycomb weathering (N29°32'14.24", E34°53'46.74");* ***(b)*** *Samar Formation; medium-grained and variably pink and white in colour (N29°33'39.08", E34°53'15.92");* ***(c)*** *Amir Formation; coarse-grained, variably dark and light pink and poorly-cemented (N9°40'21.47", E34°57'17.33").*

Cretaceous carbonate rocks (∼99.6-65.5 Ma) In the early Upper Cretaceous, deposition is dominated by limestones and dolostones, passing into deeper water chalks and marls, with periods of limestone deposition (Garfunkel, 1988). Typical exposures of Cretaceous rocks are shown in Figure 2.12.

The main units that have been studied here are the lower Cretaceous (Cenomanian) Hazera Formation (Fig. 2.12a,b), the mid Upper Cretaceous (Turonian) Grofit Formation (Fig. 2.12c) (both of the Judea Group) and the Upper Cretaceous Ghareb Formation marl (Fig. 2.12d) (part of the Mount Scopus Group) (Fig. 2.4a). There is quite a lot of local variation within these units, and the Hazera Formation is sub-divided into four members: the dolomitic Hevyon Member; the clay and marl En Yorqe'am Member; and the limestone Zafit and Yotvata members. It should be noted though that even within these members there is variation below map resolution, and it is not uncommon to find interbedded shale and limestone at the centimetre scale.

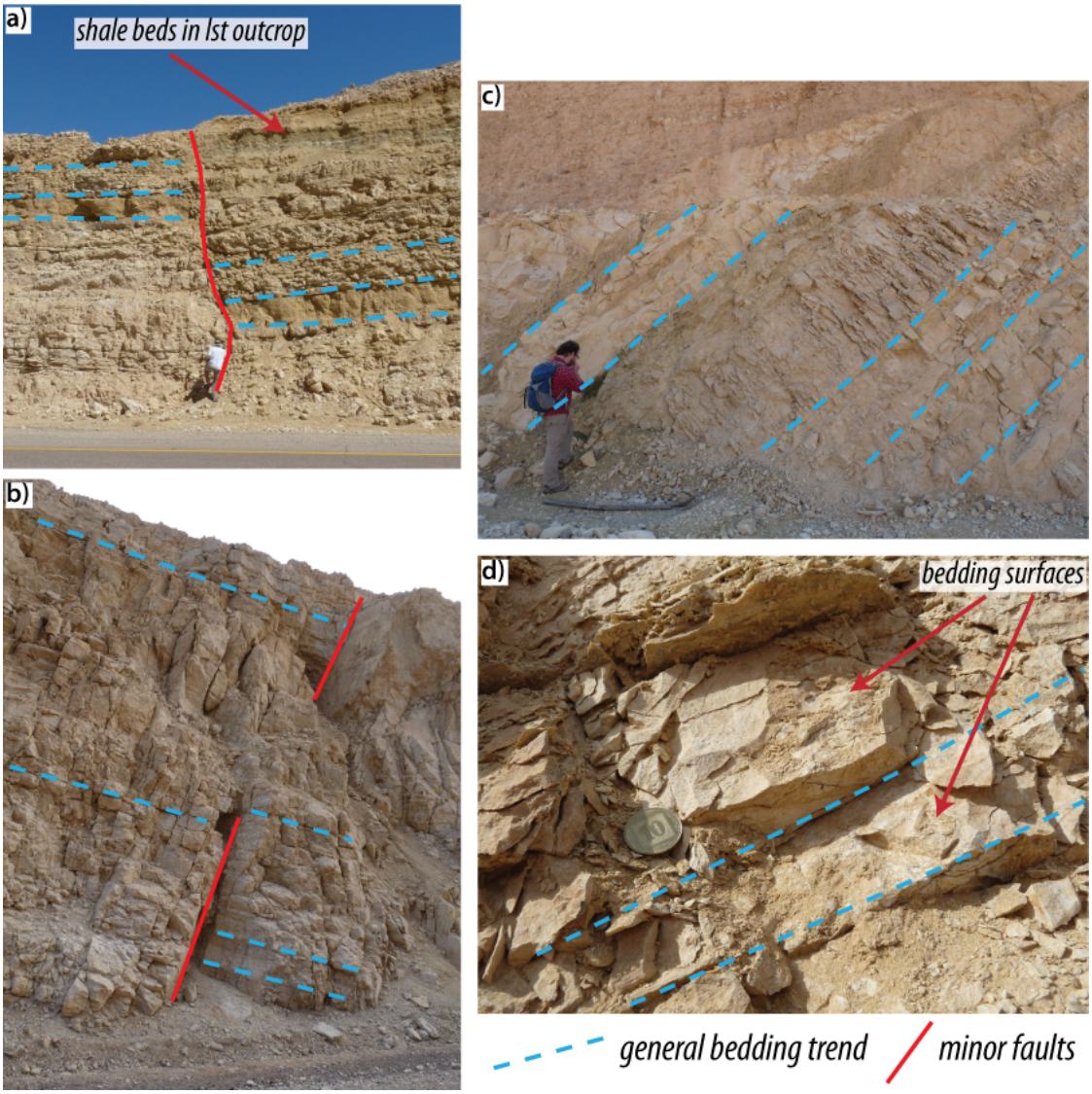

Figure 2.12: *Photographs showing the typical appearances of Cretaceous carbonate rocks:* ***(a)*** *Hazera Formation; sequence of interbedded (cm-scale) limestone and shales (N29°35'15.13", E34°52'50.22");* ***(b)*** *Hazera Formation; massively bedded limestone (N29°35'7.31", E34°53'9.72");* ***(c)*** *Grofit Formation; a typical tilted sequence of carbonates (N29°33'35.82", E34°53'21.61");* ***(d)*** *Ghareb Formation; finely-laminated and friable marl (N29°32'52.09", E34°53'31.30").*

Cretaceous Ora shale (∼94-91.5 Ma) The Ora Formation is a very distinctive upper Cretaceous marine shale, that was deposited in a basin 50 – 100 m deep (Beyth et al., 2011). The outcrop of relatively undeformed shale studied here (Fig. 2.13a) is from the lower part of the formation; at the mesoscale it is relatively homogeneous in appearance, being very fine-grained, pale green in colour and with very few clasts (Fig. 2.13b). It is finely laminated and very friable, with often numerous gypsum veins, 20-30° mm wide, running largely parallel to the foliation but also sometimes cutting across it at an angle of 20 – 30° (Fig. 2.13b), indicating that they post-date deposition. The formation is highly mobile and forms several intrusive diapirs in the area, thought to be related at least in part to movement on the Dead Sea Fault (Beyth et al., 2011).

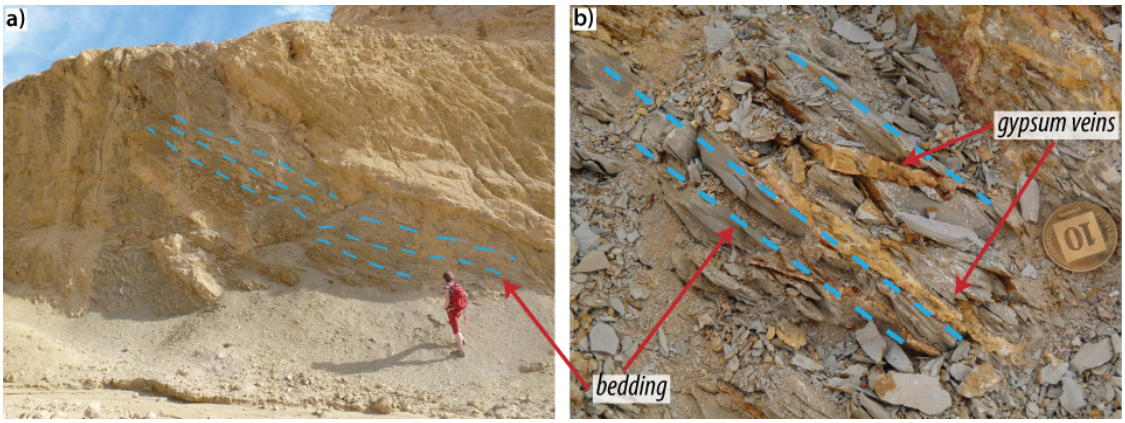

Figure 2.13: *Photographs showing typical appearance of the Ora Formation shale: (**a**) moderately dipping beds; (**b**) close-up of finely-laminated and friable shale (N29°34'20.02", E34°53'24.32").*

2.4.3 Quaternary - Recent sediments (∼1.8-0.01 Ma)

Outcrops of Eocene – Quaternary sedimentary cover are widespread and occur in significant amounts within the transform (Arava) valley. Thinner accumulations are found along the coast and in the network of dried river valleys, also known as wadis locally, (e.g. Fig. 2.14) in the mountains unconformably overlying basement, Cambrian and Cretaceous rocks. In the coastal area, well exposed Plio-Pleistocene successions are found, consisting of generally sub-horizontal conglomerates and poorly-consolidated sands. Clasts within the conglomerate range in size from a few millimetres to approximately 60 cm, and are composed of the whole range of rocks found in the area; carbonate, sandstone and igneous/metamorphic basement. Clasts range in shape from angular to well-rounded with carbonate clasts generally being well-rounded whereas those composed of basement material are more angular. Sorting within individual beds is poor and beds themselves are generally poorly-defined and the boundaries gradational. Sandy beds may be up to a metre or more in thickness and are in general poorly-lithified, appearing to have undergone very little compaction or cementation.

Figure 2.14: *Photograph showing typical horizontal and unfaulted Quaternary deposits; beds range in thickness from cm- to m-scale and alternate being clast-rich, conglomerate beds and clast-poor, sandstone beds (N29°35'0.42", E34°55'0.64").*

2.5 Pre-Dead Sea Fault System structures

The most significant and definitively pre-Miocene/DSFS structures are ductile in origin and occur within the Precambrian crystalline basement, including the fabrics of gneissic and schistose rocks, and igneous intrusions into these and with brittle structures across the basement rocks. Gneisses of the Elat Block display a range of S- and L-fabrics, whilst schists in both the Elat and Roded

blocks have a strong schistosity. These basement rocks are also heavily fractured, though it is less immediately clear if these pre-date movements on the DSFS.

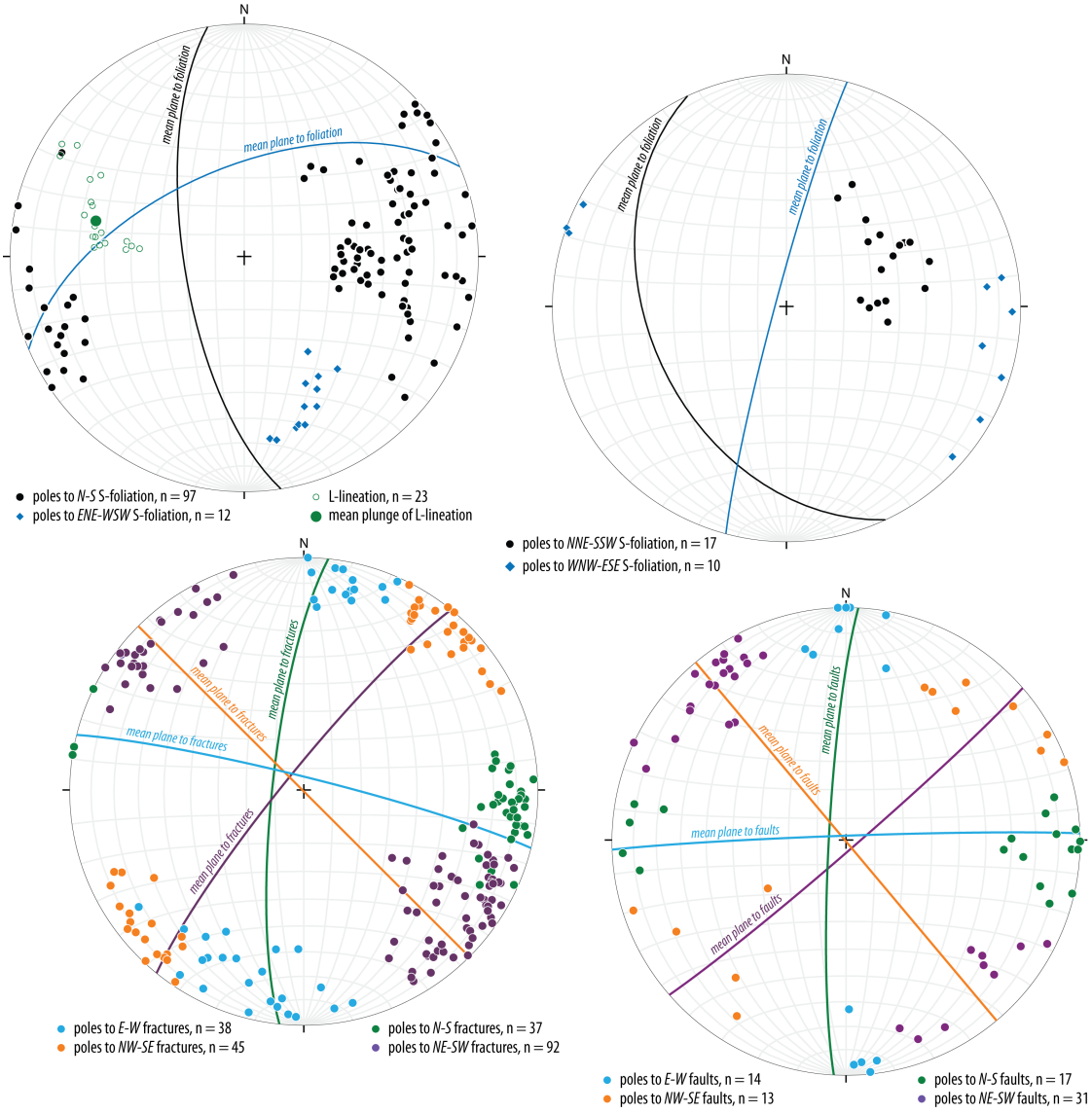

Figure 2.15: *Stereonets summarising principal basement structures:* ***(a)*** *ductile gneiss fabrics;* ***(b)*** *ductile schistose foliation;* ***(c)*** *fractures in basement rocks;* ***(d)*** *minor faults in basement rocks.*

The fabrics of the Taba Gneiss (part of the Elat block) were studied in detail during the present study. They are variably dominated by L- and S-fabrics. L-fabrics plunge moderately and consistently to the W (mean 23/276). There is more variation in the orientation of S-foliations, but the dominant strike direction is N-S, with a mean of 001/34E (Fig. 2.15a). The foliation of the Elat Schist is also variable, though with a less well-defined principal orientation. The variations in strike are from WNW-ESE to N-S with a moderate dip, and also a sub-vertical NE-SW striking foliation (Fig. 2.15b). Brittle fractures and minor faults in the basement across the area vary in strike but are for the most part sub-vertical (Fig. 2.15c). Across different lithologies, fractures can be split into four distinct groups: N-S-, NE-SW-, E-W- and NW-SE-trending. Of these, it is likely that the NE-SW set at least may be related to the DSFS. The range of dips of all of these fractures is between ~60 and 90° (but frequently >80°), with the exception of the NE-SW-trending fractures which have a wider range and dips as shallow as 40°. Minor normal faults follow a similar pattern (Fig. 2.15d) and the NE-SW-trending set appear to be dominant in both cases.

2.6 The Dead Sea Fault System in the Elat region

Although the structures of the Dead Sea Fault System now occupy a very narrow zone, several studies have noted that faulting once occupied a much broader region. For example, when mapping the eastern Sinai, Eyal et al. (1981) noted a 30 km-wide region of N-S to NE-SW-trending faults located to the west of the Gulf of Elat-Aqaba in the eastern Sinai desert (in Egypt, south of the current area of study). These faults sinistrally offset by 24 km a series of early-Miocene dykes and so are believed to be related to movement on the Dead Sea Fault (Eyal et al., 1981).

Figure 2.16 summarises the local geology, using a satellite image and cross-section, of the area surrounding the northern tip of the Gulf of Elat-Aqaba. A series of NNE-SSW-trending horst and graben structures are preserved, exposing the darker Precambrian and Cambrian rocks and younger, paler Cretaceous and younger sedimentary rocks at approximately the same topographic level. East of the Arava Valley, in Jordan, are the dark Precambrian and Cambrian rocks of the Edom Mountains.

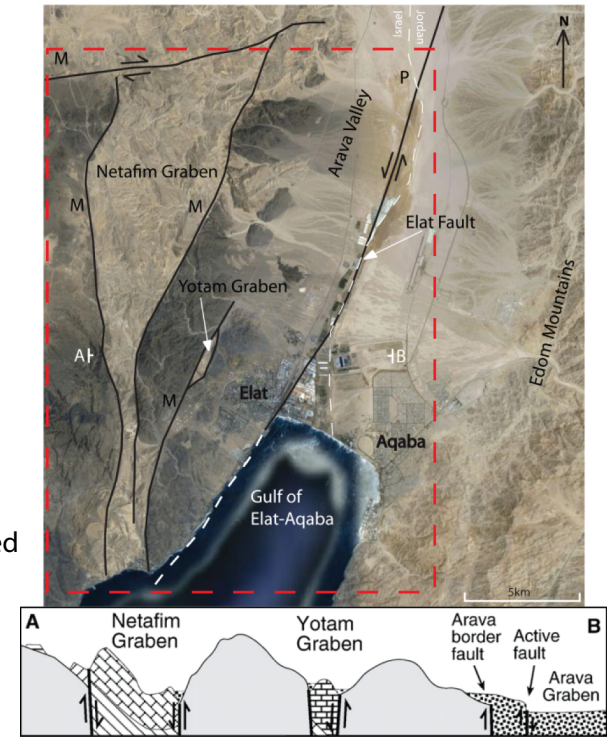

Figure 2.16: *Satellite imagery and schematic cross-section showing main geological features around Elat. Miocene faults (M), the active Dead Sea Transform strand (P). The area covered by the geological map in Fig. 2.4b is denoted by the red box (modified from Marco (2007), after Garfunkel (1970)).*

The graben-bounding faults are well-constrained as DSFS structures since they offset the middle Miocene Reham conglomerate (found at the eastern edge of the Netafim graben, Figures 2.4b & 2.16) but are overlain by Plio-Pleistocene terraces (Marco, 2007). Local folding on cm- to km-scales (wavelengths up to ~1 km) is also associated with later Miocene activity, affecting Cambrian, Cretaceous, Eocene and Miocene sedimentary rocks (Fig. 2.4b). The largest folds can be grouped according to their orientations and relationships to the major faults. The approximate mean hinge line orientation (based on map data) of these folds is 048°.

Several studies, (e.g. Avni et al. (2000); Marco (2007)) have suggested that the graben-bounding faults exposed west of Elat may represent parts of a wider fault zone, up to 50 km across, active during earlier stages of activity on the southern DSFS, which has subsequently localised into a narrower zone (20-30 km), centred around the Arava Valley (onshore) and Gulf of Elat-Aqaba (offshore). Decreasing fault zone complexity has been considered previously in relation to fault zones in many regions, including New Zealand, Canada, Turkey and the U.S.A (Stirling et al., 1996), in the East African Rift of Ethiopia (Ebinger and Casey, 2001) and Tibet (Cowgill et al., 2004). Data from the Dead Sea basin and Sea of Galilee, as well as around Elat, have been used to suggest that there may have been cycles of fault zone localisation coinciding with periods of a stable

regional stress field, coupled with re-widening of the zone when changing plate motions lead to a rearrangement of the far-field stress directions (Marco, 2007). The Euler pole for the DST has changed over time, migrating eastwards to a Plio-Quaternary position close to the north African coastline (32.8°N, 22.6°E, Garfunkel, 1981, 4 – 5° away from its pre-Pliocene position, (Butler et al., 1998), Fig. 2.17). It is suggested that these changes have led to the pulsed localisation and widening of the southern DSFS (Marco, 2007). Although southern Israel has been extensively mapped since the mid-20th century (e.g. Beyth et al., 2014; Druckman et al., 1993; Garfunkel et al., 2000; Shaw, 1947, amongst others), little attention has been paid to the mode(s) of faulting in the area.

The area of the present study, located near the town of Elat, has been chosen since the faults exposed here provide exhumed analogues for the currently active segment of the DST, the Arava Fault, which is not exposed in the transform valley immediately to the NE of Elat. In addition, there are good exposures of the Cretaceous and older lithologies, which elsewhere along the length of the fault are often covered with more recent sedimentary deposits. Depths of deformation are estimated at 2 – 3 km (based on the presence of type I twins in calcite crystals, Janssen et al., 2004) for the Arava Fault. The faults chosen for this study cut a variety of lithologies, including crystalline quartzo-feldspathic basement, together with carbonate and clastic cover rocks. They are both graben-bounding and intra-graben faults. These faults are well-exposed in several locations and the arid nature of the climate means that relatively little weathering and alteration has taken place at the surface. A summary of the faults studied, including their names, nature, wall rock lithologies (at the location/s studied) and location is given in Fig. 2.18a. Each is described in more detail in Section 2.6.2. The faults studied here follow the broad N-S - NE-SW trend of the active DSF and are located within 10 km to the west/northwest of the active Dead Sea Fault (Fig. 2.18b). They have been chosen as they vary in length and host lithologies, and are assumed to represent a range of deformation mechanisms and resulting fault rocks. The fault trace lengths vary from 0.5 – 12.3 km.

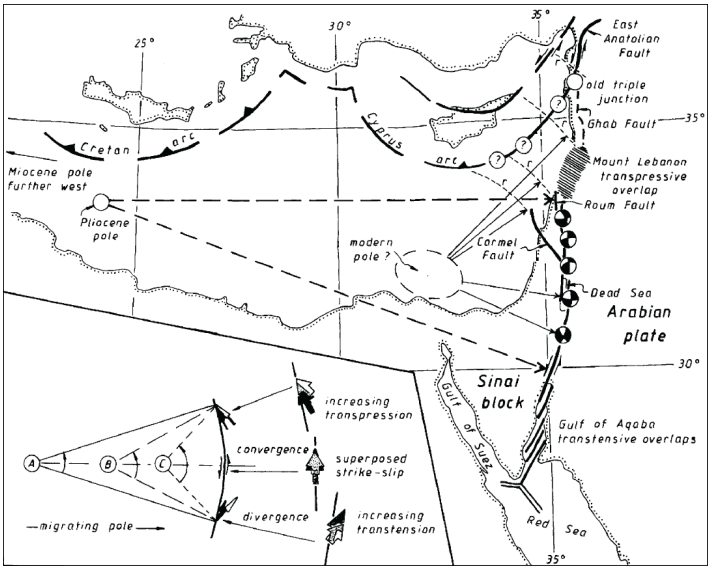

Figure 2.17: *Simplified map showing Pliocene position of DST Euler pole and possible current position (modified from Butler et al., 1998).*

(a) *Table summarising fault and outcrop names, nature, wall rock lithologies and locations used throughout (text colours correspond to fault trace colours used in Fig. 2.18b).*

Fault	Fault style	Wall-rock lithologies	Outcrop name	Latitude	Longitude
Tzefahot	Graben-bounding	Crystalline basement, carbonate cover	F1	29°32'18.31"N	34°54'9.25"E
Shelomo	Graben-bounding	Crystalline basement, carbonate cover	F2a	29°32'45.03"N	34°53'34.01"E
Shelomo		Crystalline basement, carbonate cover	F2b	29°33'49.66"N	34°53'29.99"E
Yehoshafat	Intra-graben	Carbonate, clastic, shale cover	F3	29°33'40.03"N	34°53'17.22"E
Yotam	Graben-bounding	Crystalline basement, carbonate cover	F4	29°34'5.15"N	34°55'6.93"E
Roded	Graben-bounding	Crystalline basement, clastic cover	F5a	29°36'50.21"N	34°54'52.70"E
Roded		Crystalline basement, clastic cover	F5b	29°35'58.22"N	34°54'25.98"E
R12	Intra-graben	Carbonate, clastic cover	F7	29°35'15.39"N	34°52'48.81"E
Nizoz	Graben-bounding	Crystalline basement, clastic cover	F8	29°40'20.11"N	34°56'56.64"E

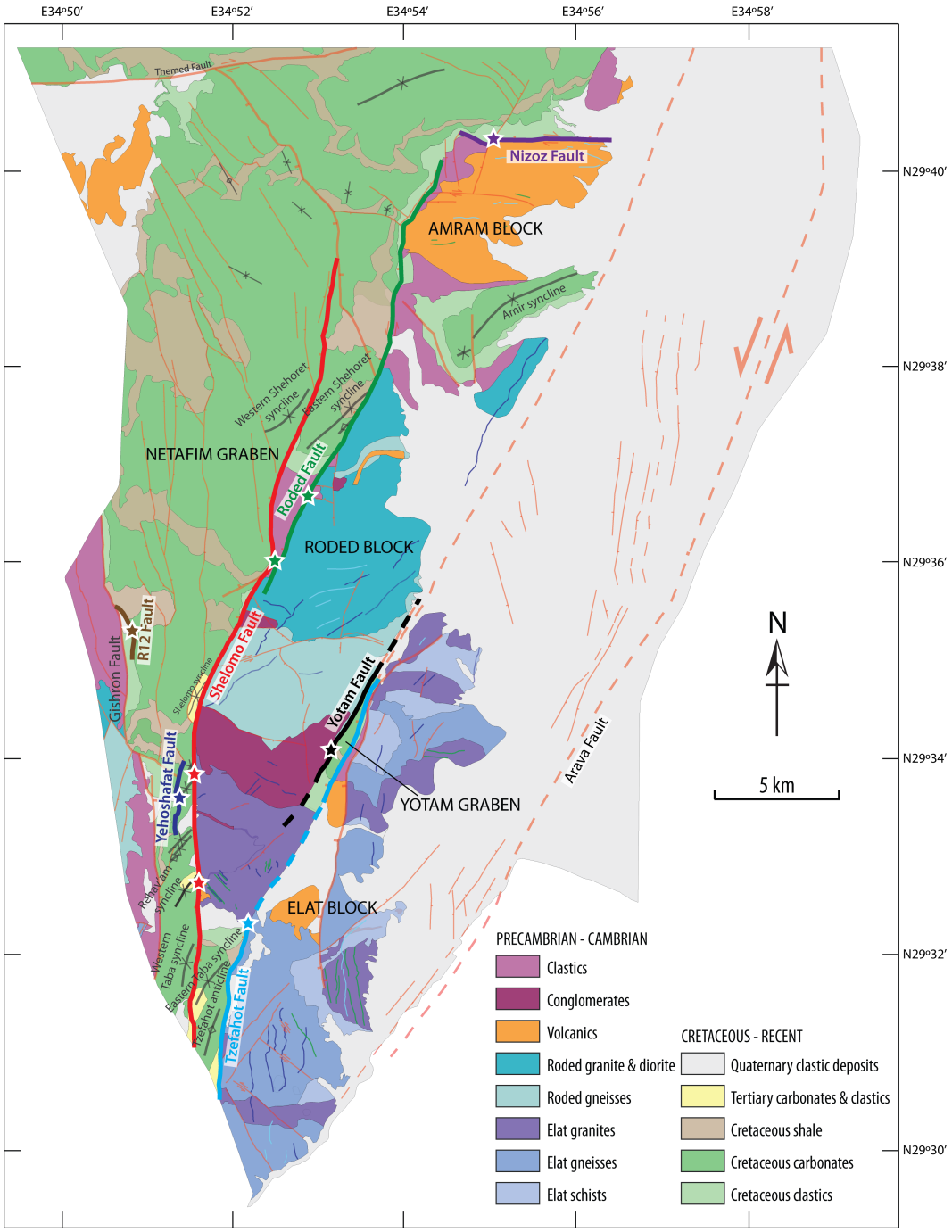

(b) *Simplified geological map with studied faults highlighted; fault trace colours correspond to text colour in Fig. 2.18a (modified from Beyth et al. (2013), Geological Map of Israel, Sheet 26 Elat, scale 1:50,000).*

Figure 2.18: ***(a)*** *table and* ***(b)*** *map showing locations of studied faults.*

2.6.1 Displacement estimates

Although the area has been extensively mapped, little consideration has been given to the faults in the area as individual structures and their properties have not been studied. Since no existing displacement data are available and there is an absence of known offset markers in the field area, we have estimated fault displacements using the stratigraphic separation across faults and measured slip vectors. This was done in two steps: firstly, by combining the dip of the fault plane and throw, or stratigraphic separation (Fig. 2.19, triangle 1 in blue), and secondly, by using the solved hypotenuse of triangle 1 and pitch (rake) of measured slickenlines to find the hypotenuse of triangle 2, which is equivalent to the displacement (Fig. 2.19, triangle 2 in purple). At all but one studied outcrops, slickenline lineations were measured on the main fault planes (as well as on any subsidiary faults) where visible. These were used to determine mean slip vectors and, in cases where there were distinct groups with different orientations, these were considered using separate displacement calculations. Where multiple sets of lineations were observed (at four of the seven studied faults), no clear evidence of over-printing, to indicate relative age relationships, could be determined. Measured slickenline pitches ranged across all faults from 7°-88°, preserving evidence of both strike-slip and dip-slip fault movement. However, intermediate (32°-52°) pitches were most commonly observed, suggesting oblique-slip movement dominated on these faults.

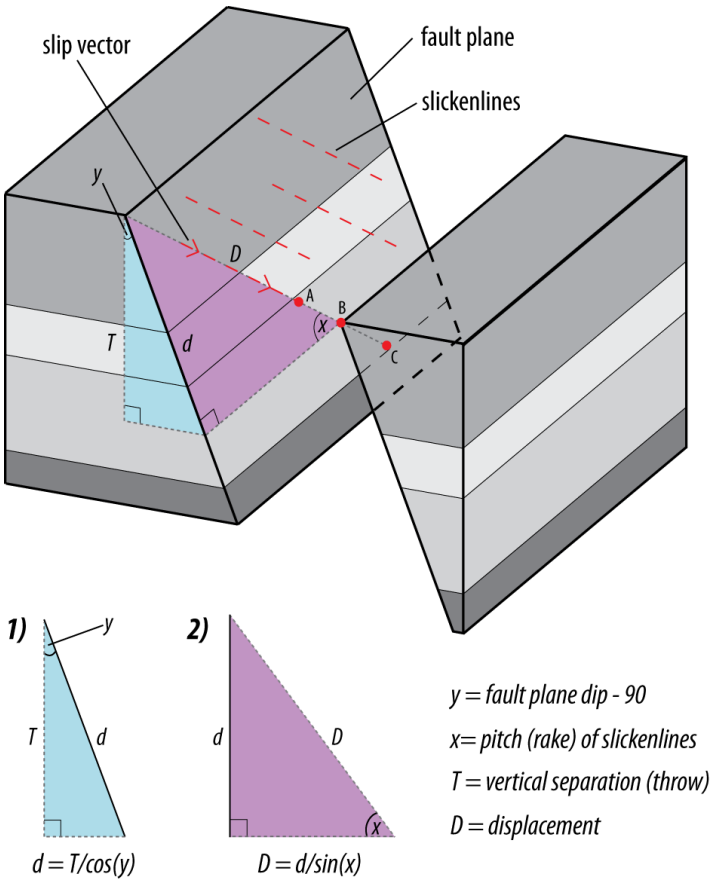

Figure 2.19: *Schematic 3D block diagram illustrating trigonometric method used for calculation of fault displacement estimates; known values for the dip of fault plane (y = dip - 90) and throw (T) enables solving of triangle 1, which is combined with the pitch of slickenlines (x) to solve triangle 2 and find displacement (D).*

Relative stratigraphic positions were constrained using the most recent geological map (Beyth et al., 2014) and accompanying stratigraphic column (Beyth et al., 2011) published for the area. In order to account for the maximum range of stratigraphic offsets theoretically possible, where variable thicknesses are given for sedimentary cover units (e.g. the thickness of the Cretaceous Samar Formation has a given range of 80-130 m, Figure 2.4a), fault offsets were calculated using the median unit thicknesses (e.g. 105 m for the Samar Formation). The difference in total possible stratigraphic offsets using this method range from approximately 100-300 m across the entire stratigraphic column. It was not always possible in the field to determine the exact position within a unit, for example, whether point A, B or C in the block represented in Figure 2.19, adding a further

element of uncertainty. In order to mitigate for this effect, minimum and maximum estimates have been calculated in all cases; minimum estimates refer to base hanging wall unit to top footwall unit (minimum stratigraphic offset), whilst the maximum estimates refer to top hanging wall unit to base footwall unit (maximum stratigraphic offset), though this is not possible to determine for the crystalline basement so only the thickness of cover units has been used.

Stratigraphic offsets have been combined with both the steepest (88°) and shallowest (7°) striae measured across the entire field area to give the widest range of offsets possible. In addition to minimum and maximum values for both stratigraphic offset and plunge of lineations, a "most confident" value of displacement has been determined using the estimated position within a stratigraphic unit based on map data, and the main set of lineations for individual fault zones. Table 2.1 summarises the range in calculated displacement estimates. It is immediately clear from the data that pure strike-slip faulting cannot have been the principal mode of displacement on these faults, as some of the maximum displacement estimates exceed the known fault lengths.

Table 2.1: *Fault lengths and minimum, maximum and most confident displacement estimates. Note that the Nizoz Fault is a dextral antithetic fault.*

Fault	Fault length	Estimated displacement			Disp. as %	Striae (pitch)
		Min.	*Max.*	***Most confident***	of length	
Shelomo	12.3 km	560 m	9919 m	**1350 m**	11%	7° S, 52° S
Tzefahot	11.7 km	329 m	4425 m	**1188 m**	10%	32° S
Roded	6.6 km	235 m	4059 m	**908 m**	14%	33° N
Yotam	5.0 km	438 m	6032 m	**599 m**	12%	16° N, 47° N, 83° N
Nizoz	2.8 km	185 m	14552 m	**250 m**	9%	--
Yehoshafat	1.5 km	126 m	3089 m	**189 m**	13%	47° N, 85° S
R12	1.1 km	57 m	1579 m	**57 m**	5%	88° N

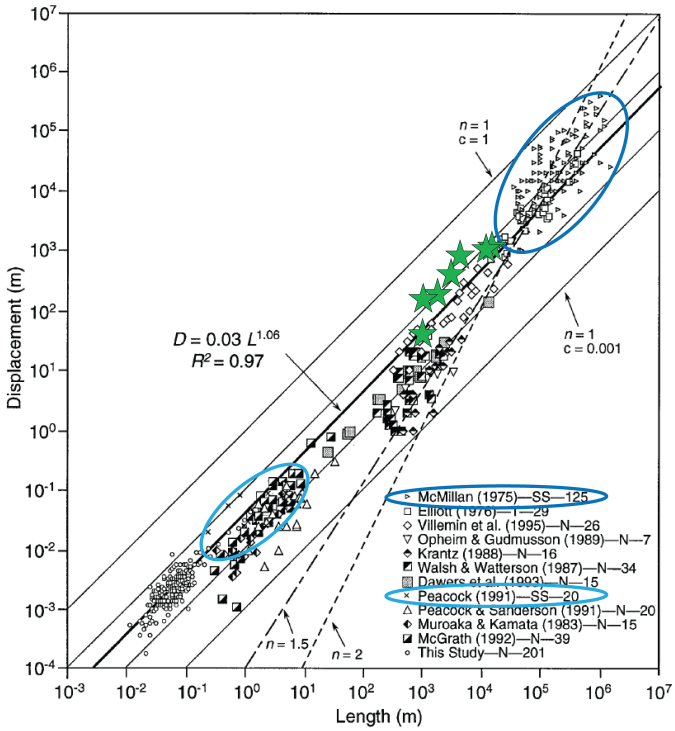

Figure 2.20: *Synthesis of published fault-length displacement relationships for thrust (T), strike-slip (SS) and normal (N) faults (modified from Schlische et al., 1996), blue ellipses highlight data for strike-slip faults. Most confident estimates for studied faults are shown with green stars.*

The fault displacement estimates given above are therefore not absolute values, but a range of minimum and maximum possible values, with a most confident estimate that incorporates new field data with existing published data. The values do, however, fit broadly with published length-displacement data for strike-slip faults (Fig. 2.20). Data relating specifically to oblique-slip faults are not available for a direct comparison.

2.6.1.1 Summary

Estimated displacement data for the studied faults cover a range of distances, from less than 100 m to more than 1 km; the majority of the faults, however, fall within a range of a few percent (9-14%) in terms of displacement as a proportion of fault

length, with the exception being the shortest and lowest displacement fault (the R12 Fault). Uncertainty in the displacement estimates arises from two areas: in presence of slickenline striae in multiple orientations on the observed fault planes for four of the seven studied faults; and in the lack of certainty regarding stratigraphic position within the sedimentary cover units. However, the most confident estimates fall within the expected range for strike-slip faults, according to the work of McMillan (1975) and Peacock (1991). We have also demonstrated that these faults (excluding the antithetic Nizoz Fault) account for only a relatively small proportion (∼4%) of the overall regional displacement of the DSFS, ∼4.3 km of the total 105 km. In the following sections we will focus on fault zone architecture, using the estimated displacement as a proxy for strain and subsequently the intensity of deformation expected. Faults are presented in order of decreasing displacement, in order to gain an understanding of the fault zone architecture of the most evolved faults first and create a framework for subsequent analysis.

2.6.2 Fault zone architecture

Seven faults (listed in Table 2.1) have been chosen in the area immediately west of Elat and have been studied at nine locations. The outcrops vary in the wall rock lithologies involved as well as the fault rocks produced, and estimated displacements range over two orders of magnitude (57-1350 m). *Protoliths* refer to the (relatively) undeformed examples of the rocks that are found within a fault zone; any deformation seen in these rocks is assumed to pre-date the faulting being studied here. A *damage zone* is defined as the relatively competent rock immediately adjacent to the fault core that is brittly deformed (by fractures and minor faults, for example) but has not undergone any significant grain-size reduction or internal displacement during faulting, i.e. it is more or less 'in situ' relative to the wall rocks. The *fault core* is defined as the most intensely deformed part of a fault zone. The material within it generally has a contrasting appearance to the immediately adjacent wall rocks; this may to due differing composition, grain size, amount of fracturing, or any combination of these. The *principal slip zone* (PSZ) is the narrow zone along which most of the slip is thought to have taken place and is commonly recognised at the mesoscale as the boundary between contrasting lithological domains within the fault core. The PSZ is typically found towards the centre the fault core, but may also be at the edge. Where the occurrence of *clay* or *clay-rich* material is described, this is used in reference to grain-size (individual grains not visible with a hand lens) and not a specific mineralogy. We have used the terms *cataclastic gouges* and *shale gouge* to distinguish the two distinct types of fault gouges observed in the field, but these are not comprehensive terms for the type of deformation that may have led to the formation of these rocks.

2.6.2.1 Shelomo Fault

The Shelomo Fault is a graben-bounding, N-S striking structure (mean 004/73 W) that is studied here at two localities (Fig. 2.18a, Fig. 2.18b): *(a)* an approximately across-strike section at the eastern edge of the Rehavam syncline; *(b)* an oblique-to-strike road-cut 2 km to the north of the first outcrop. At these outcrops, the fault juxtaposes Cretaceous and Tertiary cover units to the west against crystalline basement units to the east. The fault extends for at least 12.3 km along strike,

with minimum and maximum displacement estimated as 560 m and 9919 m, the most confident estimate being approximately 1165 m (Table 2.1).

Locality A The fault zone here is comprised of a fault core of ~0.7 m width and damage zones either side (Fig. 2.21a,b): to the east, the damage zone extends for approximately 10 m, across which the deformation is observed to decrease in intensity until a 'background' level is reached. To the west, the extent of the damage zone is harder to determine since after ~10 m there is the edge of a very steep-sided gully. The mean orientation of the fault at this locality is 004/76W (Fig. 2.21d).

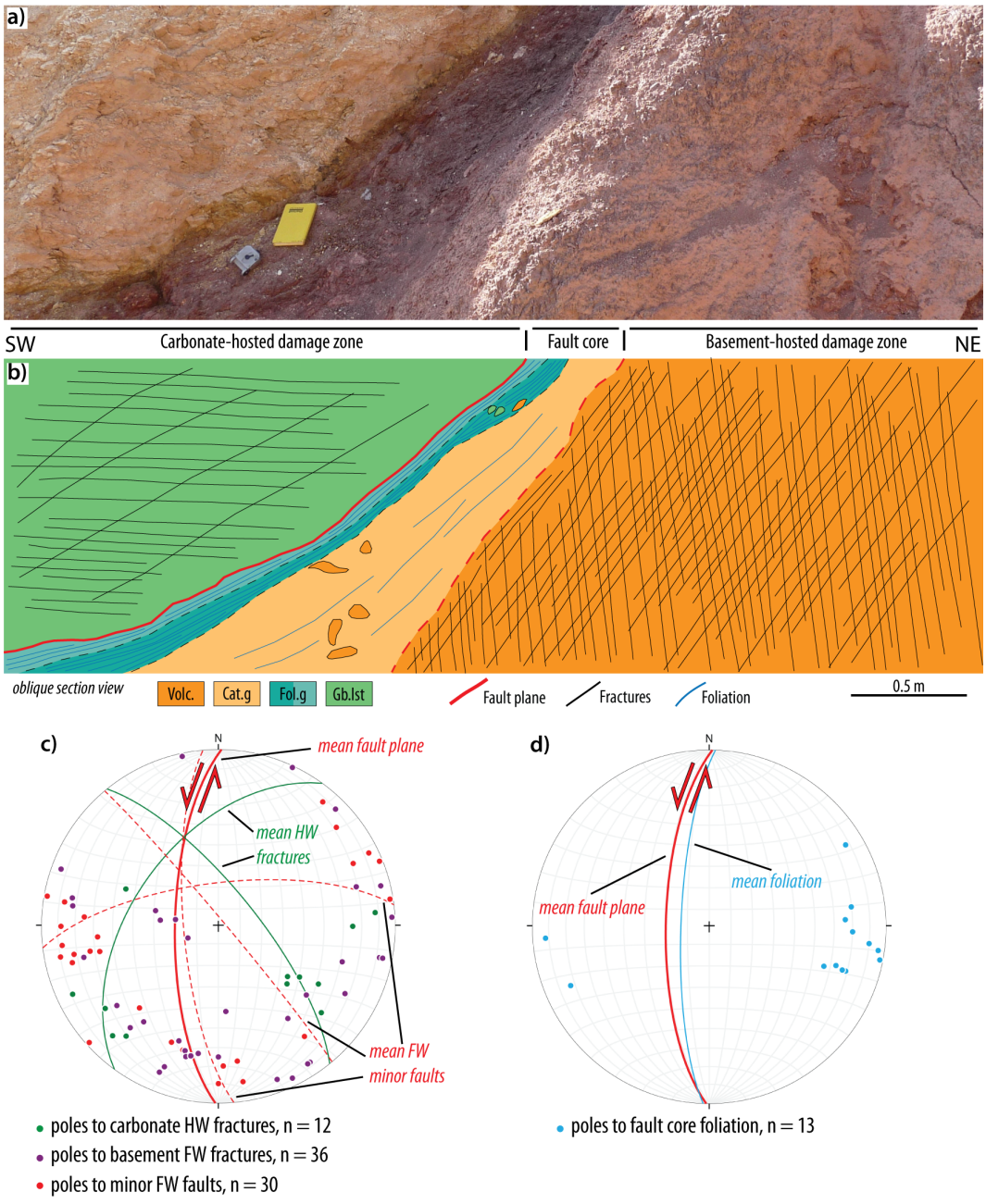

Figure 2.21: *Summary section of Shelomo Fault, Locality B:* ***(a)*** *Photograph of fault section;* ***(b)*** *Oblique section view with lithologies and main structures highlighted. Two narrow bands of foliated gouges are found adjacent to the carbonate damage zone to the west of the fault core, in the east of the fault core is a wider band of cohesive cataclasite. The carbonate damage zone is cohesive close to the fault plane but is heavily fractured 10s of cm away, the basement damage zone is intensely fractured and incohesive;* ***(c & d)*** *stereonets showing the main structural trends of the fault zone: (**c**) brittle fractures and minor faults; (**d**) fault core foliation, approximately parallel to fault orientation.*

Protoliths At Locality A, the Upper Cretaceous Ghareb Formation marl is juxtaposed against the locally outcropping Precambrian Ramat Yotam silicic volcanic rocks (Fig. 2.4b). The marl is a very pale-cream, uniformly fine-grained and fissile due to the presence of sub-parallel fractures (mean orientation 040/70W), spaced every 3-10 cm. It contains abundant calcite veins, sub-parallel to the lamination. Northwards-plunging striae are present on some calcite veins, likely indicating flexural slip along these surfaces. There are few fresh outcrops of this unit as it weathers very easily and surfaces become covered in scree. The outcrop of the volcanic rocks to the east is dark red/purple in colour and is fine-grained with very few individual crystals visible; some phenocrysts, generally <1 mm in size, of quartz and K-fsp are present.

Carbonate-hosted damage zone The marls of the carbonate damage zone are intensely fractured and are friable, easily breaking apart along fracture planes (Fig. 2.22a), though the undeformed rock is also very friable (Sections 2.4.2.2 and 2.6.2.1). The easily-weathered nature of this lithology means that although it crops out at the top of a hill, it is not well-exposed and is covered with loose, clay-like material. Directly adjacent to the fault core, however, there is a layer approximately 10-15 cm wide of much harder, more competent material (Fig. 2.22b). Within this are veins of calcite, generally 1-3 mm wide but sometimes up to 5 mm, that appear to be randomly oriented. It is possible that although initial fault-related fracturing may weaken the marl initially, subsequent influx of carbonate-rich fluids and precipitation of calcite may result in an overall strengthening. The boundary between the carbonate damage zone and the fault core is sharp and there is a smooth, polished fault plane on the carbonate side.

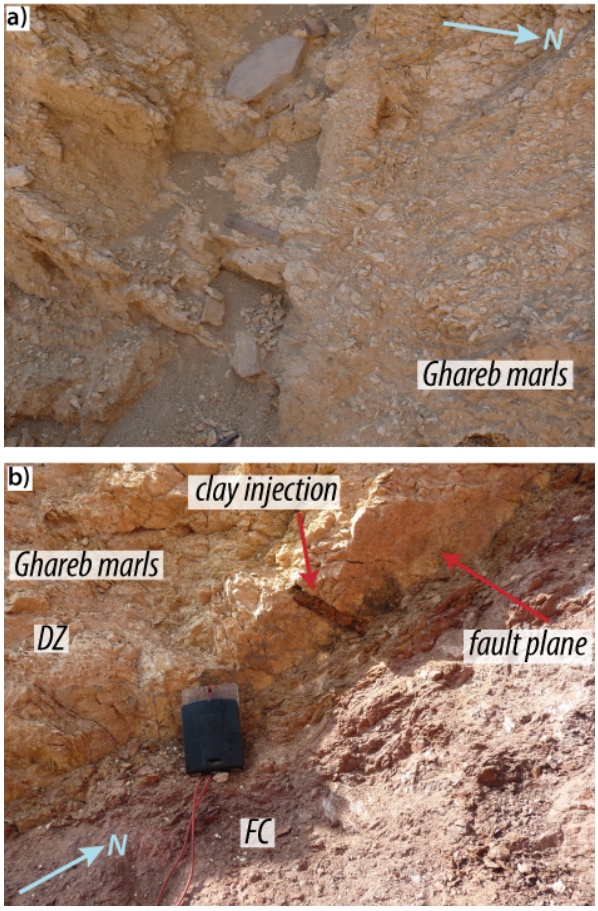

Figure 2.22: *Photographs of the Shelomo Fault, Locality A carbonate-hosted damage zone:* ***(a)*** *Heavily fractured Ghareb Formation marls approximately 2 m west of the fault core;* ***(b)*** *discrete fault plane forming the boundary between the damage zone (DZ) and fault core (FC).*

Basement damage zone The most intensely deformed part of the damage zone lies on the eastern side of the fault zone and is 2-3 m wide. After this, the intensity of fracturing is less and the rock appears more competent, though because of the relatively limited exposures of this volcanic unit it is difficult to quantify what proportion of fracturing further away from the fault is directly related to DSFS structures.

The damage zone directly adjacent to the fault core is red in colour with fractures that are spaced every 3-10 mm (average 5 mm), making the rock extremely friable (Fig. 2.23a). These fractures have a range of orientations, from NE-SW-striking to NW-SE, and with dips ranging from 40-78°,

but there are no clear preferred orientations.

Further to the east, the rock is more competent with fewer fractures (Fig. 2.23b). Approximately 10 m away from the main fault there is a narrow (<2 m at its maximum) gully formed by a minor fault, oriented obliquely to the main fault.

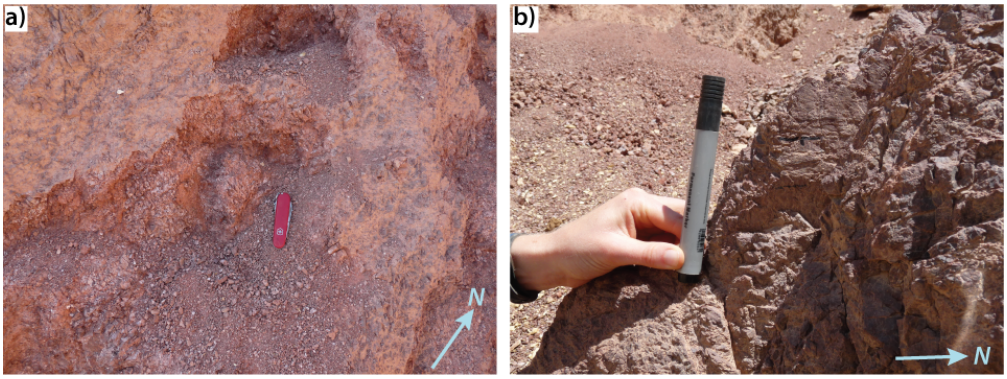

Figure 2.23: *Photographs of the Shelomo Fault, Locality A basement-hosted damage zone:* ***(a)*** *intensely fractured volcanic rocks, approximately 3 m east of the fault core;* ***(b)*** *less heavily fractured volcanic rocks approximately 7 m east of the fault core.*

Fault core At this locality the fault core is 0.7 m wide, comprising of two narrow (10-20 cm) bands of very fine-grained, clay-rich fault gouge, and a wider band (~50 cm) of cataclasite (Fig. 2.24a). Within the clay-rich gouges are small (generally <1 cm but occasionally up to 5 cm) clasts of both carbonate and igneous material; the foliation in this part of the fault core is wrapped around clasts locally, but is in general oriented parallel/sub-parallel to the main trend of the fault (Fig. 2.21d).

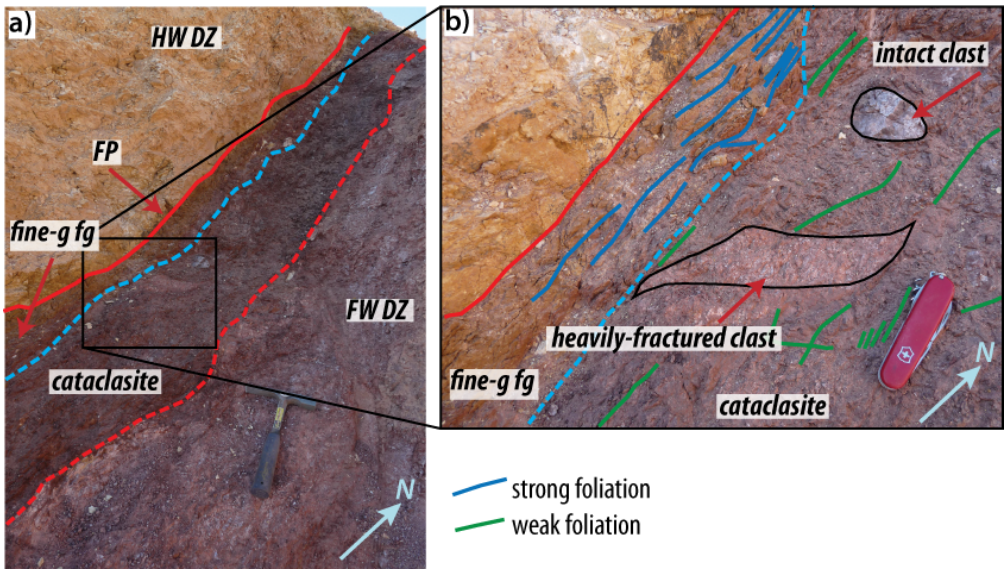

Figure 2.24: *Photographs of the Shelomo Fault, Locality A fault core:* ***(a)*** *oblique section view of the fault core;* ***(b)*** *detailed view of structures within the fault core; narrow band of foliated brown and red gouges to the east, adjacent to the principal fault plane hosted in limestone, cohesive cataclasite in the western part of the fault core with both relatively intact and heavily fractured lithic clasts. The heavily fractured clast is sigmoidal, indicating sinistral offset.*

The cataclasite, in the eastern part of the fault core, has a very weak foliation with a similar orientation to that in the clay-rich gouge. There are fewer clasts in this part of the fault core, but those that are present are larger (10-20 cm) and composed of igneous basement material (Fig. 2.24b).

Locality B Though the exposed section is oblique to the strike of the fault (due to the position of a road), the angle of the road cut is such that cover rocks approximately 2 m west of the main fault plane are exposed (Fig. 2.25). East of the fault plane, however, there is little exposure. The fault core at this location is approximately 1 m wide, but it is difficult to quantify the width of the damage zones due to the lack of exposure. The mean orientation of the main fault plane (described below) here is 003/70W, very similar to at Locality A.

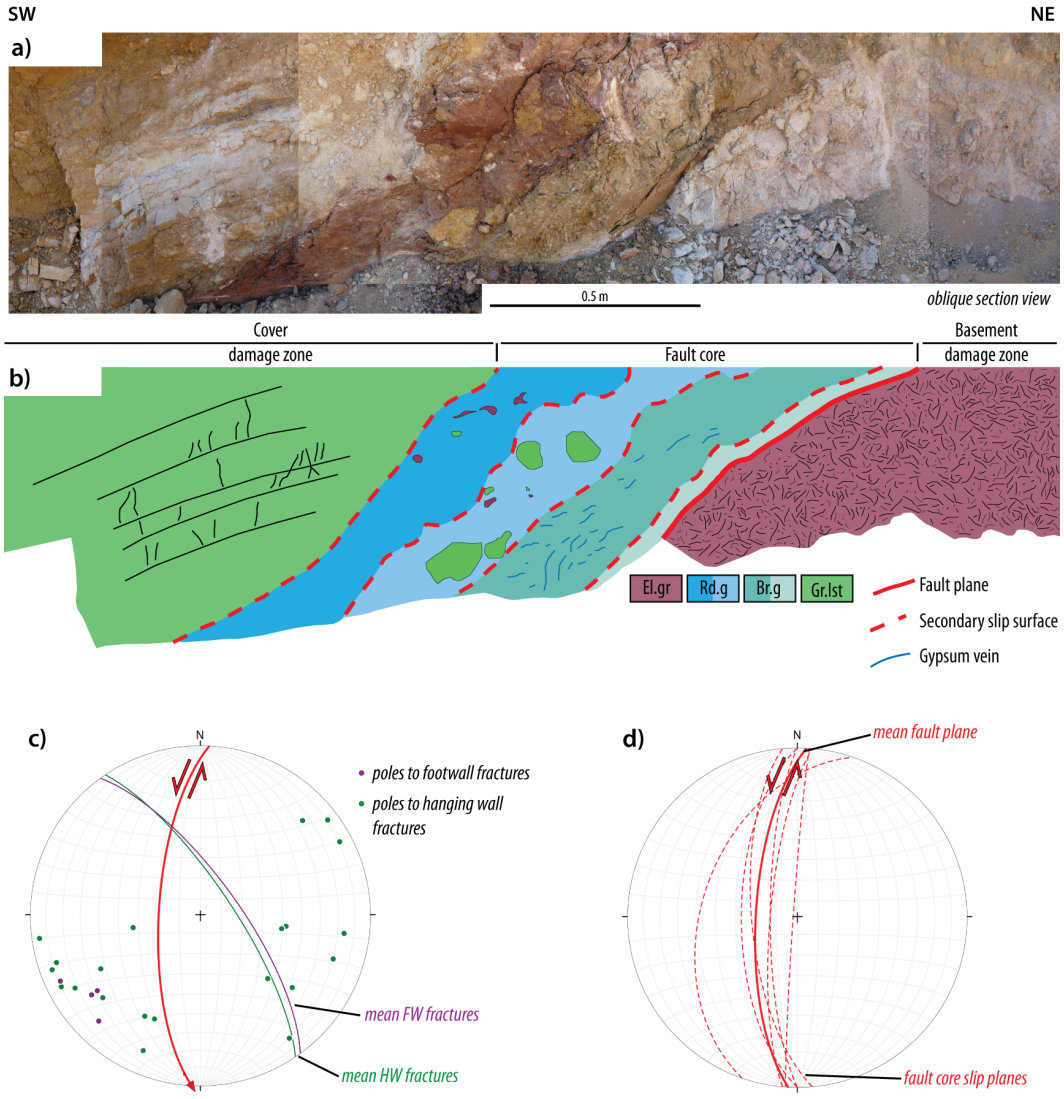

Figure 2.25: *Summary section of Shelomo Fault, Locality B:* ***(a)*** *Photograph of fault section;* ***(b)*** *Oblique section view with lithologies and main structures highlighted. The fault core is divided into four layers, separated by discrete slip surfaces. The basement damage zone to the north-east is intensely fractured and incohesive whilst the carbonate cover damage zone to the south-west contains few fractures and bedding is still visible;* ***(c & d)*** *stereonets highlighting main structural features of the fault zone at this locality:* ***(c)*** *fractures in the hanging and footwalls have similar mean orientations, striking NW-SE, oblique to fault orientation;* ***(d)*** *slip planes and foliation within the fault core sub-parallel to mean fault plane.*

Protoliths The protolith rocks at Locality B consist of Cretaceous Grofit Formation limestones in the hanging wall, juxtaposed against the Elat Granite in the footwall to the east. At this location the Elat Granite is relatively coarse-grained and contains abundant K-fsp but little biotite, giving it an overall pink appearance. The Grofit Formation consists of limestone (beds 15-30 cm thick) and blocky cherty beds up to 1 m thick. Beds strike N-S, dipping moderately (45-60°) to the W.

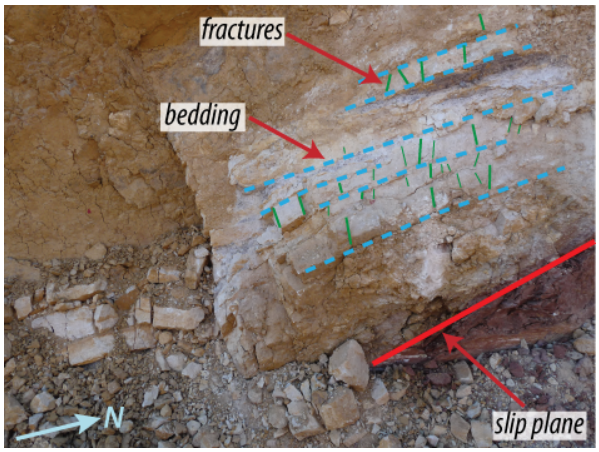

Figure 2.26: *Photograph of the Shelomo Fault carbonate-hosted damage zone: beds are ~5 cm thick and sub-vertical; fractures are spaced every 1-5 cm and are orthogonal to bedding.*

Carbonate damage zone The limestone of the western damage zone appears relatively weakly-deformed; the original bedding is still visible and fractures are generally perpendicular to it and oblique to fault orientation (Fig. 2.25b,c, Fig. 2.26). These joints are commonly continuous for <10 cm, spaced irregularly every 1-5 cm and do not appear to have any shear offset.

Basement damage zone The Elat Granite of the eastern damage zone extends for at least 3 m, after which the outcrop tapers out to road level. It is intensely deformed directly adjacent to the fault core and has a powdery white appearance with original crystal shapes of quartz, K-feldspar and biotite still visible to the naked eye (Fig. 2.27a) and is similar in appearance to the damage zone seen at the Tzefahot Fault (Section 2.6.2.2). Fractures, spaced every 5-10 cm and 10-40 cm long, oblique to the fault orientation (Fig. 2.25c), run throughout the outcrop and are often coated with a thin layer of very fine-grained (clay-size) pale-green material. Although individual crystals of the relatively coarse-grained granite can be seen with the naked eye, the rock is incohesive and crumbles easily. There is not continuous exposure directly northwest (following the road) of this area, but after 20 m the granite is competent again and is fractured on a 5+ cm spacing, with no other obvious signs of deformation at the mesoscale.

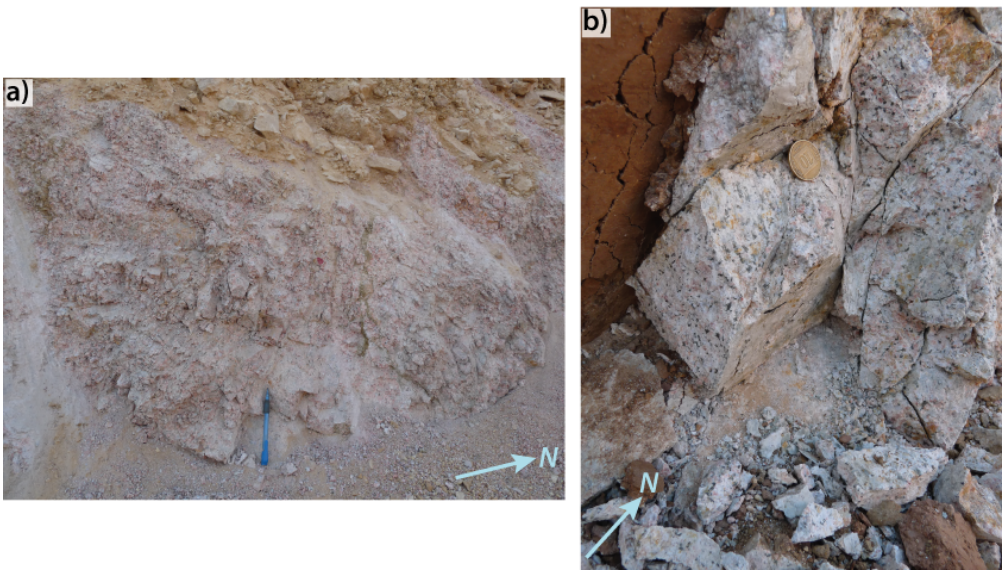

Figure 2.27: *Photographs of the Shelomo Fault basement-hosted damage zone:* ***(a)*** *intensely-fractured Elat granite that is powdery and incohesive and paler in colour than the undeformed protolith;* ***(b)*** *enlarged view showing white, opaque nature of qtz crystals and fractures in basement damage zone immediately adjacent to the fault core on the north-eastern side.*

Fault core The fault core here is approximately 1 m wide (slightly wider than at Locality A) and comprises two distinct types of fault gouge: a clast-poor, brown coloured unit approximately 40 cm wide in the eastern part of the core, and a red-coloured unit with abundant clasts that is approximately 60 cm wide (Fig. 2.28a). The boundary between the fault core and eastern damage zone is marked by a discrete, polished slip surface (Fig. 2.28b). There are three other similar slip surfaces within the fault core (Fig. 2.25d). At the western edge, there is a relatively sharp contact between the fault core and carbonate damage zone, but no single slip plane is evident.

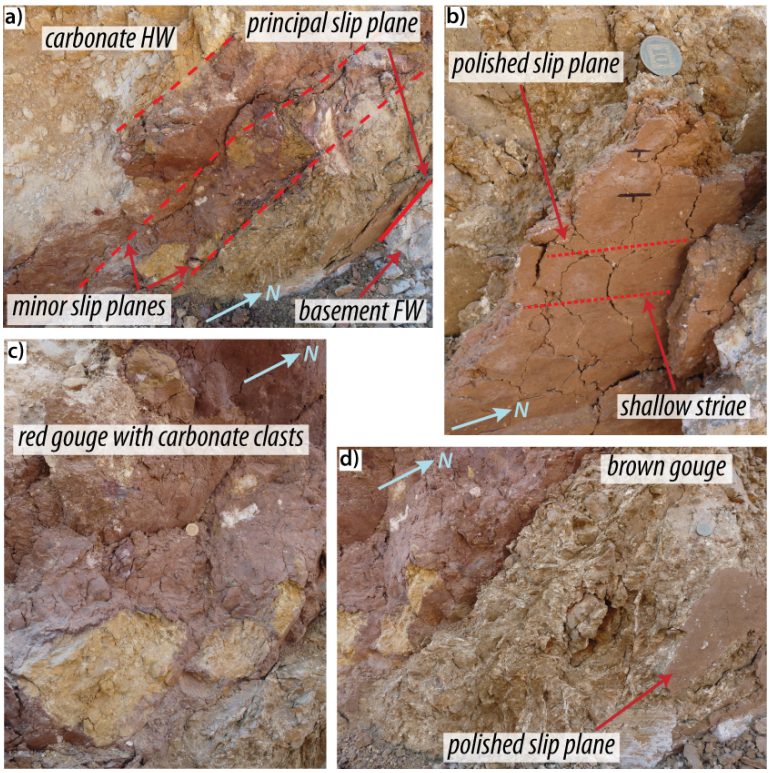

Figure 2.28: *Photographs of the Shelomo Fault, Locality B fault core:* ***(a)*** *red, fine-grained gouge with large carbonate clasts within;* ***(b)*** *discrete, polished slip surface at eastern margin of fault core;* ***(c)*** *red gouge with lack of obvious fabric;* ***(d)*** *brown gouge with few clasts and pervasive, discontinuous gypsum veins.*

The red gouge appears at the mesoscale to have no fabric and clasts are much more prevalent than in the brown gouge (Fig. 2.28c). These range in size from <1 – 10 cm and often their edges are poorly-defined. The brown gouge is very fine-grained overall, with occasional clasts of fractured carbonate material that are <2 cm in size (Fig. 2.28d). The two slip surfaces that cut through this unit are polished and coated in a red-brown clay material, with a mean orientation of 000/75W (sub-parallel to the main fault plane) though they do range in dip from 55-89°.

Summary The Shelomo Fault is a graben-bounding fault at the eastern side of the Netafim Graben, juxtaposing Precambrian crystalline basement in the eastern footwall against Cretaceous carbonate rocks in the western hanging wall, and is the fault of greatest length and estimated displacement (12.3 km and 1350 m, respectively). We have studied this fault at two localities and fault zone architecture varies considerably between them. At Locality A (Section 2.6.2.1), a discrete, polished fault plane is hosted in the carbonate hanging wall and the fault core consists of a clay-rich, foliated gouge alongside a cataclasite; the two fault core materials are separated by a relatively diffuse boundary (Fig. 2.24). At Locality B, there is no such discrete fault plane in the carbonate hanging wall rocks but there are instead several discrete slip planes within the clay-rich fault core gouge. At this locality there is no cataclasite within the fault core. Deformation appears to be more intense in the granitic footwall of Locality B, where the rock is pulverised and fractures are expected to be randomly oriented and spaced at the micron scale, whereas in the volcanic rocks of Locality A, fractures are more regular and spaced every few millimetres. Since the volcanic rocks of Locality A form only a localised part of the footwall (Fig. 2.4b), Locality B has been chosen

as a type-locality and a schematic summary of the fault zone is presented in Fig. 2.29.

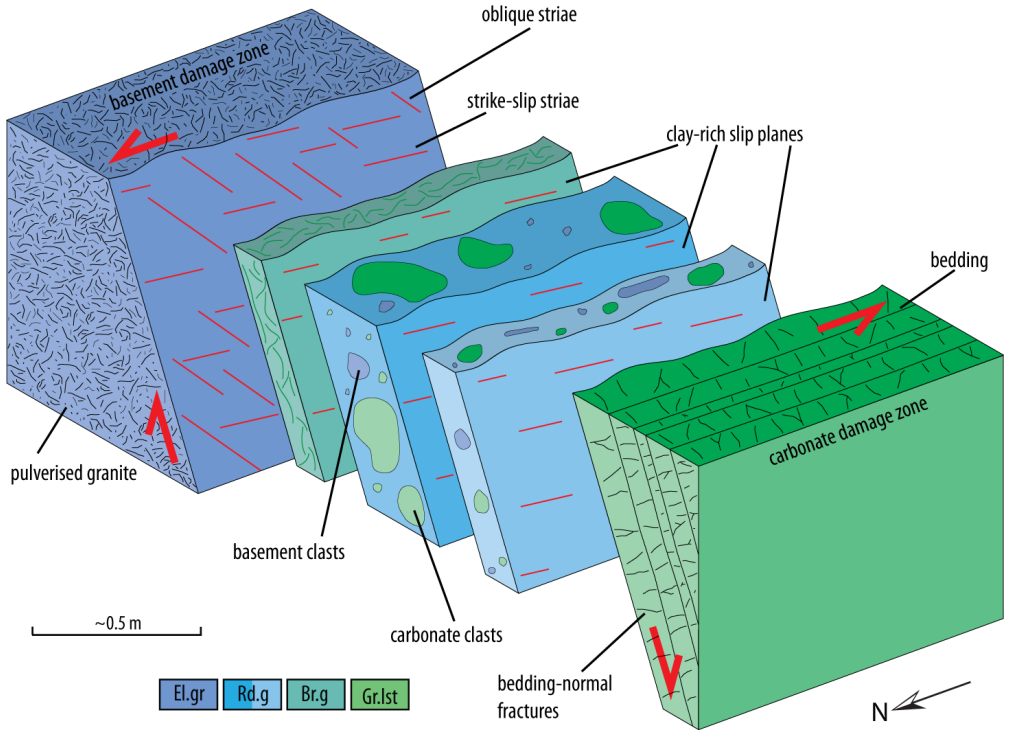

Figure 2.29: *Schematic block diagram summarising the structural features of Shelomo Fault: the basement-hosted damage zone is intensely deformed by pulverisation fracturing whilst the carbonate cover-hosted damage zone is less intensely deformed and bedding is still visible; the fault core is composed of fine-grained gouge that is separated by discrete slip surfaces. Rounded clasts of both carbonate and basement material are found within the fault core and oblique-slip and strike-slip striae are also observed.*

2.6.2.2 Tzefahot Fault

The NNE-SSW striking Tzefahot Fault is exposed in an approximately across-strike section in a dry river bed (Wadi Shelomo) and dips steeply to the NW (mean fault plane 036/74 NW). The studied section is approximately 25 m wide in total, comprising a fault core (5 m) and associated damage zones (at least 10 m either side, after which distance there is no further exposure). The fault is 11.7 km long and displacement estimates range over an order of magnitude, between 330 and 4425 m, the most confident estimate from measured slickenlines being 725 m (Table 2.1).

The fault core is defined by a 5 m wide zone of foliated gouge (Fig. 2.30a,b) that appears to have accommodated the most strain and displacement, bounded to the east in the basement by a discrete fault plane and to the west in the cover rocks by a more gradational transition into the damage zone. At the outcrop scale, the eastern fault plane does not have a smooth, polished surface; it is rough due to frequent spacing of fractures and subsequent weathering. Slickenlines are present, but due to the fracturing and weathering of the fault plane, are not frequently visible. Those measured plunge to the south-west (Fig. 2.30c) have a mean pitch of 32 SW on the main fault plane (036/74 NW), indicating that there has been an element of oblique-slip on the fault. At the western edge there is no discrete fault plane, but a gradation from fault core gouge to wall rock over a distance of approximately 1 m (Fig. 2.30a).

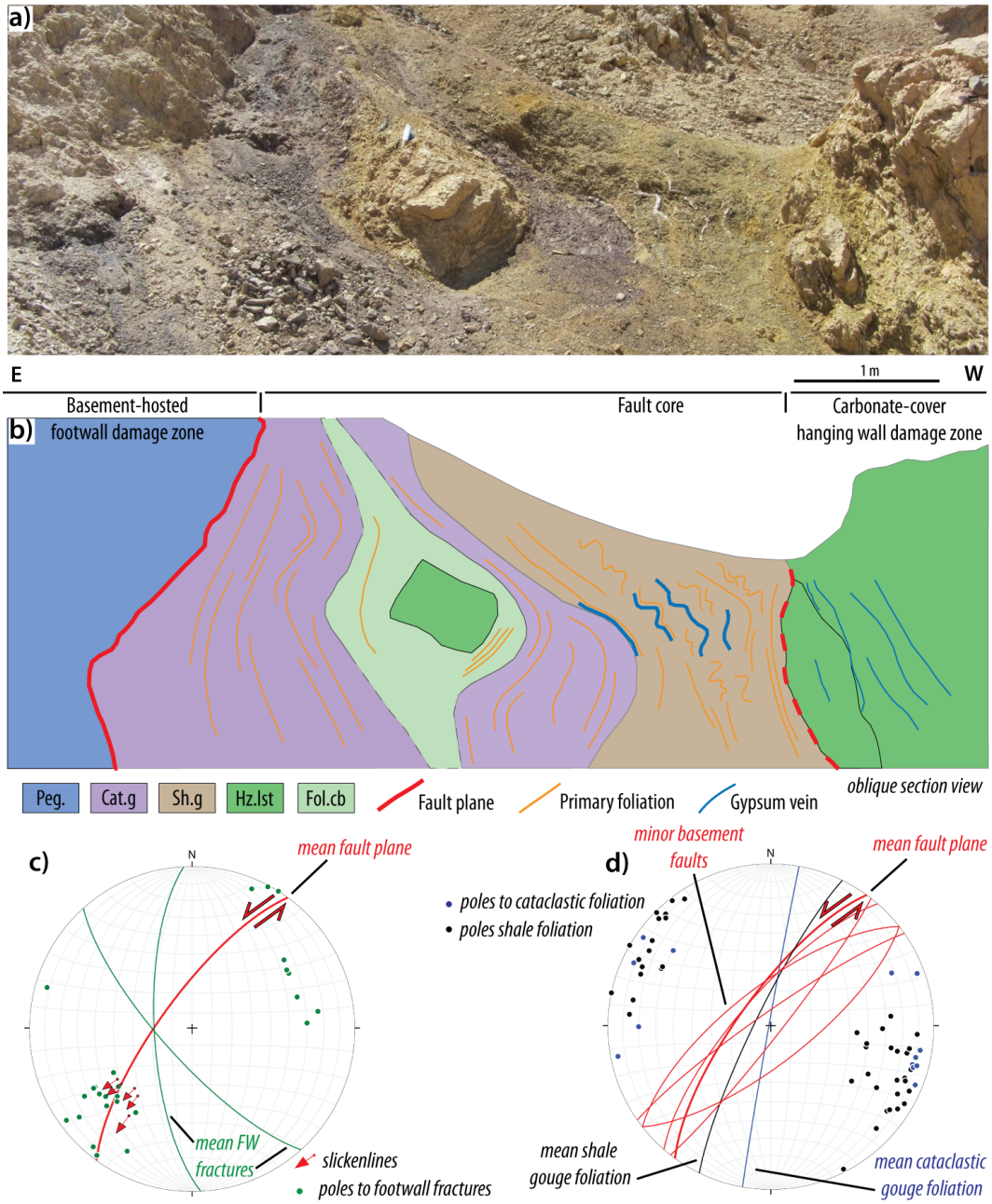

Figure 2.30: *Summary section of Tzefahot Fault:* ***(a)*** *Photograph of fault section;* ***(b)*** *Oblique section view with lithologies and main structures highlighted (Pg: pegmatite vein; Cat.g: cataclastic gouge; Hz.lst: Hazera Limestone; Fol.cb: Foliated carbonate);* ***(c & d)*** *stereonets summarising structural features of the fault zone:* ***(c)*** *damage zone fractures and slickenlines measured on basement-hosted main fault plane;* ***(d)*** *foliation planes within cataclastic and shale gouges of fault core are parallel - oblique to the main fault orientation, minor faults in the footwall gneiss are approximately parallel to the fault.*

Protoliths The footwall protolith of the Tzefahot Fault is the Taba Gneiss of the Elat Block (Section 2.4.1.1), with a local, metre-wide pegmatite vein also present at this outcrop; in the hanging wall, to the west, is the Hevyon member of the Hazera formation, a dolomitic Cretaceous cover unit (Section 2.4.2). The Taba Gneiss at this location has an L-S fabric, with the L-lineation being more prominent. The rock is relatively quartz-rich and the lineation is defined by this mineral. The pegmatite vein exposed here is also quartz-rich and is much less pink in appearance than many other veins in the area of study. Near-vertical fractures are present within the pegmatite, spaced every 10-30 cm and striking NE-SW. However, it should be noted that the location chosen for the protolith pegmatite description is relatively close (3 m east of) the fault zone since it is only a localised feature, so some fractures may be related to deformation of the Tzefahot Fault rather

than be pre-existing features. The rock determined as the protolith is significantly less-intensely deformed than that in the damage zone immediately adjacent to the fault core.

The carbonate protolith is extremely hard due to the presence of dolomite and is heavily fractured, making outcrops generally very unstable in nature with scree slopes at the base of elevated sections. Close to the exposure of the Tzefahot Fault section bedding has a mean orientation of 003/70W, forming the eastern limb of a large, open antiform that has an approximate wavelength of 1 km, between the Tzefahot and Shelomo faults.

Igneous/metamorphic basement damage zone The eastern damage zone is a minimum of 10 m wide, forming a prominent outcrop approximately 10 m high. It comprises of a metre-wide pegmatite vein (directly adjacent to the fault core) and gneiss. Pervasive fracturing of the pegmatite gives the outcrop a rather blocky appearance, with a main sub-vertical set (Fig. 2.30c) and a secondary sub- horizontal set (Fig. 2.31a). They do not appear to have accommodated any shear movement. The sub-vertical fractures are spaced every 2 – 15 cm and many continue for a metre or more, whilst the sub-horizontal are more widely-spaced, every 30 – 50 cm, and less continuous, generally up to 50 cm long. Within the pegmatite vein damage zone, there is a lens of intensely deformed material that is relatively incohesive and has a white, powdery appearance (Fig. 2.31b), but original grain shapes are still visible. The lens is approximately 40 cm wide and extends for at least 2 m. This lens is bounded by layers of clay-rich material that appear to have been injected into the damage zone from the fault core. These layers are 5 – 10 cm wide, reducing in width north-eastwards away from the fault core-damage zone boundary until they pinch-out after 50 – 100 cm.

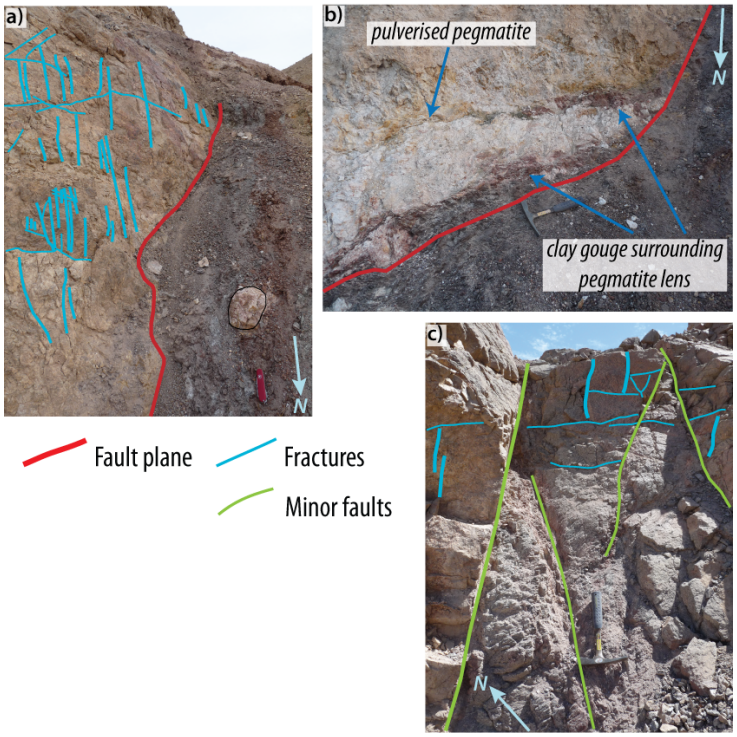

Figure 2.31: *Photographs of the Tzefahot Fault basement-hosted damage zone:* ***(a)*** *sub-vertical fractures within pegmatite veins in the footwall directly adjacent to the fault core;* ***(b)*** *pulverised lens of pegmatite with clay gouge at the margins;* ***(c)*** *minor faults and fracture in gneiss directly east of pegmatite veins in the footwall damage zone.*

In the gneiss there are minor faults which contain narrow bands (<5 mm) of red cataclasite (Fig. 2.31c). These faults strike NE-SW and dip steeply (70 – 85°) to the northwest and southeast. The deformation within this domain is evenly distributed at the metre-scale, with moderately regular spacing of fractures, but is not continuous. There is no obvious deformation at the decimetre-scale and below.

Carbonate damage zone Directly adjacent to the fault core on the western side is an area of moderately damaged limestone and dolostone that is 0.5 – 1 m wide (Fig. 2.32). This domain is pale yellow in colour and consists of a finely laminated (mean 015/80 NW), incohesive granular matrix enclosing clasts of carbonate material that have their long axes aligned approximately parallel to the lamination and general orientation of the fault. The clasts range in size from <5 cm to approximately 100 cm long, and have the appearance of broken up, disrupted bedding. 50 cm from the western boundary between the fault core and damage zones, there are three large (50 – 100 cm), boudinaged clasts of solid dolomite that have been incorporated into the fault core (long-axes parallel to the foliation), with another 15 cm of clay-rich gouge between them and the damage zone. This layer of gouge forms a mixed zone, where angular clasts from the damage zone (2 – 5 cm) are incorporated into it. There is evidence of book-shelf faulting in one of the larger clasts, indicating there has been some degree of ~N-S extension. Between the clasts, within the granular matrix, are gypsum veins. These vary in width between 1 and 15 mm (mean ~3 mm) and whilst they are generally parallel to the trend of the fault, there are some which obliquely cross-cut the main trend. Fibre growth orientation within the veins is perpendicular to vein edges, indicating that they are tensile fractures. Other fractures, filled with calcite, are also present and there are at least two generations that cross-cut each other, displaying sinistral offset.

Figure 2.32: *Photograph of the Tzefahot Fault carbonate-hosted damage zone: laminated carbonate with relatively few fractures, but gypsum veins parallel/sub-parallel to the lamination and fault zone boundary. Shear fracturing in a larger clast indicates ~N-S extension.*

Fault core There are two distinct domains within the core of the Tzefahot Fault; to the east, a zone of apparently basement-derived cataclasite and fault gouge, and to the west, a zone of entrained shale gouge.

The eastern domain is approximately 3 m wide and appears as a zone of fine-grained, purple-coloured clay-rich material. It contains numerous clasts of heavily fractured pegmatite, gneiss and carbonate material, ranging in size from 5 mm – 20 cm (Fig. 2.33a). In addition to the relatively small clasts within this zone, there is also a large clast of carbonate material, approximately 2 m long and 1 m wide, with the long axis following the approximate trend of the fault zone (Fig. 2.33b). The clast has sigma-type asymmetry, indicating a sinistral sense of shear. It is composed of a relatively solid 'core' of carbonate, surrounded by a 20-30 cm wide mantle of foliated material that tapers off towards the top and bottom of the exposure. This foliated zone is composed of layers of finely-laminated, pale yellow carbonate and clasts (a few millimetres to 5 cm wide), layered with slightly darker clay-sized material which is also finely-laminated.

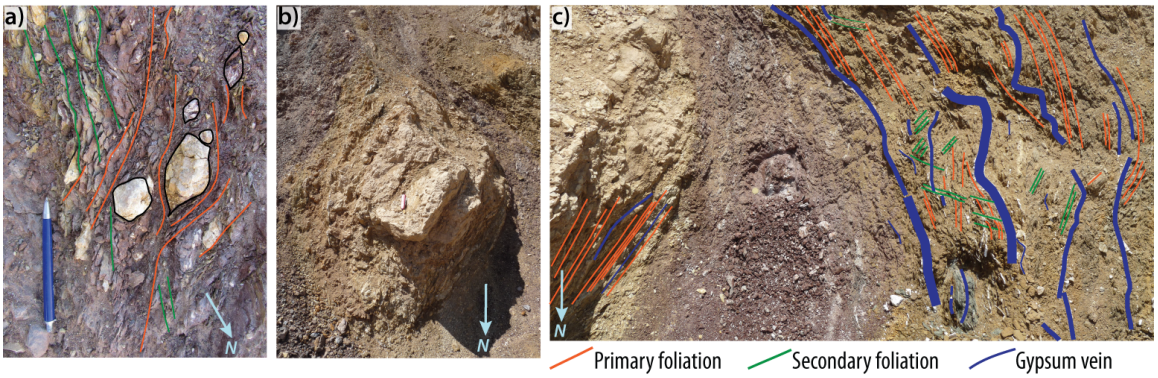

Figure 2.33: *Photographs of the Tzefahot Fault core:* ***(a)*** *small, cm-scale clasts of carbonate material with purple cataclastic gouge;* ***(b)*** *large, m-scale clast of carbonate material within cataclastic gouge;* ***(c)*** *strongly-foliated shale gouge forming the western part of the fault core.*

At the surface, the eastern domain fault core material is very friable but upon removal of the weathered layer is relatively cohesive and competent. The rock is moderately foliated, with the fabric generally parallel/sub-parallel to the main fault plane (Fig. 2.30d). However, it is wrapped around clasts, which sometimes show a weak sinistral sense of shear. There are bands within this domain which vary in colour: a dark-red band of very fine-grained cataclasite and gouge have the strongest foliation here, whilst grey bands of protocataclasite are more obviously derived from the leucocratic basement wall rocks, locally retaining some gneissic foliation. The protocataclasite forms two clear bands, approximately parallel to the fault plane, and are 30 cm and 10 cm in thickness, 30 and 50 cm away, respectively, from the fault plane at the eastern margin of the fault core.

The western portion of the fault core is composed of strongly-foliated, orange-brown material that is 1.5 – 2 m wide, which at the mesoscale is relatively homogeneous in terms of grain size (< 0.5 mm) and lacks clasts (Fig. 2.33c). This unit is extremely friable and incohesive, even beneath the weathered surface. There are "ductile" folds of the foliation (frictional sliding is the deformation mechanism, Section 1.6.2) within the gouge with wavelengths on the order of 15 cm that verge to the south-east and hinges plunging to the south-west (mean 56/231, Fig. 2.34). Gypsum veins are present across the domain, ranging in thickness from approximately 2 – 30 mm (mean 8 mm), spaced every 10-30 cm. Wider veins (> 7 mm) are frequently continuous for over a metre but narrower veins are often broken-up, though also traceable at the metre-scale. Fibre growth directions of the gypsum veins are approximately orthogonal to vein edges, indicating they are tensile structures. Veins are typically parallel to the main fault trend and foliation (Fig. 2.34), and are folded with the foliation in places. Gypsum fibres in veins are reoriented around fold hinges, suggesting they pre-date at least some of the ductile folding deformation in this zone.

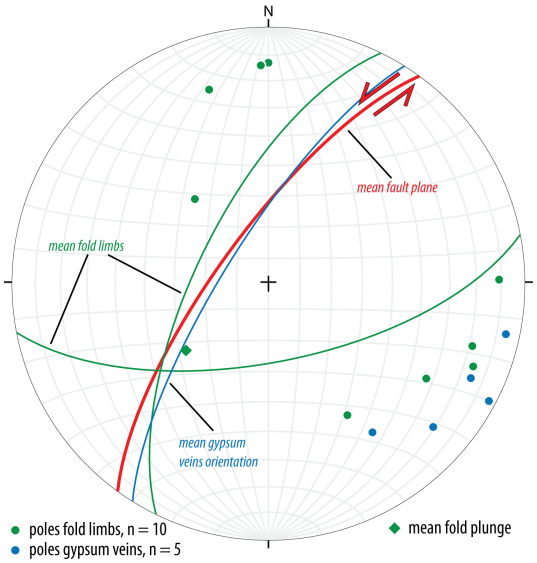

Figure 2.34: *Stereonet showing orientation of folds and gypsum veins in Tzefahot Fault shale gouge: gypsum veins are ~parallel to orientation of fault zone; fold limbs dip moderately and hinges plunge to the SW.*

Across the entire fault core, the foliation is predominantly NE-SW striking, sub-parallel to the fault plane (mean 032/88W), forming C-planes; secondary foliation planes strike ENE-WSW (mean 069/74S), forming S-planes (Fig. 2.30c). The development of such an S-C fabric indicates there has been a significant amount of shear across the entire fault core and that for part of its history at least, both domains acted as a single mechanical unit.

Summary The Tzefahot Fault is another graben-bounding fault, comparable in length (11.7 km) and estimated displacement (1188 m) to the Shelomo Fault, and juxtaposes a Precambrian pegmatite vein and gneisses in the footwall (to the east) against Cretaceous Hazera Limestone in the western hanging wall. The 4 m wide fault core is bounded by an undulating and relatively discrete fault plane in the basement footwall (Fig. 2.35), although this is disrupted by two sets of fractures.

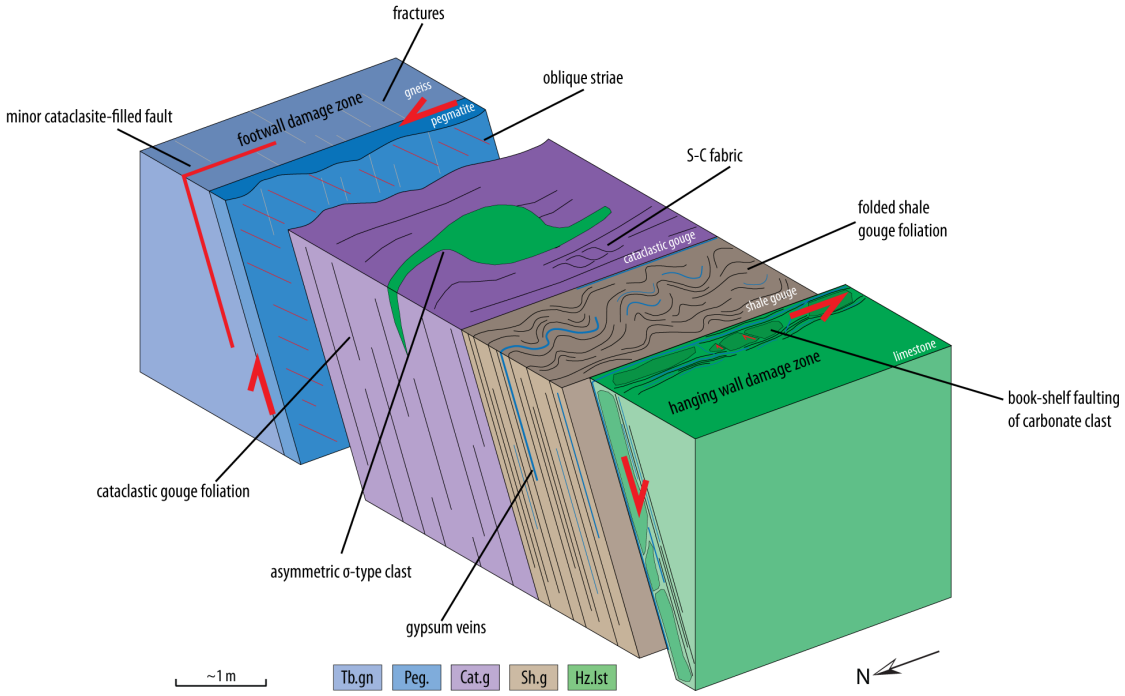

Figure 2.35: *Schematic block diagram of Tzefahot Fault summarising structural features: slickenline striae are found on the fault plane marking the boundary between the fault core and basement-hosted damage zone, sub-vertical fractures are also found here. The carbonate-hosted damage zone is composed of laminated material and fault zone-parallel gypsum veins. The fault core is divided into two types of fine-grained fault gouge, a moderately-foliated cataclastic gouge and a strongly-foliated shale gouge that also contains abundant gypsum veins parallel to the foliation.*

Within the footwall damage zone there is also a lens of intensely deformed, white powdery pegmatite, suggesting that pulverisation has occurred. Surrounding this lens on both sides is a thin layer of clay material, similar to that observed within the fault core. The boundary between the fault core and hanging wall damage zone on the western side of the fault section is less well-defined and there is a gradational transition from foliated shale to relatively intact carbonate.

The fault core of the Tzefahot Fault consists of two distinct types of fault rock: a dark purple, moderately foliated gouge containing clasts of both basement and carbonate to the east, and a brown, strongly foliated gouge containing very few clasts to the west. It is proposed that the purple gouge is cataclastic in origin whilst the brown gouge is entrained shale of the Ora Formation, to which it is very similar in appearance.

2.6.2.3 Roded Fault

The Roded Fault is a 6.5 km long graben-bounding fault, which has accumulated a most-confident estimated displacement of 432 m (minimum and maximum of 235 m and 4059 m, respectively). At its southern end it overlaps with the northern tip of the Shelomo Fault and extends north-north-eastwards towards the E-W trending Themed Fault. The fault dips steeply, with an average orientation of 008/88E and slickenlines lie in a range of orientations, with pitches from 11-40°N (Fig. 2.36c), the mean being 33°N. Two localities have been studied (Fig. 2.18a), along the central portion and close to the southern fault tip in the overlap zone with the Shelomo Fault; since the outcrops are similar in terms of lithology and structure, they are considered together below. Locality B is also poorly-exposed due to its position across a footpath so images presented are from Locality A, unless otherwise stated; structural data were collected at both localities.

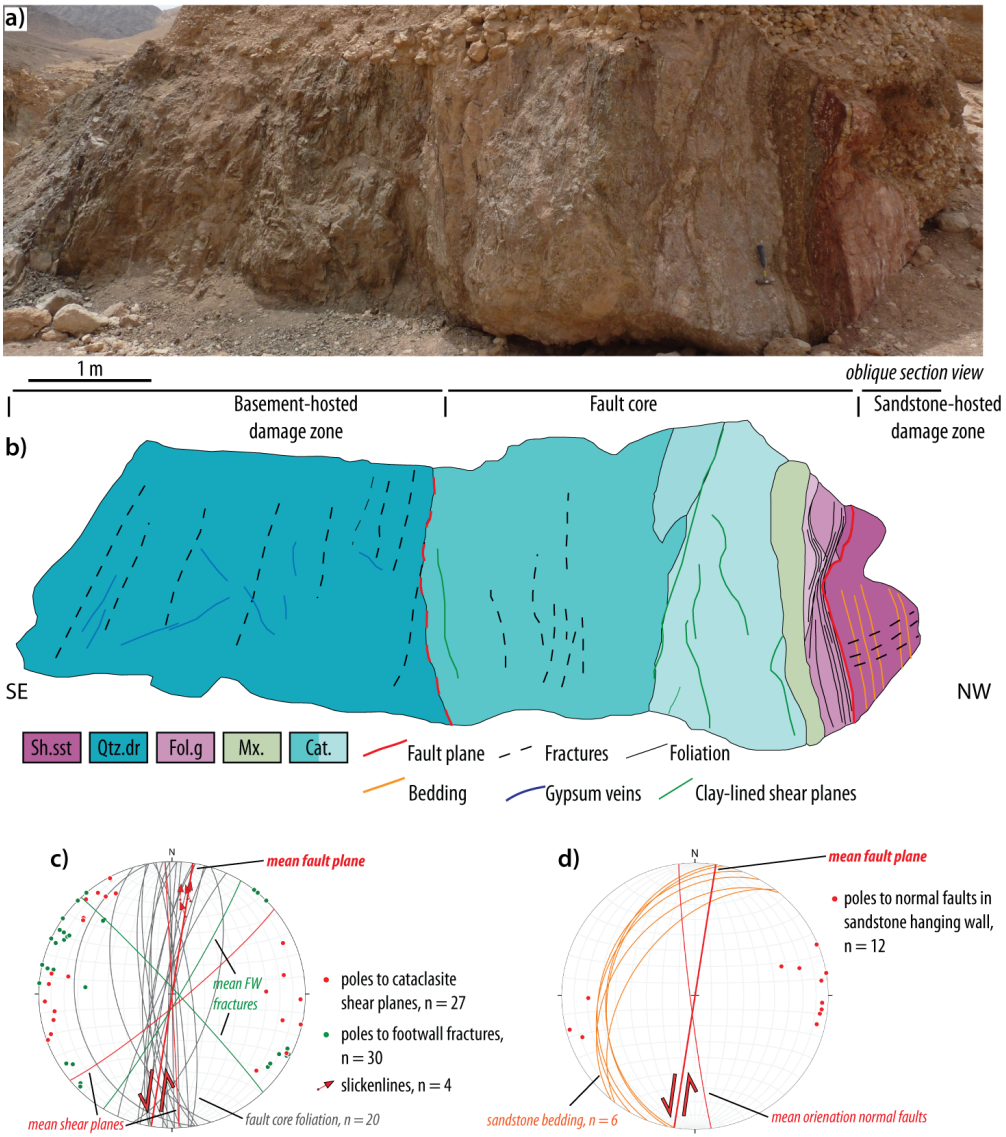

Figure 2.36: *Summary section of Roded Fault:* ***(a)*** *Photograph of fault section (Locality A);* ***(b)*** *Oblique section view with lithologies and main structures highlighted (Locality A): there is a relatively narrow zone of fine-grained, foliated fault gouge in the western part of the fault core adjacent to the clastic cover-hosted damage zone and the eastern part of the fault core is composed of cohesive cataclasite. The clastic hanging wall damage zone appears to be relatively undeformed but bedding is tilted to the vertical; the basement footwall damage zone is fractured with the dominant orientation being sub-vertical;* ***(c & d)*** *stereonets showing main structural features of the fault zone:* ***(c)*** *fault core foliation is sub-parallel to the mean fault plane and fault core shear planes show some rotation in strike from N-S to NE-SW, footwall fractures show similar orientations (localities A and B combined);* ***(d)*** *normal faults in the sandstone hanging wall strike ~N-S and dip steeply, similar to the main fault orientation (Locality B).*

Locality A is exposed by a bend in a dry river bed (Wadi Roded), revealing two sides of the outcrop, oriented approximately across- and parallel to strike (Fig. 2.36). The entire exposure is 6 m in width and 2 m high, with the across-strike portion being 3 m wide. The fault core is approximately 2 m wide, although it is only clearly defined at its western margin where the main fault plane and PSZ is located; the eastern boundary is missing due to the orientation of the outcrop. Within the fault core there are well-defined zones of very fine-grained, foliated gouge and more disordered zones of breccia and cataclasite.

At locality B the same wall rocks are observed and the outcrop is also oriented approximately perpendicular to strike. Here, the total section is approximately 20 m wide but is not continuous as it is obscured by two small gullies and a footpath. The fault core appears to be approximately 5 m wide, though it is difficult to clearly define it due to the position of the gullies and footpath. Within the fault core are once again two distinct zones of fine-grained foliated gouge and coarser breccia/cataclasite. At this outcrop it is clearer that these appear to represent the most deformed examples of the sandstone (foliated gouge) and diorite (cataclasite) wall rocks.

Protoliths At Locality A the western footwall is hosted in the Roded Quartz Diorite, juxtaposed against a Shehoret Formation Cambrian sandstone (variegated member) in the eastern hanging wall. The quartz diorite is grey-green in colour and weathered in such a way that surfaces are quite uniform in appearance, with few crystals apparent; those that are are generally 0.5-1 mm grains of quartz. At Locality B the diorite is coarser grained, with many crystals of quartz and K-fsp up to 5 mm in size visible to the naked eye.

The Shehoret Sandstone is present at both studied sections and is well-lithified and -cemented, and is much more competent than the Cretaceous sandstones of the area. Beds range in thickness from a few millimetres to approximately 15 cm and there is no obvious difference between red and white beds, other than the colour; grain size is consistently medium-grained and one colour bed does not appear more resistant to weathering than the other. It is not always obvious that an outcrop is of the variegated member without removing the red coating that forms as the result of weathering to reveal fresh surfaces.

Basement damage zone At locality A, the quartz diorite of the eastern damage zone extends for at least 5 m, though the section is cut oblique-to-strike by the Wadi Roded, so it is likely we do not see the full extent of the damage zone. It is heavily fractured by sub-vertical, NNE-SSW to NE-SW-trending fractures (mean 040/89W, Fig. 2.36c) that are spaced every 5-10 cm and continuous at the metre-scale (Fig. 2.37a). Fractures within the first $\sim$3 m east of the fault plane sometimes have a gypsum infill, though it is fine-grained and powdery in appearance, and individual grains are not visible. Within this zone the rock is also deformed at the sub-centimetre scale by fractures that are <1-2 mm wide (Fig. 2.37b), randomly oriented and cemented (the fill at the surface is weathered, and pink and powdery in appearance). These are spaced every 5-10 mm and are cross-cut by the later, through-going fractures.

The fractures at locality B follow a similar pattern, with a slightly increased range in strike from N-S to NE-SW (mean 029/87E, Fig. 2.36c). The diorite in the wall rocks here is much more coarser-grained

and as such the fractures do not appear to cut through the rock so sharply, and give a blockier appearance. They have a similar continuity but slightly wider spacing than those at locality A, on the order of 10-20 cm. There is also a pair of basaltic dykes within the basement damage zone, intruding into the quartz diorite and trending NW-SE (162/82W). These are dextrally offset by a minor, steeply-dipping oblique fault (073/87S). Fractures within the dykes follow the same trend as in the diorite, but are more closely spaced, every 5-10 cm.

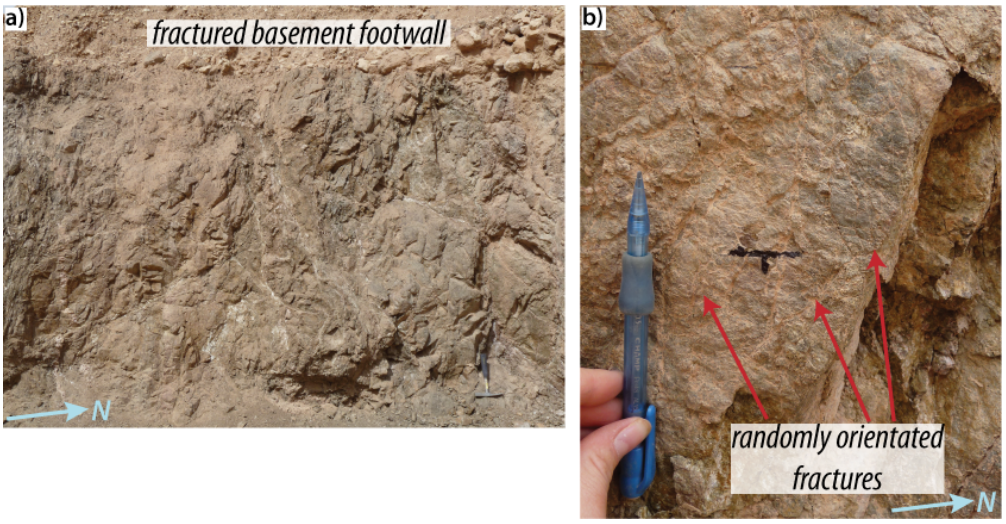

Figure 2.37: *Photographs of the basement-hosted damage zone of the Roded Fault, Locality A:* ***(a)*** *fractured footwall damage zone approximately 3 m east of the fault core;* ***(b)*** *randomly oriented microfractures in the same part of the fault core.*

Sandstone cover damage zone There is little exposure of the damage zone on the western side of the fault at locality A (Fig. 2.36a), but in the metre immediately adjacent to the fault core the variegated red and white beds are tilted to the near-vertical (from a dip of ∼64°), approximately parallel to the fault plane (Fig. 2.38). There are sub-horizontal fractures in this zone (Fig. 2.38) that, were it not for the variegated nature of this unit, might easily be confused for bedding. Some of these fractures are open (up to 1 cm), and gypsum crystals are observed growing perpendicular to fracture edges. Five metres to the north of the main outcrop, into the damage zone, bedding has a shallower dip of 50-60°NW, suggesting fault drag of this unit may have occurred.

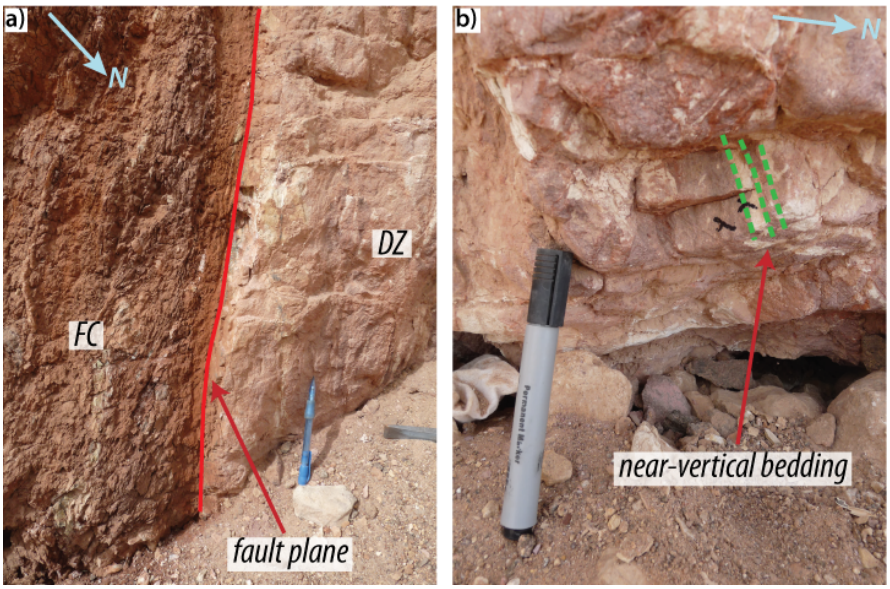

Figure 2.38: *Photographs of the Roded Fault hanging wall damage zone, Locality A:* ***(a)*** *discrete fault plane between fault core and hanging wall, in which there is a lack of obvious structures;* ***(b)*** *near-vertical bedding in hanging wall damage zone.*

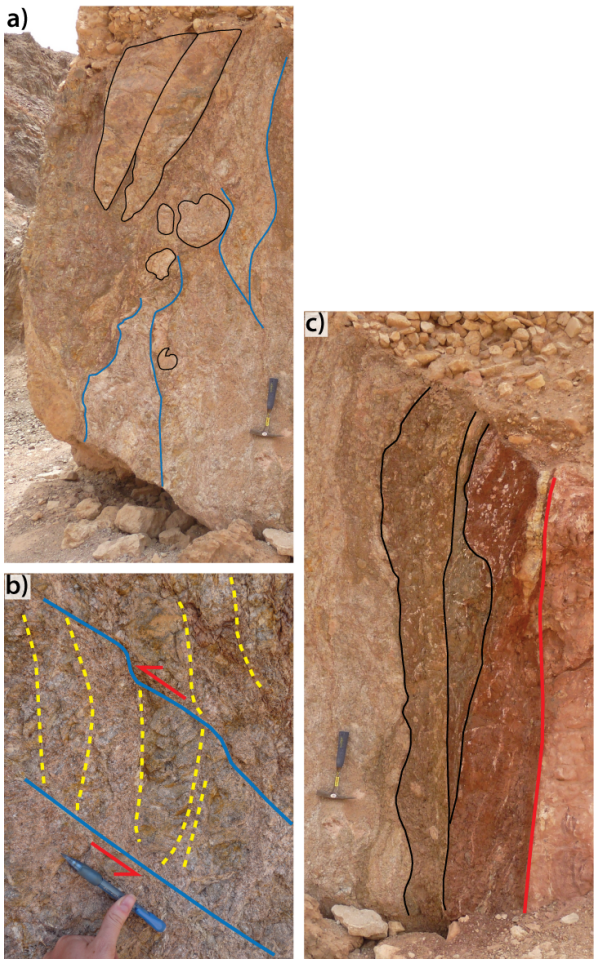

Figure 2.39: *Photographs of the Roded Fault core, Locality A:* ***(a)*** *cataclasite zone on eastern side of fault core;* ***(b)*** *shear planes within fault core cataclasite;* ***(c)*** *foliated gouge at western edge of fault core.*

At locality B, more of the sandstone damage zone a few metres away from the fault is exposed (immediately adjacent to the fault core is it cut by a footpath). Once again the sandstone is the variegated member, with beds ranging in thickness from 0.5-10 cm and a mean orientation of 025/37NW. The majority of deformation is concentrated along numerous discrete normal faults. These dip moderately and range in strike from NW-SE to NE-SW (Fig. 2.36d), but the dominant orientation is N-S (mean 173/86W). Offsets are easily distinguishable due to the distinctive bedding and range from 0.5-5 cm.

Fault core The Roded Fault has a 2-3 m wide fault core that consists of both a brecciated zone of crystalline material (Fig. 2.39a) and fine-grained, foliated, zone (Fig. 2.39c). At locality A, the PSZ appears to be at the edge of the fault core and forms the boundary between the foliated material and the more competent sandstone of the damage zone (Fig. 2.40a), whilst at locality B it lies in the centre, at the boundary between the breccia and foliated material (Fig. 2.40b). At both outcrops there are two kinds of fault core material; incohesive, foliated clay-rich gouge and coarser-grained breccia and cataclasite. The foliated gouge is thought to be derived from the sandstone wall rocks, whilst the cataclastic material is derived from the crystalline basement.

There are three different coloured bands of foliated material at locality A, with a combined width of 50-80 cm (Fig. 2.39c). Closest to the fault plane is a 30-40 cm vertical band of dark red, strongly foliated material that lies sub-parallel to the fault plane (mean 013/86E, Fig. 2.36c). There is no obvious secondary foliation here. There are relatively few clasts within this zone but there are occasional gypsum veins parallel to the foliation and 5-7 mm wide. A brown-coloured, fine-grained gouge forms the next 15-30 cm. It has a weaker foliation than the red domain and has many more clasts, ranging in size from <1-10 cm. The clasts are composed of both basement and cover lithologies.

At locality B there are two types of fine-grained, foliated material. Directly adjacent to the PSZ is a 20 cm wide band of red material, similar to that seen at locality A. Adjacent to the red band is a purple foliated gouge, also very fine-grained, but which appears to have some relatively intact clasts of sandstone within it (where intact bedding is visible over approximately 30 cm). The boundary between the gouge and intact block is relatively sharp, but irregular and wavy. The main foliation here trends sub-parallel to the mean fault plane, but there is also a NE-SW striking

secondary foliation which may represent the S-planes of an S-C fabric (Fig. 2.36c).

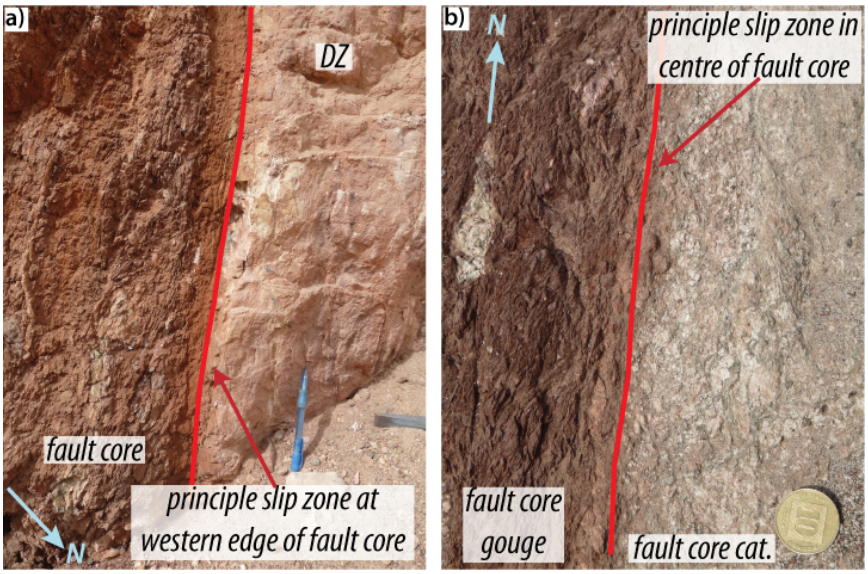

Figure 2.40: *Photographs of the principal slip surface of the Roded Fault:* ***(a)*** *at the western edge of the fault core at Locality A;* ***(b)*** *in the centre of the fault core at Locality B.*

The transition from foliated gouge to cataclasite is markedly different across the two localities (Fig. 2.41). At locality A, the boundary is sharp but irregular, and there is some gentle mixing of clay-rich gouge into the cataclastic zone (Fig. 2.41a) whereas at locality B it is sharp and straight (Fig. 2.41b). At locality B there is also a 5-10 mm wide layer of hard, sandy material between the two domains and this is thought to represent the principal slip zone. At locality A, there is no secondary material between the two domains, it is just a sharp fault.

The cataclastic zone also differs at the two outcrops since at B the deformation appears to be distributed and continuous resulting in an intensely fractured and friable rock, the only variation in grain size or material being where part of a basaltic dyke has been incorporated into the fault core. There is no foliation in this zone, but there are two sets of steeply-dipping shear planes, striking NE-SW and N-S, with mean orientation of 051/84E and 177/90 respectively (Fig. 2.36c). At locality A, however, the rock is much more competent and contains more clasts (up to 20 cm) as well as shear planes along which there appears to be some fine-grained clay material. The clasts are randomly oriented and spaced and are generally of basement rather

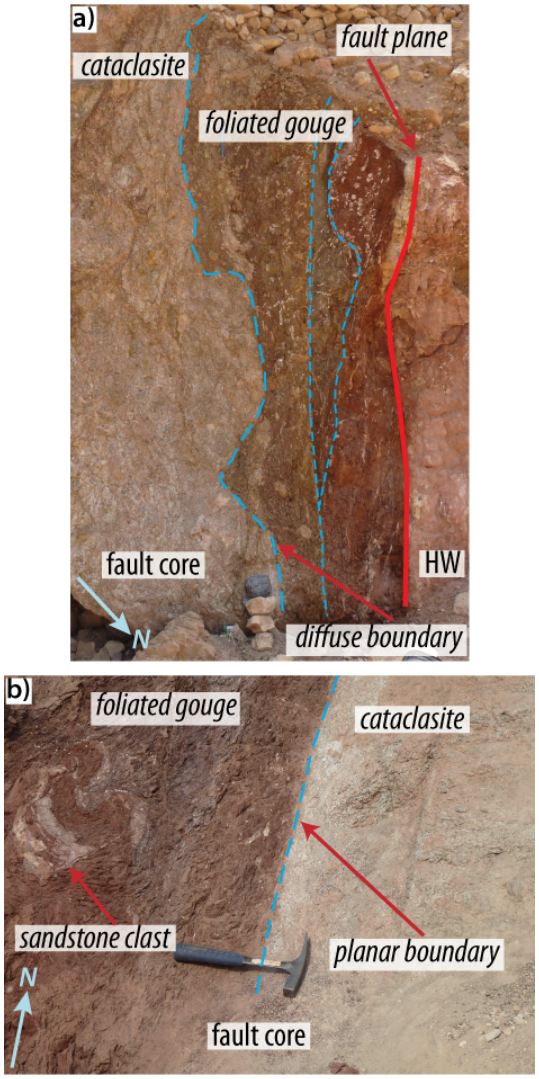

Figure 2.41: *Photographs comparing the boundary between cataclasite and foliated gouge within the fault core:* ***(a)*** *Locality A, diffuse boundary between foliated gouge and cataclasite;* ***(b)*** *Locality B, planar boundary between foliated gouge and cataclasite.*

than cover material. The deformation of the breccia at this location is much less evenly distributed. It appears that the cataclasite at Locality B represents a higher strain example of the breccia/cataclasite at Locality A.

Summary The graben-bounding Roded Fault forms the eastern margin in the northern part of the Netafim Graben and juxtaposes a range of Cretaceous rocks in the hanging wall against Precambrian crystalline rocks and Cambrian clastic sedimentary rocks to the east; at the studied locations (Fig. 2.18), Roded Quartz Diorite in the footwall is juxtaposed against the variegated member of the Cambrian Shehoret Sandstone in the hanging wall. The fault cores at both localities are 2-3 m wide and consist of a zone of foliated, fine-grained gouge to the west and breccia/cataclasite to the east.

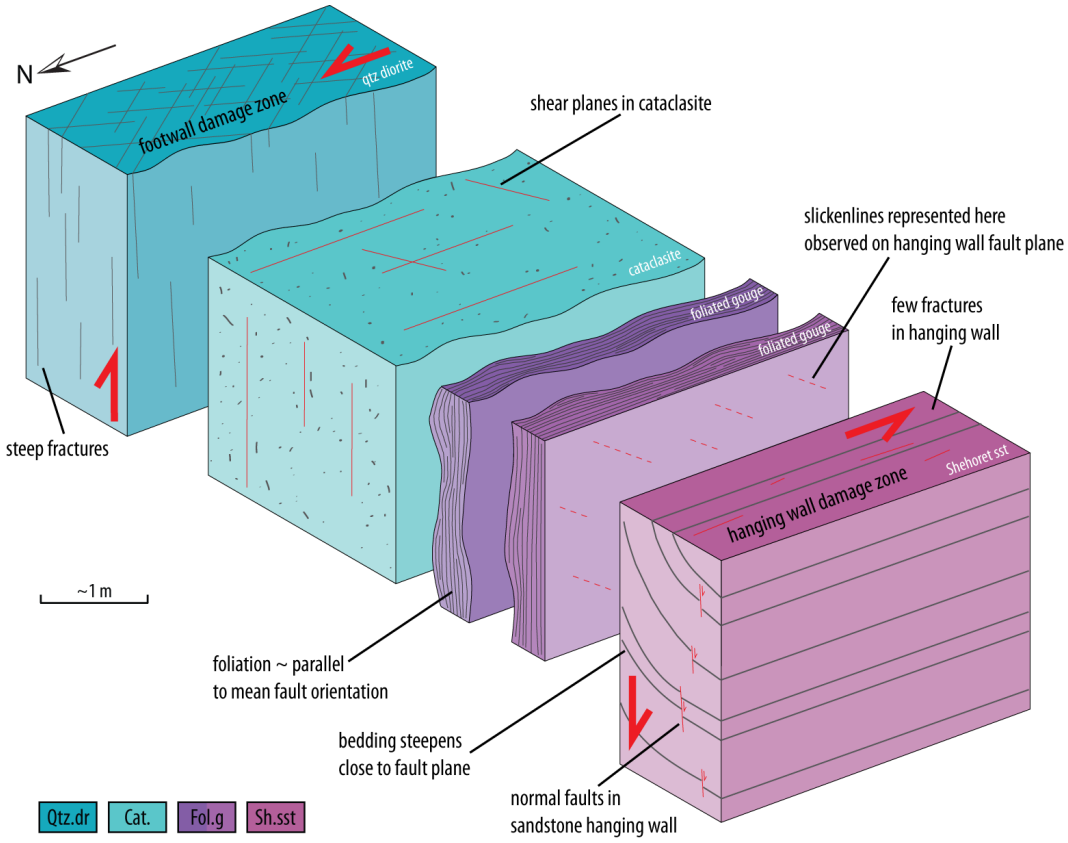

Figure 2.42: *Schematic block diagram, summarising the structural features of the Roded Fault: the footwall basement-hosted damage zone is variably fractured with the prevalent orientation being sub-vertical; there are few fractures in the hanging wall clastic-hosted damage, but there are normal faults with cm offsets. The fault core is composed of a foliated, fine-grained fault gouge in the western part and cohesive - incohesive cataclasite in the eastern part.*

There is less variation between the two studied localities of the Roded Fault than those of the Shelomo Fault, likely because of the similar wall rock lithologies, although the principal slip surface appears to vary in position between them; at Locality A, there is a sharp, discrete surface in the sandstone of the hanging wall, between it and the foliated gouge of the fault core (Fig. 2.40a). At Locality B, however, such a surface is present in the centre of the fault core, forming the boundary between the foliated gouge and cataclasite (Fig. 2.40b). At Locality A the boundary between foliated gouge and cataclasite is more diffuse and irregular (Fig. 2.39c). A schematic block diagram of the Roded Fault is provided in Fig. 2.42.

2.6.2.4 Yotam Fault

The Yotam Fault trends NNE-SSW and is the northwestern bounding fault of the Yotam Graben, forming the boundary between it and the Roded igneous-metamorphic block to the northwest. It extends for approximately 5.6 km and the range of possible displacements is 438-6032 m, with a best-estimated displacement of 600 m (Table 2.1) and has a mean orientation of 019/80NE (Fig. 2.43c). The section studied here (see Fig. 2.18a for location) is perpendicular to strike and approximately 15 m wide. It juxtaposes a pair of dykes (rhyolitic and basaltic) to the west against Hazera Formation limestone to the east (Fig. 2.43a,b). The basaltic dyke is directly adjacent to the fault core at this location.

The fault zone consists of a 1-1.5 m fault core, which can itself be divided into several distinct zones. It is bounded to the east by a discrete fault plane in the limestone that is smooth and polished, and to the west by a more diffuse transition into the basement rocks. Slickenlines are present on the limestone fault plane and range in pitch from 17-88°N, suggesting movement on the fault has varied from oblique/strike-slip to almost pure dip-slip.

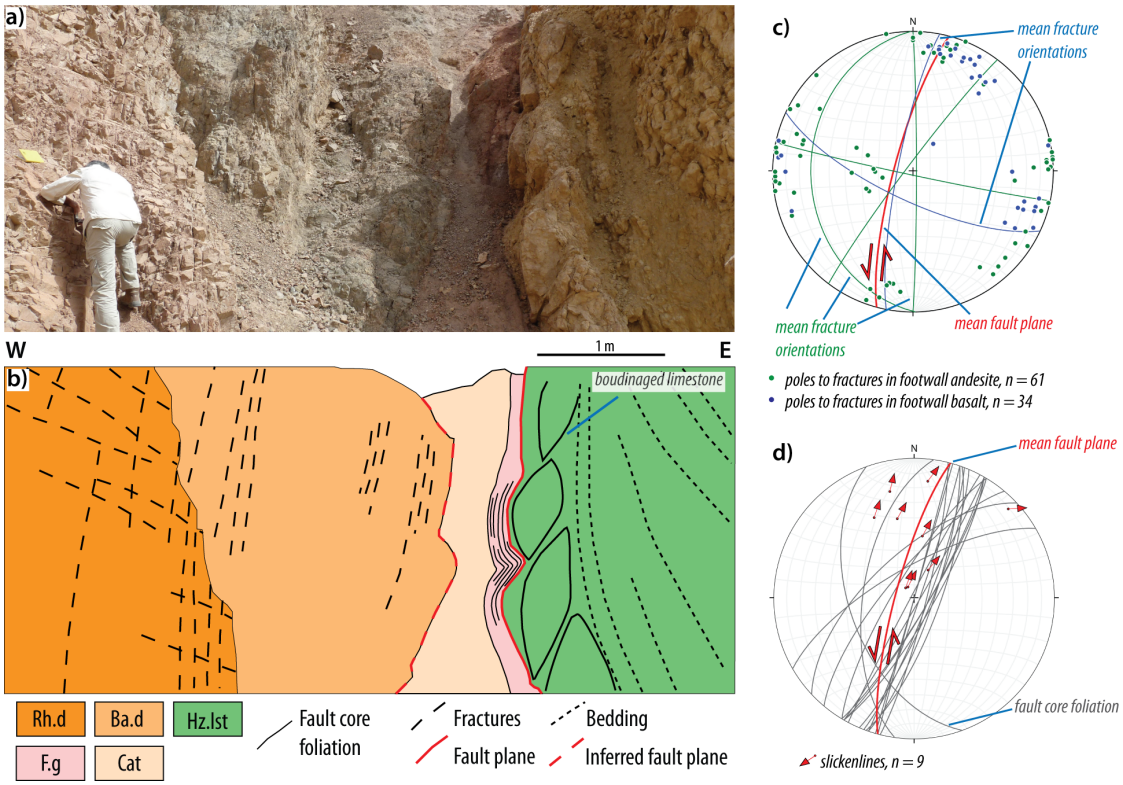

Figure 2.43: *Summary section of the Yotam Fault:* ***(a)*** *Photograph of fault section;* ***(b)*** *Oblique section view with lithologies and main structures highlighted: the narrow fault core comprises foliated, fine-grained gouges adjacent to the carbonate wall rocks to the east and cohesive cataclasite adjacent to basement wall rocks to the west. In the carbonate hanging wall damage zone there are alternating limestone and shale beds; the basement footwall damage zone is heavily fractured (Rh.d: rhyolitic dyke; Ba.d: basaltic dyke; Gr.lst: Grofit Limestone; F.g: foliated gouge; cat: cataclasite);* ***(c & d)*** *stereonets summarising main structural features:* ***(c)*** *fractures in the footwall dykes dip steeply and sub-horizontally, striking ∼N-S and E-W;* ***(d)*** *fault core foliation is mainly sub-parallel to the main fault plane and striae plunge consistently to the north with variable dips.*

Protoliths Although the footwall of the Yotam Fault is mapped as Precambrian conglomerate at the studied section (Fig. 2.18), the wall rocks are in fact composed of a pair of dykes that are andesitic and basaltic in composition. Both are very fine-grained and individual crystals are not

seen at the mesoscale; the basaltic dyke is grey-green in colour, while the andesitic dyke is pink. In the hanging wall, on the eastern side of the fault, are Grofit Formation limestones. Beds of carbonate material are interbedded with clay-rich beds; the thickness of beds of both materials can be up to ~1 m, but are generally on the order of 15-50 cm.

Basement damage zone There are two lithologies in the damage zone at this location; andesitic and basaltic dykes form a zone which is at least 10 m wide and lie at the base of a 100+ m hill (Fig. 2.44), unconformably overlain by the Precambrian Elat Conglomerate. The deformation across both lithologies is evenly distributed, but not continuous and concentrated along discrete fracture planes. In the basalt, closest to the fault core, there are two main trends of fractures; a steeply dipping, NNW-SSE - NNE-SSW set and a near vertical WNW-ESE set (Fig. 2.43c). This part of the outcrop is quite friable at the surface and fractures do not tend to form sharp, straight planes, which may in part be the result of weathering as well as proximity to the fault core. In the closest 2 m to the fault core, N-S striking fractures are dominant but an E-W group is also present. These are more closely spaced at every 2-10 cm.

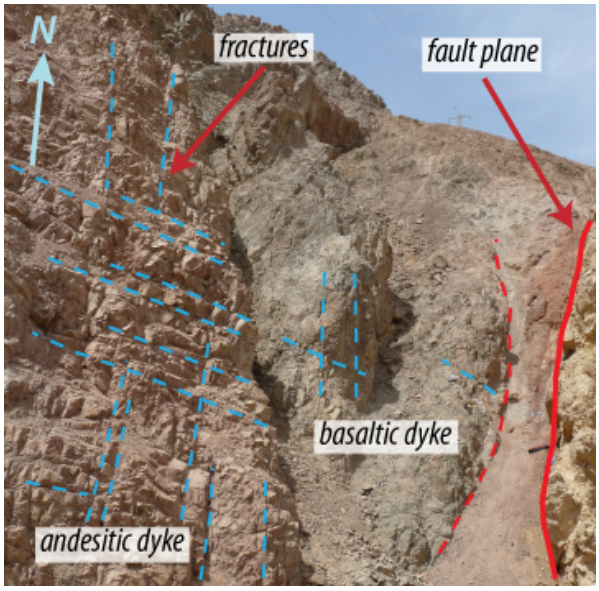

Figure 2.44: *Photograph of the footwall damage zone of the Yotam Fault: the andesite dyke has three clear sets of fractures, steeply dipping striking N-S and E-W and a sub-horizontal set; the basaltic dyke does not appear as heavily fractured by data collected (Fig. 2.43c) show it hosts fractures of the same orientations.*

Within the andesite, which starts 2 m away from the fault zone, there are three main trends of fractures. Two sub-vertical groups, N-S and E-W trending, spaced every 5-30 cm and a shallow, eastward dipping group that have a wider spacing of 30-40 cm. There is also a secondary set of fractures that is parallel/sub-parallel to the NNE-SSW trend of the fault. The rock does not show any obvious signs of deformation other than the fractures, which give the outcrop a blocky and unstable nature overall, but fragments below fracture-scale are competent and undeformed at the mesoscale. Relatively little weathering of the andesite appears to have occurred, and fracture edges are sharp, forming angular blocks of material.

Carbonate cover damage zone The carbonate damage zone, forming the western limit of the narrow Yotam Graben (Fig. 2.16), is well-exposed but less accessible than the basement rocks due to a combination of steeply-dipping beds and a gully cutting away the base of the outcrop. Immediately to the east of the fault plane is a 50-70 cm thick bed of relatively competent limestone. Within this bed are secondary shear planes, which give parts of the bed a boudinaged appearance (Fig. 2.43b). On the other side of this limestone bed is 1-2 m of finely laminated shale, which to the east passes back into limestone which is blocky in appearance. The dip of beds in all of these layers is near vertical, and standing approximately 100 m further south on higher ground (looking

northwards) it can be observed that this is the result of fault drag; after only a few tens of metres to the east the beds return to a much shallower dip (∼48°). Abundant striae are visible on the smooth, polished limestone fault plane, both predominantly dip-slip (Fig. 2.45a) and strike-slip (Fig. 2.45b), although no cross-cutting was observed so it was not possible to determine the relative age relationship.

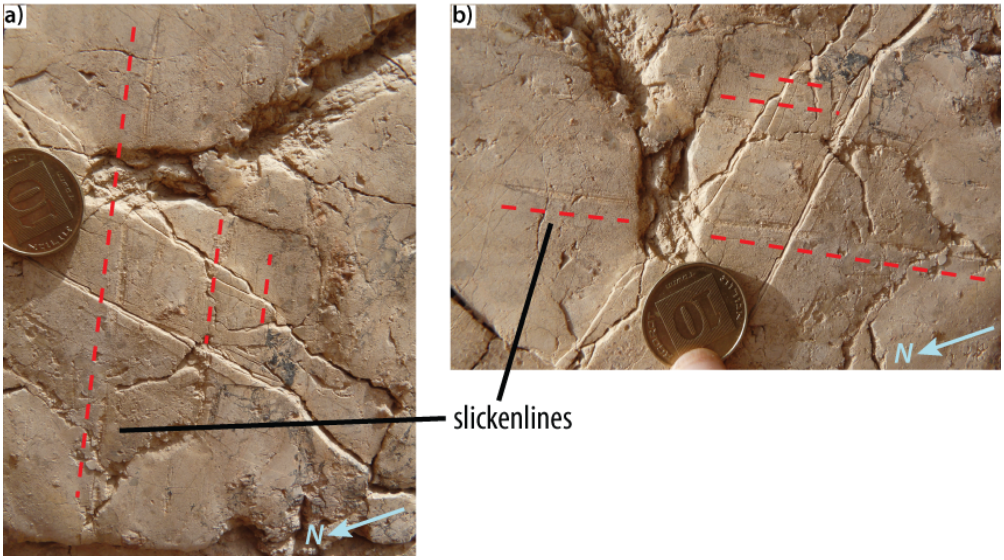

Figure 2.45: *Slickenline striae on the main fault plane:* ***(a)*** *sub-vertical, dip-slip;* ***(b)*** *sub-horizontal, strike-slip striae.*

Fault core The fault core of the Yotam Fault is narrow, approximately 1 m wide on average, but highly heterogeneous and consists of four distinct types of fault rock (Fig. 2.46a); the boundaries between these materials represent discontinuities in the product of deformation (due either to lithological variations or intensity of deformation). Closest to the fault plane at the eastern boundary is a 20-25 cm wide zone of friable, strongly foliated and clay-rich gouge (Fig. 2.46d). The foliation is sub-parallel to the mean trend of the fault plane (mean 028/90, Fig. 2.43d). Closest to the fault plane, the gouge is yellow in colour and after 5-10 cm grades into red. There are clasts of carbonate material across this zone, ranging in size from 0.5-3 cm, but it is not immediately obvious that this material is similar in composition to either wall rock lithology at this location.

The central part of the fault core is more obviously derived from basement wall rocks (Fig. 2.46d), as large, crystalline lithic fragments (5-7 cm) form a 40 cm wide band of breccia. The breccia is pink in colour and throughout this layer there are discrete shear planes (with a mean orientation of 049/69W) that are lined with what appears to be a green clay mineral. This zone is more competent that the gouge closest to the fault plane but is relatively incohesive; the clasts themselves are intensely fractured and crumble with a little pressure. To the west of this breccia, there is a further 5-10 cm of red, foliated clay-rich material containing clasts of basement rather than carbonate wall rocks. The foliation is once again sub-parallel to the main fault plane, with a mean orientation of 015/90. West of the breccia is a 30 cm wide zone of cohesive cataclasite ((Fig. 2.46c) that also appears to be derived from basement material, but in which there are few obvious clasts visible. There are also few obvious structures at the mesoscale.

The fourth material within the core of this fault, closest to the western boundary is a protocataclasite (Fig. 2.46b). It has a similar pale pink and green colour to the central portion but is relatively

cohesive and has a much finer overall grain size, with clasts being angular and generally <1 cm. There do not appear to be any discrete shear planes in this zone and there is also an absence of any clay material, but there is gypsum precipitated along fractures in the 10 cm closest to the edge of the fault core. Within this area there are also clasts that are darker red in colour and possibly derived from the Precambrian conglomerate (which overlies the dykes at this location) rather than from crystalline basement rocks.

Summary The Yotam Fault forms the western margin of the relatively smaller Yotam Graben (Fig. 2.18b) and along its length juxtaposes a range of Cretaceous sedimentary rocks in the eastern hanging wall against both crystalline and sedimentary Precambrian units in the footwall on its western side; at the locality studied the wall rocks are comprised of limestone in the hanging wall and a pair of rhyolitic and basaltic dykes (which are below map resolution) in the footwall. The fault is approximately 5 km long and has accumulated an estimated displacement in the region of 600 m. The narrow, 1 m fault core consists of a foliated clay-rich and coarser grained cataclasite, similar to the fault rocks of the Roded Fault. In the limestone hanging wall original beds are still apparent within the 2 m closest to the fault core, which appear to have undergone some degree of fault drag; the presence of shale within the formation may have enabled the carbonate sequence to act in a more 'ductile' manner than if it consisted of only limestone. There is a sharp, discrete fault plane in the limestone that hosts numerous striae, ranging from almost pure dip-slip to strongly strike-slip (Fig. 2.45). In the footwall damage zone, deformation appears to be confined to brittle fracturing and there are two principal set of fractures within the dykes, making the rocks rather friable overall. There does not appear to be any sub-cm scale deformation in either the basement footwall or carbonate hanging wall on either side of the fault, suggesting deformation quickly localised along

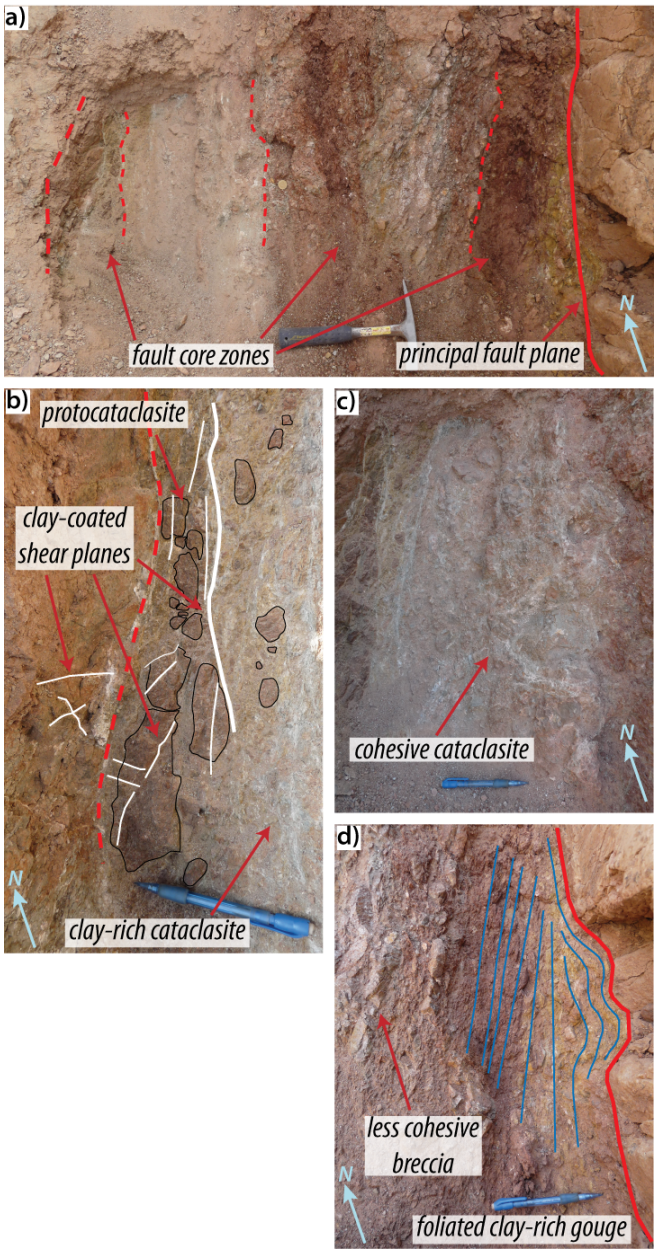

Figure 2.46: *Photographs of the Yotam Fault core:* ***(a)*** *along-strike view of fault section;* ***(b)*** *protocataclasite at western edge of fault core;* ***(c)*** *brecciated central portion of the fault core;* ***(d)*** *foliated, clay-rich fault gouge at the eastern edge of the fault core, adjacent to the hanging wall.*

a relatively planar feature and that there were few, if any, splays outside of the present fault core zone. A summary of the structure of the Yotam Fault is provided in Fig. 2.47.

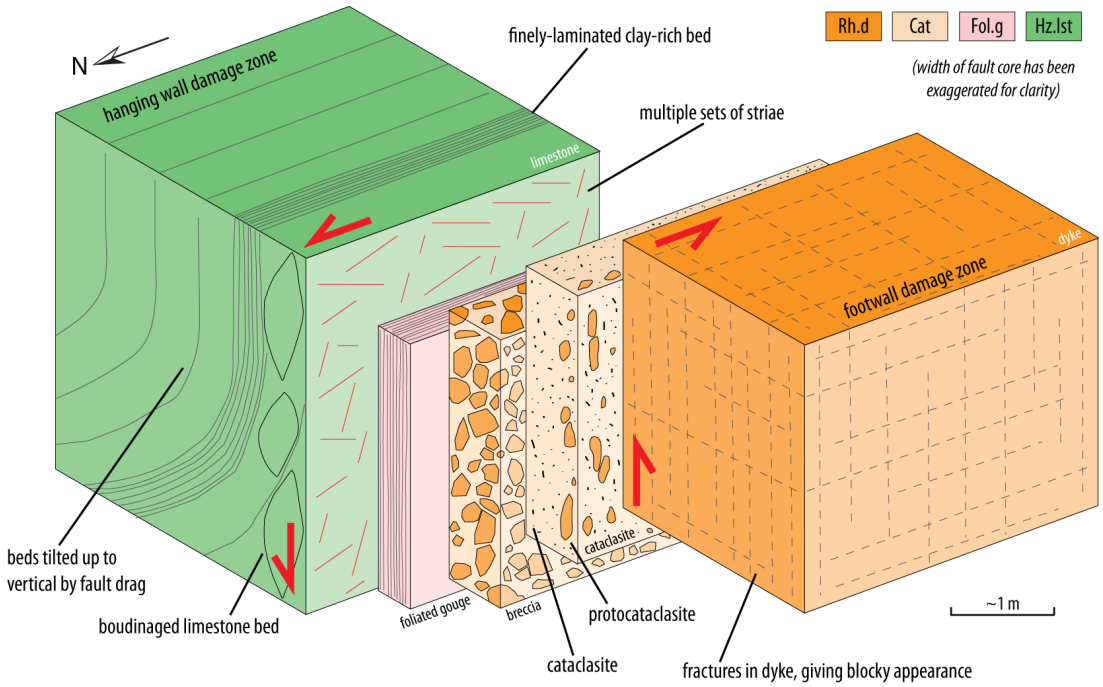

Figure 2.47: *Schematic block diagram, summarising the structural features of the Roded Fault: the footwall basement-hosted damage zone is variably fractured with the prevalent orientation being sub-vertical; there are few fractures in the hanging wall clastic-hosted damage, but there are normal faults with cm offsets. The fault core is composed of a foliated, fine-grained fault gouge in the western part and cohesive - incohesive cataclasite in the eastern part.*

2.6.2.5 Nizoz Fault

The Nizoz Fault is a 2.86 km long, E-W trending structure that has an estimated dextral displacement of approximately 250 m. It is an antithetic fault to the main NE/SW-trending faults of the southern DSFS. Close to the studied location it is sinistrally offset by approximately 100 m by a NNE-SSW trending fault (Fig. 2.18). The mean trend of the fault is 092/85S. The section of the main outcrop (Fig. 2.48) is cut at a high angle to the fault strike by a dried river bed, but reveals a 6 m wide by (maximum) 1 m high, exposure. The fault core is 2 m wide and is bounded on either side by fractured wall rocks, though it is not possible to determine exactly how wide the damage zones are due to lack of exposure.

A 30 m section, slightly oblique to fault strike, is exposed a few metres south of the main outcrop on the opposite of the river bed, so it is possible to observe structures in both the hanging and foot walls adjacent to the fault that are not well-exposed at the main section. A secondary outcrop, some 100 m to the west of the main outcrop has also been considered but the exposure is limited to a very narrow gully.

Protoliths At the main outcrop, the footwall is the Amram Granite Porphyry and the hanging wall is the Lower Cretaceous Amir Formation sandstone (Fig. 2.48a,b). At the secondary outcrop, the

hanging wall is the same but the footwall is composed of the variegated member of the Cambrian Shehoret sandstone.

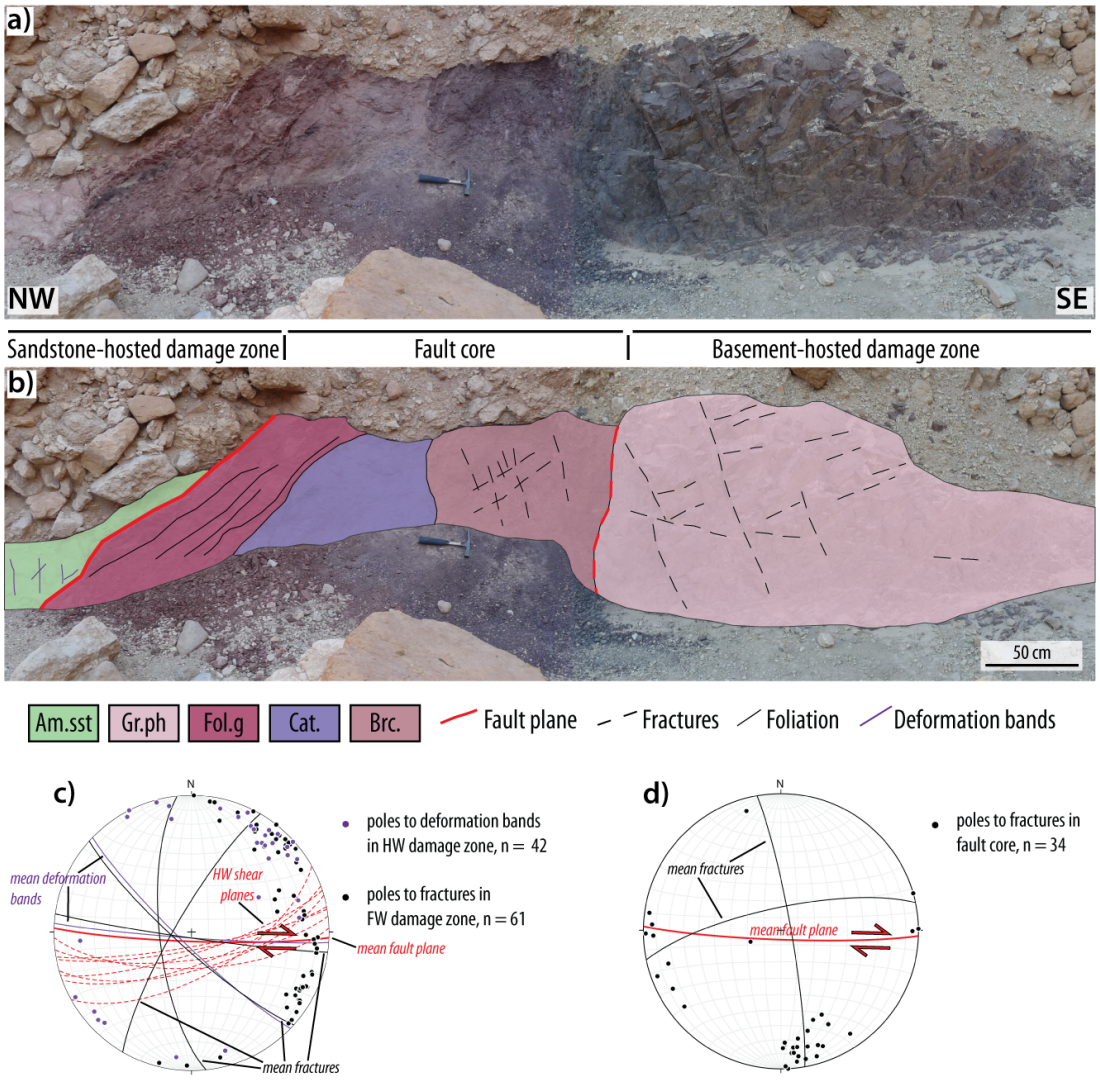

Figure 2.48: *Summary of Nizoz Fault:* ***(a)*** *Photograph of fault section;* ***(b)*** *Oblique section view with lithologies and main structures highlighted: the fault core is comprised of three zones, a foliated, fine-grained red material in the north-western part; an incohesive, light-pink coloured, fine-grained proto-gouge in the centre and a dark purple, coarser-grained breccia on the south-eastern side. The footwall, basement-hosted damage zone is fractured and cohesive, there are few fractures but deformation bands in the hanging wall clastic cover-hosted damage zone;* ***(c & d)*** *stereonet summarising main structural features:* ***(c)*** *damage zone structures: shear planes in the hanging wall damage zone are slightly oblique to the mean fault plane and fractures in both the hanging and footwall damage zones dip steeply and vary from NW-SE to NE-SW in strike;* ***(d)*** *fault core structures: fractures are largely sub-parallel to the mean fault plane (E-W striking), though some secondary fractures strike ~N-S.*

Basement damage zone On the south side of the river bed along which the main fault trends, the Amram Granite Porphyry forms a 15+ m high cliff. The granite is heavily fractured with sub-vertical structures that can be divided into three dominant groups according to strike: NW-SE, N-S and NE-SW striking (Fig. 2.48c); there is also a fourth group, sub-parallel to the trend of the fault itself. The fractures are closely spaced, every 3-30 cm for the dominant orientations, and give the outcrop a columnar appearance (Fig. 2.49a). There is no shear offset apparent on the majority of the fractures, though there are minor faults in both the NW-SE and E-W orientations, that have narrow zones (up to 3 cm) of cataclastic fill. On one such E-W trending minor fault strike-slip slickenlines, plunging 10 °N, were observed.

In 2 m of the footwall damage zone closest to the fault core (on its southern side), the rocks are more intensely fractured than in the cliff section; fractures are spaced every 2-10 cm, continuous for at least 30 cm, and the occur in at least two distinct orientations that strike at approximate right angles to each other (Fig. 2.49b). Mean orientations of the groups of fractures are N-S, NE-SW and NW-SE (Fig. 2.48c) The rock is generally quite competent, but where fractures are closely spaced and cross-cut clasts may easily fall away. It is hard to determine if there has been any shear offset along either fracture set, but there is no cataclastic fill.

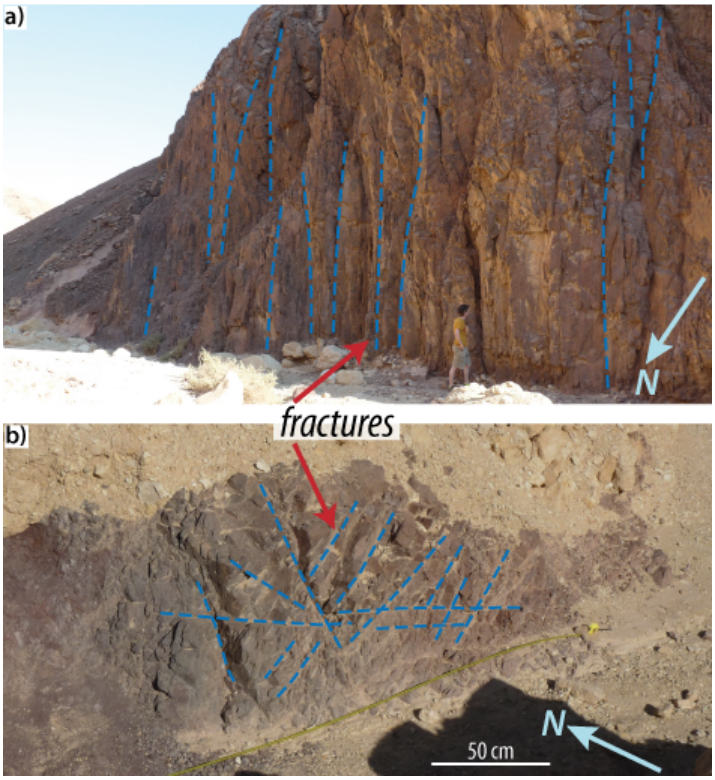

Figure 2.49: *Photographs of the Nizoz Fault footwall damage zone:* ***(a)*** *vertical fractures in footwall damage zone (Amram Rhyolite);* ***(b)*** *footwall damage zone on the southern side of the studied section (Amram Granite Porphyry).*

Sandstone cover damage zone Although there is little exposure of the hanging wall damage zone at this location, due to cover by recent stream deposits, it is apparent that there are relatively few discrete fractures when compared to the footwall damage zone; deformation is instead concentrated along deformation bands, visible due to their resistance to weathering relative to the surrounding rock (Fig. 2.50a). Deformation bands vary in strike from E-W to NE-SW, with moderate to steep dips, and have the same mean orientation as basement footwall fractures (Fig. 2.48c); some display small normal shear offsets, in the range of 1-10 cm, and there is very little evidence of other mesoscale deformation apparent in the hanging wall damage zone. At the secondary outcrop, ~100 m west of the main outcrop, there is an exposure of near-vertical planes in the sandstone hanging wall (Fig. 2.50b); these are not thought to represent the main fault plane as they are slightly set back to the north from the expected position of the fault plane at the bottom of the gully, though this is not exposed.

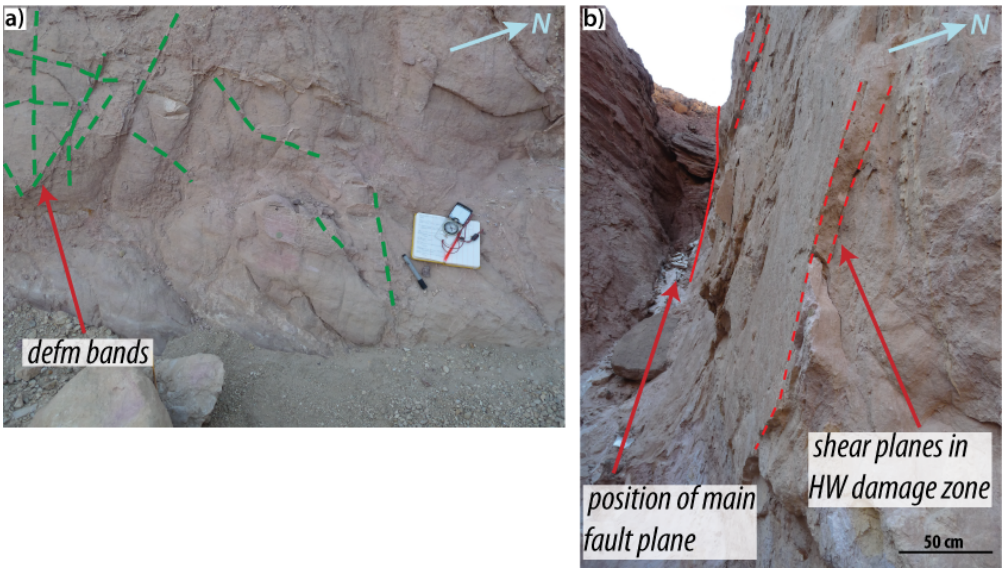

Figure 2.50: *Photographs of the Nizoz Fault hanging wall damage zone:* ***(a)*** *shear planes in sandstone hanging wall directly behind main fault plane to the north;* ***(b)*** *deformation bands in sandstone hanging wall, approximately 10 m N of the main fault plane.*

Fault core The fault core of the Nizoz Fault can be subdivided into three distinct zones (Fig. 2.51a): a 50 cm wide zone of dark purple breccia forms the southern part of the fault core (Fig. 2.51b); in the centre is a 75 cm wide band of pale purple/pink proto-gouge (Fig. 2.51c); and the northern-most part of the fault core comprises a band of thinly-bedded Cambrian Shehoret Sandstone (Fig. 2.51c,d).

In the brecciated zone, the rock is relatively friable and incohesive but there is a general lack of matrix material. The rock has a very uneven surface that appears to be formed by randomly oriented fractures, spaced every 5-20 mm and have similar mean orientations to footwall fractures (Fig. 2.48c,d) and that are pervasive throughout this zone (Fig. 2.51b). Individual clasts do not appear to have undergone any obvious deformation and are similar in appearance to the granite porphyry of the damage zone (Fig. 2.48a).

The central portion of the fault core is the most intensely deformed; it is extremely friable and there are no obvious fractures, rather there has been significant comminution and the majority of clasts are smaller than 1 cm in size, with very few large than 2 cm (Fig. 2.51c). Clasts generally have a rounded appearance, suggesting there has been deformation by rolling and cataclasis. Clasts are for the most part composed of the granite porphyry and supported by a coarse sand-sized matrix that appears to be of similar composition. There is very little clay material within this part of the fault core.

On the northern side of the fault core, directly adjacent to the hanging wall sandstone, is a layer of apparently relatively competent dark red sandstone (Fig. 2.51d); within it are apparent both continuous layers of white material, as seen in the variegated member of the Shehoret Sandstone, and rounded clasts of the same rock (Fig. 2.51e). It is hard to determine from mesoscale observations whether this layer is, in fact, more or less intact sandstone or whether it is a competent gouge/cataclasite, as may be inferred by the presence of rounded sandstone clasts.

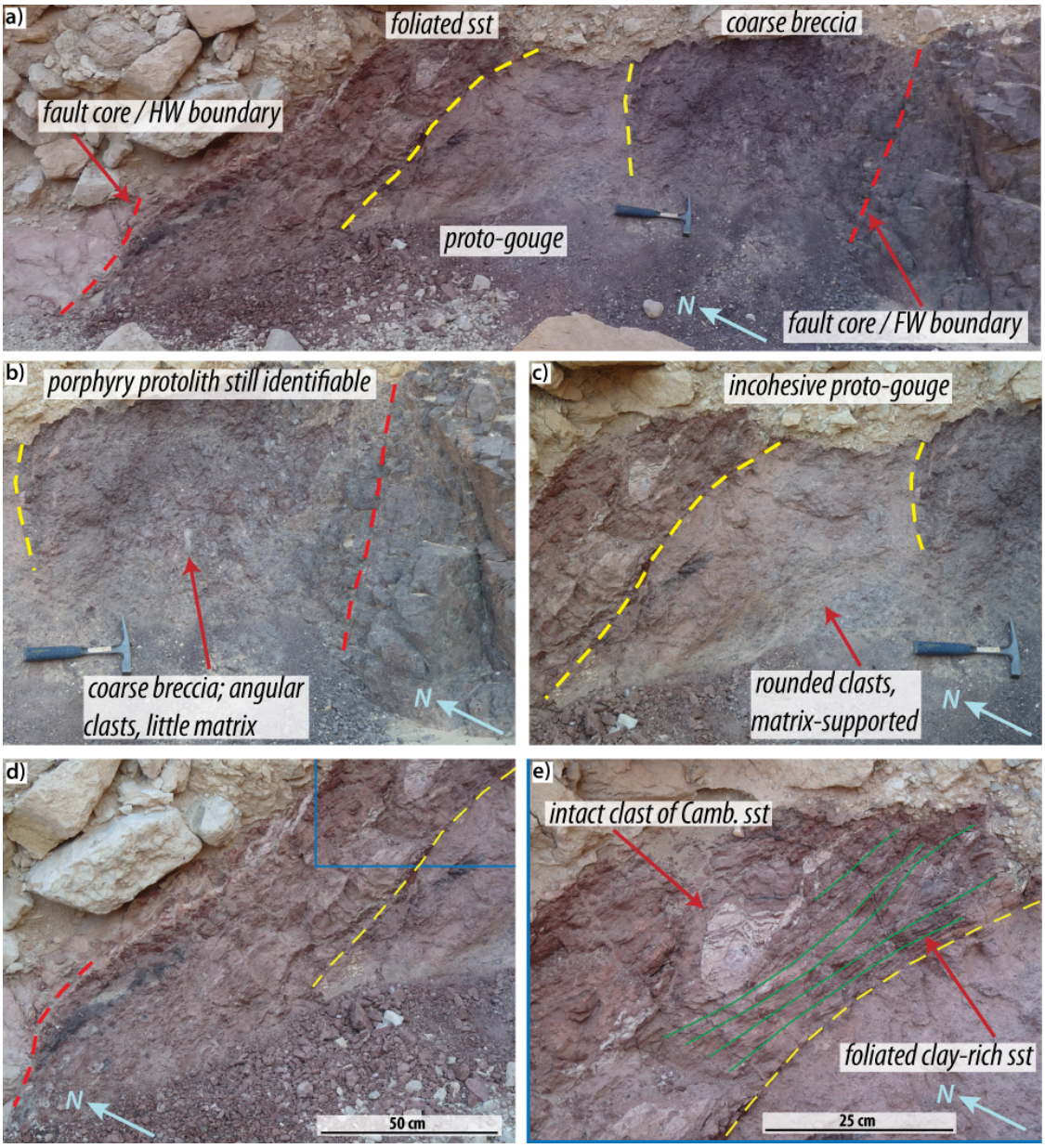

Figure 2.51: *Photographs of the Nizoz Fault core:* ***(a)*** *oblique to-strike view of fault section showing relative positions and appearance of foliated sandstone (sst), proto-gouge and coarse breccia;* ***(b)*** *coarse breccia in southern part of fault core, adjacent to basement footwall. The rock is heavily fractured, clasts are angular but there is little matrix;* ***(c)*** *incohesive proto-gouge in the centre of the fault core. Small (mostly <1 cm) clasts are rounded and matrix supported;* ***(d)*** *foliated sandstone on northern edge of fault core, adjacent to sandstone hanging wall;* ***(e)*** *enlarged image of (d), showing intact clast of Cambrian sandstone within the foliated material.*

Summary The Nizoz Fault is the only studied fault that doesn't follow a broad NE-SW - N-S trend and which is not immediately grouped with the other faults as an obvious DSFS-related structure. It is an E-W striking fault that is approximately 3 km in length and has an estimated displacement of 250 m, which is in the lower part of the range for basement-cover faults (Table 2.1). The fault juxtaposes a range of Precambrian plutonic, volcanic and Cambrian sedimentary rocks of the Amram Block in the footwall to the south, against Cretaceous clastic and carbonate rocks in the hanging wall to the north (Fig. 2.4b); at the studied location the fault juxtaposes the Amram Granite Porphyry against the lower Cretaceous Amir Sandstone (Fig. 2.4). Here, the fault core is approximately 1.5 m wide and consists mainly of fault breccia and cataclasite; there is no evidence of any clay-rich gouge observed at the other faults.

Deformation in the damage zones on either side of the fault appears to be limited to mm - cm scale fractures at the mesoscale. Both the granitic and sandstone rocks of these zones remain relatively intact and competent.

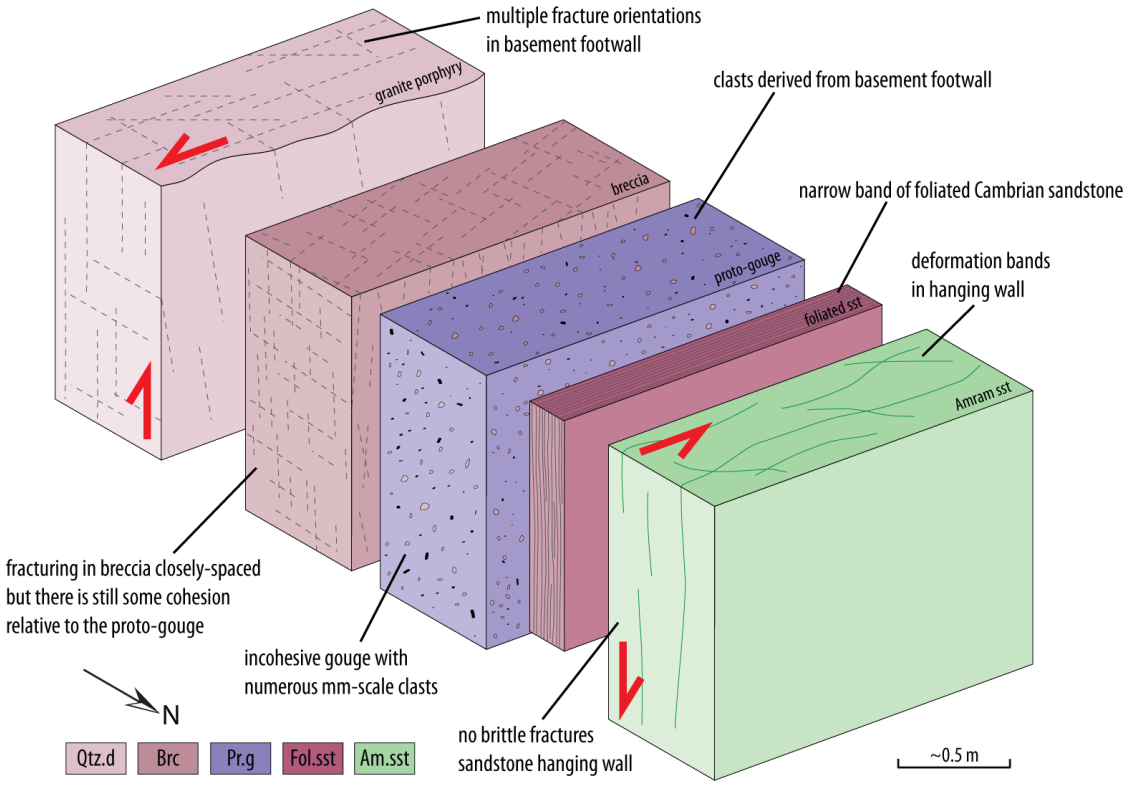

Figure 2.52: *Schematic block diagram, summarising the structural features of the Roded Fault: the footwall basement-hosted damage zone is variably fractured with the prevalent orientation being sub-vertical; there are few fractures in the hanging wall clastic-hosted damage, but there are normal faults with cm offsets. The fault core is composed of a foliated, fine-grained fault gouge in the western part and cohesive - incohesive cataclasite in the eastern part.*

2.6.2.6 Yehoshafat Fault

The Yehoshafat Fault is a 1.5 km long, generally N-S striking, dominantly dip-slip, intra-graben fault that transects Lower- to Mid-Cretaceous cover rocks. Displacement estimates range from 129-3089 m, with a most confident of 190 m (Table 2.1). For approximately 500 m along the central portion there is a 5-10 m wide fault core, which consists of entrained shale from the adjacent wall rocks . At the locality studied (Fig. 2.18a), the fault forms a steep, high-sided gully with a discrete, sub-vertical fault plane defining the eastern margin. The fault plane is sub-vertical and curviplanar, with a mean orientation of 000/89W at this location.

Protoliths At the studied section, the hanging wall to the east is composed of the Upper Cretaceous Grofit carbonates, whilst in the western footwall is the Lower Cretaceous Samar formation sandstone (Fig. 2.53a,b). The sandstone is massively bedded with few features being observed when close to the outcrop; it is only when standing a few tens of metres away that beds become apparent. The sandstone is medium grained, relatively well-lithified and pale pink in colour; fresh surfaces are quite rare, with most outcrops being covered in a fine-grained weathered coating. On the hanging wall side, the Grofit carbonates consist of massively bedded limestone

(with beds in excess of 1 m thick) along with interbedded limestone and shale; the beds here are much thinner, generally 5-10 cm for the limestone and finely laminated at the millimetre-scale for the shale.

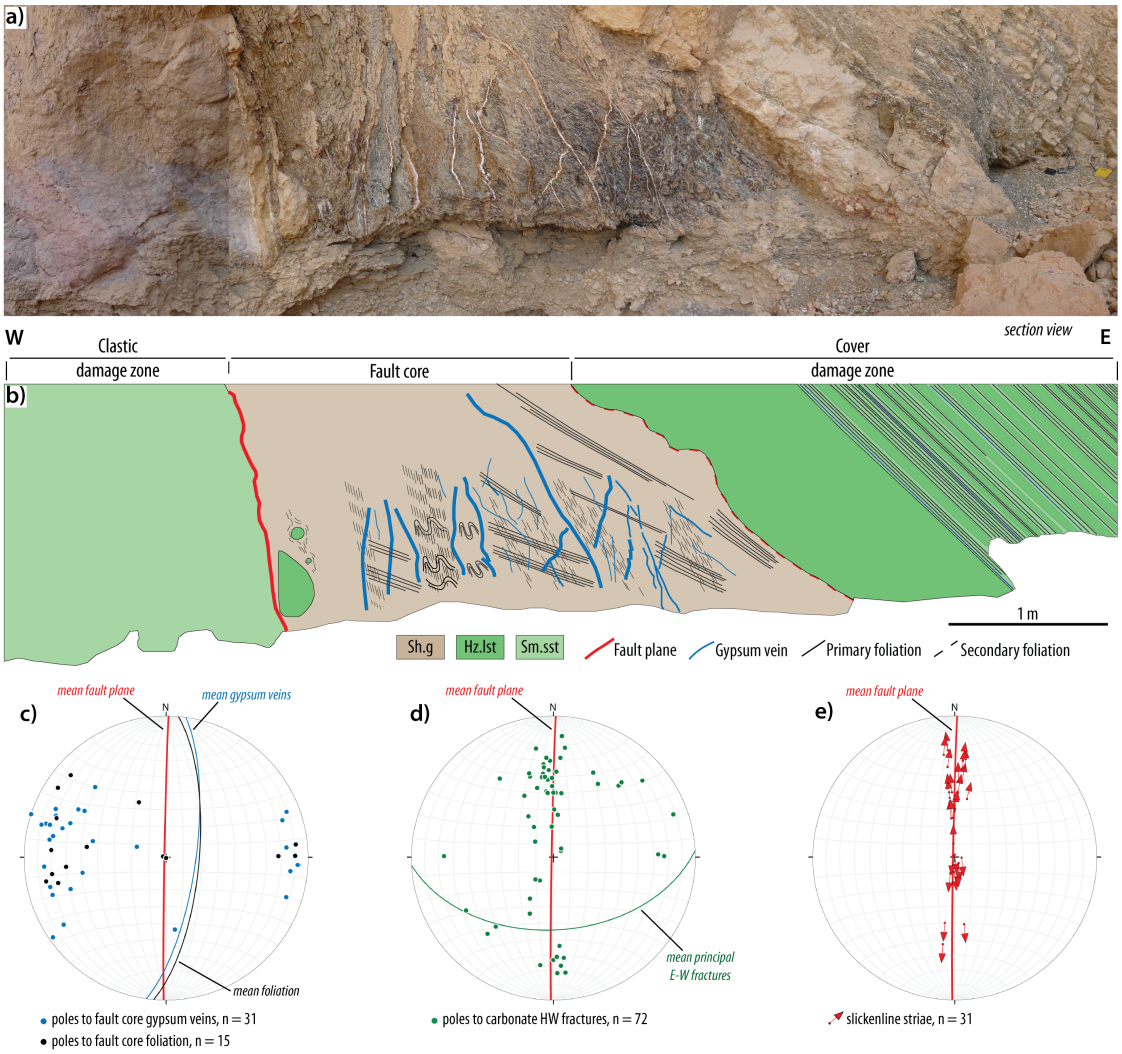

Figure 2.53: *Summary section of the Yehoshafat Fault:* ***(a)*** *Photograph of fault section;* ***(b)*** *Oblique section view with lithologies and main structures highlighted: the fault core is composed of foliated shale gouge. The dominant foliation is approximately parallel to the bedding in the hanging wall damage zone and there is a secondary, less obvious sub-vertical foliation. In the western part of the fault core, close to the main fault plane, the primary foliation is folded with ~vertical axial planes;* ***(c-e)*** *stereonets showing main structural features of the fault zone:* ***(c)*** *fault core foliation and gypsum veins; gypsum veins are parallel to the foliation and both dip steeply, sub-parallel to the mean fault plane;* ***(d)*** *carbonate hanging wall fractures; there is some scatter but the main trend is E-W, dipping moderately to the south;* ***(e)*** *slickenline striae on the main fault plane; there are three groups of slickenline orientations, those that dip sub-vertically and those that dip obliquely to the north and the south, suggesting multiple phases of movement on the fault.*

Sandstone cover-hosted footwall damage zone The sandstone of the footwall damage zone is pale pink and massively bedded, weathering at the base of the outcrop obscures them (Fig. 2.54), but the beds have an apparent dip of 30-35°E (Fig. 2.54). It is a relatively coarse-grained sandstone and does not appear to have a significant amount of cementation between grains; it is competent but not very cohesive, and grains can easily be scraped away with a hammer.

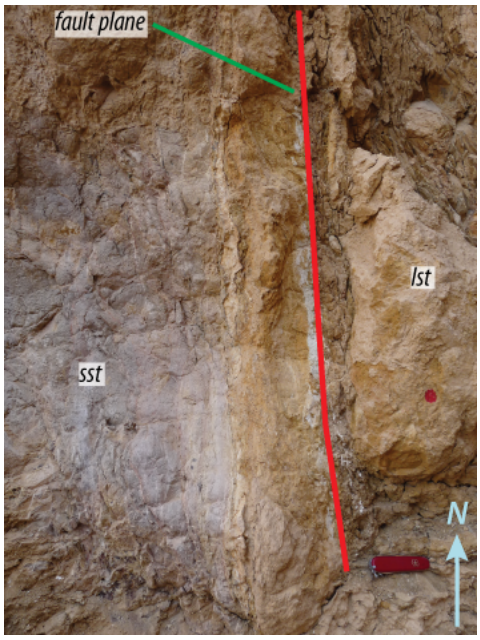

Figure 2.54: *Photograph of the Yehoshafat Fault footwall damage zone.*

At the mesoscale, deformation is confined to through-going fractures that are poorly-defined; within approximately 5 m of the fault core there are variations in colour, suggesting there has been fluid flow and subsequent alteration or precipitation of minerals along these pathways. Although the fault plane is not exposed in the bottom of the gully, there is a sharp, sub-vertical boundary between the sandstone damage zone and the fault core (Fig. 2.54).

Carbonate cover-hosted hanging wall damage zone

The hanging wall damage zone consists of interbedded marly limestone and shale (Fig. 2.55a), passing into limestone further from the fault core, and does not preserve evidence of any extensive brittle deformation. Beds vary in thickness from <5 cm (marly limestone) to massive (>1 m, limestone). The shale layers are extremely friable and relatively brittle. The mean orientation of the bedding in the damage zone close to the fault is 000/65E and there are also parallel gypsum veins. Fibre-growth orientation of gypsum within the veins is normal to vein walls, and are therefore interpreted as tensile fractures.

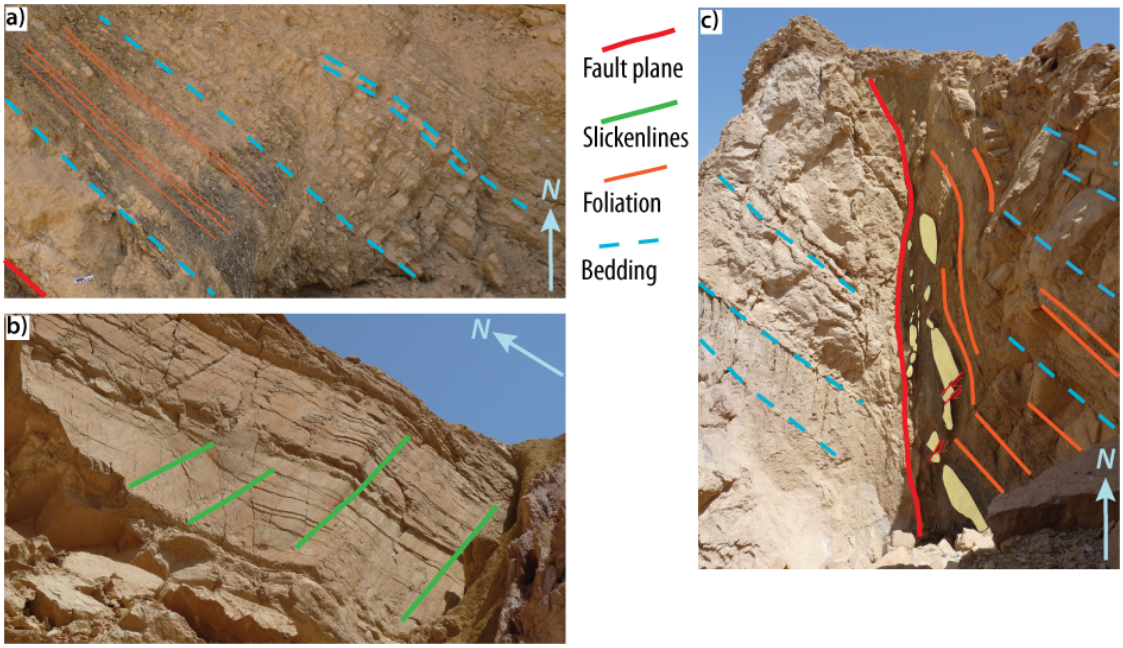

Figure 2.55: *Photographs of the Yehoshafat Fault zone hanging wall:* ***(a)*** *interbedded limestone and shale of carbonate-hosted damage zone;* ***(b)*** *carbonate-hosted fault plane with metre-scale striae (height of cliff exposure is ~30 m);* ***(c)*** *entrained shale within fault core.*

Although not exposed in the bottom of the gully, the eastern edge of the fault core is defined by a sub-vertical, curviplanar limestone fault plane, which is exposed approximately 50 m south of the main outcrop. This plane is smooth and polished, and slickenlines of varying pitches are present. Slickenlines can be divided into two main groups, plunging near vertically and more moderately (48°) to the north, indicating there have been multiple phases of movement. There are no clear overprinting relationships between these two groups, suggesting movement on the fault may

have been stepped, rather than in distinct phases of oblique- and dip-slip. Large-scale, oblique slickenlines, continuous over several metres, are visible when standing 10s of metres away from the outcrop (Fig. 2.55b). Bedding here dips much more shallowly (~27°), suggesting there may have been an element of fault-drag where more mobile lithologies, such as shale, are present and that the limestone behaves more rigidly (Fig. 2.55c).

There are 'steps' within the limestone-hosted fault plane, which may initially appear to suggest that the sandstone is the down-thrown side (Fig. 2.55b), the position of Samar Sandstone relative to the Grofit Limestone in the stratigraphy (it is older, Fig. 2.4a) does not allow for this to be the case. The likely explanation for this feature, then, is that there has been some degree of slip along eastward-dipping limestone beds, causing them to protrude slightly from the fault plane (Fig. 2.55c and shown schematically in Fig. 2.57). The relative timing of this must post-date movement on the fault, and may be related to exhumation.

Fault core The Yehoshafat Fault is unique in that the exposed section studied is approximately 30 m in height and we can observe the fault core approximately parallel to the fault orientation as well as orthogonal to it. The fault core consists entirely of shale, which is present along the fault for the entire height of the cliff at this location (Fig. 2.55b). The shale is finely foliated (mean orientation 017/39E; similar to damage zone bedding but with a rotation of strike to the east) and friable, appearing relatively homogeneous in grain size; it is very fine-grained with no clasts visible at the mesoscale. The foliation is locally folded on the order of tens of centimetres, generally with steep ~N-S axial planes verging to the west (Fig. 2.56a). On occasion, however, some folds appear to have been tilted to near-recumbent, with axial planes dipping gently towards the east. There is a secondary, steeper foliation which cross-cuts the bedding-parallel foliation at a high angle (Fig. 2.56b).

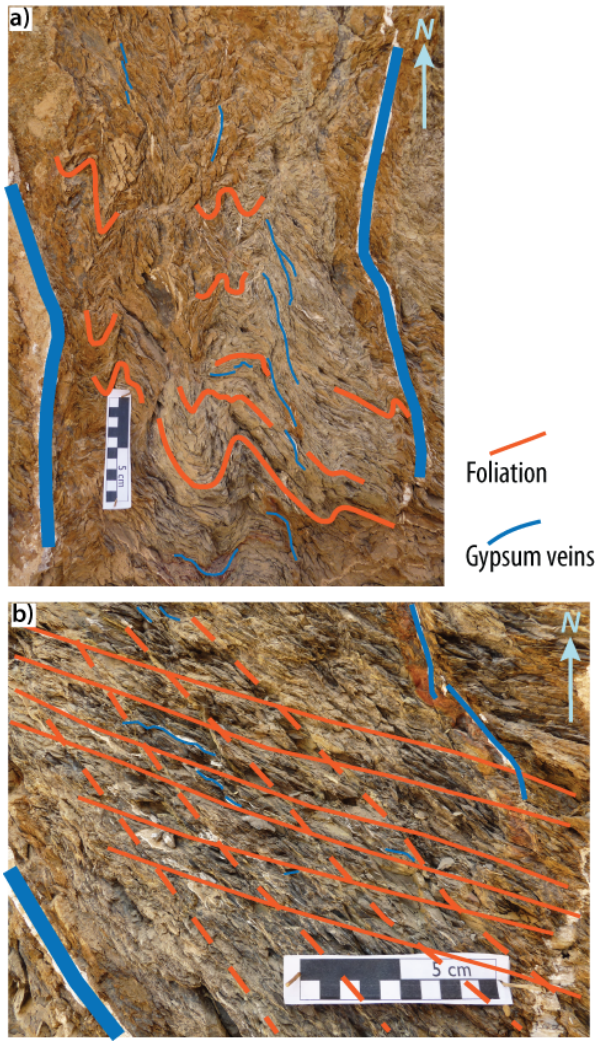

Figure 2.56: *Photographs of the foliated shale within the Yehoshafat Fault core:* ***(a)*** *folds in shale gouge;* ***(b)*** *oblique foliations in shale gouge.*

The foliation has a mean orientation of 173/85E and appears to be axial planar to the upright folds. The orientation of the secondary foliation relative to the main foliation indicates that an S-C fabric developed during faulting. Gypsum veins are present and have a similar, if more varied, orientation to the secondary shale foliation, with strikes of NNW-SSE - NNE-SSW and dips ranging from 18-90° (mean 188/73E). The strong foliation across the width of the fault core

preserves evidence of distributed and continuous deformation at the mesocale, with no obvious zones of shear localisation.

Summary The Yehoshafat Fault is a relatively short (1.5 km) fault within the Cretaceous cover sequence of rocks; it has an estimated displacement of approximately 190 m, which falls within the upper part of the range of displacements as a percentage of total fault length (13%). Fault rocks within the core of the fault consist only of shale, which appears to have been incorporated into the fault zone from the Ora Formation shales of the hanging wall carbonate sequence. At the studied location the hanging wall rocks on the eastern side of the fault consist of Grofit Limestone (the unit directly overlying the Ora Shales, Fig. 2.4a) and the western footwall rocks are the Samar Formation sandstone. There is little obvious deformation in the footwall rocks, but in the hanging wall there appears to have been a significant amount of fault drag, tilting the interbedded shales and limestone to the near vertical close to the fault core; bedding within the fault core shales is also very steeply dipping (Fig. 2.55).

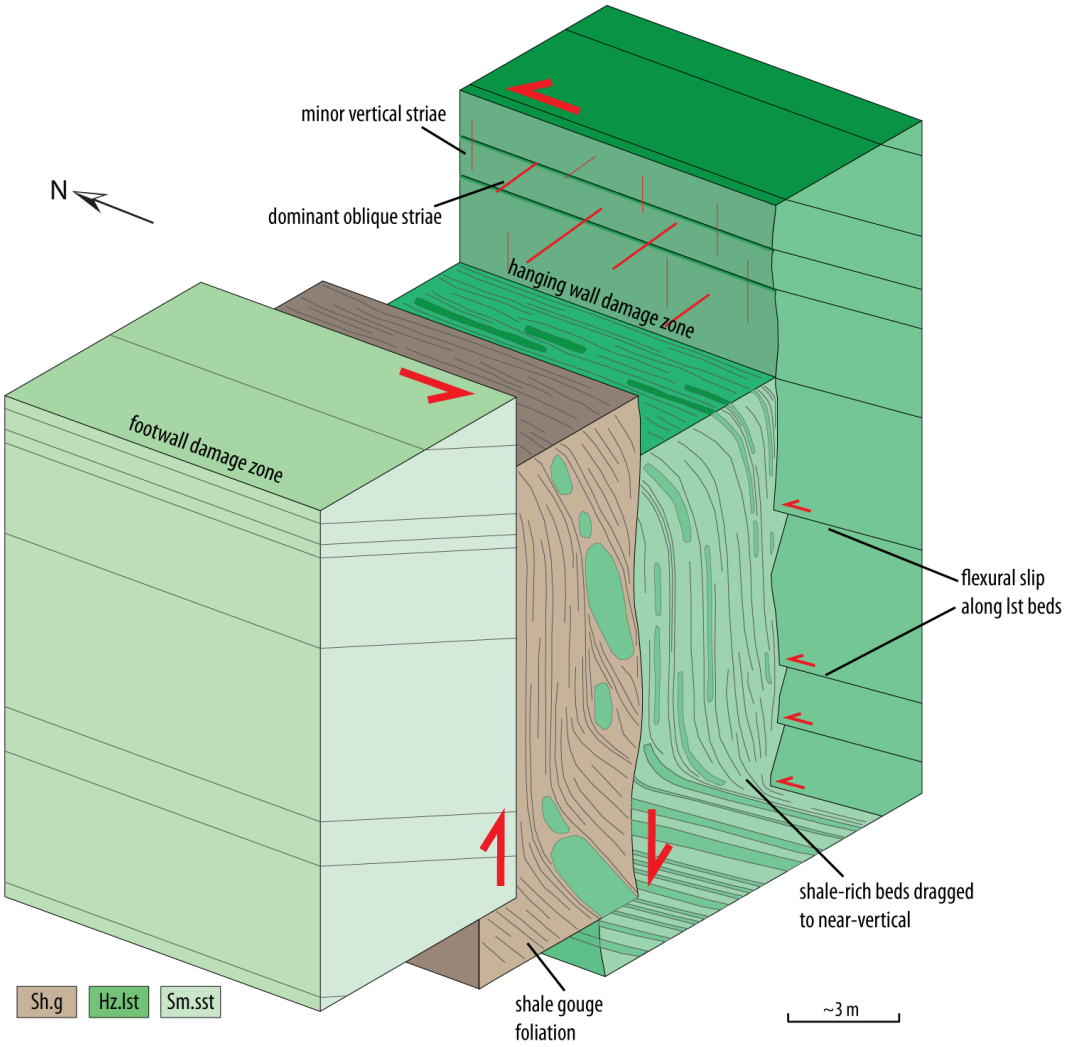

Figure 2.57: *Schematic block diagram summarising structural features of Yehoshafat Fault zone: a wide fault core of foliated shale gouge is bounded by a sandstone footwall and carbonate interbedded with shale hanging wall. There appears to be very little brittle deformation, with few fractures in the damage zones closest to fault core There is evidence of fault drag in the thinner beds of the hanging wall carbonates and shale, whilst the more rigid, massive limestone beds are more resistant. Bedding-parallel slip in the massive limestone gives the appearance of steps in the limestone fault plane. Small-scale dip-slip slickenline striae are present on the fault plane, but oblique-slip striae are dominant.*

2.6.2.7 R12 Fault

The R12 fault is a minor, intra-graben fault with an estimated displacement of 57 m (the minimum and most confident estimate, the maximum being 1579 m), making it the lowest (estimated) displacement fault of this study. The outcrop is located along the R12 road, which cuts the fault approximately perpendicular to its strike. The trace of the overall fault in map view is curvilinear, but at this location trends ~N-S and has a mean orientation of 170/75E. The studied section is 30 m long, though most of this is concentrated in the carbonate hanging wall since in the footwall the outcrop is cut by an access road. Although the Hazera Formation is generally relatively competent and can form massive bedding, in the area around the R12 Fault zone it is much more thinly bedded (<10-~40 cm) and is interbedded with thin layers of shale.

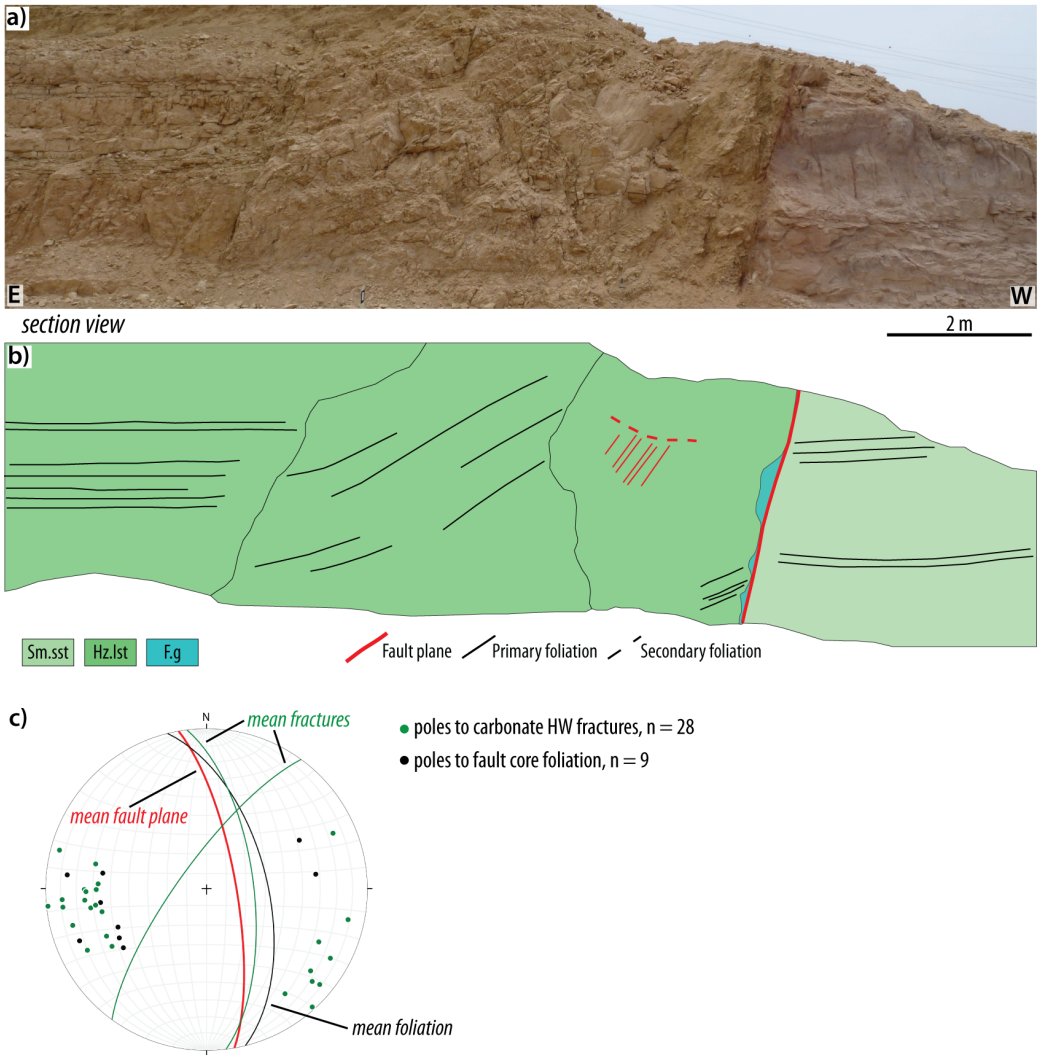

Figure 2.58: *Summary section of the R12 Fault:* ***(a)*** *Photograph of fault section;* ***(b)*** *Section view with lithologies and main structures highlighted: bedding in the footwall damage zone appears relatively undisturbed, even very close to the fault core; bedding in the hanging wall can be seen to steepen westwards towards the fault core and may indicate some degree of fault drag. Bedding is disturbed and less obvious in the damage zone immediately adjacent to the fault core (Hz.lst: Hazera limestone; Sm.sst: Samar sandstone: F.g: fault gouge);* ***(c)*** *stereonet summarising main structural features: the fault core foliation and one group of hanging wall fractures are sub-parallel to the main fault orientation, whilst a second group of hanging wall fractures are oblique to it.*

Protoliths The footwall of the R12 Fault is composed of Samar Formation sandstone, as described in Section 2.6.2.6, although there is not sufficient exposure to see if bedding is on the same massive scale. In the hanging wall is a sequence of Upper Cretaceous Hazera Formation carbonates,

which is conformable with the Samar sandstone in the unfaulted stratigraphy, supporting the low displacement estimate presented in Table 2.1. The carbonate sequence at this location consists of interbedded limestone and shale, with bed thicknesses ranging from approximately 5-100 cm. Bed thickness does not alternate uniformly.

Carbonate damage zone The carbonate damage zone is approximately 5 m wide and can be subdivided into three domains, each preserving evidence of decreasing intensity of deformation. In the metre adjacent to the fault to the east the limestone is fractured and fragmented but the bedding is still visible (Fig. 2.59a). This zone is incohesive and friable, and although the bedding is still apparent beds are composed of 10-30 cm slices (Fig. 2.59b). 1-1.5 m east of the fault is a 1 m wide zone of breccia where no intact bedding is present. Clasts in this zone are angular and randomly oriented, and are held within a relatively loose, sandy matrix. The rock as a whole is incohesive and can easily be chipped away with a hammer. In the area 2.5-5 m east of the fault the original bedding can be seen, but it is tilted up to an apparent dip of 20-30° and gradually returns to the sub-horizontal approximately 5 m away from the main fault plane. At the edge of the brecciated zone, towards the top of the outcrop, there is a curviplanar fault plane with almost vertical slickenlines (88° apparent pitch). This minor fault plane is oriented obliquely, almost perpendicularly, to the main fault, and curves convexly with the strike rotating from NE around to the SE.

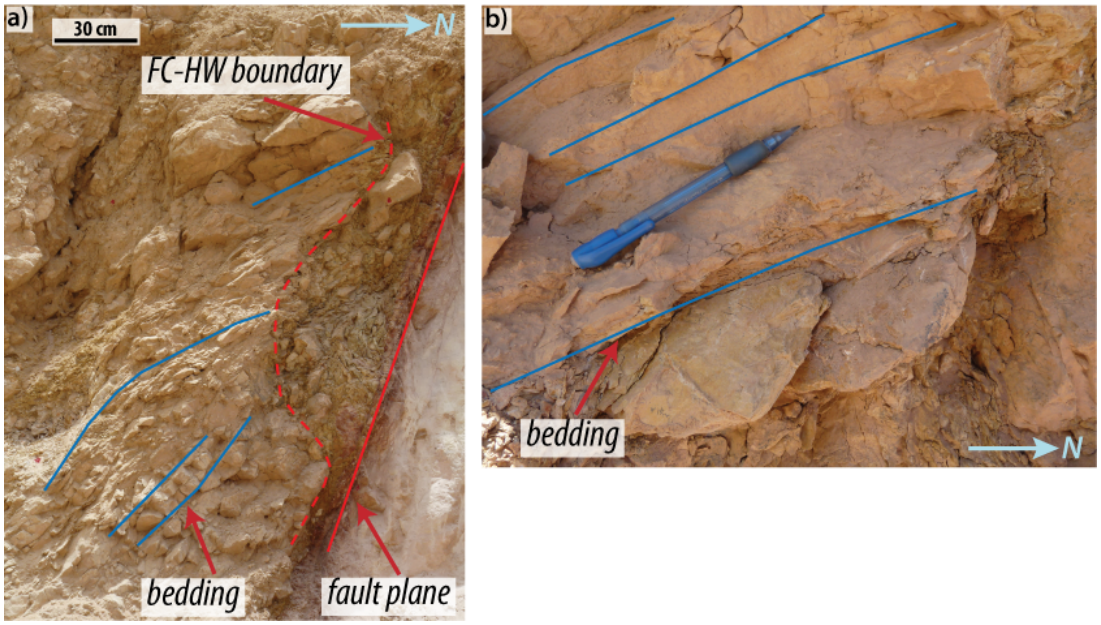

Figure 2.59: *Photographs of the R12 Fault carbonate-hosted hanging wall damage zone:* ***(a)*** *fractured carbonate hanging wall damage zone that is intensely fractured but bedding is still visible;* ***(b)*** *fractured limestone slices between bedding planes.*

Sandstone damage zone Mesoscale deformation in the sandstone footwall is much less obvious. The sandstone is poorly-cemented and very powdery in appearance, and as such few obvious fractures are preserved (Fig. 2.60a). Close to the fault (<1 m) however, there are some poorly-defined fractures. These occasionally form discrete planes, but more often do not appear to mark any obvious discontinuity in the rock other than a red-coloured discolouration along them and they appear to be slightly more resistant to weathering (Fig. 2.60b). The general trend of these fractures is sub-parallel to the fault plane and they are continuous for ~20-100 cm (1-3 mm wide),

though there is also a similar red discolouration along short (<10 cm long, 1 mm wide), curvilinear zones which are oblique to the main fault plane. Bedding on this side of the fault is sub-horizontal and does not appear to be disturbed as it approaches the fault.

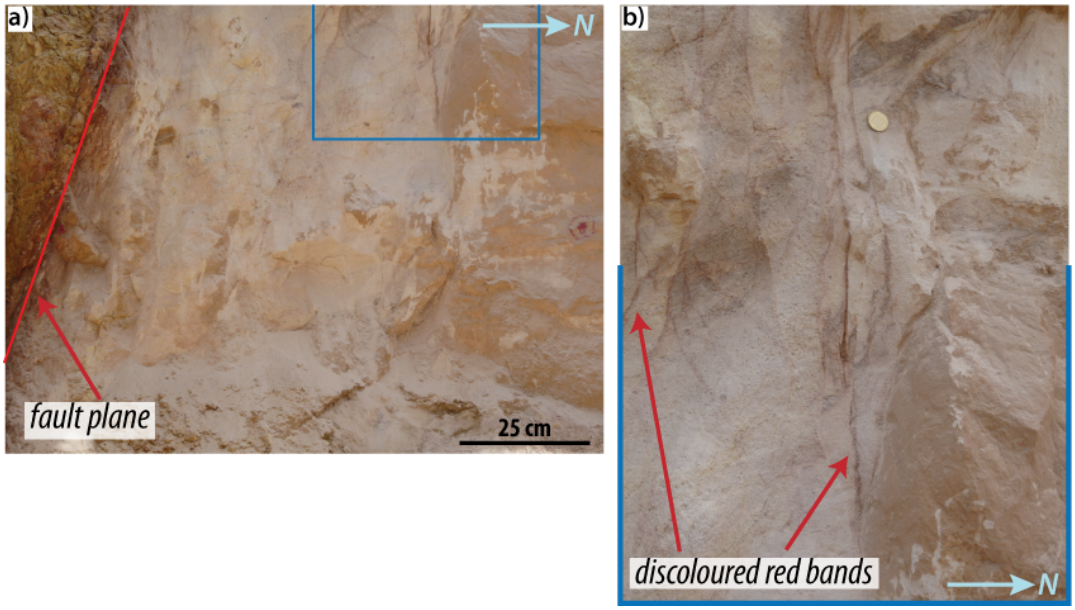

Figure 2.60: *Photographs of the R12 Fault footwall:* ***(a)*** *footwall damage zone directly adjacent to the fault core. There are few obvious signs of brittle deformation at the mesoscale but the rock is extremely incohesive and powdery in appearance;* ***(b)*** *poorly-defined 'fractures' that are defined by a red discolouration and slight resistance to weathering compared to the surrounding rock.*

Fault core At this location, the fault core is narrow and ranges from 10-40 cm in thickness (Fig. 2.61a). It can be divided into three layers: a sandstone layer at the western edge, which is ~5 cm wide, with a fault-parallel lamination but which is cohesive, and is poor in clasts (Fig. 2.61b); another 5 cm-wide layer that has a very fine-grained, red coloured matrix with abundant clasts of both carbonate and sandstone, ranging in size from 1-10 mm; and a green/brown-coloured foliated clay-rich layer that varies in width from 5-40 cm, the widest part appearing to bulge away from the main fault plane.

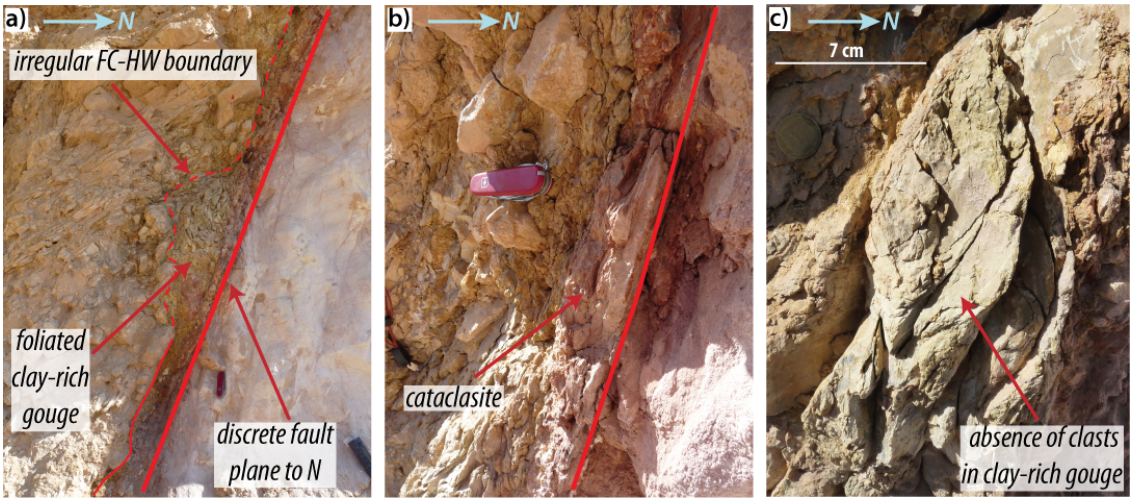

Figure 2.61: *Photographs of the R12 Fault core;* ***(a)*** *fault core varies in width from 5-40 cm due to presence of clay-rich gouge. The boundary between the fault core and the damage zone is a discrete fault plane to the north and a more diffuse, irregular boundary on the southern side;* ***(b)*** *the northern part of the fault core, adjacent to the footwall sandstone, is composed of a 5-10 cm wide band of cohesive cataclasite;* ***(c)*** *the clay-rich gouge contains no clasts of foot- or hanging wall rocks and is similar in appearance to the shale interbeds seen in the adjacent limestone stratigraphy.*

The foliation of the clay-rich layer is generally sub-parallel to the fault, except in the wider zone. There are relatively few clasts in this layer, although there does appear to be evidence of intermixing of the sand-rich and clay-rich layers as there are occasional, elongate 'pods' of red, clast-rich material within the clay zone (Fig. 2.61c).

Summary The R12 Fault is the smallest in terms of length (1.1 km) and estimated displacement (60 m) and juxtaposes two units that are conformable within the unfaulted succession (the Samar Sandstone and Hazera Limestone, Fig. 2.4a). The fault core comprises both a narrow band of cataclasite that is uniformly approximately 5 cm wide (Fig. 2.61a), and a foliated, clay-rich fault gouge that varies in width from approximately 10-40 cm (Fig. 2.61a). A schematic summary of the R12 Fault zone is shown in Fig. 2.62.

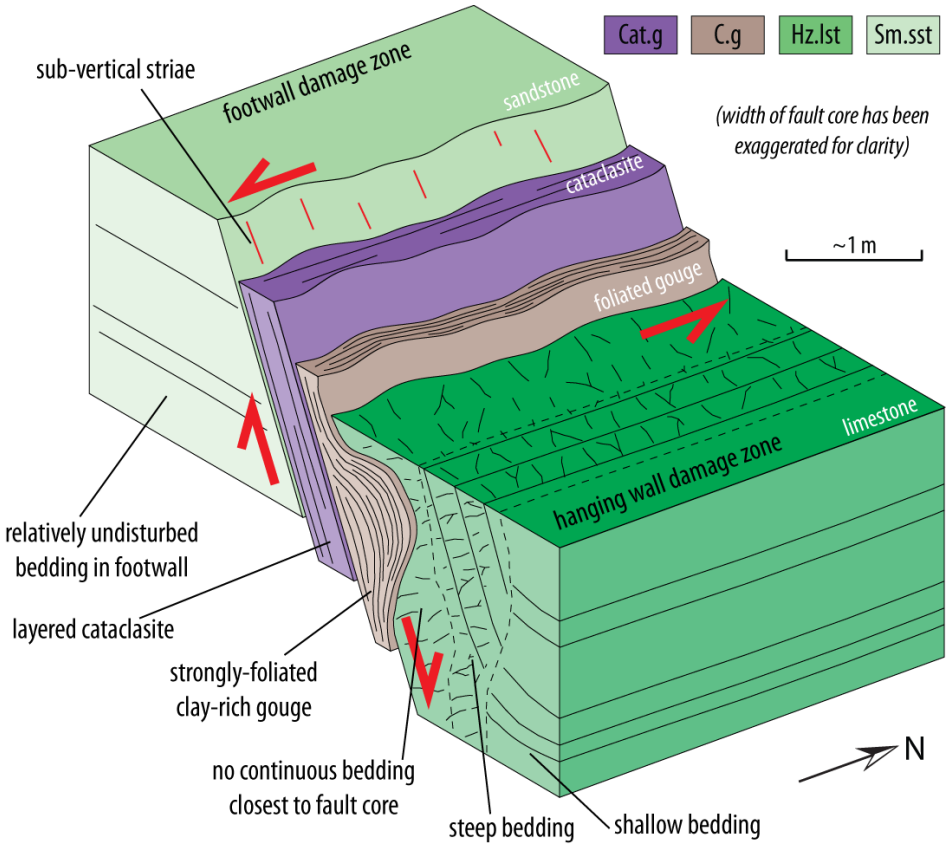

Figure 2.62: *Schematic block diagram summarising the structural features of the R12 Fault: the fault core is divided into two distinct zones, a well-defined, cohesive cataclasite to the north, adjacent to the footwall and a friable, foliated clay-rich gouge to the south, adjacent to the carbonate hanging wall. In the sandstone footwall there is little evidence of brittle deformation but the rock is extremely incohesive and powdery, whilst the hanging wall is more intensely fractured, though the bedding is still visible.*

2.7 Discussion

2.7.1 Nature and significance of DSFS structures

The faults presented here represent structures of a range of length, displacement and lithologies and as such are highly variable in terms of both geometry and fault rocks. There is no clear relationship between fault length or displacement and fault core width (Fig. 2.63); indeed, the Yehoshafat Fault is the shortest structure with the second lowest estimate displacement and yet has the widest fault core, joint with the Tzefahot Fault at 4 m. The thickness of the shale fault core of the Yehoshafat Fault is supportive of the low displacement estimate of this fault, as had displacement been greater we would expect a thinner layer of shale within the fault core as it is progressively smeared out (Fig. 1.5). The Yehoshafat and Tzefahot faults share the common feature of having entrained shale gouge within the fault cores, suggesting that the incorporation of shale has an influence fault core width. It cannot be the only factor, however, as even without considering this mechanism there is still no clear relationship between fault core width and displacement; the Tzefahot and Shelomo faults, for example, are of comparable length and estimated displacement yet the cataclastic part of the Tzefahot Fault core is still more than twice the width (2.5 m) than that of the Shelomo Fault (1 m) (Fig. 2.63).

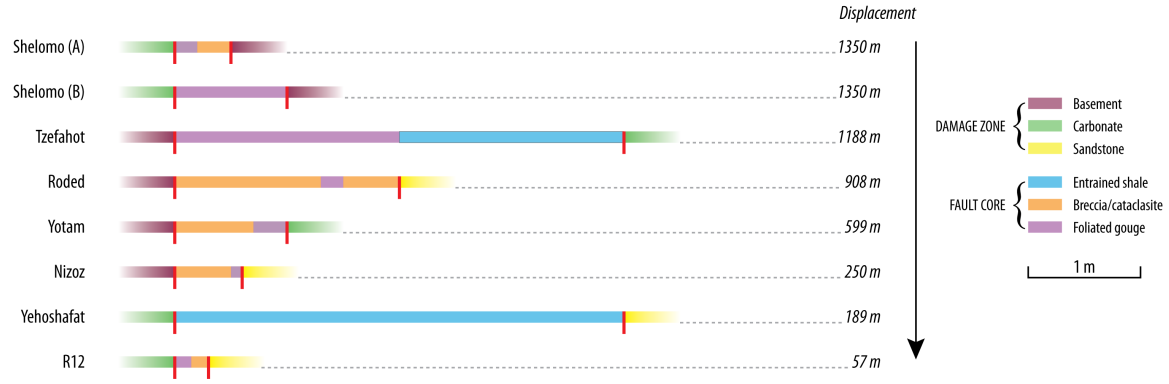

Figure 2.63: *Scale diagram showing relationship between fault core width and estimated displacement: there is no linear relationship between the amount of estimated displacement and fault core width. Fault cores where entrained shale gouges are present are the widest, though, even where displacement is low. Fine-grained fault gouges and cataclasites/breccias are present in all but one fault core and vary in width from 0.25-2.5 m.*

Brittle fault products within the fault zones also vary and can be broadly distinguished as very fine-grained, variably foliated gouges that are generally very friable, and coarser-grained breccias and cataclasites that vary in cohesiveness. There does appear to be some relationship between fault displacement and the nature of fault core materials as the highest estimated displacement faults (the Shelomo and Tzefahot faults) contain the highest proportion of fine-grained gouge, whilst the intermediate displacement faults (the Roded and Nizoz faults) also contain a significant amount of coarser breccia and cataclasite. It may be inferred from this that the fine-grained gouges form later during the fault history and are the product of continued grain comminution, of which cataclasites are an earlier stage product.

However, this hypothesis makes it at first sight difficult to account for the presence of very fine-grained, apparently clay-rich material in the fault core of the R12 Fault, which has the lowest estimated displacement (57 m). A possible explanation for this is that the clay-rich gouge at this

location is actually entrained rather than cataclastic in origin; the Hazera formation limestones at the location of the R12 Fault outcrop contain numerous shale beds interbedded with the carbonate and it is possible that some of these were incorporated into the fault core. This is supported by the general lack of clasts within this portion of the fault zone, a feature also observed in the shale gouges of the Tzefahot and Yehoshafat faults. Whether the gouge is entrained or cataclastic in origin can only be determined by describing its mineralogy and textures in thin section (see Chapter 3).

It is also interesting to note that fine-grained, clay-rich gouges and cataclasites are generally present as distinct zones; we do not frequently observe mixed zones of cataclasite and fine-grained material at the mesoscale. If the process of gouge-formation described above is correct, this indicates there may have been some degree of strain partitioning within the fault zones, leading to either narrow zones (e.g. Roded and Yotam fault) or more significant sections (e.g. Tzefahot and Shelomo faults) of the fault cores accommodating more strain and becoming more intensely deformed as a result.

Although we would usually expect deformation to be most intense towards the central portion of a fault and dying out towards the tips, it may be the case here that since the Roded Fault overlaps with the Shelomo Fault in the south (Fig. 2.4a), the deformation was actually more intense towards its southern tip.

2.7.1.1 Initial model of fault zone development

The exhumed faults studied in the area around the town of Elat may be categorised in three ways: those containing cataclastic fault rocks (cataclasites and gouges); those containing cataclastic and entrained fault rocks (Ora Shale from the adjacent formation); and those containing only entrained fault rocks. In faults where no entrained shale is present, we expect initial deformation to be accommodated by processes typically associated with the formation of fault gouges (Engelder, 1974); that is, by brittle fracturing and frictional sliding, and that as displacement (and strain) increases, by rotation and comminution of grains (Fig. 2.64, stages 1 and 2). The Nizoz (stage 1) and Roded and Yotam (stage 2) faults are thought to represent examples of this.

However, the formation of fine-grained fault gouge through cataclastic processes does not account for the strongly foliated nature of gouges observed in many of these faults, particularly the Shelomo and Tzefahot faults (Fig. 2.64, stage 3). Although Engelder (1974) noted the alignment of microfractures within fault gouge (parallel to σ_1), the presence of such features would not account for a through-going foliation that appears to be defined by the alignment of grains (possibly clay minerals). In addition, the foliation seen here is generally sub-parallel to the fault plane and not parallel to σ_1. It is therefore inferred that other microscale processes, in addition to cataclasis, have taken place to form the type of fault rocks observed in the highest displacement faults and this model will be revisited after detailed mineralogical and microstructural analysis of the fault zones (Chapter 3).

In the case of fault zones where entrained shale is present within the fault cores (principally the Tzefahot and Yehoshafat faults, and possibly also the R12 Fault), we believe that the time at which

shale is incorporated is a critical influence on the type of fault rocks formed, since it may cause an interruption of cataclastic deformation within the fault core. Although clay minerals have a range of friction coefficients, from approximately $\mu = 0.6$ for kaolinite (Byerlee, 1978) down to $\mu < 0.15$ for wet smectite (Saffer and Marone, 2003; Moore and Lockner, 2007), it is likely that shales contain at least some weak material and even a relatively small volumetric content may be sufficient to significantly affect the overall frictional strength of a material if it is present as continuous layers (Rutter et al., 2013), which is likely to be the case in the strongly foliated Ora Shale. In this case, the introduction of a relatively large volume of a frictionally weak material into a fault core is likely to result in the majority of the strain being accommodated by 'ductile' deformation in this zone. The effect of the incorporation of shale into a fault zone at various stages of fault development is shown in Fig. 2.64, stages 1a-3a. At the Yehoshafat Fault only entrained shale is found within the fault core and there is very little evidence of any cataclastic deformation, suggesting shales were incorporated relatively early in the fault history. At the Tzefahot Fault, however, entrained shale accounts for approximately half of the width of the fault core, whilst the other part consists of cataclastic fault gouge; in this case, it is inferred that shales were incorporated relatively late in the evolution of the fault, when significant cataclasis had already occurred. This model will be revisited in the following chapter after microstructural and mineralogical analyses (Chapter 3).

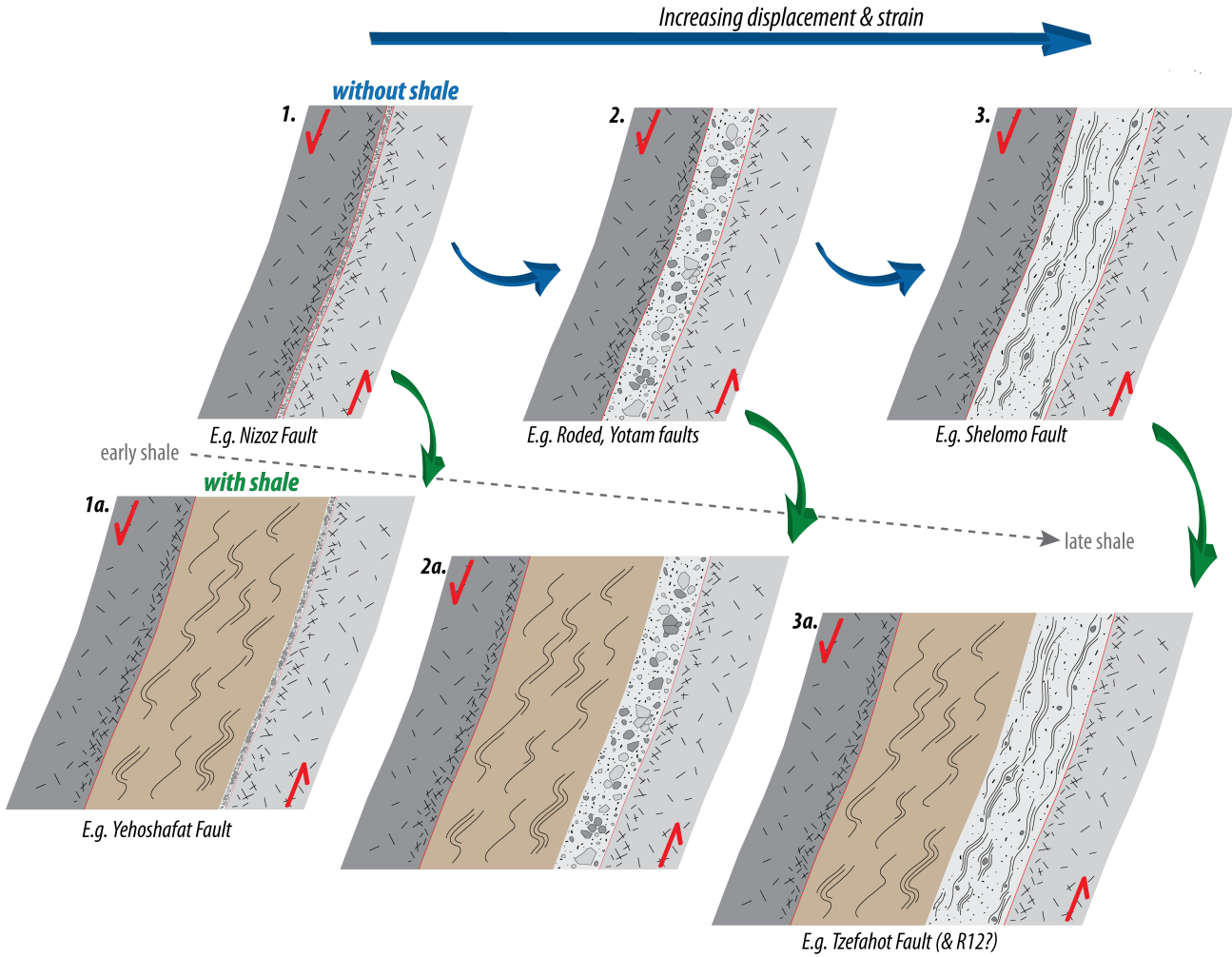

Figure 2.64: *Schematic model of fault zone development, showing possible effect of shale entrainment: where no shale is present (1 - 3), deformation is largely cataclastic and fault cores remain relatively narrow, but may show some increase in width with increasing strain and displacement. There is the development of a foliation in well-developed fault gouges, though it is unclear at this stage whether this is only the product of cataclasis and brittle processes or whether some other mechanism is also involved. The incorporation of shales into fault cores (1a - 3a), can lead to faults of low displacements having wide fault cores. It is possible that the stage at which shales, which potentially have low frictional strengths, depending on their mineralogy, may control when cataclasis stops and strain is instead accommodated by frictional sliding along the pre-existing shale foliation.*

2.7.2 Regional transtension and local structures

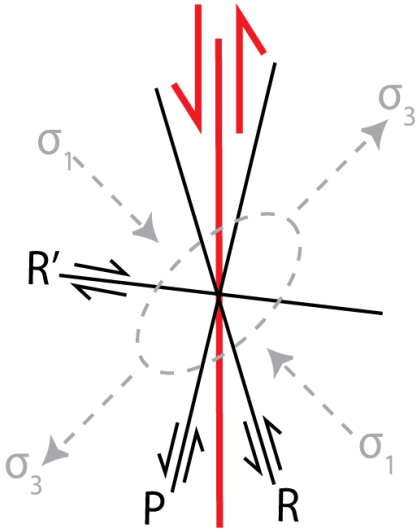

Figure 2.65: *Schematic summary of minor structures associated with strike-slip faults: R = synthetic shears; R′ = antithetic shears (conjugate with R); P = secondary synthetic shears.*

Previous descriptions (e.g. Garfunkel, 1981; Ben-Avraham et al., 2008) of the DSFS have noted the presence of pull-apart basins and compressional ridges along its length in areas of fault bends and overlaps, indicating local areas of transtension and transpression (e.g. Quennell, 1958; Reches, 1987; Eyal et al., 1986; Marco et al., 2005). However, combining field data with regional stress orientations, we observe that the southern part of the DSFS also fits into a broader transtensional regime, as described by Quennell (1984) and in contrast to the pure strike-slip in the southern Arava Desert determined by Le Pichon and Francheteau (1978).

Whilst it is relatively easy to predict the arrangement of minor structures relative to a conventional strike-slip fault (Fig. 2.65), the same set of structures, in the same orientations relative to the main fault, cannot be expected where there is an oblique transpressional or transtensional element to the regional stress field. In cases such as these, the structures associated with the main fault will be a result of the combination of pure and simple shear acting on it, and we must use their orientations to determine the relative influence of these shear components on the fault zone. Transpressional and transtensional fault systems can be classified as wrench-dominated (WD, where simple shear dominates) and compression- (for regions of transpression) or extension- (for regions of transtension) dominated (C/ED, where pure shear dominates, e.g. the South Island of New Zealand, Teyssier et al., 1995), and commonly as a combination of both (e.g. the Northumberland Basin, UK, De Paola et al. (2005); the western U.S. Cordillera, Oldow (2003); central California, Teyssier et al. (1995); and experimentally, Withjack and Jamison (1986); Smith and Durney (1992)).

In order to describe the type of strike-slip motion and degree of obliquity of the southern DSFS, we must constrain certain geometric properties of the region; the *transport direction*; the *boundary fault orientation* (orientation of the main DSF trace); and the maximum and minimum *horizontal stresses*. By examining the relationship between these properties and local structures, we can build a model describing the style of local faulting as follows.

The angle between the transport direction and the boundary fault is expressed as α; the angle between the infinitesimal maximum extension axis (or σ_3 for our purposes) and the boundary fault is expressed as β. α and β can be plotted together to determine whether an area is under extension- or wrench-dominated transtension. Since we do not know the palaeo-transport direction, we have carried out a simple stress inversion analysis, using a combination of the major structures in the area along with minor structures in the basement and cover rocks, to determine the palaeostress orientations of the region (Fig. 2.66a). Results yield an E-W extension (271°) which, when combined with the orientation of the boundary fault (020°, Beyth et al., 2014), give a β value of 71°; α is determined using the α vs. β plot shown in (Fig. 2.66b), and in this

case is approximately 50°, placing the region well within extension-dominated transtension. An α value of 50° equates to a transport direction of approximately 070°. Eyal (1996) determined a regional minimum horizontal stress (SH_{min}) direction of 074° during the Miocene (based on the assumptions described in Zoback (1992), such as that SH_{max} has a predictable relationship to the orientation of major fold axes, large strike-slip structures, tectonic stylolites and also using earthquake focal mechanism data), which, although is slightly rotated to the north from our E-W calculation, would yield a β value of 54° and still result in EDT. Present day global GPS velocity data (Kreemer et al., 2014) give a current transport direction of 030° (for the Arabian plate relative to the Sinai sub-plate), which is markedly different to our calculated palaeo-direction of 070°, suggesting there has been significant rotation of the regional stress field between the mid-Miocene and the present day.

These results at first appear to contrast with the work of De Paola (2004), who used focal mechanism solutions of modern earthquakes (1976-2004, Fig. 2.67) to determine the local stress field and calculated an overall α value of ≈10°. However, these results are divided into two components according to earthquake focal mechanisms (oblique-slip along the main fault trace, and strike-slip along marginal faults, Fig. 2.67). The data relating to oblique-slip faults only yield α and β values of 60° and 75°, respectively, which are broadly in accordance with our findings here (Fig. 2.66). Previous models have explained the local assemblage of faults by invoking block rotation (Eyal and Reches, 1983; Woodcock and Fischer, 1986), or a partly ductile (Reches, 1987) or weak (Sagy et al., 2003) crust beneath the Gulf of Elat-Aqaba (see De Paola, 2004, for a summary of these). However, with the exception of Sagy et al. (2003), these models only account for minor extension orthogonal to the main DSF. Our results indicate a vertical σ_1, suggesting strongly extensional transtension, with predominantly vertical rather than horizontal displacements in the marginal zone to the west of the main DSF. We suggest, therefore, that the

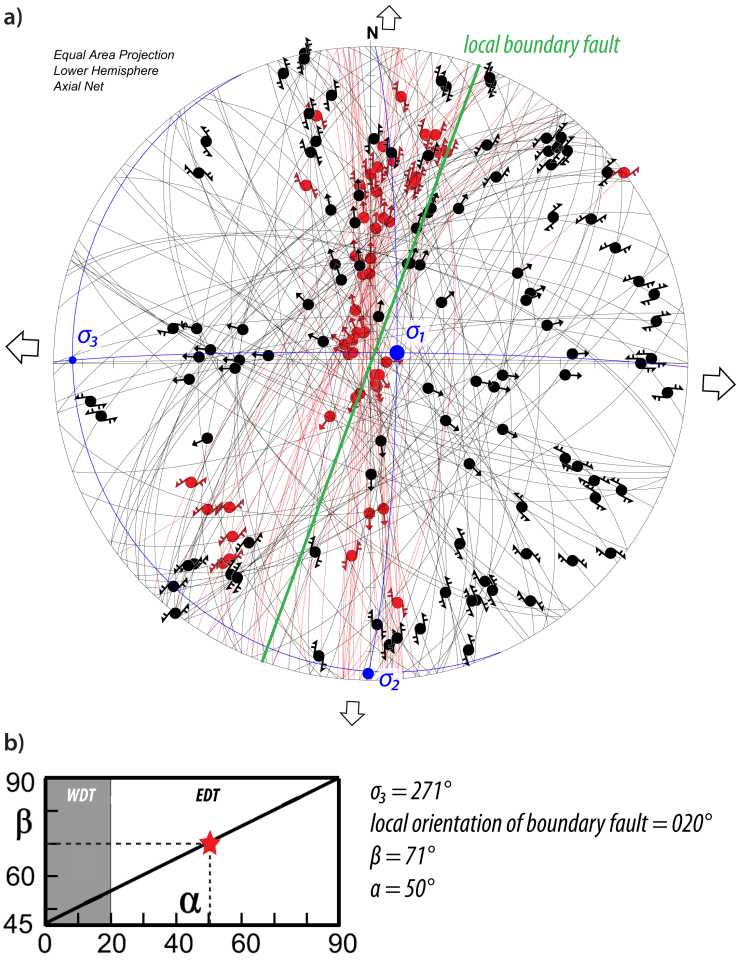

Figure 2.66: *Stress inversion analysis using structures in the region around Elat:* ***(a)*** *Stereonet showing major (red) and minor (black) structures of the region, with resulting palaeostress directions. The orientation of the boundary fault is shown in green;* ***(b)*** *α vs. β plot showing areas of EDT and WDT (modified from De Paola et al., 2005). Red star represents α and β for the southern DSFS and places the fault system in extension-dominated transtension.*

studied faults may well represent a relatively early local partitioning of strain, explained by the model proposed by De Paola (2004), at a time when the fault zone covered a much wider area, as suggested by Marco (2007), and the studied faults may have formed part of the central zone (Fig. 2.67e).

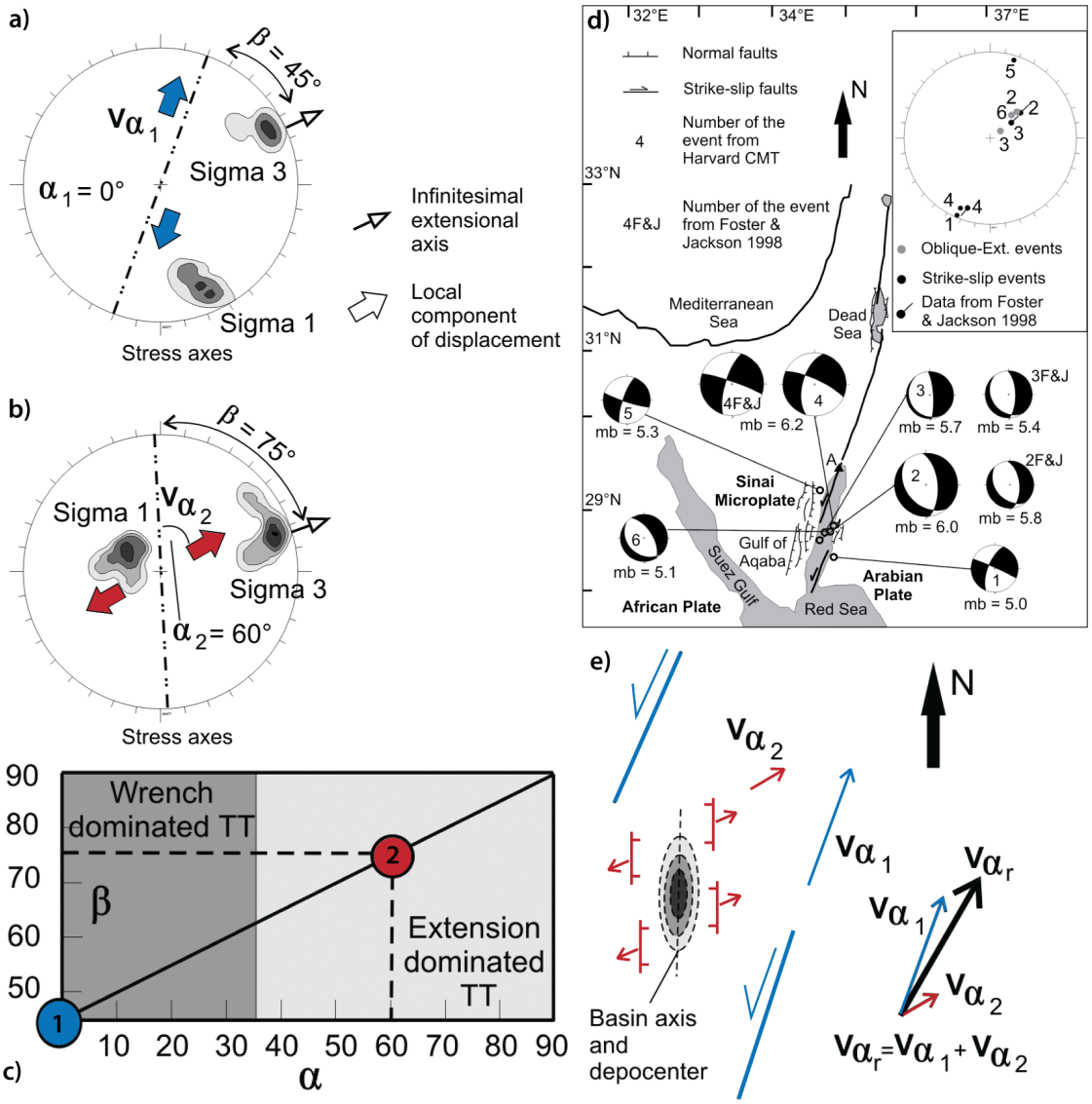

Figure 2.67: *Strain partitioning model for the southern DSFS proposed by De Paola (2004):* ***(a)*** *stress axes for strike-slip earthquakes;* ***(b)*** *stress axes for oblique-slip earthquakes;* ***(c)*** α *vs.* β *showing calculated* β *values based on information in (a) and (b);* ***(d)*** *earthquake focal mechanisms derived by the Harvard CMT (now known as the Global CMT) and Foster and Jackson (1998);* ***(e)*** *structural model showing oblique-slip faults in the centre of the Gulf of Elat-Aqaba and strike-slip faults at the margins.* $V\alpha_1$ *is transport direction of strike-slip faults,* $V\alpha_2$ *is transport direction for oblique-slip faults and* $V\alpha_r$ *is the regional transport direction (modified from De Paola, 2004).*

2.7.2.1 Influence of pre-existing basement structures on Miocene faulting

Although, as shown in Section 2.7.2, the arrangement of faulting in the area fits with an extension-dominated transtensional regime, there is some deviation of major structures away from this trend, most notably in the N-S orientation of the Tzefahot and Shelomo faults along their southern portions, and it is hard to explain this without invoking an additional influence, other than regional stresses.

Where the Tzefahot and Shelomo faults (along with the Gishron Fault, which has not been studied here because of its proximity to the border with Egypt) deviate to a N-S strike, there is also a strong N-S preferred orientation of ductile basement fabrics. The S-foliation of the Taba Gneiss, which outcrops most extensively in the Elat Block to the east of the N-S striking portion of the Tzefahot Fault, and to the south-west of the Gishron Fault, has a mean orientation of 001/34E. Although the dip of the foliation is much shallower than that of the main faults, we suggest that the strong preferred orientation of strike may create a sufficient plane of weakness to be exploited by the fault.

2.8 Conclusions

The macroscale study of exhumed faults in the area around Elat, southern Israel has demonstrated that not only are these faults related to movement of the DSFS, but also that the region was undergoing extension-dominated transtension at the time (likely mid-Miocence). However, it is likely that a strong pre-existing fabric in metamorphic basement rocks (specifically those of the Taba Gneiss), resulted in three structures (the Shelomo, Tzefahot and Gishron faults) deviating from a typical EDT-favourable orientation (NE-SW), to approximately N-S.

At the mesoscale, we have shown that displacement on the faults in this region accounts for <5% of the total displacement on the DSFS. Fault rock materials are variable and can be broadly defined as shale gouge, cataclastic gouge and cataclasite. There does not appear to be a simple link between the amount of displacement on a fault and the type of fault rocks present, nor is the influence of various lithologies (crystalline, carbonate and clastic rocks) immediately obvious. However, the presence of shale gouge is controlled by the presence of Ora Shale in the wall rocks and it may be that the timing of entrainment of these shales into the fault zones does markedly influence fault zone development. It remains to be addressed if the gouges of the cataclastic parts of the fault zones have been formed by brittle processes alone, or if mineralogical changes have also taken place. This will be considered through microstructural observations and analysis of fault rock mineralogy in Chapter 3.

3 The microstructural and mineralogical evolution of shallow crustal, heterogeneous fault zones

3.1 Introduction

We present observations and data here from six of the fault zones described in the previous chapter, comprising: two basement against carbonate cover faults (the Shelomo and Tzefahot faults); two basement against clastic cover faults (the Roded and Nizoz faults) and two carbonate cover against clastic cover faults (the Yehoshafat and R12 faults). These faults represent structures of varied estimated displacement (57-1350 m), nature (intra-graben and graben-bounding) and orientation (N-S, NE-SW and E-W). The results of the mesoscale study presented in Chapter 2 reveal that there are at least two distinct types of fault gouge present within the fault cores of the studied faults; *entrained shale gouge*, which has probably been mechanically incorporated ('smeared') into the fault zone directly from shales in the adjacent stratigraphy; and *cataclastic gouge*, of which the protolith/s has not yet been determined. It was not possible to definitively determine the protolith or mineralogy of either type of very fine-grained fault core gouge in the field and so it is important to do so using the methods presented below, in order to define not only the mineralogy and likely protoliths, but also to constrain the processes and mechanisms of deformation across the fault zones by. The following methods were used:

- Describing the microstructure of the fault zones and how these vary in terms of displacement and lithology;
- Describing the mineralogy of these fault zones and assessing its relationship to wall rocks and protoliths;
- Using these findings to describe the microstructural and mineralogical evolution of these shallow fault zones, and determine possible reasons for their observed heterogeneity.

The hypotheses to be tested are: *(1)* that the protolith of the *shale gouge* is the Ora shale and that it has undergone little to no change in mineralogy during deformation; and *(2)* that the protoliths of the *cataclastic gouges* are those rocks found in the hanging and footwall zones of each fault, and have undergone intense comminution of grains and/or mineralogical changes in order that very fine-grained gouges are produced. It is important to determine the mineralogy and microstructure of fault rocks as these properties can profoundly influence fault zone attributes such as fabric, permeability and frictional strength, which in turn can be used to determine potential fault behaviour. They also give insights into the role played by fluids during deformation and influence the fault zone porosity-permeability structure.

3.2 Methods, approaches and assumptions

Fault rock analysis was carried out on 60 polished thin sections and 51 powdered clay fraction samples (the number of samples analysed by XRD is fewer than those thin sections as not all samples contained enough clay material for analysis, see ix 2B for details). Polished thin sections were analysed using a Nikon Eclipse optical microscope (with attached DS-Fi2 camera) and a Hitachi SU-70 field emission scanning electron microscope (FE-SEM) at 15 kV accelerating voltage.

Sample mineralogy was determined using energy dispersive X-ray (EDX) for thin sections, and X-ray diffraction (XRD) of powdered clay fraction samples in a Bruker D8 Advance fixed plate X-ray diffractometer. EDX was performed using Oxford Instruments INCA software and was predominantly used to determine the mineralogy of crystalline minerals, which appear in grey-scale in back-scattered electron (BSEM) and secondary electron (SE) images. EDX does not have the resolution to identify many clay minerals due to their variable chemistry and propensity to take on impurities (kaolinite is a common exception). However, where samples were found (using XRD) to contain a single clay mineral, EDX was used to semi-quantitatively determine chemical composition. Where comments have been made on the chemical composition of clay minerals (e.g. Mg-bearing) this is the result of EDX analyses.

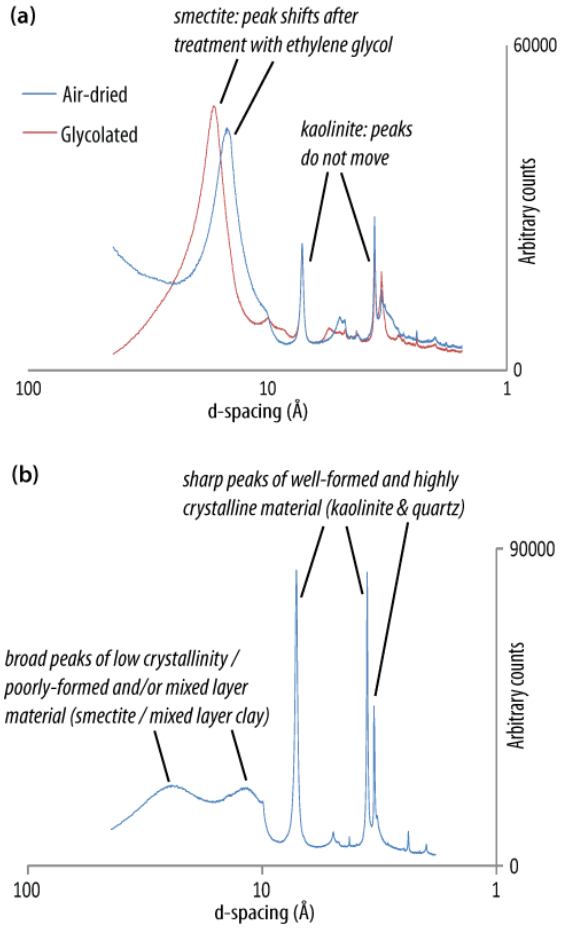

Figure 3.1: *Example XRD diffractograms:* ***(a)*** *diffractograms for a single sample after air-drying (blue) and treatment with ethylene glycol (red); the peak relating to smectite has shifted after glycol solvation due to the physical expansion of its interlayer space, whereas kaolinite is not an expandable clay and its layers remain unchanged;* ***(b)*** *diffractogram highlighting difference in peaks produce by high-crystallinity - kaolinite, quartz, sharp peaks - and low-crystallinity smectite, mixed layer clay - broad peaks.*

Samples for XRD were prepared according to the methods outlined in Moore and Reynolds (1989): first by gentle crushing in a fly press and treatment in a weak solution of acetic acid for between 1 and 48 hours to remove carbonate material. The clay-sized fraction (0.2 – 2 µm grain size) was separated by centrifuging according to Stoke's Law; mounted slide samples were prepared by pipetting a small amount (~1 ml) of the clay fraction, suspended in deionised water, to produce gravity settled samples where the (001) planes are approximately parallel to the sample surface, in order that clear diffraction patterns are achieved. Samples were left to dry at room temperature and ambient humidity for 24-48 hours, rather than in a 90 °C oven for 1 hour as suggested by Moore and Reynolds (1989), in order to prevent any damage to or changes in the clay minerals. Analyses were carried out at 2-50 ° 2-theta, with a step size of 0.02 2-theta and step time of 0.85 seconds/step, resulting in 2344 data points per analysis. After analysis of air-dried samples, those that were found to contain

swelling material (e.g. smectite, expandable chlorite, mixed layer materials) were further treated with ethylene glycol at 60 °C for a minimum of 8 hours in order to accurately identify these minerals (Fig. 3.1a). Diffractograms are plotted as d-, or interplanar-, spacing (Å) rather than the diffraction angle (degrees 2-theta) as using the former with a log x-axis prevents crowding in the 10-17 Å d-spacing region, where many clays plot.

The absolute value of diffractogram peaks is not important and the y-axes units are 'arbitrary counts'; the shape and relative intensity of peaks are, however, significant as these attributes reflect the crystallinity of the material (Moore and Reynolds, 1989). Materials with a high crystallinity, such as quartz or other framework silicates, are represented by high intensity (sharp), narrow peaks (Fig. 3.1b) representing concentrated scattering of X-rays from a crystalline surface, whereas amorphous materials such as glass are represented by a low intensity, broad 'peaks', representing diffuse scattering of X-rays from the material. Mixed layer clays also produce broad peaks since the peaks of both phases (e.g. illite and smectite) will be combined within a single peak on the diffractogram (the peaks of the separate phases are essentially 'bridged', Fig. 3.1b). This variation in peak intensity is caused by the relative internal order of a material, which influences how X-rays are diffracted. For crystalline materials, X-rays are diffracted in a predictable pattern, but since there is no internal order to amorphous material, X-rays are diffracted at a large range of angles. Since clay minerals are generally planar in structure, it is important to prepare oriented samples as described above in order to facilitate the maximum diffraction of X-rays from the crystal faces along these planes. As such, clay minerals that are 'well-formed' and have a high crystallinity will produce diffractograms with relatively sharp peaks, whereas minerals that do not have well-developed crystal faces (for example those that form as the result of alteration, that are the product of transition from one clay mineral to another or that have been degraded through weathering processes) will tend to produce relatively broad peaks.

We have presented the data below according to wall rock lithology (at the studied locations), focusing on the mineralogy and microstructure of the protolith rocks before considering those of the damage zones and subsequently of the fault core gouge material.

3.2.1 Overview of samples

Oriented samples were collected from both the fault zone sections and representative protoliths described in Sections 2.4 and 2.6.2, for the purpose of thin-sectioning and XRD analysis. The number of samples collected for each fault zone varied according to the architecture and the types of fault rock present (locations shown in Fig. 3.2). We aimed to collect at least one sample for each type of fault rock material across the fault cores and damage zones in order to be able to accurately and completely describe the microstructure and mineralogy of fault and protolith rocks, and qualify fault-related changes in these properties. Samples were collected according to the methods described in Section 1.8.1. and were cut perpendicular to the mean fault plane and parallel to the mean orientation of striae at each location. The position within each fault zone (where applicable) and a brief description of samples is provided in Tables 3.1 and 3.2, comprehensive sample information is provided in Appendices 2A (field photos) and 2B (XRD raw data, where appropriate).

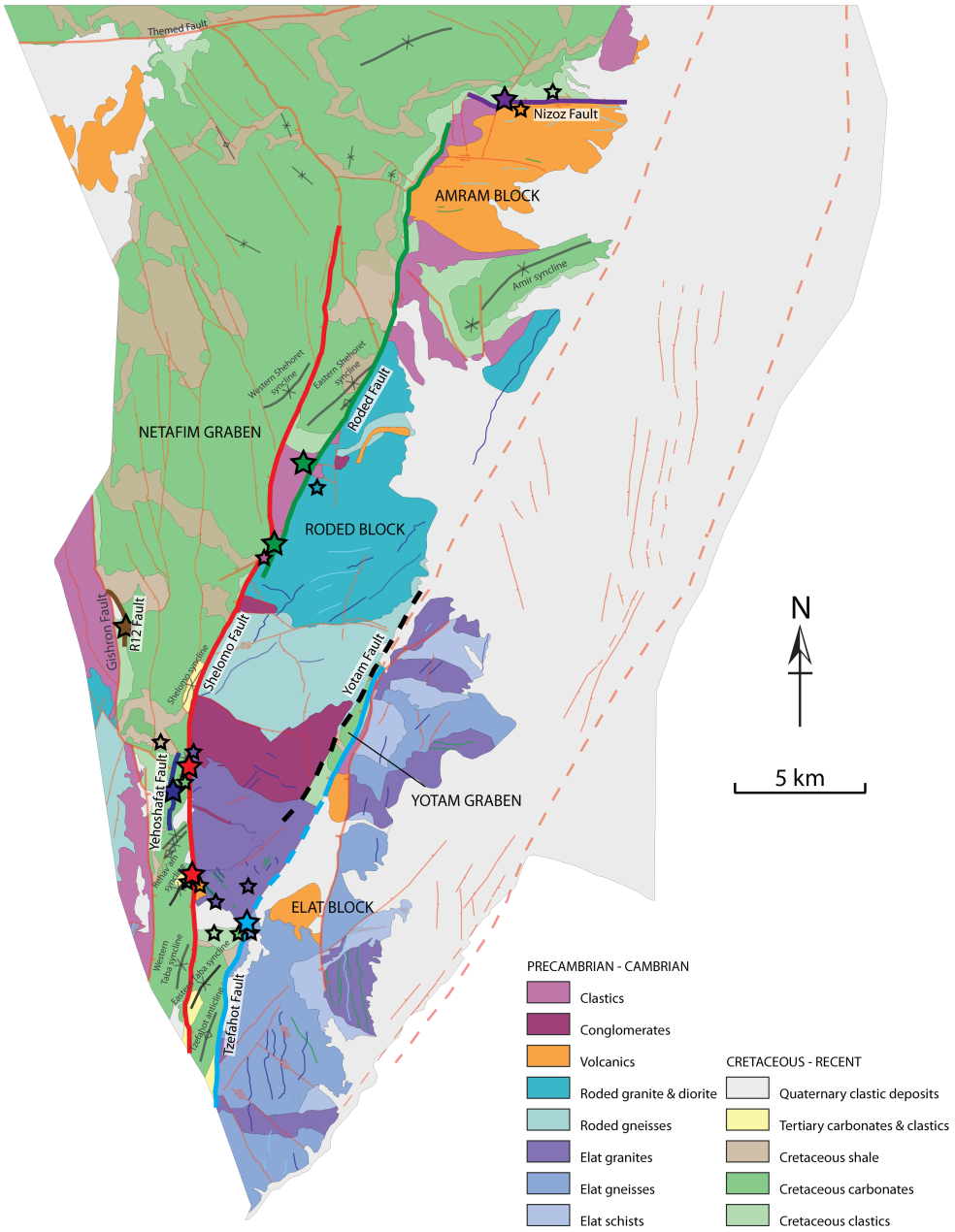

Figure 3.2: *Simplified geological map showing location of fault rock and protolith samples. Large stars represent fault rock samples, smaller stars protoliths (as shown on Fig. 2.4b); colours are representative of relevant fault/protolith colour used.*

Table 3.1: *Table summarising sample numbers and lithology of protolith samples.*

Sample no.	Lithology	Notes	Associated fault/s
22.13	Elat Granite	*Leucocratic member*	Shelomo
23.12	Ramat Yotam Volcanics		Shelomo
23.14	Taba Gneiss	*L-S tectonite*	Tzefahot
F1-9	Pegmatite vein		Tzefahot
F2b-9	Elat Granite		Shelomo
F3-10	Cretaceous sandstone (Samar Fm)		Yehoshafat, R12
F5a-4	Cambrian sandstone (Shehoret Fm)	*Variegated member*	Roded, Nizoz
F5a-5	Roded Quartz Diorite		Roded
F8c-1	Amram Rhyolite		Nizoz
F8c-10	Cretaceous sandstone (Amir Fm)		Nizoz
F8c-11	Amram Granite Porphyry		Nizoz
KUH	Cretaceous limestone (Hazera Fm)		Tzefahot, R12
KUG	Cretaceous limestone (Grofit Fm)		Shelomo
KUO	Cretaceous shale (Ora Fm)		Yehoshafat, Tzefahot (?), R12 (?)

Table 3.2: *Table summarising sample numbers and lithology for each fault zone (colours represent sample position within fault zone and rock type: basement damage zone ; carbonate damage zone ; clastic damage zone ; fault core).*

Fault	Sample no.	Protolith lithology (formation)	Description/name
Shelomo (F2)			
Locality A	F2a-5	Marly limestone (Ghareb Fm)	*Carbonate damage zone*
	F2a-6	Marly limestone (Ghareb Fm)	*Fault plane*
	F2a-7	??	*Foliated brown gouge*
	F2a-8	??	*Foliated red gouge*
	F2a-9	Ramat Yotam Volcanics	*Fractured basement damage zone*
Locality B	F2b-1	Elat Granite	*Basement damage zone*
	F2b-2	Elat Granite	*Basement damage zone*
	F2b-3	??	Brown fault gouge with slip surface
	F2b-4	??	*Brown fault gouge*
	F2b-6	??	*Red fault gouge*
	F2b-7	Limestone (Grofit Fm)	*Carbonate damage zone*
Tzefahot (F1)			
	F1-1	Limestone (Hazera Fm)	*Carbonate damage zone*
	F1-2	??	*Brown shale gouge*
	F1-3	??	*Green shale gouge*
	F1-4	??	*Cataclastic gouge*
	F1-5	Limestone clast (Hazera Fm)	*Carbonate fault core clast*
	F1-6	??	*Clast-rich cataclastic gouge*
	F1-7	??	*Gneissic cataclastic gouge*
	F1-8	Pegmatite vein	*Basement damage zone*
Roded (F5)			
	F5a-1	Cambrian sandstone (Shehoret Fm)	*Variegated sandstone damamge zone*
	F5a-3	Quartz diorite (Roded Quartz Diorite)	*Fractured basement damage zone*
	F5a-5	Quartz diorite (Roded Quartz Diorite)	*Fractured basement damage zone*
	F5a-6	Cambrian sandstone (Shehoret Fm)	*Sandstone fault plane*
	F5a-7	??	*Red foliated gouge*
	F5a-8	??	*Fault core cataclasite*
Nizoz (F8)			
	F8-2	Amram Rhyolite	*Basement damage zone*
	F8-3	Amram Rhyolite	*Basement damage zone*
	F8-4	??	*Fault core-rhyolite*
	F8-5	??	*Fault core-rhyolite*
	F8-6	??	*Basement cataclasite*
	F8-7	??	*Foliated fault core*
	F8-8	??	*Clastic cataclasite*
	F8-9	Cretaceous sandstone (Amir Fm)	*Clastic damage zone*
Yehoshafat (F3)			
	F3-1	(Ora Fm)	*Fault core shale-west*
	F3-3	(Ora Fm)	*Fault core shale-centre*
	F3-6	Laminated shale (Grofit Fm)	*Carbonate damage zone (shale)*
	F3-7	Limestone (Grofit Fm)	*Carbonate damage zone (lst)*
	F3-8	Sandstone (Samar Fm)	*Clastic damage zone*
	F3-9	(Ora Fm)	*Fault core shale-east*
R12 (F7)			
	F7-1	Cretaceous sandstone (Samar Fm)	*Foliated cataclasite*
	F7-2	??	*Fault gouge*
	F7-4	Cretaceous limestone (Grofit Fm)	
	F7-6	Cretaceous sandstone (Samar Fm)	*Powdery clastic damage zone*
	F7-8	??	*Clay-rich fault gouge*

3.3 Fault zone microstructure and mineralogy

3.3.1 Protolith rocks

3.3.1.1 Taba Gneiss

The Taba Gneiss is fairly typical in texture and composition for a quartz diorite gneiss; it contains a high proportion of quartz (40-50%) along with feldspars (K-feldspar and plagioclase, 25-35%) and biotite (∼25%) (Fig. 3.3a) and has a foliated, medium-grained gneissic texture. There is large variation in grain size, with some quartz grains being >1 mm, but the average grain size of quartz and feldspar is on the order of 200 µm. Biotite crystals are commonly >500 µm in length and range from <50-∼200 µm wide. Quartz and feldspar grains are relatively equant and show a weak shape preferred orientation (SPO) but >90% of biotite crystals are aligned parallel/sub-parallel to each other, defining the foliation that is seen at the outcrop-scale. Most grains of feldspar and quartz are fractured by intragranular fractures but these are randomly oriented, tensile and have no shear offset; occasionally they are filled with a calcite cement. Though biotite crystals are aligned, they are not generally arranged in bands more than a maximum of 500 µm wide. The sample chosen as a representative protolith was collected at 29°32'18.30"N, 34°54'11.47"E which, although relatively close to the Tzefahot Fault zone, was collected here to mitigate against the effect of textural and slight mineralogical changes within the Taba Gneiss across a relatively small area (Section 2.4.1.1); this rock type sample is most similar to that involved in the Tzefahot Fault zone.

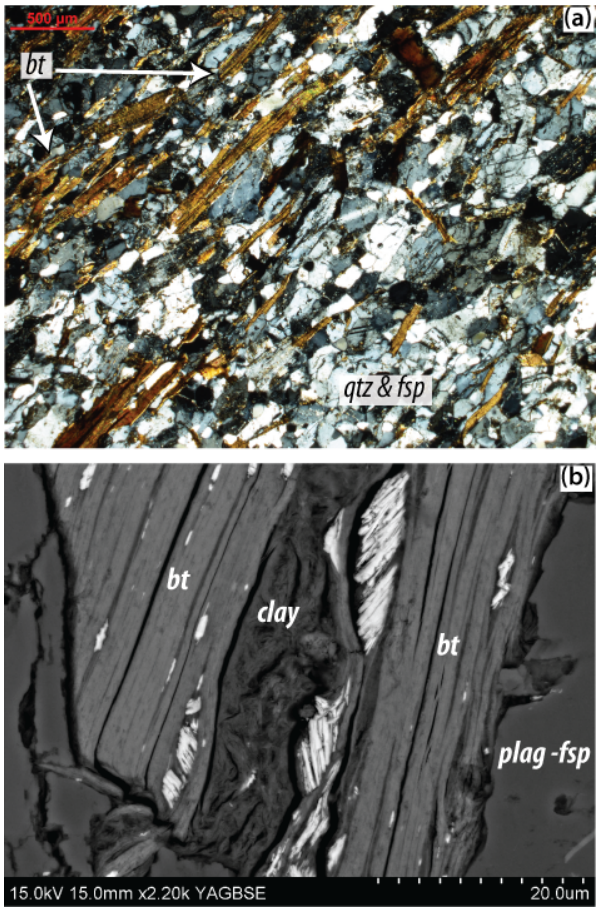

Figure 3.3: *Photomicrographs of the Taba Gneiss:* ***(a)*** *typical mineralogical and microstructural assemblage (XPL);* ***(b)*** *evidence of alteration of micaceous minerals to clay minerals (BSEM).*

It was not possible to extract enough clay material from the sample to perform XRD analysis, but EDX reveals two types of clay mineral: one with high SiO_2 and Al_2O_3 content (50-65 and 20-35 weight%, respectively), with minor K_2O (<2 weight%), which we interpret to be kaolinite (Fig. 3.3b); and another with a higher K_2O content (up to 8 weight%) which is likely illite. These clay minerals are present in very small amounts (<5%, they are only apparent in the SEM and not in optical microscopy) and we infer their presence to be the result of surface weathering processes. We suggest that the close to zero permeability of such a metamorphic rock would not allow the ingress

of fluids needed for the widespread alteration of framework aluminosilicate minerals to clays at depth.

3.3.1.2 Elat Granite

The Elat Granite varies in composition across the area of study (Section 2.4.1.2) but is principally composed of quartz (40%), feldspars (K-fsp and Na-plagioclase, 50%) and mica (10% biotite and minor white mica). It has a coarse-grained, phaneritic texture and mean grain sizes are on the order of 500 µm in size, with some individual crystals exceeding this (Fig. 3.4a), and there is no discernible fabric. Crystals of quartz and feldspar are generally sub-anhedral with an interlocking texture, whilst those of mica are more commonly euhedral but have no preferred orientation.

Small amounts of clay minerals (kaolinite) are present, which appear to be alteration products of feldspar (Fig. 3.4b), although there is not a sufficient volume for XRD analysis. Alteration of biotite to chlorite is also observed and is concentrated along cleavage planes (Fig. 3.4c). There are very few microfractures within the samples analysed.

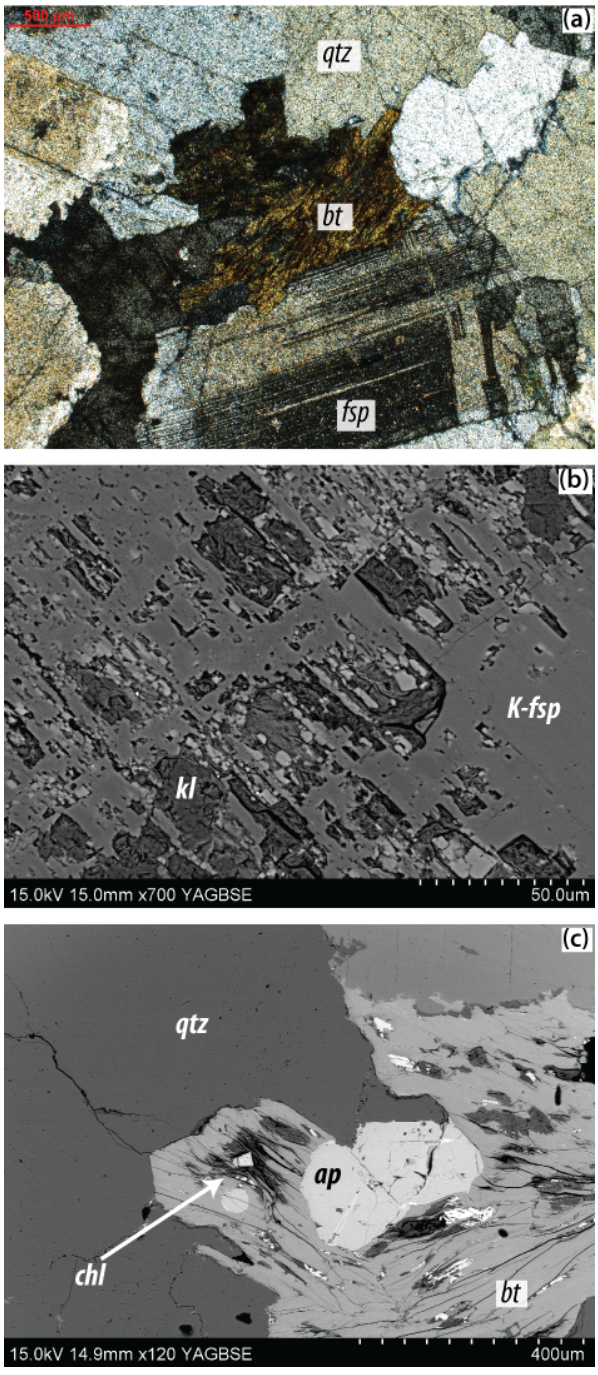

Figure 3.4: *Photomicrographs of the Elat Granite:* ***(a)*** *general texture and mineralogy (XPL);* ***(b)*** *replacement of plagioclase to clay minerals (BSEM);* ***(c)*** *retrograde alteration of biotite to chlorite (BSEM).*

3.3.1.3 Roded Quartz Diorite

The Roded Quartz Diorite is a relatively coarse-grained rock, composed principally of quartz (40%), feldspars (K-fsp and plagioclase, 25%), biotite and chlorite (30%), along with a small amount of Fe-oxide (<5%) (Fig. 3.5). Grain size is generally on the order of 50-500 µm, with a mean of 200-300 µm, and quartz and feldspar crystals are an-subhedral and interlocking, whilst those of biotite and chlorite are sub-euhedral and are more commonly parallel/sub-parallel to each other in small clusters. All minerals are ~evenly distributed throughout the rock and there is no preferred orientation of grains. The rock is moderately fractured, though there is no preferred orientation of these structures, and they are filled with

either calcite, comminuted grains or a mixture of both. There is a small amount of clay material present, likely the result of weathering along fractures, though it was not possible to extract enough for XRD analysis. Its identity cannot be determined using EDX; we can only say that as well as Al, Si and O, it also contains Mg and small amounts of Fe and/or K, so is likely illite or a member of the smectite or chlorite groups.

As well as signs of limited brittle deformation, there is also evidence of (partial) retrograde alteration of biotite to chlorite (Fig. 3.5b). This does not occur along fractures, but rather along cleavage planes of biotite.

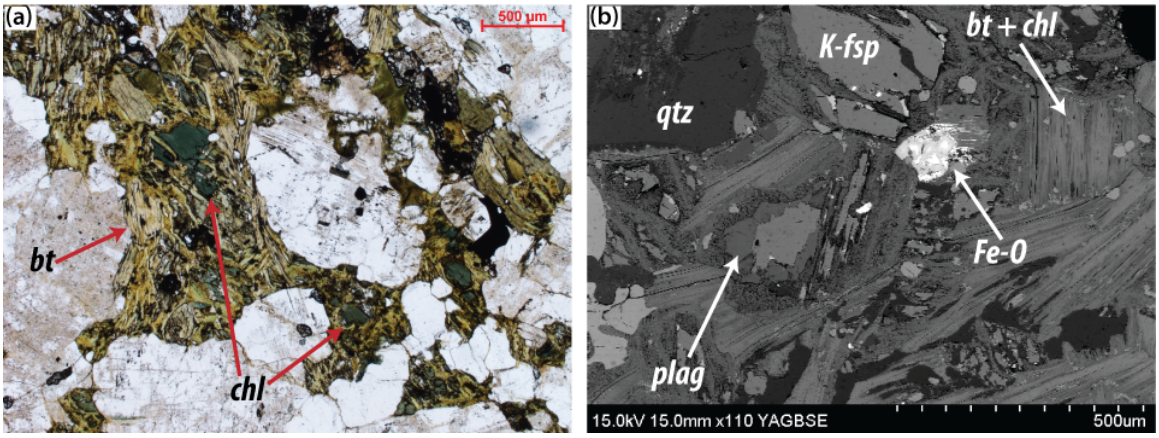

Figure 3.5: *Photomicrographs of the Roded Quartz Diorite:* ***(a & b)*** *the general texture and composition, and retrograde alteration of biotite (a: PPL, b: BSEM).*

3.3.1.4 Amram Rhyolite

The Amram Rhyolite is aphanitic in texture (individual grains are <2 mm and not visible to the naked eye), with subhedral porphyroclasts of quartz and K-feldspar up to ~2 mm in size. Groundmass composition is quartz, K-fsp and Na-plag, and crystals within it are very small and anhedral. It is difficult to determine mean grain size and proportion of each mineral, but we estimate this to be in the region of 60:40 quartz:feldspars and most 'grains' are <20 µm in size (Fig. 3.6a). Feldspars and quartz appear to be relatively evenly mixed within the groundmass. There has been some replacement of plagioclase by kaolinite (Fig. 3.6b) and small flecks (<10 µm), sometimes aggregating into larger grains, of iron oxide are disseminated interstitially throughout the rock (accounting for <2% total volume). There are occasional open, tensile intergranular microfractures of no preferred orientation (Fig. 3.6a).

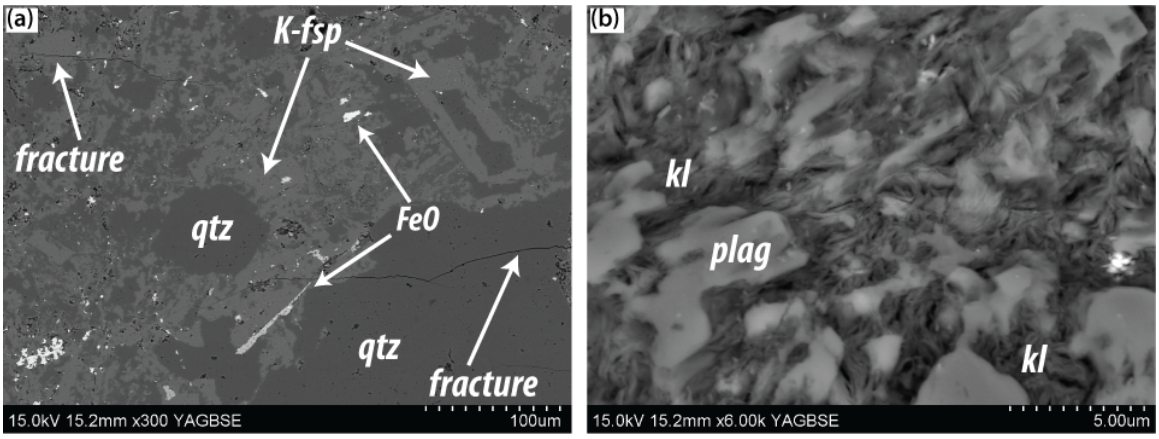

Figure 3.6: *Photomicrographs of the Amram rhyolite (BSEM):* ***(a)*** *fine-grained, aphanitic matrix of quartz and K-fsp with porphyroclasts of the same minerals,* ***(b)*** *alteration of plagioclase to kaolinite.*

3.3.1.5 Amram Granite Porphyry

The granite porphyry of the Amram Block is very similar in composition to the rhyolite; the main difference is in grain size and shape. The Amram Granite Porphyry is also porphyritic (porphyroclasts of quartz and feldspar generally 200-500 µm) with an aphanitic groundmass composed of quartz and K-fsp (Fig. 3.7a), but within the groundmass crystals are larger (10-50 µm) and sub- rather than anhedral, with better defined boundaries of relatively equant grains (Fig. 3.7b). The proportion of quartz:feldspar is approximately 50:50 and in the groundmass these minerals are evenly distributed and there is a lack of pervasive fabric to the rock. There is also iron oxide distributed across the groundmass (<5%), occurring between quartz and feldspar grains as interstitial material, giving the rock its overall dark red/brown colour (Fig. 3.7b).

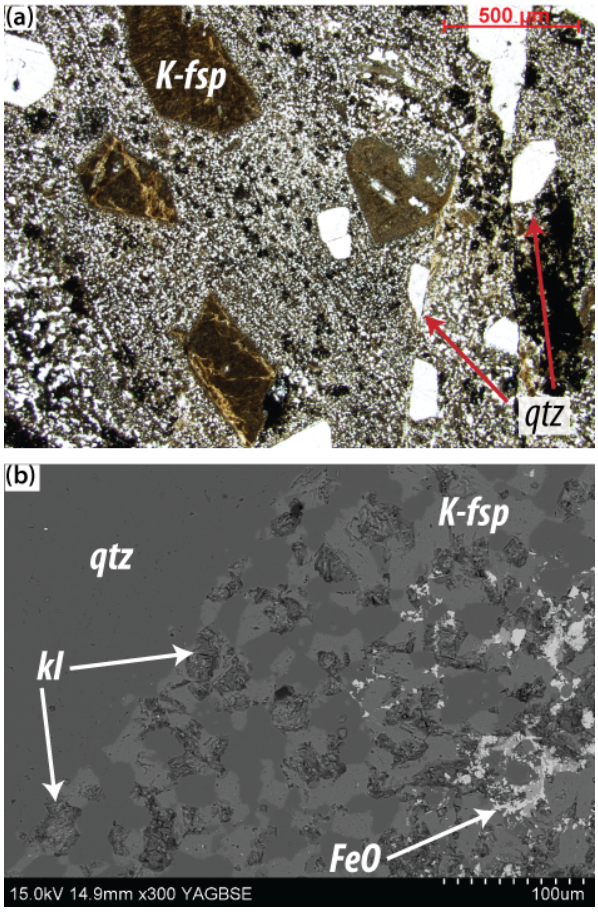

Figure 3.7: *Photomicrographs of the Amram Granite Porphyry:* ***(a)*** *fine-grained, aphanitic matrix with porphyroclasts (PPL);* ***(b)*** *alteration of plagioclase to kaolinite (BSEM).*

Replacement of Na-rich plagioclase by kaolinite is common (Fig. 3.7b) and since this does not appear to occur preferentially along fractures or other structures, we assume that this is largely related to surface weathering processes. There is a general lack of fractures at the microscale and little other evidence of any other brittle deformation.

3.3.1.6 Ramat Yotam volcanics

Volcanic rocks of the Ramat Yotam group are very fine-grained, aphanitic in texture with often large, euhedral porphyroclasts of K-feldspar and quartz (Fig. 3.8a). Porphyroclasts range in size from 50 µm-2 mm and are distributed throughout the sample; grain size of the groundmass is frequently as fine as <10 µm and crystals are anhedral (Fig. 3.8b). The groundmass is composed of quartz (50%) and K-fsp (50%) with a small amount of Fe-oxide disseminated throughout the rock (<2%). There are some irregularly spaced, randomly oriented tensile fractures up to 200 µm wide that are filled with fluorite (Fig. 3.8c). There is no other evidence of deformation in this rock, but there is occasional alteration of Na-fsp to kaolinite (accounting for <5% of feldspar crystals).

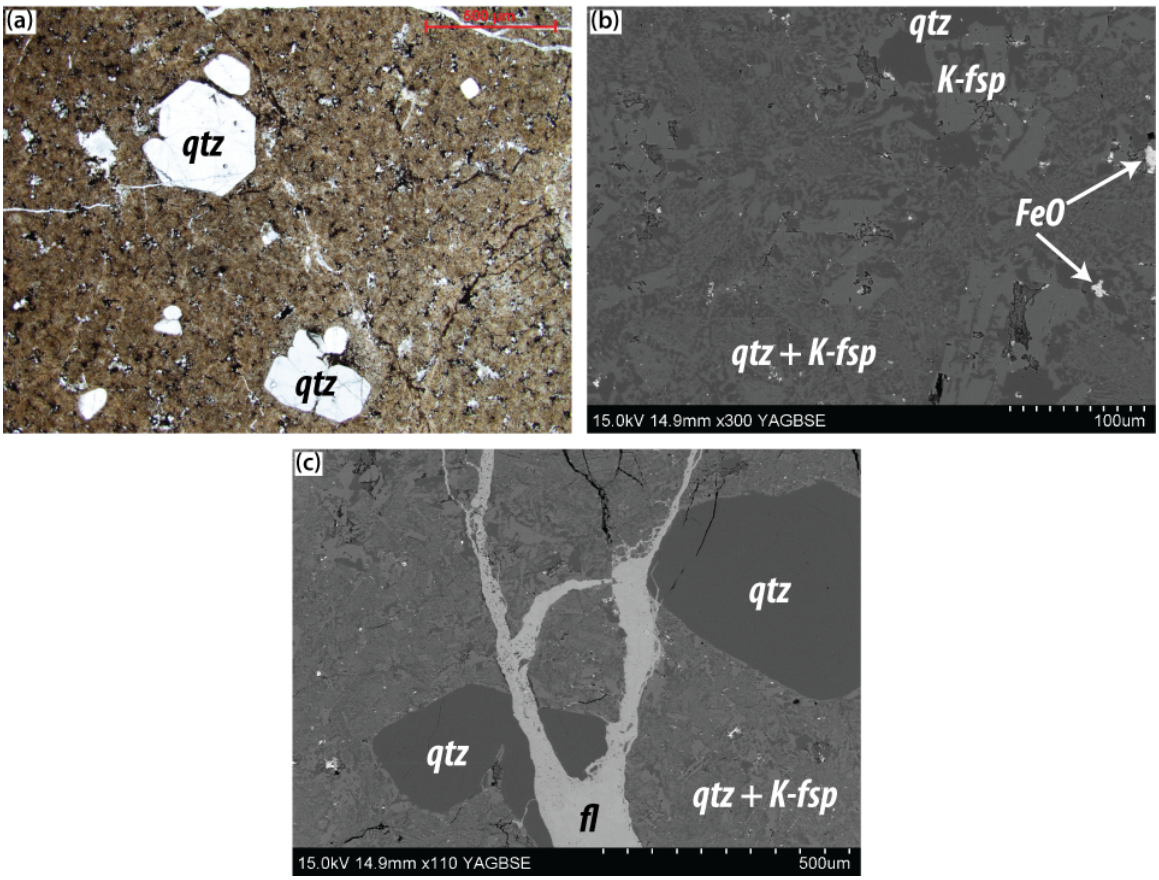

Figure 3.8: *Photomicrographs of the Ramat Yotam volcanics:* ***(a & b)*** *fine-grained, aphanitic matrix of quartz and K-fsp with porphyroclasts (a: PPL, b: BSEM), and* ***(c)*** *tensile fluorite-filled fracture (BSEM).*

3.3.1.7 Pegmatite vein

Pegmatite veins are a common feature across the igneous/metamorphic basement in the area of study. They vary somewhat in composition in terms of proportion of quartz/K-fsp but are largely composed of only these two minerals, with very few occurrences of micaceous minerals. The pegmatite vein analysed here is composed almost entirely of K-fsp (microcline) and quartz, with occasional crystals of muscovite (Fig. 3.9a). Grains are very coarse and the majority of crystals are >1 mm in size. There is extensive, randomly oriented intragranular microfracturing throughout the sample (Fig. 3.9b). Due to local compositional variations, we have chosen the 'protolith' described here from the same vein that is adjacent to the studied fault section (Section 2.6.2.2) and as such it is not possible to determine the timing of the observed fracturing relative to faulting.

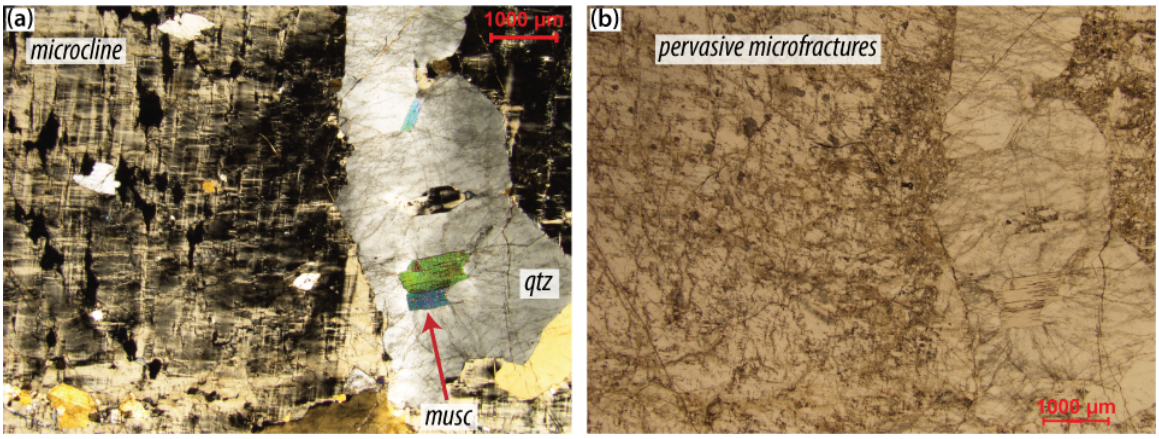

Figure 3.9: *Photomicrographs of the pegmatite vein:* ***(a)*** *large feldspar (microcline) crystal with smaller quartz (qtz) and muscovite (musc) crystals (XPL);* ***(b)*** *image of same area showing pervasive fracturing throughout (PPL).*

3.3.1.8 Cambrian sandstones

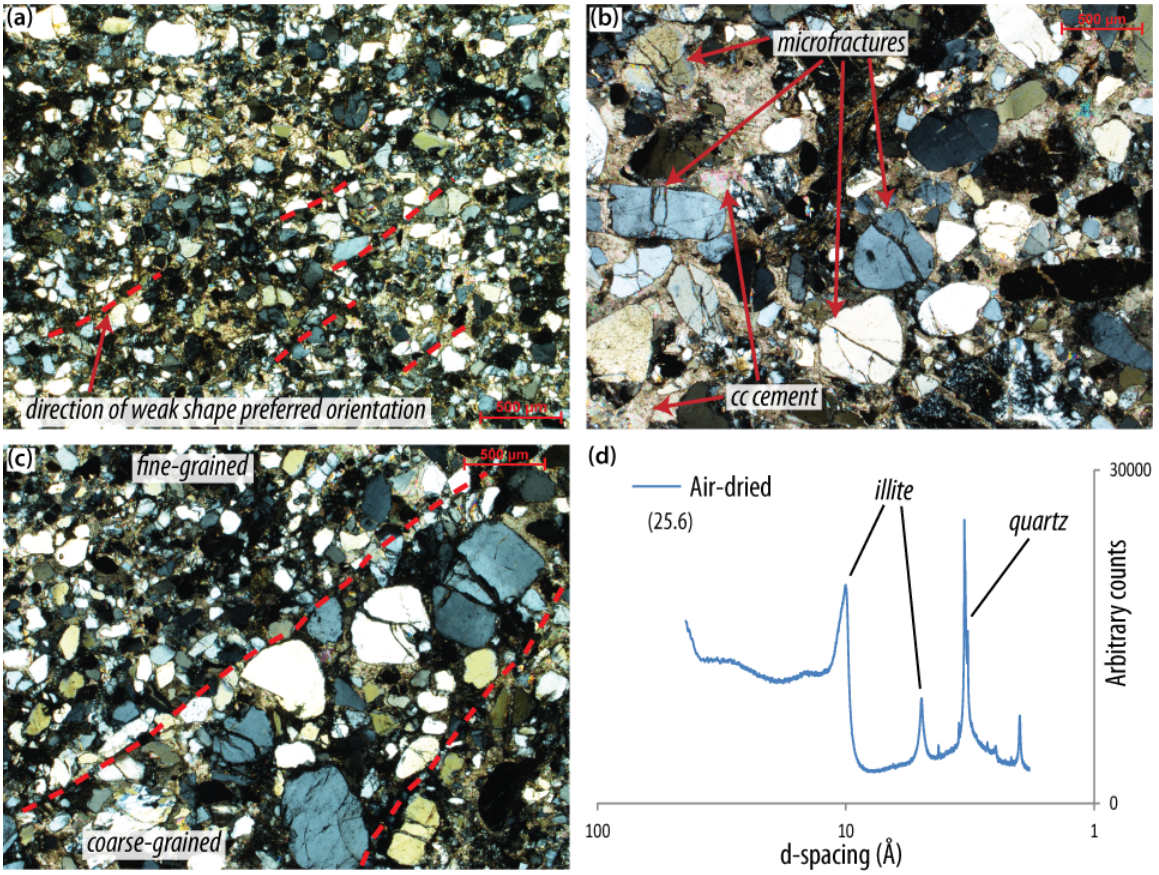

Figure 3.10: *(a-c): XPL photomicrographs of the Shehoret sandstone:* ***(a)*** *grain size and weak alignment of grains;* ***(b)*** *intragranular microfracturing of quartz grains;* ***(c)*** *stratification of grains by grain size.* ***(d)****: An XRD diffractogram of the mineralogy of the clay fraction: illite only.*

The most common outcrops of Cambrian sandstones, adjacent to the studied faults in the area, are of the Variegated Member of the Shehoret Formation (Fig. 2.4b). The average grain size of this unit is ~200 µm and the range is <20 -600 µm. Grains of quartz (>90%) and occasional feldspar are generally angular to moderately well-rounded and have a moderate sphericity (Fig. 3.10a,b) and many (30-50%) contain randomly oriented intragranular microfractures (Fig. 3.10b); there do not appear to be any intergranular microfractures, even where grains touch. There is some stratification of larger and smaller grains, although within these beds sorting is still generally

fairly poor (Fig. 3.10c) and there is a very weak preferred orientation of grains with low sphericity (Fig. 3.10a-c). The matrix is composed of a mixture of very fine-grained clay-sized material and calcite.

The grain to matrix ratio is variable but overall is approximately 60:30; the rock is grain-supported although there are some areas where few grains are touching (e.g. Fig. 3.10b). The composition of interstitial clay material is dominated by illite, though there is also minor kaolinite (Fig. 3.10d).

3.3.1.9 Cretaceous sandstones

The three Cretaceous sandstones generally consist of sub-angular to well-rounded, well-sorted quartz grains, with a relatively uniform grain size of 100-200 µm (Fig. 3.11). Quartz content of the Avrona and Amir formation sandstones is >90% quartz and there is interstitial cement present consisting of large and fragmented grains of detrital kaolinite (Fig. 3.12a,b) along with illite (Fig. 3.12c); the overall proportion of clasts in the rock is ~40% and ~60% matrix. Nearly all grains (>90%) contain at least one intragranular microfracture that are open and free of any fracture fill (Fig. 3.12b); there is no preferred orientation to these fractures and they are the only apparent deformation in the sample.

Figure 3.11: *Photomicrograph of typical Cretaceous sandstone: grain composition is >90% quartz and grains are relatively well-sorted and range from sub-angular to well-rounded in shape. Sphericity is moderate to low.*

The youngest (Albian) Samar formation sandstone differs somewhat as there is more variation in grain size, from <50 µm to the occasional grain of >500 µm, with the average in the region of 150-200 µm (Fig. 3.13a,b) and is better sorted overall, though still relatively poorly. Grains are moderately well-rounded and have a moderate sphericity and fewer host intragranular fractures (Fig. 3.13a,b). There is also some stratification by grain size (Fig. 3.13a) and in general the Samar sandstone is matrix-supported (Fig. 3.13b), whereas the Avrona and Amir sandstones are grain-supported (Fig. 3.12a,d); the clast:matrix ratio is on the order of 30:70. The clay mineralogy of the Samar formation sandstone is also in contrast to the older Cretaceous sandstones as kaolinite is the only mineral present (Fig. 3.13c). Kaolinite grains are visible using scanning electron microscopy, with some grains being in excess of 20 µm large (Fig. 3.13d).

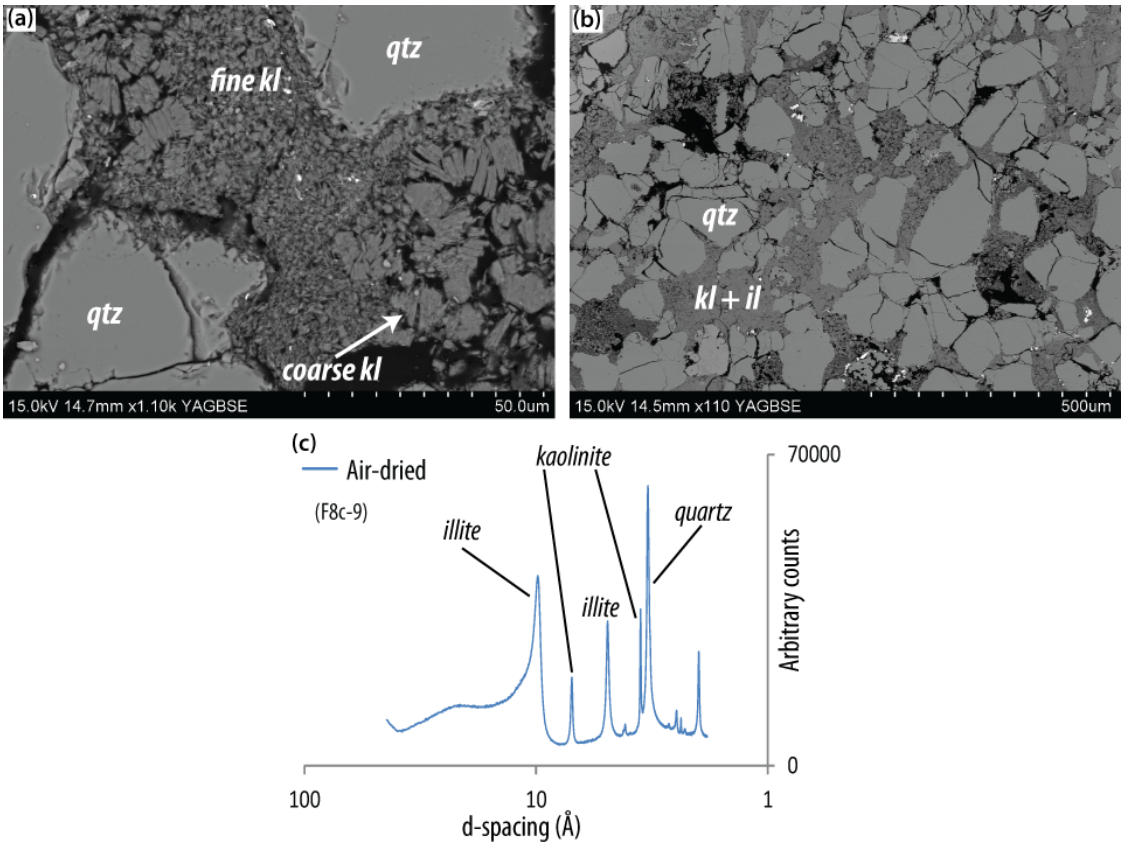

Figure 3.12: *Photomicrographs of and XRD diffractogram for the Cretaceous (Amir Formation) sandstone:* ***(a)*** *photomicrograph showing angular quartz grains and both fine and coarse kaolinite (kl) cement (BSEM);* ***(b)*** *angular quartz grains, some microfractured, supported by kaolinite illite (il) clay matrix (BSEM);* ***(c)*** *XRD diffractogram showing mineralogy of the clay fraction: kaolinite and illite.*

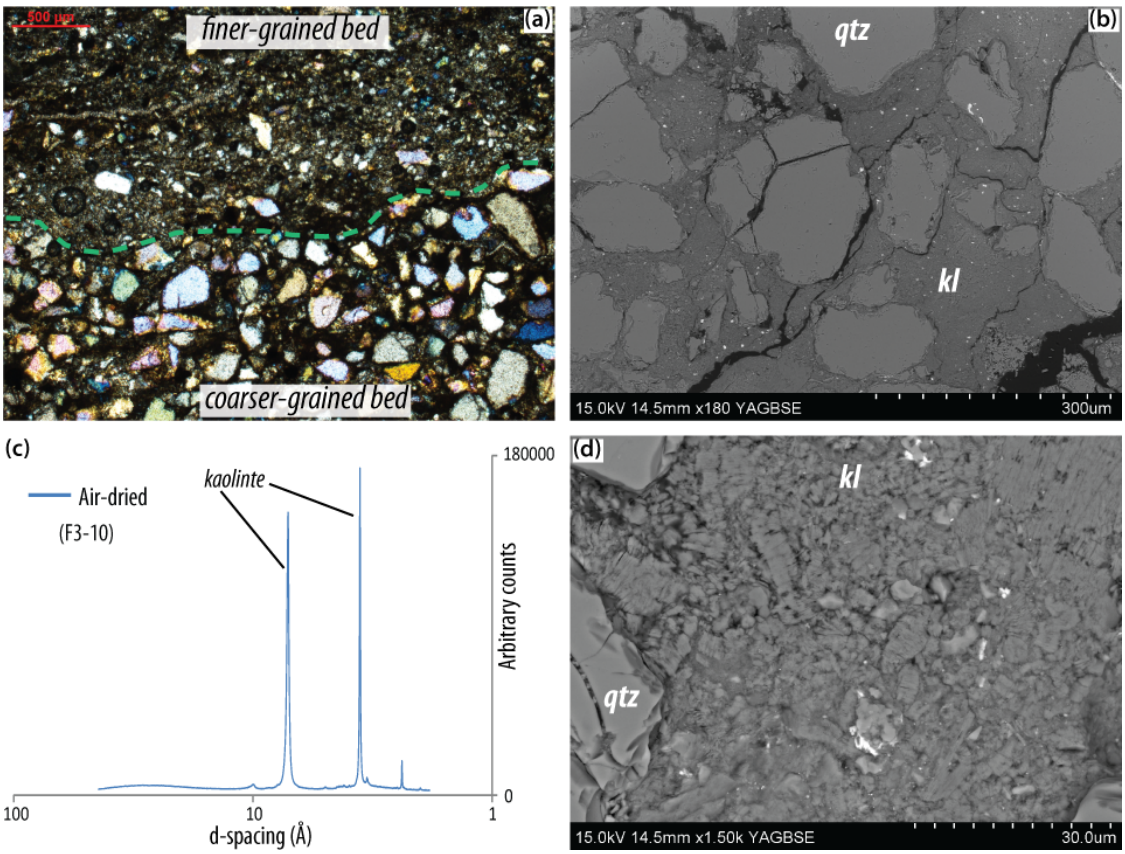

Figure 3.13: *Photomicrographs of and XRD diffractogram for Cretaceous sandstones (Samar Formation):* ***(a)*** *grain size variation and sorting (XPL);* ***(b)*** *matrix-supported quartz grains (BSEM);* ***(c)*** *XRD diffractogram showing mineralogy of clay fraction: kaolinite only;* ***(d)*** *texture of interstitial kaolinite cement (BSEM).*

3.3.1.10 Cretaceous limestones

There are a number of Cretaceous carbonate units in the area, ranging from the Cenomanian (base of the Upper Cretaceous) all the way through to the top Cretaceous Maastrichtian, but since the fault sections studied here involved only the Hazera, Grofit and Ghareb formations (Section 2.6.2), we present data relating to these three formations here.

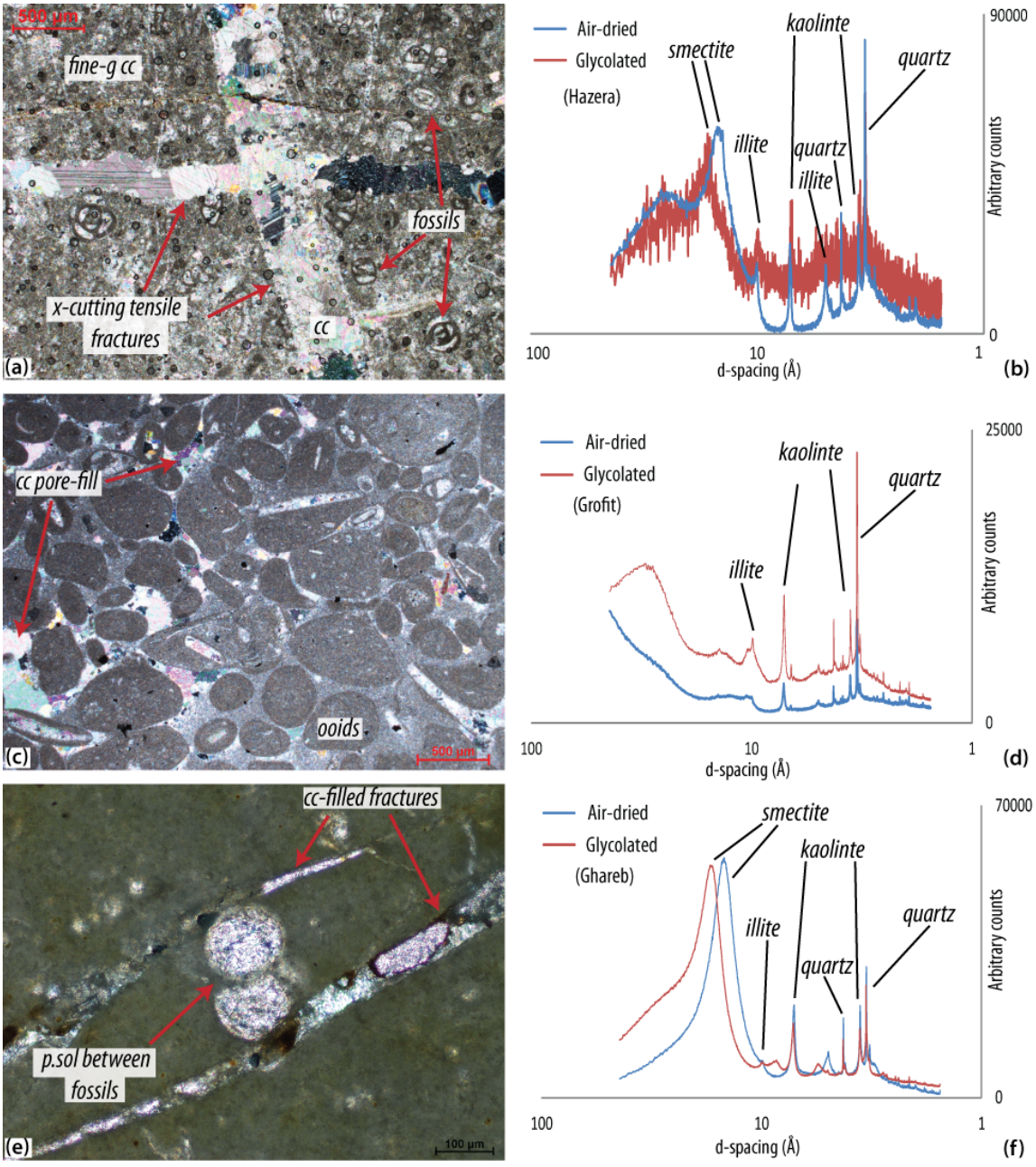

Figure 3.14: ***(a)*** *cross-cutting, calcite-filled tensile fractures with fossils (XPL);* ***(b)*** *XRD diffractogram for clay fraction of Hazera limestone: smectite, illite and kaolinite;* ***(c)*** *oolitic Grofit limestone (XPL);* ***(d)*** *XRD diffractogram for clay mineral composition of Grofit limestone: illite and kaolinite;* ***(e)*** *Ghareb limestone, calcite-filled fractures and localised pressure solution;* ***(f)*** *XRD diffractogram for clay mineral composition of Ghareb limestone: smectite and kaolinite with minor illite.*

The Hazera Formation limestone is the oldest Cretaceous limestone, and is composed of fine-grained calcite with numerous fossil fragments (Fig. 3.14a). Tensile fractures are present in various orientations but as there is no shear offset it is not possible to determine age relationships of these. The clay minerals present in this unit are smectite, illite and kaolinite (Fig. 3.14b). The Grofit Formation limestone is oolitic in nature at the studied location (Fig. 3.14c) and also contains

a fine-grained cement. There is relatively little clay material in this sample, with small amounts of kaolinite and illite (Fig. 3.14d). The Ghareb Formation is a fine-grained marl with occasional grains of calcite and calcite-filled fractures (Fig. 3.14e). Smectite is the most abundant clay mineral present (Fig. 3.14f) and there is also minor kaolinite. It should be noted that in the case of all of these carbonate rocks there is significant variation in texture and mineralogy throughout each unit (Fig. 2.4a), and the rocks described here are representative of the protolith rocks adjacent to the studied faults and not representative of the entire vertical stratigraphy.

3.3.1.11 Ora Shale

The Cretaceous Ora Shale appears relatively homogeneous in terms of grain size at the field-scale (Section 2.4.2.2) and is much the same at the micro-scale; mean grain size is not discernible even with electron microscopy and there are few clasts (generally quartz and feldspars) >50 μm in size (<5%, Fig. 3.15a- c). The shale is strongly-foliated at the sub-micron scale (Fig. 3.15d), defined by the alignment of clay minerals parallel to their long axes, and the foliation has a somewhat 'wavy' appearance overall (Fig. 3.15c,d). Evidence of brittle deformation is rare but not absent, and occasional brittle fractures, which are continuous over several millimetres have a few tens of microns of shear offset, cross-cut the foliation (Fig. 3.15a). Fractures are open, though this may be an artefact of thin section preparation due to the presence of swelling clays (smectite, mixed layer material, Fig. 3.15d) which may have expanded on contact with water and contracted when dried. These types of brittle features are isolated and not distributed across the rock, whereas the foliation is pervasive.

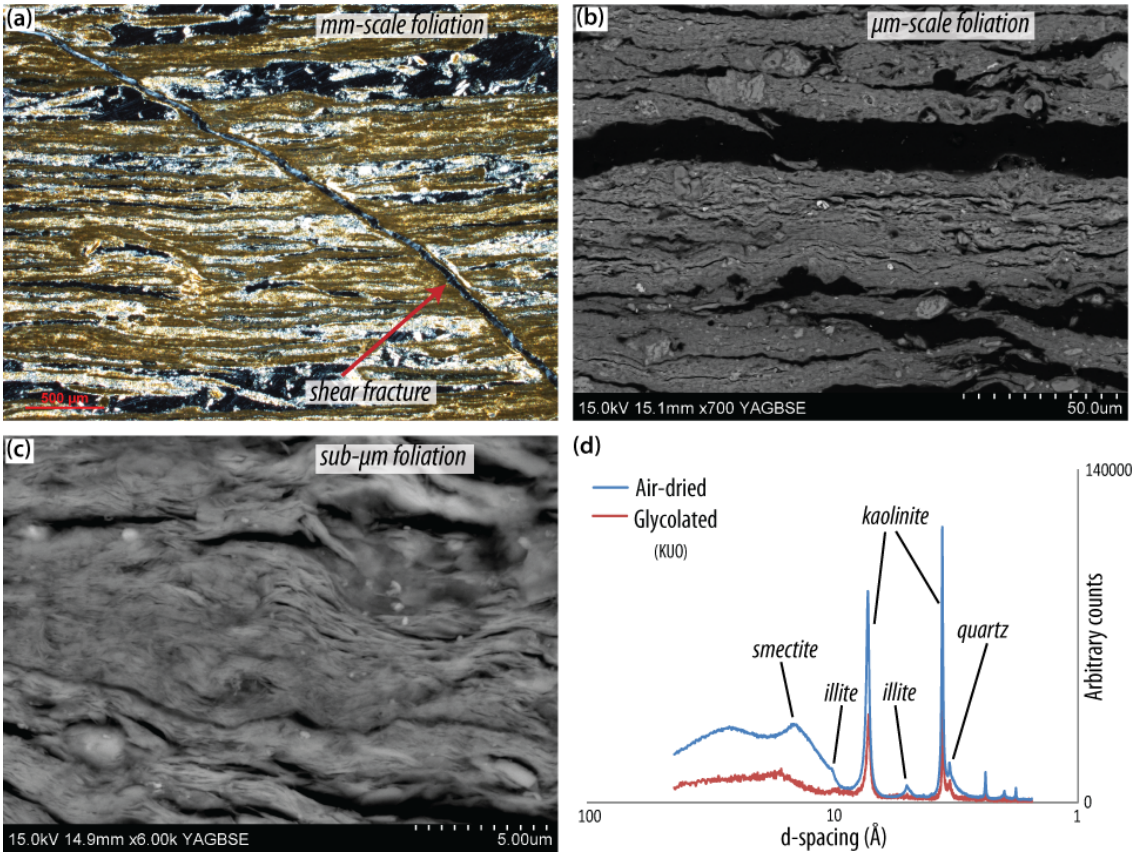

Figure 3.15: *Photomicrographs of the Ora Shale:* ***(a)*** *shear fracture cross-cutting foliation (XPL);* ***(b)*** *clast-poor area of foliated clay (BSEM);* ***(c)*** *relatively clast-rich area (BSEM);* ***(d)*** *XRD diffractogram showing clay mineral composition of the clay fraction: smectite and kaolinite with minor illite.*

Clay mineralogy of this unit is dominated by kaolinite (Fig. 3.15e) but there is also minor illite and smectite/chlorite-smectite, causing the shale to swell when wet (wetting and subsequent shrinkage on drying during thin section preparation is responsible for the voids observed in Fig. 3.15a-c). Although kaolinite is comparable in frictional strength to more cohesive rocks (Byerlee, 1978), smectite has a much lower coefficient of friction (as low as $\mu = 0.15$ when wet, Moore and Lockner, 2007), the significance of which will be discussed in Section 3.4.4.

3.3.2 Basement-hosted damage zones

3.3.2.1 Shelomo Fault

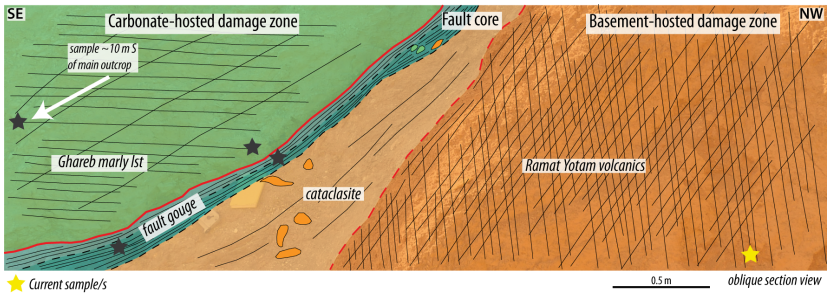

Figure 3.16: *Schematic log of Shelomo Fault, Locality A section showing position of basement-hosted damage zone sample.*

Locality A The basement damage zone at Locality A of the Shelomo Fault comprises Ramat Yotam silicic volcanic rocks, unconformably overlying Elat Granite (that does not outcrop at this location). The incohesive nature of the rocks (described in Section 2.6.2.1) is reflected in the microstructures; clasts of more or less intact volcanic rock are surrounded by a clay matrix (Fig. 3.17a,b) of smectite and kaolinite (Fig. 3.17c). Clasts of K-feldspar, quartz or combinations of the two range in size from <5 - >500 µm and their shape is largely size-dependent; clasts larger than 50 µm are generally less angular than those below this size, and smaller clasts also have a lower sphericity. Aggregate clasts which also include clay material may be up to 1000 µm in size (Fig. 3.17a) and are the most well-rounded. Many grains host intragranular microfractures (Fig. 3.17b) and more continuous intergranular fractures may persist for several centimetres and are commonly a few tens of microns wide and filled with fine-grained clay material. There is no microscale fabric in this damage zone as fractures are too irregularly spaced and oriented, and there is no pervasive preferred orientation of clasts or clay minerals.

There is a clear distinction between the occurrence of the kaolinite and smectite clay minerals. Kaolinite occurs as fracture-fills (Fig. 3.18a,b) and as the alteration product of feldspar minerals (Fig. 3.18b). In the Ramat Yotam Volcanics protolith <5% of feldspar grains are altered to kaolinite, but here it is closer to 30-50%. Kaolinite is also present as the matrix in localised zones of cataclasis (Fig. 3.17b) and in these cases grains are randomly oriented. In the case of smectite, however, it is only present as very thin coatings (<20 µm) at the edges of large, aggregate grains (Fig. 3.18c,d). The alignment of grains is parallel/sub-parallel to the edge of the grain that the smectite surrounds (the void between the grain and smectite coating in this case is an artefact of section preparation). Although we have not quantified the proportion of clay minerals present in this damage zone, we qualitatively estimate this to be on the order of 10-20% and believe this would account for the highly friable and incohesive nature of the outcrop.

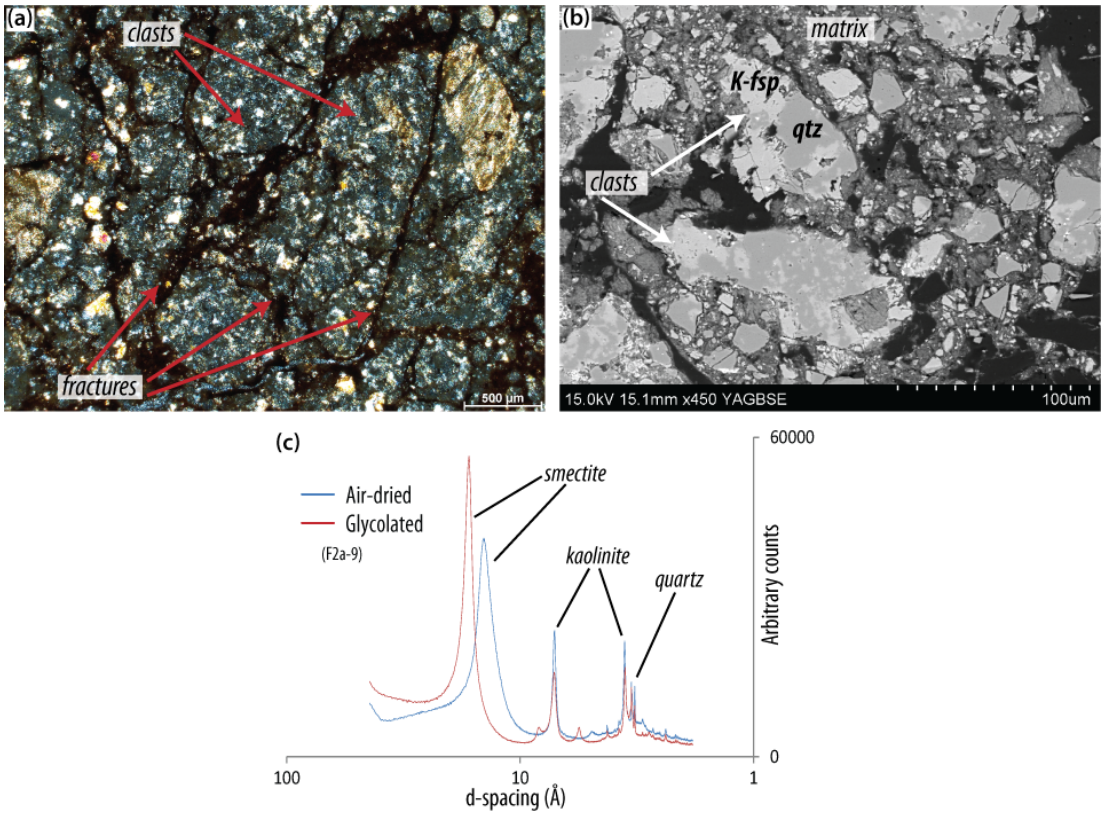

Figure 3.17: ***(a&b)*** *Photomicrographs of Shelomo Fault basement damage zone:* ***(a)*** *large, rounded clasts of volcanic material with cross-cutting fractures (XPL);* ***(b)*** *angular clasts of varying sizes of quartz and K-fsp in a fine-grained clay matrix (BSEM);* ***(c)*** *XRD diffractogram showing clay mineral composition of the clay fraction: smectite and kaolinite.*

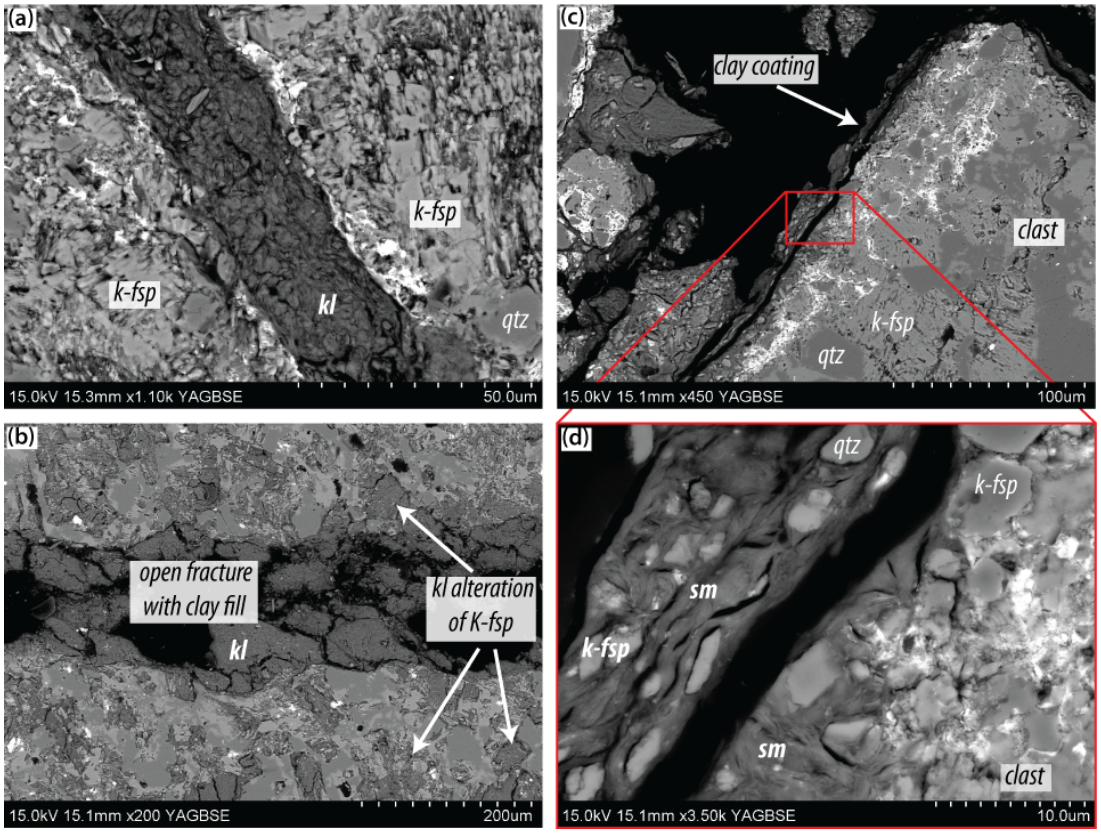

Figure 3.18: *BSEM photomicrographs of Shelomo Fault basement damage zone:* ***(a)*** *fracture filled with kaolinite arranged in random orientations;* ***(b)*** *kaolinite present both as fracture fill and as replacement of plagioclase crystals;* ***(c)*** *fine-grained clay material lining a large clast;* ***(d)*** *foliated smectite at clast edge, containing very small clasts of quartz and K-fsp.*

Microscale deformation in the basement damage zone at Locality A is distributed but by no means continuous. Evidence of a range of processes is preserved, including fracturing, cataclasis and growth of new minerals through alteration and precipitation, indicating there has been some degree of fluid flow through this part of the fault zone.

Locality B At Locality B, the basement wall rock is the Elat Granite (Fig. 3.19). Directly adjacent to the fault core the outcrop is powdery white and extremely incohesive, though grains of quartz, biotite and K-feldspar can be seen with the naked eye.

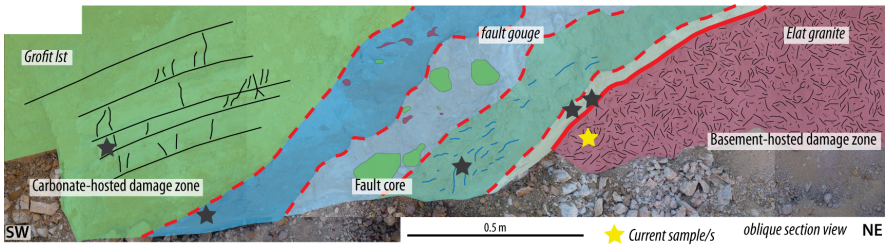

Figure 3.19: *Schematic log of Shelomo Fault, Locality B section showing position of basement-hosted damage zone sample.*

Grain size is extremely variable as there are grains of quartz and K-fsp, in excess of 1000 µm in size, that are intensely fractured but retain their original grain boundaries (e.g. Fig. 3.20a), along with localised zones of cataclasis where comminution has occurred and clasts are <10 µm in size (Fig. 3.20c). Grains of all sizes are highly angular (Figs. 3.20 and 3.21).

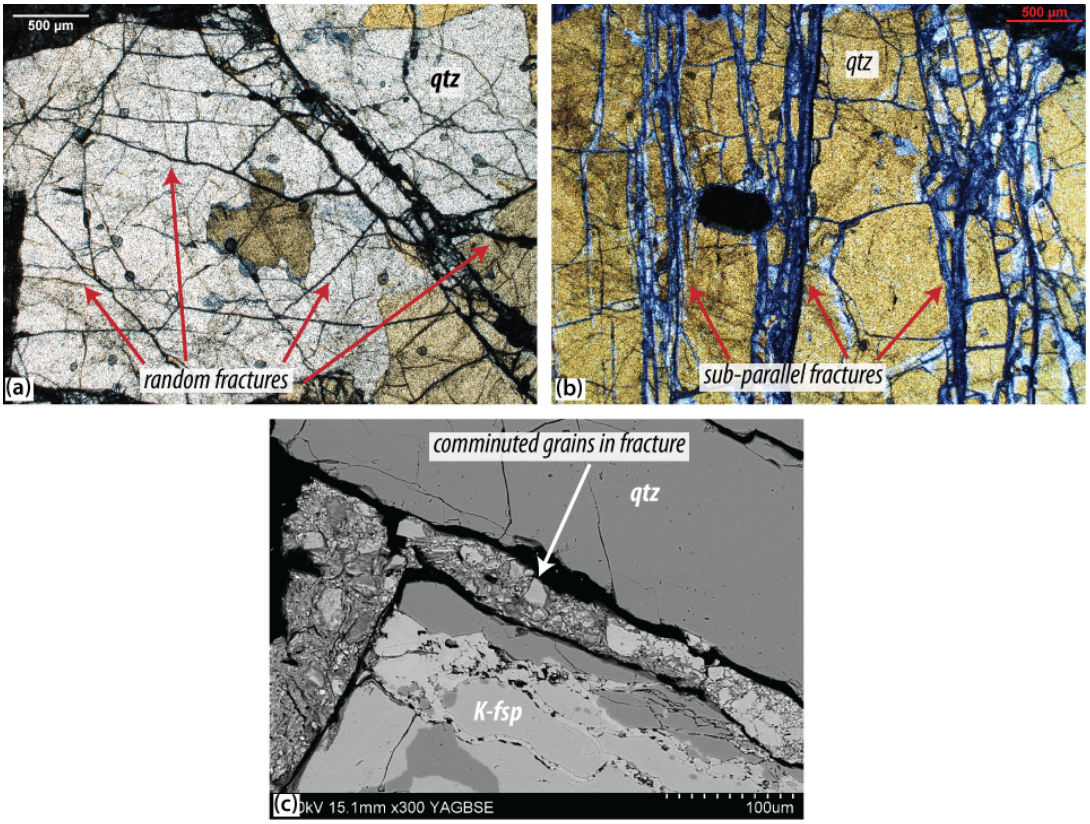

Figure 3.20: *Photomicrographs of Shelomo Fault basement damage zone: **(a)** randomly oriented fractures within a grain that retains its original boundaries (XPL); **(b)** sub-parallel group of fractures cross-cutting earlier randomly oriented fractures shown in (a) (XPL); **(c)** cataclasis and grain comminution at fracture edges (BSEM).*

At the microscale, we observe randomly oriented microfractures, along which there are been little or no shear offset (Fig. 3.20a,b). These fractures are cross-cut by later, parallel/sub-parallel fractures that are closely spaced (<50-750 µm, Fig. 3.20b), some of which are filled with very fine-grained cataclastic material (Fig. 3.20c). A third set of fractures are filled with calcite (Fig. 3.21a-c); these are tensile fractures with no shear offset, indicating that fracturing and cementation were synchronous, and that Ca-rich fluids were present at the time of faulting. There appears to be no overall fabric in this zone, and although there are groups of aligned fractures, overall the features of brittle deformation have no preferred orientation.

Clay material is present both in cataclastic matrix (Fig. 3.22a) and along fractures and grain boundaries (Fig. 3.22b), and is composed of Mg-bearing smectite(Fig. 3.22c). Between fractures, clay grains have a weak shape-preferred orientation that is interrupted by the presence of clasts also within the fractures; the fabric tends to be wrapped around, and generally parallel to the long edges of, clasts.

Deformation across this zone is brittle and as such not continuous, but it is distributed though varies in intensity. Over the space of a few millimetres we see grains still in their original shape and position (Fig. 3.20a) and intense comminution of grains by cataclasis, forming fractures filled with a fine-grained, incohesive gouge (Fig. 3.22a). In addition there has been alteration and/or precipitation of authigenic clay (Mg-smectite) that is not present in the adjacent wall rocks.

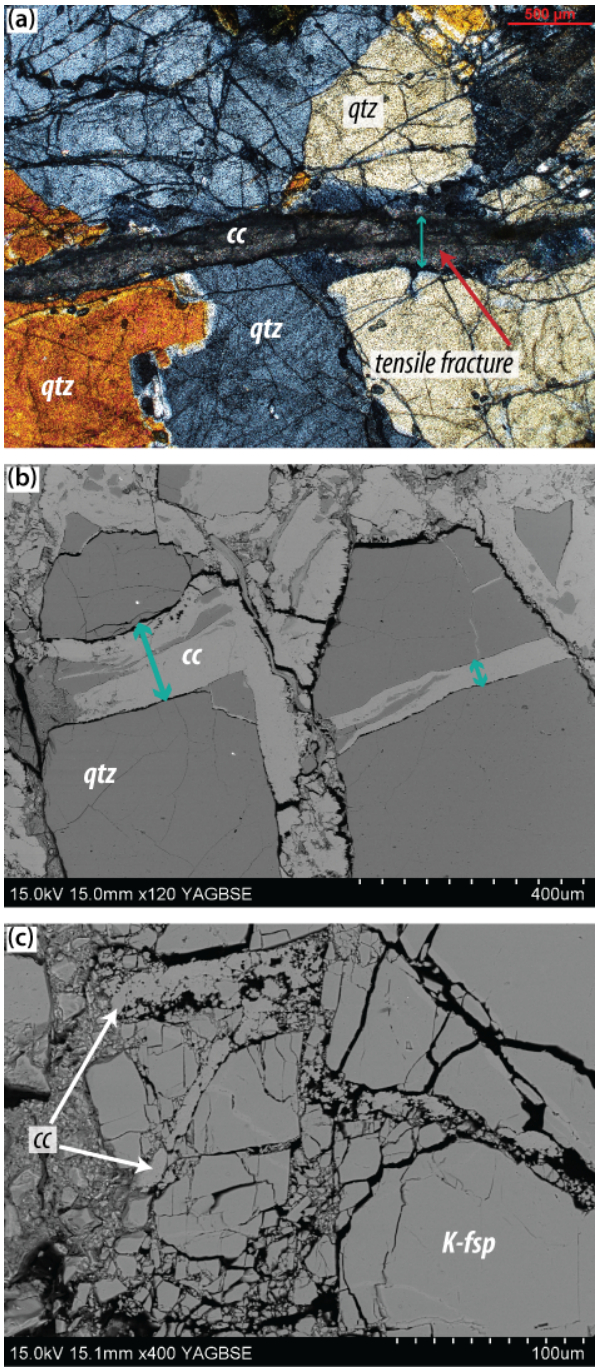

Figure 3.21: *Photomicrographs of Shelomo Fault basement damage zone:* ***(a & b)*** *tensile, calcite-filled fracture (a: XPL, b: BSEM);* ***(c)*** *fractured calcite veins (BSEM).*

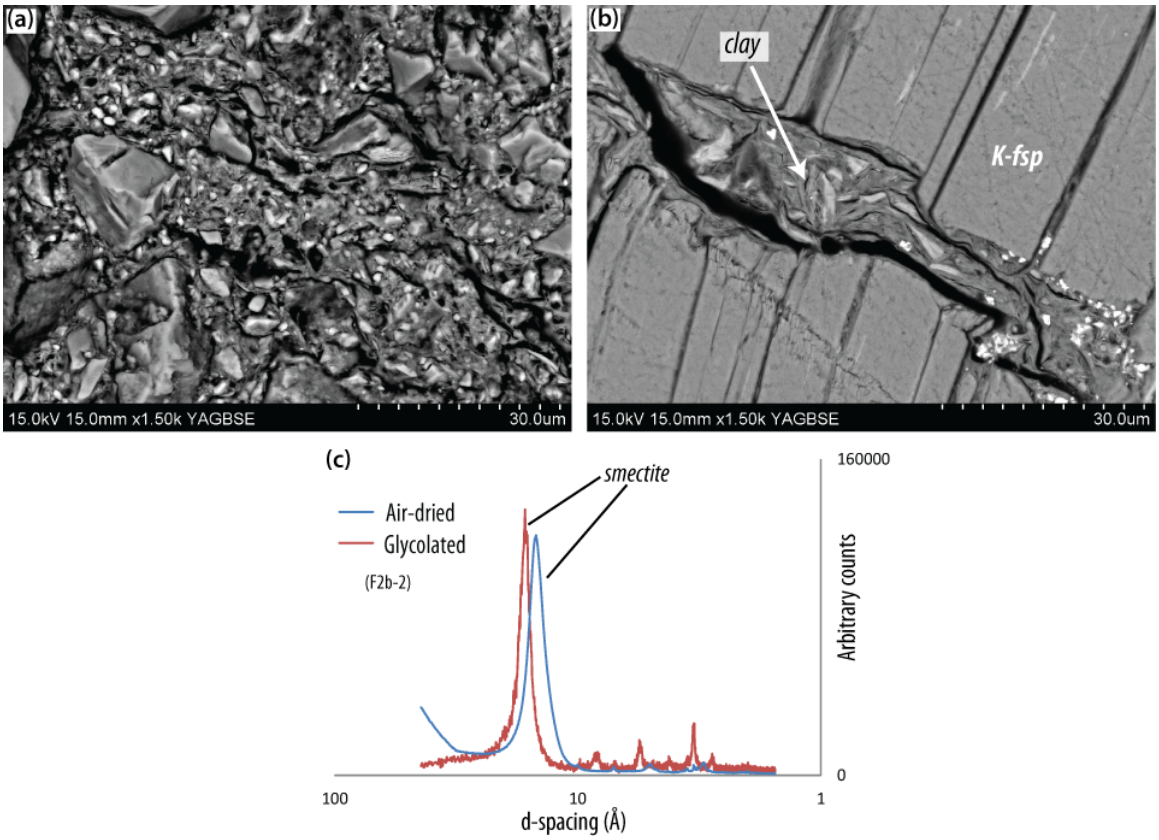

Figure 3.22: ***(a & b)*** *Photomicrographs of Shelomo Fault basement damage zone:* ***(a)*** *combined clay and mechanical matrix (BSEM);* ***(b)*** *clay material within a fracture (BSEM);* ***(c)*** *XRD diffractogram showing clay mineral composition of the clay fraction: smectite only.*

3.3.2.2 Tzefahot Fault

On the eastern side of the Tzefahot Fault zone (Fig. 3.23), the basement damage zone is composed of a pegmatite vein (∼1 m wide) followed by an outcrop of Taba Gneiss, though it is the pegmatite vein that appears to have accommodated the most deformation as it is visibly more intensely deformed at the field-scale (Section 2.6.2.2).

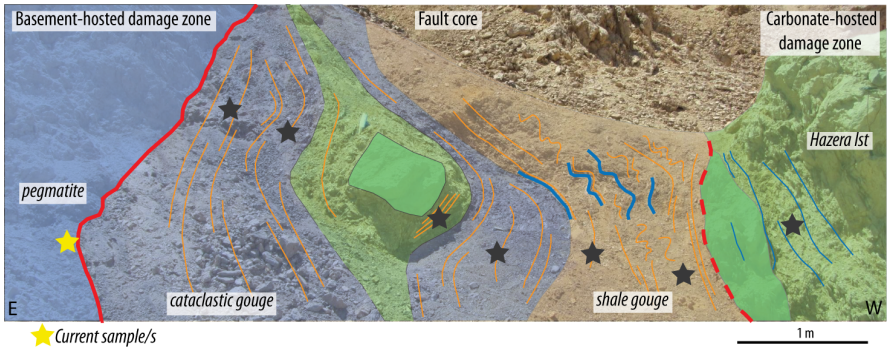

Figure 3.23: *Schematic log of Tzefahot Fault section showing position of basement-hosted damage zone sample.*

In a sample collected from the most intensely deformed lens of pegmatite (Section 2.6.2.2), we observe at the microscale fracturing of quartz and feldspar grains that is predominantly intragranular, with few fractures crossing multiple grains. There is no alignment of intra- or intergranular microfractures. Within the boundaries of original grains that are in excess of 500 µm in size, we see new grains smaller than 5 µm formed by this fracturing (Fig. 3.24a,b). It is possible to determine original grain boundaries within the sample as there has largely been little

or no shear offset along these microfractures within quartz and feldspars. The new grains formed by this fracturing are highly angular.

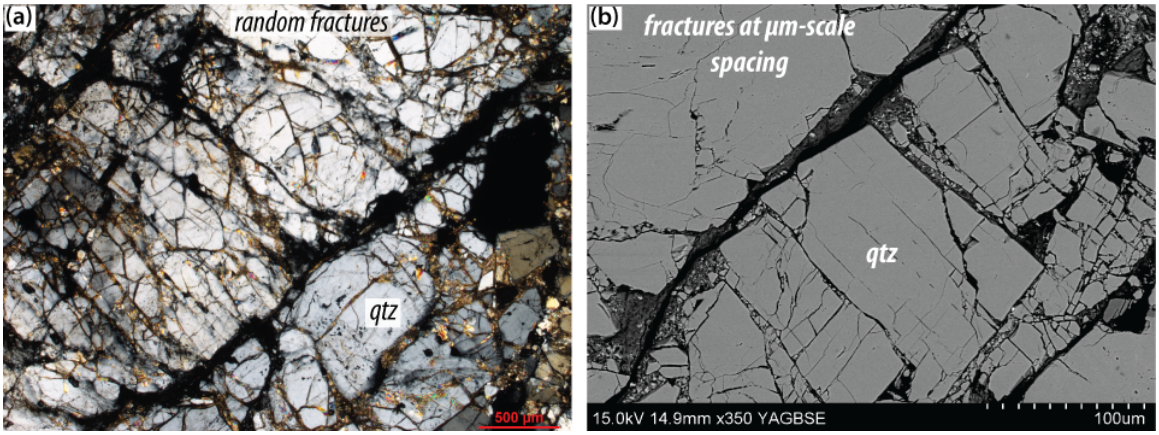

Figure 3.24: *Photomicrographs of the Tzefahot Fault basement damage zone:* ***(a & b)*** *heavily fractured grains of quartz within still visible original grain boundaries (a: XPL, b: BSEM).*

This type of fracturing is very similar in appearance to that observed by (Mitchell et al., 2011, their Fig. 6), which was described as being caused by a 'pulverisation' mechanism whereby the rocks were fractured without having undergone any change in position within the fault zone, relative to adjacent rocks. The powdery appearance observed at the macro-scale (Section 2.6.2.2) is also consistent with pulverisation (described by Dor et al., 2006) and is a result of the intense tensile microfracturing seen in Fig. 3.24.

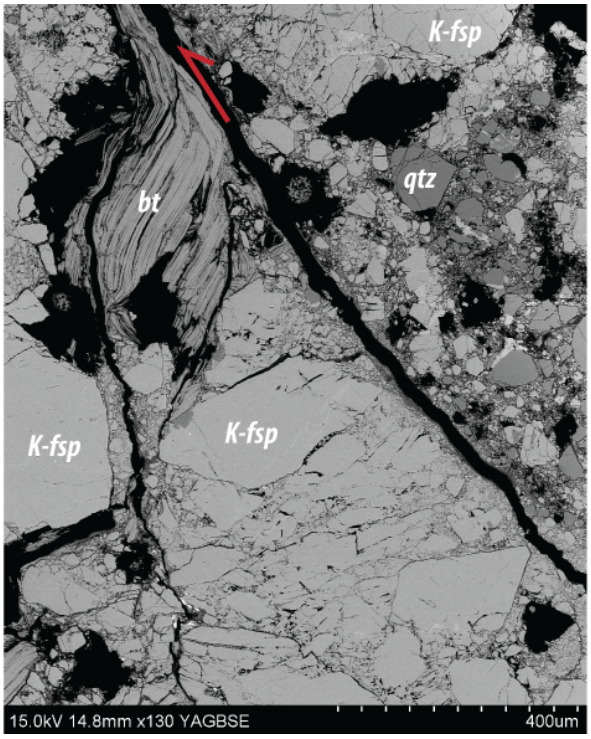

Figure 3.25: *Photomicrograph of the Tzefahot Fault basement damage zone: shear deformation of a grain of mica and grain comminution at fracture edges (BSEM).*

Although there are relatively few grains of micaceous minerals within the pegmatite, where they do occur we see that they have accommodated the deformation very differently. Rather than being fractured, these grains have often split along their cleavage planes and preserve evidence of shearing (Fig. 3.25), indicating there has been some shear movement within this zone, but which has concentrated along minerals with inherent internal weaknesses (i.e. cleavage planes). There is also comminution of grains at grain edges in areas where evidence of shear deformation is preserved, indicating localised deformation by cataclasis. We observe grains of moderate rounding and sphericity that are on average <100 µm and supported by a very fine-grained matrix. This matrix is only observed where cataclasis has occurred and is not evenly distributed throughout the rock. Deformation is distributed across the pegmatite damage zone but the mechanism varies. Pulverisation-style fracturing is the most evenly distributed throughout the sample, whilst cataclasis is more localised. Since randomly oriented fractures dominate the deformation style in

this part of the fault zone, there is no overall fabric to the rock.

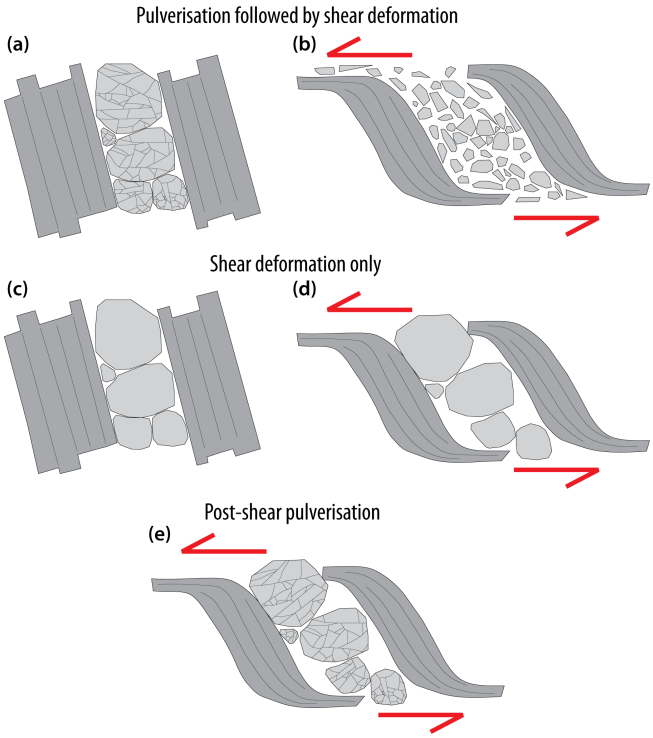

Figure 3.26: *Schematic diagram illustrating relative timing of pulverisation and shear deformation in the Tzefahot Fault footwall:* ***(a & b)*** *pulverisation of quartz/feldspar followed by shear;* ***(c-e)*** *shear deformation only* ***(d)*** *followed by pulverisation* ***(e)****, producing sheared mica grains and fractured quartz/feldspar with intact original grain boundaries.*

Microstructures relating to both tensile and shear deformation indicate multiphase faulting with shearing occurring first. If pulverisation had occurred first, we would not expect to individual 'new' grains within the existing boundaries of an original crystal, but would expect this incohesive 'grain' to also have been sheared along with the platy, cleaved minerals (Fig. 3.26a,b). That we do not see this indicates the more competent quartz and feldspar crystals were resistant to the initial phase of shear deformation (Fig. 3.26c-e).

Also present within this part of the fault zone is a very fine-grained clay mineral material (grain size too small to determine using scanning electron microscopy) that is frequently present within fractures (Fig. 3.27a, b). In these cases the grains are strongly aligned parallel/sub-parallel to each other and the fracture walls and grains of quartz are sometimes also found in these clay-filled fractures. This clay mineral is Mg-bearing smectite, and is the only clay mineral present within the part of the damage zone (Fig. 3.27c). The strong foliation of the smectite suggests that it has not grown in situ but rather has been injected from elsewhere in the fault zone, since there is no smectite in the pegmatite or gneiss protoliths. It is unlikely that the foliation is of shear origin since it is sub-parallel to fracture walls wherever it is observed, and there is no indication of a sigmoidal fabric that may be expected had the foliation developed in this way (Fig. 3.27).

There are two potential mechanisms for the presence of small grains of quartz (<10 μm) within these fractures. They may indicate early-stage cataclasis, resulting in comminuted grains lining fractures, that occurred before the smectite was injected. Alternatively, these grains may have been injected along with the smectite and also originate from the fault core. The latter mechanism could explain the very small grain size of quartz within these fractures, relative to the larger grains elsewhere in this part of the fault zone (Figs. 3.24 and 3.26), and is therefore the more likely. Either processes indicates at least two phases of deformation; an early stage of brittle fracturing, possibly including some degree of cataclasis, followed by a later stage of pulverisation, which we suggest was coeval to clay injection.

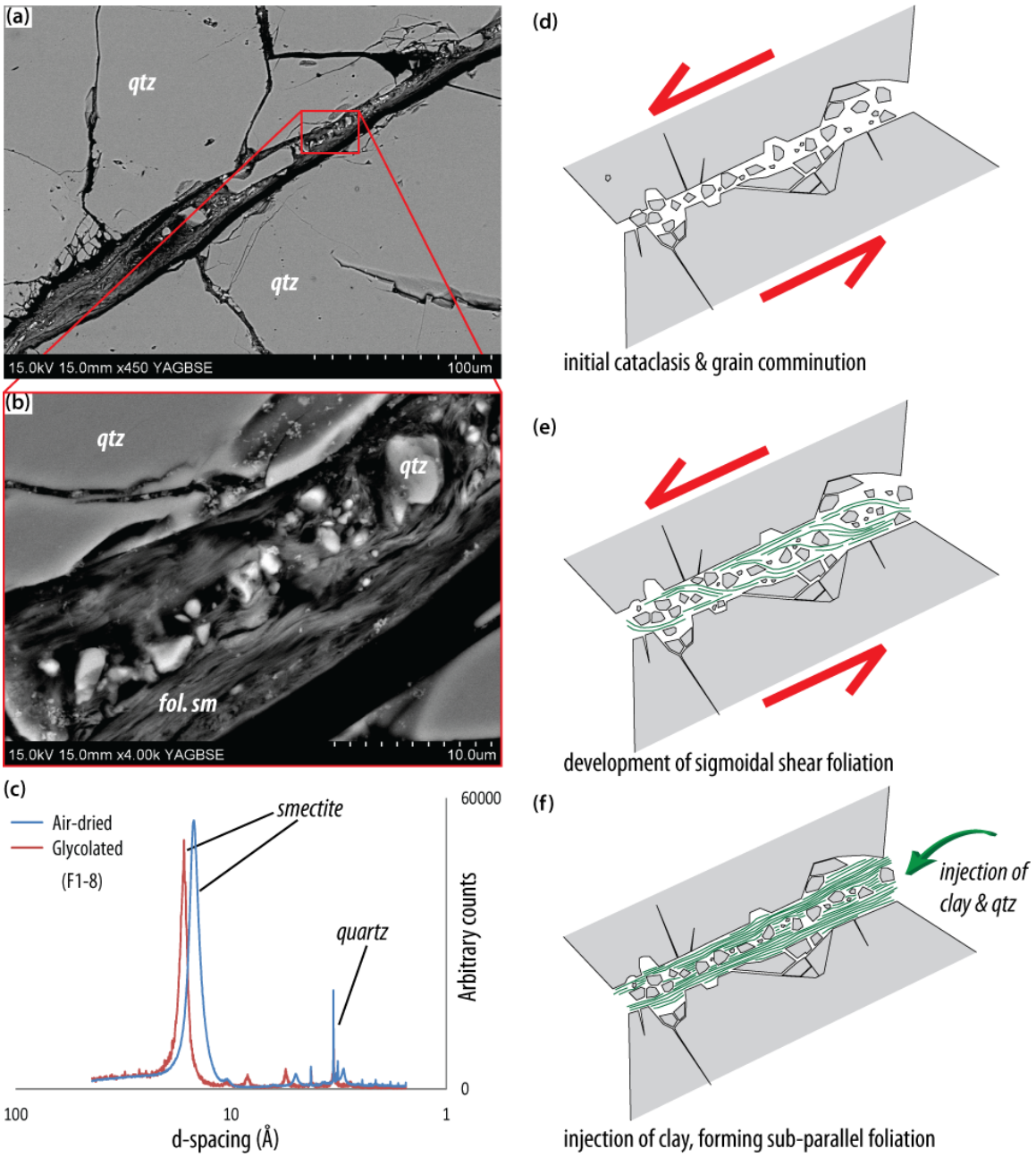

Figure 3.27: ***(a & b)*** *photomicrographs showing clay with foliation (fol.sm) parallel to fracture walls through a quartz (qtz) grains (BSEM);* ***(c)*** *XRD diffractogram for pulverised zone in footwall pegmatite;* ***(d-f)*** *schematic diagrams illustrating mode of development of foliation in smectite.*

3.3.2.3 Roded Fault

The footwall rocks of the Roded Fault damage zone, on its eastern side, are composed of Roded Quartz Diorite (Fig. 3.28). The rock is variably fractured; by intragranular microfractures in almost all quartz and feldspar grains (Fig. 3.29a), by tensile intergranular fractures filled with a calcite cement (Fig. 3.29a) and by shear fractures, filled with comminuted grains (Fig. 3.29b). Grain size is similar to the protolith for the most part, the only change (reduction) being in areas of comminution by cataclasis, where a fine-grained matrix is formed.

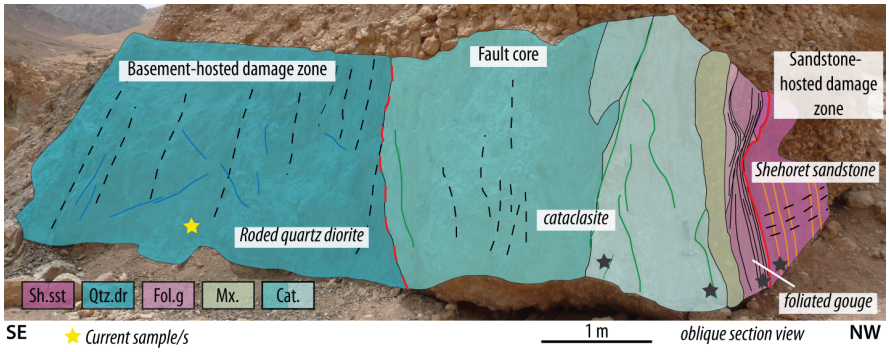

Figure 3.28: *Schematic log of Roded Fault section showing position of basement-hosted damage zone sample.*

Only occasional clay material (<5%) is present within this part of the fault zone, along fractures rather than as part of the framework of the rock. Here there is kaolinite and chlorite (Fig. 3.29d) and the diffractogram peaks of both are sharp, indicating they have well-formed crystal planes. The origin of the chlorite is likely comminution of altered biotite (Fig. 3.29) and the kaolinite an alteration product of weathering of feldspars along fractures.

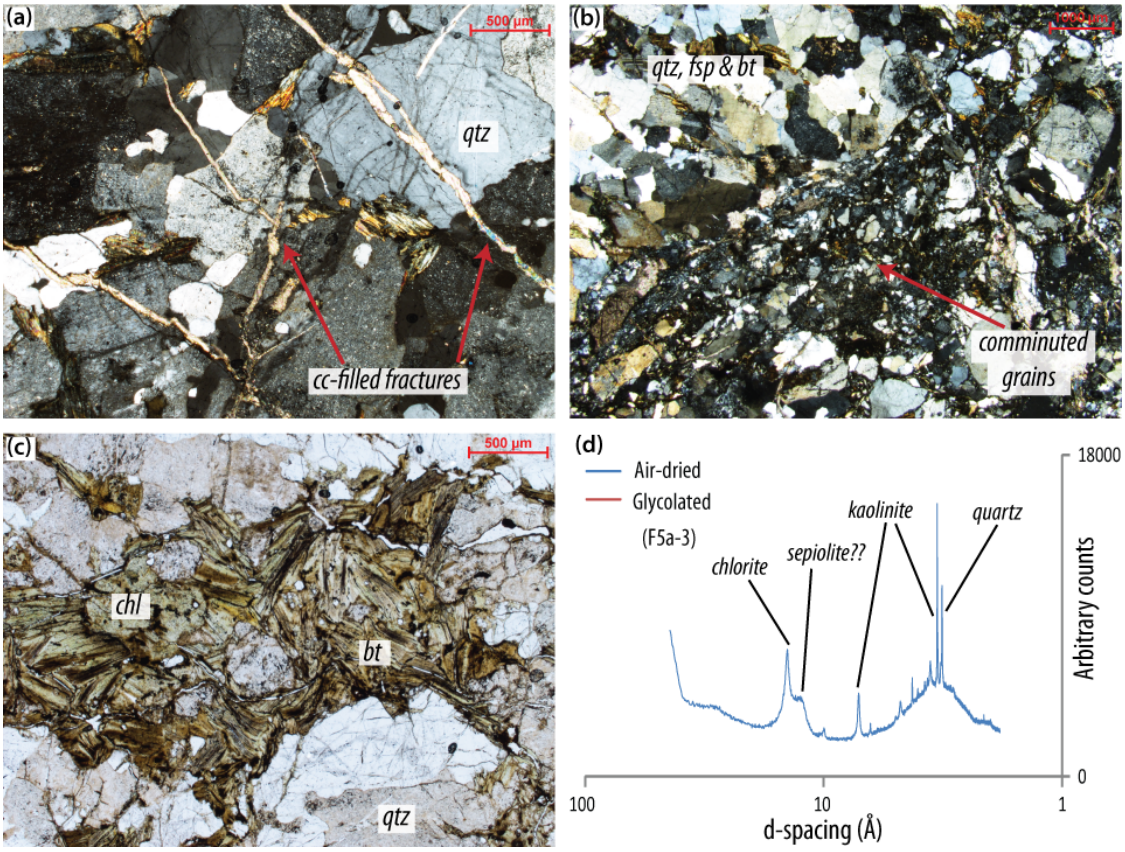

Figure 3.29: ***(a & b)*** *Photomicrographs of the Roded Fault basement damage zone:* ***(a)*** *Intragranular fractures within quartz grains, and intergranular fractures filled with calcite (XPL);* ***(b)*** *zone of cataclasis and grain size comminution (XPL);* ***(c)*** *retrograde alteration of biotite to chlorite (PPL);* ***(d)*** *XRD diffractogram showing clay mineral composition of the clay fraction: chlorite, kaolinite and possibly sepiolite (sample has not been glycolated due to lack of expandable clay minerals revealed during air-dried analysis).*

3.3.2.4 Nizoz Fault

At the section of the Nizoz Fault studied (Fig. 3.30), the damage zone immediately adjacent to the east of the fault core is comprised of the Amram Rhyolite and shows very little evidence of

deformation below the cm-scale fractures observed in the field (Section 2.6.2.5).

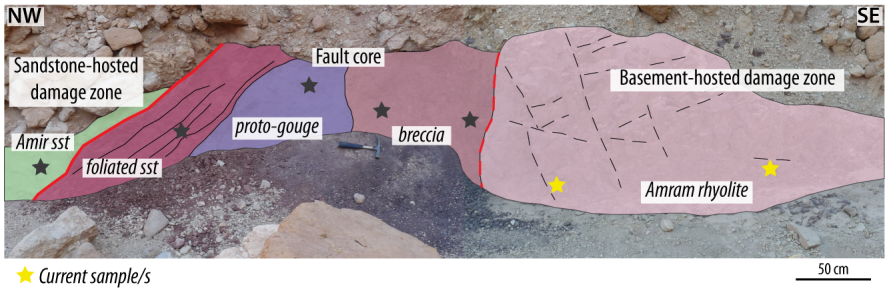

Figure 3.30: *Schematic log of Nizoz Fault section showing position of basement-hosted damage zone sample.*

The aphanitic texture observed in the protolith remains and the mineralogy is principally quartz, K-feldspar and Na-plagioclase (~50% quartz, 50% feldspars), although there is some apparent alteration of feldspar minerals to clays. There is not sufficient clay material within this part of the fault zone to extract for XRD analysis, but EDX suggests that the clay mineral is likely illite (Fig. 3.31b). It is difficult to determine average grain size of the matrix due to the aphanitic texture of the rock (Fig. 3.31a), although there are abundant phenocrysts of quartz and K-feldspar that together account for 5-10% of the total rock volume.

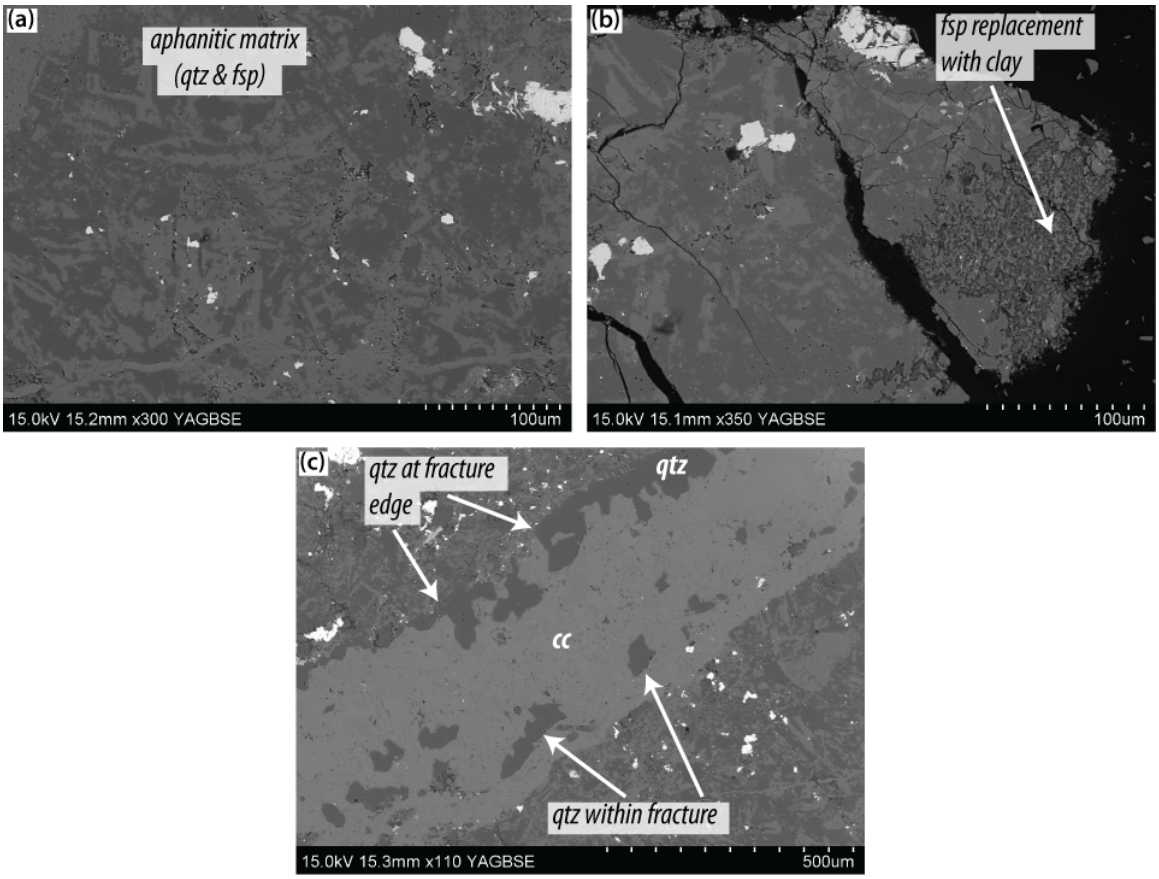

Figure 3.31: *Photomicrographs of the Nizoz Fault rhyolitic basement damage zone (BSEM): **(a)** aphanitic texture; **(b)** alteration of feldspars to kaolinite; **(c)** calcite-filled fracture with quartz grains at edges and in centre of the fracture, indicating quartz was the first phase of fracture cementation, followed by calcite after a second stage of fracturing.*

Fractures, spaced every few millimetres, of between 10 and 500 µm in width are present; they are occasionally filled with calcite but do not appear to have any preferred orientation. In the case of the larger fractures, quartz crystals of a much more regular shape than in the general matrix are sometimes present (Fig. 3.31c), ranging in size from approximately 50-100 µm. These are observed

to both line the fracture edges and be supported by the calcite fracture-fill, and it is proposed that the presence of quartz represents an earlier stage of fracture-fill that has been superseded by a later phase of fracturing and cementation.

3.3.2.5 Summary of basement-hosted damage zones

A range of deformation mechanisms and intensity are observed across the various basement damage zones. At the fault sections with lower estimated displacements (Roded, Nizoz faults), deformation is generally brittle and for the most part confined to tensile Mode 1 fracturing. In some cases these fractures are filled with cement (calcite and fluorite) and as such the damage zones remain relatively competent. There is occasional evidence of shear fracturing and associated grain size reduction by cataclasis but overall the grain size and texture in the damage zones of the Roded and Nizoz faults is relatively similar to the protolith rocks. The mineralogy is also generally the same as in the protoliths, except for an increase in alteration of feldspars to clay minerals, likely weathering-related due to the increase in permeability and surface area caused by the presence of non-cemented fractures.

In the higher displacement Shelomo and Tzefahot faults, however, deformation is more intense and evidence of a greater degree of shear deformation is seen together with tensile fracturing. Possible evidence of seismogenic rupture is also observed in the presence of pulverisation textures and clay injection. In the case of these faults, a significant amount of grain size reduction has occurred to produce a fine-grained matrix; this matrix is composed of both comminuted grains of rock as well as authigenic clay material, which is not present in the adjacent wall rocks.

3.3.3 Carbonate cover-hosted damage zones

3.3.3.1 Shelomo Fault

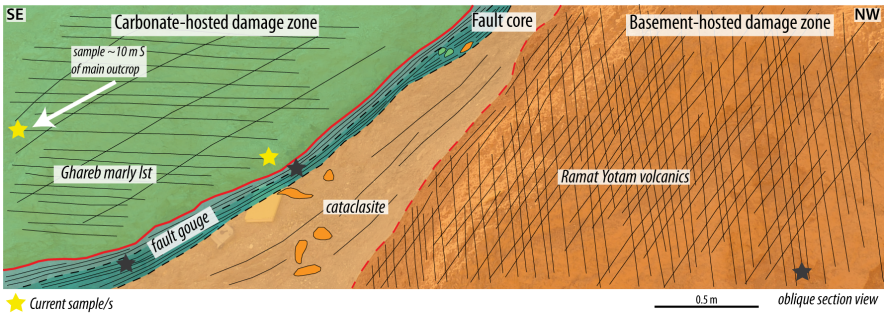

Figure 3.32: *Schematic log of Shelomo Fault, Locality A section showing relative position of carbonate-hosted damage zone samples to main fault section.*

Locality A Although the hanging wall wall rock on the western side of the Shelomo Fault is a relatively soft marl (Ghareb Formation, Section 3.3.1.10 and Fig. 3.32), the carbonate damage zone at Locality A is very hard and competent. The rock is almost entirely calcite in composition, occurring in two phases: the matrix is composed of a very fine-grained (generally <20 µm) calcite cement with anhedral grains (Fig. 3.33a). There is very fine-grained interstitial material between the fine-grained, micritic calcite (Fig. 3.33a), so we can assume that the clay content is confined

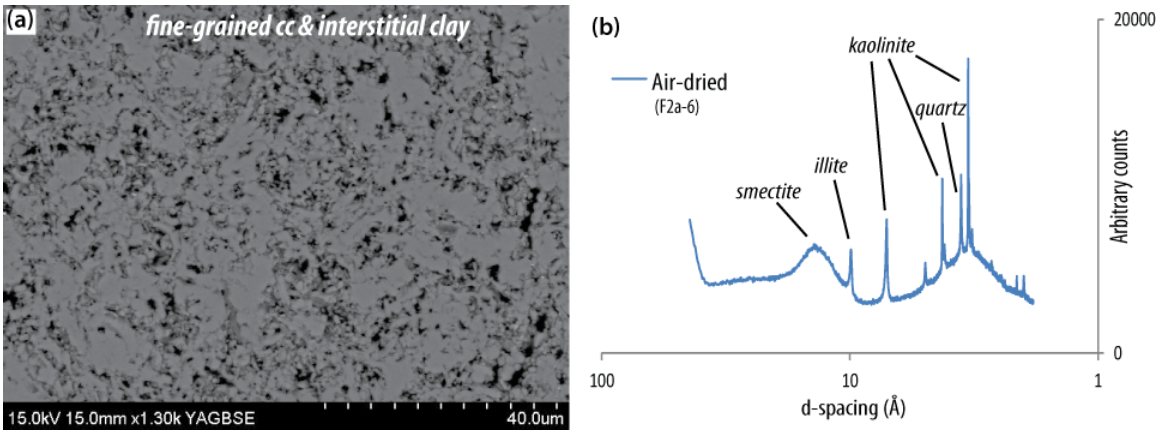

Figure 3.33: ***(a)*** *anhedral calcite with interstitial clay material (BSEM);* ***(b)*** *XRD diffractogram showing clay mineral composition of the clay fraction: smectite, illite and kaolinite.*

to the marl. The clay mineralogy is a mix of kaolinite, illite and smectite (Fig. 3.33b). There are abundant fractures, filled with a sparry calcite (Fig. 3.34a,b), which locally account for up to 40% of the rock volume. The calcite in these fractures is equant and blocky, with individual crystals up to 700 µm in size (mean 200-300 µm), indicating there was a tensile component to the fracturing along with shearing, or that tensile fracturing occurred as a second phase after shear fracturing, and calcite crystals have a vuggy texture (Fig. 3.34a,b). There are multiple phases of randomly oriented fractures that cross-cut each other (Fig. 3.33a), although shear offsets are present but minimal (10s of µm). There is also evidence of crack-seal fracturing that is indicative of repeated phases of fracturing and fluid flow (Fig. 3.34b).

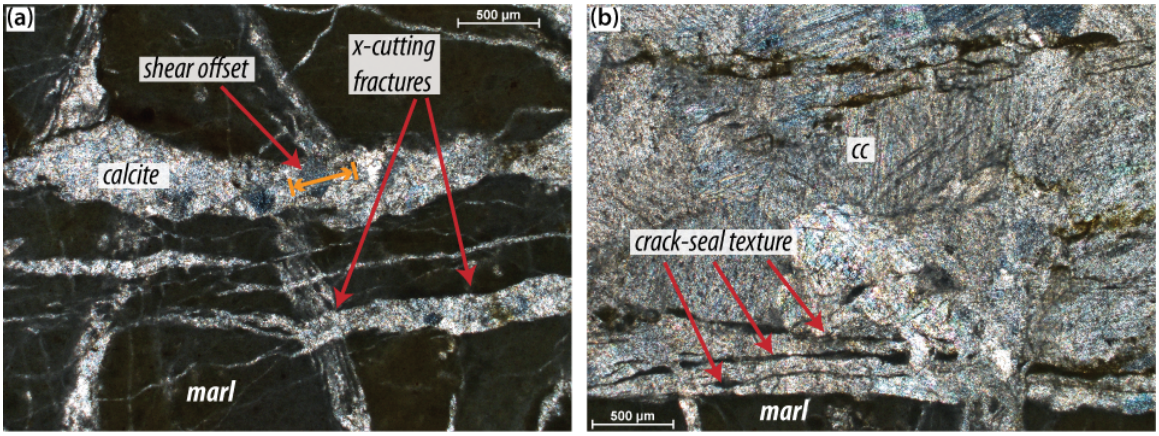

Figure 3.34: ***(a)*** *multiple generations of cross-cutting, fractures filled with sparry calcite (XPL);* ***(b)*** *evidence of crack-seal fracturing, indicating multiple phases of fracturing and cementation (XPL).*

Locality B Locality B is located 1750 m north of Locality A, and here the carbonate wall rock of the hanging wall is part of the Cretaceous Grofit Formation (Section 3.3.1.10).

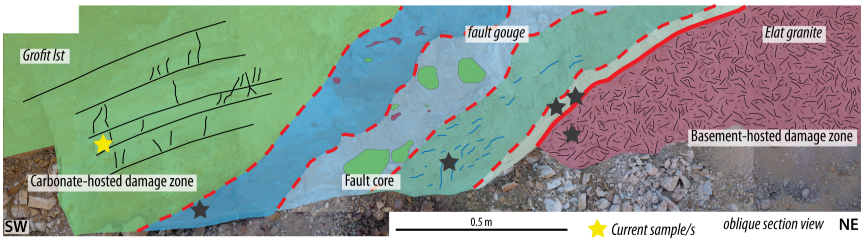

Figure 3.35: *Schematic log of Tzefahot Fault section showing position of basement-hosted damage zone sample.*

Although the sample was collected from within 50 cm of the fault core (Fig. 3.35), there are very few microscopic fractures (Fig. 3.36a,b) and the rock is very similar in appearance to the undeformed protolith (Fig. 3.14b). It is mainly composed of ooids with crystalline filling the primary porosity. There is some layering with fine-grained calcite and iron-stained layers (Fig. 3.35b), although there is no appreciable clay content in the sample, with only trace amounts of illite and kaolinite being detected by XRD (Fig. 3.35c).

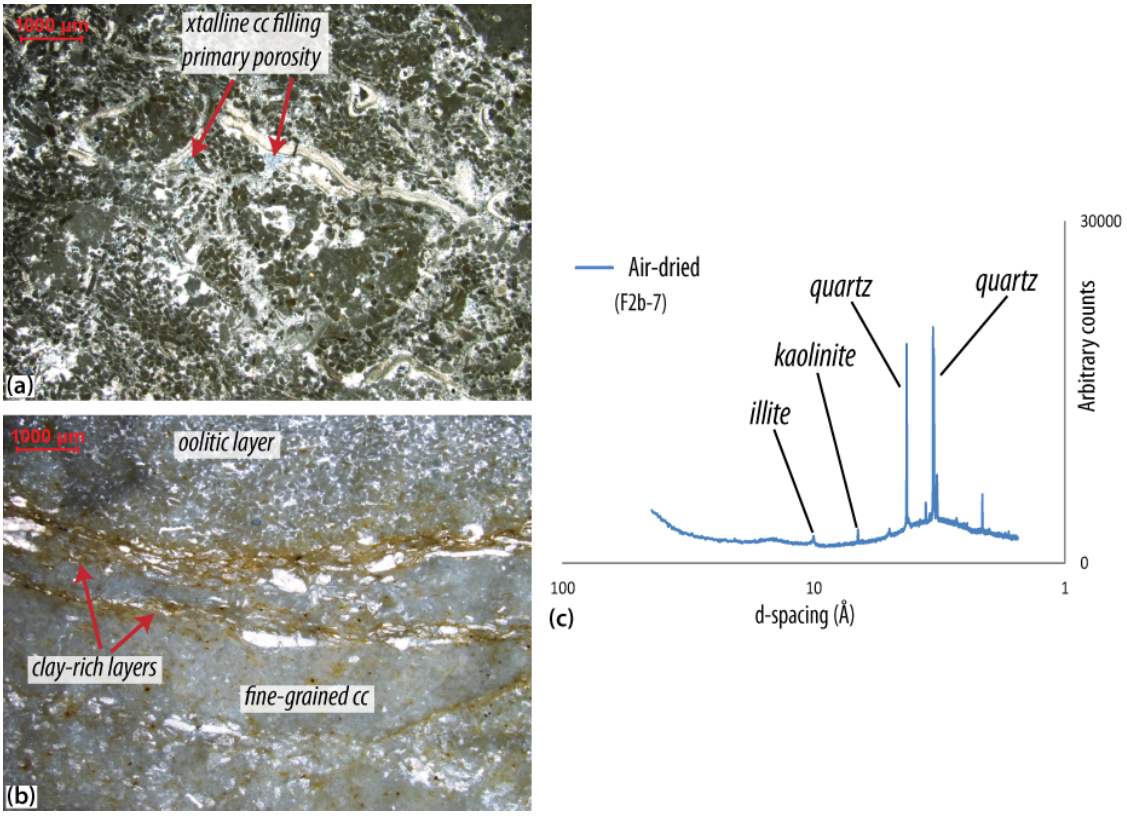

Figure 3.36: ***(a)*** *Photomicrograph showing oolitic texture of carbonate-hosted hanging wall (XPL);* ***(b)*** *defined layers of oolitic calcite, fine-grained calcite and mud layers (XPL); (c) XRD diffractogram showing lack of clay minerals.*

3.3.3.2 Tzefahot Fault

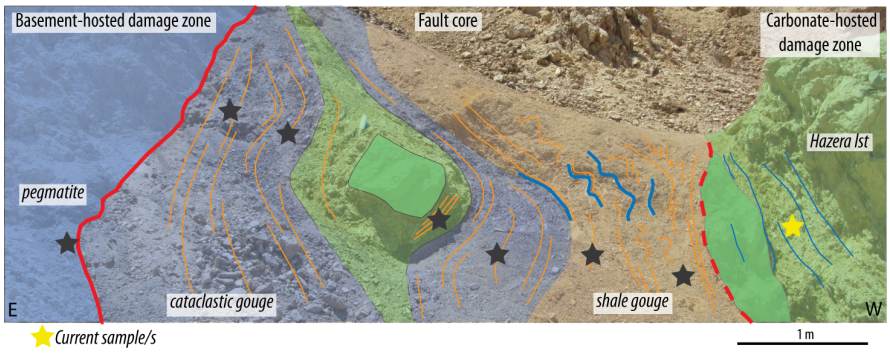

Figure 3.37: *Schematic log of Tzefahot Fault section showing position of fault core samples.*

The western hanging wall of the Tzefahot Fault (Fig. 3.37) is Upper Cretaceous Hazera Formation carbonate (Fig. 2.4). At this location the carbonate-hosted damage zone is composed of a mix of micritic calcite and rhomb-shaped dolomite (Fig. 3.38). The micritic calcite is very fine-grained

(<10 μm) and grains are anhedral (Fig. 3.38a) whilst the dolomite rhombs have a mean grain size of ~100 μm and are euhedral.

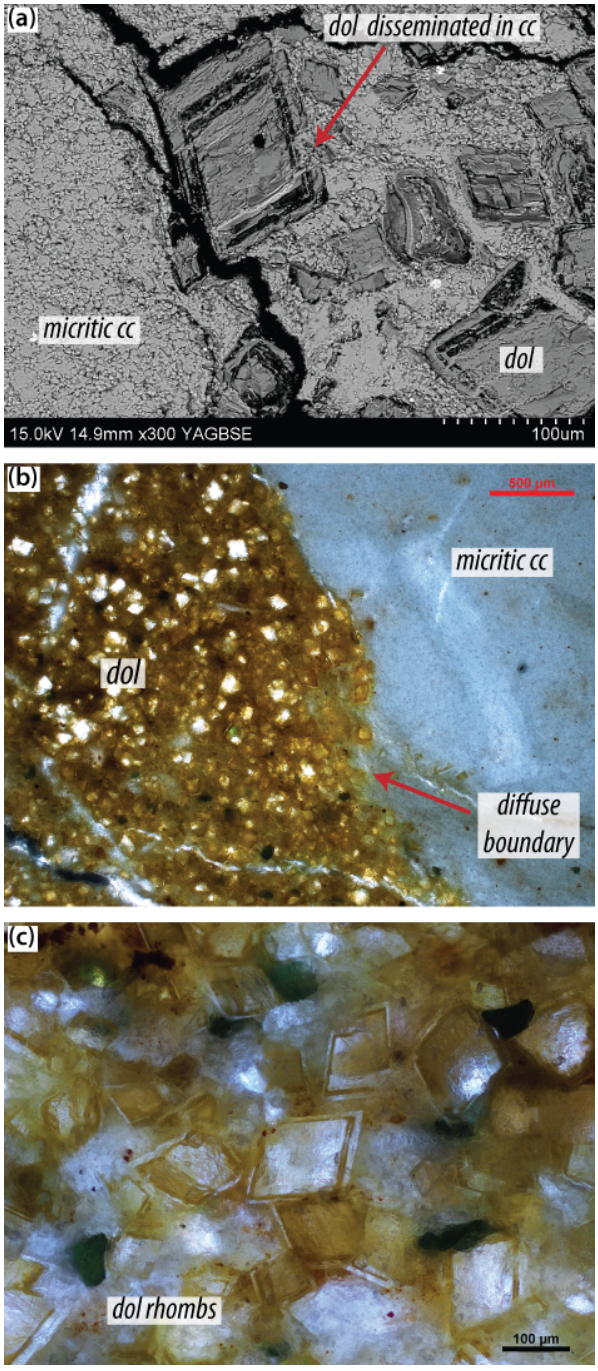

Figure 3.38: *Photomicrographs of the Tzefahot Fault carbonate damage zone:* ***(a)*** *dolomite (dol) rhombs within a very fine-grained calcite (cc) matrix (BSEM);* ***(b)*** *adjacent zones of dolomite and calcite with diffuse boundary (XPL);* ***(c)*** *euhedral dolomite crystals (XPL).*

There are occasional shell fragments within the micrite, some of which may be up to 1 mm in size. There is occasionally a distinct boundary between the micrite and dolomite (Fig. 3.38a), but more commonly there appear to be areas of higher concentrations of one or the other mineral, without a clear boundary between. In some areas the dolomite crystals appear to be disseminated within a micritic matrix (Fig. 3.38a), whilst elsewhere the dolomite crystals appear to support each other (Fig. 3.38b,c). The rock is sparsely-fractured at the microscale with calcite-filled fractures that formed in at least two stages, demonstrated by cross-cutting relationships (Fig. 3.39a). There is possible evidence of shearing within the calcite fill of fractures (Fig. 3.39a), indicating that more than one phase of deformation may have occurred along single fractures.

The clay mineralogy is dominated by kaolinite, but illite, smectite and a mixed layer clay (likely chlorite-smectite) are also present (Fig. 3.39b) as interstitial material between the micritic calcite (Fig. 3.39c,d). Although there are numerous macroscopic fractures present in the hanging wall carbonate rocks, density of fractures at the microscale is much lower. Overall, relatively few microfractures are observed and deformation appears confined to these discrete structures. There is no apparent relationship between the location of clay grains and fractures, and as such we infer the clays to be detrital/diagenetic in origin and not to be related to faulting. Deformation is not continuous across the damage zone at the microscale, but is confined to localised fractures that are spaced every few millimetres throughout the sample. The random orientation of these fractures does not produce a fabric at this scale, despite a macroscale fabric being apparent (Section 2.6.2.2). As observed in the carbonate damage zones of the Shelomo Fault, clay minerals are generally observed as interstitial material between calcite and dolomite grains. There is no evidence of clay material within fractures or in large volumes elsewhere, so we believe these minerals to be diagenetic in origin.

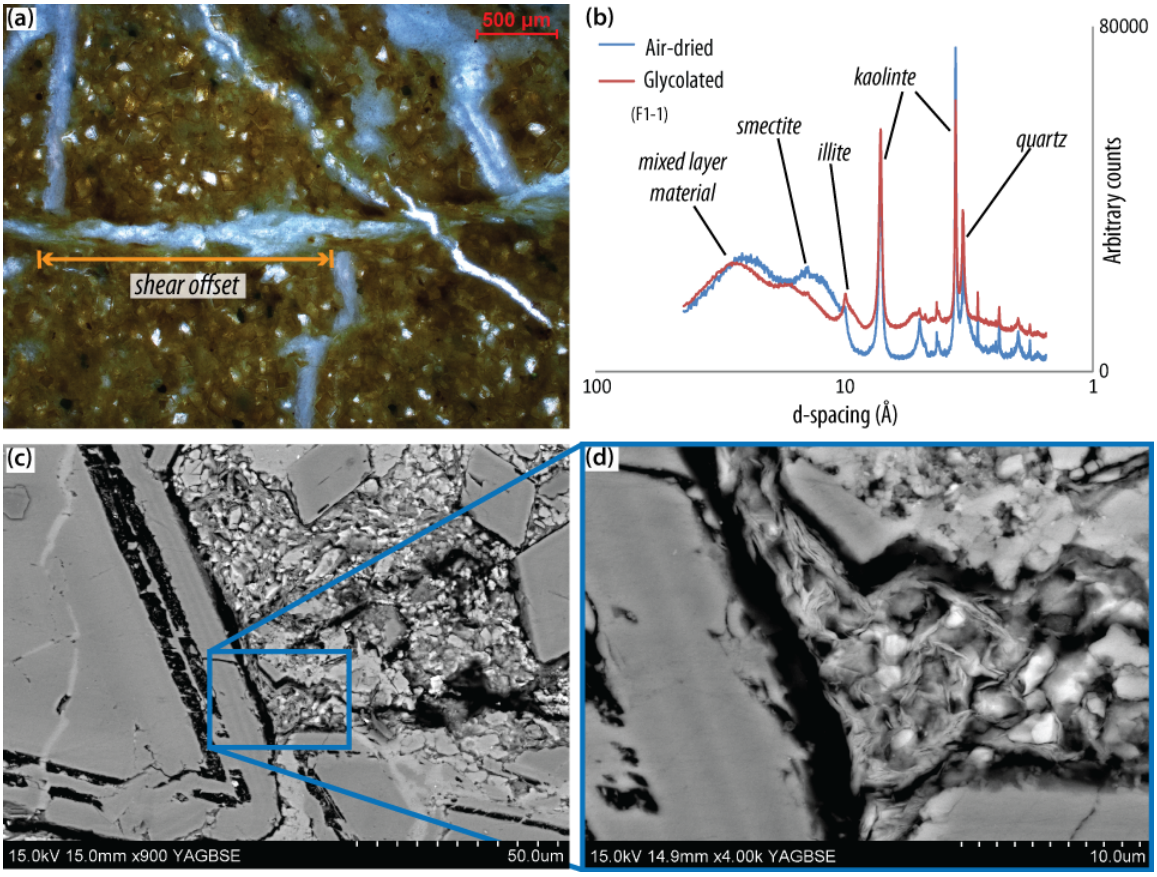

Figure 3.39: ***(a)*** *Photomicrograph of cross-cutting, calcite-filled shear fractures in the Tzefahot Fault carbonate damage zone (XPL);* ***(b)*** *XRD diffractogram showing clay mineral composition of the clay fraction: smectite, mixed layer material, kaolinite and illite;* ***(c & d)*** *photomicrographs showing interstitial clay between micritic calcite (BSEM).*

3.3.3.3 Yehoshafat Fault

The carbonate damage zone of the hanging wall side of the Yehoshafat Fault is composed of the lower, clay-rich section of the Grofit formation and at this location consists of interbedded micritic limestone and shale (Fig. 3.40 and Section 2.6.2.6).

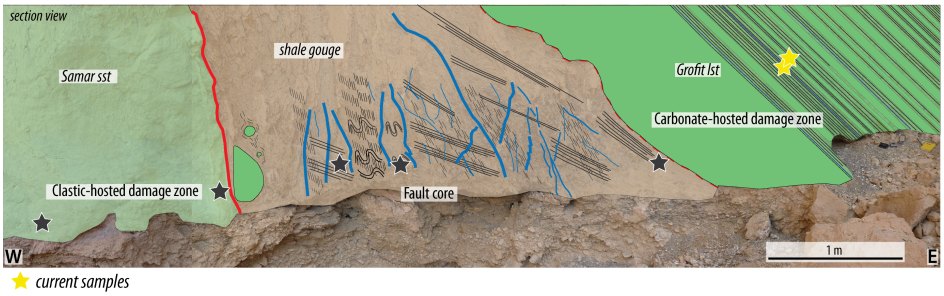

Figure 3.40: *Schematic log of Yehoshafat Fault section showing position of carbonate-hosted damage zone sample.*

At the macroscale, the shale beds are very similar in appearance to the Ora Shale (Section 2.6.2.6). There is little evidence of brittle deformation and the rock has a strong, pervasive foliation (Fig. 3.41a). There are very few clasts present (< 5% rock volume), composed of quartz, calcite and dolomite, and these vary in roundness and sphericity. The clay mineral composition is near-identical to the Ora Shale, consisting of kaolinite, illite, low crystallinity smectite and some mixed layer chlorite-smectite (Fig. 3.41b).

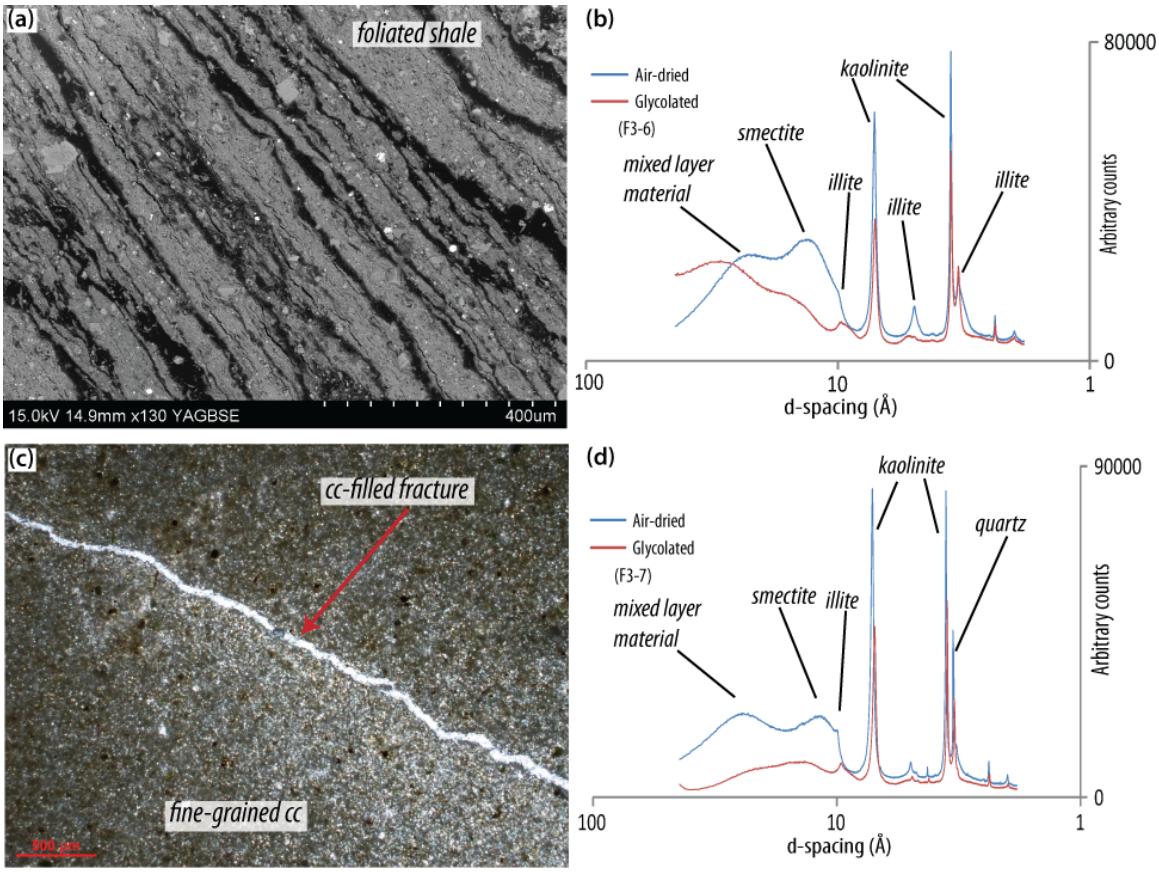

Figure 3.41: ***(a)*** *Photomicrograph of the carbonate hosted damage zone, shale bed (BSEM);* ***(b)*** *XRD diffractogram showing clay mineral composition of the clay fraction in the shale beds of the Yehoshafat Fault carbonate damage zone: smectite, mixed layer material, kaolinite and minor illite;* ***(c)*** *photomicrograph of the Yehoshafat Fault carbonate damage zone, limestone bed (XPL);* ***(d)*** *XRD diffractogram showing clay mineral composition of the clay fraction: smectite, mixed layer material, kaolinite and minor illite.*

The limestone beds are generally relatively homogeneous in terms of grain size, consisting solely of micritic grains <10 µm in size. There is very little, if any, biogenic material and the only evidence of deformation is in tensile fractures filled with sparry calcite (Fig. 3.41c). Clay minerals are present interstitially between the fine-grained calcite, and the composition is very similar to that of the shale beds. There is well-formed kaolinite with smaller amounts of illite, smectite and mixed layer chlorite-smectite (Fig. 3.41d).

3.3.3.4 R12 Fault

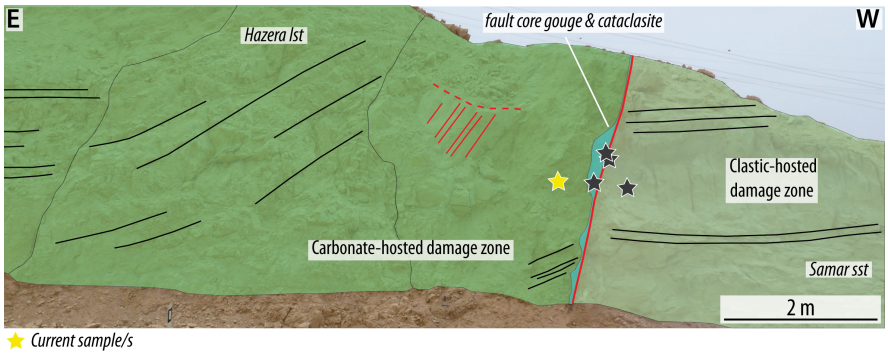

Figure 3.42: *Schematic log of R12 Fault section showing position of carbonate-hosted damage zone sample.*

The carbonate damage zone directly adjacent to the fault core of the R12 Fault (Fig. 3.42) comprises heavily fractured limestone, although thin section analysis shows that individual clasts are not necessarily intensely deformed (Fig. 3.43a,b), indicating that microscopic brittle deformation is not pervasive. Calcite grains vary in size but are small and generally <20 μm, although they frequently form aggregate clasts up to ~60 μm (Fig. 3.43c). Grains are anhedral, which together with the fine grain size, gives the rocks a micritic texture overall. There is evidence of extensive pressure solution, in the form of through-going stylolites (Fig. 3.43a) and dissolution seams at the contacts between many grain boundaries (Fig. 3.43b,c). Approximately 60-70% of the rock volume is calcite with the rest being interstitial clay material; it is composed of kaolinite, illite and low crystallinity smectite (Fig. 3.43d).

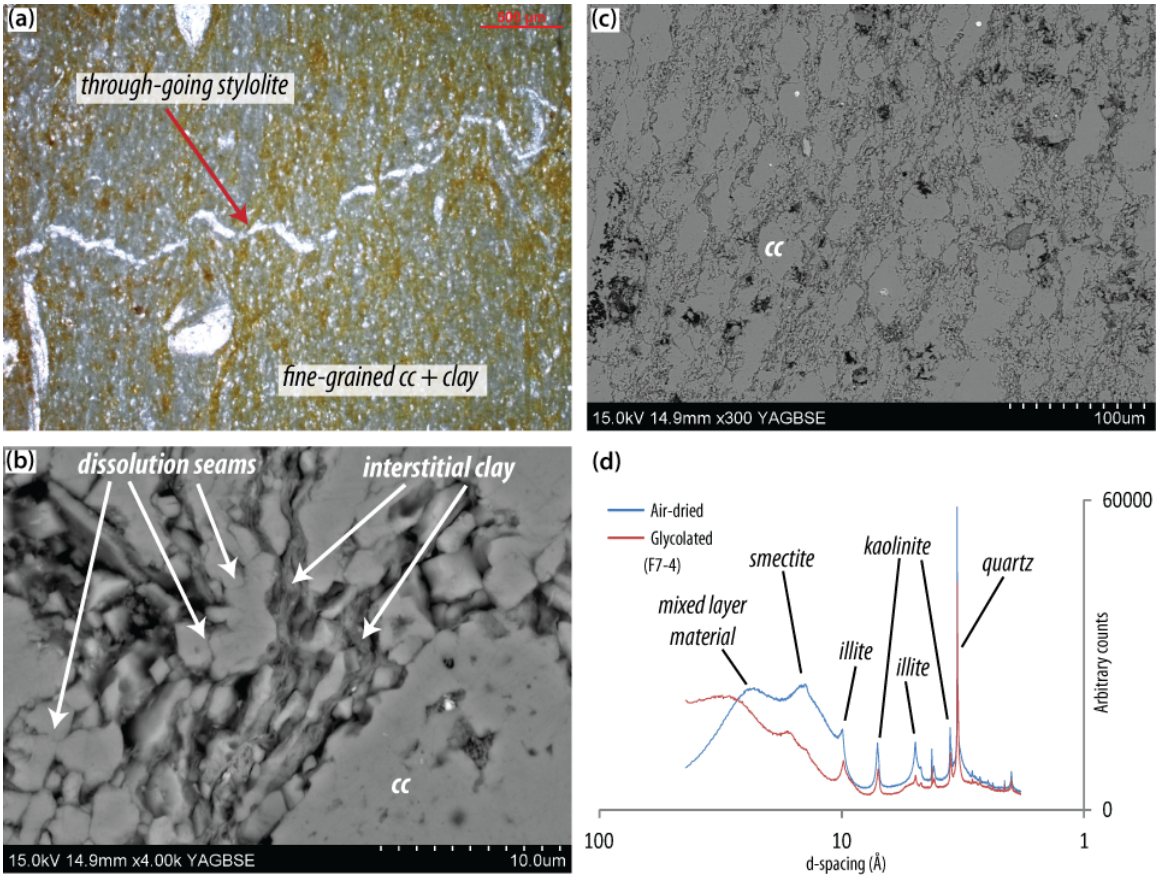

Figure 3.43: ***(a-c)*** *photomicrographs of the R12 Fault carbonate-hosted damage zone:* ***(a)*** *through-going pressure solution seam (XPL);* ***(b)*** *interstitial clay between grains of calcite (BSEM);* ***(c)*** *poorly-defined boundaries of individual calcite grains and contacts between grains (BSEM);* ***(d)*** *XRD diffractogram showing clay composition of the sample: smectite, mixed layer material, kaolinite and minor illite.*

3.3.3.5 Summary of carbonate cover-hosted damage zones

Deformation in the carbonate damage zones appears to be much less intense than in the basement equivalents on a microscale, even in the case of the highest estimated displacement faults (the Shelomo and Tzefahot faults). There is occasional evidence of shear fracturing (e.g. Fig. 3.39a) but we have not observed any evidence of widespread grain size reduction through cataclasis. The degree of fracturing does vary across the fault zones, with the rocks of the Shelomo Fault being the most intensely fractured. However, there does not seem to be a great deal of difference in the intensity of fracturing in the Tzefahot and R12 damage zones, suggesting that this is not solely

linked to the amount of displacement on a fault. At the Shelomo Fault there is evidence of both high pore fluid pressure syn-tectonic cementation (calcite-filled tensile fractures) and repeated cycles of fracturing and fluid ingress (crack-seal fractures).

3.3.4 Clastic cover-hosted damage zones

3.3.4.1 Roded Fault

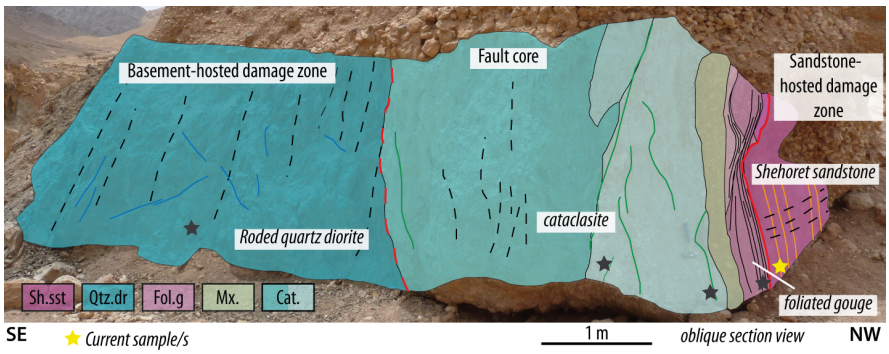

Figure 3.44: *Schematic log of Roded Fault section showing position of basement-hosted damage zone sample.*

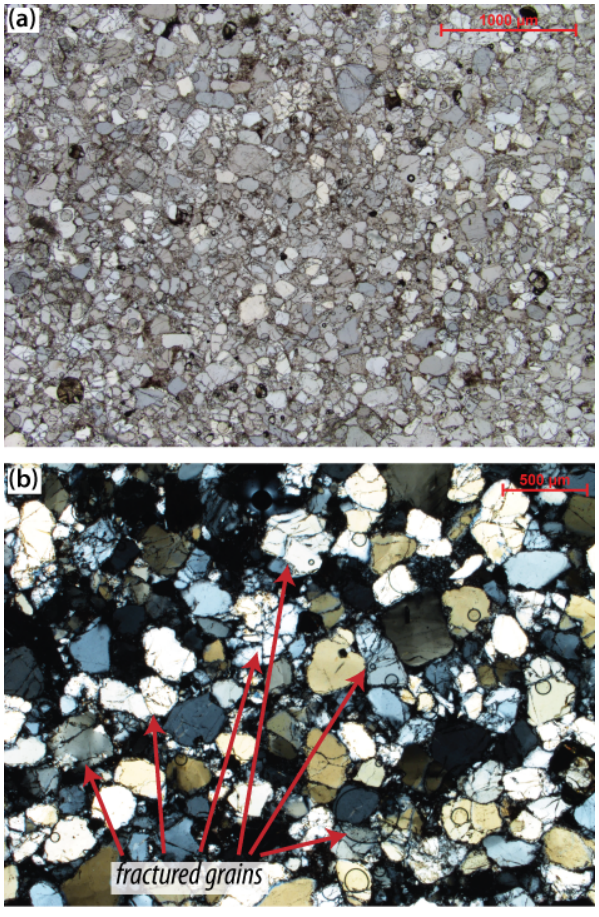

Figure 3.45: *Photomicrographs of the Roded Fault sandstone-hosted damage zone:* ***(a)*** *grain size range and poor sorting (PPL);* ***(b)*** *intragranular microfracturing (BSEM).*

The Variegated Member of the Shehoret Formation sandstone forms the hanging wall rocks on the western side of the Roded Fault (Fig. 3.44). It does not appear to be intensely deformed and the mean grain size is approximately 200 µm though the range is ~50-500 µm (Fig. 3.45a). Grains are moderately-well rounded with a moderate sphericity. Shape and rounding do not appear to be size-dependent as there is a range of each at all sizes and the grains are not well-sorted.

Evidence of fault-related deformation is preserved in the randomly-oriented, intragranular micro- fracturing of 80-90% of grains within the sandstone (Fig. 3.45a,b), in contrast to the 30-50% observed in the protolith (Section 3.3.1.8), and in addition many grains appear to host numerous fractures, though few propagate across multiple grains (Fig. 3.45b). Deformation by intragranular microfracturing is distributed more or less evenly across the damage zone and may be described as relatively continuous since the spacing of fractures is at the 10s µm scale. The random orientation of these fractures does not produce a fabric in the damage zone rock.

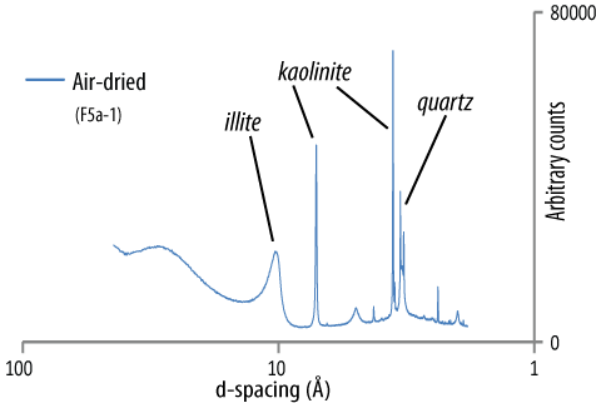

Figure 3.46: *XRD diffractogram showing clay mineralogy of Roded Fault sandstone-hosted damage zone: illite and kaolinite.*

Composition of grains is the same as in the protolith (>95% quartz) but clay mineral compositions differ somewhat as in the damage zone kaolinite is present in addition to illite (Figs. 3.10 and 3.46d). The sharpness of the kaolinite peaks of the XRD pattern suggests it has a high crystallinity and is very similar in form to kaolinite in other sandstones (Section 3.3.1.9), so we infer its presence to be the result of a local variation in detrital deposits rather than to being a fault-related mineral.

3.3.4.2 Nizoz Fault

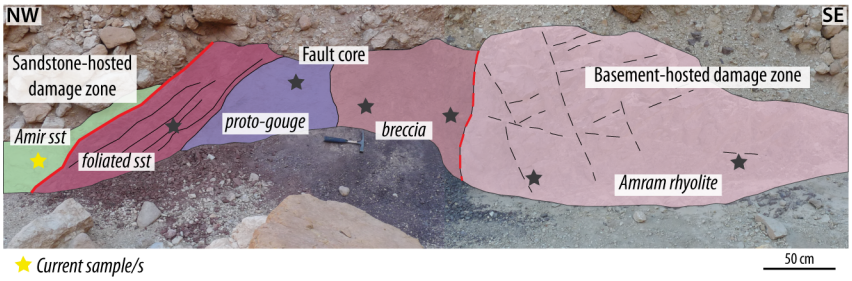

Figure 3.47: *Schematic log of Nizoz Fault section showing position of clastic-hosted damage zone sample.*

The damage zone immediately adjacent to the fault core of the Nizoz Fault (Fig. 3.47) is very similar in appearance to the older Cretaceous sandstone protoliths (grains are moderately-rounded to angular and composed largely of quartz and K-fsp, Fig. 3.12), with the exception of the presence of red-coloured bands (Fig. 3.48a).

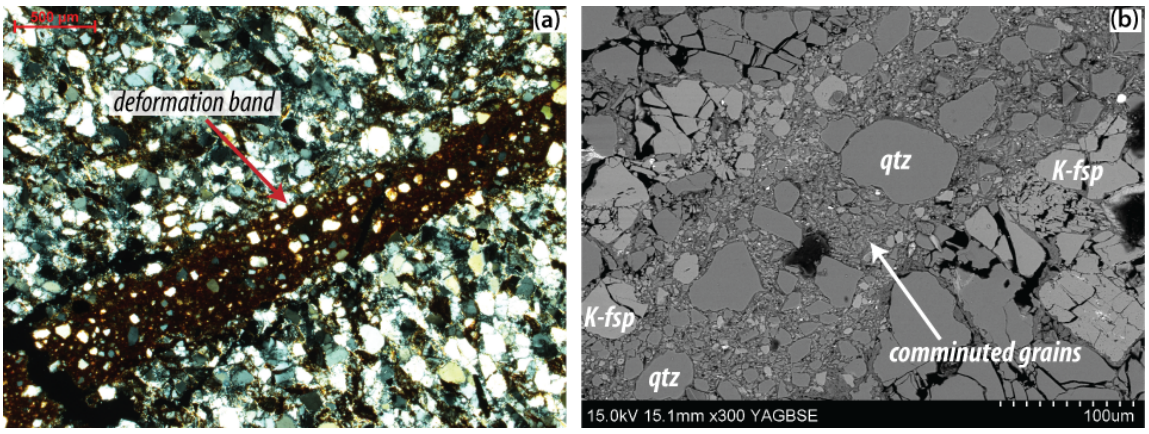

Figure 3.48: *Photomicrographs of the Nizoz Fault hanging wall sandstone:* ***(a)*** *deformation band identifiable by red-coloured material containing small, rounded grains (XPL);* ***(b)*** *BSEM image of same area, band containing intensely comminuted grains.*

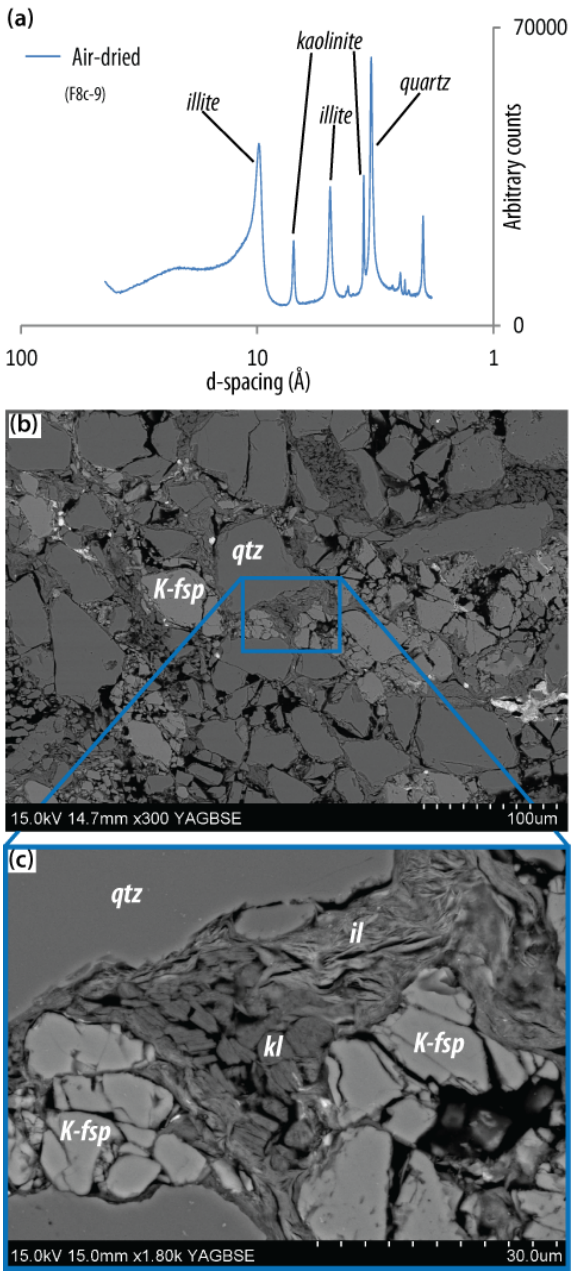

Figure 3.49: *Photomicrographs and XRD diffractogram of the Nizoz Fault clastic-hosted damage zone:* ***(a)*** *XRD diffractogram showing clay mineral composition: illite and kaolinite;* ***(b)*** *angular clasts of varying sizes (BSEM);* ***(c)*** *two phases of clay minerals between quartz (qtz) and K-fsp grains: foliated illite (il) and stacks of kaolinite (kl) (BSEM).*

These bands are generally <1 mm wide, though occasionally are up to 3 mm, and continuous up to 10 cm; because of the width of these structures and small grain size, it is not possible to observe any sense of shear offset. In optical mineralogy these bands appear dark brown and contain grains of quartz that are significantly smaller (< 100 µm) than the average grain size (on the order of 200 µm) of the rest of the rock. These grains are suspended in an ultra fine-grained matrix (<5 µm) that is composed of both comminuted quartz and feldspar grains along with clay mineral/s (Fig. 3.48b).

Although the thin section analysed has not been stained with blue epoxy resin, it is nevertheless possible to see that there is a lack of pore space (black space on SEM images) within the bands compared to outside them, and that, together with extreme grain comminution, leads us to interpret that these are cataclastic deformation bands. Grains of quartz and feldspar outside of the deformation bands are angular and variably fractured with intragranular microfractures (Fig. 3.48b). There are no through-going intergranular fractures that continue across multiple grains; deformation is confined to deformation bands and intragranular fractures and there is no overall fabric to the sandstone. Deformation by both cataclasis (forming deformation bands) and microfracturing is discontinuous and not evenly distributed across the damage zone; the spacing of deformation bands is on the millimetre scale, whilst the intensity of microfracturing is greatest at, but exclusive to, deformation band margins.

It was not possible to separate deformation bands from the rest of the sample for XRD analysis, but the clay mineralogy of the entire sample is composed of kaolinite and illite (Fig. 3.49a). It is possible, in some cases, to determine the composition of clay minerals outside of deformation bands using EDX and we can observe both kaolinite and illite in the matrix of the sandstone; whilst kaolinite occurs as discrete 'stacks' a few microns in length and height, illite occurs as more continuous, foliated material (Fig. 3.49b,c). In addition there is a slight difference in grey-scale colour in backscattered electron images, indicating a variation in atomic weight (and therefore chemical composition) between these two phases. Since both minerals are present within the matrix, we infer that the deformation bands are the product of cataclasis-only and there has been

little alteration or new mineral growth within them. Clay minerals account for approximately 30% of the total rock volume and, although it is grain-supported, this accounts for the relatively grainy texture observed in the field.

3.3.4.3 Yehoshafat Fault

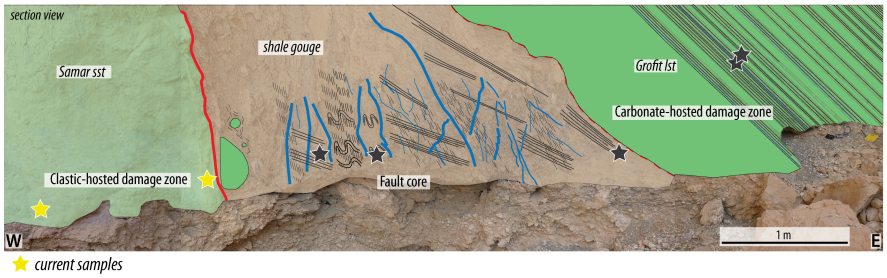

Figure 3.50: *Schematic log of Yehoshafat Fault section showing position of sandstone-hosted damage zone sample.*

The Cretaceous Avrona sandstone forms the footwall on the western side of the Yehoshafat Fault at the studied section (Fig. 3.50). Quartz grains are highly angular and range in size from <5 µm-∼200 µm with a mean of ∼100 µm (Fig. 3.51a,b). There is an interstitial kaolinite cement and though there is contact between some quartz grains, the rock is matrix-supported with an overall clast:matrix ratio of approximately 60:40.

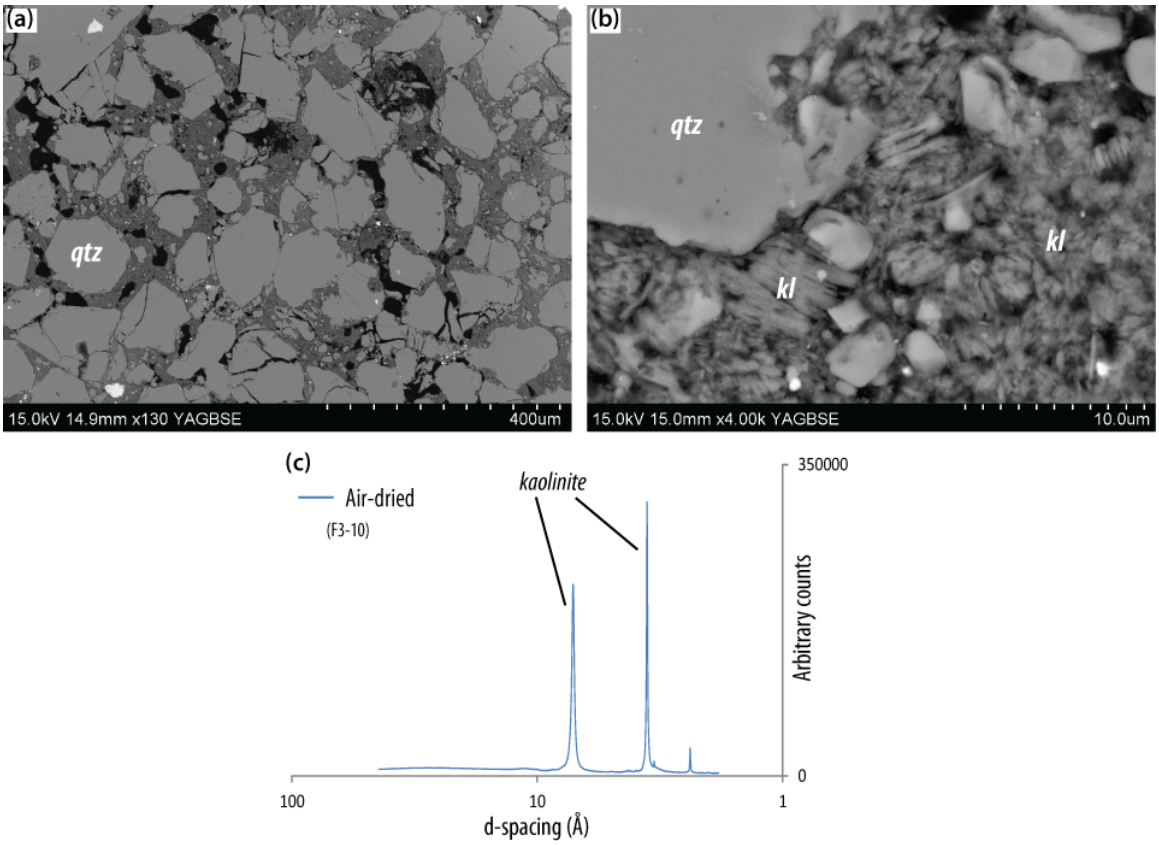

Figure 3.51: *Photomicrographs of and XRD diffractogram for sandstone-hosted damage zone of the Yehoshafat Fault:* ***(a)*** *angular quartz (qtz) grains with interstitial clay;* ***(b)*** *stacks of interstitial kaolinite (kl);* ***(c)*** *XRD diffractogram showing clay mineral composition of sandstone footwall damage zone.*

There has been significant comminution of grains compared to the protolith rock, (where there

are few grains <50 µm Fig. 3.13). There does not appear to be any size-related stratification of quartz grains or shape preferred orientation and there is no pervasive fabric. There is relatively little microfracturing of individual grains, with <10% overall being internally fractured, though larger grains (<100 µm) are preferentially affected and >50% of grains of this size are fractured. Intragranular fractures are random in orientation and there are few/no intergranular fractures as overall, few clasts are in contact with each other. Deformation is distributed more or less evenly across the damage zone and there are no areas of concentrated, localised deformation.

The clay content of this sample, including the inferred principal slip zone at the eastern edge of the fault core (Section 2.6.2.6 and Fig. 3.52b,c), is near identical to that of the protolith rock (Fig. 3.13e), containing only kaolinite (Fig. 3.51c). The kaolinite is observed as fragmented individual grains with randomly oriented stacks of plates up to 5 µm thick (Fig. 3.51b). However, in the 2-3 mm directly adjacent to the fault plane, there is a dark red/brown staining of the cement, reflecting an enrichment of FeO rather than a mineralogical change (Fig. 3.52a,b). This is distributed relatively evenly through the kaolinite cement (Fig. 3.52a-c), suggesting fluid flow close to the fault plane.

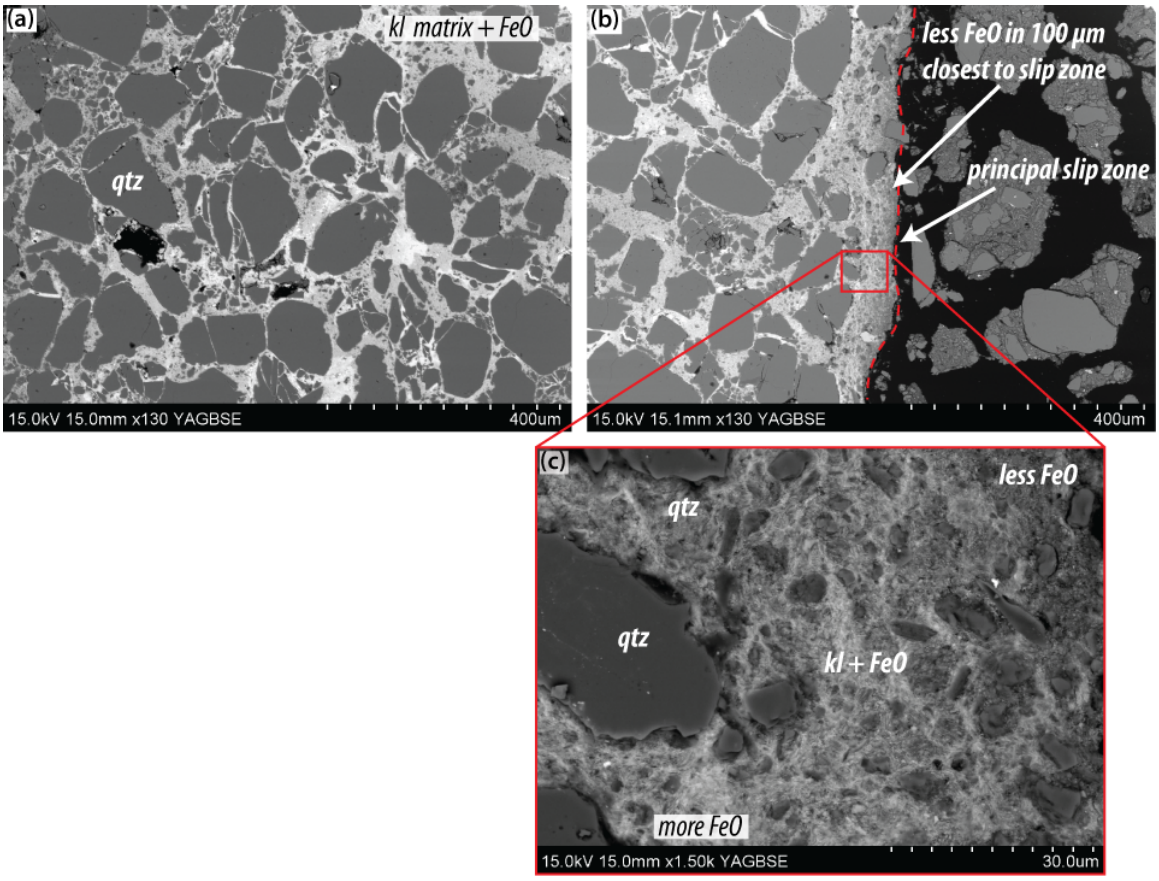

Figure 3.52: *Photomicrographs of the Yehoshafat Fault sandstone-hosted damage zone:* ***(a)*** *angular grains in a kaolinite (kl) and FeO matrix;* ***(b)*** *comminution of grains and lower concentration of FeO in 100 µm closest to the fault plane;* ***(c)*** *enlarged image of matrix close to fault plane with fewer clasts and lower concentration of FeO nearest the fault plane to right of image.*

In the 100-200 µm closest to what we believe from field evidence to be the fault plane (Section 2.6.2.6) there is intense comminution of kaolinite grains with the majority being smaller than 10 µm in size (Fig. 3.52b). Fe-staining is slightly less intense here (Fig. 3.52b,c), suggesting a possible reduction in permeability through compaction during cataclasis. Deformation in this part of the fault zone is confined to brittle fracturing and comminution of grains, there is no evidence of fluid assisted DMT or alteration processes taking place.

3.3.4.4 R12 Fault

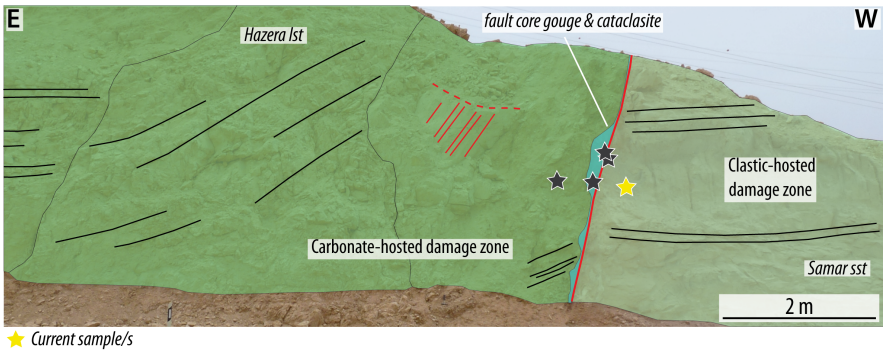

Figure 3.53: *Schematic log of R12 Fault section showing position of carbonate-hosted damage zone sample.*

The incohesive nature of the Samar sandstone in the footwall damage zone of the R12 Fault (Fig. 3.53) meant that it was not possible to collect a sample for sectioning, although we were able to collect material for XRD analysis. As with the damage zone of the Yehoshafat Fault, the only clay mineral this rock contains is kaolinite (Fig. 3.54). Deformation appears to be distributed and continuous across the damage zone, and XRD analysis confirms that it contains no authigenic clay material.

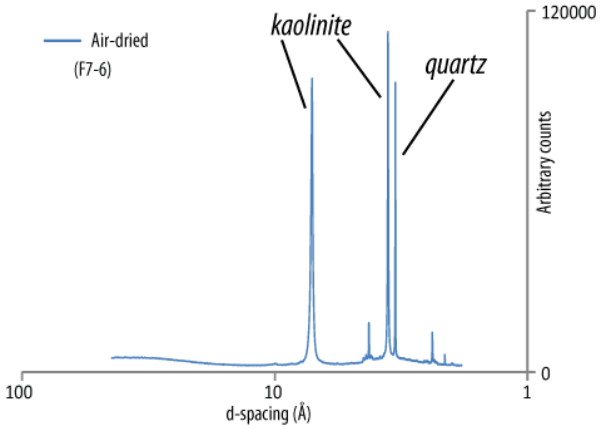

Figure 3.54: *R12 Fault clastic damage zone: XRD diffractogram showing clay mineral composition of the clay fraction: kaolinite only.*

3.3.4.5 Summary of clastic cover-hosted damage zones

Deformation in the clastic damage zones are similar across all the localities, regardless of estimated fault length and displacement, and of the juxtaposed wall rocks on the other side of the faults. Framework grains of feldspar and quartz are commonly microfractured, but the presence of supporting clay matrix appears to retard these fractures and they tend not to propagate through multiple grains. Comminution through fracturing and cataclasis has occurred to varying extents and it is only in the wall rocks of the Nizoz Fault that we observe significant cataclasis and formation of deformation bands. It is only close to the main fault plane (of the Yehoshafat Fault) that a layer of intensely comminuted grains is seen. Elsewhere, comminuted grains are distributed amongst larger grains, suggesting the smaller grains formed through repeated microfracturing of large grains, distributed over 10s of centimetres across the damage zones, rather than localised shear deformation along discrete, transgranular fractures. Analysis of the clay matrices reveals there to

have been no mineralogical changes between the protolith and damage zone rocks, indicating that deformation has taken place by brittle mechanisms only.

3.3.5 Fault cores

3.3.5.1 Cataclastic gouges

Shelomo Fault Two sections of the Shelomo Fault core have been studied and since their fault zone architectures and wall rock lithologies differ (Section 2.6.2.1), they will be described separately here.

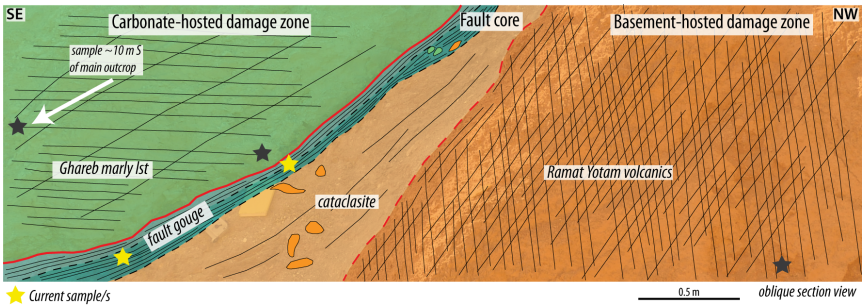

Figure 3.55: *Schematic log of Shelomo Fault, Locality A section showing position of fault core sample.*

Locality A At Locality A, the fault core consists of: *(i)* a narrow (10 cm) band of brown, foliated material located on the eastern side, directly adjacent to the fault plane; *(ii)* a slightly wider band (10-20 cm) of red foliated material; and *(iii)* a 50 cm wide layer of hard, cohesive cataclasite lacking in a pervasive fabric.

In the brown layer immediately adjacent to the fault plane, the foliated gouge is incohesive and friable along foliation planes. It contains clasts of quartz, feldspars (K-fsp, Na-plag) and less common calcite that are supported by an extremely fine-grained (<1 µm) matrix (Fig. 3.56a). Clasts vary in size from 5 µm-2 mm and as such it is difficult to quantify a mean grain size, but this is on the order of <50 µm. The proportion of clasts (>5 µm) to matrix is estimated to be >50% matrix. On the whole, clasts are poorly-sorted and angular, though some larger ones (>50 µm) are moderately well rounded (Fig. 3.56b). Preserved microfracturing is grain size-dependent, with intragranular fractures generally being confined to grains that are greater than ~40 µm in size. Where this is the case, there are occasional through-going fractures (e.g. Fig. 3.56a) but they are more common at grain margins and cause fragments to spall off (Fig. 3.56b), thereby gradually reducing the size of the large grain with each new fracture. There is a distinction between the intensity of fracturing in quartz and K-fsp grains, with quartz grains often hosting individual, discrete fractures at grain edges, whilst K-fsp grains often have a margin a few microns deep that is intensely fractured (Fig. 3.56b).

We have defined the matrix here as all material <5 µm in size, but even at this scale there is significant heterogeneity in both the composition and fabric (or lack thereof) of the matrix, and we have identified two distinct phases within it: a *mechanical gouge*, and an *authigenic clay gouge*. In the mechanical gouge, clasts smaller than 0.5 µm are visible (Fig. 3.57a) and within it there is no discernible fabric. There is no mesoscopic distinction between these two types of gouge as they

are only clearly distinguishable using electron microscopy. Backscattered SEM images show the clasts in the mechanical gouge are composed of a range of materials and we infer this gouge to have formed as the result of cataclasis described above, and resulting extreme grain comminution. The boundaries of many grains within the mechanical gouge appear poorly-defined and indistinct.

The authigenic gouge is composed of variably foliated stacks of clay minerals; the foliation is defined by alignment of individual clay grains and may be continuous over >100 µm (Fig. 3.57b) or a few (<10) microns (Fig. 3.57c), giving the fault gouge its foliated appearance at the macroscale. In the authigenic gouge there are fewer very small (<1 µm) clasts and there is a much more discrete boundary between those that are present and the matrix than is the case with clasts in the mechanical gouge. (It should be noted that though we have defined *mechanical* and *authigenic* gouge, this does not preclude the possibility that the mechanical gouge also contains some clay material, but we cannot identify it with the techniques used.) XRD analysis of this brown fault gouge reveals a mixed mineralogy of highly crystalline kaolinite, minor illite and smectite of relatively low crystallinity (Fig. 3.57c). This is similar to the clay mineral composition of the carbonate wall rocks at this location (Fig. 3.33c).

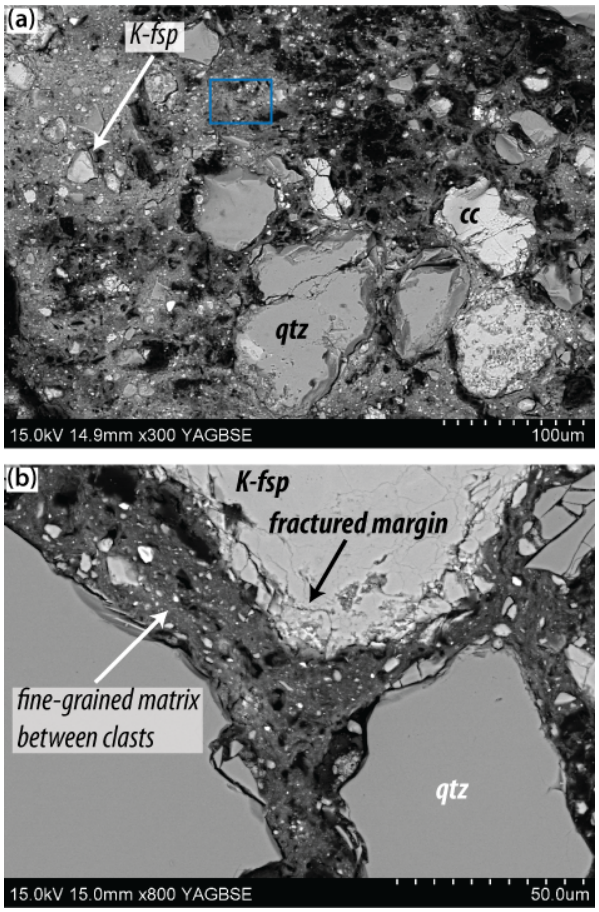

Figure 3.56: *Photomicrographs of the cataclastic gouge of the Shelomo Fault core, Locality A, showing relationships between gouge and clasts:* ***(a)*** *angular grains supported in a fine-grained matrix;* ***(b)*** *grains of quartz and K-fsp, quartz shows few fractures at grain edges whilst K-fsp grain has a margin of intense fracturing.*

The layer of red gouge to the east of the brown is similar in both the composition of clasts (quartz, feldspar, calcite) and in proportion and type of very fine-grained matrix; we see both finely-foliated clay material and very fine-grained mechanical gouge (Fig. 3.57c,d). The red authigenic gouge is extensively foliated and in some places gently folded, with wavelengths of approximately 50 µm (Fig. 3.57d). Although this layer of gouge is similar to the brown gouge in terms of mineralogy of clasts and microstructure, the clay mineralogy is somewhat different and Mg-smectite of higher crystallinity is present here (Fig. 3.57f).

It was not possible to collect a sample for sectioning from the zone of cohesive cataclasite that forms the eastern part of the fault core due to its hard but friable nature. However, field observations concluded that it is very similar in composition to the eastern, basement damage zone at this location and therefore we feel that thin section and clay mineral analysis of this part of the fault zone, along with that of the foliated gouges, is sufficient to bridge this gap in knowledge.

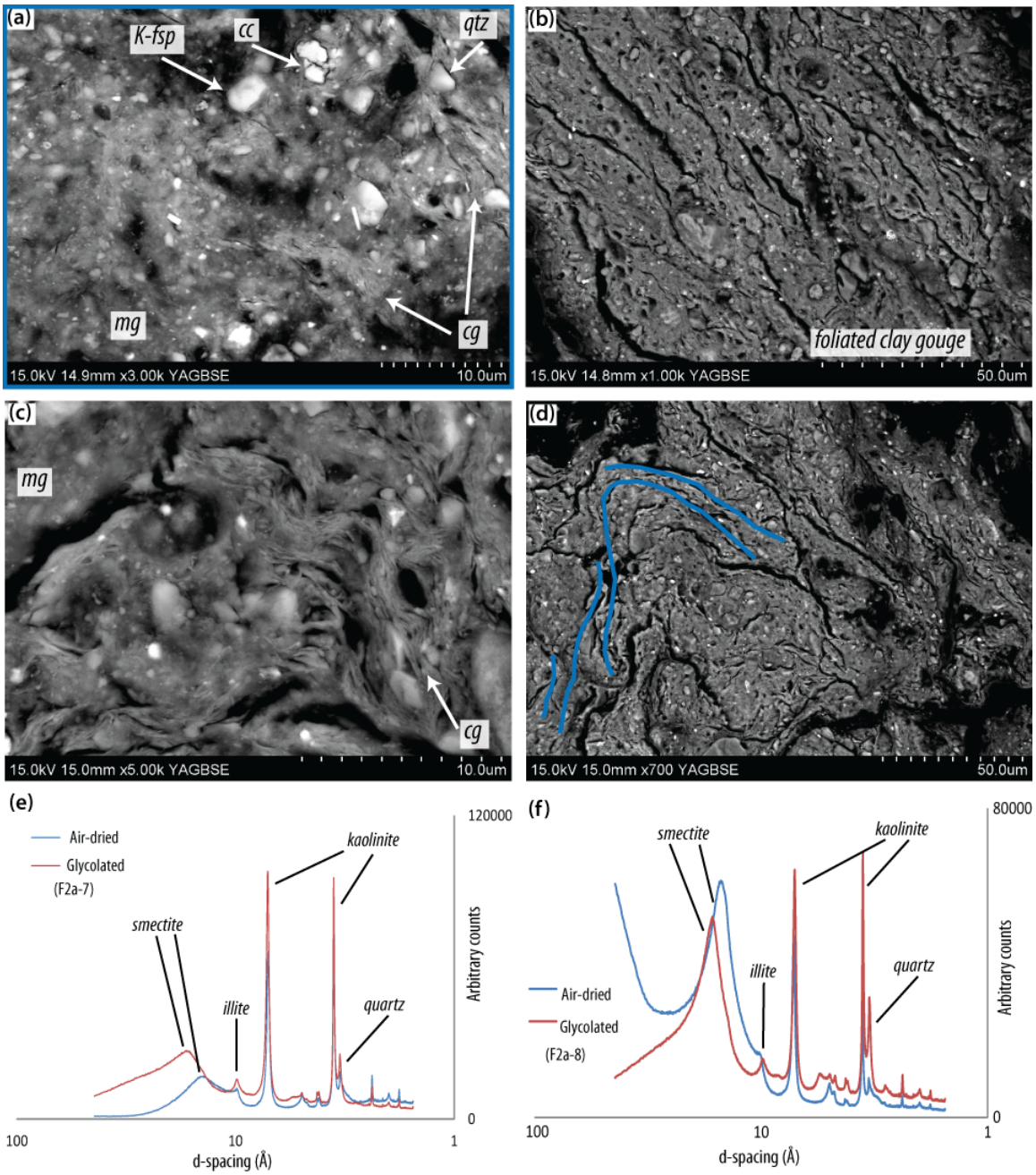

Figure 3.57: *(a & b): Photomicrographs of brown cataclastic gouge adjacent to the fault plane:* ***(a)*** *mixed mechanical gouge (mg) and authigenic clay gouge (cg);* ***(b)*** *foliated authigenic gouge* ***(c)*** *intermixed mechanical gouge and authigenic clay gouge with micron-scale foliation;* ***(d)*** *folded foliation in authigenic clay gouge;* ***(e)*** *XRD diffractogram showing clay mineral composition of the clay fraction of brown cataclastic gouge: smectite, kaolinite, minor illite;* ***(f)*** *XRD diffractogram showing clay mineral composition of the clay fraction of red cataclastic gouge: smectite, kaolinite, minor illite.*

Locality B At Locality B, the fault zone architecture is somewhat different to Locality A in that the fault core is composed of several, slip surface-bound layers of fine-grained gouge material and there is no cohesive cataclasite unit as seen at Locality A (Fig. 3.58).

In the western part of the fault core, directly adjacent to the carbonate damage zone, there is a 20-30 cm band of red, fine-grained incohesive gouge. This part of the fault core contains abundant clasts of both basement (quartz, feldspar) and carbonate (calcite) wall rocks. The clasts vary in size from approximately 5-1000 µm and even in optical microscopy it is possible to see that the gouge is heterogeneous and there are areas which contain more (Fig. 3.59a) and fewer (Fig. 3.59b) clasts.

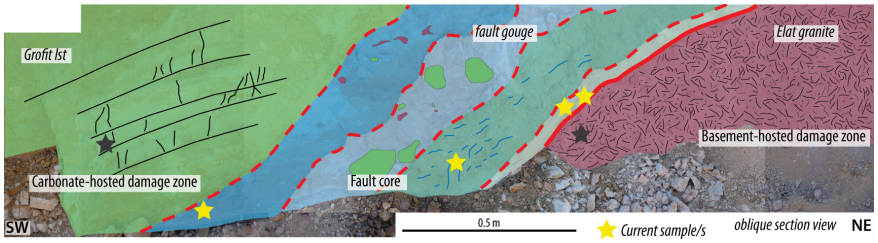

Figure 3.58: *Schematic log of Shelomo Fault, Locality B section showing position of basement-hosted damage zone sample.*

Clast-rich zones are associated with a clay-poor matrix (mechanical gouge), whilst the matrix of clast-poor zones appears to be clay-rich (authigenic clay gouge).

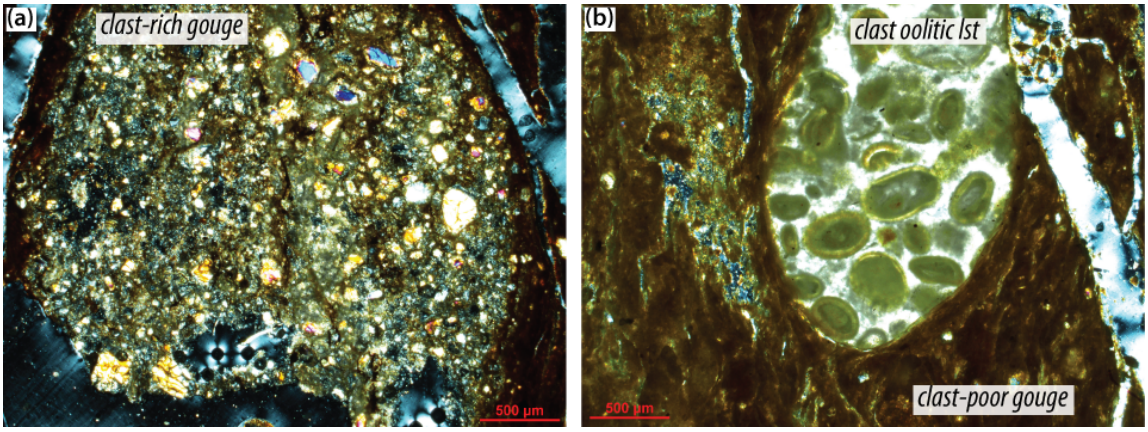

Figure 3.59: *Photomicrographs of the Shelomo Fault, Locality B core:* ***(a)*** *angular clasts supported in a fine-grained matrix;* ***(b)*** *clast-poor, foliated clay-rich gouge.*

In the areas with many clasts these are angular and matrix supported overall (Fig. 3.60a); due to the 'pockets' of clast-rich/-poor material it is hard to quantify and overall clast:matrix ratio, but we estimate that the matrix accounts for >50% of the rock volume. As at Locality A, small grains (<50 µm) tend not to be fractured and grains >5 µm have discrete grain boundaries. There is evidence of cataclasis in the fracturing at grain margins and subsequent grain-size reduction through progressive fragmentation of larger grains.

The matrix is again composed of the previously described mechanical (Fig. 3.60b) and authigenic clay gouges (Fig. 3.60c). Within the mechanical gouge there is no apparent fabric and there are small grains (<1 µm) with indistinct boundaries. Slightly larger grains (1-5 µm) are generally composed of quartz, K-fsp and calcite.

In the authigenic gouge, aligned clay grains form a foliation, but it is not as well-defined at the macroscale here as at Locality A (Section 2.6.2.1). This may be because the clay gouge is generally more interspersed with the mechanical gouge, disrupting the foliation (Fig. 3.60c). The clay mineralogy of this fault rock consists of kaolinite, illite and smectite (Fig. 3.61a). We also analysed a 'clast' of orange material (Section 2.6.2.1) and found it to contain mostly kaolinite, minor illite and a very small amount of smectite (Fig. 3.61b), which is similar (but not identical) to the clay minerals found in the carbonate wall rocks of Locality A (Fig. 3.33c) and is therefore likely to represent blocks of these that have been incorporated into the fault zone.

The second type of gouge present at this location is a brown gouge in the eastern part of the fault core, adjacent to the basement wall rocks. This material contains a higher proportion of

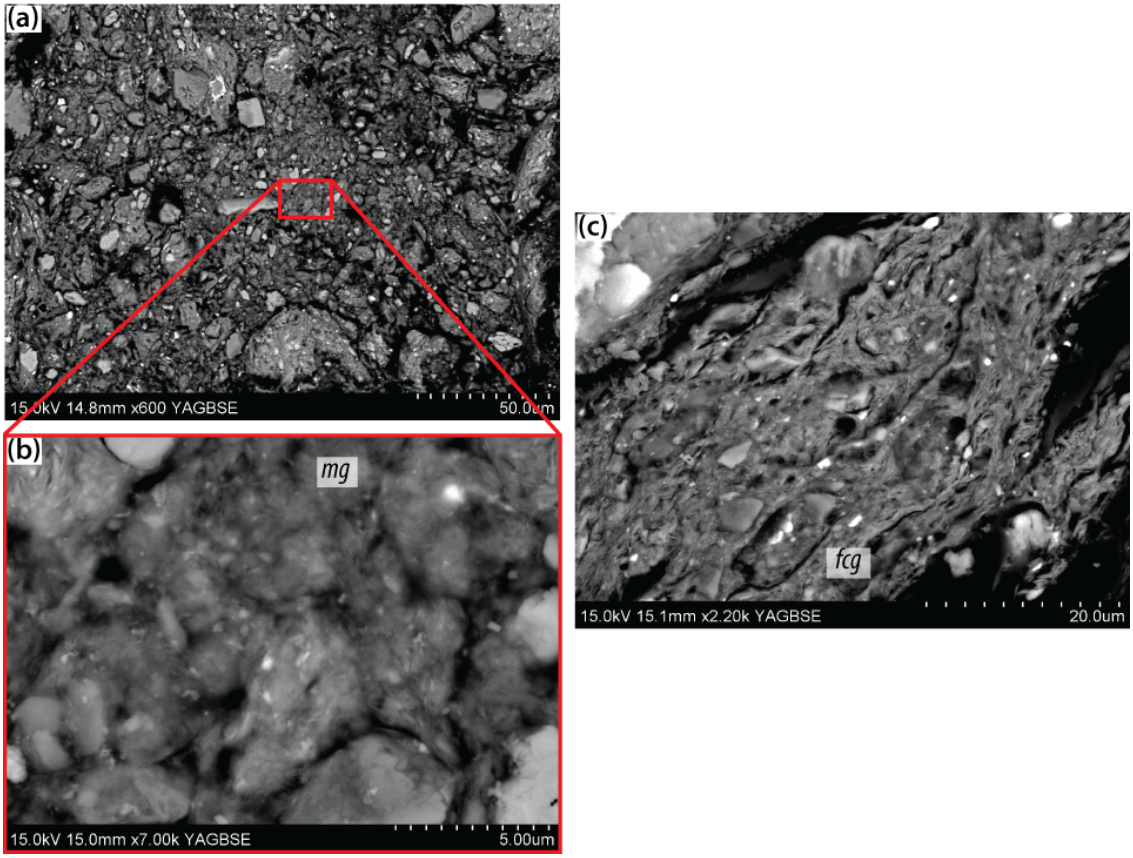

Figure 3.60: *Photomicrographs of the Shelomo Fault, Locality B core:* ***(a)*** *angular clasts supported in a fine-grained matrix;* ***(b)*** *fine-grained mechanical gouge (mg) that has no fabric;* ***(c)*** *foliated authigenic clay gouge (fcg).*

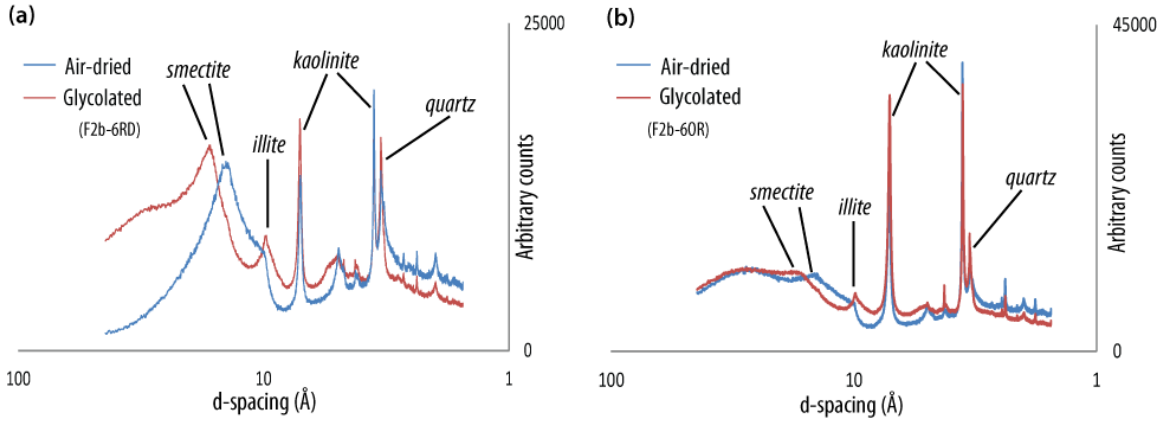

Figure 3.61: *XRD diffractogram showing clay mineral composition of the clay fraction of the Shelomo Fault, Locality B, core gouges (clay fraction):* ***(a)*** *clay mineralogy of gouge from central, red-coloured band of fault core: smectite, illite and kaolinite;* ***(b)*** *clay mineralogy of clast within red, clay-rich gouge: kaolinite with minor smectite and illite.*

foliated clay gouge matrix than the red gouge, but also more larger clasts of both carbonate and basement material, up to approximately 1 cm and commonly 2-5 mm. Clasts are distributed within the clay matrix (Fig. 3.62a) and may be single grains or clasts of multiple grains (Fig. 3.62b). On the whole, clasts are more well-rounded than those observed in other gouges (Fig. 3.62c), although as previously seen the smallest (<20 µm) are the most angular (Fig. 3.62d), and fractures are generally only present in grains/clasts larger than ~50 µm. Clasts are almost entirely supported by a fine-grained matrix (Fig. 3.62a-d).

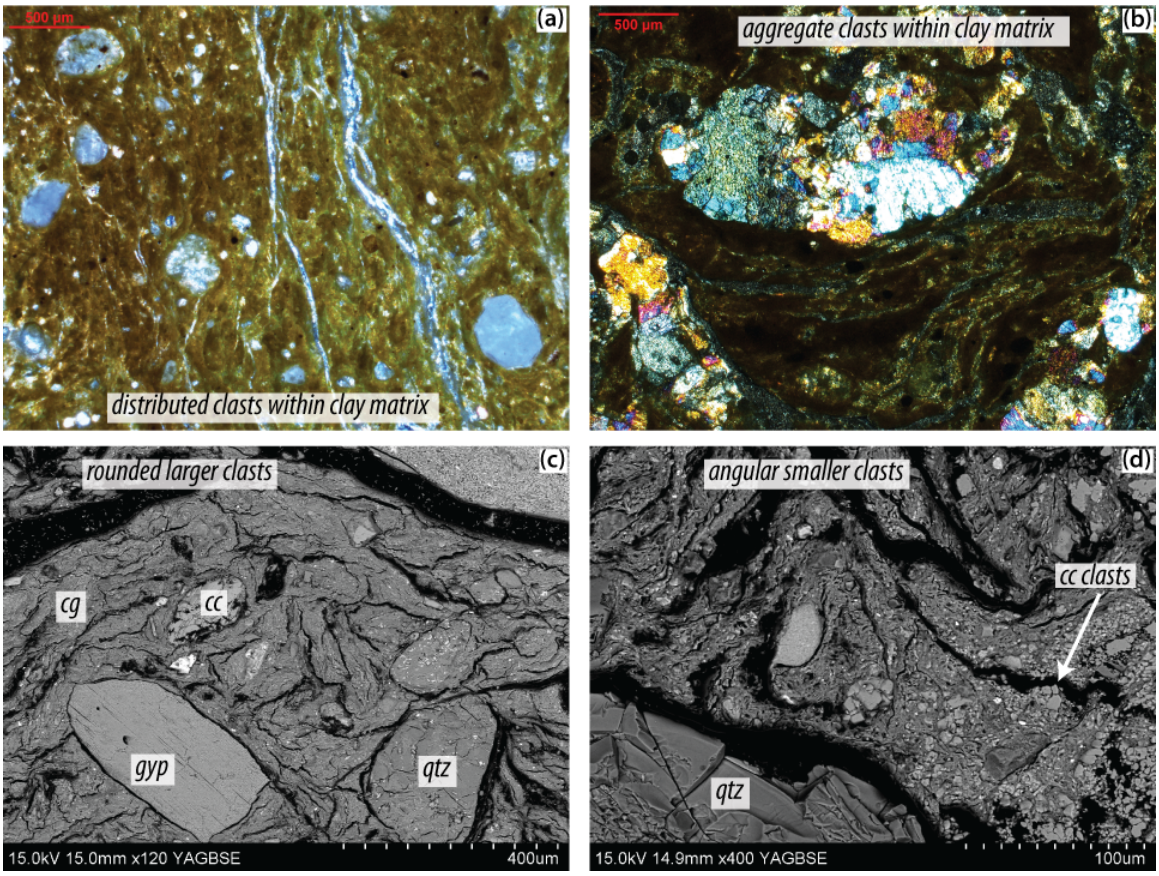

Figure 3.62: *Photomicrographs of Shelomo Fault, Locality B cataclastic gouge:* ***(a)*** *distributed clasts of calcite within clay matrix;* ***(b)*** *aggregate clasts of basement material within foliated, clay gouge;* ***(c)*** *rounded, larger clasts within fine-grained authigenic clay gouge;* ***(d)*** *smaller, angular clasts within fine-grained authigenic clay gouge.*

Much of the matrix in this part of the fault zone appears to be foliated clay gouge rather than mechanical gouge; there is a general fabric at the microscale, although this does not scale up to the macroscale since it is frequently disturbed by the presence of large clasts (e.g. Fig. 3.62c). The foliation, as with previous clay gouges described, is defined by the alignment of clay grains and can be continuous over a few millimetres where there are fewer large clasts (Fig. 3.63a) and small clasts (<10 µm) are aligned parallel to the foliation (Fig. 3.63b).

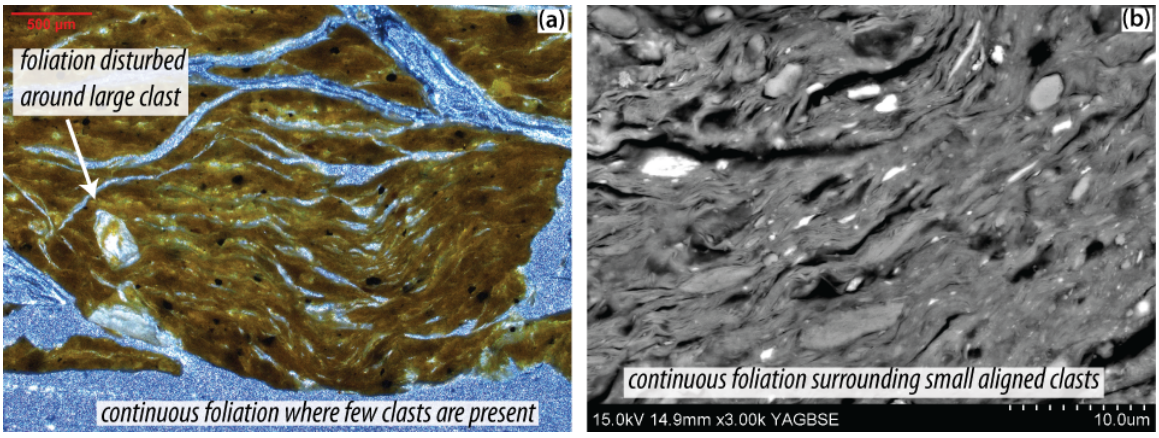

Figure 3.63: *Photomicrographs of foliated gouge from Shelomo Fault, Locality B fault core:* ***(a)*** *continuous foliation over several mm, disturbed locally around a large grain;* ***(b)*** *small grains (<10 µm) aligned parallel to the foliation.*

XRD analysis was performed on two samples from this part of the fault zone, taken from layers separated by slip surfaces, and the clay mineralogy in both is very similar: in the gouge in the

centre of the fault core, adjacent to the red gouge, high-crystallinity smectite is the predominant mineral and there is minor kaolinite and illite (Fig. 3.64a); in the gouge east of this, adjacent to the basement damage zone, there is also highly crystalline smectite but there is a lack of other clay minerals such as kaolinite and illite (Fig. 3.64b). The lack of clay minerals associated with hanging wall lithologies (Section 3.3.3.1) may be indicative of some degree of partitioning within the fault zone, or at least a lack of homogeneous mixing throughout. The neoformed clay mineral phase is the same in the fault gouges as found in the basement damage zone but in neither gouge sample do we see any evidence of the presence of the chlorite that was detected in the basement damage zone (Fig. 3.22c). The clay mineralogy, combined with the typically clast-poor, foliated nature of the gouges, indicates they are largely authigenic clay gouges, rather than mechanical gouges.

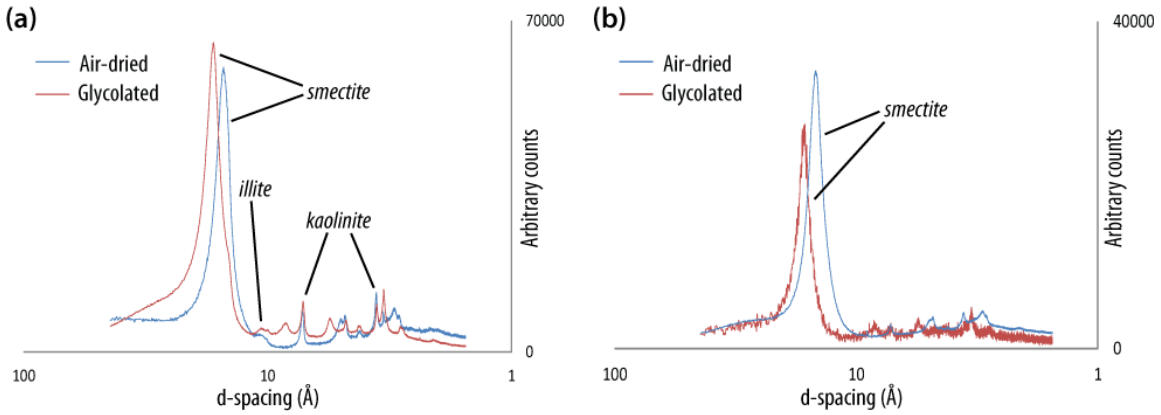

Figure 3.64: *XRD diffractograms showing clay mineral composition of the clay fraction of the Shelomo Fault, Locality B core cataclastic gouges:* ***(a)*** *central fault core clay mineralogy;* ***(b)*** *eastern fault core clay mineralogy. The mineralogy of both samples indicates they are composed of authigenic clay gouge, with neomineralised smectite, rather than comminuted mechanical gouge.*

Summary Deformation within the fault core of the Shelomo Fault is highly heterogeneous, with the sections studied both containing various deformation products. Although the basement wall rocks are of different lithologies at the two sections studied, the cataclastic gouges of the fault cores are quite similar both mineralogically and microstructurally. Both contain very fine-grained gouges formed by mechanical processes (fracturing and cataclasis) as well as the growth of new clay minerals (smectite). There is some variation in the proportion and intensity of fabric in the authigenic clay gouges, but they all contain significant amounts of smectite. This mineral is not present at all in the protolith basement units or - in this crystalline form - in cover rocks, indicating that it is likely to be authigenic in nature. In addition, though we observe retrograde alteration of biotite to chlorite in the damage zone Elat Granite associated with the Shelomo Fault, we do not detect chlorite in the gouge samples, suggesting there may have been a further breakdown of chlorite to smectite during faulting. The similarity in mineralogy of the clasts (and resultant mechanical gouge) at both locations may reflect the limited spatial distribution of the Ramat Yotam volcanic wall rocks that are present at Locality A.

Deformation is not continuous within the fault core, with some clasts exceeding 1 mm in size and showing no signs of internal deformation, whilst others have been comminuted to <1 μm. The growth of smectite appears to be relatively well distributed within the gouges, but at Locality A there is a layer of cohesive cataclasite, indicating deformation was not evenly distributed across the fault core but was concentrated within a relatively narrow (50-100 cm) zone.

Tzefahot Fault Several samples have been studied from within the cataclastic part of the fault core (Fig. 3.65), in order to fully describe the microstructures and mineralogy of the heterogeneous fault zone described in Section 2.6.2.2. These samples comprise the dark red/purple foliated gouge, a sample of an apparently more intact slice of basement material, and a sample that appears to contain carbonate material together with red gouge.

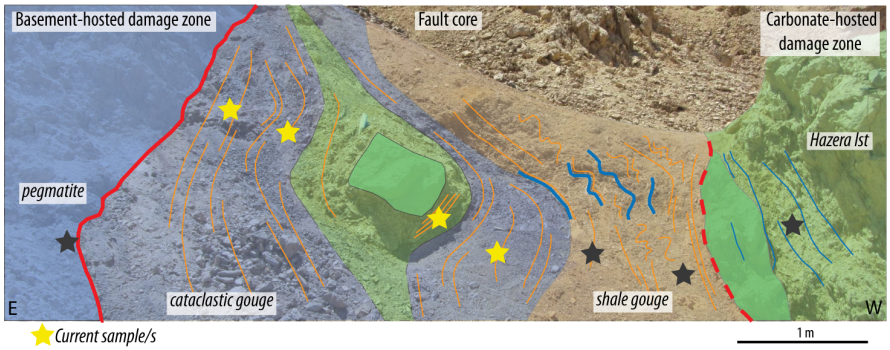

Figure 3.65: *Schematic log of Tzefahot Fault section showing position of carbonate-hosted damage zone sample.*

The composition of the cataclastic gouge of the Tzefahot Fault can be broadly divided into clasts and matrix. Clasts vary in composition (feldspars, gypsum, quartz) but the most common are quartz, in a variety of shapes and sizes. In some cases we observe rotation and subsequent comminution of rounded grains (Fig. 3.66a), leading to the formation of very fine-grained (<2-5 µm) cataclasite (Fig. 3.66b), whilst we also see in situ fracturing/pulverisation of larger (>1 mm) grains, producing textures similar to those observed in basement damage zones (Sections 3.3.2.1 and 3.3.2.2). Quartz clasts >500 µm are present but are not common and there are many in the range of 50-200 µm.

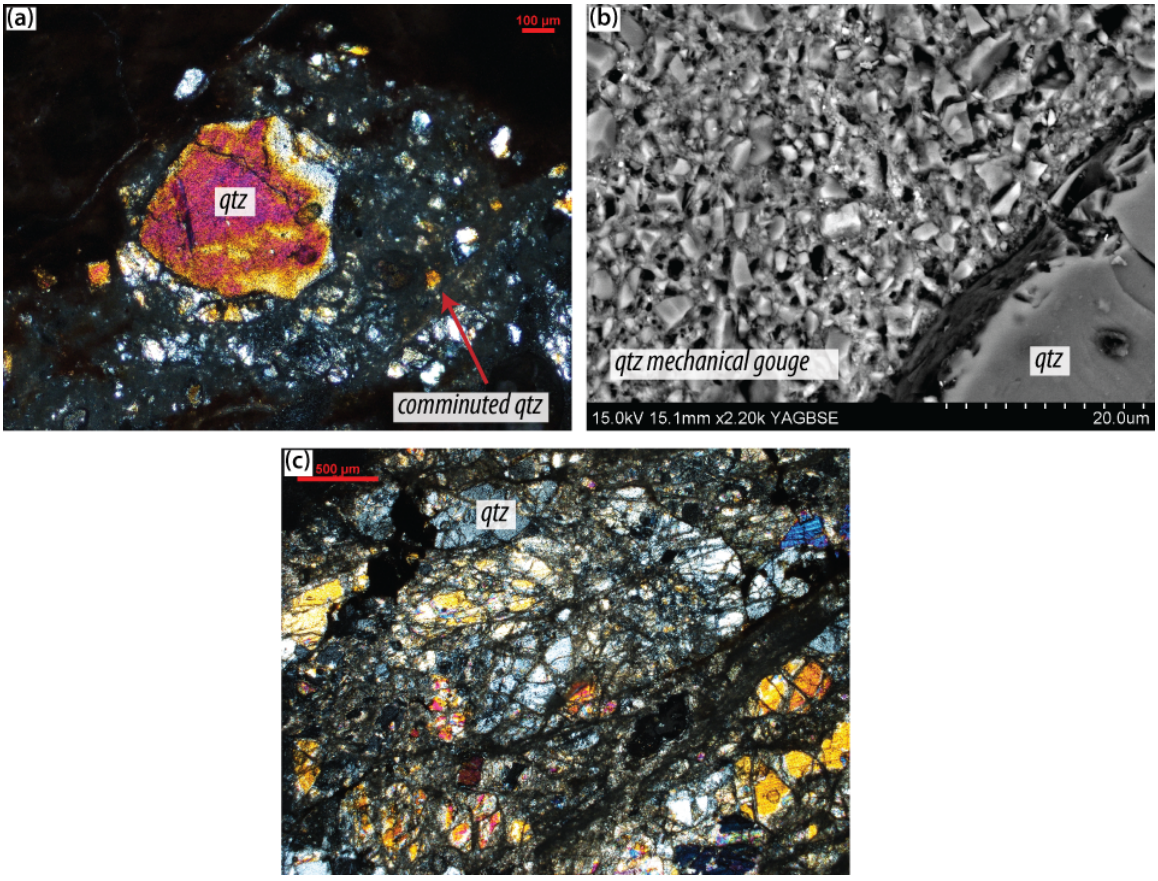

Figure 3.66: *Photomicrographs of typical deformation textures in Tzefahot Fault core:* ***(a)*** *cataclasis by grain rotation and microfracturing (XPL);* ***(b)*** *quartz mechanical gouge (BSEM);* ***(c)*** *pulverised quartz grains (XPL).*

There appear to be very few clasts of carbonate material (calcite and dolomite) at the micro-scale and, where present, it is generally as larger, aggregate clasts of up to 1 mm; smaller clasts of calcite are present surrounding the larger clasts, but are rarely seen disseminated within the matrix. Where aggregate calcite grains are observed, there is evidence of pressure solution at grain boundaries (Fig. 3.67a,b).

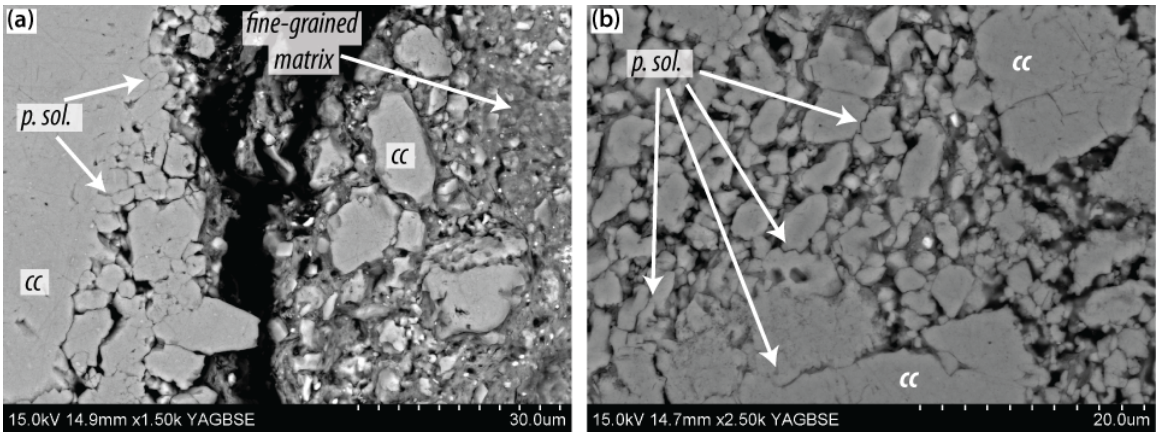

Figure 3.67: *BSEM photomicrographs of calcite clasts within Tzefahot Fault core, showing **(a)** large, aggregate clasts; **(b)** evidence of pressure solution between individual grains (cc: calcite; p. sol.: pressure solution).*

In optical microscopy there appear to be two phases of the matrix; a dark red/brown-coloured material that is relatively homogeneous in appearance, with the exception of a few grains, and a grey-coloured material that contains abundant clasts of apparently crystalline material (Fig. 3.68a,b).

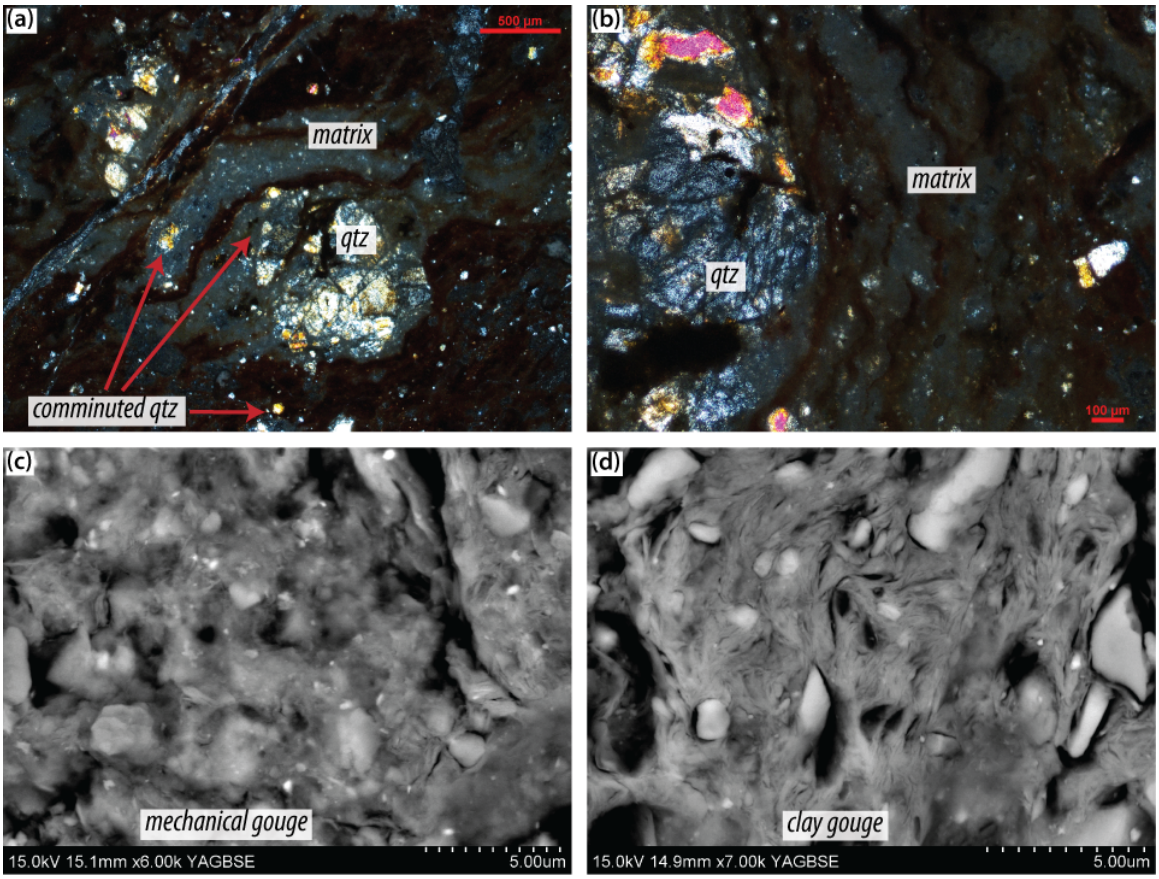

Figure 3.68: *Photomicrographs of fine-grained gouge in the Tzefahot Fault core, showing two phases of fine-grained gouge material: **(a)** a rounded qtz clast with smaller fragments in a fine-grained matrix ; **(b)** layered grey and red/brown fine-grained matrix wrapping around a quartz clast; **(c)** mechanical gouge and **(d)** foliated clay gouge that represent the grey (mechanical) and red/brown (authigenic clay) materials seen in (a) and (b).*

Scanning electron microscopy confirms the difference between these two types of gouge material: there is a mechanical gouge of varying grain size (<1-5 µm) that is similar in mineralogy to the constituent grains of the wall rocks (e.g. Fig. 3.66b), and an ultra-fine grained foliated clay material. These have been defined as distinct gouges due to the difference in fabric: the mechanical gouge has little or no apparent fabric (Fig. 3.68c), whilst the clay gouge has a strong foliation defined by alignment of individual clay grains (Fig. 3.68d). There are also differences in mineralogy and grain size: the mechanical gouge contains numerous clasts from a few millimetres to <1 µm, all of which appear to be composed of the same range of mineralogy as larger grains (predominantly quartz and feldspar), whilst the foliated clay gouge has a consistent grain size of <1 µm and clasts are of a different mineralogy (typically quartz and feldspar) than the clay matrix.

In addition to the mechanical and clay gouges, there are also localised areas where fragments of basement rock (mostly quartz) are suspended in calcite, which appears to have filled tensile fractures (Fig. 3.69a,b). These fractures are only present within larger clasts of more intact basement material, they are not present within either gouge type, so it is inferred that these are relicts of an earlier phase of deformation and mineralisation.

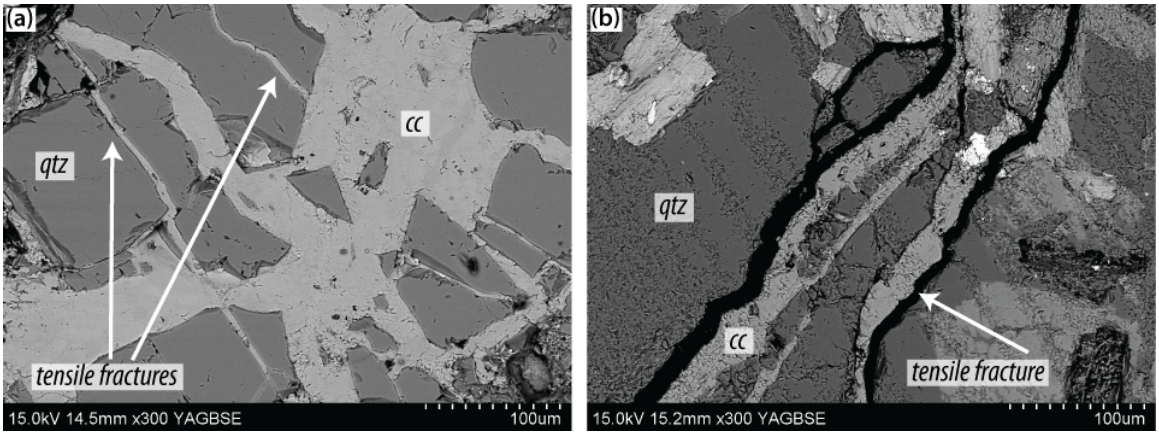

Figure 3.69: *BSEM photomicrographs of tensile, calcite filled fractures in fault core samples of the Tzefahot Fault:* ***(a)*** *calcite cement containing quartz grains and hosting later, calcite-filled tensile fractures;* ***(b)*** *single calcite-filled tensile fracture.*

The relationship between clasts and gouge, and between the two types of gouge, is highly variable. For the most part, the mechanical and clay gouges are intermixed (Fig. 3.70a,b) and there is no clear boundary between the two. In zones where there are relatively few clasts, there may be little overall fabric (Fig. 3.70a) but instead 'pockets' of clay gouge that are themselves foliated over a few microns (Fig. 3.70b). In contrast, there are also zones where a single type of gouge is present (Fig. 3.70c), and those where the mechanical and clay gouges form distinct layers (Fig. 3.70d, in this case clay gouge). This suggests that while deformation is intense and distributed across most of the fault zone, the distribution is not even, nor is the deformation continuous.

Results of XRD analysis of the clay-sized fraction of the cataclastic gouges show that the primary clay mineral present is smectite in all three samples (Fig. 3.71). The sample of foliated red material contains only Mg-bearing smectite and no appreciable amount of other clay minerals (Fig. 3.71a), whilst the two samples that contain more clasts also contain some kaolinite and illite (Fig. 3.71b,c). The smectite present within the gouges has a higher crystallinity (sharper peak) than that generally found in carbonate wall rocks (e.g. Figs. 3.33 and 3.39c). This variation in the crystallinity identifies the fault gouge smectite as a different phase to that in the sedimentary wall rocks. This, together

with the volume present, cannot be explained by simple cataclastic processes and the fact that the gouges in general appear to be derived from predominantly basement rocks, leads us to interpret the smectite as an authigenic phase of fault gouge material.

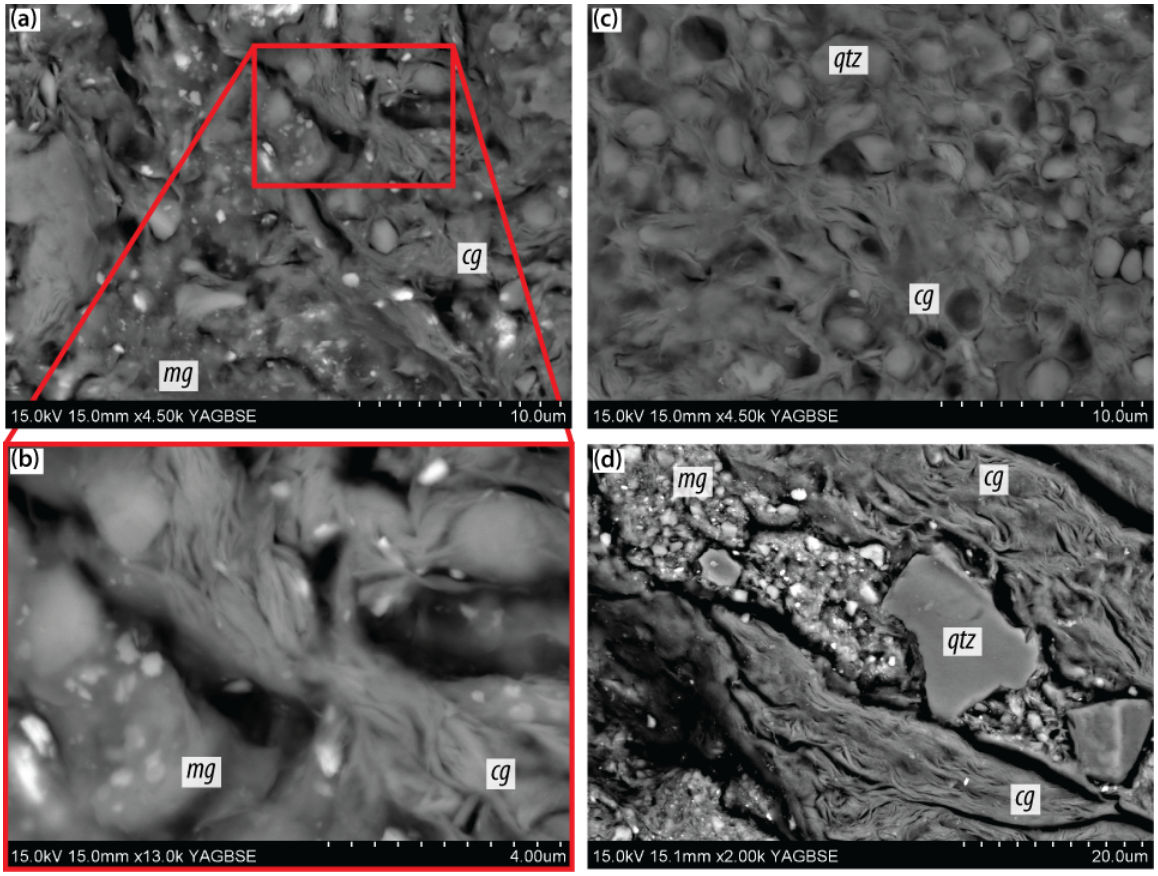

Figure 3.70: *BSEM photomicrographs of gouges in fault core samples of the Tzefahot Fault:* ***(a)*** *intermixed mechanical gouge and authigenic clay gouge;* ***(b)*** *detailed view of (a), showing aligned clay grains (cg) and fine grains and amorphous material of mechanical gouge (mg);* ***(c)*** *rounded quartz grains supported in foliated authigenic clay gouge;* ***(d)*** *discrete layers of mechanical gouge (mg) and authigenic clay gouge (cg).*

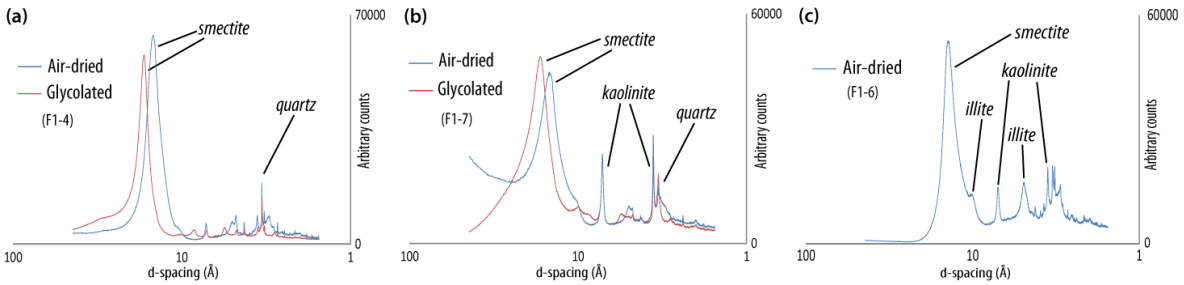

Figure 3.71: *XRD diffractograms showing clay mineralogy of fault core gouges of Tzefahot Fault:* ***(a)*** *foliated, clast-poor red gouge;* ***(b & c)*** *clast-rich samples. The principal clay mineral in all is smectite, which due to its well-formed nature is likely to have formed by neomineralisation rather than alteration, and the samples with more clasts present also contain small amounts of kaolinite +/- illite.*

Summary Cataclastic gouges within the fault core of the Tzefahot Fault are highly heterogeneous and several deformation mechanisms are observed. There is a clear distinction between gouge that has formed through cataclasis, and which is similar in mineralogy to adjacent wall rocks, and that has formed as the result of alteration and/or precipitation, introducing at least one new clay mineral (smectite) into the fault zone. Although deformation is distributed across the width of the cataclastic gouge zone of the fault section, it varies in intensity and there remain several large clasts

that are visible at the macroscale. At the microscale, there are areas of isolated clay (Fig. 3.70b) and mechanical gouges (Fig. 3.66b), as well as those where they are intermixed (Fig. 3.70a) or forming discrete layers (Fig. 3.70d), indicating that deformation is neither evenly distributed nor continuous.

Roded Fault There are two types of fault core material within the Roded Fault at the studied sections (though we have only analysed samples from Locality A here, Fig. 3.72); a fine-grained, sometimes foliated, clay-rich domain and a coarser-grained domain with little obvious fabric (Section 2.6.2.3).

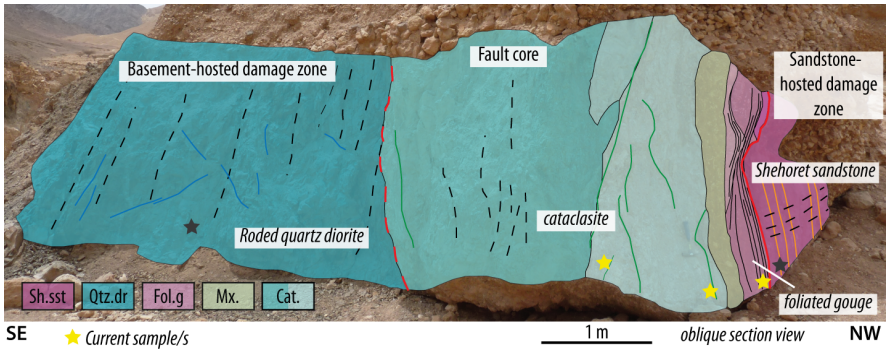

Figure 3.72: *Schematic log of Roded Fault section showing position of fault core samples.*

Within the foliated, clay-rich zone, clasts of quartz, K-fsp and occasional mica are supported by a fine-grained, foliated matrix (Fig. 3.73a-c). Clasts range in size from individual grains of <5 µm to clasts of sandstone wall rock up to 10 mm. Some clasts are relatively well-rounded but on the whole they are in contrast to the protolith rock and are angular with sharp grain boundaries (Fig. 3.73a,b), particularly those of quartz grains. Sorting is generally poor. Many larger grains (<30 µm) host microfractures but these are not present in smaller grains, and we infer the fractures to have been formed as the result of comminution of larger, original grains. The concentration of clasts is not evenly distributed across the rock (e.g. Fig. 3.73a,c) and clasts may account for as little as 30% of the rock volume in some places, and <50% overall.

The matrix can be subdivided into two phases: ultra fine-grained clay material, and clasts that are <1 µm in size. The clay material is composed of predominantly illite with minor kaolinite (Fig. 3.73d). This is somewhat similar to the mineralogy observed in the Cambrian sandstone wall rocks (Fig. 3.46b), and although within the fault core the kaolinite peaks appear suppressed relative to those of illite, we also observe a slight 'double-peak' at a d-spacing of 10 Å. This indicates that the peaks of two minerals are overlapping and since we observed mica grains in thin section, we interpret this to be muscovite that has remained in the sample after preparation. This mineral shares a similar diffraction pattern to illite and, because of its crystalline form, produces very sharp peaks. We therefore interpret the clay-rich gouge of the Roded Fault to be entirely derived from the clastic wall rocks, and no authigenic clay minerals to be present.

The clay matrix is variably foliated, depending on the amount of clasts present; where these are few, there is a moderate foliation defined by the sub-parallel alignment of clay grains (Fig. 3.73c). This foliation is frequently interrupted by the presence of even very small clasts, producing a relatively discontinuous fabric. Where there are more clasts (e.g. Fig. 3.73a), there is very little preferred orientation of clay grains (Fig. 3.73b).

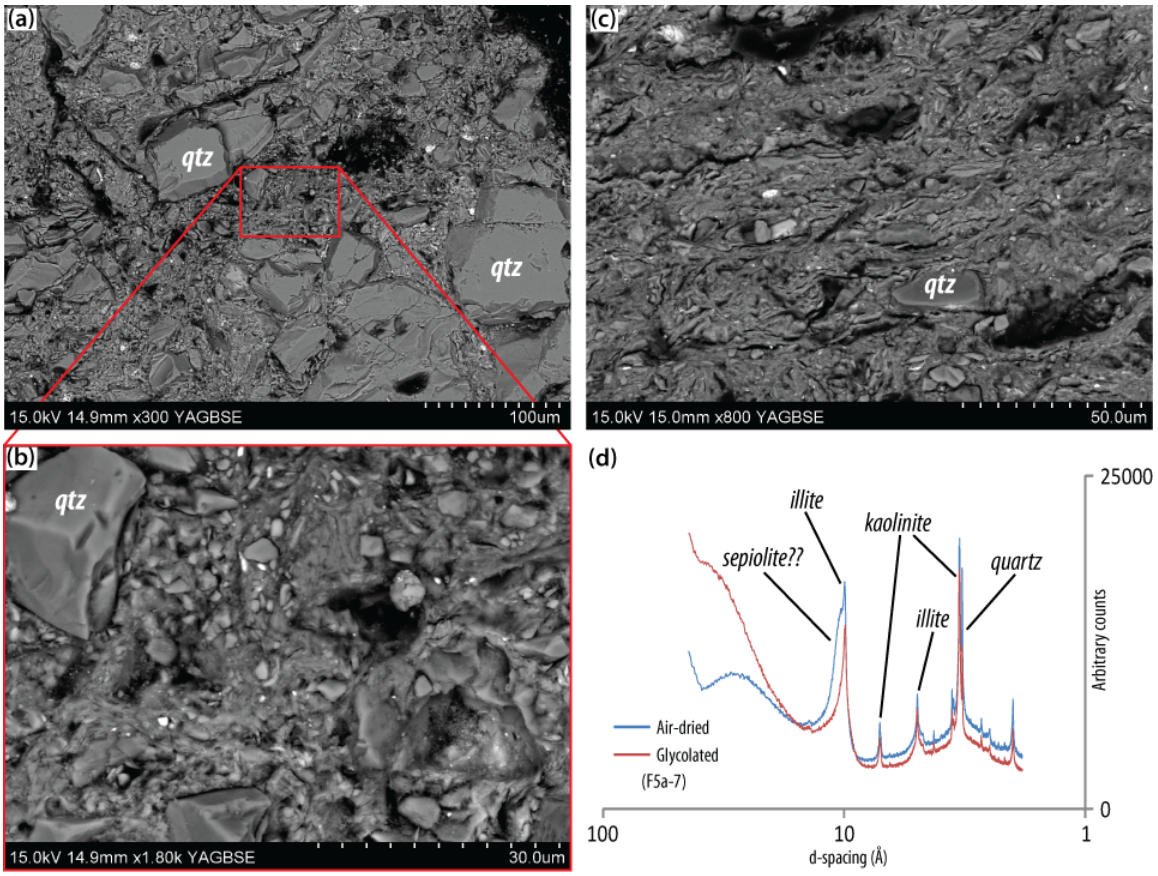

Figure 3.73: *Roded Fault foliated gouge:* ***(a-c)*** *BSEM photomicrographs:* ***(a)*** *typical clast-matrix arrangement of angular quartz grains of varying size supported in a fine-grained matrix;* ***(b)*** *enlarged image of (a) showing interstitial fine-grained matrix and small grains (<5 μm);* ***(c)*** *foliated fine-grained matrix with abundant small (<10 μm) grains;* ***(d)*** *XRD diffractogram showing clay mineral composition: there is no smectite, only illite and kaolinite, possibly also with sepiolite, indicating there has been no neomineralisation as these minerals are found in the clastic wall rocks (Fig. 3.10d).*

In the cataclasite/breccia part of the fault zone, the proportion of grains to matrix is much higher (Fig. 3.74a) and most of the very fine-grained material is only apparent in scanning electron microscopy (Fig. 3.74b). Even at the <5 μm scale individual clasts are still visible (although we have defined clasts <5 μm in size as matrix), indicating that intense comminution has taken place. Grains range in size from <5-500 μm, with the mean being in the range of 50-100 μm, and they are generally composed of quartz and K-fsp, with minor Na-rich plagioclase. Grains of all sizes are angular and for the most part contain few intragranular fractures (Fig. 3.74). There are few through-going fractures at the microscale, which we suggest is the result of the generally incohesive rock having low cohesive and tensile strength, resulting in unfavourable conditions for the propagation of fractures. Feldspar grains have less well-defined grain boundaries than quartz grains, with more intense fracturing at grain edges.

As well as shear fracturing and subsequent comminution of grains forming a relatively incohesive fault gouge, there is also local evidence of tensile fracturing and fluid flow (Fig. 3.74c). In this case the fracturing appears to have propagated through a relatively large clast of wall rock material in random orientations, with synchronous ingress of Ca-rich fluids and almost immediate cementation. The calcite cement is not fractured, and although there are few areas of this size (~500 μm x 500 μm) within this part of the fault core that relatively free of deformation, this may be a function of the size of the sample analysed. There is little other evidence of the flow

of calcite-bearing fluids through the cataclasite and it is more likely that this relates to an earlier phase of deformation.

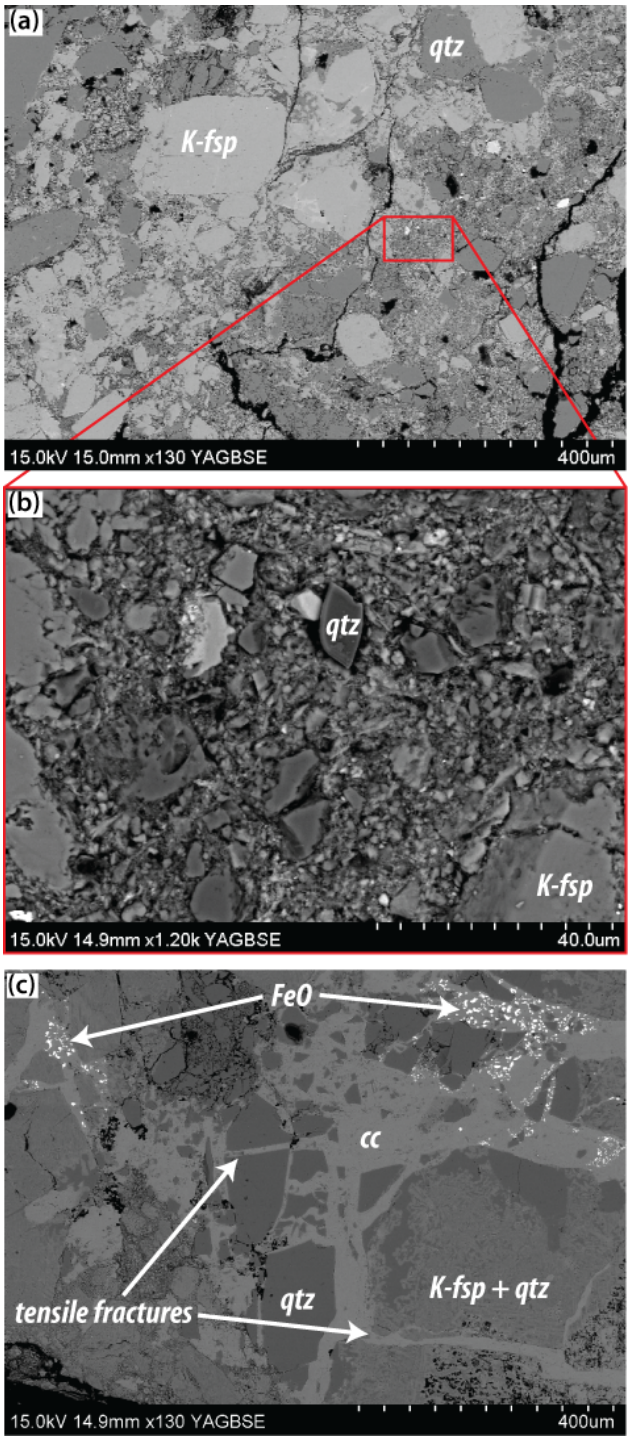

Figure 3.74: *BSEM photomicrographs of Roded Fault cataclasite:* ***(a)*** *clast-supported cataclasite with large grains (>100 μm);* ***(b)*** *enlargement of (a) showing small angular clasts with an interstitial fine-grained matrix;* ***(c)*** *calcite-filled tensile fractures.*

Though the matrix in this part of the fault zone is predominantly composed of comminuted material from larger grains (Fig. 3.74b), there is also extremely fine-grained (<1 μm) clay material (Fig. 3.75a). This is present as interstitial material in areas where grains of quartz and feldspar have been reduced to <5 μm and has no apparent fabric. The mineralogy of this clay material is exclusively Mg-bearing smectite (Fig. 3.75b) and since there is none in either of the wall rock protoliths (Section 3.3.1), it is most likely to be authigenic in origin.

Summary Deformation within the fault core of the Roded Fault appears less intense than that in the Shelomo and Tzefahot faults as there is a lack of foliated gouge material at the microscale. Although part of the fault core is foliated at the macroscale (Section 2.6.2.3), this does not persist to the microscale as there are too many large clasts of both basement and cover wall rocks that disrupt the continuity of fine-grained gouge material. In addition, smectite is not present throughout the fault core, suggesting there was some partitioning of deformation and alteration, likely due to restricted fluid flow, during deformation. Smectite is restricted to (and is the only clay mineral present in) the basement-derived cataclasite and gouges, and is not present in the strongly-foliated red gouge closest to the fault plane. In this layer, clays are similar in composition to those in both the clastic damage zone (Fig. 3.46b) and the undeformed protolith (Fig. 3.10d).

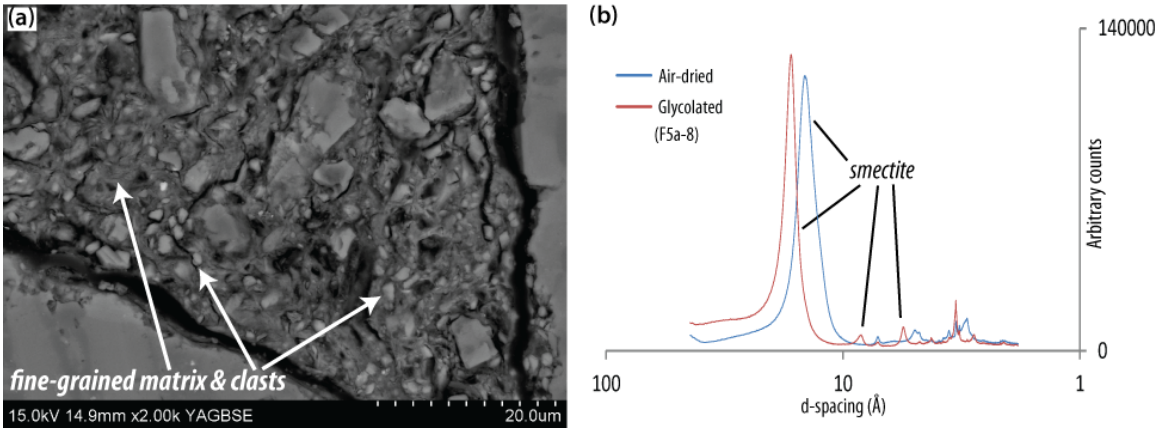

Figure 3.75: *Photomicrograph of and XRD diffractogram for breccia/cataclasite of Roded Fault:* ***(a)*** *small, angular clasts supported by a fine-grained matrix (BSEM);* ***(b)*** *mineralogy of clay fraction, containing only smectite which is interpreted as an authigenic, neomineralised phase.*

Nizoz Fault The Nizoz Fault is the fault with the lowest estimated displacement (250 m, Table 2.1) to involve both basement and cover rock lithologies, yet we still see a relatively heterogeneous fault core with three well-defined zones (Section 2.6.2.5 and Fig. 3.76).

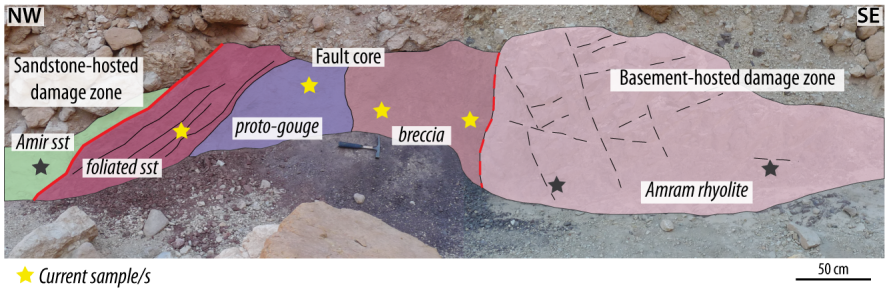

Figure 3.76: *Schematic log of Nizoz Fault section showing position of fault core samples.*

In the zone closest to the footwall on the southern side of the fault core, there is relatively little microscale brittle deformation; many fractures are observed at the mesoscale (Section 2.6.2.5) but very few are present at the sub-mm scale (Fig. 3.77a,b). Rather, there is pervasive alteration of feldspars to clay minerals (kaolinite, Fig. 3.77c,d). Clays are seen replacing grains of feldspar within their original grain boundaries and this alteration may have occurred in up to 50% of feldspar crystals, but does not appear to have occurred preferentially along the few fractures that are present (Fig. 3.77c).

Microstructures in the most intensely deformed, central part of the fault core (Section 2.6.2.5) reflect its incohesive appearance in the field. The rock here has been completely fragmented and grains of basement wall rocks are suspended in a fine grained matrix (Fig. 3.78a). Clasts are a mixture of quartz and K-fsp (either individually or combined) and appear to be derived from the granite porphyry wall rocks (Fig. 3.78b). There is a large range in clast sizes, from <1 µm to >1000 µm and the shape of clasts is size-dependant. Those smaller than ~200 µm are generally angular whilst larger clasts are a mixture of moderately well-rounded (Fig. 3.78b) - angular (Fig. 3.78a). It is hard to assess whether any of the grains of quartz are derived from the sandstone wall rocks, but we believe this to be unlikely since most clasts >50 µm are composed of both quartz and feldspar, indicating they are from an igneous/volcanic protolith as few feldspar grains are seen in the sandstone protoliths (Section 3.3.1.9).

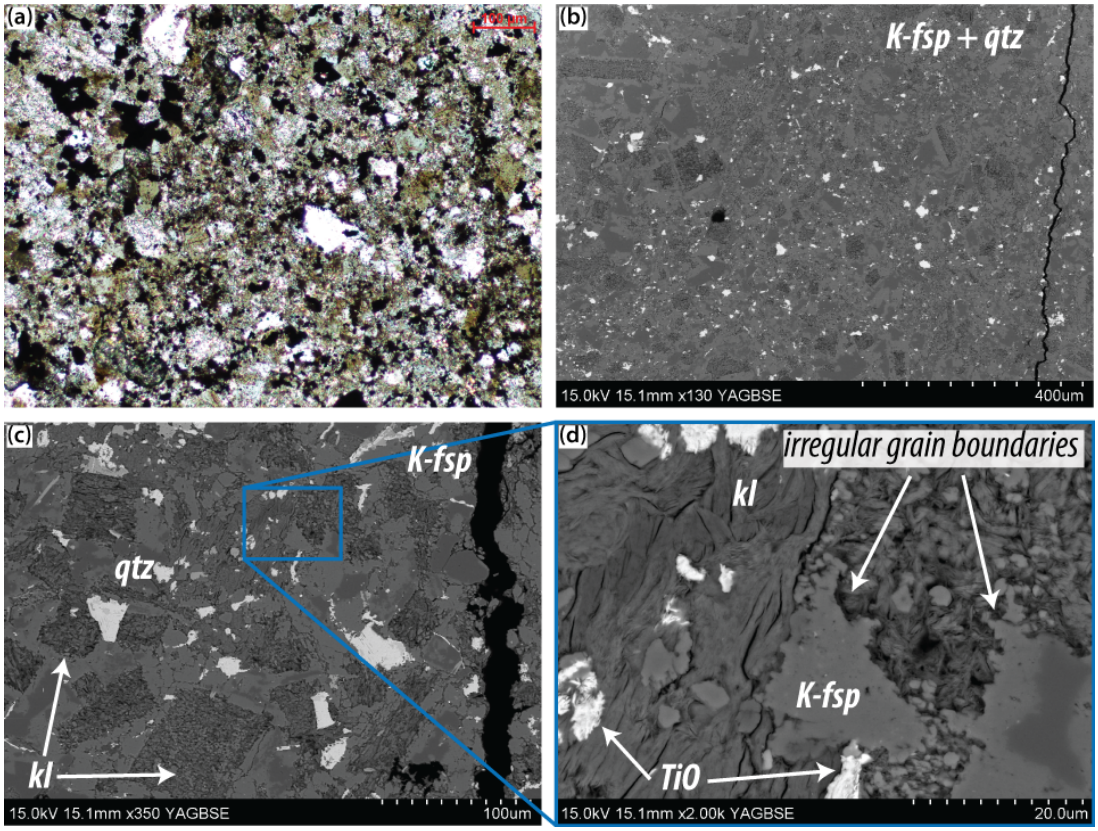

Figure 3.77: *Photomicrographs of fault core breccia of the Nizoz Fault:* ***(a & b)*** *near-intact granite porphyry (a, XPL; b, BSEM);* ***(c)*** *alteration of fsp to clay mineral with original grain boundaries still visible (BSEM);* ***(d)*** *enlarged image of (c) showing aligned kaolinite grains and irregular K-fsp grain boundaries, typical of alteration during weathering (BSEM).*

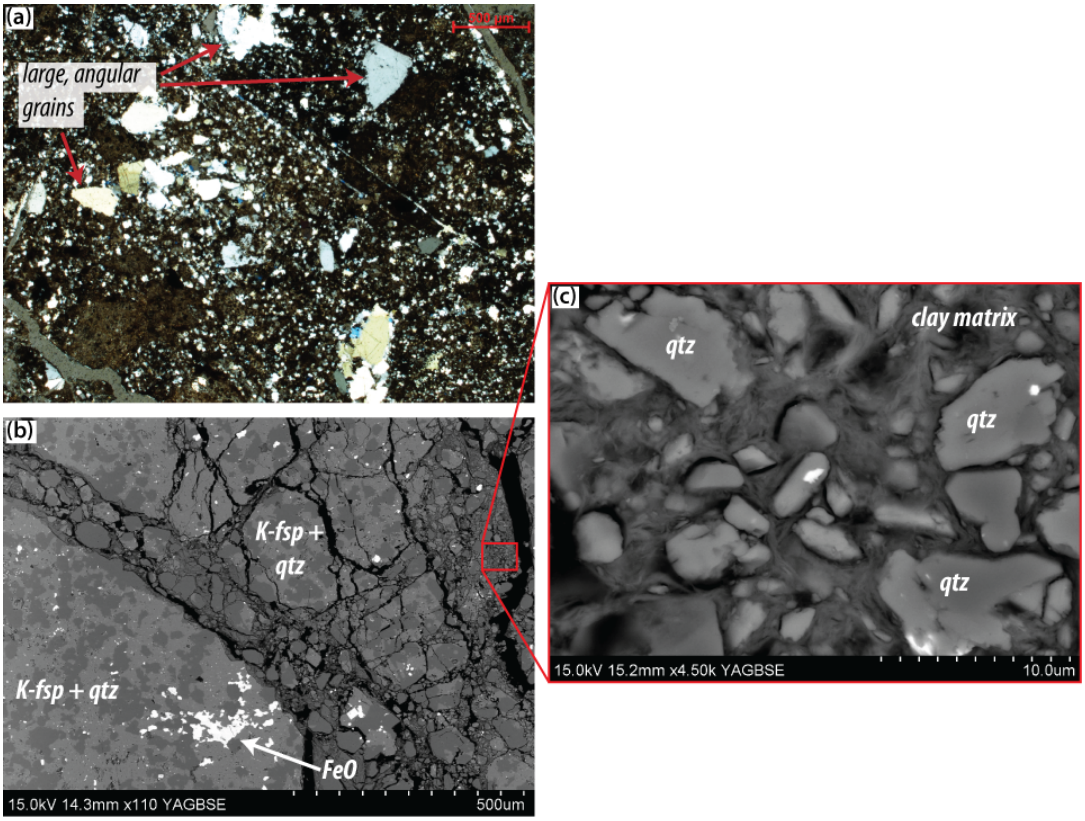

Figure 3.78: *Photomicrographs of fault core proto-grouge of the Nizoz Fault:* ***(a)*** *angular grains of basement material supported by a fine-grained matrix (XPL);* ***(b)*** *clasts of granite porphyry, large clasts are more well-rounded whilst smaller clasts are more angular. Most clasts >25 µm are composed of K-fsp and quartz, indicating they are derived from the granite porphyry rather than sandstone (BSEM);* ***(c)*** *enlargement of (b) showing small clasts supported in clay matrix (BSEM).*

Between clasts there is a very fine-grained clay matrix that appears to be formed by a fibrous/platy material, but individual grains are not as well-defined as those observed in the Shelomo and Tzefahot fault cores (Fig. 3.78c, Sections 3.3.5.1 and 3.3.5.1). However, there is a general absence of clasts much smaller than 1 µm in the matrix and this together with the definition of elongate grains, even though weak, leads us to believe that this matrix is clay material rather than being mechanically formed.

In the northern zone of the fault core, adjacent to the hanging wall, deformation is continuous and more evenly distributed than in the other parts of this fault core. The rock is very fine-grained and few clasts larger than 200 µm are present (Fig. 3.79a), although they are not entirely absent (Fig. 3.79b). There is much less variation in grain size than in the other parts of the fault core and the mean is on the order of 20 µm. Clasts are generally angular, even at relatively small sizes, and those >5 µm account for approximately 40% of the overall rock volume. Relatively few grains host microfractures and those that do are generally >40 µm in size. Clasts are composed largely of quartz and K-fsp, and there are also elongate grains of biotite.

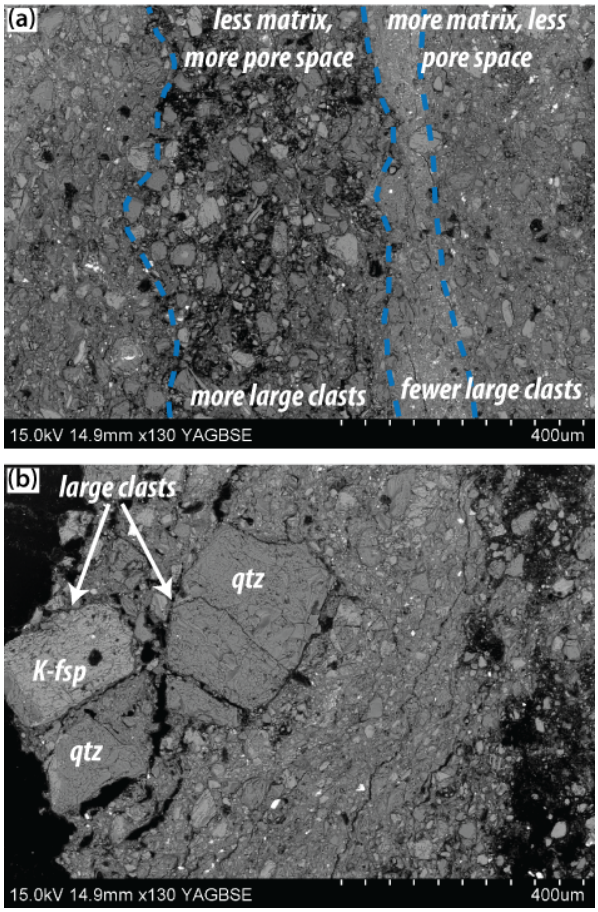

Figure 3.79: *BSEM photomicrographs of Nizoz Fault core foliated gouge:* ***(a)*** *fine-grained clasts and layering by clast size, the layers of larger clasts (centre) have less porosity than those composed of smaller clasts (to the right of the image);* ***(b)*** *occasional large clasts surrounded by matrix and clasts typically at least 10x smaller.*

The matrix in this part of the fault zone is very fine grained, and contains few grains <1 µm. As in Zone 1, some grains of phyllosilicates and clay minerals are relatively poorly-defined, but their platy nature is still apparent (Fig. 3.80a). However, there are also areas within the sample analysed where clay grains are much better defined and there is some void space between them (Fig. 3.80b). Elongate grains of clay minerals within the matrix form very localised pockets of aligned material (Fig. 3.80), but this is frequently disrupted by the presence of clasts, so there is no fabric at this scale. It is not possible to definitively determine whether this is the same clay mineral in both instances, but a possible explanation is compaction. In gouge fault rocks and shale protoliths where clays are well-defined and there is spacing between them (of <1 µm), the rocks are soft and friable; in the case of this fault rock, however, it is compacted and cohesive, and we would classify it as a cataclasite rather than fault gouge, and it may be that the difference in cohesiveness relates to the degree of compaction.

At the 10s of microns scale there is no fabric to the rock; grains are randomly oriented throughout the matrix and there are no fractures, nor is there an alignment of matrix grains. However, at the 100s of microns scale there is a clear fabric, defined by variations in grain size. Bands between 100 and 500 µm wide and continuous for the length of the sample (several centimetres, also observed

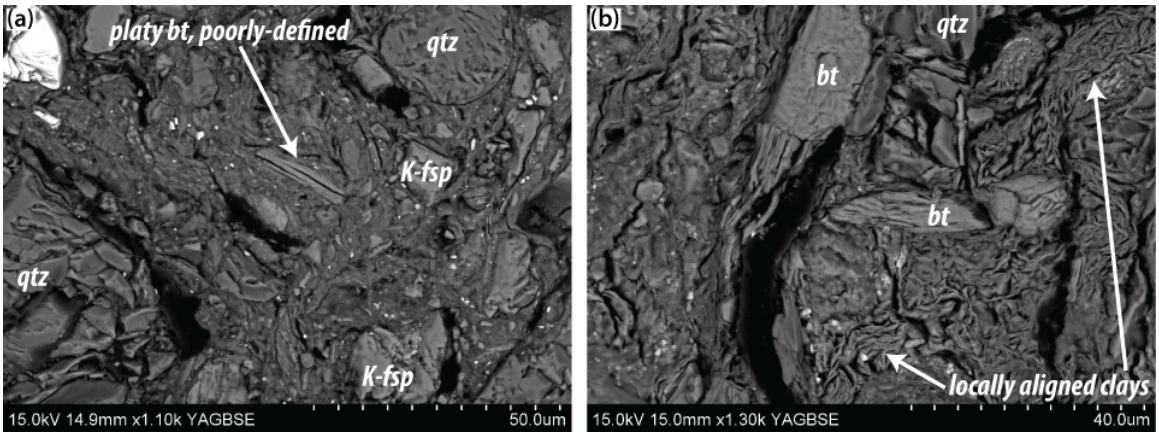

Figure 3.80: *BSEM photomicrographs of Nizoz Fault core foliated gouge matrix:* ***(a)*** *zone of fine-grained matrix supporting small, angular grains of quartz and K-fsp where individual clay and phyllosilicate (biotite) grains are poorly-defined;* ***(b)*** *zone of well-defined and locally aligned clay grains.*

at the macroscale) (Fig. 3.79a). This foliation is planar and approximately parallel to the orientation of the fault, and is not folded at the microscale.

As well as microstructurally, the different zones within the fault core also differ in terms of clay mineralogy (Fig. 3.81). In the breccia on the southern side, where the fault rocks are more competent and basement-derived, the sample analysed contains smectite and illite (Fig. 3.81a). In the central part of the fault core, in the incohesive, basement-derived gouge, the only clay mineral present is smectite (Fig. 3.81b). This is similar to the clay mineral composition of other gouges in basement-cover faults, although in this case the material is coarser grained and less cohesive. At the northern side of the fault core, clay mineral composition is illite, kaolinite and a smectite that is less well-formed (less intense peak) than that observed in the other parts of the fault core (Fig. 3.81c).

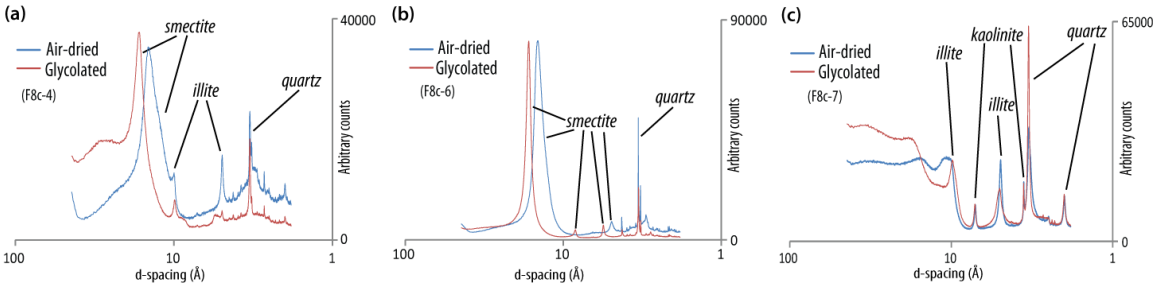

Figure 3.81: *XRD diffractograms showing clay mineralogy of the Nizoz fault core zones:* ***(a)*** *southern breccia zone containing smectite together with illite and kaolinite;* ***(b)*** *central cataclasite zone containing only smectite;* ***(c)*** *northern foliated gouge zone containing only illite and koalinite, no smectite (similar to the mineralogy of Cretaceous +/- Cambrian sandstone, Fig. 3.49a, Fig. 3.10d).*

Summary There are three well-defined zones within the core of the Nizoz Fault with two relatively cohesive layers of cataclasite at the edges, bounding an incohesive central layer. The protolith rocks of the different fault core materials are easily identifiable, with the central and southern portions consisting of only basement material, and the thinner portion in the northern part being derived from clastic wall rocks.

R12 Fault The R12 Fault is the lowest estimated displacement fault and has the narrowest fault core of the sections studied so such samples were collected from a very narrow zone (Fig. 3.82).

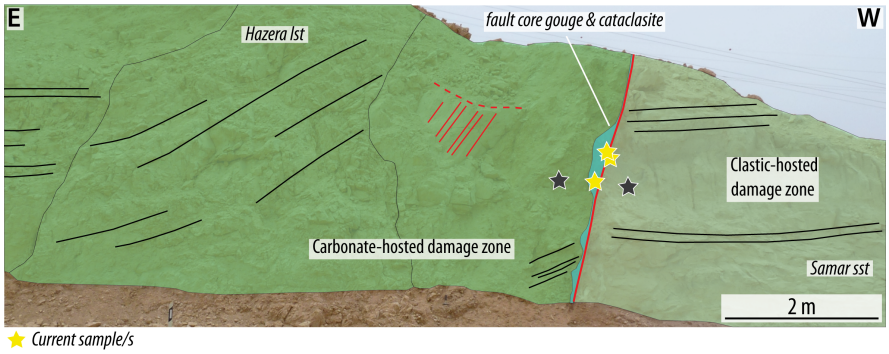

Figure 3.82: *Schematic log of R12 Fault section showing position of fault core samples.*

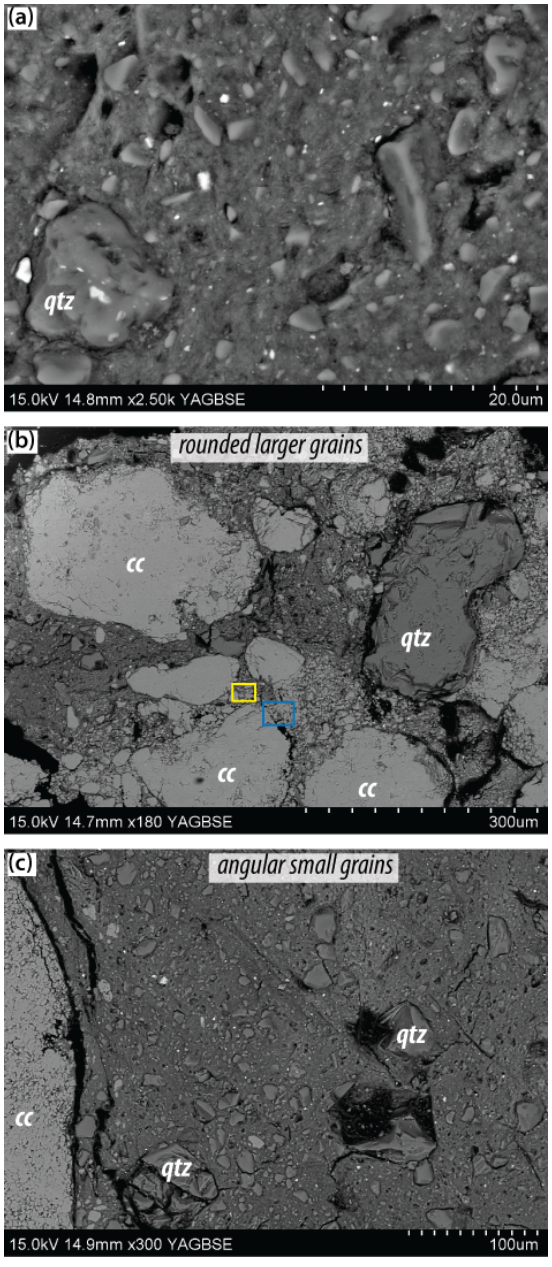

Figure 3.83: *BSEM photomicrographs showing typical relationships between clasts and matrix of the R12 Fault foliated red cataclasite:* ***(a)*** *small, angular grains within ultra fine-grained matrix;* ***(b)*** *rounded, larger grains of quartz (qtz) and calcite (cc) (blue and yellow boxes show areas represented in Fig. 3.84a,b);* ***(c)*** *small, angular clasts of quartz in close association with a large clast of calcite.*

The fault core comprises a narrow (5-10 cm) layer of cohesive, red/orange material to the east and a less cohesive brown band of clay-rich material (5-20 cm) on the western side (Section 2.6.2.7). The red band contains abundant clasts of both calcite and quartz, which vary in size from a few millimetres to <1 µm in size (Fig. 3.83a). Evidence of cataclasis is seen in the comminution of grains by spalling of small fragments from larger grains (Fig. 3.83b). The remaining larger grains are generally moderately rounded as a result and host many intragranular microfractures, while the comminuted grains tend to be more angular with few fractures (Fig. 3.83b,c). In general, there is no clast-size sorting throughout the rock and small grains (<10 µm) are seen in close association with grains >10x larger (Fig. 3.83c) The clast to matrix ratio is hard to define due to the heterogeneity of the sample, but overall it appears to be matrix-supported more often than clast-supported. However, due to the relatively cohesive nature of this sample we have defined it as a cataclasite rather than a fault gouge.

Where grains of calcite have been comminuted, there is evidence of pressure solution between some new grain boundaries and these grains appear to have thin (<5 µm) coatings of clay material (Fig. 3.84a,b); where this coating is present, grain boundaries are often poorly-defined, suggesting this clay is likely authigenic, and may have precipitated as the result of fluid-assisted diffusive mass transfer after initial pressure solution. The boundaries of small quartz grains are well-defined and there is no evidence of pressure solution between them.

The matrix in this sample is extremely fine-grained (<1 μm, Fig. 3.84c) and, in general, the mineralogy cannot be determined, although occasional stacks of kaolinite grains are observed (Fig. 3.84d). There is no apparent fabric within the matrix and we have defined it as a cataclastic fault gouge, where the grains of kaolinite observed have been incorporated as part of this process.

The brown, clay-rich, western part of the fault core is much more homogeneous in appearance and mineralogy. There are few clasts (of quartz and calcite) and the matrix consists of very fine-grained clay material (Fig. 3.84e). Although there is a foliation at the sub-micron level (Fig. 3.84f), on a larger scale across the sample this is discontinuous and frequently disturbed.

The clay mineral composition of the clay gouge and cataclasite are distinct; the clay gouge contains kaolinite, smectite and minor illite (Fig. 3.85a) and is very similar in composition to the undeformed Ora Shale (Fig. 3.15d), and therefore may represent mechanical entrainment of this rock, whilst the cataclasite is predominantly composed of kaolinite (Fig. 3.85b) and is very similar in composition to the sandstone wall rocks (Fig. 3.54). The similarity of the two fault core materials to wall rock lithologies suggests there have been very few mineralogical changes within the fault core. The distinct clay compositions of the two materials to each other suggests, in addition, that there has been relatively little mechanical mixing of materials within the fault core.

Summary Although the R12 Fault has a low estimated displacement (57 m) and the studied section is relatively narrow (Section 2.6.2.7), the fault core itself is heterogeneous and two distinct zones within it are observed; a narrow, cohesive layer of cataclasite that is very similar in composition to the footwall wall rocks, and a clay layer of varying width that is similar in composition to the Ora Shale.

Summary of cataclastic gouges We have presented here microstructural evidence that within the fault gouges defined as 'cataclastic', there are actually two phases of very fine-grained (<1 μm) gouge: a *mechanical gouge* that formed by cataclasis and intense comminution of grains that is lacking in fabric; and an *authigenic gouge* that is foliated at the sub-micron scale and is weakly-moderately foliated. This foliation is always visible at the microscale, but not always at the macroscale. The mineralogy of the cataclastic gouges is dominated by smectite, and though it was not possible to separate the mechanical and clay gouges for analysis, we believe that this is present largely in the clay gouges. Smectite is present in the gouges of all fault zones, apparently regardless of wall rock mineralogy. The presence of foliated, interconnected smectite may have significant implications for the frictional properties and behaviour of faults (see Sections 3.4.2 to 3.4.4). In the case of framework minerals such as quartz and feldspars, feldspars crystals are consistently more intensely fractured than those of quartz, which is consistent with observations that feldspar is weaker than quartz at very low grade (<300 °C) metamorphic conditions (Chester and Logan, 1987; Evans, 1988).

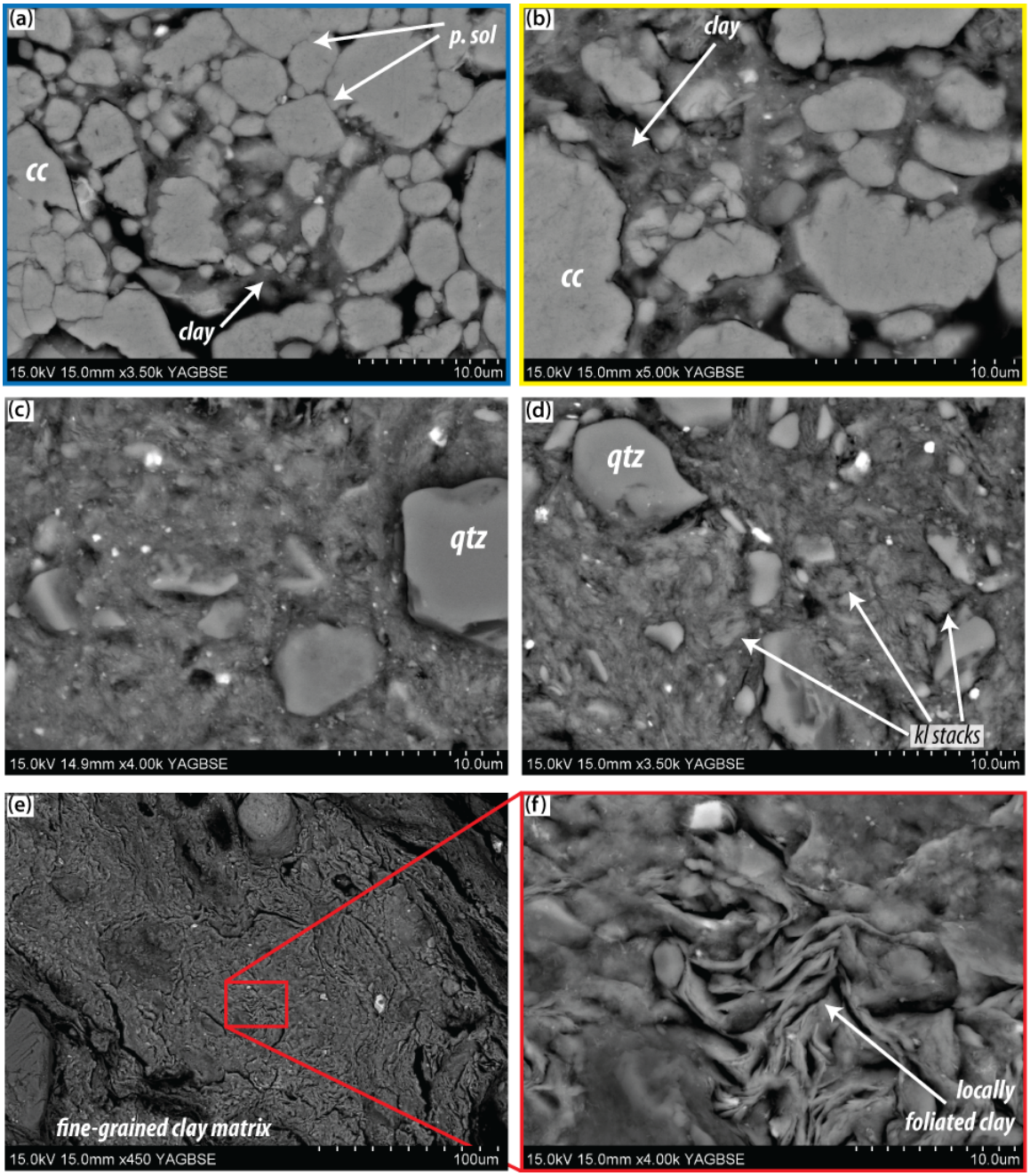

Figure 3.84: *BSEM photomicrographs showing grain-scale features of the R12 Fault cataclastic gouge:* ***(a)*** *pressure solution at grain contacts of calcite grains;* ***(b)*** *clay coatings between calcite grains;* ***(c)*** *ultra fine-grained clay matrix with no visible structure or fabric;* ***(d)*** *locally stacked kaolinite;* ***(e)*** *fine-grained clay matrix with few clasts;* ***(f)*** *enlargement of (e), well-defined, locally folded clay grains.*

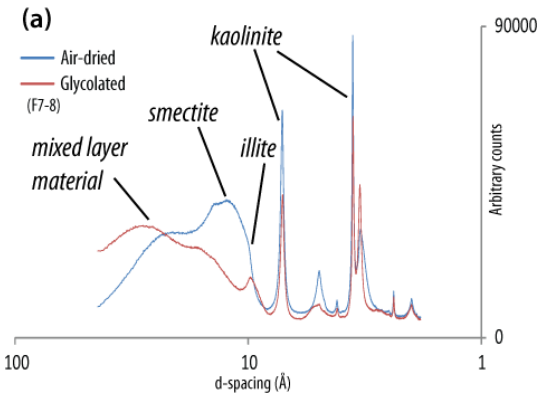

Figure 3.85: *XRD diffractogram showing clay mineralogy of R12 Fault cataclastic gouge: kaolinite, smectite, mixed layer material and smectite.*

3.3.5.2 Shale gouges

Tzefahot Fault At the studied section of the Tzefahot Fault, approximately half of the fault core width is composed of what we have given the field definition of 'shale gouge' (Fig. 3.86 and Section 2.6.2.2). As suggested by field observations, the shale gouge is strongly foliated at the microscale (Fig. 3.87a), a fabric that is defined by the alignment of clay grains. The spacing of this foliation is at the sub-micron scale (Fig. 3.87c) At the mesoscale we observed folds on the centimetre-scale (formed by frictional sliding, Section 1.6.2) and these are also present at the millimetre (Fig. 3.87b) and micron (Fig. 3.87c) scales and indicate sliding along the platy clay minerals formed these "ductile" structures. Analysis of the gypsum veins observed in the field confirms that they are tensile fractures, with gypsum crystals growing orthogonal to vein walls (Fig. 3.87d).

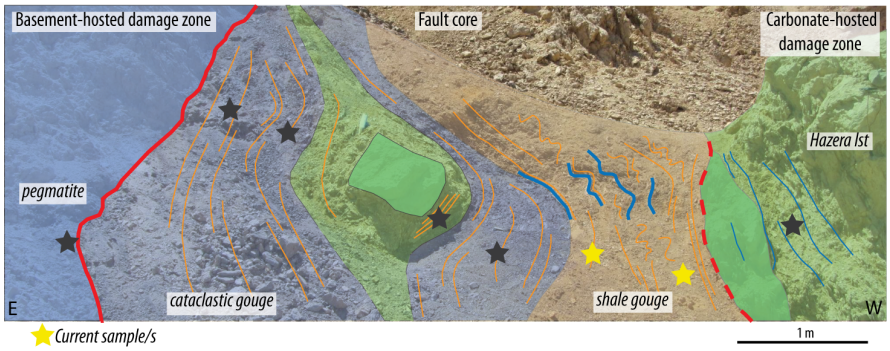

Figure 3.86: *Schematic log of Tzefahot Fault section showing position of shale gouge fault core samples.*

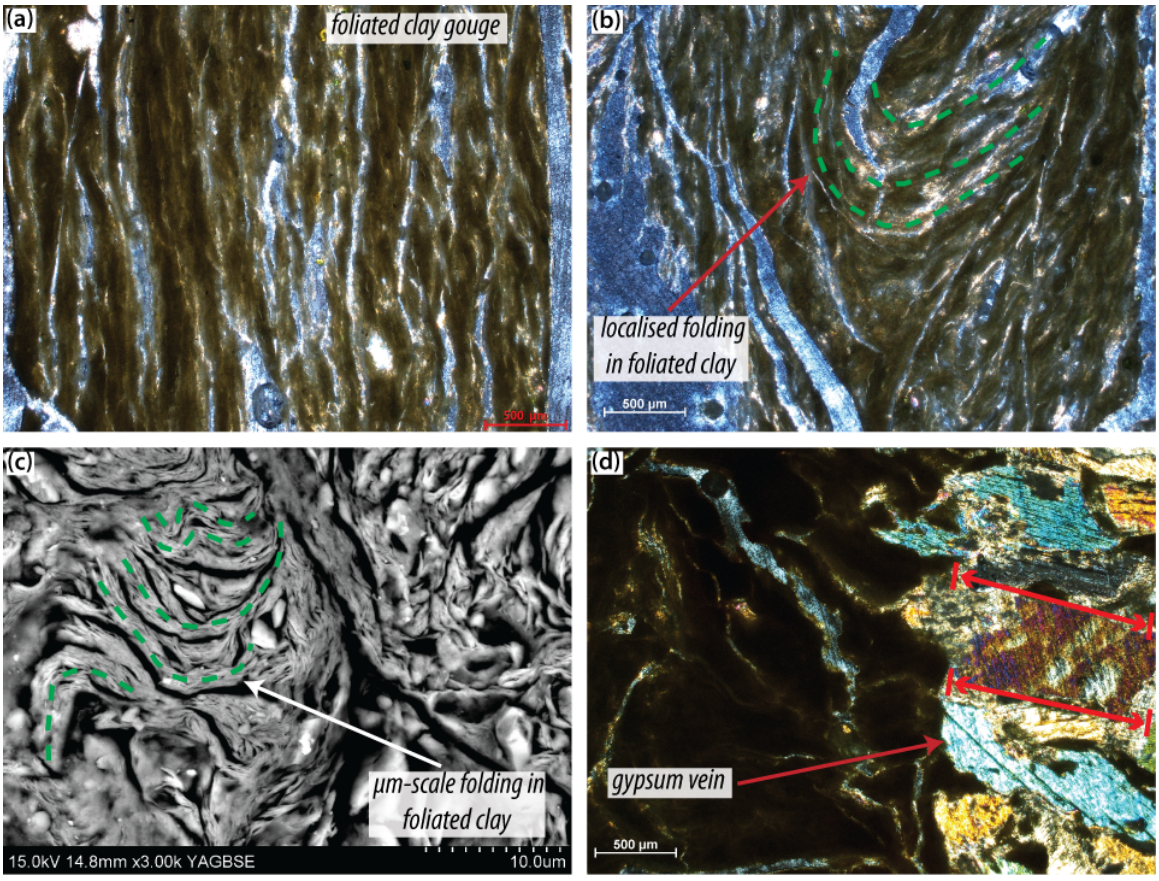

Figure 3.87: *Photomicrographs showing the typical appearance of the Tzefahot Fault core shale gouge:* ***(a)*** *foliated, clast-poor shale (XPL);* ***(b)*** *mm-scale fold within the shale (XPL);* ***(c)*** *micron-scale folding in the shale (BSEM);* ***(d)*** *gypsum vein with fibre-growth sub-perpendicular to the vein wall (XPL).*

The clay mineralogy of this gouge is composed of kaolinite together with minor smectite and illite (Fig. 3.88a), which is almost identical to the composition of the Ora shale, with the exception that this is no mixed layer material in this sample (Fig. 3.15e). The general lack of clasts and foliated nature of the shale gouge is also very similar in appearance to that of the Ora shale. However, the gouge is somewhat heterogeneous as there are areas where the foliation has been disturbed in a more brittle manner; that is, it is interrupted and becomes discontinuous over short distances, rather than being folded (Fig. 3.88b). Despite this, deformation across this part of the fault core is much more continuous than in the cataclastic gouges and is more evenly distributed.

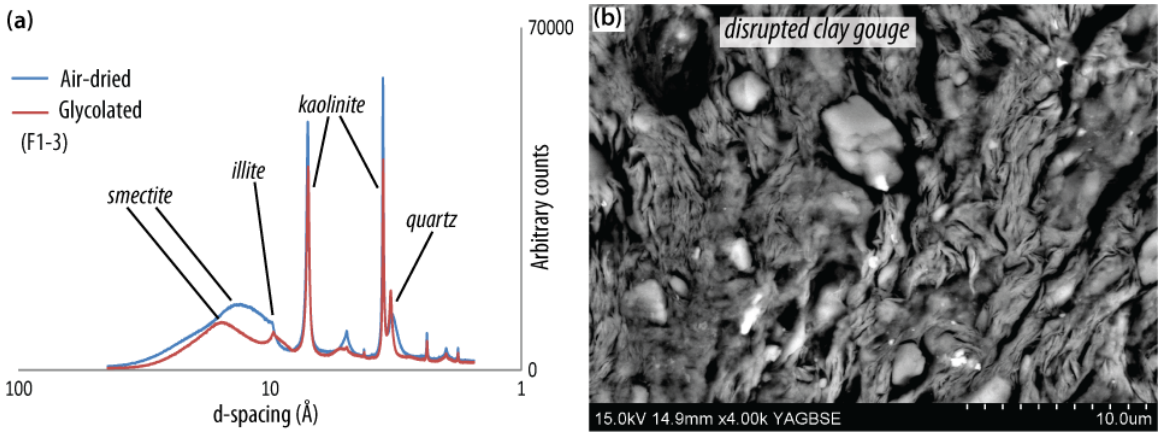

Figure 3.88: *Appearance and mineralogy of the Tzefahot Fault shale gouge:* ***(a)*** *XRD diffractogram showing clay mineralogy of shale gouge: smectite, kaolinite and minor illite;* ***(b)*** *Photomicrographs showing shale foliation disrupted by the presence of clasts (BSEM).*

Yehoshafat Fault In contrast to the Tzefahot Fault, shale gouge is the only material present within the fault core of the Yehoshafat Fault (Fig. 3.89). The fabric observed at the macroscale is also present at the microscale, with the foliation defined at the sub-micron scale by the shape preferred orientation of clay minerals.

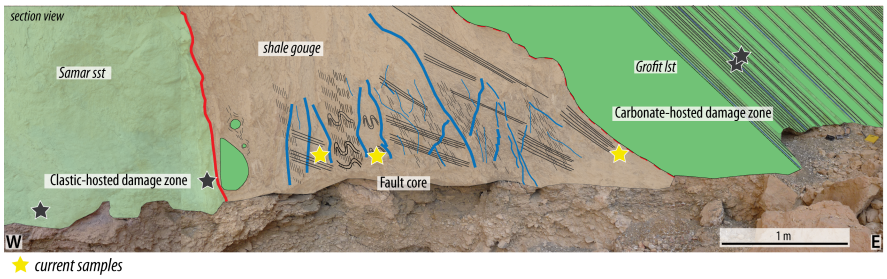

Figure 3.89: *Schematic log of Yehoshafat Fault section showing position of fault core samples.*

There is some variation in the concentration of clasts across the fault core, which appears to reflect the difference in appearance of the gouge laterally across this zone (described in Section 2.6.2.6). Gypsum veins are present throughout the fault core and the direction of crystal growth is sub-perpendicular to vein edges, suggesting these are tensile structures.

At the western side of the fault core, closest to the sandstone footwall, the shale is strongly foliated and clasts (mostly composed of quartz) are generally 10 µm in size or less, and rarely >30 µm (Fig. 3.90a). In the eastern part of the fault core, however, where the gouge is more brittle and darker in appearance, there is an increase in the concentration of round nodules of a material composed of S, K, Al, Si and Fe, with occasional quartz grains (Fig. 3.90b). These nodules

of sulphur-rich silicate material range in size from <5 - ~50 µm and form aggregate clasts that are often relatively well rounded with diffuse boundaries; we infer that these have grown in situ as the result fluids passing preferentially through this region of the fault core. This may be the case if fluids are sourced in the carbonate hanging wall as we would not expect them to travel far laterally across the fault zone, due to a low assumed permeability of a strongly-foliated shale. However, no such nodules are observed in the hanging wall shales in the damage zone of the fault section.

Although the shale material of the eastern damage zone is very similar in appearance to that of the western part of the fault core (Section 2.6.2.6), there is some variation in the clay mineralogy (Fig. 3.91). To the east, the clay mineralogy is very similar to that of the damage zone (Fig. 3.41b) and the smectite peak in the XRD diffractogram is relatively subdued (Fig. 3.91c); moving westwards, however, this peak becomes more prominent. Although we have not performed quantitative XRD, the increase in relative intensity of this peak (in comparison to those for kaolinite and illite, which remain approximately the same) indicates a relative increase in the amount of smectite within the shale gouge. Although we still conclude from its appearance in the field and thin section, and from the overall clay mineralogy that the shale gouge is entrained Ora shale, the variation in smectite content suggests additional precipitation of this authigenic mineral and that this is not evenly distributed throughout the fault zone.

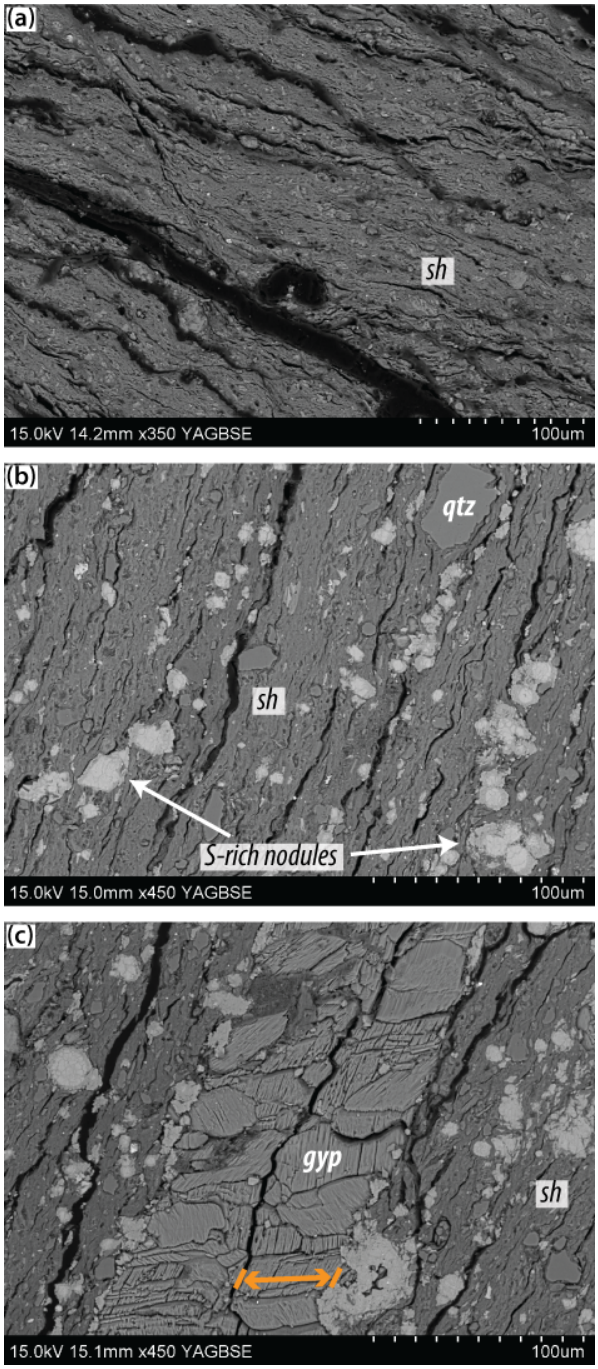

Figure 3.90: *BSEM photomicrographs of the Yehoshafat Fault core shale:* ***(a)*** *strongly foliated shale;* ***(b)*** *S-rich nodules and quartz clasts in eastern part of fault core;* ***(c)*** *gypsum vein, sub-parallel to foliation and crystal growth sub-orthogonal to vein wall.*

Summary of shale gouges The presence of shale gouges within the Tzefahot and Yehoshafat fault cores is in contrast to cataclastic gouges as they are not derived from wall rocks directly adjacent to the fault cores of the studied sections. Instead, the shale gouges are derived from mechanically entrained ('smeared') units of the Ora Shale formation and have undergone very little cataclastic deformation.

Whilst the gouges within the Tzefahot Fault section have undergone very few mineralogical changes, there is an increase in the relative amount of smectite present from east to

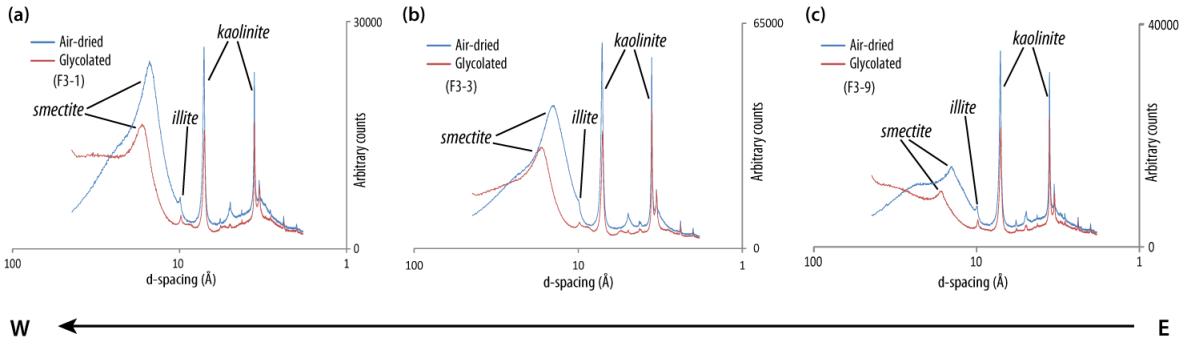

Figure 3.91: *[XRD diffractograms showing clay mineralogy of Yehoshafat Fault shale gouge:* ***(a)*** *highest concentration of smectite to the west, closest to fault plane;* ***(b)*** *intermediate concentration of smectite in central part of fault core;* ***(c)*** *smectite concentration in eastern part of fault core similar to that in damage zone (Fig. 3.41).*

west within the fault core of the Yehoshafat Fault. The Tzefahot and Yehoshafat faults also differ in that shale gouge is the only fault core material present in the Yehoshafat Fault section, but at the studied exposure of the Tzefahot Fault this material accounts for approximately half of the fault core width.

3.3.6 Summary of microstructures and mineralogy

Evidence of a range of deformation mechanisms has been observed in the studied suite of fault zones, and can be broadly separated into three styles: *(i)* brittle deformation by micro- fracturing (shear and tensile), frictional sliding and grain-size reduction through cataclasis; *(ii)* 'ductile' deformation by creep, folding and entrainment of clay-rich material; and *(iii)* neomineralisation, by alteration to and/or precipitation of new clay minerals (the possible mechanisms of which are discussed further in Section 3.4.3). Deformation in the damage zones is mostly confined to brittle fracturing +/- cementation of fractures and protolith rocks are easily identifiable at the mesoscale. By contrast, fault core deformation produces intense microstructural and mineralogical changes, and probable protolith rocks can only be determined by carrying out more detailed, microscopic analysis. The result of intense deformation within these zones is the production of two distinct types of fault gouges: cataclastic gouges, by mechanical and chemical processes, and shale gouges, by ductile processes.

Although distinct mechanisms of deformation within the fault cores have been identified (i-iii, above), they do not occur in isolation and brittle deformation and mineralogical changes appear to be closely linked. Ductile deformation, with the exception of very small-scale features, is confined to shale gouges, and as such is believed to be able to occur due to the specific mechanical properties of clay minerals. The deformation of shale gouges is still closely linked to fault zone evolution, however, as it appears to serve to arrest, or at least significantly reduce, further cataclastic deformation and mineralogical changes. Authigenic smectite is consistently Mg-rich, containing little to no Fe. A summary of the deformation mechanisms, mineralogy and resultant fault rocks is provided in Table 3.3.

Table 3.3: *Table summarising dominant mineralogy and deformation mechanisms of the studied fault sections, arrow represents decreasing displacement (qtz: quartz; bt: biotite; cc: calcite; dol: dolomite; sm: smectite; kl: kaolinite; ilt: illite; chl: chlorite;* ***bold*** *minerals represent the principal phase present).*

Fault	Location	Mineralogy		Dominant deformation mechanisms	Matrix type
		Crystal/grain	*Clay*		
Shelomo Fault					
Locality A	Basement damage zone	K-fsp, qtz	sm, kl	Tensile fracturing, localised cataclasis	*Mechanical* gouge & *authigenic* clay gouge
	Carbonate damage zone	calcite	kl, sm, ilt	Tensile & shear fracturing, clay injection	
	Fault core	qtz, K-fsp	**kl**, sm (ilt)	Cataclasis & precipitation of authigenic clay material	
Locality B	Basement damage zone	qtz, K-fsp, bt	sm	Fracturing, localised catalcasis, pulverisation	
	Carbonate damage zone	calcite	kl, ilt, sm	Cataclasis & precipitation of authigenic clay material	
	Fault core	K-fsp, qtz, bt, cc	**sm** +/- **kl**		*Mechanical* gouge, *authigenic* & clay gouge
Tzefahot Fault					
	Basement damage zone	qtz, K-fsp	sm	Shear fracturing, pulverisation, localised cataclasis, clay injection	*Mechanical* gouge & *authigenic* clay gouge
	Carbonate damage zone	cc, dol	chl-sm, kl, ilt, sm	Shear & Tensile fracturing	Undeformed
	Fault core	qtz	**sm** (kl, ilt)	Wholesale cataclasis & precipitation of authigenic clay material + 'ductile' folding and precipitation of gypsum veins	*Mechanical* gouge, *authigenic* clay gouge & *shale* gouge
Roded Fault					
	Basement damage zone		chl (??), kl, (ilt)	Tensile fracturing, localised cataclasis	
	Clastic damage zone	qtz, K-fsp	kl, ilt	Intragranular microfracturing	Not present
	Fault core		**ilt**, **sm**, kl	Cataclasis, DMT processes, precipitation of authigenic clay material	*Mechanical* gouge & *authigenic* clay gouge
Nizoz Fault					
	Basement damage zone	qtz, K-fsp		Mescoscale fracturing	
	Clastic damage zone	qtz	kl, ilt	Microfracturing	
	Fault core	qtz, K-fsp	**sm**, ilt (kl)	Tensile & shear fracturing, localised cataclasis, & precipitation of authigenic clay material	*Mechanical* gouge & *authigenic* clay gouge
Yehoshafat Fault					
	Carbonate damage zone	cc	chl-sm, kl, ilt, sm	Tensile fracturing	Undeformed
	Clastic damage zone	qtz	kl	Intragranular microfracturing, localised cataclasis	Undeformed + FeO precipitation
	Fault core		**kl**, ilt, sm	'Ductile' folding and precipitation of gypsum veins	*Shale* gouge
R12 Fault					
	Carbonate damage zone	cc	sm, ilt, kl	Localised pressure solution	
	Clastic damage zone	qtz	chl-sm, kl, ilt, sm	??	
	Fault core	qtz	**kl**, (sm, ilt)	Cataclasis	*Mechanical* gouge & *authigenic* clay gouge

displacement

3.4 Discussion

3.4.1 Deformation mechanisms and syn-tectonic evolution of mineralogy

3.4.1.1 Damage zones

Deformation within the damage zones is for the most part by brittle fracturing, with varying effects of fluid-rock interaction, but the mechanisms by which fractures form are distinct within the three types of wall rock lithology. In carbonate damage zones, both tensile and shear fractures, continuous for several millimetres, are common; these are frequently filled with blocky, equant calcite and the presence of 'floating' fragments of grains within the calcite fracture-fill that have not undergone any shear displacement allows us to constrain the timing of these fluids as syn-tectonic, since a space between a grain and the fragment is not sustainable without the presence of fluid pressure to maintain the distance. In addition, crack-seal textures at the Shelomo Fault indicate that fluid flow involved cyclical increases in pore-fluid pressure over time due to repeated ingress of fluids into the fault system.

The fracturing and subsequent cementation of rocks in the damage zone with a relatively strong material (calcite) may serve to strengthen this part of the fault zone, but any increase in pore fluid pressure will reduce the effective normal stress within the fault zone. This effect may be compounded by a reduction in permeability in the wall rocks (by cementation of fractures), serving as a baffle to fluid flow across the fault zone. The extent to which fluids may become trapped within faults depends also on the permeability of both the fault core materials and rocks within the footwall damage zones, as well as confining pressure (e.g. Caine et al., 1996; Evans et al., 1997; Faulkner and Rutter, 2001; Mitchell and Faulkner, 2012).

Deformation within basement damage zones is more varied than in carbonate equivalents and likely reflects the varying lithologies, that whilst are similar in mineralogy overall, are distinct in fabric and texture. Calcite-filled tensile fractures are also common within granitic, dioritic and rhyolitic basement damage zones (but were not observed in volcanic rocks), suggesting permeability was also relatively low in these rocks and fluids may have been prevented from escaping, leading to elevated pore fluid pressures. It is also possible that the effect of low permeability in the wall rocks may have helped to facilitate clay transformations within fault core, as a result of trapped fluids being present in larger volumes and/or for longer periods of time. The fact that Ca-rich fluids are present in both the carbonate cover and igneous/metamorphic basement damage zones suggests either at least some degree of cross-fault fluid flow, or a source shallower or deeper than the fault that has allowed fluids to penetrate either side of (and within ?) the structure.

Cemented tensile fractures are not the only brittle deformation feature present in the basement wall rocks. Shear fractures, intra- and intergranular microfractures are also present. Narrow zones of comminuted material suggest localised cataclasis and this, together with randomly oriented, pulverisation-style fracturing observed at the Shelomo and Tzefahot faults serve to reduce the cohesiveness of these zones, as well as increase permeability in crystalline rocks (e.g. Zoback and Byerlee, 1975; Zhu and Wong, 1997). The relative timing of tensile fractures is determined to have

preceded shear deformation as the calcite fill is also fractured in places (e.g. Fig. 3.21), so it is possible that high pore fluid pressures were only maintained during the early evolution of the fault zones.

Where footwall rocks include volcanic material, however, no such tensile fractures and calcite cement are observed. In the case of Locality A of the Shelomo Fault, fractures are generally filled with clay material (kaolinite and smectite, Fig. 3.18) and there is no sign of calcite. With the exception of pulverised zones, volcanic rocks in damage zones are also the most intensely deformed and least cohesive of all the basement units. The mineralogy and texture of these rocks is similar to those of the porphyritic and rhyolitic rocks that are present at the Nizoz Fault, and displacement magnitude along this fault is comparable to the Tzefahot Fault, so it is hard to explain this difference in terms of lithology or displacement. Instead, it is possible that these rocks had already undergone an initial phase of deformation related to the minor faults that are oblique to the main fault trace (Section 2.6.2.1).

A further mechanism of deformation of which there is evidence in the basement damage zones of the Shelomo and Tzefahot faults is pulverisation. This style of deformation is widely considered as indicative of seismogenic slip (e.g Brune, 2001; Ben-Zion, 2001; Reches and Dewers, 2005; Wilson et al., 2005; Mitchell et al., 2011). In addition, at both of these faults we also observed clay-rich gouge material injected from the fault cores into the damage zones (on the basement side at the Tzefahot Fault and the cover side at the Shelomo Fault), which may be a further indication of seismogenic behaviour (e.g. Lin, 1996; Rowe et al., 2012; Fagereng et al., 2014). In addition to evidence that these faults have accommodated seismic slip at some point in their history, the presence of pulverisation textures is also an indicator of fault asymmetry (contrast in seismic velocities of host rocks), since this is recognised as a necessary condition for this type of deformation (Dor et al., 2006; Mitchell et al., 2011). It is generally believed that a contrast in seismic velocities is required in order for pulverisation to occur, in the rocks with higher seismic velocities (Ben-Zion and Huang, 2002; Dor et al., 2006; Mitchell et al., 2011). Since it is likely that the faults propagated through cover rock sequences relatively late in their history, we may infer from this that seismic slip also occurred relatively late; there would not have been the necessary contrast in seismic properties of hanging- and footwall rocks when the faults were basement-hosted at depth. Several authors (Reches and Dewers, 2005; Wilson et al., 2005; Dor et al., 2006) have also noted that pulverisation textures are produced at shallow depths, supporting this interpretation. Notably, this evidence of seismogenic behaviour, in addition to clay injections, is only observed at the two largest displacement faults. This may indicate that coseismic ruptures initiate in deeper parts of the crust, where frictionally-weak smectite is not present (transformed to illite or chlorite), and propagate to more shallow depths through smectite-bearing fault zones towards the surface (see Section 3.4.4 for further discussion of this).

In clastic damage zones, there are few through-going fractures and little evidence of circulating fluids generally, with the exception of close to the fault plane at the Yehoshafat Fault (e.g. Fig. 3.52). Fracturing, for the most part, occurs as intragranular microfractures since there is a high volume of intergranular clay cement. However, discrete shears do form deformation bands, although these are usually <1 mm wide and have a spacing of up to 10s of centimetres, so are by no means abundant nor are thought to have a significant impact on the overall competency of the rocks. The competency of clastic damage zone varies from there being little obvious change compared to the

protolith (Roded and Nizoz faults) to a drastic reduction in cohesiveness and apparent competency (R12 Fault). We believe this to be related to the nature of the different sandstone formations. The Cambrian Shehoret sandstone (present at the Roded Fault outcrop), for example, is a well-lithified, well-cemented rock, whereas the youngest Cretaceous sandstone (Samar formation, present at the R12 fault outcrop) is not as well-lithified and contains a relatively high proportion of intergranular clay cement (up to 70%), and is therefore not expected to be as resistant to deformation.

3.4.1.2 Cataclastic gouges

Deformation within the cataclastic gouges is highly heterogeneous and it is in this part of the fault zones that the most pervasive changes in both structure and mineralogy occur. A common feature of these gouges is that in all fault zones with igneous/metamorphic basement wall rocks, clast mineralogy largely consists of silicate minerals (quartz, feldspars, biotite) that are igneous/metamorphic in origin. In fault cores where carbonate wall rocks are present (Shelomo and Tzefahot Faults), there are some clasts of this material present at the mesocale, but very few are observed at the sub-millimetre scale. Although it is harder to determine the origin of all quartz grains within fault cores, at the basement-clastic Nizoz Fault, the basement wall rocks tend to be aphanitic (Sections 3.3.1.4 and 3.3.1.5) and evidence of this texture is seen in many of the clasts within the core of this fault (Figs. 3.78 and 3.79), leading us to infer these are also igneous/metamorphic in origin. This evidence suggests that cataclastic gouges are, for the most part, derived from basement wall rocks, although small volumes of carbonate rocks at least have been incorporated into the fault cores to some extent.

This is particularly evident at the exposure of the Tzefahot Fault, where there is a large, metre-wide clast of carbonate material within the cataclastic gouge. No basement clasts of comparable size were observed at any of the studied fault sections and we infer that the faults initiated within basement rocks before propagating to shallower depths and incorporating cover rocks through increasing displacement. In this scenario, the most displacement on these oblique-slip faults would occur when both the hanging- and footwalls were comprised of the same, or similar, aluminosilicate materials and it would only be in the later stages that relatively shallow carbonate and clastic cover rocks are incorporated into the fault zones (on the hanging wall side). In this case it may be possible for both large clasts of cover wall rocks to remain relatively intact, having been incorporated into the fault core relatively late in its history, whilst basement-derived material has been subjected to more intense deformation over a longer period of time, resulting in a significant reduction in grain size not seen in cover-derived rocks. Evidence of cataclastic deformation is widespread within these gouges, in both the microfracturing of individual grains of quartz, feldspars and mica, and in intense comminution of grains; small clasts of quartz and feldspars down to 1 μm in size or less are observed. Within this mechanically-formed part of the gouge, the principal deformation mechanism is inferred to be frictional sliding. However, fault gouges are not formed solely by simple cataclastic processes, as XRD analyses reveal the development of a clay mineral (smectite) that is not present in adjacent wall rocks, confirming there is an authigenic phase within the cataclastic gouge.

Smectite is ubiquitous in the fault gouges and appears to be present regardless of wall rock lithology. It is present in two distinct phases: as a well-formed, 'fresh' phase in basement against

carbonate cover faults (Shelomo and Tzefahot), basement against clastic cover faults (Roded and Nizoz) and carbonate cover against clastic cover Yehoshafat Fault and as a weathered, more irregularly-formed phase in the R12 Fault, also carbonate cover against clastic cover. At the Shelomo, Tzefahot, Roded and Nizoz faults, the clay mineralogy of the cataclastic gouges is dominated by smectite (Fig. 3.92), indicating it is the only authigenic phase. At the Shelomo and Tzefahot faults there are also minor amounts of illite and kaolinite, likely sourced from carbonate wall rocks that are not present at the Roded and Nizoz faults.

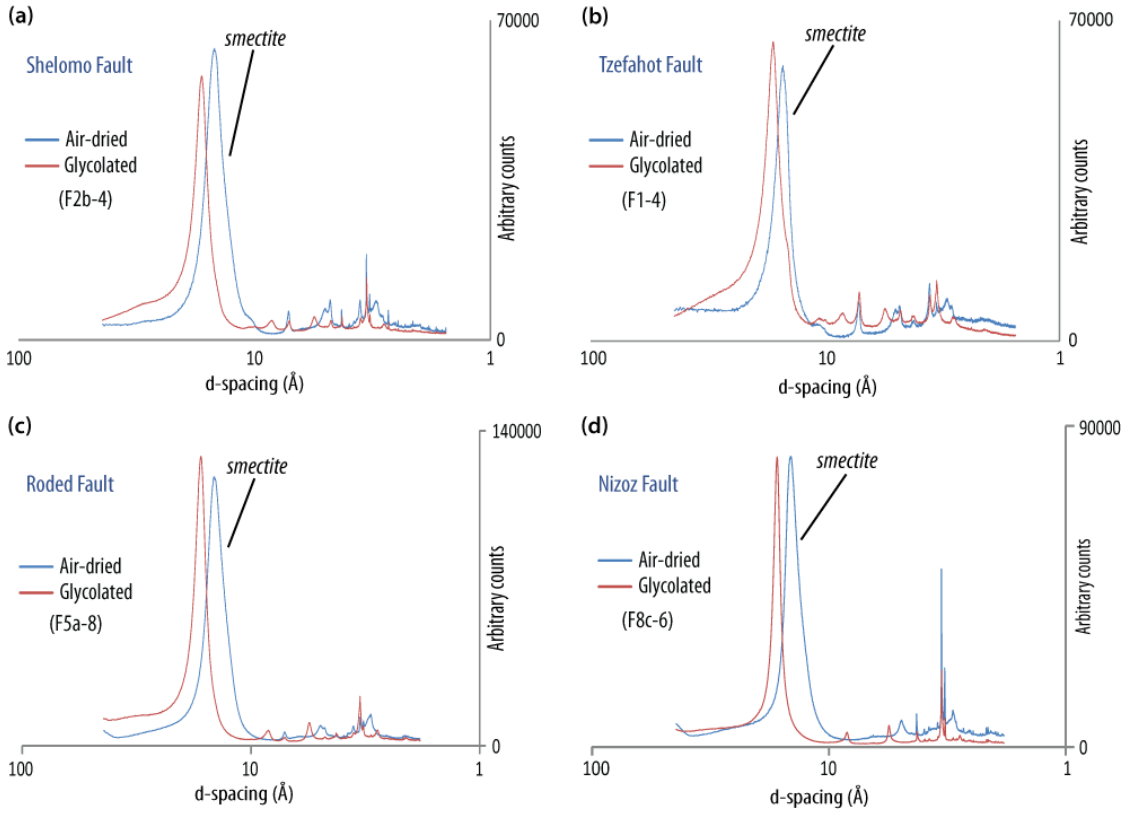

Figure 3.92: *Clay mineralogy of cataclastic fault core gouges, showing neoformed smectite as principal mineral in all:* ***(a)*** *Shelomo Fault;* ***(b)*** *Tzefahot Fault;* ***(c)*** *Roded Fault;* ***(d)*** *Nizoz Fault.*

Smectite is stable only at low temperatures (<100 °C) and, in the case of these faults, we are likely to be at the low end of the temperature range since we see only pure smectite and no mixed layer material, which would signal the start of the transition to chlorite or illite. Faulting must therefore have been shallow; assuming a normal geothermal gradient of 30 °C/km, a 3 km depth is the maximum but 1 km is more probable due to the purity of smectite present. The well-formed nature of the smectite also indicates it represents new mineral growth and is not the product of retrograde alteration of chlorite or illite on exhumation of the faults.

3.4.1.3 Shale gouges

Within the shale gouges of the Tzefahot and Yehoshafat faults, the dominant style of deformation is ductile and there is very little evidence of brittle deformation apart from occasional shear planes that cut across the foliation. The few clasts that are present in the clay matrix are not generally fractured and have a similar range in size and distribution as those within undeformed shales. Microfolds on the meso- to micro-scale are consistent with distributed, ductile deformation during

aseismic creep (e.g. Holdsworth et al., 2011; Hadizadeh et al., 2012; Bullock et al., 2014).

Deformation is for the main part continuous and distributed, with the exception of the shear planes which are discontinuous and localised. This, along with the lack of extensive brittle deformation leads us to infer that this is a unit of mechanically entrained shale, dragged into the fault core from shales in the adjacent sedimentary formations; the foliation is also believed to be inherited from the (relatively) undeformed shales.

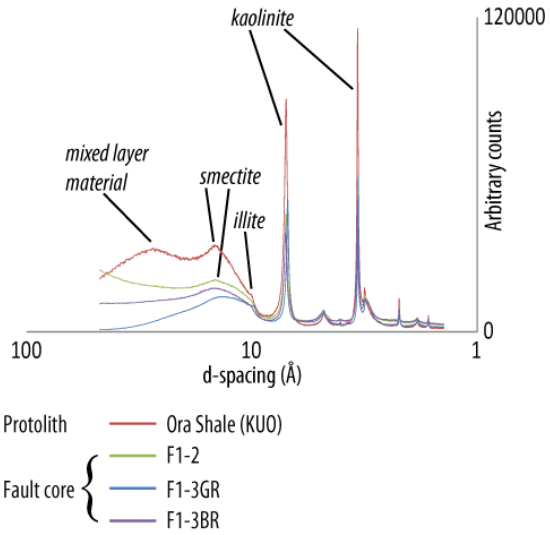

Figure 3.93: *Combined XRD diffractograms for shale gouges of the Tzefahot Fault and undeformed Ora Shale (air-dried only), showing similarity in clay mineral composition of the gouges and protolith shale.*

XRD analysis of the phyllosilicate content of the shale gouges show a general similarity to the undeformed Ora shale, but there are subtle differences. The shale gouges of the Tzefahot Fault are lacking in the mixed layer material that is present in the shale protolith (Fig. 3.93). This may be due to the collapse of this crystal structure due to increases in effective normal stress during deformation. There is no change laterally across the fault zone in the clay mineral composition of the shale gouges at the outcrop of the Tzefahot Fault.

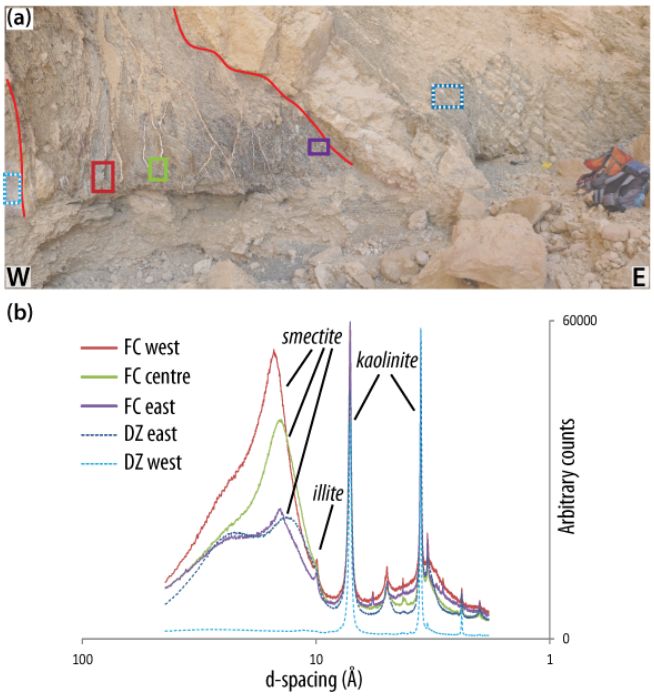

Figure 3.94: *Clay mineral evolution in Yehoshafat Fault core: **(a)** fault section showing location of samples; **(b)** combined XRD diffractograms (air-dried only) for the fault section: the shale gouge from the eastern part of the fault core, close to the carbonate hanging wall, is very similar in composition to the shale of the hanging wall Grofit Formation. Moving westwards towards the sandstone footwall, the intensity of the smectite peak increases, suggesting the precipitation of authigenic smectite in this part of the fault core. There is no smectite in the sandstone footwall, ruling this out as the source of smectite.*

At the Yehoshafat Fault, however, which is the only structure we have observed to have a fault core composed entirely of shale gouge, there is a lateral change in clay mineralogy across the fault section (east to west, perpendicular to the orientation of the N-S striking fault). In this case, the shale gouge in the eastern part of the fault core is similar in composition to both the Ora shale and the shale beds forming part of the base of the Grofit formation (Fig. 2.4a), but moving westwards towards the principal slip zone, there is both an increase in the relative amount and in the crystal form of smectite (Fig. 3.94). This indicates the growth of authigenic smectite within the fault core, likely due to an increase in strain close to the fault plane, but in contrast to other faults where this has been observed, there has neither been significant cataclasis nor are aluminosilicate minerals present in the

wall rocks at this location.

Folding within the shale gouges suggests deformation by aseismic creep during at least part of the Yehoshafat and Tzefahot fault histories, which is in contrast to the evidence of seismogenic behaviour also observed in association with the Tzefahot Fault. In the case of the Yehoshafat Fault, this can be easily explained by entrained shale gouge being the only fault core material, and we infer that shale was incorporated into the fault relatively early in its history. In this scenario, slip is concentrated on the low frictional strength of smectite layers within the shale. The coefficient of friction within the fault remains low and sliding is in the stable regime. Cataclastic deformation does not take place because strain is accommodated by distributed shear in relatively frictionally weak clay minerals within the shale.

In the case of the Tzefahot Fault, however, the fault core is heterogeneous (cataclastic and shale gouges are both present) and there is evidence of seismogenic behaviour (pulverisation and clay injectite), suggesting fault zone evolution was complex and that deformation style may have varied temporally. Evidence indicates that the pulverisation episode postdates the majority of shear deformation (Section 3.3.2.2), and though we may expect unstable, seismogenic slip to be unlikely in velocity-strengthening, frictionally weak material, recent studies by Faulkner et al. (2011) and Bullock et al. (2015) have recognised the importance of slip velocity on the role of clay minerals in seismogenic faulting. There is no evidence of mechanical mixing between the cataclastic and shale gouges, supporting the idea that these two foliated, frictionally-weak materials simply slid past each other. The possible effects of this on the evolution of faults in this study is discussed further in Section 3.4.4.

3.4.2 Model for fault zone development: revisited

Microstructural observations and mineralogical analysis of the clay minerals present within the studied fault zones reveal that fine-grained gouges are formed by a combination of cataclasis and authigenic precipitation of smectite. The initial model for fault zone development (Fig. 2.64) can thus be developed further to include inferred relative timing of authigenesis and incorporation of sedimentary cover wall rocks (Fig. 3.95). In this model, initial cataclasis (stage 1) is necessary to disaggregate grains of the crystalline wall rocks, both increasing the surface area of grains and permeability, allowing for possible fluid flow within and/or across the narrow fault core. It is expected that cataclasis continues as the principal deformation mechanism into stage 2, forming the fine-grained mechanical gouge observed within the faults, since the precipitation of frictionally weak smectite may be expected to retard cataclasis at the microscale in the same way that the incorporation of shale gouges are expected to at the mesoscale (Section 2.7.1.1).

In stage 3, precipitation of authigenic smectite occurs and continued shearing leads to the development of a foliation within the fault gouge; cataclasis continues to some degree, particularly during the early stages of smectite precipitation. In basement-cover faults, very little sedimentary material (both carbonate and clastic in origin) is observed within the fault gouges at the microscale, and from this we infer that the cover rocks were incorporated into the fault zones relatively late in fault history (stage 4). The presence of relatively large clasts (>5 mm, up to 1 m) of cover material within the Tzefahot and Shelomo fault sections (Sections 2.6.2.1 to 2.6.2.2) suggests some

degree of brittle deformation involving the cover rocks has occurred, but that comminution was not as intense as in the basement material. This supports the hypothesis that cover rocks were incorporated relatively late in fault history.

The effect of incorporation of shale gouges into the fault zones follows the scheme described in Section 2.7.1.1. In the case of the Tzefahot Fault, which is inferred to have reached stage 4 (Fig. 3.95) prior to the incorporation of shale gouge, the consequence of this is to produce a wide (up to 5 m at the studied section) zone of foliated, frictionally weak material within the fault core. There is no microstructural or mineralogical evidence for any mechanical mixing between the cataclastic and shale gouges. This further supports the model presented suggesting late incorporation of shale gouges into faults, since otherwise we would expect to see some evidence of mixing as the result continued shearing. The current hypothesis for the origin of gouges, presented in Fig. 3.95, is that shale gouges are derived from the Ora Shale, whilst cataclastic gouges are derived from largely basement wall rocks. We will further test this hypothesis by carrying out a detailed elemental analysis of protolith and fault rocks in Chapter 4.

3.4.3 Source of smectite

Many authors have described smectitic fault gouges in a variety of locations and structural settings, for example the continental transform San Andreas Fault (e.g. Marone, 1998; Holdsworth et al., 2011; Moore and Lockner, 2013; Lockner et al., 2011; Schleicher et al., 2012), low angle normal faults in the western USA (Haines and van der Pluijm, 2012), the Alpine Fault Zone, New Zealand (Warr and Cox, 2001) and the Gokasho-Arashima Tectonic Line, Japan (Sone et al., 2012). A common feature of these fault zones is that the gouges are generally derived from relatively Mg-rich rocks (e.g. serpentinite and other mafic lithologies) which are lacking in the southern Dead Sea Fault region; wall rocks are either sedimentary or felsic igneous/metamorphic and the only minerals with any appreciable Mg-content are biotite and dolomite. Our results contrast with previous works that have attributed illite +/- smectite gouges as being typical in association with quartzo-feldspathic wall rocks (e.g. Surace et al., 2011; Haines and van der Pluijm, 2012). We observe very little illite in any of our samples. Since authigenic, Mg-rich smectite is present across the range of fault zones in the area of study (for example, in basement-clastic as well as clastic-carbonate faults) we must consider either separate mechanisms of formation, since there is no consistency of likely Mg-source rocks across the fault sections, or that there is more complex linkage of faults and involvement of other lithologies and fluid flow at depth. Given the relative scarcity of dolomite in carbonate wall rocks (Fig. 2.4a, Section 3.3.3), we propose that the principal source of Mg is biotite in the basement rocks and that fault linkage and/or fluid flow along faults is responsible for the precipitation of authigenic smectite where there are no basement rocks at the surface section (the Yehoshafat Fault).

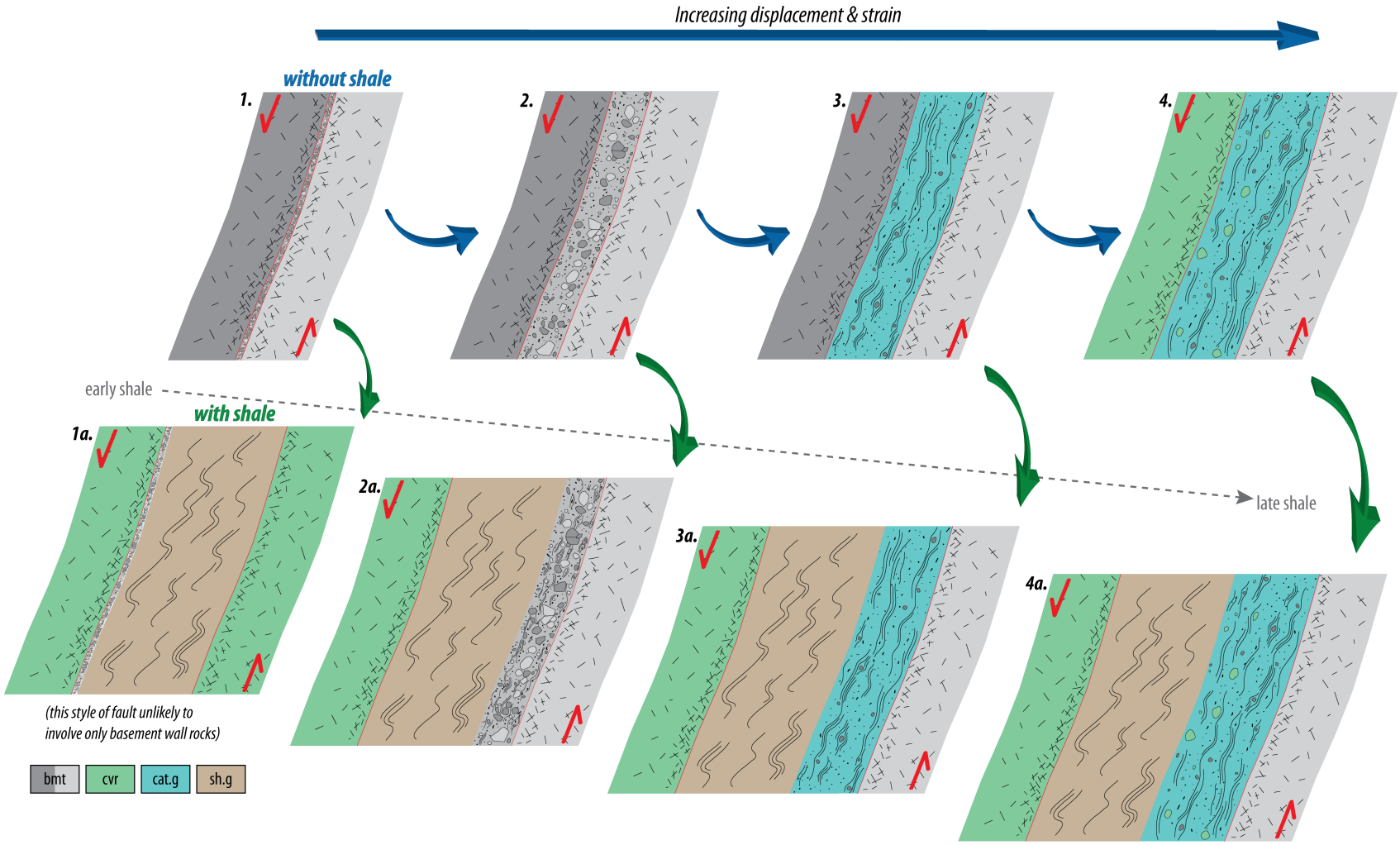

Figure 3.95: *Revised schematic model of fault zone development, showing timing of cover rock involvement relative to gouge formation: in stages 1 and 2 cataclasis through brittle fracturing and frictional sliding is the principal deformation mechanism; in stage 3, as strain and displacement increase, and with increased permeability allowing the ingress of fluids into the fault zone, precipitation of authigenic smectite occurs; in stage 4, as the fault propagates to shallower depths to cut through sedimentary cover rocks, brittle fracturing leads incorporation of these rocks into the fault zone. However, their relatively late stage involvement and reduced intensity of cataclasis due to the presence of smectite leads to lower levels of comminution of cover material taking place. The effect of incorporation of shale gouges (stages 1a-4a) is as described in Fig. 2.64 (bmt: basement rocks; cvr: cover rocks; cat.g: cataclastic gouge; sh.g: shale gouge).*

A possible reaction pathway for the formation of smectite may be via initial retrograde alteration of biotite to chlorite (observed in the Roded Quartz Diorite and Elat Granite, Sections 3.3.1.2 and 3.3.1.3), and subsequent chlorite to smectite alteration (as described by Nieto et al., 1994). However, this process would need to be complete since smectite is the only clay mineral found in many parts of the fault cores and it is difficult to anticipate that there would be no trace of chlorite remaining were this the case. It is also hard to account for the volume of smectite-rich gouges found via the alteration of biotite alone, which although relatively abundant in some lithologies (most notably the Taba Gneiss and Roded Quartz Diorite, Sections 3.3.1.1 and 3.3.1.3), is relatively rare in others (such as the Amram Rhyolite and Granite Porphyry, Sections 3.3.1.4 and 3.3.1.5), and smectite is still the predominant clay mineral at faults where there is little biotite in the wall rocks (such as the Nizoz Fault, where basement mineralogy is primarily K-fsp and quartz). Other studies have described the direct transformation of biotite to other clay minerals during weathering (Banfield and Eggleton, 1988), negating the need for initial in situ alteration to chlorite, but the products in these cases were vermiculite and eventually kaolinite, not smectite.

Another possible route for the formation of smectite, described by several authors in the context of weathering rather than fault zones, is via retrograde alteration of feldspars (plagioclase and K-feldspar) to smectite (e.g. Wilson, 1971; Banfield and Eggleton, 1990). Wilson (1971) described the weathering of both K- and plagioclase feldspars to a low-Fe montmorillonite smectite, whilst Banfield and Eggleton (1990) recorded alteration of plagioclase to a Ca-Fe-K smectite and K-feldspar to an Fe-rich smectite, which is in contrast to our observations of low-Fe/high-Mg authigenic smectite. Also in contrast to the results obtained by Banfield and Eggleton (1990) we observed no other authigenic products (such as kaolinite) in the cataclastic gouges.

However, alteration by any mechanism does not account for the well-formed smectite that is seen consistently across the authigenic gouges, and it is much more likely that smectite is a neoformed phase. Evans and Chester (1995) invoke the following hydrolysis reactions (as described in Garrels, 1984; Faure, 1998; Noh and Boles, 1993):

$$\underbrace{SiO_2}_{\text{quartz}} + H_2O \leftrightarrow \underbrace{H_4SiO_4}_{\text{dissolved silica}} \tag{3.1}$$

$$\underbrace{2NaAlSi_3O_8}_{\text{albite}} + 9H_2O + 2H+ \leftrightarrow \underbrace{Al_4Si_4O_{10}(OH)_8}_{\text{kaolinite}} + 2Na^+ + \underbrace{8H_4SiO_4}_{\text{dissolved silica}} \tag{3.2}$$

$$\begin{aligned} &\underbrace{7Al_2Si_2O_5(OH)_4}_{\text{kaolinite}} + 8SiO_2 + Fe^{2+} + Mg^{2+} \\ &\leftrightarrow 6[\underbrace{(Al_4(Fe - Mg^{2+})_{0.167})(Si_{3.67}, Al_{0.33})O_{10}(OH)_2}_{\text{Fe-Mg montmorillonite}}] + 7H_2O + 2H^+ \end{aligned} \tag{3.3}$$

and it is possible that a similar reaction pathway is seen here, but where the principal feldspar contribution is from K-fsp rather than albite. It is not known, however, if this reaction produces the well-formed smectite as is found in these faults. Wilson (1971) described the resistance to weathering of plagioclase and K-fsp to be less than that of micas (biotite and muscovite), which

were in turn less resistant that quartz, so it is possible that initial breakdown of feldspars took place within the fault cores and transformation to smectite (rather than illite or kaolinite) took over once Mg was released from the subsequent breakdown of biotite.

It has not been possible thus far to determine the source of fluids necessary for alteration reactions to take place, but one hypothesis is that they were marine fluids that percolated to relatively shallow depths from the overlying Gulf of Elat-Aqaba, which may fit with the reactions described in Eqs. (3.1) to (3.3). Magnesium is an abundant element in sea water and present day concentration is an average of 1540 mg/L (Friedman, 1968, samples taken from northern, central and southern locations in the Gulf of Elat-Aqaba), which may explain the precipitation of Mg-rich smectite rather than a more common Fe-rich phase. Alternatively, fluids may be sourced from within the crust or from much deeper within the mantle, though there are not known to be any mafic source-rocks in the area that may yield Mg-rich fluids. The nature of fluid-rock interactions within the fault zones will be addressed in Chapter 4.

3.4.4 Implications for fault strength and behaviour

The development of authigenic smectite has significant implications for fault strength. Whilst we might expect mechanical gouge to have a similar frictional strength to wall rock lithologies ($\mu \approx 0.6$-0.85, Byerlee, 1978), smectite can have frictional strengths as low as $\mu = 0.15$ when wet (e.g. Moore and Lockner, 2007; Saffer and Marone, 2003). Even relatively low volumes of weak material (10 wt%) may significantly lower the frictional strength if it is present in continuous layers (Rutter et al., 2013; Bullock et al., 2015). The presence of intermixed layers of both relatively weak (authigenic smectite-bearing gouge) and potentially strong (cataclastic gouge, $\mu \approx 0.6$-0.85) material raises uncertainties regarding the assessment of relative fault strength. Whilst it is possible that in the shale gouge layer the overall friction behaviour is controlled by weak layers, it is less easy to determine whether the properties of the cataclastic or authigenic gouge will control the overall behaviour of this intermixed layer that has a much weaker fabric. More likely, they will interact and fault core properties will continue to evolve over time. Extrusion of smectite from fault cores into adjacent damage zones suggests pore fluid pressure was high during at least some stage of fault history, although it is not possible to say whether this was for a sustained period of time or short-lived. High pore fluid pressure could also serve to further reduce friction within fault zones and likely contributed to the overall frictional weakness of these structures.

The presence of microfolds in both the authigenic smectite and shale gouges are consistent with creep in a weak material. In the damage zone, there is evidence of possible seismogenic behaviour, such as pulverisation style fracturing and mechanical injection of gouge material along brittle fractures, consistent with a spatially and temporally heterogeneous fault zone. However, although the presence of folds suggest aseismic creep during at least a period of fault history, the presence of the frictionally weak, hydrous smectite itself does not preclude the possibility of seismogenic slip. Although hydrous phyllosilicate minerals such as smectite are recognised as inherently frictionally weak, particularly when saturated (e.g. Saffer and Marone, 2003; Ikari et al., 2007; Moore and Lockner, 2007; Tembe et al., 2010) and thus velocity-strengthening, recent experiments by Faulkner et al. (2011) and Bullock et al. (2015) have found that they do not always contribute to the inhibition of earthquake propagation in the shallow, upper crust. These authors have found that although

at relatively low slip velocities frictionally weak clays may behave in a velocity- strengthening manner and inhibit earthquake propagation, but where slip velocities are higher, they may be velocity-weakening and allow for seismogenic rupture propagation. The localisation of slip onto discrete surfaces, rather than distributed throughout a wide zone, appears to be necessary for the attainment of high slip velocities (Bullock et al., 2015). We suggest that whilst it is possible that slip localisation may have occurred in the heterogeneous cataclastic gouges, it is unlikely to have done so in the more homogeneous shale gouges where the pre-existing foliation provides frequent, distributed surfaces along which frictional sliding could take place. As such, whilst it is possible that a seismogenic rupture may have propagated through the frictionally weak, smectite-rich cataclastic gouges, we find it unlikely that such behaviour could have occurred once shale gouges were incorporated into a fault zone.

3.5 Conclusions

Detailed microstructural and mineralogical analysis of a range of fault rocks from the southern Dead Sea Fault System has revealed that there is a great deal of heterogeneity of deformation mechanisms within the fault zones. Cataclastic deformation has occurred to varying degrees. At the Yehoshafat Fault this is confined the clastic footwall damage zone, whilst at the Tzefahot Fault there is a 2 m wide zone of cataclastic fault gouge. Also present is evidence of 'ductile' deformation and growth of authigenic clay minerals, and fault core materials can be broadly subdivided into two parts; cataclastic gouges, which have formed by a combination of mechanical and chemical processes, and shale gouges, which were incorporated into the fault zones by entrainment and deformed predominantly by ductile processes. There is evidence that fault slip occurred both seismogenically (Sections 3.3.2.1 and 3.3.2.2) and as aseismic creep (Section 3.3.5.1), suggesting an evolution of fault properties over time.

Authigenesis does not appear to be controlled by fault length or displacement and occurs at all but one studied fault sections. The product in all cases is Mg-smectite. XRD diffractograms show the smectite to be well-formed, suggesting growth in a relatively free space and microstructural analysis shows these grains interacting in a variety of ways with surrounding mechanical gouge and grains: as grain coatings around large clasts (Fig. 3.18c,d), interstitially between grains (Figs. 3.70 and 3.75c), mixed with very fine-grained mechanical gouge (Fig. 3.70a,b) and as continuous, foliated layers (Figs. 3.63 and 3.70d). When wet, smectite has been reported to have extremely low friction coefficients and due to the volume present in the fault gouges, is likely to have a profound weakening effect on the faults. However, the presence of injected smectite in the damage zones of the Shelomo and Tzefahot faults suggest there was not a linear evolution from strong (before precipitation of smectite) to weak (after precipitation of smectite) faults, since these features are themselves indicative of seismogenic behaviour.

There are no outcrops of mafic rocks in the area, which have been shown in previous work to be the source of smectitic fault gouges, but we conclude that the quartzofeldspathic crystalline basement is the most likely origin of the smectite. Initial breakdown of feldspars served to release Al, Si and small amounts of Ca, to which Mg was added following subsequent breakdown of biotite. All authigenic mineral growth occurred after initial and significant cataclastic deformation, with the

exception of that seen in the shale gouges of the Yehoshafat Fault. Faulting was most likely active at relatively low temperatures (~100 °C) and therefore also relatively shallow depths (max. 3 km), due to the presence of smectite.

4 Geochemical constraints on the origin of fault gouges

4.1 Introduction

Although fault zone architecture, microstructure and mineralogy have been characterised in Chapters 2 and 3, further information is needed in order to better constrain the origin of fault core gouges, as well as the extent of mechanical and geochemical mixing within the fault zones. These questions have been addressed by analysing the elemental composition of a range of rocks; of relatively undeformed protoliths from the area, and representative sample of damage zone and fault core rocks from each fault section. The aims of this chapter are to:

- quantify the elemental composition of a variety of (relatively) undeformed wall rocks and intensely deformed fault rocks;
- determine the protolith/s for each fault zone by assessing the similarity in elemental composition of fault core material to adjacent wall rocks. This will include a comparison to the Ora shale (Fig. 2.4a), which is not present as wall rocks directly adjacent to any fault sections studied, in order to test the hypothesis that two types of fault core gouges are present within these fault zones: 'cataclastic' and 'shale' gouges, as proposed in Section 3.4;
- place further constraints on the source of the Mg needed to form authigenic smectite, specifically whether it is exotic as suggested in Section 3.4.3.

94 samples in total, comprising specimens collected across eight fault exposures (of six faults) as well as representative samples of fault rock protoliths, have been analysed. Ten major element oxides and loss on ignition (LOI) have been analysed by fusion inductively coupled plasma (FUS-ICP), and 35 trace elements and ten rare earth elements (REE) by fusion inductively coupled plasma mass spectrometry (FUS-ICP/MS) by Actlabs Ltd (Ancaster, Ontario, Canada; method 4Litho. Detection limits for each major element oxide and trace element, REE are provided along with the raw data in Appendix 3A). REE have been considered separately from the other trace elements as they show distinct concentration trends across the fault zones (see Sections 4.4.1.2, 4.4.2.2 and 4.4.3.2).

4.2 Information on methods, approaches and assumptions

We have presented elemental concentrations as both raw data (for fault rock protoliths, Section 4.3) and normalised to assumed protoliths (wall rocks at the studied sections, Section 2.6.2). Normalised data are presented in order to mitigate against the "constant sum effect" (Rollinson, 1993, p.37),

which arises from the fact that compositional data are expressed as percentages, 100% is the constant sum, and so where one component increases, one or all of the others must decrease relatively. Using this method of normalisation, a value of 1 for any given element represents the same concentration in the compared samples, and values >1 or <1 represent enrichment or depletion, respectively, in the fault rock sample relative to the protolith. The further a value deviates from 1, the greater the enrichment or depletion of a given sample; we have quantified a "significant" enrichment/depletion as a difference of approximately a factor of 10 in the fault rocks samples relative to a protolith (values of $\sim$10 for enrichments and $\sim$0.1 for depletions).

Trace element and rare earth element (REE) data have been plotted as multi-element spider diagrams (or spidergrams) and have been normalised relative to protolith lithologies in the same way as the major element oxides (in cases where an element or oxide is not present in the protolith or fault rock sample, it has been omitted from the resulting plots). Because all of the studied fault zone sections have contrasting wall rock lithologies on either side of the fault, there are (at least) two potential protoliths for each fault zone and fault rock data have been normalised to both. For trace element spidergrams, the elements considered to be more mobile (large ion lithophile elements, LILE; Ba, Sr, Rb, Cs, Pb, Albarède, 2003) have been plotted to the left, followed by transition elements (Sc, V, Cr, Ni) and generally immobile elements (high field strength elements, HFSE; Ti, Zr, Y, Nb, Hf, Ta, U and Th), to the right on all plots. In the case of REEs, light REEs (LREE; La, Ce, Pr, Nd, Sm) are plotted to the left whilst heavy REEs (HREE; Eu, Gd, Tb, Dy, Ho, Er, Tm, Yb, Lu) are plotted to the right. LILE are the most mobile in fluid-rock interactions, whilst HFSE, transition elements and REEs are considered relatively immobile (Cann, 1970; Floyd and Winchester, 1975). The distribution of both types of elements across a fault zone can aid in assessing the relative degree of mixing that has taken place (Section 4.4.5).

In addition to presenting the element concentration data for individual samples, we have used the mean concentrations of cataclastic and shale gouges for each fault zone in order to assess the compatibility of gouges with basement and cover rock protoliths (Section 4.4.4) through statistical analysis. We have used a method similar to the isocon method used by Gresens (1967) and Grant (1986) to assess the relative mobility of elements in a geochemical system. However, we have not been able to quantify element mobility in this way since for each fault zone there are at least two protolith lithologies and we cannot discount the possibility that changes (or lack thereof) in element concentrations may be a result of mixing of two or more lithologies, rather than true element mobility/immobility. The equations used for this analysis are provided in Section 4.4.4.

The purpose of this analysis is to determine a most-likely protolith/s for each fault zone and provide a quantitative aspect to the hypothesis presented in Chapter 3 that cataclastic gouges are largely derived from wall rocks on one side of the fault (at the surface sections), and that these are basement rocks, with the exception of the R12 Fault. Mean gouge compositions (of cataclastic and shale gouges at each fault section) have been used in order to mitigate against the localised variations in fault core composition. The cores of faults studied here are heterogeneous, and samples were collected from zones of contrasting appearance or composition specifically in order to describe fault zone microstructure and composition as comprehensively as possible. In elemental analysis, however, it is necessary to use mean compositions so that localised concentrations of a particular mineral or rock type (by way of large clasts within the fault core, for example) do not bias the results. Comparisons of elemental concentrations between the fault

gouges and assumed protoliths will also allow for a qualitative insight into fluid-rock ratios during gouge formation, since gouges that are very similar in elemental concentration to their protolith are not normally indicative of open-system behaviour with high fluid fluxes.

In order to constrain the possible source of the Mg necessary for the precipitation of smectite, we focussed particularly on concentrations of this element in the protolith rocks, and how this varies across the fault core rocks. If the source of Mg is from overlying seawater percolating down into the fault zones or from mantle fluids at depth, we will expect to see significant enrichment of the fault core materials with respect to the protolith rocks, especially relative to the basement wall rocks since sedimentary cover rocks (with the exception of dolomite), composed predominantly of calcite and quartz and are not potential sources of Mg.

4.3 Fault rock protoliths

Fault rock protoliths have been selected based on field observations described in Section 2.6.2 and represent not only a range in age (Precambrian - Upper Cretaceous) but also of the wall rock lithologies for the studied fault exposures. It should be noted that they do not represent all the *possible* wall rock lithologies that may be involved within an individual fault zone since time and access constraints did not allow for collection of all possible protoliths in the area, but they do represent all the observed wall rocks from the eight localities studied. Representative samples of the major units of crystalline basement and cover rocks have been chosen (Fig. 2.4b); 16 protolith rocks in total have been analysed, comprising eight basement units (Elat Granite, Taba Gneiss, Elat Schist, a pegmatite vein, Ramat Yotam Volcanics, Roded Quartz Diorite, Amram Rhyolite and Amram Granite Porphyry) and eight cover units (Hazera limestone, Grofit limestone, Grofit cherty limestone, Avrona sandstone, Amir sandstone, Samar sandstone, Shehoret sandstone and Ora shale).

4.3.1 Crystalline basement rocks

A summary of the raw concentration data (wt%) for major element oxides of the crystalline basement rocks is presented in Fig. 4.1a, highlighting the overall similarities of this group of aluminosilicate rocks. Most similar are the Taba Gneiss, Roded Quartz Diorite and Elat Schist, with the main constituents of SiO_2 and Al_2O_3 at similar levels (60-68 and 15-18 wt%, respectively), and similar levels of Fe_2O_3, CaO and Na_2O (4-6, 2-6 and 3-5 wt%, respectively). All of the basement protoliths are relatively low in Fe_2O_3 and MgO, but the Elat Granite, pegmatite and the Amram Rhyolite are especially so (<1.5 and <0.5 wt%, respectively). LOI is predictably low for all samples (<3 wt%, Fig. 4.1a) since we do not expect to find significant amounts of volatile material (e.g. water or CO_2) within these little altered crystalline rocks.

Trace element concentrations reveal that the basement rocks of the Elat Block is geochemically distinct from those of the Roded and Amram blocks (Fig. 4.1c&d), and that there is consistency between the rocks of the Elat Block (Fig. 4.1c), which (with the exception of the pegmatite) contain Ba in the range of 625 - 955 ppm, Sr 275 - 450 ppm and Cr 40 - 90 ppm. The Taba Gneiss and Elat

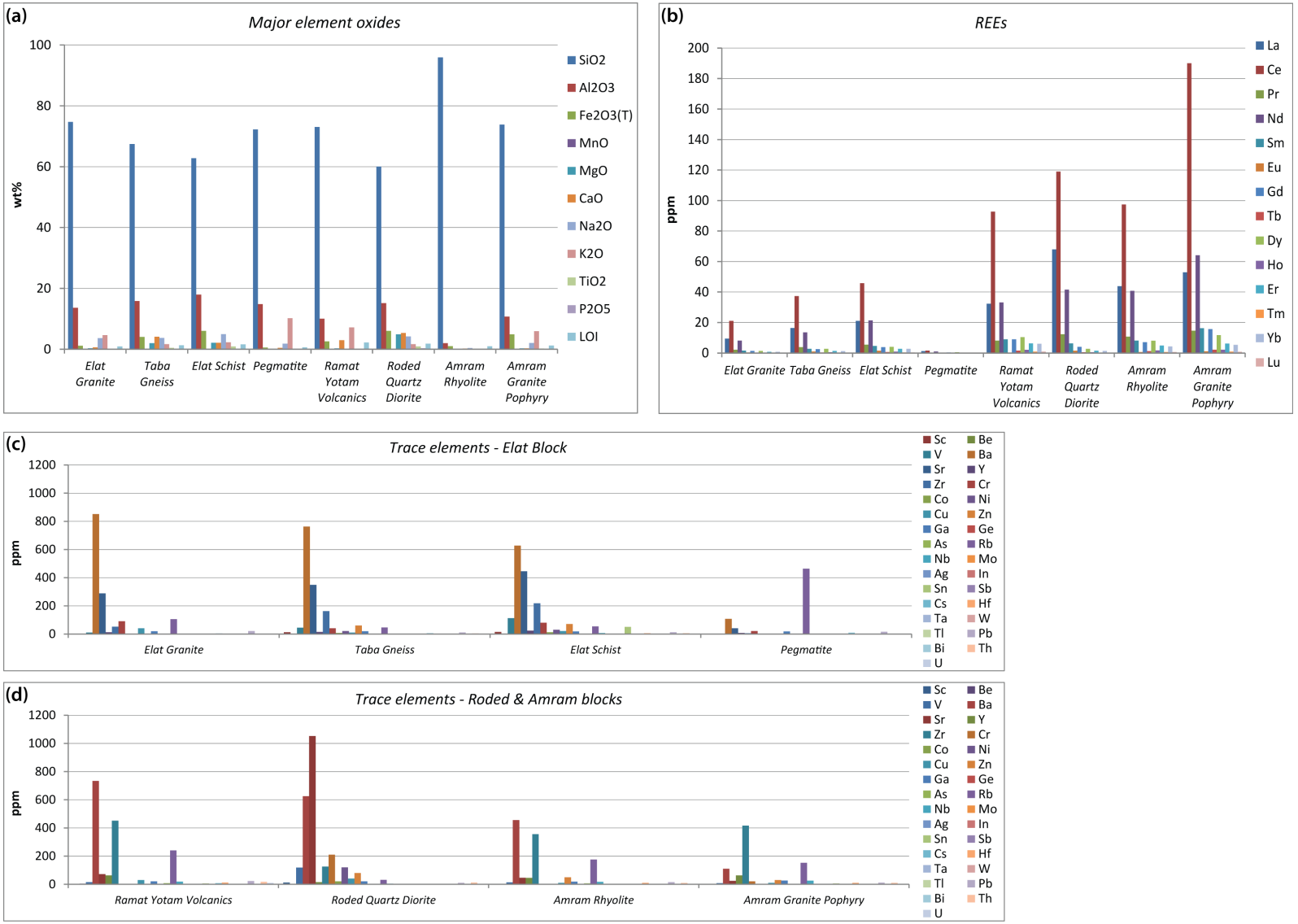

Figure 4.1: *Graphs showing **(a)** major element oxide concentrations (wt%); **(b)** rare earth element concentrations (ppm); **(c)** trace element concentrations of the Elat Block (ppm) and **(d)** trace element concentrations of the Roded & Amram blocks (ppm).*

Schist also both contain a significant proportion of Zr (150 - 225 ppm). The pegmatite vein sampled (at the Tzefahot Fault section) differs from the other rocks of this block and is relatively low in all trace elements (<50 ppm and frequently <10) except Rb (464 ppm) and Ba (108 ppm), but this may be expected as the pegmatite is likely different in age (younger, since it intrudes an outcrop of the Taba Gneiss) and source to the Elat Granite, Taba Gneiss and Elat Schist. The pegmatite is rich in Rb (464 ppm) with a smaller concentration of Ba (108 ppm). The elevated Rb in the pegmatite, and relative enrichment of Sr in the rest of the block, may reflect the inferred younger age of the pegmatite, as Sr is a daughter isotope of Rb (Rollinson, 1993).

The rocks of the Roded and Amram blocks show a greater range in trace elements than those of the Elat block (Fig. 4.1d), which likely reflects the more varied source and ages of these rocks. The extrusive Ramat Yotam Volcanics and Amram Rhyolite contain the highest concentrations of the same elements (Fig. 4.1d), with the greatest concentrations of Ba (734 and 455 ppm, respectively), Zr (451 and 355 ppm) and Rb (240 and 175 ppm), whilst the Roded Quartz Diorite contains a relatively very high concentration of Sr (1052 ppm) and significant amount of Ba (625 ppm). All other trace element concentrations in the quartz diorite are $\leqslant$210 ppm (Fig. 4.1d). High concentrations of Sr may be the result of breakdown of Rb in feldspar minerals. The Amram Granite Porphyry contains a relatively high concentration of Zr (416 ppm) but is low in other trace elements, although concentrations of Rb (152 ppm) and Ba (110 ppm) are elevated relative to other elements in this sample.

Rare earth elements (REEs) show a similar trend in concentrations (Fig. 4.1b), once again with a clear distinction between the rocks of the Elat Block compared to the Roded and Amram blocks; the pegmatite is also distinct, with very low concentrations of all REEs. All rocks (except the pegmatite) show the greatest concentrations of Ce, but in the Elat block these are between 20 and 50 ppm and in the Roded and Amram blocks the levels are much higher, between 90 and 200 ppm. La and Nd are also elevated, and again concentrations are 1.5 - 4 x higher in the Roded and Amram blocks than in the Elat Block. Both trace element and REE data indicate that the Elat Granite, Taba Gneiss and Elat Schist have a common source, and whilst the trace element concentrations of the Roded and Amram block rocks are more varied, the REE data indicate some commonality of source.

4.3.2 Cover rocks

The cover protolith rocks reveal similarly predictable major element concentrations to the basement rocks (Fig. 4.2a). The Hazera and Grofit formation limestones contain <4 wt% of any oxide other than CaO (and 45 wt% LOI, corresponding to the loss of CO_2) and the Cretaceous Avrona and Amir formation sandstones contain >90 wt% SiO_2 (Fig. 4.2a), indicating they are composed almost entirely of quartz, with very little in the way of accessory minerals (e.g. feldspars or clay). The Samar formation sandstone (also Cretaceous in age) contains >10 wt% Al_2O_3, which, along with an elevated LOI (4.5wt%, compared to <1 wt%), suggests it contains slightly more clay material than the Avrona and Amir sandstones (due to the loss of bonded water during combustion by dehydroxylation from within clay minerals). The Cambrian Shehoret sandstone is somewhat different in composition to the Cretaceous sandstones, containing greater amounts of CaO, Na_2O and K_2O (3 - 5 wt%, Fig. 4.2a), which likely indicate the presence of feldspars, minor calcite and/or clay minerals. The significant oxides of the Cretaceous Ora formation shale are SiO_2 (54.5 wt%),

Al_2O_3 (23 wt%), with minor amounts of Fe_2O_3 (4.5 wt%), K_2O (2wt%) and MgO (1.5 wt%), which correlate with the clay mineral composition of shales. The LOI is 12.5 wt%, though it is not possible to determine from this measurement alone how much of this loss is due to dehydroxylation of clay minerals and how much may relate to loss of organic material.

Trace element analysis reveals relatively low concentrations of most elements (Fig. 4.2c&d), with the exception of Sr in all of the limestones (ranging between 185 and 880 ppm) and Nb (340 ppm) in the Hazera formation (Fig. 4.2c). The clastic rocks are more varied (Fig. 4.2d) with the Cretaceous Avrona and Amir sandstones being similar (highest concentrations of Cr, Zr and Cu), but the Samar sandstone contains 1005 ppm Zr and also higher concentrations of Ba (102 ppm) and Sr (94 ppm), suggesting it is composed of material from a different source location. The Cambrian Shehoret sandstone contains much higher levels of Ba (675 ppm) and Rb (117 ppm), which are not present in any significant amounts in the other sandstones. An enrichment of Ba and Sr in the Shehoret sandstone (relative to the younger units) may reflect the fact this formation directly overlies the crystalline basement (Fig. 2.4a) and was also likely sourced from these rocks. The Ora shale contains a number of trace elements at low levels (20 - 200 ppm, Fig. 4.2d), including (in descending order) Zr, V, Cr, Ba, Rb, Zn, Ni, Sc and Cu, which likely reflects both the varied mix of trace elements in the marine water in which the shale was deposited and high cation exchange adsorption rates of trace elements onto some clay minerals.

Concentrations of REEs show a similar distinction between the Samar sandstone and the Avrona and Amir sandstones (Fig. 4.2b), with the former having much higher concentrations of Ce (144 ppm), Nd (71 ppm) and La (54 ppm) than the latter two, where these elements are all found in concentrations $\leqslant$5 ppm. The Shehoret sandstone and Ora shale have very similar concentrations of REEs as the other clastic rocks, containing the highest amounts of Ce, La and Nd. The Hazera and Grofit limestones also show very low concentrations ($\leqslant$5 ppm) of all REEs (Fig. 4.2b).

4.3.3 Summary

The raw elemental data of the fault rock protoliths reveal that in the case of the basement rocks, they are all aluminosilicates in which SiO_2 and Al_2O_3 make up a combined total of >75 wt% in each. In addition, trace element and REE show there are two chemically distinct groups; rocks belonging to the Elat block, and those belonging to the Roded and Amram blocks. This suggests that although we have analysed both igneous and metamorphic, and intrusive and extrusive rocks, the two groups of rocks each have a common source. In the cover protoliths, the carbonates are revealed to be relatively pure with few accessory minerals, as are two of the Cretaceous sandstones. However, the Cambrian Shehoret Sandstone is composed of more varied major oxides, which we believe reflects the fact it both directly overlies the crystalline basement that was its source.

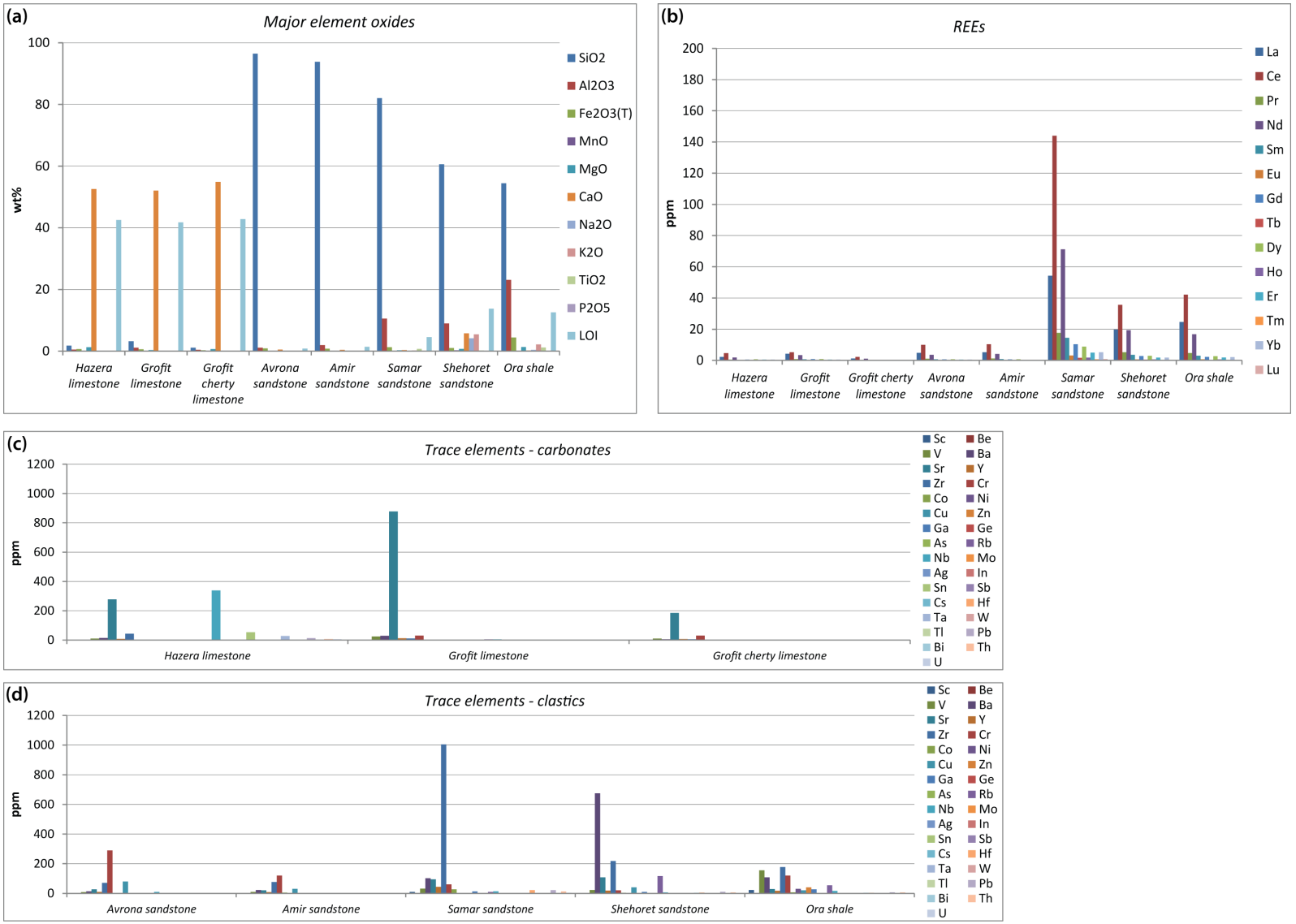

Figure 4.2: *Graphs showing* ***(a)*** *major element oxide concentrations (wt%);* ***(b)*** *rare earth element concentrations (ppm);* ***(c)*** *trace element concentrations of carbonate rocks (ppm) and* ***(d)*** *trace element concentrations of the clastic rocks (ppm).*

4.4 Fault zone whole-rock analysis

The fault zone sections studied here (as described in Section 2.6) comprise a range of protolith rocks, not only across the different faults but also at different exposures of the same fault (Shelomo Fault A & B, Roded Fault A & B). For each fault, samples have been collected from each different domain within the fault core, as well as from the damage zones on either side. As summarised in Fig. 2.18a, the faults can be divided into three groups according to wall rock lithologies: crystalline basement-carbonate cover; crystalline basement-clastic cover; carbonate cover-clastic cover (Table 4.1) and their geochemical properties will be discussed here within this framework.

Table 4.1: *Table summarising wall rock lithologies of the studied fault zones (Ca: Cambrian; Cr: Cretaceous).*

Fault	**Wall rock lithologies**		
	Basement - carbonate	*Basement - clastic*	*Carbonate - clastic*
Tzefahot	✓ (gneiss/pegmatite-limestone)		
Shelomo A	✓ (granite/volcanic-limestone)		
Shelomo B	✓ (granite-limestone)		
Roded A		✓ (diorite-Ca.sandstone)	
Roded B		✓ (diorite-Ca.sandstone)	
Nizoz		✓ (rhyolite-Cr.sandstone)	
Yehoshafat			✓ (limestone-Cr.sandstone)
R12			✓ (limestone-Cr.sandstone)

4.4.1 Basement - carbonate faults

Whole-rock analysis has been carried out on two basement-carbonate faults at three locations (Table 4.1); the Tzefahot Fault juxtaposes Cretaceous Hazera formation limestone against Precambrian Taba Gneiss of the Elat Block and a local pegmatite vein (Fig. 4.3a), whilst the Shelomo Fault juxtaposes Cretaceous Grofit formation limestone against Precambrian Elat Granite (Fig. 4.3b), and at Locality A a small outcrop of the overlying Ramat Yotam Volcanics is also present (Figs. 2.4b and 4.3b). Based on field and microstructural/mineralogical observations, described in Section 2.6.2 Section 3.3.5, respectively, we have classified the gouges within fault cores of the Tzefahot and Shelomo faults as 'cataclastic gouges' (samples F1-4, F1-6, F1-7, F2a-7, F2a-8 and F2b3 - 6R) and 'shale gouges' (samples F1-2 and F1-3). The position of the samples within the fault zones is shown in Fig. 4.3.

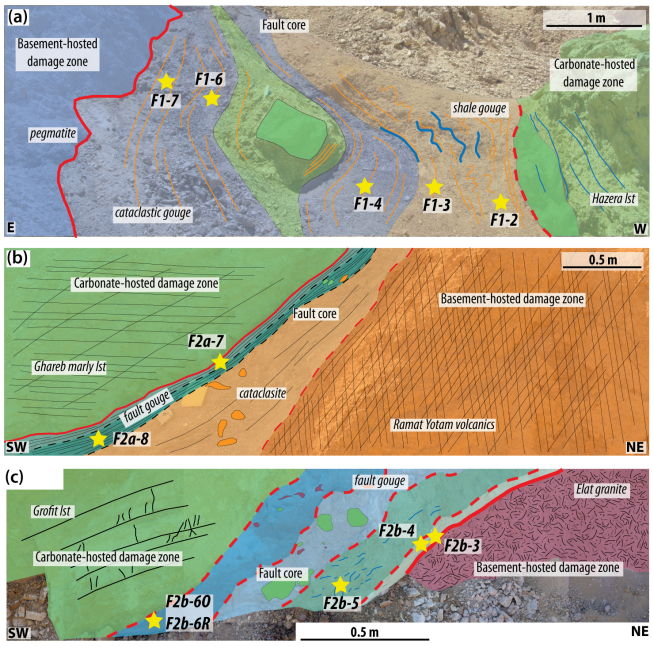

Figure 4.3: *Sketch section showing position of analysed samples in:* ***(a)*** *Tzefahot Fault;* ***(b)*** *Shelomo Fault, Locality A;* ***(c)*** *Shelomo Fault, Locality B.*

4.4.1.1 Major element oxides

Fig. 4.4 shows the major element data from the cataclastic gouges of the three outcrops normalised to each crystalline basement wall rock lithologies of the Tzefahot and Shelomo faults (Taba Gneiss, Elat Granite, Elat Schist, Ramat Yotam Volcanics and a pegmatite vein). The gouges of both faults show little enrichment or depletion of any major element oxides with respect to the gneiss (Fig. 4.4a) except for NaO, which may suggest alteration of feldspar during faulting. There is also a significant increase in LOI, which supports the interpretation of feldspar alteration to clay minerals. There is more variation in the same gouges relative to the granite (Fig. 4.4b); NaO is again depleted in the gouges, but there is enrichment of CaO, TiO_2, MgO and P_2O_5.

When normalised to the Ramat Yotam Volcanics found at the Shelomo Fault, Locality A outcrop, the cataclastic gouges of the Tzefahot and Shelomo faults are relatively consistent and there is only slightly less disparity between the between the gouges from that locality (F2a-7 and F2a-8) than to the samples from other outcrops (Fig. 4.4c). Three samples from Locality B (F2b-3, F2b-4, F2b-5) are enriched in Al_2O_3 and TiO_2 but the pattern in the remainder of oxides is similar to Locality A samples. In general there is slight enrichment of a number of oxides (MgO, TiO_2, MnO, Na_2O), with the gouges from the Shelomo Fault-B outcrop in particular being enriched in MgO and TiO_2, and slight depletion of SiO_2 and K_2O across all the samples, reflecting the higher initial K_2O content (wt%) of the volcanic rocks then the gneiss and pegmatite (Fig. 4.1a).

Of the basement wall rocks, the cataclastic gouges are the least similar to the pegmatite vein (Fig. 4.4d), showing relative enrichment of TiO_2, MgO, CaO and Fe_2O_3, and depletion of K_2O. This is unsurprising as the pegmatite is a very local feature to the outcrop studied and the raw major element oxide data (Fig. 4.1a) show it contains >97 wt% SiO_2, Al_2O_3 and K_2O, suggesting it is composed almost entirely of quartz and K-feldspar.

Relative to the Hazera limestone (Fig. 4.4e), the cataclastic gouges show enrichment in many of the major oxides (TiO_2, Al_2O_3, SiO_2, K_20, Na_2O, P_2O_5 and Fe_2O_3). Along with a depletion in CaO and LOI (both of which are high in carbonate rocks), the data show that the gouges are much more similar in major oxide composition to the basement wall rocks, particularly the Taba Gneiss, than to the carbonate cover rocks.

At the studied outcrop of the Tzefahot Fault (Section 2.6.2.2), as well as the cataclastic gouge there is also a second gouge that is very similar in appearance to the Cretaceous Ora shale in the area (Section 2.6.2.2). Since it does not appear that the shale gouge is cataclastic in nature (Section 3.4.1.3), we have also normalised the samples to the Ora Shale, the assumed protolith, and Fig. 4.5 shows that they are very similar in major element composition. There is enrichment of CaO, which can be explained by the presence of gypsum veins (Section 2.6.2.2) and inferred flow of Ca-rich fluids through these gouges, and of P_2O_5, but the other major element oxides are present at levels consistent with those measured in the protolith shale. The hypothesis that cataclasis is not the only mechanism resulting in clay-rich fault cores is therefore supported by major oxide geochemical data.

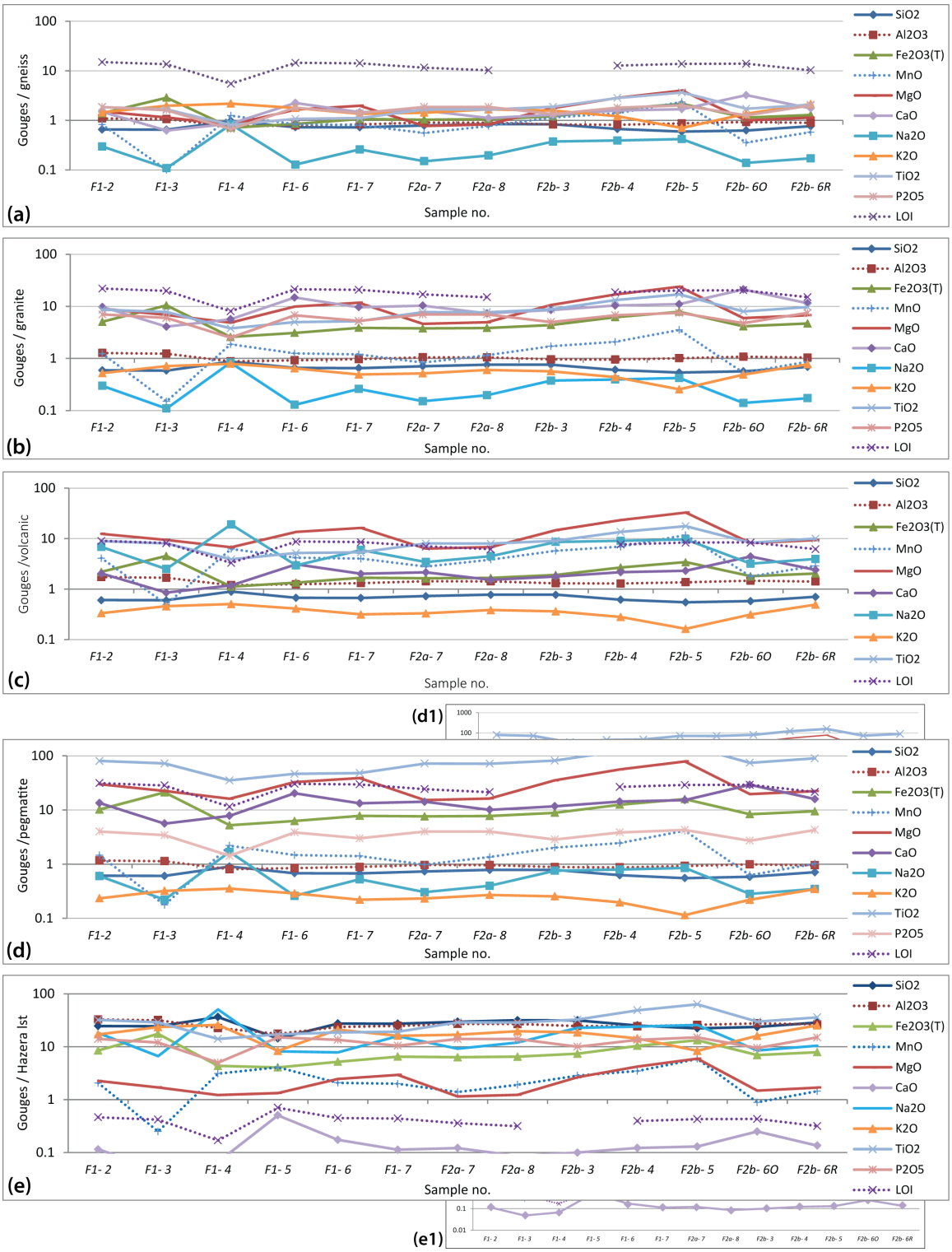

Figure 4.4: *Graphs showing major element oxide concentrations for fault gouges of Tzefahot Fault (F1) and Shelomo Fault (F2a & b) normalised to:* ***(a)*** *Taba Gneiss;* ***(b)*** *Elat Granite;* ***(c)*** *Ramat Yotam Volcanics;* ***(d)*** *pegmatite vein;* ***(e)*** *Hazera limestone. (Insets* ***(d1)*** *and* ***(e1)*** *show missing data due to main graphs being plotted at the same scale for visual comparison.)*

4.4.1.2 Trace elements & REEs

Across the five protoliths at the Tzefahot and Shelomo Fault exposures, we observe similar enrichment/ depletion trends in the gouge trace element and REE data as in the major oxide data; they are again the most similar to the Taba Gneiss (Fig. 4.6a). Notable spikes are depletion of Ba in some gouges and enrichment of Nb and Ta in one of the Shelomo Fault samples (F2b-3).

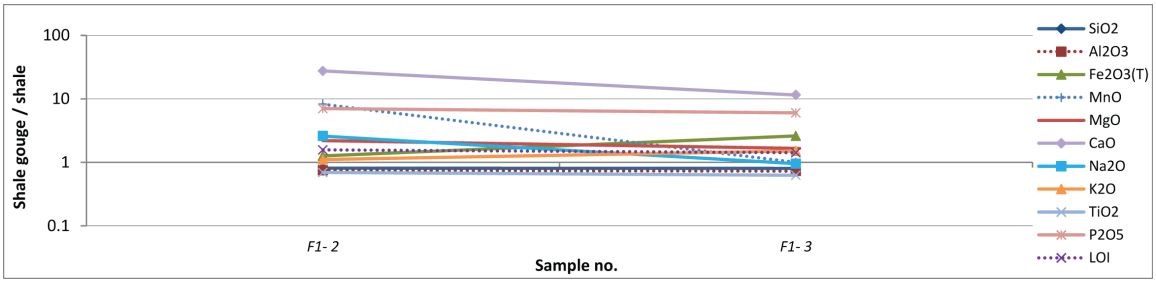

Figure 4.5: *Major element oxide data for Tzefahot Fault shale gouges normalised to the Ora shale.*

Ba is commonly found as a trace element in feldspars and biotite, so depletion of this element in gouge samples may represent alteration/break down of these minerals during faulting.

When normalised to the granitic and volcanic wall rocks, trace element concentrations of the gouge samples show a similar trend, but the deviation from 1 is more pronounced than when normalised to the gneiss (Fig. 4.6b&c). The main difference is in the enrichment in the gouges of Co, a trace element found in biotite, relative to granite and of V relative to both the granite and gneiss wall rocks.

When the gouges are normalised to the pegmatite vein, there is much more variation in the relative enrichment/depletion of many of the trace elements (Fig. 4.6d); there is significant enrichment of Zr and Th in all samples, and Ba, Nb and Sn in some of the gouge samples (Ba: F2a-8, F2b-5; Nb: F2b-3; Sn: F2a7). Rb and Tl are depleted relative to the pegmatite in all of the fault rock samples. The only elements for which there is a notable divergence in the trend of the relative gouge compositions are Ba (most samples are enriched, F1-2, F1-3 and F2b-6O contain approximately the same amount), Cs (mixture of enrichment, depletion and no difference across the gouges) and Ta (enrichment in F2b-3).

Fig. 4.6e shows the fault gouge samples normalised to the Hazera limestone. All samples follow the same trend, with all except Sr, Y, Hf, Pb, Th and U being either enriched or depleted. The raw trace element data show that the Hazera limestone is relatively rich in Sr and Nb, and the depletion of Nb in the gouge relative to the protolith indicates that it is either a highly mobile element that has left the system during faulting, or that the gouges are largely not derived from carbonate wall rocks. We believe the latter to be the more likely explanation due to the highly variable relationship (elements are not consistently enriched or depleted) between the gouge samples and the Hazera limestone. Whilst it is possible that fluids have entered the fault system, these data need to be considered in relation to the gneiss-normalised data (Fig. 4.6a), where the gouges are very similar in composition to this wall rock. Hence the simplest explanation is that the variation arises from the limestone having contributed little material to the cataclastic fault gouges. In addition, since fault gouges from two different faults are represented on (Fig. 4.6e), and explanation invoking significant fluid flux would require fluids of a very similar composition to be present within the two fault zones. Although this is possible, we find it unlikely that fluids passing through wall rocks of differing lithology would have near-identical trace element compositions.

The concentration of REEs in the fault gouges of both faults is closest to that in the gneiss wall rocks (Fig. 4.7a) but varies significantly relative to the volcanic (depletion to some extent of all elements except Eu, Fig. 4.7c), pegmatite and limestone wall rocks (enrichment in all elements, Fig. 4.7d&e).

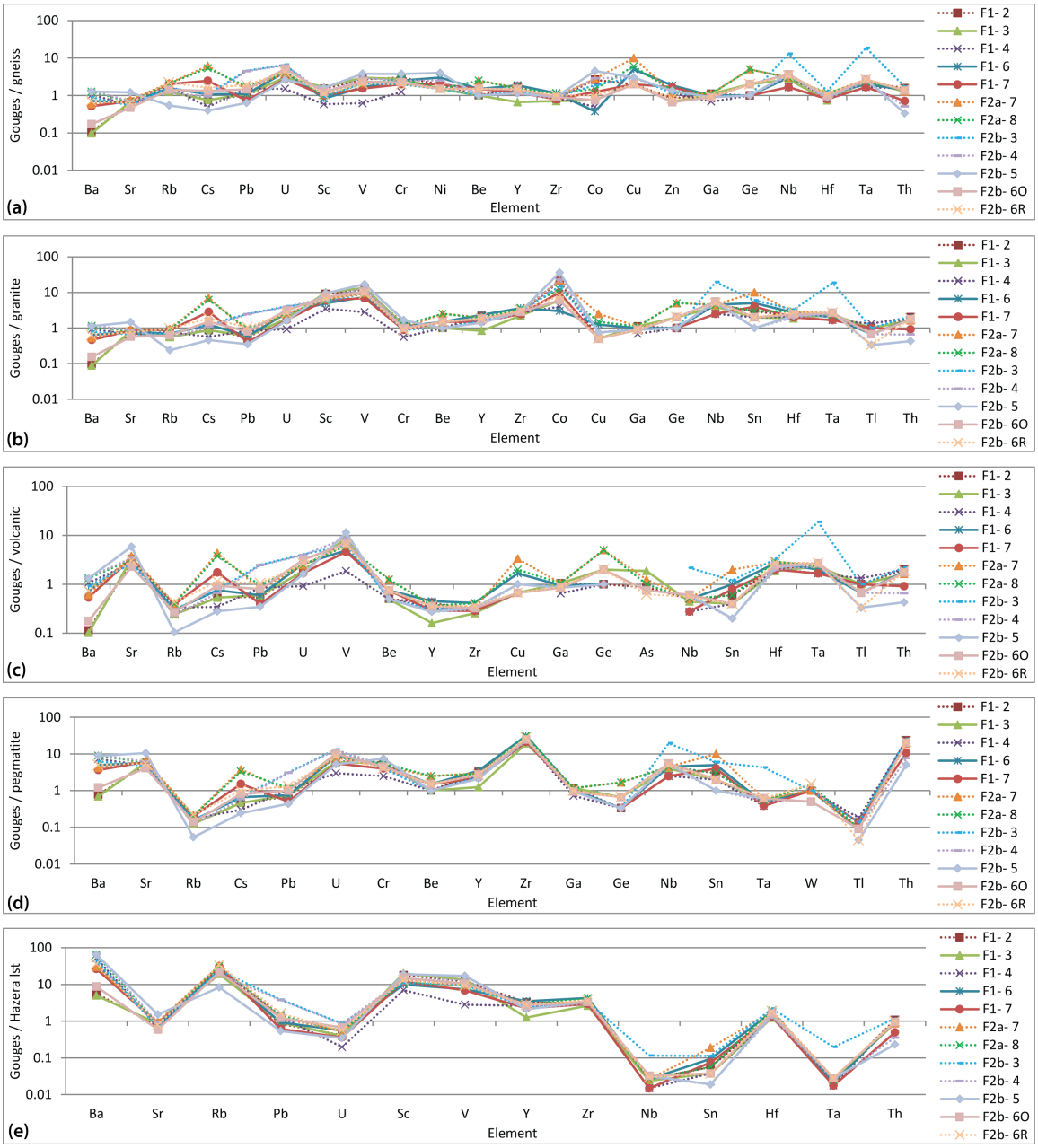

Figure 4.6: *Graphs showing trace element concentrations for fault gouges of Tzefahot Fault (F1) and Shelomo Fault (F2a & b) normalised to:* ***(a)*** *Taba Gneiss;* ***(b)*** *Elat Granite;* ***(c)*** *Ramat Yotam Volcanics;* ***(d)*** *pegmatite vein;* ***(e)*** *Hazera limestone.*

These results follow the trends of the major oxides and trace element data, pointing to the Taba Gneiss as the principal protolith rock for the cataclastic fault gouges of the Tzefahot and Shelomo faults.

4.4.1.3 Summary

Major and trace element data of basement-carbonate fault zones show similar trends; fault gouge samples are consistently the most similar to the Taba Gneiss and overall have more similarity to the basement wall rocks than to the limestone wall rocks. The exception to this is the pegmatite vein, relative to which the gouge data vary significantly. This is perhaps not surprising, since the pegmatite vein is a local feature and therefore not expected to contribute a significant amount of

material to the cataclastic fault gouge. The disparity of both the major and trace element data of the gouges relative to the Hazera Limestone wall rocks suggests that these fault rocks are likely composed of basement-derived rather than carbonate-derived material, for the most part. There is a strong correlation between the elemental composition of the shale gouges and the Ora shale protolith (Fig. 4.5), supporting the hypothesis proposed in 2.6.2.2 that these gouges are derived directly from entrainment of the Ora Shale, rather than by cataclastic deformation of basement or carbonate wall rocks.

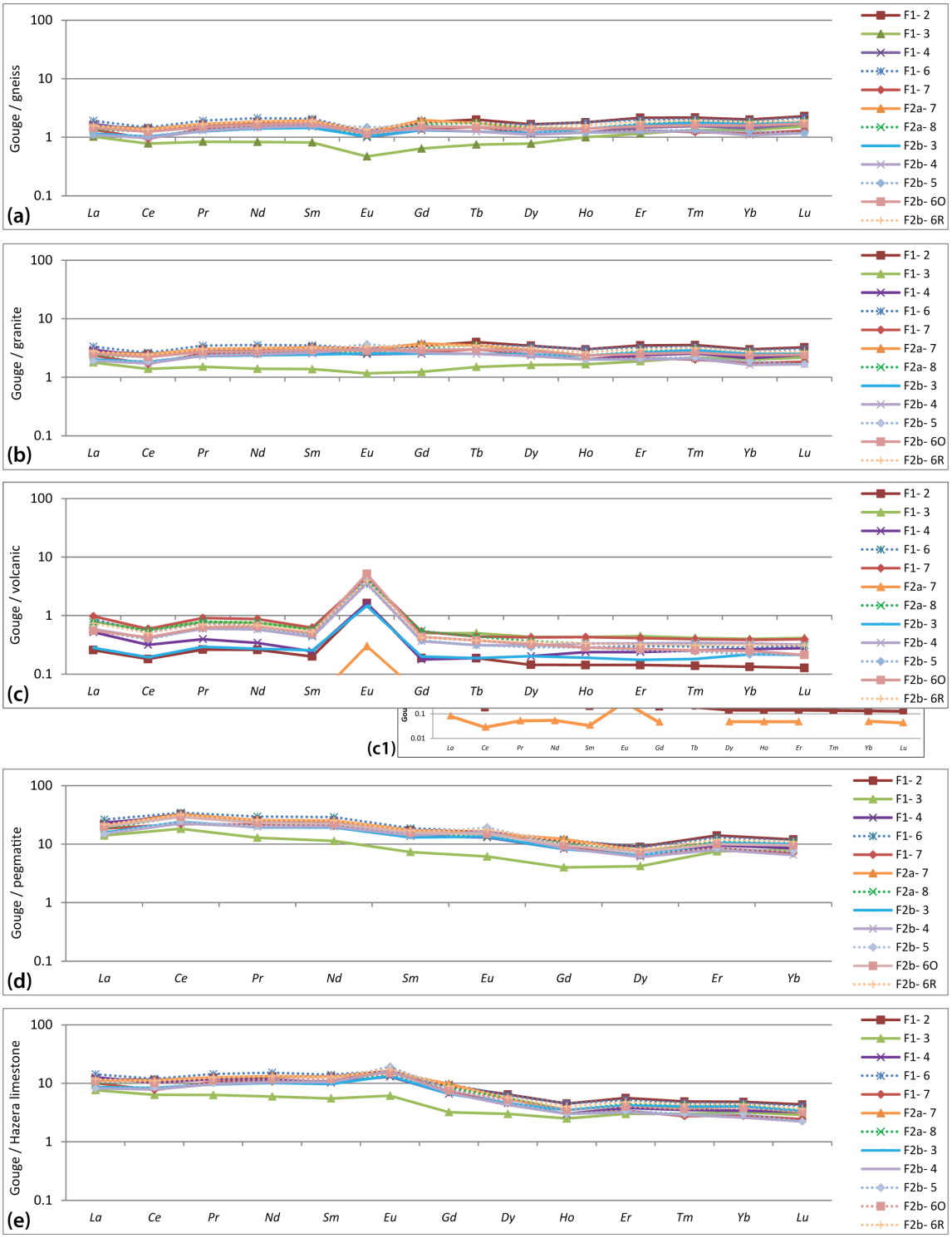

Figure 4.7: *Graphs showing REE concentrations for fault gouges of Tzefahot Fault (F1) and Shelomo Fault (F2a & b) normalised to:* ***(a)*** *Taba Gneiss;* ***(b)*** *Elat Granite;* ***(c)*** *Ramat Yotam Volcanics;* ***(d)*** *pegmatite vein;* ***(e)*** *Hazera limestone. (Inset* ***(c1)*** *shows missing data due to main graphs being plotted at the same scale for visual comparison.)*

4.4.2 Basement - clastic faults

Examples of basement-clastic fault zones studied here are the Roded and Nizoz faults (Fig. 2.4b, Fig. 2.18a); the Roded Fault juxtaposes Roded Quartz Diorite against Cambrian Shehoret sandstone (Fig. 4.8a,b) and the Nizoz Fault juxtaposes Amram Rhyolite against Cretaceous Amir sandstone (Fig. 4.8c). In the case of Nizoz Fault, the Amram Granite Porphyry underlies the younger volcanics and the Shehoret sandstone is present in the footwall a few metres from the studied outcrop, so these two lithologies have also been considered as wall rocks here. The Roded Fault has been studied at two localities with an along-strike separation of approximately 1700 m. The same wall rock lithologies are present at both outcrops (Section 2.6.2.3). The position of the samples within the fault zones is shown in Fig. 4.8

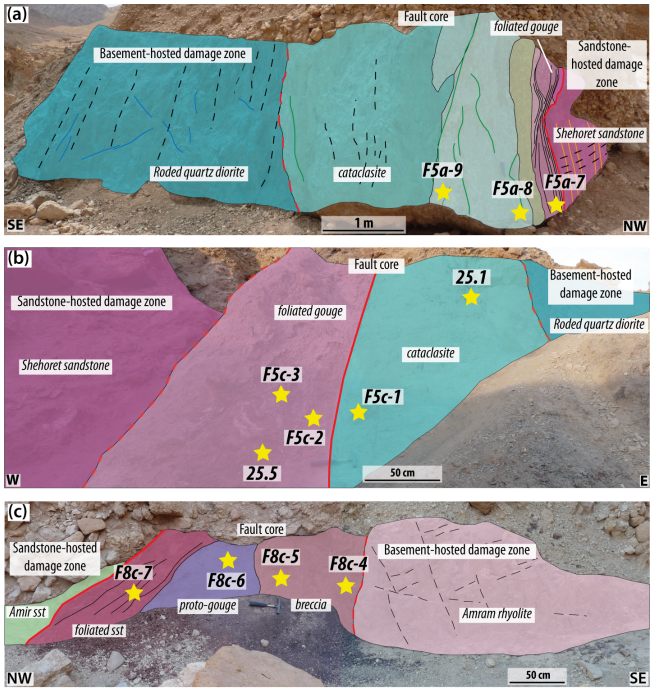

Figure 4.8: *Sketch section showing position of analysed samples in:* ***(a)*** *Roded Fault, Locality A;* ***(b)*** *Roded Fault, Locality B;* ***(c)*** *Nizoz Fault.*

4.4.2.1 Major element oxides

Major element oxide concentrations for all of the gouge samples normalised to the various wall rocks are shown in Fig. 4.9. There is relatively little enrichment/depletion of the Roded Fault gouges measured against the diorite (Fig. 4.9a), although there are slight dips in Na_2O and CaO in two of the samples, which may relate to breakdown of plagioclase feldspars during faulting. There is a slight increase in LOI across the samples, suggesting that the gouges are not only composed of crystalline basement material but may also contain some clay minerals. It is less likely to be carbonate material than in the basement-carbonate faults, though this cannot be completely discounted as it is possible these faults cut carbonate rocks in the subsurface. Although the diorite is not believed to be present within the Nizoz fault zone, the gouges from this fault show a broadly similar trend, but with depletion of Na_2O and CaO across the four samples.

When compared to the granite porphyry and rhyolite protoliths, all of the gouges show a similar trend (Fig. 4.9b&c), which reflects the fact these two basement lithologies are very close in mineralogical composition. All gouges show some enrichment in MgO and P_2O_5, but the other oxides are generally enriched/depleted by a factor of <10, i.e. not significantly. LOI is slightly higher in the gouges than in the rhyolite and granite wall rocks, again suggesting the possible presence of clay minerals.

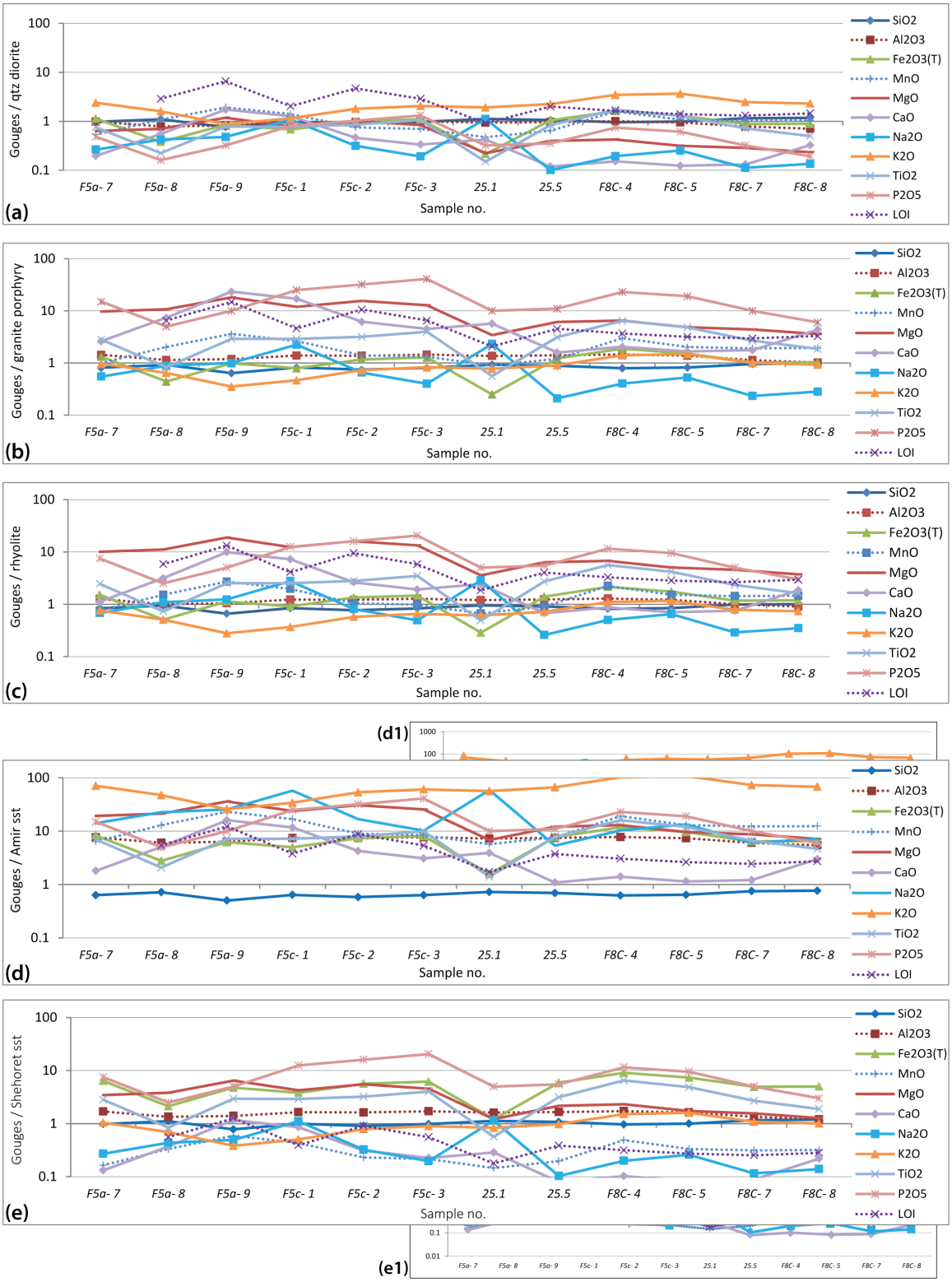

Figure 4.9: *Graphs showing major element oxide concentrations for fault gouges of Roded Fault (F5) and Nizoz Fault (F8) normalised to:* ***(a)*** *Roded Quartz Diorite;* ***(b)*** *Amram Granite Porphyry;* ***(c)*** *Amram Rhyolite;* ***(d)*** *Amir sandstone;* ***(e)*** *Shehoret sandstone. (Insets* ***(d1)*** *and* ***(e1)*** *show missing data due to main graphs being plotted at the same scale for visual comparison).*

The Cretaceous Amir sandstone is a relatively pure sandstone, composed of >90 wt% SiO_2 (Fig. 4.2a), and as such it is not surprising that when the fault gouges are normalised to it, they are enriched in almost all of the major element oxides except for SiO_2 (Fig. 4.9d). All of the gouges are particularly enriched in K_2O, but there is a distinction between those of the Nizoz and Roded faults as the Nizoz gouges show in general lower concentrations of CaO (and lower LOI) than those of the

Roded Fault. There is less disparity between the gouges and the Cambrian Shehoret sandstone (Fig. 4.9e), which may reflect the fact that this rock contains more Al_2O_3, CaO, Na_2O and P_2O_5 than the Amir sandstone (Fig. 4.2a). In the Roded Fault gouges there is a slight enrichment of MgO, Fe_2O_3 and P_2O_5, whilst the Nizoz Fault gouges show enrichment of Fe_2O_3, P_2O_5 and TiO_2, and depletion in Na_2O as well as lower LOI. The reduction in LOI relative to the Shehoret Sandstone wall rocks is likely to reflect a lower clay content of the gouges.

4.4.2.2 Trace elements & REEs

Trace element data for the Roded and Nizoz faults are presented in Fig. 4.10 and show a varied pattern across the two fault zones. The greatest similarity between gouges and wall rocks are seen between the Roded Quartz Diorite and Shehoret Sandstone wall rocks (Fig. 4.10a&e), with enrichment/depletions of > x10 in one or more samples only recorded for two elements; depletion of Sr in the Nizoz Fault gouges and enrichment of Cs for one Roded Fault sample relative to the diorite (Fig. 4.10a), and enrichment of Sn and Hf in two different Roded Fault gouges relative to the Cambrian (Shehoret) sandstone (Fig. 4.10e). Relative to the rhyolite, granite porphyry and Cretaceous (Amir) sandstone, there is slightly more variation in composition of the gouges (V, Sr, Ba, Y, Cr, Cs, Fig. 4.10b-d), especially in the Amir sandstone, which reflects the trends observed in the major element data (Fig. 4.9) and indicates that this wall rock does not contribute significantly to these gouges.

In contrast to the other trace elements, REE concentrations show more consistent trends (Fig. 4.11a-e) with enrichment/depletion factors of $\sim$10 being more or less the limit. There is enrichment of Eu in the gouges relative to the Amram Granite Porphyry and Amram Rhyolite (Fig. 4.11b,c), which may be due to the gouges containing more feldspar than these protolith rocks. The REE content of the gouges is most similar to the Roded Quartz Diorite and Cambrian Shehoret sandstone (Fig. 4.11a&e), a pattern also observed in the trace element data (Fig. 4.10a,e).

4.4.2.3 Summary

Similar trends are observed for the major and trace element data of all the basement-clastic faults studied. Fault gouge samples of both the Roded and Nizoz faults show greatest parity with the Roded Quartz Diorite, although there are subtle differences between gouges of the Roded Fault and those of the Nizoz Fault, particularly in the major element oxides. Trace element and REE data are more consistent across the two fault zones. Normalisation of fault gouge samples against the Cretaceous Amir Sandstone reveals little parity, with the gouges showing an overall pattern of element enrichment compared to the other plots. For the Cambrian Shehoret Sandstone, however, the trace element and REE data particularly show a much closer association, with only two elements (Sn and Cs) in two samples (F5a-7 and F5c-2, respectively) being enriched by a factor greater than 10. Major element data broadly fall within this range too, with the exception of P_2O_5, which is often enriched by > x10 in the gouges relative to the Cambrian sandstone, and CaO, which is depleted by the same amount in gouges of the Nizoz Fault.

Figure 4.10: *Graphs showing trace element concentrations for fault gouges of Roded Fault (F5) and Nizoz Fault (F8) normalised to:* ***(a)*** *Roded Quartz Diorite;* ***(b)*** *Amram Granite Porphyry;* ***(c)*** *Amram Rhyolite;* ***(d)*** *Amir sandstone;* ***(e)*** *Shehoret sandstone.*

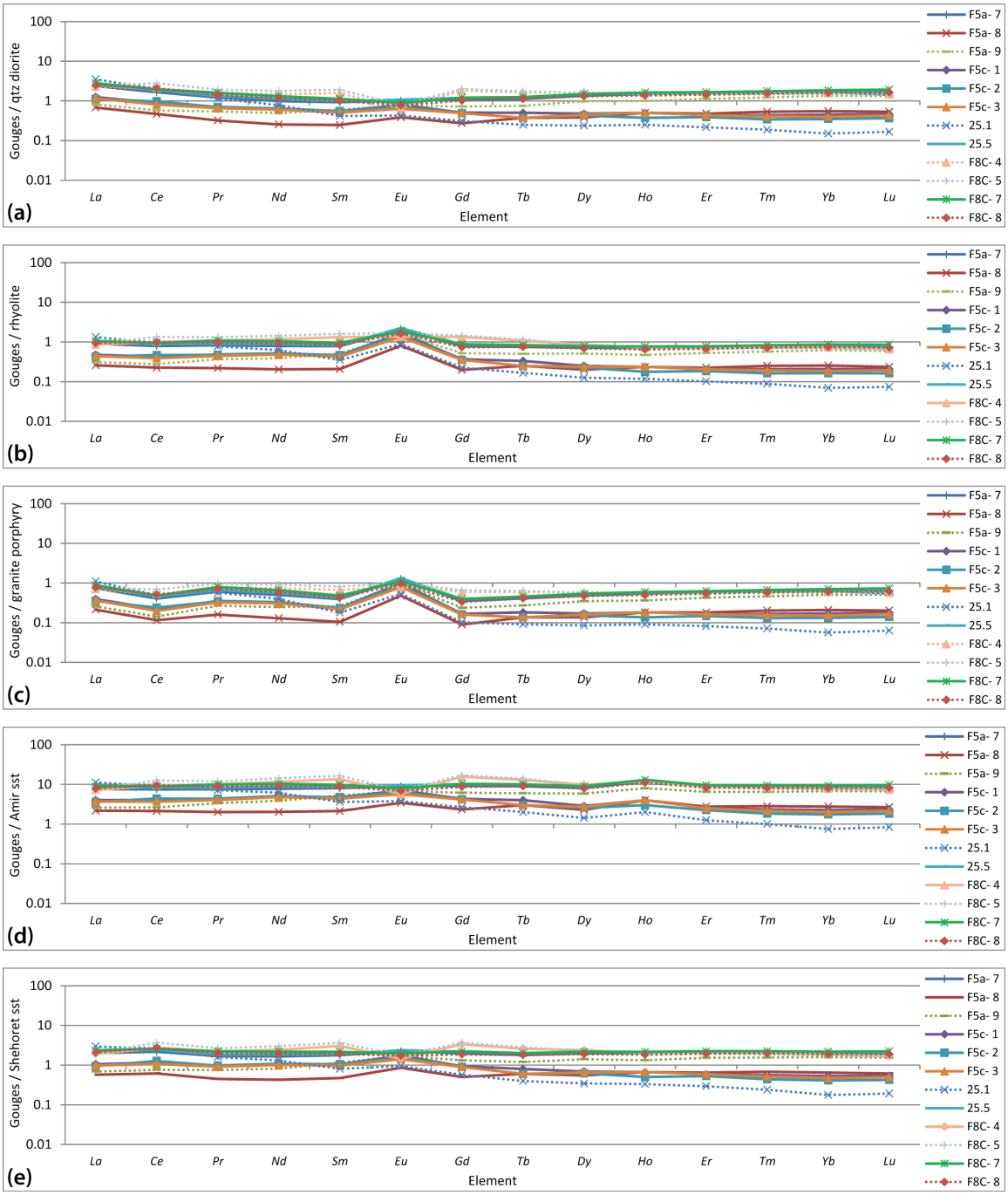

Figure 4.11: *Graphs showing REE concentrations for fault gouges of Roded Fault (F5) and Nizoz Fault (F8) normalised to:* ***(a)*** *Roded Quartz Diorite;* ***(b)*** *Amram Granite Porphyry;* ***(c)*** *Amram Rhyolite;* ***(d)*** *Amir sandstone;* ***(e)*** *Shehoret sandstone.*

4.4.3 Carbonate - clastic faults

Major and trace element analysis has been carried out on two intra-graben faults that, at the surface, involve only cover rocks. At the location studied (Fig. 2.18a), the R12 Fault juxtaposes Upper Cretaceous Hazera formation limestone against Lower Cretaceous Samar sandstone (Fig. 4.12b); the Yehoshafat Fault (Fig. 2.18a) juxtaposes Upper Cretaceous Grofit formation limestone also against Samar formation sandstone (Fig. 4.12a). In the case of the Yehoshafat Fault, these wall rock lithologies are not directly adjacent for approximately 500 m along its central portion (Fig. 2.18b) but are separated by a narrow zone of Ora formation shale (Section 2.6.2.6, Fig. 2.4a). The fault gouge of the Yehoshafat Fault at this location have been classified as 'shale gouges' (Section 2.6.2.7) so the Ora Shale has also been considered as a wall rock lithology for the purpose of whole-rock analysis. The position of the samples within the fault zones is shown in Fig. 4.12

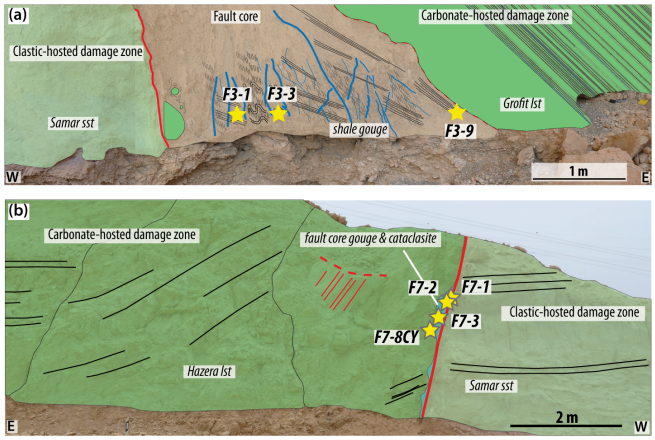

Figure 4.12: *Sketch section showing position of analysed samples in:* ***(a)*** *Yehoshafat Fault;* ***(b)*** *R12 Fault.*

4.4.3.1 Major element oxides

Major element oxide data for the Yehoshafat and R12 (samples numbered F3 and F7, respectively) faults reveal a very similar trend when gouge concentrations are normalised to both the Grofit and Hazera limestones (Fig. 4.13a&b). The gouges are very strongly depleted in calcite (by a factor of >100 in the case of sample F7-8CL), and enriched in SiO_2, Al_2O_3 and TiO_2, indicating sandstone wall rocks are the major source of fault gouge material. This is supported by the sandstone-normalised data (Fig. 4.13c) where relative SiO_2 and Al_2O_3 concentrations are close to 1. The exception to this is in samples F7-1 and F7-2 of the R12 Fault, which are enriched in CaO relative to the Samar sandstone and depleted relative to the limestones, suggesting these gouges may be of a more mixed origin, from a combination of both sandstone and limestone material. Gouges of the Yehoshafat Fault have also been normalised to the Ora shale (Fig. 4.13d) and reveal similar concentrations of major oxides to this rock. There is enrichment of CaO in these gouges, which may be the result of the circulating fluids which resulting in the precipitation of gypsum veins (see Section 2.6.2.6 for a description).

4.4.3.2 Trace elements & REEs

Relative trace element concentration data are presented in Fig. 4.14 and follow a similar trend to the major element oxide concentrations: the gouges show the biggest variation in composition relative to the limestone protoliths (Fig. 4.14a&b) and more similarity to the sandstone protolith

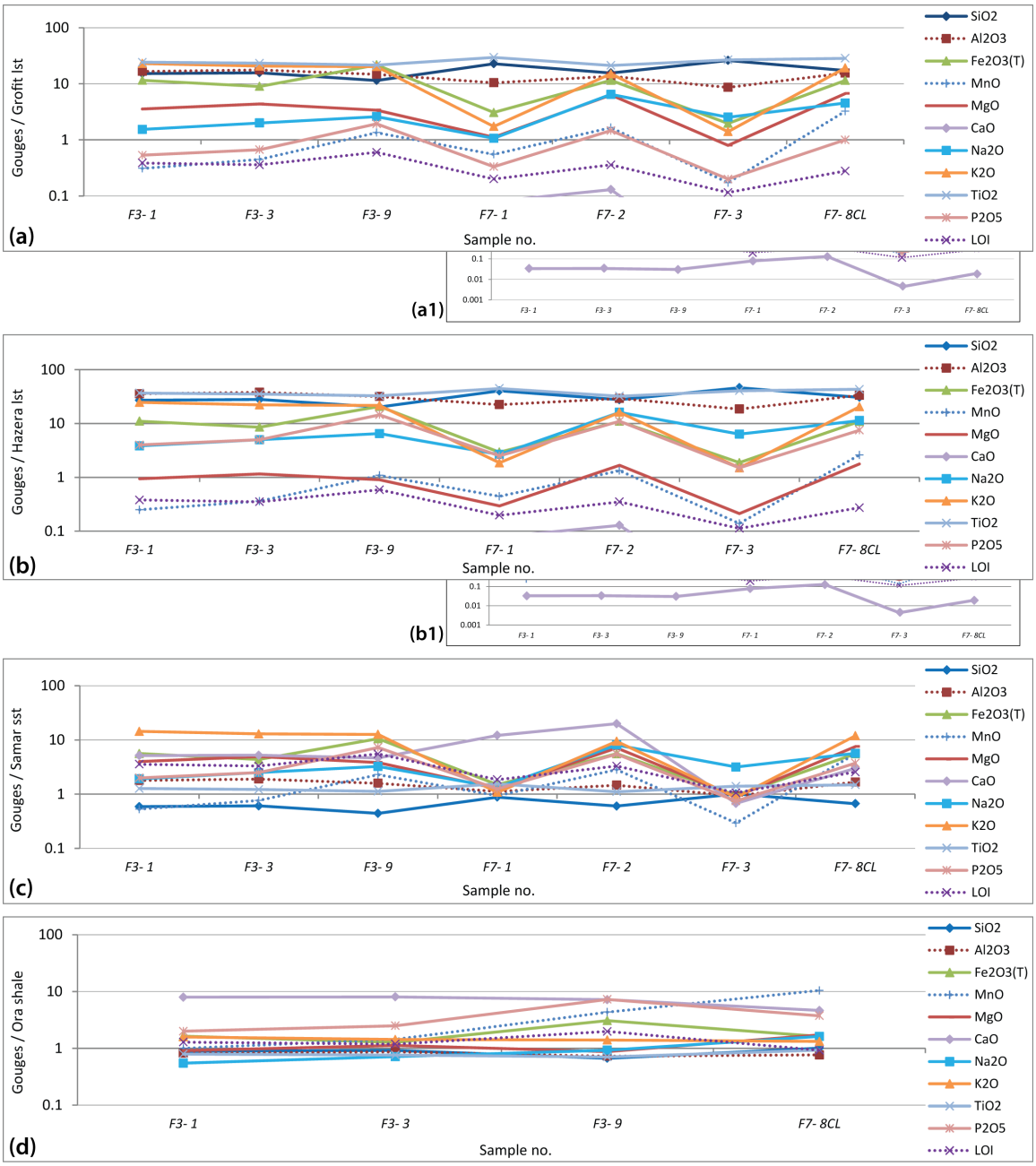

Figure 4.13: *Graphs showing major element oxide concentrations for fault gouges of Yehoshafat Fault (F3) and R12 Fault (F7) normalised to:* ***(a)*** *Grofit limestone;* ***(b)*** *Hazera limestone;* ***(c)*** *Samar sandstone;* ***(d)*** *Ora shale. (Insets* ***(a1)*** *and* ***(b1)*** *show missing data due to main graphs being plotted at the same scale for visual comparison.)*

(Fig. 4.14c). Of particular significance is the depletion of Sr in the gouges relative to both the Hazera and Grofit limestone, since Sr is an element known to coprecipitate with calcite (e.g Morse and Bender, 1990; Malone and Baker, 1999). Depletion of Sr in the fault gouges therefore supports the interpretation of major element data that limestone wall rocks have not significantly contributed to fault gouge composition. When normalised to the Samar sandstone, the gouges from both faults show a broader spread of relative concentrations (Fig. 4.14c), especially in the case of Sr, Co and Rb. The most significantly depleted elements are Zr and Co, and those enriched are Rb and Cs. Yehoshafat Fault gouges are very similar in trace element composition, albeit with some Sr enrichment in samples F3-1 and F3-9 (Fig. 4.14d). This enrichment in Sr is likely to be the result of the calcium-rich circulating fluids described above and the lack of enrichment in sample F3-3 may be the result of local variations in the presence of these fluids.

Figure 4.14: *Graphs showing trace element concentrations for fault gouges of Yehoshafat Fault (F3) and R12 Fault (F7) normalised to:* ***(a)*** *Grofit limestone;* ***(b)*** *Hazera limestone;* ***(c)*** *Samar sandstone;* ***(d)*** *Ora shale.*

REE concentrations show much less scatter than the other trace elements (Fig. 4.15); the gouges are enriched overall relative to the limestone wall rocks and slightly depleted relative to the sandstone. As for major and trace elements, the composition of shale gouges of the Yehoshafat Fault is almost identical to that of the Ora Shale protolith (Fig. 4.15d), whilst the same gouges along with those of the R12 Fault show greater discrepancy when normalised to the other possible protoliths (Fig. 4.15a-c).

4.4.3.3 Summary

Fault gouges of the carbonate-clastic faults show little similarity to the limestone wall rocks in the case of both major and trace elements. The major elements are strongly depleted in CaO and enriched in SiO_2, suggesting they are more closely related to a sandstone protolith than carbonate one, and trace element and REE concentrations are also highly variable relative to the limestone protoliths. Elemental compositions of the fault gouges much more closely resembles those of the Samar Sandstone wall rock, with major, trace and REE concentrations generally being within one order of magnitude to those found in the protolith sample. Exceptions to this are seen in slight enrichments of K_2O in gouges of the Yehoshafat Fault and of CaO in two of the apparently sandstone-derived samples of the R12 Fault (F7-1 and F7-2), suggesting that, at this location, there

is some contribution from the carbonate wall rocks to the gouges. As with the shale gouges of the Tzefahot Fault, those of the Yehoshafat Fault are also very similar to the Ora Shale protolith and are also enriched in CaO.

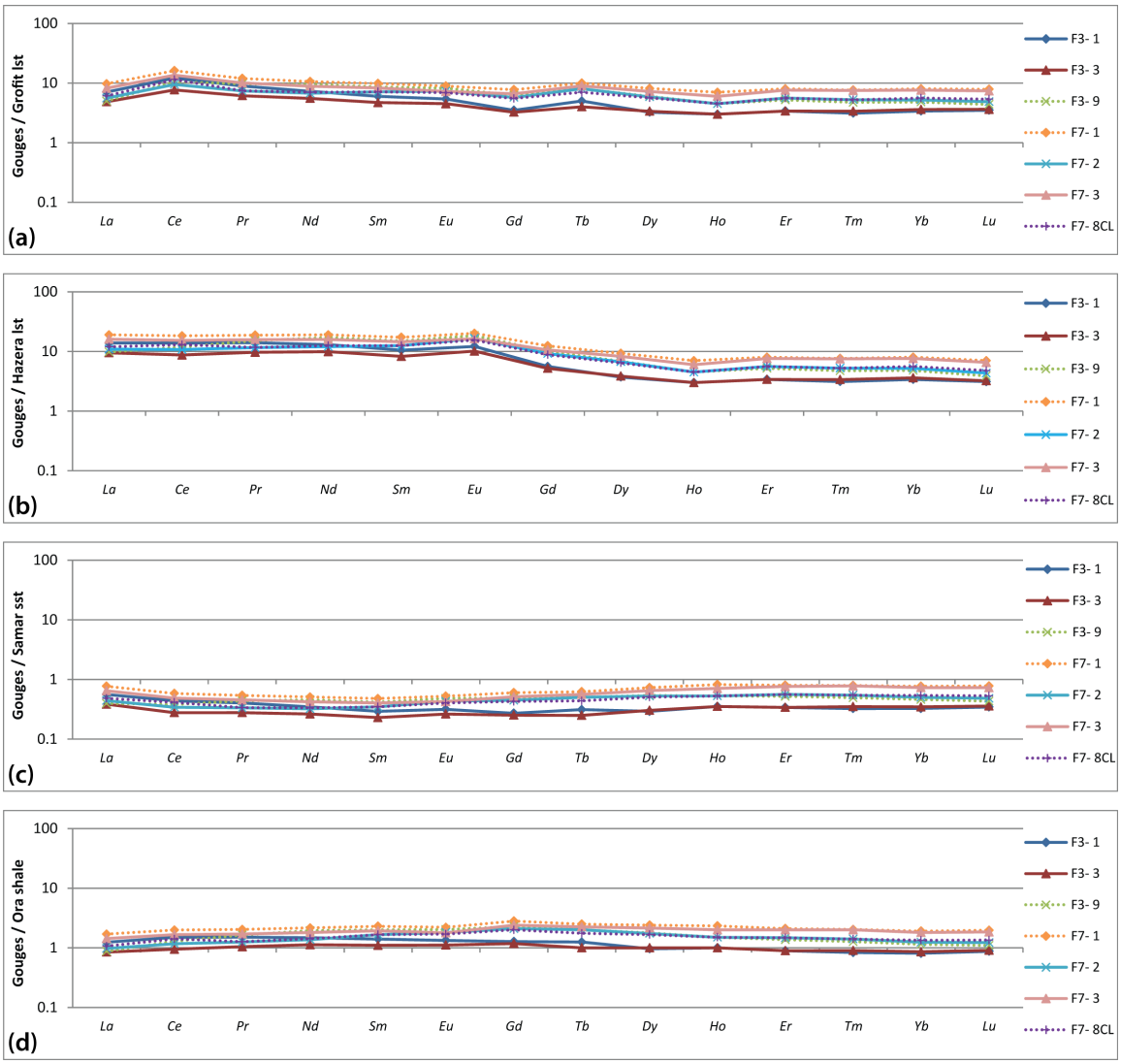

Figure 4.15: *Graphs showing REE concentrations for fault gouges of Yehoshafat Fault (F3) and R12 Fault (F7) normalised to:* ***(a)*** *Grofit limestone;* ***(b)*** *Hazera limestone;* ***(c)*** *Samar sandstone;* ***(d)*** *Ora shale.*

4.4.4 Mean gouge compositions

As well as considering the normalised elemental data for each individual sample across the six fault zones studied, we have also compared the mean gouge composition from each fault zone against the most likely protolith in the footwall and hangingwalls, in order to quantify the similarity of the fault gouges to these wall rocks. Where there is more than one potential protolith in a given footwall/hanging wall, we have chosen the lithologies which the gouges resemble the most geochemically, based on the data presented in the preceding sections (Sections 4.4.1 to 4.4.3).

4.4.4.1 Statistical methodology

In order to do this, we have plotted the mean elemental concentrations (in parts per million) for the gouges of each fault zone against those of the wall rocks on x-y plots. A line of constant composition (gradient=1) is added to the graph, allowing us to infer that elements lying on the line are unchanged in concentration in the gouges relative to wall rocks, whilst those that lie significantly above or below the line are enriched or depleted, respectively.

We have quantified this similarity by calculating a coefficient of determination, or "R^2", value for each plot, though we have slightly varied the method to do this. The purpose of calculating R^2 is normally to show how much of the scatter in a give data set can be explained by the predicted model ('least ordinary squares' method), this model being the trendline of the data. The equation is given as:

$$R^2 = 1 - \frac{SSe}{SSt} = \frac{\sum(y_i - \hat{y}_i)^2}{\sum(y_i - \bar{y})^2} \tag{4.1}$$

where SSe is the sum of squared errors, SSt is the sum of squared totals, y = *elemental concentration of mean gouge* , y_i = *actual* y, $\hat{y}_i$ = *predicted* y and $\bar{y}$ = *mean* y. According to this equation, a value of 1 is a perfect correlation where 100 % of the scatter can be explained by the model, and a value of 0.1 is a very poor correlation where only 10% of the scatter can be explained by the model. Since this essentially describes how well data fit a trendline, it is possible to have an R^2 of $\simeq$1 where the actual values differ, as long as the relationship is the same (e.g. a data set where y = 2x would return R^2 = 1).

However, as the purpose here is to determine how close the gouge compositions are to initial wall rock composition, the model (or trendline) we must use is a line where x = y (along which element concentration in the fault gouge is the same as in the wall rock), described by the equation:

$$\text{"}R^2\text{"} = 1 - \frac{\sum(y_i - \bar{x})^2}{\sum(y_i - \bar{y})^2} \tag{4.2}$$

where predicted $\hat{y}$ becomes $\bar{x}$, the mean elemental concentration of protolith. Using this method, we are able to describe the composition of the fault gouges relative to a reference model of constant composition, rather than the correlation of the data themselves. Where we have used the term "R^2" in the following text, all values were calculated using Eq. (4.2). It should be noted that using this method is more likely to return R^2 values of zero than when using a least ordinary squares approach even where the data do not appear to have a completely random scatter, since we are using a reference model that is independent of the data themselves (S. Dixon, pers. comm., June 2015).

Other statistical methods can be used to further quantify the relative contribution of each protolith rock to a fault gouge. This can be done by using a least squares method (Eq. (4.3), Evans and Chester, 1995) to find a best-fit model for the percentage contribution of two wall rocks to a fault gouge, and the results obtained by Evans and Chester (1995), for example, show a clear relationship

between the model and observed values.

$$X_{opt} = min \sum [E_{fault} - X[E_A] + ([1 - X]E_B)]^2 \tag{4.3}$$

where X_{opt} is the optimised contribution (fraction) of protolith A to form the observed composition of the gouge; X is the modelled fraction of protolith A; $1 - X$ is the modelled fraction of protolith B; E_{fault} is the observed composition; E_A is the observed composition in protolith A (footwall in our case); and E_B is the observed composition in protolith B (hanging wall in our case). The sum relates to the combination of elements that can be used, which are chosen according to their relative immobility, and the part of the equation $E_{fault} - X[E_A] + ([1 - X]E_B)$ is repeated for the chosen elements.

We attempted this method using the major oxide elements Mn, Ti and P, as per Evans and Chester (1995), and were not able to produce a reasonable model to fit the observed data. We also used a variety of relatively immobile, HFS, trace elements (Y, Zr, Ta, Hf, U) and found the models produced also did not fit well with the observed data. We suggest that this is due to uncertainty in protolith lithology and the possible contribution, perhaps in relatively small amounts, of additional lithologies which although may be similar in bulk mineralogy (e.g. crystalline basement rocks) may have significantly different geochemical signatures.

4.4.4.2 R^2 modelling

The data for the Tzefahot, Shelomo, Roded, Nizoz, Yehoshafat and R12 faults are plotted in figures 4.16 and 4.17, below. In addition, data from the proposed shale-derived gouges from the Tzefahot and Yehoshafat faults have been plotted against the Ora shale protolith (Fig. 4.17b).

In the case of basement-cover faults, it is immediately apparent that there is a greater disparity between the fault gouges and the cover wall rocks (particularly limestones) than the basement wall rocks. Elemental concentrations for the fault gouges are plotted against those of the basement wall rocks (Fig. 4.16a1 & b1), the data tend to cluster around the reference line and R^2 values are 0.94 and 0.69 for the Tzefahot and Shelomo faults, respectively, whereas more data points lie further away from this reference line when plotted against the carbonate wall rocks (Fig. 4.16a2 & b2) and R^2 values of 0 are returned, indicating there is no correlation between these materials.

The pattern is somewhat different in the case of basement-clastic faults (Fig. 4.16c-d), where once again the gouges show a strong similarity to the basement wall rocks (R^2 = 0.99, Fig. 4.16c1 & d1) but the gouges also show a relatively strong similarity to the cover wall rocks (R^2 = 0.97 and 0.73 for the Roded and Nizoz faults, respectively, Fig. 4.16c2 & d2). A possible explanation for this is that the undeformed clastic wall rocks are more similar in composition to the crystalline basement than carbonate rocks are, particularly in the case of major element oxides (Fig. 4.1a and Fig. 4.2a). As well as a general similarity due to the content of silicate minerals, the sandstones of the area are sourced from many of the crystalline basement rocks so it is expected that trace element and REE compositions will also be similar.

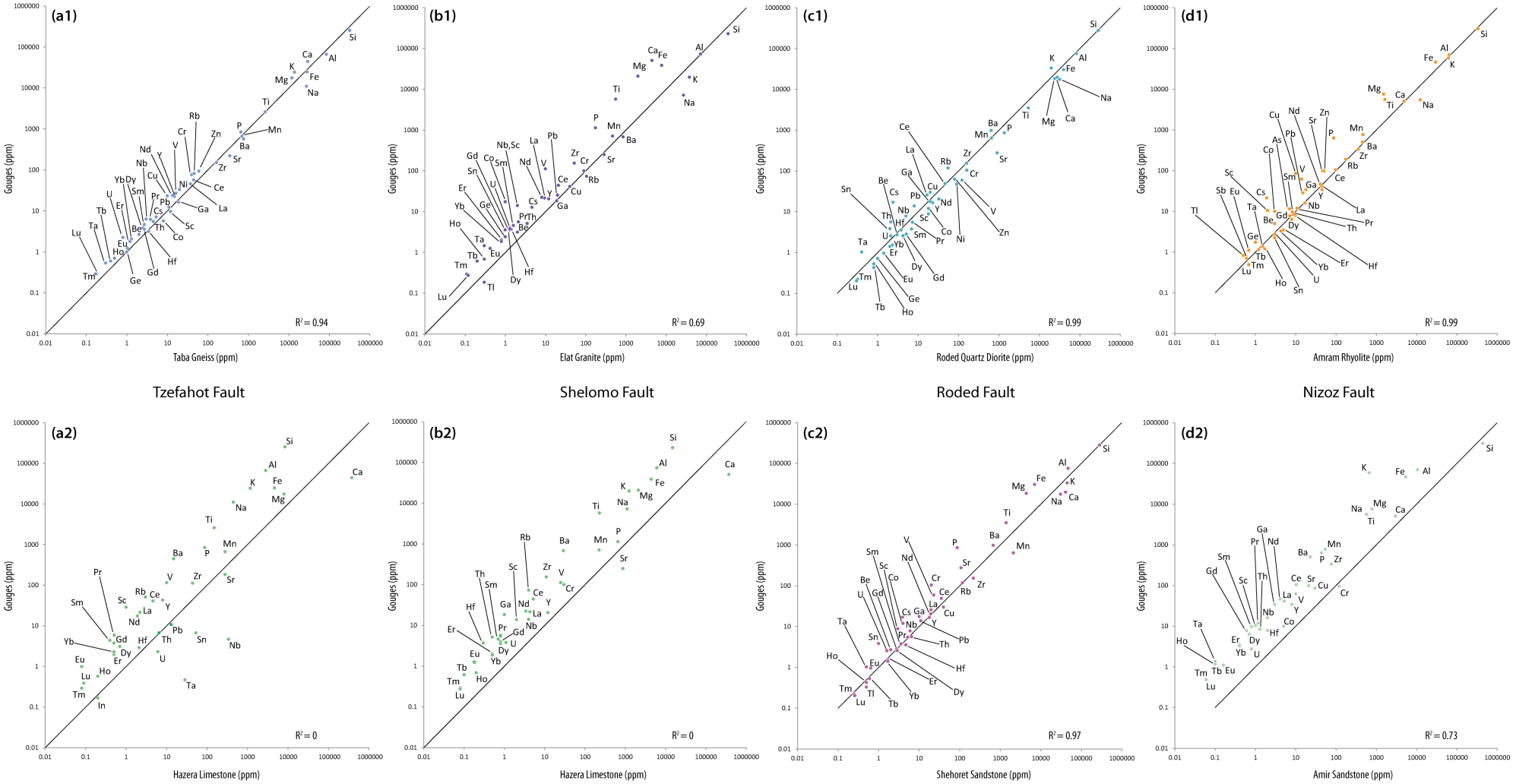

Figure 4.16: *Element compatibility charts for basement-cover faults:* ***(a)*** *Tzefahot Fault,* ***1.*** *Mean gouge composition/gneiss protolith,* ***2.*** *Mean gouge composition/limestone protolith;* ***(b)*** *Shelomo Fault,* ***1.*** *Mean gouge composition/granite protolith,* ***2.*** *Mean gouge composition/limestone protolith;* ***(c)*** *Roded Fault,* ***1.*** *Mean gouge composition/quartz diorite protolith,* ***2.*** *Mean gouge composition/sandstone protolith;* ***(d)*** *Nizoz Fault,* ***1.*** *Mean gouge composition/rhyolite protolith,* ***2.*** *Mean gouge composition/sandstone protolith.*

Based on mean gouge concentration data alone, it is therefore more difficult in the case of basement- clastic rocks to say with as much confidence as for the basement-carbonate faults that the basement wall rocks are the primary source of fault gouge material. However, when considering the x-y plots themselves (Fig. 4.17c1-d2), a greater scatter of the data is observed when the fault gouges are plotted against the clastic wall rocks. In the case of the Roded Fault, this is particularly notable in the major element oxides (Fig. 4.17c2), whereas the Nizoz Fault data show that almost all elements, with the exception of Si and Cr, are enriched in the gouges relative to the wall rock. That the elemental concentrations of the Nizoz Fault gouges are consistently enriched relative to the clastic wall rocks suggest that these are not the primary source of gouge material, despite the high R^2 value.

The data are somewhat more varied in the case of cover-cover faults (Fig. 4.17), but still appear to reveal one primary protolith for the fault gouges. R^2 values for the Yehoshafat Fault gouges compared to clastic and carbonate wall rocks are 0.36 and 0, respectively (Fig. 4.17a1 & a2). Compared to the R^2 value of 0.93 returned when compared to the Ora Shale (Fig. 4.17a3), it is clear that there is a much stronger relationship between the shale gouges and the shale protolith than either of the adjacent wall rocks at this location.

At the R12 Fault there is a very close relationship between the fault gouges and the clastic wall rocks (R^2 = 0.95, Fig. 4.17b1) but a no significant correlation between the same gouges and the carbonate wall rocks (R^2 = 0, Fig. 4.17b2).

4.4.4.3 Summary

Determining the R^2 values of the x-y plots shown in Fig. 4.16 and Fig. 4.17 has enabled us to quantify the degree of similarity between fault gouges and adjacent wall rocks described in Sections 4.4.1 to 4.4.3. The data show that for basement-carbonate and cover-cover (carbonate-clastic) faults, there is a strong correlation only between the composition of the fault gouges and the basement or clastic wall rocks (R^2 0.69-0.99) and not between the gouges and the carbonate wall rocks (R^2 = 0).

In the case of basement-clastic fault zones, however, whilst there is a very strong correlation between the composition of the basement wall rocks and fault gouges (R^2 = 0.99), there is also a relatively strong correlation between the gouges and the clastic wall rocks (R^2 = 0.97 & 0.73). Raw elemental data show, as expected, that the chemical composition of the clastic cover rocks are much more similar to the crystalline basement than carbonate rocks are (Fig. 4.1a and Fig. 4.2a). It is therefore not possible, using geochemical data alone, to quantify how much of this similarity is a result of close initial composition of the basement and clastic wall rocks, and how much is due to mixing of the two wall rocks within the fault zone.

4.4.5 Mixing trend analysis

Whilst the data presented in Sections 4.4.1 to 4.4.4 show that fault gouges are most likely derived from a single protolith rock, elemental composition data can also be used to describe lateral

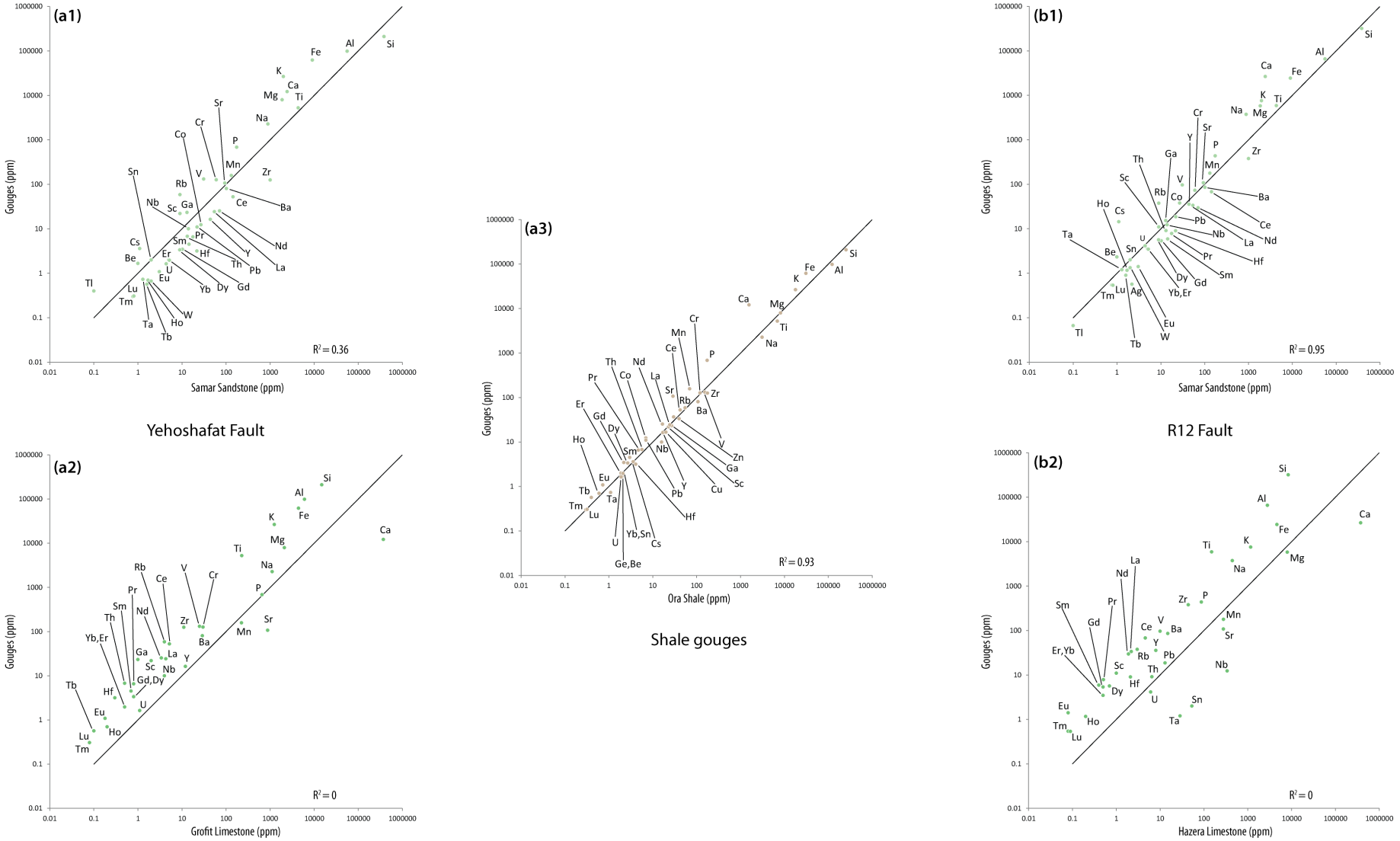

Figure 4.17: *Element compatibility charts for cover-cover faults:* ***(a)*** *Yehoshafat Fault,* ***1.*** *Mean gouge composition/sandstone protolith,* ***2.*** *Mean gouge composition/limestone protolith,* ***3.*** *Shale gouge composition/shale protolith;* ***(b)*** *R12 Fault,* ***1.*** *Mean gouge composition/sandstone protolith,* ***2.*** *Mean gouge composition/limestone protolith.*

variations in fault zone composition. This is useful as a means of assessing the degree of mixing of different materials within fault cores.

4.4.5.1 Low-displacement faults (<500 m)

The three faults with estimated displacements of <500 m, the Nizoz, Yehoshafat and R12 faults, show relatively little mixing of both footwall and hanging wall rocks, with fault core materials generally having similar compositions of major element oxides, trace elements and REEs as a single protolith lithology (Fig. 4.18). At the Nizoz Fault, where protolith rocks on both sides of the fault are quartz-rich, there is a slight elevation in the concentration of K_2O in the fault core breccia and cataclasite (F8-4, F8-5, Fig. 4.18a), which may be the result of precipitation of illite in this zone (Fig. 3.81a). Of the trace elements, Ba and Zr are the most variable across the fault zone (Fig. 3.81b), at levels higher than either protolith rock, indicating they may have become concentrated through accumulation after breakdown of minerals (such as feldspars and biotite), or are sourced from exotic fluids. At the Yehoshafat Fault, major, trace and RE element concentrations in the shale gouge samples are near-identical to the shale protolith, with only a minor increase in Fe_2O_3 seen in the eastern-most fault core sample. This suggests there has been no mixing between rocks directly adjacent to the fault at the studied location.

Elemental concentrations across the R12 Fault zone show the most variation (Fig. 4.18g-i), with trace element concentrations being the least consistent (Fig. 4.18h). In the fault core, concentration of Zr varies even between the two cataclasite samples (F7-1 and F7-2), and is close to zero in the damage zone (F7-6) despite being the most abundant trace element in the protolith sample (F3-10). In two of the core samples (F7-2 and F7-8CY) there is an elevated concentration of Zn, despite this element only being present at very low concentrations in the wall rocks of both the hanging- and footwalls. This suggests there has been some fluid flow within the fault zone, possibly along the boundary between the cataclastic part of the fault core (F7-2) and the clay-rich part (F7-8CY). REE concentrations show little change across the fault core samples (F7-1 - F7-3) but do contain higher concentrations than the damage zone sample, which may further support the possibility of fluid flow along the fault. CaO is slightly more abundant in the cataclasite samples than the sandstone protolith, reflecting the minor contribution of carbonate material to these fault rocks.

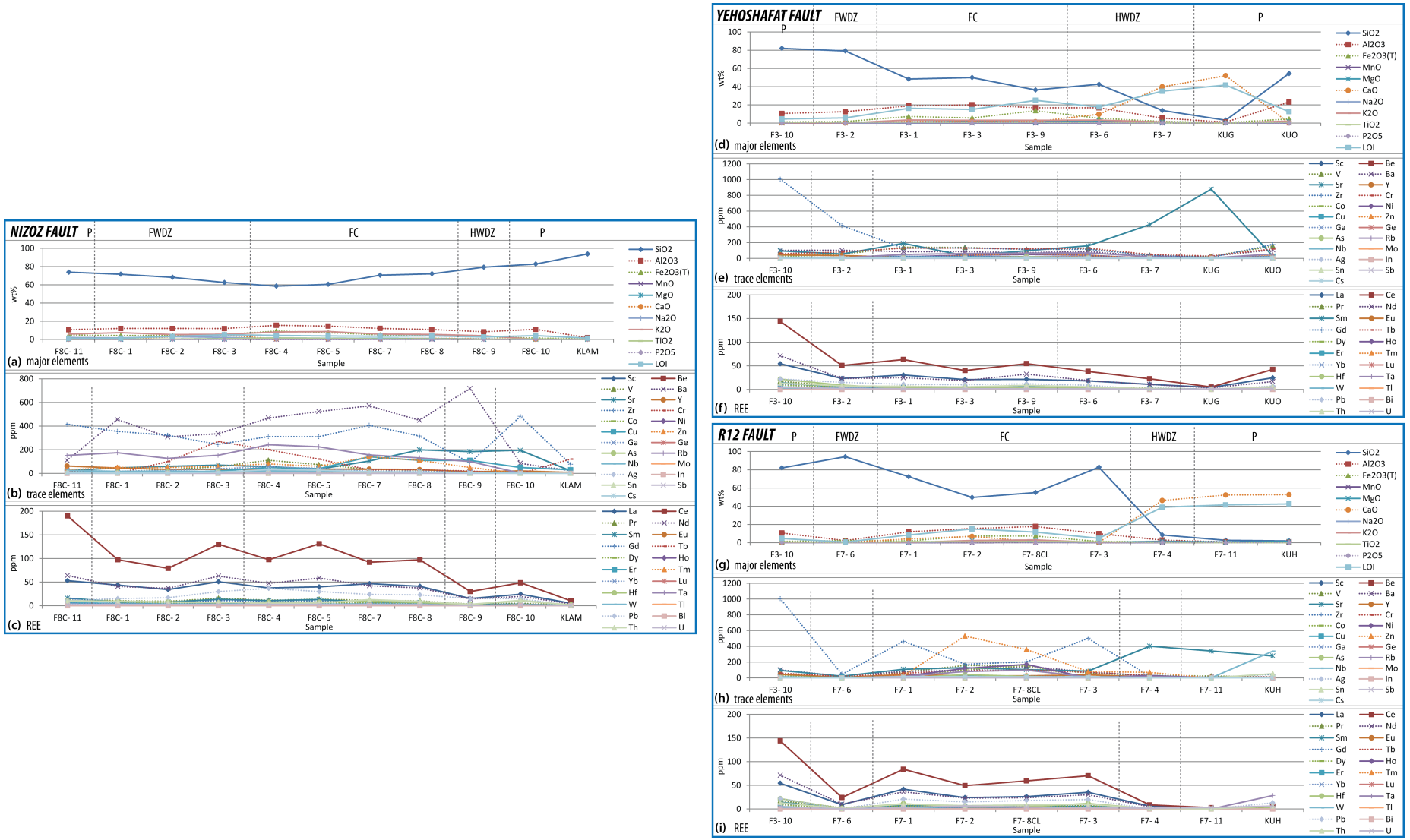

Figure 4.18: *Raw data plots showing lateral variation of major, trace and REE across high-displacement (>500 m) faults:* ***Nizoz Fault****,* ***(a)*** *major elements;* ***(b)*** *trace element;* ***(c)*** *REE.* ***Yehoshafat Fault****,* ***(d)*** *major elements;* ***(e)*** *trace element;* ***(f)*** *REE.* ***R12 Fault****,* ***(g)*** *major elements;* ***(h)*** *trace element;* ***(i)*** *REE. (Footwall basement rocks are to the left on all plots, hanging wall cover rocks to the right. P: protolith; FWDZ: footwall damage zone; HWDZ: hanging wall damage zone; FC: fault core.)*

4.4.5.2 High-displacement faults (>500 m)

In the high displacement faults, those with estimated displacements of >500 m, variable degrees of mixing are observed. In the case of major elements (Fig. 4.19a,d,g,j) the clear relationship between cataclastic gouges and basement wall rocks, and shale gouges and shale wall rocks, is observed; the gouges are rich in the major element oxides that are present in high concentrations in basement and shale wall rocks. However, there are also slight increases in oxides from the hanging wall rocks (carbonate and clastics), indicating some mixing has taken place. In the case of Shelomo Fault, Locality B, where four samples were collected from across the fault core, the amount of LOI and concentration of CaO is slightly elevated in the gouge samples relative to the basement wall rocks, but both are still <10wt% (compared to >50wt% in the carbonate protolith). There does not appear to be a decrease in these components from E (F2b-6R, adjacent to basement wall rocks) to W (F2b-3, adjacent to carbonate wall rocks) across the fault zone, suggesting that any mixing that occurred was homogeneous throughout the fault core (in this part of the fault zone). A similar pattern is seen in the gouges of Shelomo Fault, Locality A and of the Tzefahot Fault.

It is less immediately clear in the case of the Roded Fault, a basement-clastic fault, since SiO_2 is the principal oxide in both quartz diorite footwall rocks and the sandstone hanging wall and there is no distinguishing oxide in either wall rock that is not present in the other (like CaO in the case of basement-carbonate faults). However, the major oxide concentrations of the cataclasite (F5a-9, F5a-8) and foliated gouge (F5a-7) of the fault core are near identical in concentration to the basement protolith and SiO_2 and Al_2O_3 (Fig. 4.19). There is little to no lateral variation across the fault core samples, with the exception of slightly elevated CaO and LOI in the western-most sample, closest to the basement footwall, suggesting possible fluid flow through this zone. The parity between the cataclasite and gouge samples also indicates that the fine-grained gouge is a more intensely comminuted example of the cataclasites. In the case of both basement-carbonate and basement-clastic rocks there is no evidence of a gradational chemical change from an initial protolith towards the fault zone, as there is very little change in concentration of major element oxides between the protolith and damage zone rocks, nor any exotic elements in the damage zone rocks.

Concentrations of trace elements and REEs are relatively consistent overall between fault core samples and inferred protoliths, and highly variable between fault core samples and rocks not inferred to be protoliths, further supporting the single-protolith hypothesis (Fig. 4.19b,c,e,f,h,i,k,l). The exceptions to this are in elevated concentrations of Ba in the fault gouges of the Shelomo Fault at both localities (Fig. 4.19b,e) and at the Roded Fault, relative to the basement footwall rocks. It is possible that this increase is the result Ba released during the progressive breakdown of feldspars and biotite being adsorbed by newly precipitated clay minerals rather than leaving the fault system, resulting in an accumulation in the fault cores.

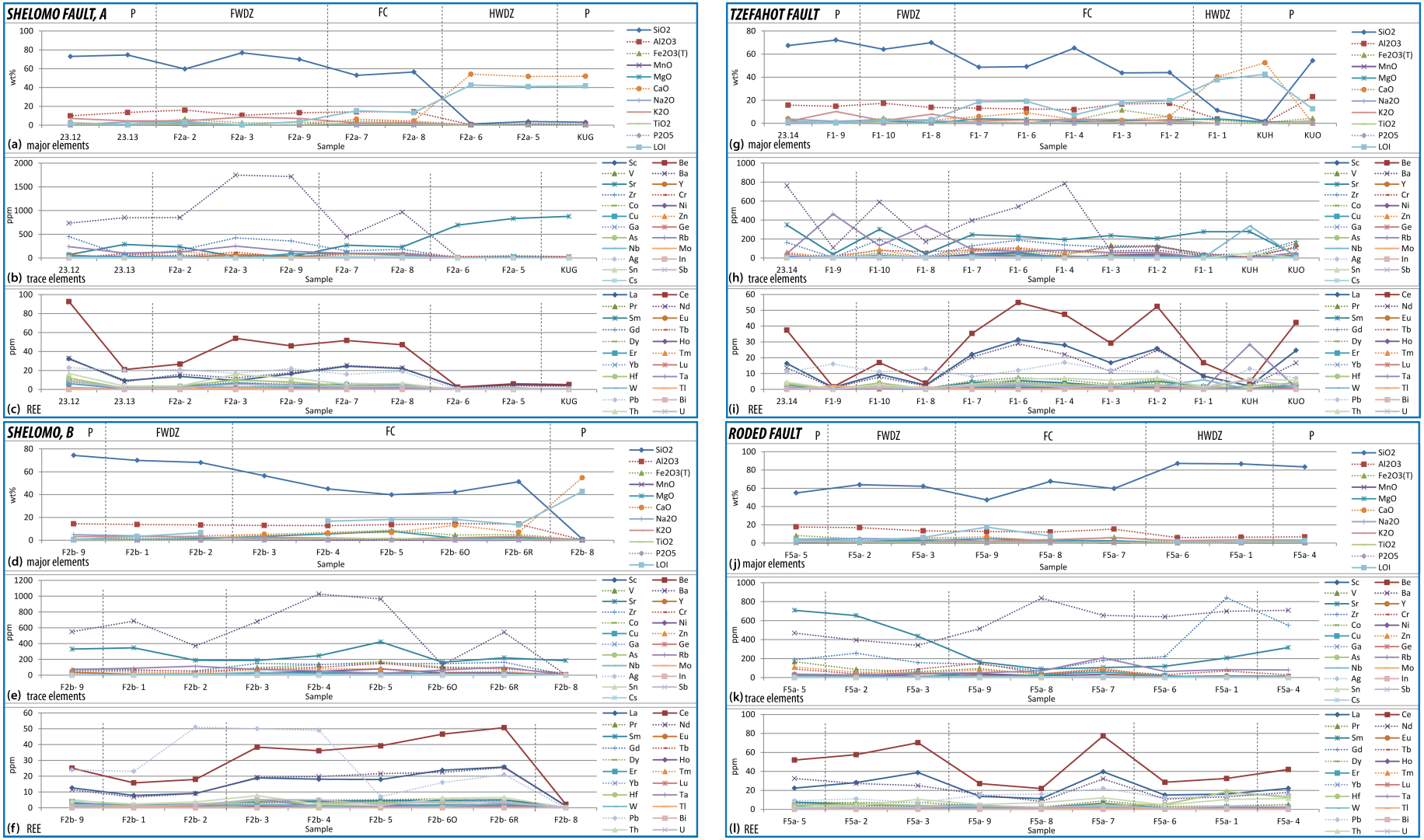

Figure 4.19: *Raw data plots showing lateral variation of major, trace and REE across high-displacement (>500 m) faults:* ***Shelomo Fault****, Locality A,* ***(a)*** *major elements;* ***(b)*** *trace element;* ***(c)*** *REE;* ***Shelomo Fault****, Locality B,* ***(d)*** *major elements;* ***(e)*** *trace element;* ***(f)*** *REE;* ***Tzefahot Fault, (g)*** *major elements;* ***(h)*** *trace element;* ***(i)*** *REE;* ***Roded Fault (j)*** *major elements;* ***(k)*** *trace element;* ***(l)*** *REE. (Footwall basement rocks are to the left on all plots, hanging wall cover rocks to the right. P: protolith; FWDZ: footwall damage zone; HWDZ: hanging wall damage zone; FC: fault core).*

4.5 Discussion

4.5.1 The origin of fault core gouges

4.5.1.1 Cataclastic gouges

Detailed geochemical analysis of major and trace element data confirm that cataclastic fault gouges are, for the most part, derived from a single protolith. We have considered the faults according to their wall rock lithologies, classifying them as basement-carbonate, basement-clastic and carbonate-cover and found that despite these lithological and estimated displacement differences (Section 2.6.1), the gouges from all of the fault zones display a similar geochemical pattern. There is some ambiguity in the case of the basement-clastic (Roded and Nizoz) faults since the wall rocks in both the hanging- and footwall have similar elemental compositions.

Mean gouge concentration data for all four basement-cover faults show that the gouges are much closer in elemental composition to the assumed basement protoliths than their cover equivalents (Fig. 4.16a-d). This is not only seen in the major oxide data, which may be considered the most straightforward way by which to track mineralogical changes, but also in trace element and REE data. That the major, trace and REE data for given fault zones are consistently the most similar to the same wall rock very strongly implies that this is indeed the protolith. This pattern is observed regardless of the cover lithologies involved (Cretaceous limestone, Cretaceous sandstone and Cambrian sandstone), implying that the crystalline igneous/metamorphic aluminosilicate rocks are the principal lithologies contributing to fault gouges. Whilst there could be a mechanical reason for this, we suggest (as proposed in Section 3.4) that these faults initiated in the basement at depth and that the cover rocks were only incorporated into the fault zones in the later stages of deformation. Whilst this might seem unusual in a predominantly strike-slip system, we have shown in Chapter 2 that the faults studied here have a significant component of oblique movement. It is entirely possible that, for the majority of a fault's history, it propagated through a single basement lithology, resulting in fault gouge largely derived from a single protolith. Relatively late incorporation of a secondary, cover lithology may account for the relatively small amount of contributory material we have observed from these rocks.

Although we infer a single protolith to be the main source for the fault gouges of basement-cover faults, the clay contents of these fault rocks (described in Chapter 3) suggest that we are not observing a simple case of brittle cataclasis by comminution of grains alone. This is supported here by the increase in LOI seen in most gouges when normalised to their respective igneous/metamorphic protoliths, as smectite contains both bonded water within its crystal structure and, as a swelling clay, water in the interlayer space also. The contribution of small amounts of carbonate material or interstitial clays from sedimentary wall rocks to fault gouges could also serve to increase the LOI, and it is not possible with the techniques used to differentiate between these two potential sources of volatile material. However, it is more probable that the increase in LOI in fault gouges is related to the precipitation of authigenic smectite, since the gouges that show the greatest increase in LOI (those of the Tzefahot and Shelomo faults, Fig. 4.4a, and to a lesser extent the Roded Fault, Fig. 4.9a) do not show corresponding enrichments in CaO (Tzefahot and Shelomo faults) or SiO_2 (Roded Fault) that we might expect if significant comminution of cover

wall rocks and subsequent mechanical mixing of lithologies has taken place.

In the case of the cover-cover R12 Fault, where no basement lithologies are involved, fault core cataclasite is much closer in elemental composition to a single protolith, in this case the sandstone rather than the carbonate. Although the fault core in this case is very narrow (<40 cm, Section 2.6.2.7) the cataclasite samples (F7-1, F7-2, F7-3) show little enrichment or depletion of major oxides relative to the sandstone protolith (Fig. 4.13c) and a much greater disparity with the limestone protoliths. In particular, when normalised to the limestone protoliths (of the Hazera and Grofit formations, Fig. 4.13a&b), the gouges display the most significant depletion in CaO and the most significant enrichments in SiO_2 and Al_2O_3; the raw data for the Samar Formation sandstone show that it contains a significant amount, 10 wt%, of Al_2O_3, whereas the limestones contain $\leqslant$1 wt%.

As well as indicating a single-protolith origin, the close relation of fault gouge compositions to those of the wall rocks suggests there were low fluid-rock ratios within the fault system; had there been higher fluid-rock ratios, we would expect to observe much higher discrepancies between wall rock and fault gouge composition due to the differing composition, particularly of trace elements and REEs, of exotic fluids. Although fault systems appear to have been largely isochemical in nature, the possible transformation of feldspar and mica minerals to clays (as suggested by elevated LOI in fault gouges) means that we cannot entirely disregard the presence of some syn- or post-tectonic fluids.

4.5.1.2 Shale gouges

The elemental data also confirm that two distinct types of gouges have been observed in the cores of the studied faults. Whilst there is evidence to support the occurrence of alteration alongside cataclastic processes in the "cataclastic" gouges, we have also shown that the so-called "shale gouges" are distinct from these since they are elementally almost identical to the Ora shale protolith. Combined with the field and microstructural observations made in Chapters 2 and 3, which highlighted the strong foliated nature and relative homogeneity of grain size and appearance, the elemental data confirm that they are most likely to be entrained ('smeared') shale gouges that have undergone very little alteration or brittle comminution. The parity in composition is seen across the major, trace and REE data and it is hard to explain this using any other mechanism for deformation. Elemental data also confirm that the clay-rich gouges at the R12 Fault section are very similar in composition to the Ora shale. In this case, it is more likely that this shale gouge originates from shale beds with the Hazera limestone rather than the Ora shale itself (as the carbonate wall rocks along the R12 road contained interbedded shale and limestone). Once again, the closer similarity to a shale protolith, together with microstructural and mineralogical observations, suggest that it is more likely an entrained shale gouge than cataclastic in nature.

The presence of entrained shale material within fault zones may have significant implications for deformation mechanisms taking place during faulting as the frictional properties of clay minerals found in shales may be vastly different to the aluminosilicates, calcite and quartz that dominate the other protoliths (Byerlee, 1978). Any changes in frictional behaviour will, of course, be dependent

on the specific clay mineralogy of the shales, as well as other factors such as fabric and pore fluid pressure (the possible influence of which is discussed in Chapter 3). The confirmation that the shale gouges present in the Tzefahot and Yehoshafat fault outcrops are the Ora Shale also tells us that this unit is highly mobile and prone to acting in a "ductile" manner, as seen in the extensive macro-scale folding observed (Section 2.6.2.2 and Section 2.6.2.6). Evidence of this is also seen in the presence of shale diapirs in the area (Fig. 2.4b), but the occurrence of such ductile deformation mechanisms within fault zones demonstrates that even within largely brittle fault zones, the Ora Shale is still able to accommodate strain in this way. The relative mobility of this, and other, shales could also mean that relatively little material is needed to have a significant effect on the frictional strength of a fault zone, depending on the mineralogy of the shale.

Entrainment in this way of the highly mobile shales is significant as, along with the potential reduction of friction within the fault zone, its presence may serve to isolate the hangingwall and footwall protoliths from one another, thereby terminating or limiting the involvement of hanging wall rocks in cataclastic processes. Evidence of this may be seen in the similarity of fault gouges to respective basement wall rocks at the Tzefahot and Shelomo faults. Where gouges of the Tzefahot Fault show a very strong correlation to Taba Gneiss wall rocks (R^2 = 0.94, Fig. 4.16a1), gouges of the Shelomo Fault are less similar to the Elat Granite wall rock (R^2 = 0.69, Fig. 4.16b1). There is enrichment in the Shelomo Fault gouges of CaO relative to the granite, suggesting the carbonate wall rocks may have contributed more material to these gouges than at the Tzefahot Fault.

4.5.2 Fault zone mixing

Results of the mixing trend analysis presented in Section 4.4.5 provide further evidence that fault gouges are largely derived from a single protolith. However, they also show that in the case of basement-/clastic-carbonate faults there has been limited carbonate contribution to the fault gouges, as well giving further insight into the possibility of fluid flow across and along faults.

There is no appreciable increase in the abundance of MgO in any of the smectite-rich fault gouges with respect to their assumed basement protoliths (Figs. 4.18 and 4.19), confirming that the source of smectite-forming Mg is not exotic, as proposed in Chapter 3, but must have been released from minerals in the adjacent wall rocks. As very few Mg-bearing minerals have been observed with the fault core gouges (Section 3.3.5), it would appear that all the available Mg has been taken up by authigenic smectite, even in the case of a relatively low displacement fault (the Nizoz Fault, 250 m estimated displacement). This suggests that far from being a process confined to the highest strain (and displacement) faults, that the precipitation of authigenic smectite can occur relatively early in fault zone evolution in the right conditions.

These results are somewhat similar to those obtained by Evans and Chester (1995) in relation to the San Gabriel Fault, southern California, part of the San Andreas Fault system. Here, the authors described neomineralisation of clay and zeolite (smectite and laumonite), in association with cataclasis, within a narrow fault core along a section of the northern branch of the San Gabriel Fault. From coupled microstructural and geochemical analysis they inferred that clay and zeolite mineralisation had taken place under relatively low fluid-rock interaction conditions (or chemically inert fluids, at least), in a system where fluids were localised close to the fault zone.

By comparison, Evans and Chester (1995) also studied a different segment of the same fault and noted a zone that they argued was part of a more open system, due to relative enrichments of immobile elements and depletions of mobile elements in the fault core. Of the closed vs. open system hypothesis present by Evans and Chester (1995), our results much more closely resemble that of a relatively closed system, with fluid-rock interactions limited to the fault core, since we see no precipitation of smectite outside of the fault cores (Section 3.3.5). Other authors (O'Hara and Blackburn, 1989; Goddard and Evans, 1995) have also noted much more significant variations in fault zone geochemistry in the case of open systems, where fluid-rock interactions are high.

4.6 Conclusions

We have demonstrated here the most-likely protoliths for the six fault zones studied, as summarised in Table 4.2. The data show that where cover and basement lithologies are juxtaposed, the basement rocks are the primary source of fault gouge material, although we propose that this is the result of late-stage involvement of the cover rocks in the faulting rather than being for specific mechanical reasons. "Cataclastic" fault core material is believed to have been formed by both cataclastic deformation and localised alteration processes under relatively closed geochemical conditions. We have also confirmed the process of entrainment of shale from the adjacent formation in both low (Yehoshafat) and high (Tzefahot) displacement faults, confirming that the Ora Shale is a highly mobile unit and susceptible to "ductile" deformation even where crystal plastic processes are not involved.

Table 4.2: *Table summarising the inferred primary gouge protolith lithology for each fault zone studied.*

Fault	**Primary protolith**
Tzefahot	Taba Gneiss
Shelomo	Elat Granite
Roded	Roded Quartz Diorite
Nizoz	Amram Rhyolite
Yehoshafat	Ora Shale
R12	Amar Sandstone

Geochemical analysis of fault rocks and their assumed protoliths from three types of lithologically distinct fault zones indicates that fault gouges are derived from predominantly one lithology; in the case of basement-cover faults this is observed to be the basement wall rocks, and in the cover-cover faults from clastic wall rocks. Gouges are much more chemically similar to crystalline basement protolith rocks than to carbonate or clastic equivalents. This is observed across the trends of major, trace and REE concentrations.

In addition to constraining a single, primary protolith for the fault gouges observed within each fault zone, we have also shown that gouge-formation processes are near isochemical and that fluid-rock ratios during faulting are likely to have been low.

5 Discussion, conclusions and suggestions for further research

5.1 Discussion

5.1.1 Introduction

The results presented in Chapters 2 to 4 show that smectite-bearing fault gouges are a common product of faulting in the southern Dead Sea Fault System and that neomineralisation of this clay mineral is likely dependent on wall rock lithology, with most cataclasis occurring during basement against basement faulting. Data show that fluid-rock interactions have been limited and though it has not been possible to quantify the proportion of individual protoliths that contribute to the fine-grained fault gouges, possible mechanisms for mixing will be discussed here. Wall rock lithologies also play an important role where sedimentary cover rocks are involved by the mechanical entrainment of shale into fault zones, providing a second mechanism for introducing smectite into fault cores. The presence of smectite in the shallow portions of faults may have significant implications for their frictional behaviour and this will also be addressed.

5.1.2 The significance of distributed vs. localised deformation in relation to seismic activity of the southern Dead Sea Fault system

Although the studied faults share the common feature of smectite-rich fault cores, whether by neomineralisation or incorporation of smectite-bearing shales from adjacent formations, fault zone architecture is nevertheless variable. Only the Roded Fault has an obvious PSZ within the fault core (Fig. 2.40) and in this case it is only present at one outcrop (Locality B), indicating it is not continuous along the length of the fault (as may be expected, Sibson, 2003). At the other faults, we observe wide fault cores, of several metres width in some cases (Tzefahot and Yehoshafat faults), but with little evidence of slip localisation within the fault core. Whilst this can easily be explained in the case of the Yehoshafat Fault by the mode of shale incorporation proposed in the preceding chapters, the absence of a PSZ in fault zones that preserve other evidence of seismogenic rupture (pulverisation and clay injection at the Shelomo and Tzefahot faults) is somewhat more peculiar.

One possible explanation for the lack of PSZ at the Shelomo and Tzefahot faults is that coseismic slip occurred relatively early in fault history and evidence of such behaviour within the fault core has since been overprinted by structures resulting from later, aseismic creep. This may especially be the case if the PSZ was initially located in the centre of the fault core, rather than at the fault core - damage zone boundary; if a PSZ formed sufficiently early during fault zone evolution, when wall rocks were igneous-metamorphic basement on both sides of the fault, it is possible that the

cataclasis and neomineralisation required to form the observed fine-grained, smectite-rich fault gouge occurred either side of the PSZ and it was eventually incorporated into the gouge. Such an explanation favours an evolution from early, localised slip to later, distributed slip, which may explain the fault zone architecture of the Tzefahot Fault but is rather more problematic in the case of the Shelomo Fault, where multiple localised slip surfaces are found in smectite-bearing gouges (Locality B).

In the case of the Shelomo Fault, though early localisation followed by later distribution of slip and accompanying overprinting of a PSZ may have occurred, discrete slip surfaces within the smectite-bearing gouge indicate a later stage of slip localisation. Evidence of coseismic slip in frictionally-weak clays may be explained by factors such as elevated pore pressure (leading to a reduction in effective normal stress, Saffer et al., 2001), increases in slip velocity (Faulkner et al., 2011) and saturation of clays (Ikari et al., 2007; Bullock et al., 2015), which have been shown to affect the frictional behaviour of clay minerals so that they are not always velocity-strengthening (Saffer and Marone, 2003; Ikari et al., 2009). In such cases, it is expected that the rupture nucleates elsewhere in more conventionally velocity-weakening rocks rather than in the frictionally-weak zone (Bullock et al., 2015). There are, therefore, several factors that may facilitate the propagation of seismogenic ruptures, and associated slip localisation, through material which may otherwise inhibit such behaviour, making it difficult to interpret the specific cause of slip localisation in smectite-bearing gouges. However, we suggest that the localisation onto multiple slip planes within the smectite-bearing gouge, rather than onto a single PSZ, is indicative of wet gouges where the localisation process is by frictional sliding and not cataclasis (Moore and Lockner, 2004, 2007; Bullock et al., 2015).

It may also be the case that no slip localisation, and resulting PSZ, ever occurred in the shallow, smectite-bearing portion of the seismogenic Shelomo and Tzefahot faults. Direct evidence of seismogenic behaviour is only observed at the two largest displacement faults (Shelomo and Tzefahot faults, 1.2 km and 1.4 km, respectively) and possible indication of seismogenic behaviour, in the form of a PSZ, at one further fault (Roded Fault, 0.9 km). Rather than displacement occurring in a localised zone for the entire slipping segment of a fault, it could be possible that displacement becomes distributed when clay-rich gouges are encountered. However, in this scenario with rupture energy distributed across the fault zone, it is less likely that pulverisation of the damage zone would occur as little energy is required for rupture propagation to continue through wet clays with low coefficients of friction (Faulkner et al., 2011). Though this mechanism may apply to later seismic ruptures on mature faults, it is not favoured for the production of pulverisation textures observed in the basement damage zones of the Shelomo and Tzefahot faults.

Although we cannot definitively correlate the evidence of coseismic slip in smectite-bearing fault gouges to a specific fault attribute, the evidence presented shows that fault zone evolution is likely complex and that the presence of frictionally-weak gouges within fault zones does not necessarily predicate the end of seismic activity on a fault. It does, however, suggest that although earthquakes may still propagate through clay-rich regions of the fault zones, they are not likely to nucleate in such regions. This may help to explain why, although the southern DSFS is less seismically active than other faults of similar nature and scale, there are still relatively frequent and moderate earthquakes in the region.

5.1.3 The influence of wall rock lithology and fluid-rock interactions in the development of fault rocks in the shallow, upper crust

It has been demonstrated throughout Chapters 2 to 4 that the nature of fault rocks, specifically fine-grained fault gouges, is strongly influenced by wall rock lithology. In the region to the west of Elat, in southern Israel, the lithostratigraphy is dominated by Precambrian quartzo-feldspathic basement rocks and Cretaceous cover rocks that include carbonates, sandstones and shales.

5.1.3.1 Crystalline basement rocks

Of the six faults studied at the meso-, micro- and elemental-scales, four are major graben-bounding structures (Shelomo, Tzefahot, Roded and Nizoz faults) that juxtapose crystalline basement units in footwalls against carbonate and clastic cover rocks in hanging walls. Fault gouges are very similar in clay mineralogy, major, trace and rare earth element composition in all of these faults, regardless of hanging wall lithology. It is therefore inferred that crystalline basement rocks contribute a greater proportion to fault rock development than the cover lithologies. In footwall damage zones, brittle deformation is by cataclasis, tensile fracturing and pulverisation. Protoliths of damage zone rocks are identifiable at the mesoscale and mineralogy is relatively unchanged from the protolith rocks (Sections 3.3.1 and 3.3.2). Fault cores consist of fault gouge +/- breccia and cataclasite and in the case of gouges, where the deformation is most intense, it is not possible to determine protoliths from mesoscale observations. Microscale observations show that as well as intense comminution of grains, there is also a neomineralised phase of clay material present; the authigenic clay in all cases is Mg-rich smectite.

The most abundant grains in fault core gouges are K-fsp and quartz and they accommodate cataclasis differently; whilst quartz grains typically have few fractures at grain edges, K-fsp grains more commonly have an intensely deformed margin of a few µm. This suggests that K-fsp is more susceptible to fracturing under the conditions of deformation, which agree with low temperature deformation (<300 °C) in a quartz-K-fsp aggregate rock. The preferred comminution of K-fsp over quartz may serve to not only more rapidly reduce grain size within the fault rock than if stronger minerals such as quartz or mafic minerals were the dominant phase/s, but also to increase the surface area of feldspar available for reaction. It has therefore been proposed that the breakdown of feldspars is a key initial stage in the precipitation authigenic smectite Section 3.4.3. It is also likely that initial cataclasis would result in dilatancy and increased permeability within the fault zone, allowing the ingress of fluids necessary to fuel reactions leading to the neomineralisation of smectite. The combination of: *(1)* preferential fracturing; *(2)* resulting increased permeability; and (3) the increased availability of feldspar reaction surfaces may mean that the prevalence of highly-felsic rocks in the region is an essential factor in the propensity for the formation of smectite-bearing gouges in these faults. However, it should be noted that previous studies (e.g. Haines and van der Pluijm, 2012) have not found smectite to be the principal authigenic clay mineral resulting from faulting in quartzo-feldspathic rocks. They instead found illite-smectite in such fault zones, and smectite was present as a retrograde alteration product of a chloritic gouge, indicating factors other than simply wall rock lithology may also play a part in the development of clay-rich fault gouges (see Section 5.1.3.3).

It is also interesting to note that previous studies that have reported the presence of authigenic, Mg-rich smectite (saponite) have interpreted the source of Mg as mafic (serpentinite) bodies adjacent to the fault zone (e.g. Moore and Rymer, 2012), yet there are no such Mg-bearing rocks in the southern region of Israel/northern Sinai that could act as the source of Mg. Whilst the results of our geochemical analyses indicate there is no additional Mg in the fault core gouges than is found in the most biotite-abundant basement protoliths (Taba Gneiss and Roded Quartz Diorite), there is also a much lower concentration of Mg in these rocks than is found in serpentinites, so we are left with a paradox of creating an Mg-rich clay minerals, from relatively Mg-poor protoliths but without an obvious source for the addition of any further Mg. Although it is difficult to quantify the proportion of smectite in the cataclastic gouges, due to the intermixing with mechanically-derived gouge, field evidence of clay-rich fault zones coupled with XRD evidence that smectite is the only authigenic clay mineral produced during faulting suggest there are significant volumes of it in the basement against cover fault zones.

5.1.3.2 Cover rocks

Cover rocks appear to play a relatively minor role in the development of fault core gouges; there is a much lower agreement in elemental composition between the gouges and cover rocks than between gouges and basement rocks (Section 4.4.4). Nevertheless, this is not necessarily simply controlled by lithology as the cover lithologies are only likely to have been juxtaposed against basement-involved faults at a late stage in their displacement history. However, in the case of cover against cover faults it does appear that a single protolith is the main contributor to fault gouges and there is still relatively little mechanical mixing of foot- and hanging wall rocks. Clastic rocks appear to preferentially contribute to the formation of cataclastic gouges, but only one carbonate against clastic cover rock has been studied here (R12 Fault) so we cannot say with certainty that this observation is universal.

The effect of shales, as either a stratigraphic unit in their own right (the Ora shale) or as part of a carbonate unit (the Grofit limestone) may be classed as equally important in the development of fault core gouges, but the processes involved here are very different. Whereas sandstone and carbonates are observed to deform by shear fracturing and cataclasis, deformation within shales is typically confined to frictional sliding (a few, isolated, shear fractures are present but are not common) along a pre-existing foliation created by alignment of clay minerals during deposition. Shales are easily incorporated into fault cores if they are in a favourable position relative to the propagating fault plane (the fault must directly cut through a shale bed/unit) meaning the potential for influence on fault behaviour is limited to localised segments of faults.

5.1.3.3 Other factors affecting the development of smectite-rich fault gouges

Although wall-rock lithology is the principal controlling factor of the nature of fault gouges, they can also be influenced by other factors such as depth of faulting (and associated temperature) and the presence, composition and timing of fluids.

Depth and temperature Smectite is recognised as being stable only at low temperatures and the process of conversion to illite and chlorite with increasing temperature is well-documented. An increase in the proportion of illite in an illite-smectite mixed layer material has been observed at temperatures as low as 40 °C (Day-Stirrat et al., 2010) and the fact that all of the smectite in the studied samples is well-formed and shows no signs of illitisation suggests a very low-temperature environment. A very shallow fault system may explain the differences in results between this studied and that of Haines and van der Pluijm (2012), as the presence of illite-smectite as the product of faulting in quartzo-feldspathic rocks they observed may be the result of a slightly elevated temperature due to increased depth during faulting.

Fluids Whilst we have been unable to determine the source of fluids involved in the deformation that produced the studied faults, it is nevertheless recognised that for the neomineralisation of smectite to occur, the presence of some fluids is essential to facilitate the chemical reactions that allowed this, and the precipitation of smectite in this case is the result of the specific composition of these fluids, as well as wall rock composition. It is likely that any slight variation in the composition of fluids, even though fluid-rock interactions are predicted to have been low, would lead to a different evolution of fault core mineralogy. For example, K-rich fluids may have resulted in the precipitation of illite rather than smectite or Fe-rich fluids montmorillonite rather than Mg-rich smectite.

5.1.4 Fault zone development and mixing

The geochemical analyses carried out in Chapter 4 support the hypotheses proposed in Chapter 2 that the cataclastic fault gouges are largely derived from a single protolith, although it has not been possible to determine the exact proportions, and that where shale gouges are present, they are consistently derived from a shale unit in the adjacent wall rock stratigraphy. These findings would seem to suggest that very little carbonate material should be found in the fault cores of major graben-bounding faults that juxtapose carbonate wall rocks against those of the crystalline basement. This is not the case. Rather, there appears to be a size dependency on the presence of carbonate clasts within the cataclastic gouges, with those below the cm-scale very rare and the largest up to 2 m in length (at the Tzefahot Fault). This suggests that rather than incorporation by gradual fracturing of wall rocks adjacent to the fault core, carbonate material is incorporated as relatively large blocks. The lack of clasts apparent at the microscale supports the proposal that the cover sequences of rocks only became involved in the fault relatively late during their development. The lack of comminution suggests either there was not sufficient time for carbonate clasts to undergo substantial cataclasis, or that the already well-developed, smectite-rich gouges inhibited cataclasis because strain was accommodated by frictional sliding in the weak gouges surrounding the clasts.

The question remains of how relatively large clasts are incorporated not only into the outer zone of the fault core that is closest to carbonate wall rocks/damage zone, but also into the central part of the fault core, as is seen at the Tzefahot Fault exposure (Section 2.6.2.2). Sibson (2003) describes "anastomosing shears" in damage zones and such structures, possibly an arrangement of Riedel-type (R, R', P) shears, may cause relatively large segments of wall rocks to become

incorporated into a developed fault core (Fig. 5.1-4,4.1), much as small fragments of individual grains spall away from the parent grain during cataclasis at the microscale. In order for clasts to move away from the fault core - damage zone boundary, it is envisaged that continuing creep of the clay-rich gouge, behaving in a relatively "ductile" manner, could lead to the clasts becoming mixed into the fault core gouge (Fig. 5.1-4.2).

It is evident from the asymmetric, sigmoidal shape of these clasts that some shearing continued to occur after their incorporation. In addition, the precipitation of authigenic smectite in the carapace of the large carbonate clast within the core of the Tzefahot Fault indicates that the chemical conditions were still favourable for the neomineralisation of smectite later in fault zone evolution, despite the mechanism for this being driven by fluid-assisted diffusive mass transfer after dissolution at grain contacts (Fig. 3.67) rather than by initial cataclasis. It is thought that the effect of shale incorporation into the fault zone would have the same effect of halting the majority of cataclastic deformation in other rock units, as described in Section 3.4.2 and Fig. 3.95 (Fig. 5.1-3a-4.2a).

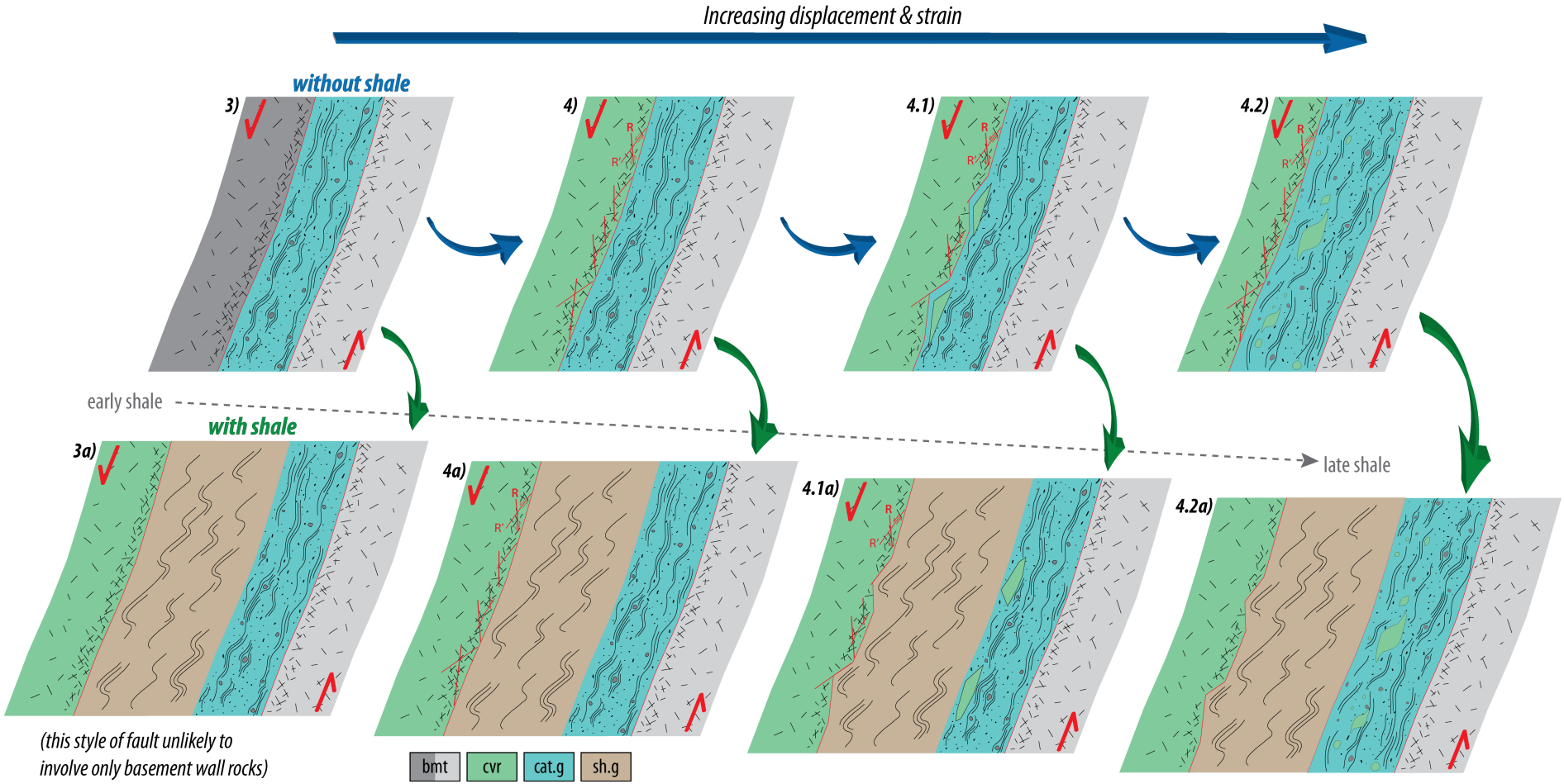

Figure 5.1: *Schematic model of fault zone development, expanding on final two stages (3 & 4) proposed in previous models (Figs. 2.64 and 3.95): the formation of R and R' shears (Sibson, 2003) in the hanging wall damage zone (4) allows the shearing off of relatively large clasts of carbonate material (4.1). It is possible that this happens preferentially in sedimentary hanging wall rocks and not the crystalline basement due to pre-existing weaknesses, such as bedding, that are not present in the basement. Creep in frictionally weak, smectite-bearing gouges allows for distribution of these clasts within the fault gouge without further substantial cataclasis (4.2). The influence of entrained shale is expected to be as described in Section 3.4.2 and Fig. 3.95, and inhibit further cataclastic deformation within the fault core when it is incorporated (3a - 4.2a).*

5.2 Conclusions

The importance of using a multi-disciplinary approach when assessing the origin and evolution of fine-grained fault rocks

1. Although field (mesoscale) and microstructural (microscale) studies are common research methods in the field of structural geology, the importance of using laboratory methods other than optical or scanning electron microscopy, such as XRD, for mineralogical identification and the further use of mass spectrometry to determine elemental composition, has been demonstrated here. Whilst the use of XRD for identification of clay phases in fault rocks has increasingly been used over the last two decades (e.g. Vrolijk and van der Pluijm, 1999; Saffer and Marone, 2003; Collettini et al., 2009; Carpenter et al., 2011; Haines and van der Pluijm, 2012; Schleicher et al., 2012; Buatier et al., 2015), relatively few authors have sought to investigate the geochemical history of fault zones by assessing elemental compositions and those that have have not combined this with XRD studies, either because techniques were not widely available at the time (e.g. Evans and Chester, 1995) or because clay minerals were not abundant in the fault zones (e.g. Imber, 1998; Jefferies, 2006). It is important to consider the wide range of variables that may influence our interpretation of fault zone mechanisms and processes, and recognise that it is not always possible to accurately constrain fault zone evolution using a limited number of techniques. The use of elemental-scale analysis has proved important in this study, in order to resolve that deformation took place in a relatively closed geochemical environment. Had the study not been extended to this level, we could have concluded it likely that the origin of fluids was the overlying Gulf of Elat-Aqaba marine basin or the underlying mantle, whereas in actual fact this is unlikely to be the case. The use of mean gouge compositions (Section 4.4.4) and mixing analysis (Section 4.4.5) also allowed for the determination of the predominantly single-protolith origin that would not have been possible without the use of mass spectrometry.

Field relationships

2. The exhumed faults studied, situated to the west of the active DSF, form part of the palaeo-DSFS and were active in an extension-dominated transtensional zone. A simple stress inversion suggests that deformation may have be partitioned, with strike-slip displacement dominating in the centre of the broad fault zone and dip-slip at the margins. This is in agreement with the work of De Paola (2004), which focussed on recent movements, suggesting the regional stress regime has been relatively stable since the mid-Mioence (Section 2.7.2).
3. With the exception of the antithetic Nizoz Fault, the measured faults account for <5 % of the total displacement (105 km) of the DSF, suggesting displacement localised onto the main fault trace relatively early in its history (Section 2.6.1).
4. There is no simple relationship between fault displacement and fault core width or material present. One of the lowest displacement faults (Yehoshafat Fault) has one of the widest fault cores, whilst the highest displacement fault (Shelomo Fault) has a relatively narrow fault core. Rather, fault core architecture appears to be much more strongly linked to wall rock lithology

and the incorporation of shale gouge, in particular, into a fault zone may lead to a wide fault core forming irrespective of the total displacement (Section 3.3.1.11).

Smectite-rich fault gouges

5. Fault core gouges can be distinguished as shale gouges and cataclastic gouges. The shale gouges have undergone little to no cataclastic deformation and are formed almost exclusively by frictional sliding, whilst cataclastic gouges have undergone intense cataclastic deformation coupled with neomineralisation of an Mg-rich smectite (Section 3.4.1).
6. The precipitation of Mg-rich smectite as the authigenic clay phase is the result of neomineralisation within a relatively closed geochemical system. Fluid-rock interactions are deemed to be low since there is little flux in or out of the system of elements relative to the wall rocks of the footwall and/or hanging wall (Section 5.1.3).

Fault zone protoliths

7. The two types of fault core gouges are largely the product of a single protolith. Footwall basement rocks are the main contributors to cataclastic gouges of graben-bounding faults whilst the same can be said for clastic cover rocks in intra-graben faults. Shale gouges are almost entirely derived from shales in the local stratigraphy, whether this is the Ora shale formation or shale beds within carbonate units (Section 4.5.1).
8. Although we have shown that cataclastic gouges are predominantly derived from a single protolith, we have been unable to quantify the exact mixing proportions of foot- and hanging wall rocks. This is believed to be the result of more than two protoliths making some contribution to these gouges, rendering a mixing model that uses only two protoliths inappropriate (Section 4.5.2). In principle, it should be possible to incorporate further protoliths into the method described by Evans and Chester (1995). However, this would require better constraints on all *possible* protoliths, which is not feasible for faults that may have propagated through a number of basement and cover units. In addition, there are likely to be significant changes in the elemental composition even within single sedimentary formations due to changes in depositional environment, for example, which may be sufficient to skew the results of a mixing model even if there are only two protoliths.

5.3 Suggestions for further research

5.3.1 Assessment of Quaternary - Recent faulting

The southern DSFS is an active fault zone (Section 2.3.3, and references therein) and there are numerous exposures of Quaternary - Recent sediments both in coastal sections west of Elat and in dry river beds further inland within the area of study (Fig. 2.4b). It would be useful to make an assessment of structures within these young sediments to determine how they fit with both recent regional-scale structures and the Miocene-age structures that have been studied here.

Documenting these small-scale structures would provide a link between the Miocene-age faulting studied here and the present day behaviour of large, seismogenic faults that are monitored via the seismograph network. This would lead to a greater understanding of the behaviour of both small- and large-scale structures relating to the southern DSFS over time.

5.3.2 Refined approach to fault zone mixing analysis

It is likely that to accurately quantify the mixing proportions of multiple protoliths, a more comprehensive analysis of elemental concentrations of the full range of country rocks in the area would need to be undertaken. However, using the statistical techniques proposed here could lead to a prohibitively complex solution. One way to mitigate against this would be to find exposed fault tip zones or low displacement faults, where displacement is relatively small and the protolith wall rocks are known, to test the statistical approach to mixing analysis used here. Since the lowest displacement faults studied here (the Yehoshafat and R12 faults) have entrained shale in their fault cores, it would be useful to find further examples of low displacement faults where cataclastic processes have dominated and a small amount of mixing is likely to have occurred. Analysis of a range of relatively low displacement faults in the basement would provide constraints on the degree of mixing between two protoliths. The reason for choosing basement rather than cover faults is because it is thought to be in the basement that the significant proportion of cataclasis and mixing has taken place (Fig. 5.1). Faults that may be suitable for this kind of analysis are those found in the Elat Block immediately to the east of the Yotam Graben (Fig. 2.4b) as they are low displacement (small offsets of dykes can be seen, Fig. 2.4b) and likely to involve only the two lithologies that are juxtaposed at the surface.

Although this method would not give quantitative mixing results for the larger displacement faults studied here, it would be possible to evaluate the behaviour of basement lithologies in the early stages of fault development and create a basis for subsequent analyses of large displacement faults. For example, it would be possible to compare the elemental compositions of fault gouges from basement against basement faults and basement against cover faults and quantify the contribution from sedimentary cover rocks as a whole in the larger faults, rather than the individual lithological units as attempted here. It would be particularly useful to find low displacement faults that contained authigenic smectite in their fault cores. In such cases, a comparison of the elemental composition of the smectite-bearing fault gouges formed in low displacement faults to the gouges found in higher displacement faults may help better constrain potential protoliths and allow a more targeted statistical analysis.

5.3.3 Stable isotope geochemistry

Though it has been shown that neomineralised smectite is unlikely to have an exotic source of Mg, we have not definitively identified the origin of fluids involved in the precipitation of this authigenic clay phase and analysis of the stable isotope composition of fault gouges may go some way to addressing this remaining question. Although previous fault zone studies have analysed the isotopic concentration of $\delta^{18}O$ and $\delta^{13}C$ in carbonate veins (e.g. Kerrich, 1986; Kenis et al.,

2000; Kirschner and Kennedy, 2001; Smith et al., 2011b), which are rarely present in the fault cores here, techniques used in studies of clay diagenesis may be applicable for isotopic analysis of the gouges in this study. Comparison of oxygen ($\delta^{18}O$) and hydrogen (δD) isotope concentrations of clay minerals against known compositions of different types of water (e.g. meteoric, marine, hydrothermal) can be used to determine fluid source, in much the same way that concentration of $\delta^{18}O$ and $\delta^{13}C$ from carbonate material is used for the same purpose (e.g. Savin, 1967; Savin and Epstein, 1970; Sheppard and Gilg, 1996). In addition, the fractionation of $\delta^{18}O$ and δD can be used to estimate the temperature of formation (Delgado and Reyes, 1996). This technique would be easily applicable to the authigenic clay gouges that contain only one clay phase (smectite), but would be more complex for analysis of fluid-shale interactions, where the rock is composed of multiple clay phases since the fractionation behaviour of different clay minerals varies. To carry out isotopic analysis of the authigenic smectite in this scenario, it would first need to be separated from the other clay minerals.

Isotopic analysis of authigenic smectite could also be combined with $\delta^{18}O$ and $\delta^{13}C$ analysis of calcite veins in carbonate damage zones (Shelomo and Tzefahot faults) to gain further insights into the evolution of fluid flow within the fault zones over time, since the carbonate cover rocks are thought to be incorporated into the fault zones relatively late in their history (Section 5.1.3). Further constraints on the timing of these Ca-bearing fluids may be achieved by conducting U-Th dating, as performed by Nuriel et al. (2012a,b) in the DSFS in central and northern Israel.

5.3.4 Friction testing of gouges

Published data on the low frictional strength of smectite, particularly when wet (e.g. Saffer and Marone, 2003; Moore and Lockner, 2007; Bullock et al., 2015) have been used to infer the low frictional strength of the smectite-bearing fault gouges of the present study, but it would be useful to conduct friction testing on these materials. Although smectite is the only authigenic mineral present in the gouges, their bulk composition is not pure smectite as they also contain variable amounts of other minerals, predominantly quartz, feldspars (K-fsp and plagioclase) and calcite. By conducting friction testing, it would be possible to constrain the friction coefficient of these polymineralic gouges under a range of conditions (e.g. dry and wet; at high and low slip velocities), and therefore characterise their possible behaviours under such conditions. The work of Bullock et al. (2015) recently showed that synthetic smectite-bearing gouges do not always act as velocity-strengthening materials under certain conditions (when wet) and a similar investigation of natural gouges would further our understanding of the frictional behaviour of these faults. It would be beneficial to conduct these experiments on intact cores of the gouges, in order to account for fabric effects, but extraction of such samples, intact and without the addition of resin, may prove challenging.

References

Albarède, F. (2003). *Geochemistry: An Introduction*. Cambridge University Press.

Allen, M. B. and Armstrong, H. A. (2008). Arabia–Eurasia collision and the forcing of mid-Cenozoic global cooling. *Palaeogeography, Palaeoclimatology, Palaeoecology*, 265(1-2):52–58.

Ambraseys, N. N. and Barazangi, M. (1989). The 1759 Earthquake in the Bekaa Valley: Implications for earthquake hazard assessment in the Eastern Mediterranean Region. *Journal of Geophysical Research: Solid Earth*, 94(B4):4007–4013.

Ambraseys, N. N. and Melville, C. P. (1988). An analysis of the eastern Mediterranean earthquake of 20 May 1202. In Lee, W. H. K., Meyers, H., and Shimazaki, editors, *Historical seismograms and earthquakes of the world*, page 181–200. Academic Press, Inc.

Amit, R., Zilberman, E., Enzel, Y., and Porat, N. (2002). Paleoseismic evidence for time dependency of seismic response on a fault system in the southern Arava Valley, Dead Sea rift, Israel. *Geological Society of America Bulletin*, 114(2):192–206.

Amit, R., Zilberman, E., Porat, N., and Enzel, Y. (1999). Relief inversion in the Avrona playa as evidence of large-magnitude historical earthquakes, southern Arava Valley, Dead Sea rift. *Quaternary Research*, 52(1):76–91.

Avni, Y., Bartov, Y., Garfunkel, Z., and Ginat, H. (2000). Evolution of the Paran drainage basin and its relation to the Plio-Pleistocene history of the Arava Rift western margin, Israel. *Israel Journal of Earth Sciences*, 49(4):215–238.

Balsamo, F., Aldega, L., De Paola, N., Faoro, I., and Storti, F. (2014). The signature and mechanics of earthquake ruptures along shallow creeping faults in poorly lithified sediments. *Geology*, 42(5):435–438.

Banfield, J. F. and Eggleton, R. A. (1988). Transmission electron microscope study of biotite weathering. *Clays and Clay Minerals*, 36(1):47–60.

Banfield, J. F. and Eggleton, R. A. (1990). Analytical transmission electron microscope studies of plagioclase, muscovite, and K-feldspar weathering. *Clays and Clay Minerals*, 38(1):77–89.

Barka, A., Akyüz, H. S., Altunel, E., Sunal, G., Çakir, Z., Dikbas, A., Yerli, B., Armijo, R., Meyer, B., Chabalier, J. B. d., Rockwell, T., Dolan, J. R., Hartleb, R., Dawson, T., Christofferson, S., Tucker, A., Fumal, T., Langridge, R., Stenner, H., Lettis, W., Bachhuber, J., and Page, W. (2002). The Surface Rupture and Slip Distribution of the 17 August 1999 İzmit Earthquake (M 7.4), North Anatolian Fault. *Bulletin of the Seismological Society of America*, 92(1):43–60.

Bartov, Y., Steinitz, G., Eyal, M., and Eyal, Y. (1980). Sinistral movement along the Gulf of Aqaba — its age and relation to the opening of the Red Sea. *Nature*, 285(5762):220–222.

Be'eri-Shlevin, Y., Katzir, Y., and Whitehouse, M. (2009). Post-collisional tectonomagmatic evolution in the northern Arabian–Nubian Shield: time constraints from ion-probe U–Pb dating of zircon. *Journal of the Geological Society*, 166(1):71–85.

Ben-Avraham, Z. (1985). Structural framework of the gulf of Elat (Aqaba), northern Red Sea. *Journal of Geophysical Research: Solid Earth (1978–2012)*, 90(B1):703–726.

Ben-Avraham, Z., Almagor, G., and Garfunkel, Z. (1979). Sediments and structure of the Gulf of Elat (Aqaba)—northern Red Sea. *Sedimentary Geology*, 23(1):239–267.

Ben-Avraham, Z., Garfunkel, Z., and Lazar, M. (2008). Geology and Evolution of the Southern Dead Sea Fault with Emphasis on Subsurface Structure. *Annual Review of Earth and Planetary Sciences*, 36(1):357–387.

Ben-Menahem, A. (1991). Four thousand years of seismicity along the Dead Sea Rift. *Journal of Geophysical Research: Solid Earth*, 96(B12):20195–20216.

Ben-Zion, Y. (2001). Dynamic ruptures in recent models of earthquake faults. *Journal of the Mechanics and Physics of Solids*, 49(9):2209–2244.

Ben-Zion, Y. and Huang, Y. (2002). Dynamic rupture on an interface between a compliant fault zone layer and a stiffer surrounding solid. *Journal of Geophysical Research: Solid Earth*, 107(B2):ESE 6–1.

Ben-Zion, Y. and Sammis, C. G. (2003). Characterization of Fault Zones. *pure and applied geophysics*, 160(3-4):677–715.

Bender, F. (1974). *Explanatory notes on the geological map of the Wadi Araba, Jordan*. Schweizerbart.

Bentor, Y. (1985). The crustal evolution of the Arabo-Nubian Massif with special reference to the Sinai Peninsula. *Precambrian Research*, 28(1):1–74.

Beyth, M., Eyal, M., and Garfunkel, Z. (2013). Geological Map of Israel. Sheet 26 Elat, scale 1:50,000.

Beyth, M., Eyal, Y., and Garfunkel, Z. (2011). The geology of the Elat sheet: Explanatory notes (Report No. GSI/22/2011). Technical Report GSI/22/2011, Geological Survey of Israel, Jerusalem.

Beyth, M., Eyal, Y., and Garfunkel, Z. (2014). The geology of the northern tip of the Arabian–Nubian Shield. *Journal of African Earth Sciences*.

Beyth, M. and Heimann, A. (1999). The youngest igneous event in the crystalline basement of the Arabian-Nubian Shield, Timna Igneous Complex. *Israel Journal of Earth Sciences*, 48(2):113–120.

Bielski, M. (1982). *Stages in the evolution of the Arabian-Nubian Massif in Sinai*. PhD thesis, Hebrew University, Jerusalem.

Billi, A., Salvini, F., and Storti, F. (2003). The damage zone-fault core transition in carbonate rocks: implications for fault growth, structure and permeability. *Journal of Structural Geology*, 25(11):1779–1794.

Blenkinsop, T. G. (1991). Cataclasis and processes of particle size reduction. *Pure and Applied Geophysics*, 136(1):59–86.

Brune, J. N. (2001). Fault normal dynamic loading and unloading: an explanation for "non-gouge" rock powder and lack of fault-parallel shear bands along the San Andreas fault. *EOS Trans. Am. Geophys. Union*, 82:47.

Buatier, M. D., Cavailhes, T., Charpentier, D., Lerat, J., Sizun, J. P., Labaume, P., and Gout, C. (2015). Evidence of multi-stage faulting by clay mineral analysis: Example in a normal fault zone affecting arkosic sandstones (Annot sandstones). *Journal of Structural Geology*, 75:101–117.

Bullock, R. J., De Paola, N., and Holdsworth, R. E. (2015). An experimental investigation into the role of phyllosilicate content on earthquake propagation during seismic slip in carbonate faults. *Journal of Geophysical Research: Solid Earth*, 120(5):2015JB011914.

Bullock, R. J., De Paola, N., Holdsworth, R. E., and Trabucho-Alexandre, J. (2014). Lithological controls on the deformation mechanisms operating within carbonate-hosted faults during the seismic cycle. *Journal of Structural Geology*, 58:22–42.

Butler, R. W. H., Spencer, S., and Griffiths, H. M. (1998). The structural response to evolving plate kinematics during transpression: evolution of the Lebanese restraining bend of the Dead Sea Transform. *Geological Society, London, Special Publications*, 135(1):81–106.

Byerlee, J. (1978). Friction of rocks. *Pure and applied Geophysics*, 116(4-5):615–626.

Caine, J. S., Evans, J. P., and Forster, C. B. (1996). Fault zone architecture and permeability structure. *Geology*, 24(11):1025.

Cann, J. R. (1970). Rb, Sr, Y, Zr and Nb in some ocean floor basaltic rocks. *Earth and Planetary Science Letters*, 10(1):7–11.

Carpenter, B., Marone, C., and Saffer, D. (2011). Weakness of the San Andreas Fault revealed by samples from the active fault zone. *Nature Geoscience*, 4(4):251–254.

Chester, F. and Logan, J. (1986). Implications for mechanical properties of brittle faults from observations of the Punchbowl fault zone, California. *Pure and Applied Geophysics*, 124(1-2):79–106.

Chester, F. and Logan, J. (1987). Composite planar fabric of gouge from the Punchbowl fault, California. *Journal of Structural Geology*, 9(5):621–634.

Chester, F. M. and Chester, J. S. (1998). Ultracataclasite structure and friction processes of the Punchbowl fault, San Andreas system, California. *Tectonophysics*, 295(1):199–221.

Chester, F. M., Evans, J. P., and Biegel, R. L. (1993). Internal structure and weakening mechanisms of the San Andreas Fault. *Journal of Geophysical Research*, 98(B1):771.

Chu, D. and Gordon, R. G. (1998). Current plate motions across the Red Sea. *Geophysical Journal International*, 135(2):313–328.

Collettini, C. and Holdsworth, R. E. (2004). Fault zone weakening and character of slip along low-angle normal faults: insights from the Zuccale fault, Elba, Italy. *Journal of the Geological Society*, 161(6):1039–1051.

Collettini, C., Niemeijer, A., Viti, C., and Marone, C. (2009). Fault zone fabric and fault weakness. *Nature*, 462(7275):907–10.

Courtillot, V., Armijo, R., and Tapponnier, P. (1987). Kinematics of the Sinai triple junction and a two-phase model of Arabia-Africa rifting. *Geological Society, London, Special Publications*, 28(1):559–573.

Cowgill, E., Arrowsmith, J. R., Yin, A., Xiaofeng, W., and Zhengle, C. (2004). The Akato Tagh bend along the Altyn Tagh fault, northwest Tibet 2: Active deformation and the importance of transpression and strain hardening within the Altyn Tagh system. *Geological Society of America Bulletin*, 116(11):1443–1464.

Day-Stirrat, R. J., Milliken, K. L., Dutton, S. P., Loucks, R. G., Hillier, S., Aplin, A. C., and Schleicher, A. M. (2010). Open-system chemical behavior in deep Wilcox Group mudstones, Texas Gulf Coast, USA. *Marine and Petroleum Geology*, 27(9):1804–1818.

De Paola, N. (2004). *The structural evolution of transtensional basins and rifted margins*. PhD thesis, University of Durham.

De Paola, N., Holdsworth, R. E., McCaffrey, K. J. W., and Barchi, M. R. (2005). Partitioned transtension: an alternative to basin inversion models. *Journal of Structural Geology*, 27(4):607–625.

Delgado, A. and Reyes, E. (1996). Oxygen and hydrogen isotope compositions in clay minerals: A potential single-mineral geothermometer. *Geochimica et Cosmochimica Acta*, 60(21):4285–4289.

Dor, O., Ben-Zion, Y., Rockwell, T. K., and Brune, J. (2006). Pulverized rocks in the Mojave section of the San Andreas Fault Zone. *Earth and Planetary Science Letters*, 245(3-4):642–654.

Druckman, Y., Weissbrod, T., and Garfunkel, Z. (1993). Sheets 25, 26: Yotvata and Elat, Geological Map of Israel 1: 100,000. *The Geological Survey of Israel, Jerusalem*.

Dziewonski, A. M., Chou, T.-A., and Woodhouse, J. H. (1981). Determination of earthquake source parameters from waveform data for studies of global and regional seismicity. *Journal of Geophysical Research: Solid Earth*, 86(B4):2825–2852.

Ebinger, C. J. and Casey, M. (2001). Continental breakup in magmatic provinces: An Ethiopian example. *Geology*, 29(6):527–530.

Ekström, G., Nettles, M., and Dziewoński, A. M. (2012). The global CMT project 2004–2010: Centroid-moment tensors for 13,017 earthquakes. *Physics of the Earth and Planetary Interiors*, 200–201:1–9.

Engelder, J. T. (1974). Cataclasis and the Generation of Fault Gouge. *Geological Society of America Bulletin*, 85(10):1515–1522.

Ernoul, Le Trésorier, B. l., and de Mas Latrie, L. (1871). *Chronique d'Ernoul et de Bernard le Trésorier*. Renouard.

Evans, J. P. (1988). Deformation mechanisms in granitic rocks at shallow crustal levels. *Journal of Structural Geology*, 10(5):437–443.

Evans, J. P. and Chester, F. M. (1995). Fluid-rock interaction in faults of the San Andreas system: Inferences from San Gabriel fault rock geochemistry and microstructures. *Journal of Geophysical Research*, 100(B7):13007–13020.

Evans, J. P., Forster, C. B., and Goddard, J. V. (1997). Permeability of fault-related rocks, and implications for hydraulic structure of fault zones. *Journal of Structural Geology*, 19(11):1393–1404.

Eyal, M., Eyal, Y., Bartov, Y., and Steinitz, G. (1981). The tectonic development of the western margin of the Gulf of Elat (Aqaba) rift. *Tectonophysics*, 80(1):39–66.

Eyal, M., Litvinovsky, B. A., Katzir, Y., and Zanvilevich, A. N. (2004). The Pan-African high-K calc-alkaline peraluminous Elat granite from southern Israel: geology, geochemistry and petrogenesis. *Journal of African Earth Sciences*, 40(3–4):115–136.

Eyal, Y. (1996). Stress field fluctuations along the Dead Sea rift since the middle Miocene. *Tectonics*, 15(1):157–170.

Eyal, Y., Eyal, M., Bartov, Y., Steinitz, G., and Folkman, Y. (1986). The origin of the Bir Zreir rhomb-shaped graben, eastern Sinai. *Tectonics*, 5(2):267–277.

Eyal, Y. and Reches, Z. (1983). Tectonic analysis of the Dead Sea Rift Region since the Late-Cretaceous based on mesostructures. *Tectonics*, 2(2):167–185.

Fagereng, k., Smith, Z., Rowe, C. D., Makhubu, B., and Sylvester, F. Y. G. (2014). Stress, strain, and fault behavior at a thrust ramp: Insights from the Naukluft thrust, Namibia. *Journal of Structural Geology*, 58:95–107.

Faulkner, D. R., Jackson, C. A. L., Lunn, R. J., Schlische, R. W., Shipton, Z. K., Wibberley, C. A. J., and Withjack, M. O. (2010). A review of recent developments concerning the structure, mechanics and fluid flow properties of fault zones. *Journal of Structural Geology*, 32(11):1557–1575.

Faulkner, D. R., Lewis, A. C., and Rutter, E. H. (2003). On the internal structure and mechanics of large strike-slip fault zones: field observations of the Carboneras fault in southeastern Spain. *Tectonophysics*, 367(3-4):235–251.

Faulkner, D. R., Mitchell, T. M., Behnsen, J., Hirose, T., and Shimamoto, T. (2011). Stuck in the mud? Earthquake nucleation and propagation through accretionary forearcs. *Geophysical Research Letters*, 38(18).

Faulkner, D. R., Mitchell, T. M., Rutter, E. H., and Cembrano, J. (2008). On the structure and mechanical properties of large strike-slip faults. *Geological Society, London, Special Publications*, 299(1):139–150.

Faulkner, D. R. and Rutter, E. H. (2001). Can the maintenance of overpressured fluids in large strike-slip fault zones explain their apparent weakness? *Geology*, 29(6):503.

Faure, G. (1998). *Principles and applications of geochemistry : a comprehensive textbook for geology students*. Prentice Hall.

Floyd, P. A. and Winchester, J. A. (1975). Magma type and tectonic setting discrimination using immobile elements. *Earth and Planetary Science Letters*, 27(2):211–218.

Fossen, H. (2010). *Structural Geology*. Cambridge University Press.

Foster, A. N. and Jackson, J. A. (1998). Source parameters of large African earthquakes: implications for crustal rheology and regional kinematics. *Geophysical Journal International*, 134(2):422–448.

Freund, R. (1965). A model of the structural development of Israel and adjacent areas since Upper Cretaceous times. *Geological Magazine*, 102(03):189–205.

Freund, R., Zak, I., and Garfunkel, Z. (1968). Age and rate of the sinistral movement along the Dead Sea Rift. *Nature*, page 253–255.

Friedman, G. M. (1968). Geology and Geochemistry of Reefs, Carbonate Sediments, and Waters, Gulf of Aqaba (Elat), Red Sea. *Journal of Sedimentary Research*, 38(3):895–919.

Garfunkel, Z. (1970). *The tectonics of the western margins of the southern Arava: a contribution to the understanding of rifting*. PhD thesis, Hebrew University.

Garfunkel, Z. (1980). Contribution to the geology of the Precambrian of the Elat area. *Israel Journal of Earth Sciences*, 29:25–40.

Garfunkel, Z. (1981). Internal structure of the Dead Sea leaky transform (rift) in relation to plate kinematics. *Tectonophysics*, 80(1):81–108.

Garfunkel, Z. (1988). The pre-Quaternary geology of Israel. *Monographiae biologicae*, 62:7–34.

Garfunkel, Z. (1999). History and paleogeography during the Pan-African orogen to stable platform transition: reappraisal of the evidence from Elat area and the northern Arabian-Nubian Shield. *Israel Journal of Earth Sciences*, 48(0):135–157.

Garfunkel, Z. and Ben-Avraham, Z. (1996). The structure of the Dead Sea basin. *Tectonophysics*, 266(1):155–176.

Garfunkel, Z., Eyal, Y., Eyal, M., Weissbrod, T., Bakler, N., Shimron, A., Peltz, S., Gutkin, V., Bartov, Y., and Druckman, Y. (2000). Geological map of the northern Gulf of Elat area. *Geological Survey of Israel, Jerusalem*.

Garrels, R. M. (1984). Montmorillonite/illite stability diagrams. *Clays and Clay Minerals*, 32(3):161–166.

Goddard, J. V. and Evans, J. P. (1995). Chemical changes and fluid-rock interaction in faults of crystalline thrust sheets, northwestern Wyoming, U.S.A. *Journal of Structural Geology*, 17(4):533–547.

Gomez, F., Karam, G., Khawlie, M., McClusky, S., Vernant, P., Reilinger, R., Jaafar, R., Tabet, C., Khair, K., and Barazangi, M. (2007). Global Positioning System measurements of strain accumulation and slip transfer through the restraining bend along the Dead Sea fault system in Lebanon. *Geophysical Journal International*, 168(3):1021–1028.

Grant, J. A. (1986). The isocon diagram; a simple solution to Gresens' equation for metasomatic alteration. *Economic Geology*, 81(8):1976–1982.

Gresens, R. L. (1967). Composition-volume relationships of metasomatism. *Chemical Geology*, 2:47–65.

Gueydan, F., Leroy, Y. M., Jolivet, L., and Agard, P. (2003). Analysis of continental midcrustal strain localization induced by microfracturing and reaction-softening. *Journal of Geophysical Research*, 108(B2).

Hadizadeh, J., Mittempergher, S., Gratier, J.-P., Renard, F., Di Toro, G., Richard, J., and Babaie, H. A. (2012). A microstructural study of fault rocks from the SAFOD: Implications for the deformation mechanisms and strength of the creeping segment of the San Andreas Fault. *Journal of Structural Geology*, 42:246–260.

Haines, S. H. and van der Pluijm, B. A. (2012). Patterns of mineral transformations in clay gouge, with examples from low-angle normal fault rocks in the western USA. *Journal of Structural Geology*, 43:2–32.

Halpern, M. and Tristan, N. (1981). Geochronology of the Arabian-Nubian Shield in southern Israel and eastern Sinai. *The Journal of Geology*, page 639–648.

Hamiel, Y., Amit, R., Begin, Z. B., Marco, S., Katz, O., Salamon, A., Zilberman, E., and Porat, N. (2009). The Seismicity along the Dead Sea Fault during the Last 60,000 Years. *Bulletin of the Seismological Society of America*, 99(3):2020–2026.

Handy, M., Wissing, S., and Streit, L. (1999). Frictional–viscous flow in mylonite with varied bimineralic composition and its effect on lithospheric strength. *Tectonophysics*, 303(1):175–191.

Haynes, J. M., Niemi, T. M., and Atallah, M. (2006). Evidence for ground-rupturing earthquakes on the Northern Wadi Araba fault at the archaeological site of Qasr Tilah, Dead Sea Transform fault system, Jordan. *Journal of Seismology*, 10(4):415–430.

Hofstetter, A., Thio, H., and Shamir, G. (2003). Source mechanism of the 22/11/1995 Gulf of Aqaba earthquake and its aftershock sequence. *Journal of Seismology*, 7(1):99–114.

Holdsworth, R. E. (2004). Weak Faults-Rotten Cores. *Science*, 303(5655):181–182.

Holdsworth, R. E., Stewart, M., Imber, J., and Strachan, R. A. (2001). The structure and rheological evolution of reactivated continental fault zones: a review and case study. *Geological Society, London, Special Publications*, 184(1):115–137.

Holdsworth, R. E., van Diggelen, E. W. E., Spiers, C. J., de Bresser, J. H. P., Walker, R. J., and Bowen, L. (2011). Fault rocks from the SAFOD core samples: Implications for weakening at shallow depths along the San Andreas Fault, California. *Journal of Structural Geology*, 33(2):132–144.

Ikari, M. (2015). Principal slip zones: Precursors but not recorders of earthquake slip. *Geology*.

Ikari, M. J., Saffer, D. M., and Marone, C. (2007). Effect of hydration state on the frictional properties of montmorillonite-based fault gouge. *Journal of Geophysical Research*, 112(B6).

Ikari, M. J., Saffer, D. M., and Marone, C. (2009). Frictional and hydrologic properties of clay-rich fault gouge. *Journal of Geophysical Research*, 114(B5).

Imber, J. I. (1998). *Deformation and fluid-rock interaction along the reactivated Outer Hebrides Fault Zone, Scotland*. PhD thesis, Durham University.

Janssen, C., Hoffmann-Rothe, A., Bohnhoff, M., Wetzel, H. U., Matar, A., and Khatib, M. (2007). Different styles of faulting deformation along the Dead Sea Transform and possible consequences for the recurrence of major earthquakes. *Journal of Geodynamics*, 44(1-2):66–89.

Janssen, C., Romer, R., Hoffmann-Rothe, A., Kesten, D., and Al-Zubi, H. (2004). The Dead Sea transform: Evidence for a strong fault? *The Journal of Geology*, 112(5):561–575.

Jefferies, S. P. (2006). *Microstructural and geochemical processes in long-lived reactivated crustal-scale fault zones: A case study from the Median Tectonic Line, SW Japan*. PhD thesis, Durham University.

Jefferies, S. P., Holdsworth, R. E., Shimamoto, T., Takagi, H., Lloyd, G. E., and Spiers, C. J. (2006a). Origin and mechanical significance of foliated cataclastic rocks in the cores of crustal-scale faults: Examples from the Median Tectonic Line, Japan. *Journal of Geophysical Research*, 111(B12).

Jefferies, S. P., Holdsworth, R. E., Wibberley, C. A. J., Shimamoto, T., Spiers, C. J., Niemeijer, A. R., and Lloyd, G. E. (2006b). The nature and importance of phyllonite development in crustal-scale fault cores: an example from the Median Tectonic Line, Japan. *Journal of Structural Geology*, 28(2):220–235.

Katz, O., Avigad, D., Matthews, A., and Heimann, A. (1998). Precambrian metamorphic evolution of the Arabian Nubian Shield in the Roded area, southern Israel. *Israel Journal of Earth Sciences*, 47(2):93–110.

Katzir, Y., Litvinovsky, B., Eyal, M., Zanvilevich, A., and Vapnik, Y. (2006). Four successive episodes of Late Pan-African dikes in the central Elat area, southern Israel. *Israel Journal of Earth Sciences*, 55(2):69–93.

Katzir, Y., Litvinovsky, B. A., Jahn, B. M., Eyal, M., Zanvilevich, A. N., Valley, J. W., Vapnik, Y., Beeri, Y., and Spicuzza, M. J. (2007). Interrelations between coeval mafic and A-type silicic magmas from composite dykes in a bimodal suite of southern Israel, northernmost Arabian–Nubian Shield: Geochemical and isotope constraints. *Lithos*, 97(3-4):336–364.

Kaufman, A., Yechieli, Y., and Gardosh, M. (1992). Reevaluation of the lake-sediment chronology in the Dead Sea basin, Israel, based on new 230thu dates. *Quaternary Research*, 38(3):292–304.

Kenis, I., Muchez, P., Sintubin, M., Mansy, J. L., and Lacquement, F. (2000). The use of a combined structural, stable isotope and fluid inclusion study to constrain the kinematic history at the northern Variscan front zone (Bettrechies, northern France). *Journal of Structural Geology*, 22(5):589–602.

Kerrich, R. (1986). Fluid infiltration into fault zones: Chemical, isotopic, and mechanical effects. *pure and applied geophysics*, 124(1-2):225–268.

Kirschner, D. L. and Kennedy, L. A. (2001). Limited syntectonic fluid flow in carbonate-hosted thrust faults of the Front Ranges, Canadian Rockies, inferred from stable isotope data and structures. *Journal of Geophysical Research: Solid Earth*, 106(B5):8827–8840.

Kolodner, K. (2007). *The provenance of the siliciclastic section in Israel and Jordan: U-Pb dating of detrital zircons*. PhD thesis, Hebrew University, Jerusalem.

Kreemer, C., Blewitt, G., and Klein, E. C. (2014). A geodetic plate motion and Global Strain Rate Model. *Geochemistry, Geophysics, Geosystems*, 15(10):3849–3889.

Kröner, A., Eyal, M., and Eyal, Y. (1990). Early Pan-African evolution of the basement around Elat, Israel,and the Sinai Peninsula revealed by single-zircon evaporation dating, and implications for crustal accretion rates. *Geology*, 18(6):545–548.

Lawson, A. C. and Reid, H. F. (1908). The California Earthquake of April 18, 1906: Report of the State Earthquake Investigation Commission. Technical Report No. 87, Carnegie institution of Washington.

Le Pichon, X. and Francheteau, J. (1978). A plate-tectonic analysis of the Red Sea—Gulf of Aden area. *Tectonophysics*, 46(3):369–406.

Li, Z. X., Bogdanova, S. V., Collins, A. S., Davidson, A., De Waele, B., Ernst, R. E., Fitzsimons, I. C. W., Fuck, R. A., Gladkochub, D. P., Jacobs, J., Karlstrom, K. E., Lu, S., Natapov, L. M., Pease, V., Pisarevsky, S. A., Thrane, K., and Vernikovsky, V. (2008). Assembly, configuration, and break-up history of Rodinia: A synthesis. *Precambrian Research*, 160(1-2):179–210.

Lin, A. (1996). Injection veins of crushing-originated pseudotachylyte and fault gouge formed during seismic faulting. *Engineering Geology*, 43(2–3):213–224.

Lindsay, N. G., Murphy, F. C., and Walsh, J. J. (1993). Outcrop studies of shale smears on fault surfaces. In Bryant, I. D. and Flint, S. S., editors, *The Geological Modelling of Hydrocarbon Reservoirs and Outcrop Analogues (Special Publication 15 of the IAS)*, page 113 – 123. John Wiley & Sons.

Lockner, D. A., Morrow, C., Moore, D., and Hickman, S. (2011). Low strength of deep San Andreas fault gouge from SAFOD core. *Nature*, 472(7341):82–5.

MacDonald, K. C., Kastens, K., Spiess, F. N., and Miller, S. P. (1979). Deep tow studies of the Tamayo transform fault. *Marine Geophysical Researches*, 4(1):37–70.

Mahmoud, Y., Masson, F., Meghraoui, M., Cakir, Z., Alchalbi, A., Yavasoglu, H., Yönlü, O., Daoud, M., Ergintav, S., and Inan, S. (2013). Kinematic study at the junction of the East Anatolian fault and the Dead Sea fault from GPS measurements. *Journal of Geodynamics*, 67:30–39.

Malone, M. J. and Baker, P. A. (1999). Temperature Dependence of the Strontium Distribution Coefficient in Calcite: An Experimental Study from 40° to 200°C and Application to Natural Diagenetic Calcites. *Journal of Sedimentary Research*, 69(1):216–223.

Marco, S. (2007). Temporal variation in the geometry of a strike–slip fault zone: Examples from the Dead Sea Transform. *Tectonophysics*, 445(3-4):186–199.

Marco, S. and Agnon, A. (1995). Prehistoric earthquake deformations near Masada, Dead Sea graben. *Geology*, 23(8):695–698.

Marco, S., Hartal, M., Hazan, N., Lev, L., and Stein, M. (2003). Archaeology, history, and geology of the A.D. 749 earthquake, Dead Sea transform. *Geology*, 31(8):665–668.

Marco, S., Rockwell, T., Heimann, A., Frieslander, U., and Agnon, A. (2005). Late Holocene activity of the Dead Sea Transform revealed in 3d palaeoseismic trenches on the Jordan Gorge segment. *Earth and Planetary Science Letters*, 234(1-2):189–205.

Marone, C. (1998). Laboratory-derived friction laws and their application to seismic faulting. *Annual Review of Earth and Planetary Sciences*, 26(1):643–696.

Mayer, H. E. (1972). *Two unpublished letters on the Syrian earthquake of 1202*.

McMillan, R. A. (1975). The orientation and sense of displacement of strike–slip faults in continental crust [Bachelor's thesis]: Ottawa. *Ontario, Carleton University*.

Meghraoui, M., Gomez, F., Sbeinati, R., Van der Woerd, J., Mouty, M., Darkal, A. N., Radwan, Y., Layyous, I., Al Najjar, H., Darawcheh, R., Hijazi, F., Al-Ghazzi, R., and Barazangi, M. (2003). Evidence for 830 years of seismic quiescence from palaeoseismology, archaeoseismology and historical seismicity along the Dead Sea fault in Syria. *Earth and Planetary Science Letters*, 210(1–2):35–52.

Mitchell, T. M., Ben-Zion, Y., and Shimamoto, T. (2011). Pulverized fault rocks and damage asymmetry along the Arima-Takatsuki Tectonic Line, Japan. *Earth and Planetary Science Letters*, 308(3-4):284–297.

Mitchell, T. M. and Faulkner, D. R. (2012). Towards quantifying the matrix permeability of fault damage zones in low porosity rocks. *Earth and Planetary Science Letters*, 339-340:24–31.

Moore, D. E. and Lockner, D. A. (2004). Crystallographic controls on the frictional behavior of dry and water-saturated sheet structure minerals. *Journal of Geophysical Research: Solid Earth*, 109(B3).

Moore, D. E. and Lockner, D. A. (2007). Friction of the smectite clay montmorillonite: a review and interpretation of data. In Dixon, H. and Moore, editors, *The seismogenic zone of subduction thrust faults*, page 317–345. Columbia University Press.

Moore, D. E. and Lockner, D. A. (2013). Chemical controls on fault behavior: Weakening of serpentinite sheared against quartz-bearing rocks and its significance for fault creep in the San Andreas system. *Journal of Geophysical Research: Solid Earth*, 118(5):2558–2570.

Moore, D. E. and Rymer, M. J. (2012). Correlation of clayey gouge in a surface exposure of serpentinite in the San Andreas Fault with gouge from the San Andreas Fault Observatory at Depth (SAFOD). *Journal of Structural Geology*, 38:51–60.

Moore, D. M. and Reynolds, R. C. (1989). *X-ray Diffraction and the Identification and Analysis of Clay Minerals*, volume 378. Oxford university press Oxford.

Morag, N., Avigad, D., Gerdes, A., Belousova, E., and Harlavan, Y. (2011). Crustal evolution and recycling in the northern Arabian-Nubian Shield: New perspectives from zircon Lu–Hf and U–Pb systematics. *Precambrian Research*, 186(1-4):101–116.

Morrow, C., Radney, B., and Byerlee, J. (1992). Frictional Strength and the Effective Pressure Law of Montmorillonite and Illite Clays. *International Geophysics*, 51:69–88.

Morse, J. W. and Bender, M. L. (1990). Partition coefficients in calcite: Examination of factors influencing the validity of experimental results and their application to natural systems. *Chemical Geology*, 82:265–277.

Nieto, F., Velilla, N., Peacor, D. R., and Huertas, M. O. (1994). Regional retrograde alteration of sub-greenschist facies chlorite to smectite. *Contributions to Mineralogy and Petrology*, 115(3):243–252.

Noh, J. H. and Boles, J. R. (1993). Origin of Zeolite Cements in the Miocene Sandstones, North Tejon Oil Fields, California. *Journal of Sedimentary Research*, 63(2):248–260.

Noy, D. (1978). A comparison of magnetic anomalies in the Red Sea and the Gulf of Aden. In Ramberg, I. B. and Neumann, editors, *Tectonics and Geophysics of Continental Rifts*, page 279–287. Springer.

Nuriel, P., Rosenbaum, G., Zhao, J.-X., Feng, Y., Golding, S. D., Villemant, B., and Weinberger, R. (2012a). U-Th dating of striated fault planes. *Geology*, 40(7):647–650.

Nuriel, P., Weinberger, R., Rosenbaum, G., Golding, S. D., Zhao, J.-X., Tonguc Uysal, I., Bar-Matthews, M., and Gross, M. R. (2012b). Timing and mechanism of late-Pleistocene calcite vein formation across the Dead Sea Fault Zone, northern Israel. *Journal of Structural Geology*, 36:43–54.

O'Hara, K. and Blackburn, W. H. (1989). Volume-loss model for trace-element enrichments in mylonites. *Geology*, 17(6):524–527.

Oldow, J. S. (2003). Active transtensional boundary zone between the western Great Basin and Sierra Nevada block, western U.S. Cordillera. *Geology*, 31(12):1033–1036.

Oppenheimer, D. H. (1990). Aftershock slip behavior of the 1989 Loma Prieta, California Earthquake. *Geophysical Research Letters*, 17(8):1199–1202.

Pascale, G. P. D. and Langridge, R. M. (2012). New on-fault evidence for a great earthquake in A.D. 1717, central Alpine fault, New Zealand. *Geology*, 40(9):791–794.

Peacock, D. C. P. (1991). Displacements and segment linkage in strike-slip fault zones. *Journal of Structural Geology*, 13(9):1025–1035.

Pollard, D. D. and Aydin, A. (1984). Propagation and linkage of oceanic ridge segments. *Journal of Geophysical Research*, 89(B12):10,017–10,028.

Quennell, A. (1958). The structural and geomorphic evolution of the Dead Sea Rift. *Quarterly Journal of the Geological Society*, 114(1-4):1–24.

Quennell, A. (1959). Tectonics of the Dead Sea rift. In *Proceedings of the 20th International Geological Congress, Mexico*, page 385–403.

Quennell, A. (1984). The western Arabia rift system. *Geological Society, London, Special Publications*, 17(1):775–788.

Reches, Z. (1987). Mechanical aspects of pull-apart basins and push-up swells with applications to the Dead Sea transform. *Tectonophysics*, 141(1-3):75–88.

Reches, Z. and Dewers, T. (2005). Gouge formation by dynamic pulverization during earthquake rupture. *Earth and Planetary Science Letters*, 235(1-2):361–374.

Rollinson, H. R. (1993). *Using Geochemical Data: Evaluation, Presentation, Interpretation*. Routledge.

Rowe, C. D., Kirkpatrick, J. D., and Brodsky, E. E. (2012). Fault rock injections record paleo-earthquakes. *Earth and Planetary Science Letters*, 335–336:154–166.

Rowe, C. D., Moore, J. C., Remitti, F., and Scientists, t. I. E. T. (2013). The thickness of subduction plate boundary faults from the seafloor into the seismogenic zone. *Geology*, 41(9):991–994.

Rutter, E., Maddock, R., Hall, S., and White, S. (1986). Comparative microstructures of natural and experimentally produced clay-bearing fault gouges. *Pure and Applied Geophysics*, 124(1-2):3–30.

Rutter, E. H., Hackston, A. J., Yeatman, E., Brodie, K. H., Mecklenburgh, J., and May, S. E. (2013). Reduction of friction on geological faults by weak-phase smearing. *Journal of Structural Geology*, 51:52–60.

Saffer, D. M., Frye, K. M., Marone, C., and Mair, K. (2001). Laboratory results indicating complex and potentially unstable frictional behavior of smectite clay. *Geophysical Research Letters*, 28(12):2297–2300.

Saffer, D. M. and Marone, C. (2003). Comparison of smectite- and illite-rich gouge frictional properties: application to the updip limit of the seismogenic zone along subduction megathrusts. *Earth and Planetary Science Letters*, 215(1-2):219–235.

Sagy, A., Reches, Z., and Agnon, A. (2003). Hierarchic three-dimensional structure and slip partitioning in the western Dead Sea pull-apart. *Tectonics*, 22(1).

Salamon, A. (2008). Patterns of Aftershock Sequences Along the Dead Sea Transform - Interpretation of Historical Seismicity. Technical Report GSI/05/2008, Ministry of National Infrastructures, Geological survey of Israel, Jerusalem.

Sammis, C., King, G., and Biegel, R. (1987). The kinematics of gouge deformation. *Pure and Applied Geophysics*, 125(5):777–812.

Savin, S. M. (1967). *Oxygen and hydrogen isotope ratios in sedimentary rocks and minerals*. PhD thesis, California Institute of Technology.

Savin, S. M. and Epstein, S. (1970). The oxygen and hydrogen isotope geochemistry of clay minerals. *Geochimica et Cosmochimica Acta*, 34(1):25–42.

Schleicher, A. M., Pluijm, B. A. v. d., and Warr, L. N. (2012). Chlorite-smectite clay minerals and fault behavior: New evidence from the San Andreas Fault Observatory at Depth (SAFOD) core. *Lithosphere*, 4(3):209–220.

Schlische, R. W., Young, S. S., Ackermann, R. V., and Gupta, A. (1996). Geometry and scaling relations of a population of very small rift-related normal faults. *Geology*, 24(8):683–686.

Schmid, S. M. and Handy, M. R. (1991). Towards a genetic classification of fault rocks: Geological usage and tectonophysical implications. In Müller, D. W., McKenzie, J. A., and Weissert, editors, *Controversies in Modern Geology*, page 339–361. Academic Press London.

Scholz, C. H. (1998). Earthquakes and friction laws. *Nature*, 391(6662):37–42.

Shalev, E., Lyakhovsky, V., Weinstein, Y., and Ben-Avraham, Z. (2013). The thermal structure of Israel and the Dead Sea Fault. *Tectonophysics*, 602:69–77.

Shaw, S. (1947). Geological map of southern Palestine with explanatory notes. Scale 1: 250,000. *Govt. Printing Office. Jerusalem*.

Sheppard, S. M. F. and Gilg, H. A. (1996). Stable isotope geochemistry of clay minerals. *Clay Minerals*, 31(1):1–24.

Sibson, R. H. (1977). Fault rocks and fault mechanisms. *Journal of the Geological Society*, 133(3):191–213.

Sibson, R. H. (1994). An assessment of field evidence for 'Byerlee' friction. *Pure and Applied Geophysics*, 142(3-4):645–662.

Sibson, R. H. (2003). Thickness of the Seismic Slip Zone. *Bulletin of the Seismological Society of America*, 93(3):1169–1178.

Smit, J., Brun, J. P., Cloetingh, S., and Ben-Avraham, Z. (2010). The rift-like structure and asymmetry of the Dead Sea Fault. *Earth and Planetary Science Letters*, 290(1-2):74–82.

Smith, J. V. and Durney, D. W. (1992). Experimental formation of brittle structural assemblages in oblique divergence. *Tectonophysics*, 216(3–4):235–253.

Smith, S. A. F., Billi, A., Toro, G. D., and Spiess, R. (2011a). Principal Slip Zones in Limestone: Microstructural Characterization and Implications for the Seismic Cycle (Tre Monti Fault, Central Apennines, Italy). *Pure and Applied Geophysics*, 168(12):2365–2393.

Smith, S. A. F. and Faulkner, D. R. (2010). Laboratory measurements of the frictional properties of the Zuccale low-angle normal fault, Elba Island, Italy. *Journal of Geophysical Research*, 115(B2).

Smith, S. A. F., Holdsworth, R. E., and Collettini, C. (2011b). Interactions between low-angle normal faults and plutonism in the upper crust: Insights from the Island of Elba, Italy. *Geological Society of America Bulletin*, 123(1-2):329–346.

Smith, S. A. F., Holdsworth, R. E., Collettini, C., and Pearce, M. A. (2011c). The microstructural character and mechanical significance of fault rocks associated with a continental low-angle normal fault: the Zuccale Fault, Elba Island, Italy. *Geological Society, London, Special Publications*, 359(1):97–113.

Solum, J. G. and van der Pluijm, B. A. (2009). Quantification of fabrics in clay gouge from the Carboneras fault, Spain and implications for fault behavior. *Tectonophysics*, 475(3-4):554–562.

Sone, H., Shimamoto, T., and Moore, D. E. (2012). Frictional properties of saponite-rich gouge from a serpentinite-bearing fault zone along the Gokasho-Arashima Tectonic Line, central Japan. *Journal of Structural Geology*, 38:172–182.

Stein, R. S., Barka, A. A., and Dieterich, J. H. (1997). Progressive failure on the North Anatolian fault since 1939 by earthquake stress triggering. *Geophysical Journal International*, 128(3):594–604.

Stein, R. S., King, G. C. P., and Lin, J. (1992). Change in Failure Stress on the Southern San Andreas Fault System Caused by the 1992 Magnitude = 7.4 Landers Earthquake. *Science*, 258(5086):1328–1332.

Stewart, M., Holdsworth, R. E., and Strachan, R. A. (2000). Deformation processes and weakening mechanisms within the frictional–viscous transition zone of major crustal-scale faults: insights from the Great Glen Fault Zone, Scotland. *Journal of Structural Geology*, 22(5):543–560.

Stirling, M. W., Wesnousky, S. G., and Shimazaki, K. (1996). Fault trace complexity, cumulative slip, and the shape of the magnitude-frequency distribution for strike-slip faults: a global survey. *Geophysical Journal International*, 124(3):833–868.

Surace, I. R., Clauer, N., Thélin, P., and Pfeifer, H.-R. (2011). Structural analysis, clay mineralogy and K–Ar dating of fault gouges from Centovalli Line (Central Alps) for reconstruction of their recent activity. *Tectonophysics*, 510(1-2):80–93.

Sutherland, R., Eberhart-Phillips, D., Harris, R. A., Stern, T., Beavan, J., Ellis, S., Henrys, S., Cox, S., Norris, R. J., Berryman, K. R., and others (2007). Do great earthquakes occur on the Alpine fault in central South Island, New Zealand? *Geophysical Monograph-American Geophysical Union*, 175:237.

Tembe, S., Lockner, D. A., and Wong, T. (2010). Effect of clay content and mineralogy on frictional sliding behavior of simulated gouges: Binary and ternary mixtures of quartz, illite, and montmorillonite. *Journal of Geophysical Research: Solid Earth (1978–2012)*, 115(B3).

Tesei, T., Collettini, C., Viti, C., and Barchi, M. R. (2013). Fault architecture and deformation mechanisms in exhumed analogues of seismogenic carbonate-bearing thrusts. *Journal of Structural Geology*, 55:167–181.

Teyssier, C., Tikoff, B., and Markley, M. (1995). Oblique plate motion and continental tectonics. *Geology*, 23(5):447–450.

Thatcher, W., Marshall, G., and Lisowski, M. (1997). Resolution of fault slip along the 470-km-long rupture of the great 1906 San Francisco earthquake and its implications. *Journal of Geophysical Research: Solid Earth*, 102(B3):5353–5367.

Ujiie, K., Yamaguchi, H., Sakaguchi, A., and Toh, S. (2007). Pseudotachylytes in an ancient accretionary complex and implications for melt lubrication during subduction zone earthquakes. *Journal of Structural Geology*, 29(4):599–613.

Vrolijk, P. and van der Pluijm, B. A. (1999). Clay gouge. *Journal of Structural Geology*, 21(8):1039–1048.

Walker, R. J., Holdsworth, R. E., Armitage, P. J., and Faulkner, D. R. (2013). Fault zone permeability structure evolution in basalts. *Geology*, 41(1):59–62.

Warr, L. N. and Cox, S. (2001). Clay mineral transformations and weakening mechanisms along the Alpine Fault, New Zealand. *Geological Society, London, Special Publications*, 186(1):85–101.

Watts, L. M., Holdsworth, R. E., Sleight, J. A., Strachan, R. A., and Smith, S. A. F. (2007). The movement history and fault rock evolution of a reactivated crustal-scale strike-slip fault: the Walls Boundary Fault Zone, Shetland. *Journal of the Geological Society*, 164(5):1037–1058.

Welton, J. E. (1984). *SEM petrology atlas*. Number No. 4 in Methods in Exploration. American Association of Petroleum Geologists Tulsa, Oklahoma.

Wibberley, C. (2007). Seismology: Talc at fault. *Nature*, 448(7155):756–757.

Wibberley, C. A. J. and Shimamoto, T. (2003). Internal structure and permeability of major strike-slip fault zones: the Median Tectonic Line in Mie Prefecture, Southwest Japan. *Journal of Structural Geology*, 25(1):59–78.

Wilson, B., Dewers, T., Reches, Z., and Brune, J. (2005). Particle size and energetics of gouge from earthquake rupture zones. *Nature*, 434(7034):749–752.

Wilson, M. J. (1971). Clay Mineral Formation in a Deeply Weathered Boulder Conglomerate in North-East Scotland. *Clays and Clay Minerals*, 19:345–352.

Withjack, M. O. and Jamison, W. R. (1986). Deformation produced by oblique rifting. *Tectonophysics*, 126:99–124.

Woodcock, N. H. and Fischer, M. (1986). Strike-slip duplexes. *Journal of Structural Geology*, 8(7):725–735.

Zhu, W. and Wong, T.-F. (1997). The transition from brittle faulting to cataclastic flow: Permeability evolution. *Journal of Geophysical Research: Solid Earth*, 102(B2):3027–3041.

Zielke, O., Arrowsmith, J. R., Ludwig, L. G., and Akciz, S. O. (2012). High-Resolution Topography-Derived Offsets along the 1857 Fort Tejon Earthquake Rupture Trace, San Andreas Fault. *Bulletin of the Seismological Society of America*, 102(3):1135–1154.

Zilberman, E., Amit, R., Porat, N., Enzel, Y., and Avner, U. (2005). Surface ruptures induced by the devastating 1068 AD earthquake in the southern Arava valley, Dead Sea Rift, Israel. *Tectonophysics*, 408(1-4):79–99.

Zoback, M. D. and Byerlee, J. D. (1975). The effect of microcrack dilatancy on the permeability of westerly granite. *Journal of Geophysical Research*, 80(5):752–755.

Zoback, M. L. (1992). First-and second-order patterns of stress in the lithosphere: the world stress map project. *Journal of Geophysical Research: Solid Earth*, pages 11,703–11,728.

Appendix 1

Supplementary data to accompany data presented in Chapter 2

Appendix 1A: High resolution stratigraphic column (page 19).

Appendix 1B: High resolution geological map (page 20).

Appendix 1A

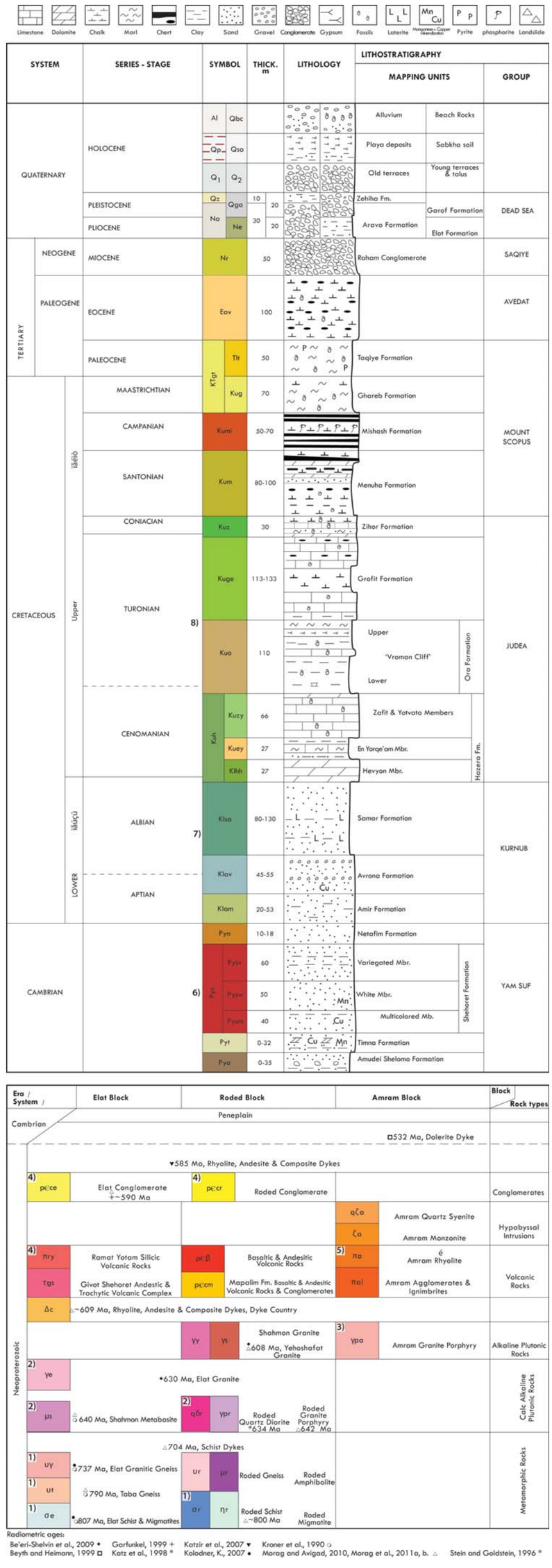

Radiometric ages:
Be'eri-Shelvin et al., 2009 • Garfunkel, 1999 + Katzir et al., 2007 ▼ Kroner et al., 1990 ↻
Beyth and Heimann, 1999 □ Katz et al., 1998 * Kolodner, K., 2007 ● Morag and Avigad, 2010, Morag et al., 2011a, b. △ Stein and Goldstein, 1996 *

Appendix 1B

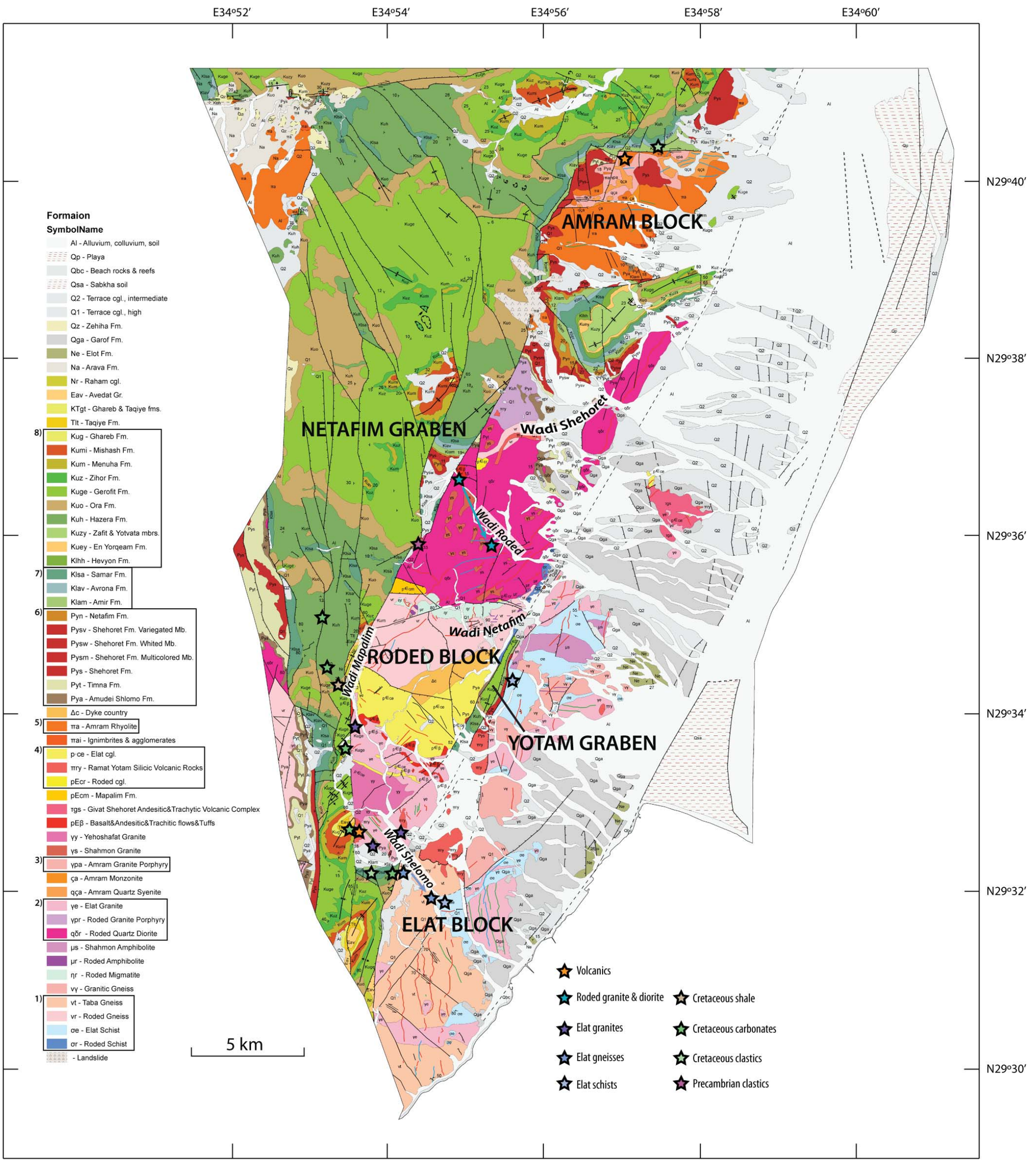
E34°52′
E34°54′
E34°56′
E34°58′
E34°60′
N29°40′
N29°38′
N29°36′
N29°34′
N29°32′
N29°30′
AMRAM BLOCK
NETAFIM GRABEN
RODED BLOCK
YOTAM GRABEN
ELAT BLOCK
Wadi Shehoret
Wadi Roded
Wadi Netafim
Wadi Mapalim
Wadi Shelomo
5 km
Formaion
SymbolName
Al - Alluvium, colluvium, soil
Qp - Playa
Qbc - Beach rocks & reefs
Qsa - Sabkha soil
Q2 - Terrace cgl., intermediate
Q1 - Terrace cgl., high
Qz - Zehiha Fm.
Qga - Garof Fm.
Ne - Elot Fm.
Na - Arava Fm.
Nr - Raham cgl.
Eav - Avedat Gr.
KTgt - Ghareb & Taqiye fms.
Tlt - Taqiye Fm.
8)
Kug - Ghareb Fm.
Kumi - Mishash Fm.
Kum - Menuha Fm.
Kuz - Zihor Fm.
Kuge - Gerofit Fm.
Kuo - Ora Fm.
Kuh - Hazera Fm.
Kuzy - Zafit & Yotvata mbrs.
Kuey - En Yorqeam Fm.
Klhh - Hevyon Fm.
7)
Klsa - Samar Fm.
Klav - Avrona Fm.
Klam - Amir Fm.
6)
Pyn - Netafim Fm.
Pysv - Shehoret Fm. Variegated Mb.
Pysw - Shehoret Fm. Whited Mb.
Pysm - Shehoret Fm. Multicolored Mb.
Pys - Shehoret Fm.
Pyt - Timna Fm.
Pya - Amudei Shlomo Fm.
Δc - Dyke country
5)
πa - Amram Rhyolite
πai - Ignimbrites & agglomerates
4)
p·ce - Elat cgl.
πry - Ramat Yotam Silicic Volcanic Rocks
pEcr - Roded cgl.
pEcm - Mapalim Fm.
τgs - Givat Shehoret Andesitic&Trachytic Volcanic Complex
pEβ - Basalt&Andesitic&Trachitic flows&Tuffs
γy - Yehoshafat Granite
γs - Shahmon Granite
3)
γpa - Amram Granite Porphyry
ça - Amram Monzonite
qça - Amram Quartz Syenite
2)
γe - Elat Granite
γpr - Roded Granite Porphyry
qδr - Roded Quartz Diorite
μs - Shahmon Amphibolite
μr - Roded Amphibolite
ηr - Roded Migmatite
vγ - Granitic Gneiss
1)
vt - Taba Gneiss
vr - Roded Gneiss
σe - Elat Schist
σr - Roded Schist
- Landslide
Volcanics
Roded granite & diorite
Elat granites
Elat gneisses
Elat schists
Cretaceous shale
Cretaceous carbonates
Cretaceous clastics
Precambrian clastics

Appendix 2

Supplementary data to accompany data presented in Chapter 3

Appendix 2A: Fault section logs showing sample positions and corresponding photographs of in situ samples (page 81 – 155).

- Shelomo Fault, Locality A
- Shelomo Fault, Locality B
- Tzefahot Fault
- Roded Fault, Locality A
- Roded Fault, Locality B
- Nizoz Fault
- Yehoshafat Fault
- R12 Fault
- Protoliths

Appendix 2B: Raw XRD data – see separate Excel file (page 81 – 155).

Appendix 2A

Shelomo Fault, Locality A samples

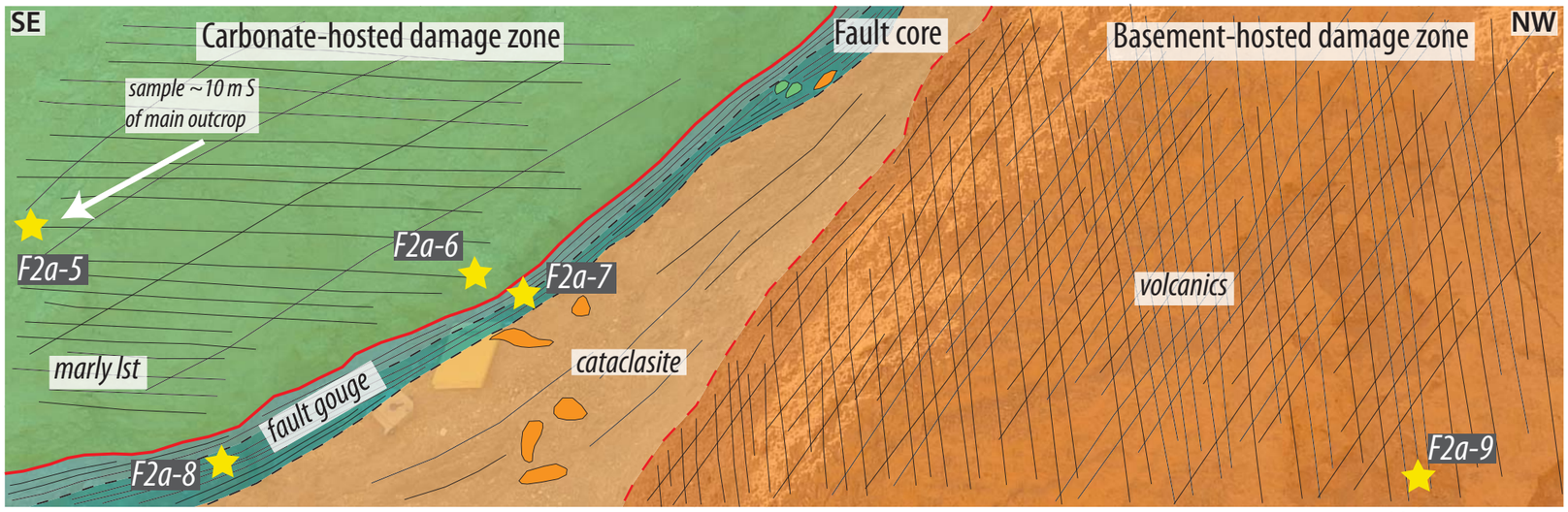

Shelomo Fault, Locality B samples

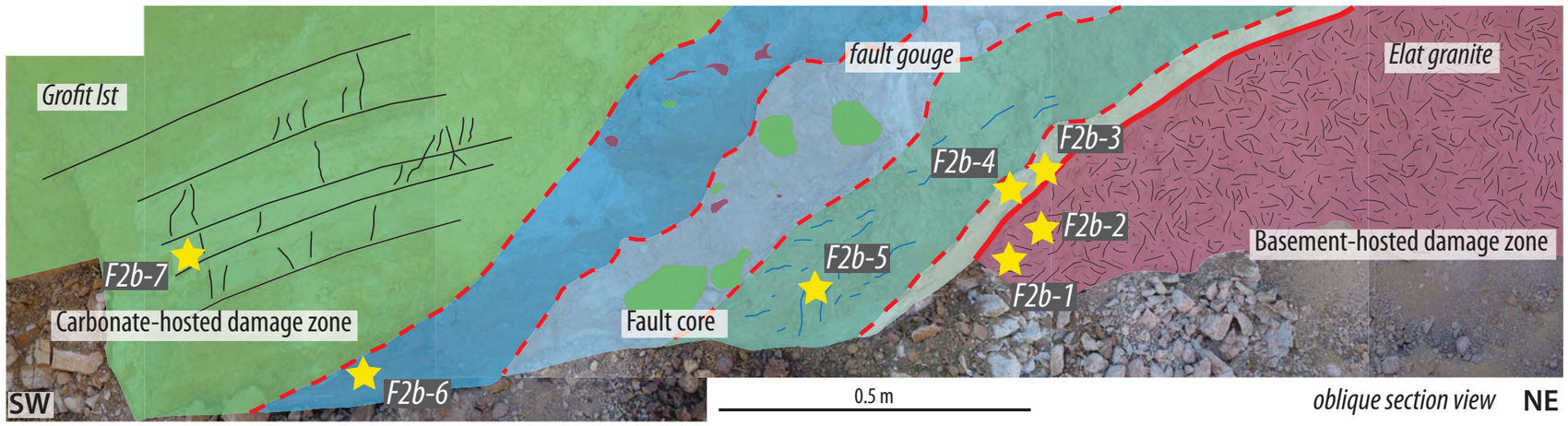

Tzefahot Fault samples

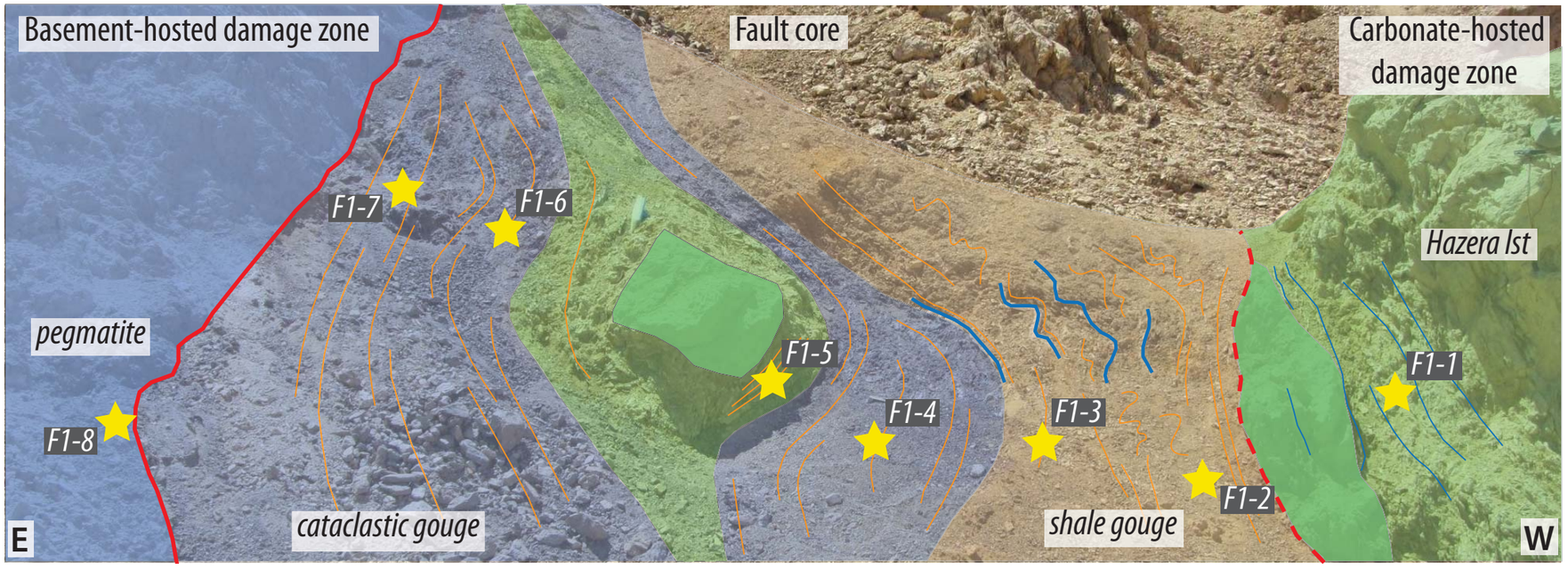

1 m

Roded Fault, Locality A samples

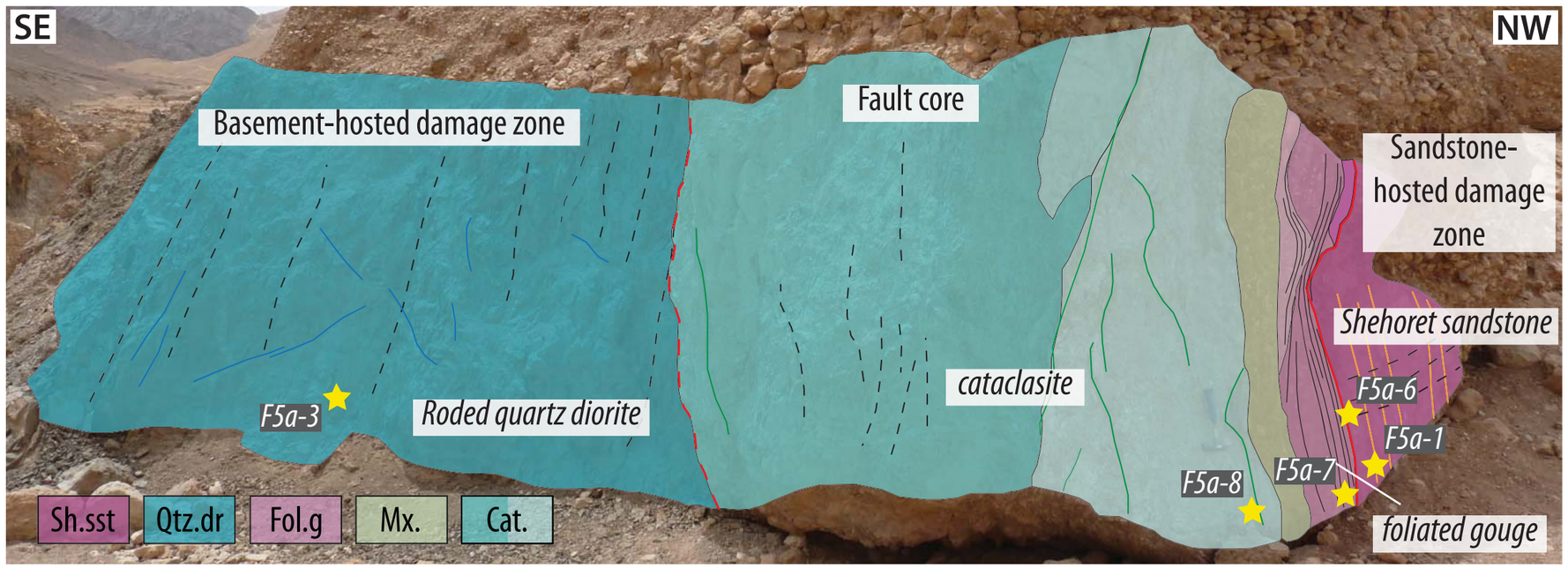

1 m

oblique section view

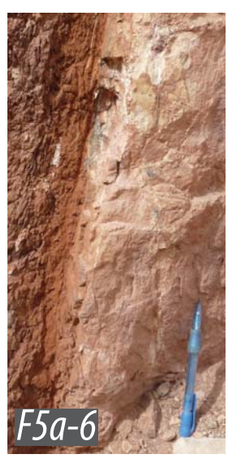

Roded Fault, Locality B samples

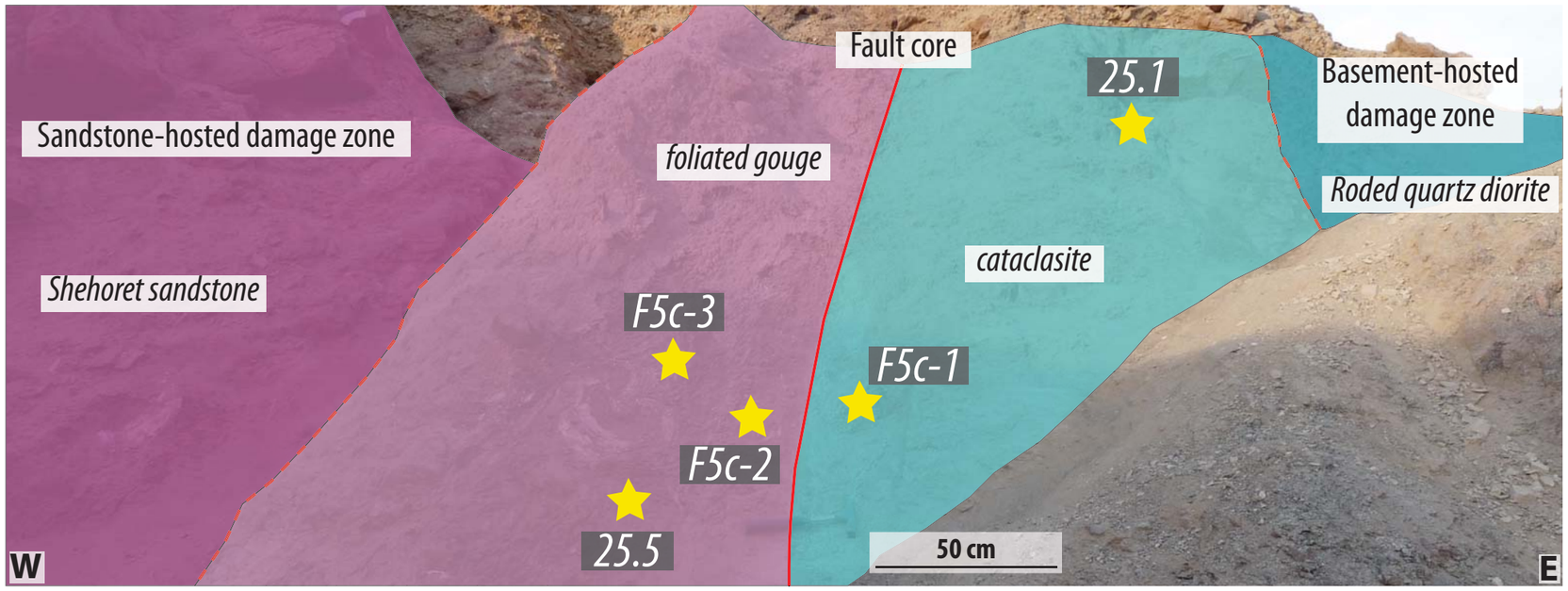

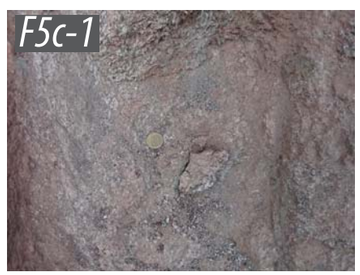

Nizoz Fault samples

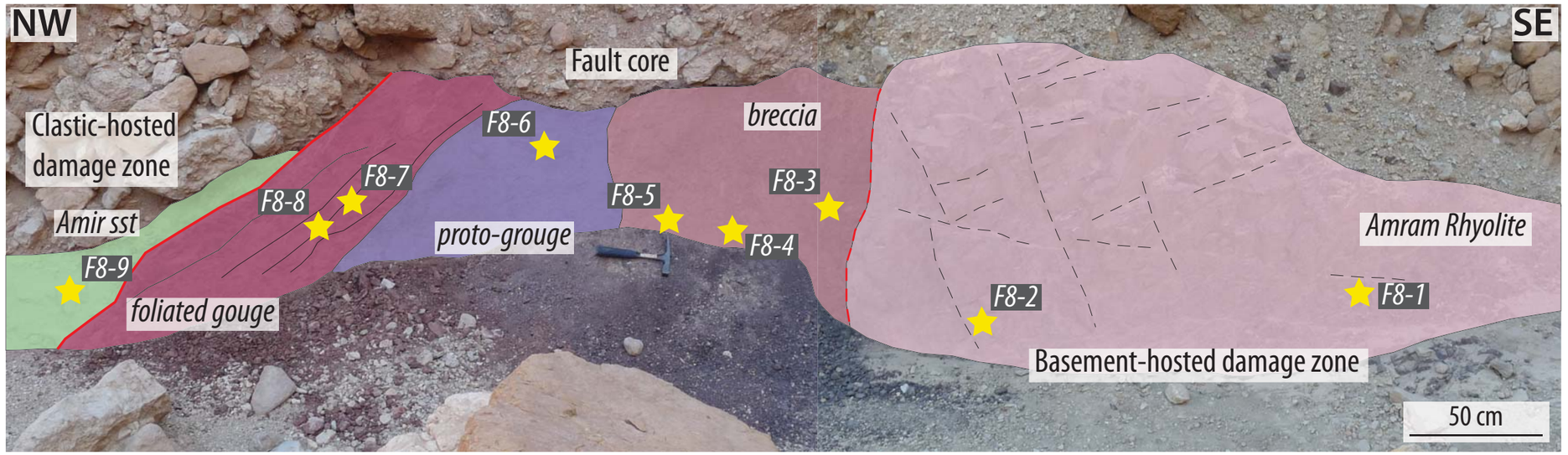

Yehoshafat Fault samples

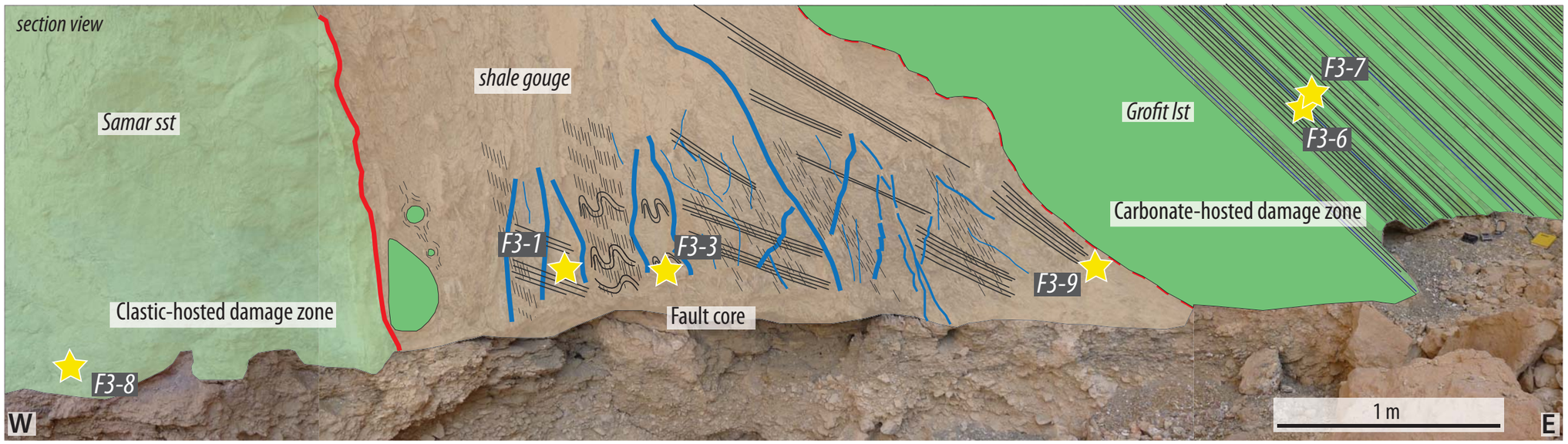

R12 Fault samples

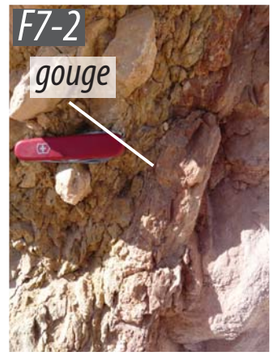

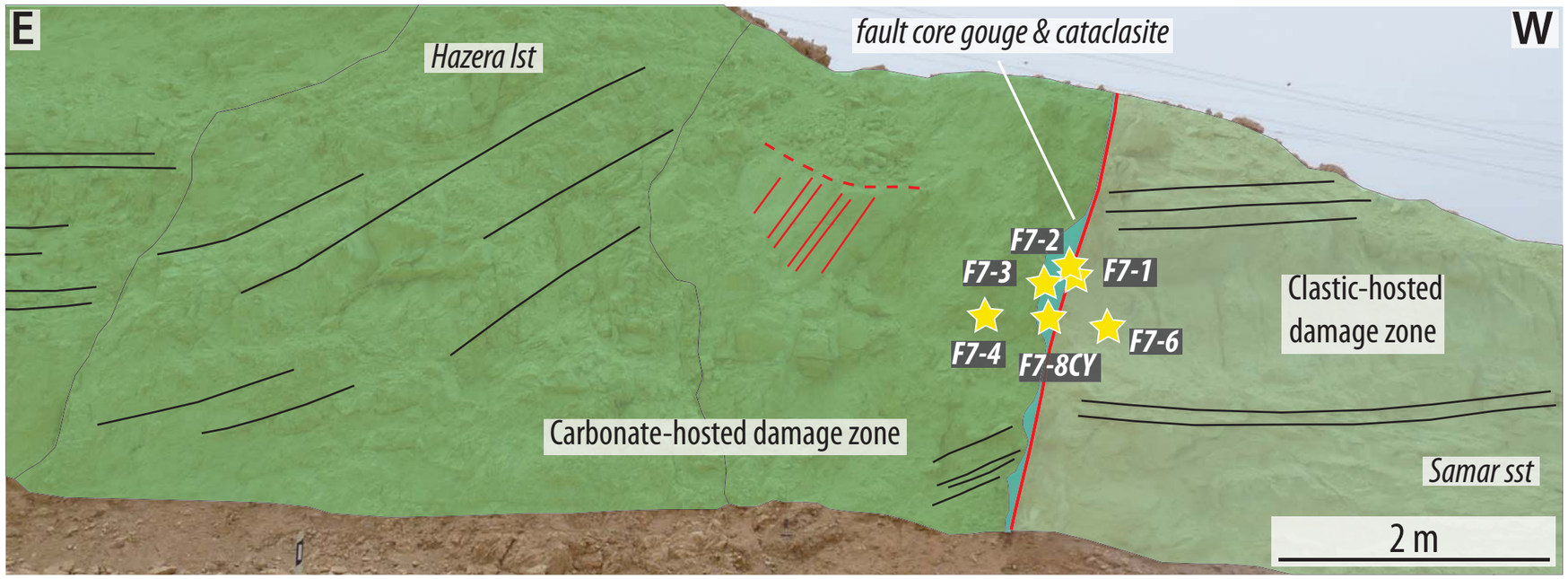

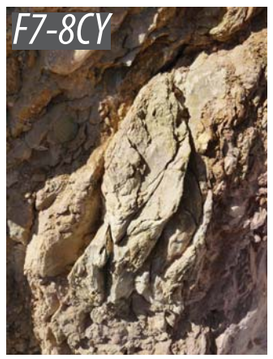

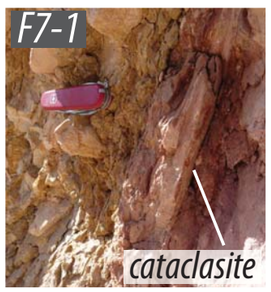

Protolith samples

Basement rocks

Elat Granite - leucocratic member

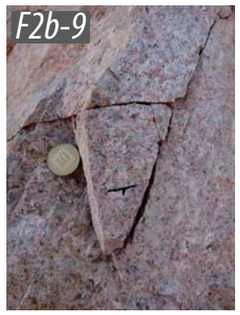

Elat Granite

Taba Gneiss

Pegmatite

Roded Quartz Diorite

Ramat Yotam Volcanics

Amram Rhyolite

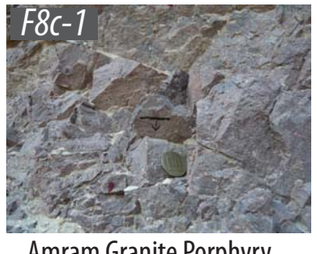

Amram Granite Porphyry

Carbonate cover rocks

Hazera limestone

Grofit limestone

Ghareb marl

Clastic cover rocks

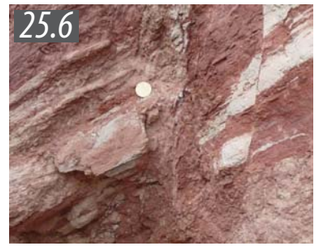

Shehoret sandstone - variegated member

Amir sandstone

Samar sandstone

Ora shale

Avrona sandstone

Appendix 3

Supplementary data to accompany data presented in Chapter 4

Appendix 3A: Raw FUS-ICP/MS data (page 157 – 191).

Results

Analyte Symbol	SiO2	Al2O3	Fe2O3(T)	MnO	MgO	CaO	Na2O	K2O	TiO2	P2O5	LOI	Total	Sc	Be	V	Ba	Sr	Y	Zr	Cr	Co	Ni	Cu
Unit Symbol	%	%	%	%	%	%	%	%	%	%	%	%	ppm	ppm	ppm	ppm	ppm	ppm	ppm	ppm	ppm	ppm	ppm
Lower Limit	0.01	0.01	0.01	0.001	0.01	0.01	0.01	0.01	0.001	0.01		0.01	1	1	5	3	2	2	4	20	1	20	10
Method Code	FUS-ICP	FUS-ICP	FUS-ICP	FUS-ICP	FUS-ICP	FUS-ICP	FUS-ICP	FUS-ICP	FUS-ICP	FUS-ICP	FUS-ICP	FUS-ICP	FUS-ICP	FUS-ICP	FUS-ICP	FUS-ICP	FUS-ICP	FUS-ICP	FUS-ICP	FUS-MS	FUS-MS	FUS-MS	FUS-MS
F1- 1	11.23	3.83	2.52	0.071	3.87	40.32	0.12	0.17	0.175	0.11	37.73	100.1	4	< 1	25	25	277	9	35	50	< 1	< 20	20
F1- 2	44.09	17.32	5.61	0.074	2.98	6.05	1.09	2.40	0.802	0.28	19.75	100.4	18	2	122	84	206	26	133	120	21	40	20
F1- 3	43.74	16.81	11.61	0.009	2.25	2.53	0.40	3.28	0.723	0.24	17.86	99.46	20	2	134	75	237	10	116	110	6	30	20
F1- 4	65.28	11.96	2.87	0.112	1.61	3.51	3.04	3.62	0.351	0.10	7.22	99.66	7	2	28	785	194	21	138	50	4	< 20	< 10
F1- 5	25.72	9.30	2.69	0.147	1.76	26.54	0.49	1.17	0.428	0.30	29.94	98.48	11	2	116	1957	407	25	67	110	6	80	30
F1- 6	49.16	12.51	3.44	0.075	3.26	9.16	0.47	2.95	0.465	0.27	19.12	100.9	10	3	74	540	228	28	188	100	3	60	50
F1- 7	48.72	13.16	4.30	0.072	3.89	5.96	0.95	2.26	0.481	0.21	18.70	98.69	12	3	69	395	245	18	129	80	10	40	20
F1- 8	70.02	13.85	0.43	0.043	0.35	2.80	2.23	7.99	0.005	0.05	3.22	101.0	< 1	3	< 5	171	44	7	11	70	< 1	< 20	< 10
F1- 9	72.25	14.82	0.55	0.051	0.10	0.45	1.81	10.22	0.010	0.07	0.63	101.0	< 1	2	< 5	108	40	8	6	20	< 1	< 20	< 10
F1- 10	64.18	17.39	4.47	0.081	2.26	3.40	3.18	2.26	0.500	0.16	2.59	100.5	10	4	52	590	302	13	191	80	9	30	10
F2a- 2	59.75	16.05	6.56	0.110	2.63	0.87	3.86	4.58	0.817	0.28	3.14	98.64	8	5	65	852	236	15	162	40	15	< 20	20
F2a- 3	76.96	10.55	2.53	0.019	0.15	0.29	0.38	8.57	0.099	< 0.01	0.52	100.1	1	2	17	1748	30	69	426	120	< 1	< 20	< 10
F2a- 5	3.86	1.41	0.96	0.020	0.29	51.81	< 0.01	< 0.01	0.053	0.12	41.03	99.56	2	< 1	25	36	833	9	11	50	< 1	< 20	20
F2a- 6	1.27	0.42	0.45	0.063	0.32	54.27	0.05	0.06	0.013	0.05	42.69	99.67	1	< 1	12	16	694	9	6	30	< 1	< 20	< 10
F2a- 7	53.02	14.30	4.18	0.050	1.52	6.39	0.55	2.37	0.720	0.28	15.30	98.67	13	5	96	447	270	24	151	90	22	< 20	100
F2a- 8	56.59	14.25	4.27	0.069	1.63	4.54	0.72	2.76	0.715	0.28	13.47	99.29	12	5	91	967	233	23	184	110	12	30	60
F2a- 9	69.99	13.26	2.80	0.020	0.48	0.35	0.38	7.21	0.202	0.01	3.88	98.59	10	2	17	1718	29	44	360	20	18	< 20	90
F2a- 10	2.91	0.40	0.36	0.021	2.45	50.56	0.06	0.09	0.019	0.18	42.20	99.26	< 1	< 1	13	36	263	8	25	40	< 1	< 20	< 10
F2b- 1	70.04	13.88	1.31	0.052	0.67	2.79	3.88	3.51	0.114	0.04	3.43	99.70	2	3	12	685	347	10	61	70	2	< 20	< 10
F2b- 2	68.12	13.45	1.68	0.123	1.23	3.93	2.83	2.46	0.131	0.04	6.74	100.7	3	3	16	371	189	15	55	50	4	< 20	< 10
F2b- 3	56.51	13.08	4.87	0.103	3.51	5.27	1.37	2.60	0.815	0.20		88.32	11	2	96	679	188	19	149	80	15	30	30
F2b- 4	45.07	12.91	6.88	0.125	5.59	6.43	1.44	2.01	1.224	0.27	16.79	98.73	14	2	133	1027	247	17	137	100	23	50	30
F2b- 5	39.94	13.73	8.74	0.212	7.87	6.84	1.54	1.17	1.587	0.30	18.20	100.1	19	2	171	965	422	17	150	150	36	80	30
F2b- 6O	42.20	14.68	4.59	0.032	1.96	13.14	0.51	2.25	0.743	0.19	18.35	98.64	15	3	105	131	165	22	147	90	6	30	20
F2b- 6R	51.30	14.13	5.20	0.052	2.23	7.13	0.63	3.54	0.898	0.30	13.53	98.93	13	3	94	544	220	22	165	80	8	30	20
F2b- 8	1.15	0.43	0.29	0.020	0.69	54.86	0.08	0.13	0.012	0.04	42.84	100.6	1	< 1	10	5	185	7	5	30	< 1	< 20	< 10
F2b- 9	74.42	14.48	1.24	0.039	0.42	0.82	5.02	3.18	0.147	0.04	0.78	100.6	2	3	13	551	331	38	64	80	2	< 20	< 10
F3- 1	48.36	18.93	7.29	0.009	1.24	1.75	0.23	3.45	0.919	0.08	16.18	98.44	25	1	141	85	190	14	130	130	6	20	20
F3- 2	79.22	12.52	1.69	0.003	0.30	0.10	0.15	0.15	0.969	0.03	5.75	100.9	9	1	51	103	55	35	415	80	7	< 20	< 10
F3- 3	49.98	20.12	5.66	0.013	1.53	1.77	0.30	3.10	0.882	0.10	14.97	98.43	21	2	139	85	33	16	133	130	11	40	20
F3- 4	82.87	9.76	1.27	0.004	0.23	0.24	0.27	0.13	1.092	0.03	4.67	100.6	9	1	60	94	59	47	548	50	10	< 20	10
F3- 5	83.93	7.17	2.52	0.053	0.47	0.96	0.12	0.26	0.702	0.05	4.55	100.8	7	1	50	110	71	34	381	100	66	30	< 10
F3- 6	42.64	16.79	5.39	0.038	2.56	9.73	0.26	3.35	0.800	0.16	17.67	99.39	19	2	124	87	159	17	116	130	14	40	10
F3- 7	13.87	5.50	1.84	0.066	1.17	39.87	0.09	1.28	0.246	0.06	35.04	99.03	7	< 1	40	27	429	13	40	50	3	< 20	< 10
F3- 8	76.23	11.84	2.33	0.006	0.30	0.17	0.76	0.31	1.485	0.04	6.03	99.50	11	2	76	134	92	83	518	80	7	< 20	10
F3- 9	36.38	16.82	13.69	0.039	1.19	1.58	0.39	3.04	0.816	0.29	24.99	99.23	20	2	115	72	98	19	114	120	20	50	10
F3- 10	82.07	10.58	1.30	0.017	0.31	0.34	0.12	0.24	0.725	0.04	4.53	100.3	9	1	31	102	94	44	1005	60	27	< 20	< 10
F5a- 1	86.62	6.40	1.26	0.007	0.23	0.29	0.26	3.52	0.630	0.05	1.61	100.9	2	1	19	699	207	18	842	70	1	< 20	< 10
F5a- 2	63.83	16.84	4.44	0.065	2.02	3.84	5.04	1.21	0.812	0.26	2.15	100.5	8	2	86	395	654	19	257	40	10	< 20	30
F5a- 3	62.13	13.33	3.71	0.083	3.05	5.71	4.28	1.64	0.511	0.16	6.20	100.8	5	2	63	341	436	14	157	90	10	40	50
F5a- 4	83.35	6.73	1.10	0.006	0.37	0.20	1.03	3.26	0.496	0.03	2.60	99.17	2	< 1	15	709	317	15	551	30	< 1	< 20	< 10
F5a- 5	54.88	17.69	8.32	0.128	4.47	4.52	4.28	1.53	1.429	0.42	3.16	100.8	20	2	168	469	709	32	187	90	18	20	20
F5a- 6	87.13	5.97	0.83	0.076	0.16	0.15	0.25	2.72	0.241	0.05	1.42	98.98	2	< 1	13	641	119	11	221	30	2	< 20	20
F5a- 7	59.60	15.25	6.44	0.045	2.52	0.76	1.13	5.68	0.667	0.15		92.24	12	6	85	656	106	38	181	80	12	30	60
F5a- 8	67.53	12.11	2.15	0.091	2.78	2.14	1.81	3.79	0.198	0.05	7.70	100.3	6	2	33	837	91	12	71	40	6	20	30
F5a- 9	47.16	12.62	4.81	0.162	4.71	6.74	2.05	2.07	0.689	0.10	17.47	98.59	14	2	95	515	165	25	141	150	13	40	10
KUH	1.79	0.53	0.66	0.036	1.32	52.59	0.06	0.14	0.025	0.02	42.56	99.73	1	< 1	10	15	278	8	44	< 20	< 1	< 20	< 10
KLAV	96.46	1.11	0.91	0.008	0.13	0.51	0.09	0.06	0.068	< 0.01	0.87	100.2	< 1	< 1	8	14	27	9	70	290	1	< 20	80

Analyte Symbol	SiO2	Al2O3	Fe2O3(T)	MnO	MgO	CaO	Na2O	K2O	TiO2	P2O5	LOI	Total	Sc	Be	V	Ba	Sr	Y	Zr	Cr	Co	Ni	Cu
Unit Symbol	%	%	%	%	%	%	%	%	%	%	%	%	ppm	ppm	ppm	ppm	ppm	ppm	ppm	ppm	ppm	ppm	ppm
Lower Limit	0.01	0.01	0.01	0.001	0.01	0.01	0.01	0.01	0.001	0.01		0.01	1	1	5	3	2	2	4	20	1	20	10
Method Code	FUS-ICP	FUS-ICP	FUS-ICP	FUS-ICP	FUS-ICP	FUS-ICP	FUS-ICP	FUS-ICP	FUS-ICP	FUS-ICP	FUS-ICP	FUS-ICP	FUS-ICP	FUS-ICP	FUS-ICP	FUS-ICP	FUS-ICP	FUS-ICP	FUS-ICP	FUS-MS	FUS-MS	FUS-MS	FUS-MS
KUG	3.18	1.14	0.63	0.029	0.35	52.08	0.15	0.15	0.038	0.15	41.76	99.65	2	< 1	25	29	877	12	11	30	< 1	< 20	< 10
TLT	31.44	15.29	3.99	0.029	1.63	19.54	0.36	0.92	0.507	0.46	26.76	100.9	14	2	136	1001	512	27	75	160	11	80	20
KUO	54.43	23.14	4.45	0.009	1.36	0.22	0.42	2.17	1.158	0.04	12.60	99.99	23	2	155	108	29	17	177	120	7	30	20
KLAM	93.83	1.99	0.77	0.007	0.13	0.42	0.08	0.08	0.095	0.01	1.42	98.85	1	< 1	10	23	21	8	77	120	5	< 20	30
F5c- 1	60.22	14.82	3.86	0.118	3.10	4.93	4.61	2.73	0.685	0.25	5.41	100.7	9	1	85	838	564	13	174	150	14	70	40
F5c- 2	54.77	14.65	5.70	0.063	4.01	1.79	1.35	4.28	0.756	0.32	12.49	100.2	10	4	46	808	208	10	134	120	16	80	20
F5c- 3	59.48	15.38	6.24	0.059	3.33	1.30	0.82	4.87	0.945	0.41	7.68	100.5	11	3	46	624	103	10	349	130	20	90	20
15.3	62.75	17.97	6.03	0.102	2.10	2.08	4.96	2.26	0.886	0.11	1.59	100.8	15	2	112	628	445	24	218	80	13	30	20
20.2	60.01	15.16	6.05	0.085	4.87	5.34	4.22	1.63	0.876	0.33	1.82	100.4	12	2	118	625	1052	15	125	210	21	120	40
20.4-2	77.86	11.74	1.23	0.009	0.12	0.31	2.96	5.58	0.078	< 0.01	0.27	100.1	1	< 1	10	154	45	23	67	160	< 1	< 20	< 10
23.12	73.06	10.04	2.56	0.018	0.24	2.97	0.16	7.17	0.090	< 0.01	2.19	98.49	< 1	4	15	734	72	62	451	< 20	< 1	< 20	30
23.13	74.68	13.59	1.11	0.060	0.33	0.62	3.65	4.59	0.093	0.04	0.90	99.66	2	2	10	851	288	12	52	90	1	< 20	40
23.14	67.45	15.84	4.04	0.090	1.97	4.07	3.67	1.66	0.434	0.15	1.32	100.7	12	2	45	762	349	15	163	40	8	20	10
25.1	68.29	14.50	1.22	0.040	0.89	1.65	4.76	4.54	0.133	0.10	2.45	98.58	< 1	1	24	2581	701	9	28	60	3	< 20	30
25.2	61.25	15.42	5.67	0.084	3.97	3.87	4.27	2.37	0.884	0.31	2.66	100.8	18	3	121	637	894	23	158	160	18	90	20
25.3	54.89	14.65	8.37	0.091	4.82	4.41	4.13	2.94	1.627	0.61	4.05	100.6	14	2	184	914	711	17	185	150	24	70	30
25.4	55.25	14.81	7.87	0.085	4.20	4.16	4.05	3.34	1.556	0.57	3.81	99.69	13	2	171	1115	720	17	202	120	23	80	40
25.5	65.09	14.94	5.96	0.054	1.58	0.46	0.43	5.32	0.742	0.11	5.31	100.0	13	4	64	630	125	34	203	70	15	40	20
25.6	60.60	9.00	1.01	0.274	0.73	5.76	4.16	5.43	0.235	0.02	13.77	101.0	3	2	23	675	108	18	218	20	4	< 20	40
Q1	57.35	15.98	7.09	0.052	1.75	2.72	1.63	2.45	1.152	0.25	9.66	100.1	15	3	142	482	220	33	259	90	17	50	30
Q2	69.79	10.32	3.81	0.031	0.88	3.95	1.37	3.28	0.923	0.16	6.21	100.7	9	2	78	772	178	32	416	60	8	30	20
Q3	52.15	7.26	2.52	0.045	1.08	17.73	0.72	1.38	0.565	0.40	16.58	100.4	7	1	61	377	198	26	232	80	5	30	20
Q4	31.42	9.76	3.39	0.039	1.18	25.67	0.52	1.31	0.487	0.40	26.28	100.5	8	2	90	141	315	22	99	90	6	30	30
F7- 1	72.36	11.89	1.94	0.016	0.39	4.13	0.16	0.26	1.122	0.05	8.39	100.7	10	2	73	82	109	41	463	60	9	20	< 10
F7- 2	49.62	15.50	7.25	0.048	2.21	6.77	0.97	2.26	0.805	0.22	14.98	100.6	15	3	158	97	129	27	173	90	104	120	20
F7- 3	82.76	9.84	1.24	0.005	0.28	0.23	0.38	0.21	1.014	0.03	4.81	100.8	8	2	59	78	86	39	502	70	1	< 20	< 10
F7- 4	8.35	2.80	1.12	0.030	1.45	46.30	0.22	0.72	0.098	0.13	38.85	100.1	3	< 1	32	25	402	13	21	30	6	30	10
F7- 5	2.03	0.63	0.42	0.009	0.40	53.68	0.23	0.12	0.017	0.02	42.35	99.90	< 1	< 1	10	8	416	6	7	< 20	< 1	< 20	< 10
F7- 6	94.31	2.16	2.42	0.021	0.08	0.15	0.16	0.10	0.054	0.02	0.63	100.1	2	< 1	12	23	22	7	46	20	2	< 20	10
F7- 8CL	54.97	17.72	7.21	0.094	2.34	1.02	0.68	2.87	1.080	0.15	11.62	99.75	18	4	149	146	105	25	203	100	155	170	20
F7- 8B	1.64	0.38	0.39	0.008	0.37	54.65	0.09	0.08	0.015	< 0.01	42.39	100.0	< 1	< 1	12	5	405	6	5	< 20	< 1	< 20	< 10
F7- 11	2.56	0.82	0.71	0.012	0.57	52.28	0.25	0.17	0.024	< 0.01	41.42	98.83	1	< 1	24	9	341	6	7	< 20	< 1	< 20	< 10
F8A- 1	95.91	2.00	1.02	0.015	0.04	0.20	0.39	0.08	0.100	0.04	0.94	100.7	< 1	< 1	7	31	174	9	104	< 20	1	< 20	20
F8A- 5	95.83	1.83	0.36	0.007	0.02	0.74	0.07	0.04	0.055	0.03	1.19	100.2	< 1	< 1	6	23	183	8	65	< 20	< 1	< 20	10
F8A- 6	74.82	10.24	3.45	0.052	0.38	1.41	0.31	7.60	0.234	< 0.01	2.21	100.7	< 1	2	26	945	40	31	408	< 20	1	< 20	30
F8A- 8	96.71	2.17	1.12	0.012	0.03	0.10	0.08	0.05	0.084	0.02	0.60	101.0	< 1	< 1	6	17	50	9	91	< 20	< 1	< 20	10
F8C- 1	71.54	12.05	4.25	0.060	0.25	0.68	1.66	7.44	0.272	0.02	1.32	99.55	2	3	14	455	46	45	355	< 20	3	< 20	10
F8C- 2	68.18	12.02	4.46	0.152	0.39	2.81	3.04	5.39	0.385	0.05	3.28	100.2	4	3	32	309	59	34	322	100	4	< 20	10
F8C- 3	62.52	11.93	5.47	0.215	0.81	4.63	2.14	5.58	0.736	0.11	5.16	99.30	9	4	57	335	70	34	245	270	6	< 20	20
F8C- 4	58.55	15.52	9.14	0.134	1.69	0.59	0.83	8.22	1.528	0.23	4.34	100.8	18	8	111	468	57	34	311	200	12	30	50
F8C- 5	60.45	14.67	7.42	0.091	1.26	0.48	1.08	8.68	1.143	0.19	3.75	99.21	13	6	74	523	36	36	310	120	9	< 20	40
F8C- 7	70.55	12.09	4.98	0.086	1.14	0.51	0.48	5.87	0.634	0.10	3.49	99.93	6	3	34	571	104	35	407	30	10	< 20	140
F8C- 8	72.07	10.87	5.04	0.087	0.93	1.26	0.58	5.46	0.444	0.06	3.88	100.7	5	3	29	449	199	32	316	30	9	< 20	110
F8C- 9	79.30	8.41	2.85	0.043	0.32	0.90	0.31	4.07	0.159	0.06	2.73	99.14	2	2	16	718	184	13	89	20	4	< 20	110
F8C- 10	82.80	11.07	1.44	0.016	0.05	0.15	0.10	0.11	0.522	0.06	4.13	100.5	3	< 1	15	85	195	21	482	< 20	< 1	< 20	50
F8C- 11	73.82	10.68	4.89	0.045	0.26	0.29	2.06	5.89	0.238	0.01	1.18	99.36	< 1	3	8	110	24	62	416	20	2	< 20	10

Results

Analyte Symbol	Zn	Ga	Ge	As	Rb	Nb	Mo	Ag	In	Sn	Sb	Cs	La	Ce	Pr	Nd	Sm	Eu	Gd	Tb	Dy	Ho	Er
Unit Symbol	ppm	ppm	ppm	ppm	ppm	ppm	ppm	ppm	ppm	ppm	ppm	ppm	ppm	ppm	ppm	ppm	ppm	ppm	ppm	ppm	ppm	ppm	ppm
Lower Limit	30	1	1	5	2	1	2	0.5	0.2	1	0.5	0.5	0.1	0.1	0.05	0.1	0.1	0.05	0.1	0.1	0.1	0.1	0.1
Method Code	FUS-MS	FUS-MS	FUS-MS	FUS-MS	FUS-MS	FUS-MS	FUS-MS	FUS-MS	FUS-MS	FUS-MS	FUS-MS	FUS-MS	FUS-MS	FUS-MS	FUS-MS	FUS-MS	FUS-MS	FUS-MS	FUS-MS	FUS-MS	FUS-MS	FUS-MS	FUS-MS
F1- 1	< 30	5	< 1	< 5	3	3	< 2	< 0.5	< 0.2	< 1	< 0.5	< 0.5	8.3	16.8	2.13	8.6	1.8	0.49	1.7	0.3	1.5	0.3	0.9
F1- 2	50	21	1	7	60	9	< 2	< 0.5	< 0.2	3	0.7	4.1	25.8	52.4	6.34	24.9	5.2	1.29	4.5	0.8	4.5	0.9	2.8
F1- 3	40	21	2	15	58	8	< 2	< 0.5	< 0.2	2	0.6	4.0	16.8	29.2	3.21	11.3	2.2	0.49	1.6	0.3	2.1	0.5	1.5
F1- 4	70	13	1	< 5	81	5	< 2	< 0.5	< 0.2	2	0.6	2.6	27.9	47.4	5.99	22.1	4.1	1.04	3.3	0.5	3.2	0.6	1.9
F1- 5	90	13	< 1	< 5	30	6	< 2	< 0.5	< 0.2	1	0.8	2.9	20.3	28.6	4.05	16.1	3.2	0.84	3.0	0.5	3.1	0.6	2.0
F1- 6	110	19	1	< 5	72	9	< 2	< 0.5	< 0.2	5	0.8	5.7	31.4	54.9	7.36	28.9	5.6	1.33	4.8	0.7	4.4	0.9	2.6
F1- 7	100	17	1	< 5	93	5	< 2	< 0.5	< 0.2	4	0.5	13.1	22.1	35.3	5.34	20.4	4.3	1.32	3.5	0.6	3.2	0.6	1.7
F1- 8	< 30	18	2	< 5	339	2	< 2	< 0.5	< 0.2	1	0.6	5.8	2.7	4.0	0.54	2.1	0.6	0.14	0.5	< 0.1	0.5	< 0.1	0.2
F1- 9	< 30	18	3	< 5	464	2	< 2	< 0.5	< 0.2	1	< 0.5	8.6	1.2	1.6	0.25	1.0	0.3	0.08	0.4	< 0.1	0.5	< 0.1	0.2
F1- 10	90	22	1	< 5	131	6	< 2	0.5	< 0.2	2	< 0.5	21.7	9.5	16.9	2.17	7.8	1.5	0.84	1.4	0.3	1.9	0.4	1.4
F2a- 2	140	30	2	9	128	4	< 2	< 0.5	< 0.2	1	1.5	8.6	13.8	26.8	3.72	16.0	3.5	0.70	2.8	0.4	2.6	0.5	1.6
F2a- 3	40	11	2	< 5	251	15	< 2	1.0	< 0.2	5	1.0	6.0	9.5	53.9	2.65	12.2	5.3	0.64	7.5	1.7	11.1	2.4	6.8
F2a- 5	< 30	2	< 1	< 5	< 2	1	< 2	< 0.5	< 0.2	< 1	< 0.5	< 0.5	5.0	6.0	0.96	3.9	0.8	0.23	0.8	0.1	0.9	0.2	0.6
F2a- 6	< 30	< 1	< 1	< 5	2	< 1	< 2	< 0.5	< 0.2	< 1	< 0.5	< 0.5	2.6	2.6	0.42	1.8	0.3	0.09	0.4	< 0.1	0.5	0.1	0.3
F2a- 7	70	21	5	10	98	9	< 2	< 0.5	< 0.2	10	< 0.5	32.5	24.6	51.7	6.44	25.3	5.2	1.21	4.9	0.7	3.8	0.7	2.1
F2a- 8	80	21	5	8	96	9	2	< 0.5	< 0.2	3	0.9	28.5	22.1	47.2	5.77	22.8	4.6	1.09	4.2	0.7	3.9	0.7	2.2
F2a- 9	< 30	15	2	< 5	144	10	< 2	0.8	< 0.2	16	0.9	2.8	16.4	46.0	4.30	17.8	5.0	0.88	5.3	1.1	7.0	1.5	4.4
F2a- 10	< 30	< 1	< 1	< 5	2	< 1	< 2	< 0.5	< 0.2	< 1	0.5	< 0.5	1.9	3.0	0.37	1.4	0.3	0.09	0.3	< 0.1	0.3	< 0.1	0.2
F2b- 1	40	18	1	< 5	89	4	< 2	< 0.5	< 0.2	2	0.5	1.7	7.8	15.8	1.87	6.8	1.5	0.41	1.1	0.2	1.1	0.2	0.6
F2b- 2	30	23	1	< 5	114	12	< 2	< 0.5	< 0.2	1	< 0.5	3.1	9.1	18.0	2.38	9.0	2.3	0.44	1.8	0.3	2.1	0.4	1.1
F2b- 3	70	18	1	< 5	74	39	2	< 0.5	< 0.2	6	0.6	5.8	18.9	38.4	4.84	19.2	3.9	1.07	3.3	0.5	3.2	0.7	2.1
F2b- 4	80	17	1	< 5	55	10	2	< 0.5	< 0.2	1	0.5	5.0	18.1	36.1	4.92	19.8	4.2	1.29	3.4	0.5	3.0	0.6	1.6
F2b- 5	80	17	1	< 5	25	11	< 2	< 0.5	< 0.2	1	< 0.5	2.1	17.9	39.2	5.11	21.6	4.5	1.54	3.9	0.6	3.4	0.6	1.7
F2b- 6O	40	17	2	6	65	11	< 2	< 0.5	< 0.2	2	0.6	7.0	23.8	46.6	5.76	22.5	4.7	1.19	3.8	0.6	3.7	0.7	2.0
F2b- 6R	50	18	2	5	102	10	< 2	< 0.5	< 0.2	2	< 0.5	8.6	25.8	50.7	6.40	25.4	5.1	1.40	4.5	0.7	4.0	0.8	2.4
F2b- 8	< 30	< 1	< 1	< 5	2	< 1	< 2	< 0.5	< 0.2	< 1	< 0.5	< 0.5	1.2	2.2	0.28	1.1	0.3	0.07	0.2	< 0.1	0.2	< 0.1	0.2
F2b- 9	50	19	1	< 5	73	4	< 2	< 0.5	< 0.2	1	< 0.5	1.5	12.6	25.1	2.97	11.4	2.9	0.51	3.5	0.8	5.2	1.1	3.5
F3- 1	< 30	25	2	9	49	10	< 2	< 0.5	< 0.2	2	0.6	3.6	30.5	63.2	7.12	24.7	4.2	0.97	2.8	0.5	2.6	0.6	1.7
F3- 2	< 30	16	1	< 5	7	12	< 2	0.8	< 0.2	2	0.7	2.1	23.2	50.7	6.02	23.4	4.6	1.09	4.3	0.8	5.5	1.2	3.8
F3- 3	40	24	2	6	61	10	< 2	< 0.5	< 0.2	2	0.6	4.4	20.9	40.0	4.92	18.8	3.3	0.81	2.6	0.4	2.7	0.6	1.7
F3- 4	< 30	15	1	< 5	6	35	< 2	0.7	< 0.2	< 1	< 0.5	1.8	32.0	87.9	12.3	52.8	11.5	2.24	9.4	1.4	8.0	1.6	5.0
F3- 5	40	10	1	< 5	12	10	< 2	0.8	< 0.2	2	0.6	2.4	27.7	63.0	7.45	30.9	6.4	1.34	5.5	0.9	5.5	1.1	3.3
F3- 6	40	20	2	6	69	9	< 2	< 0.5	< 0.2	2	0.6	3.9	18.1	38.1	4.71	18.8	3.8	0.95	3.2	0.5	3.1	0.6	1.8
F3- 7	< 30	6	< 1	< 5	21	3	< 2	< 0.5	< 0.2	< 1	< 0.5	1.1	10.9	22.5	2.63	10.6	2.0	0.53	1.6	0.3	1.6	0.3	0.9
F3- 8	30	14	1	< 5	12	20	< 2	1.1	< 0.2	3	< 0.5	2.8	42.2	85.5	10.6	45.6	10.2	2.58	11.8	2.0	12.1	2.5	7.1
F3- 9	60	21	1	19	66	10	< 2	< 0.5	< 0.2	2	< 0.5	2.8	21.5	54.5	7.74	32.4	6.0	1.48	5.0	0.8	4.8	0.9	2.6
F3- 10	< 30	13	< 1	< 5	9	14	< 2	2.2	< 0.2	2	< 0.5	1.1	54.3	144	17.7	71.2	14.4	3.07	10.3	1.6	8.9	1.7	5.0
F5a- 1	< 30	7	< 1	< 5	83	8	< 2	1.6	< 0.2	< 1	< 0.5	1.1	16.1	32.5	3.61	13.2	2.4	0.59	1.9	0.4	2.4	0.5	1.6
F5a- 2	60	23	1	< 5	28	6	< 2	0.6	< 0.2	2	0.5	1.8	28.2	57.6	6.98	27.2	5.2	1.36	3.7	0.6	3.2	0.6	1.8
F5a- 3	50	17	< 1	< 5	43	6	< 2	< 0.5	< 0.2	2	< 0.5	1.9	38.7	70.2	7.30	25.0	3.9	1.03	3.0	0.4	2.1	0.4	1.2
F5a- 4	< 30	7	< 1	< 5	80	7	< 2	1.3	< 0.2	< 1	< 0.5	1.2	22.1	42.0	4.97	17.9	2.9	0.68	2.2	0.3	2.1	0.4	1.3
F5a- 5	110	26	1	< 5	37	8	< 2	< 0.5	< 0.2	5	< 0.5	2.3	22.3	51.9	7.41	32.5	7.5	1.86	6.7	1.0	5.7	1.1	3.1
F5a- 6	< 30	6	< 1	< 5	65	4	< 2	< 0.5	< 0.2	< 1	< 0.5	1.4	15.1	28.5	3.10	10.8	1.6	0.43	1.1	0.2	1.1	0.2	0.8
F5a- 7	100	21	2	< 5	208	9	< 2	< 0.5	< 0.2	12	< 0.5	18.6	39.6	77.3	8.85	32.1	6.4	1.45	5.5	0.9	5.7	1.2	3.6
F5a- 8	40	13	< 1	< 5	71	4	< 2	< 0.5	< 0.2	7	0.5	1.9	11.3	21.9	2.34	8.3	1.7	0.55	1.4	0.3	1.6	0.4	1.1
F5a- 9	80	18	1	< 5	51	8	2	< 0.5	< 0.2	5	0.6	2.8	13.6	27.1	3.93	15.9	4.2	1.08	3.7	0.6	4.1	0.8	2.6
KUH	< 30	< 1	< 1	< 5	3	338	< 2	< 0.5	0.2	53	< 0.5	< 0.5	2.2	4.6	0.51	1.9	0.4	0.08	0.5	< 0.1	0.7	0.2	0.5
KLAV	< 30	2	< 1	< 5	< 2	9	< 2	< 0.5	< 0.2	< 1	< 0.5	< 0.5	4.8	10.0	1.05	3.6	0.7	0.15	0.6	0.1	0.7	0.2	0.5
KUG	< 30	1	< 1	< 5	4	4	< 2	< 0.5	< 0.2	< 1	< 0.5	< 0.5	4.3	5.2	0.80	3.4	0.7	0.18	0.8	0.1	0.8	0.2	0.5

Analyte Symbol	Zn	Ga	Ge	As	Rb	Nb	Mo	Ag	In	Sn	Sb	Cs	La	Ce	Pr	Nd	Sm	Eu	Gd	Tb	Dy	Ho	Er
Unit Symbol	ppm	ppm	ppm	ppm	ppm	ppm	ppm	ppm	ppm	ppm	ppm	ppm	ppm	ppm	ppm	ppm	ppm	ppm	ppm	ppm	ppm	ppm	ppm
Lower Limit	30	1	1	5	2	1	2	0.5	0.2	1	0.5	0.5	0.1	0.1	0.05	0.1	0.1	0.05	0.1	0.1	0.1	0.1	0.1
Method Code	FUS-MS	FUS-MS	FUS-MS	FUS-MS	FUS-MS	FUS-MS	FUS-MS	FUS-MS	FUS-MS	FUS-MS	FUS-MS	FUS-MS	FUS-MS	FUS-MS	FUS-MS	FUS-MS	FUS-MS	FUS-MS	FUS-MS	FUS-MS	FUS-MS	FUS-MS	FUS-MS
TLT	140	20	2	< 5	38	12	< 2	< 0.5	< 0.2	1	< 0.5	3.4	35.4	57.1	6.89	25.0	4.6	1.12	3.9	0.6	3.6	0.8	2.2
KUO	40	27	2	< 5	55	16	< 2	< 0.5	< 0.2	2	< 0.5	3.6	24.6	42.2	4.71	16.7	3.0	0.73	2.2	0.4	2.7	0.6	1.9
KLAM	< 30	3	< 1	< 5	< 2	2	3	< 0.5	< 0.2	< 1	< 0.5	< 0.5	5.2	10.3	1.17	4.1	0.8	0.16	0.6	0.1	0.7	0.1	0.4
F5c- 1	60	20	< 1	< 5	53	3	< 2	< 0.5	< 0.2	< 1	< 0.5	2.0	20.8	42.0	5.14	21.0	3.8	1.12	2.6	0.4	2.0	0.4	1.0
F5c- 2	80	20	2	< 5	232	3	< 2	< 0.5	< 0.2	< 1	< 0.5	71.6	18.7	45.4	5.07	20.9	3.8	1.02	2.5	0.3	1.8	0.3	0.9
F5c- 3	80	20	< 1	< 5	156	28	< 2	< 0.5	< 0.2	3	< 0.5	22.3	19.3	37.7	4.75	19.6	3.5	0.90	2.5	0.3	1.9	0.4	1.0
15.3	70	18	1	< 5	54	7	< 2	< 0.5	0.2	51	< 0.5	1.6	21.0	45.8	5.50	21.4	4.6	1.50	3.8	0.6	4.0	0.9	2.8
20.2	80	21	1	< 5	31	4	< 2	< 0.5	< 0.2	1	< 0.5	1.2	68.0	119	12.2	41.6	6.3	1.45	4.0	0.5	2.8	0.5	1.5
20.4-2	< 30	17	1	< 5	85	< 1	< 2	< 0.5	< 0.2	< 1	< 0.5	< 0.5	20.6	41.9	5.15	19.3	4.3	0.12	3.9	0.6	3.5	0.7	1.8
23.12	< 30	20	1	8	240	18	< 2	1.3	< 0.2	5	< 0.5	7.5	32.3	92.7	8.12	33.1	9.0	0.30	9.0	1.6	10.4	2.1	6.3
23.13	< 30	19	1	< 5	105	2	< 2	< 0.5	< 0.2	1	< 0.5	4.6	9.4	21.0	2.12	8.1	1.6	0.42	1.3	0.2	1.3	0.3	0.8
23.14	60	19	1	< 5	46	3	< 2	< 0.5	< 0.2	< 1	< 0.5	5.3	16.4	37.4	3.83	13.6	2.7	1.04	2.5	0.4	2.7	0.5	1.3
25.1	< 30	12	< 1	< 5	52	< 1	< 2	< 0.5	< 0.2	< 1	< 0.5	< 0.5	58.2	93.9	8.33	25.4	2.9	0.61	1.6	0.2	1.0	0.2	0.5
25.2	80	20	1	< 5	55	5	< 2	< 0.5	< 0.2	2	< 0.5	2.4	16.6	46.8	7.24	32.4	6.9	1.42	5.1	0.8	4.2	0.8	2.3
25.3	100	20	1	< 5	59	6	< 2	< 0.5	< 0.2	< 1	< 0.5	1.1	35.7	76.3	9.75	40.2	7.4	2.17	5.3	0.7	3.4	0.6	1.6
25.4	100	20	1	7	65	6	< 2	< 0.5	< 0.2	< 1	< 0.5	0.6	36.7	77.5	9.74	38.6	7.1	2.25	5.3	0.7	3.5	0.6	1.6
25.5	60	20	1	14	141	8	< 2	< 0.5	< 0.2	2	< 0.5	10.3	42.7	87.3	9.70	36.1	6.8	1.52	6.1	1.0	6.2	1.3	3.6
25.6	< 30	10	< 1	< 5	117	6	< 2	< 0.5	< 0.2	1	< 0.5	3.9	19.7	35.6	5.23	19.4	3.6	0.64	2.8	0.5	2.9	0.6	1.7
Q1	90	21	2	5	86	15	5	< 0.5	< 0.2	2	< 0.5	6.9	41.9	88.9	9.92	37.4	7.5	1.77	5.9	1.0	6.0	1.2	3.4
Q2	50	12	1	< 5	76	8	3	< 0.5	< 0.2	2	< 0.5	3.3	32.9	65.5	7.80	29.4	5.6	1.26	4.9	0.8	5.2	1.1	3.3
Q3	50	10	< 1	< 5	37	7	< 2	< 0.5	< 0.2	1	< 0.5	2.8	20.6	42.0	4.94	19.4	3.8	0.85	3.6	0.5	3.1	0.6	1.9
Q4	70	12	< 1	< 5	36	7	4	< 0.5	< 0.2	< 1	< 0.5	3.3	24.1	44.6	5.51	21.1	4.2	1.01	3.3	0.5	3.1	0.6	1.8
F7- 1	30	14	2	< 5	19	13	< 2	0.6	< 0.2	2	< 0.5	16.5	41.8	84.0	9.57	36.1	6.9	1.61	6.2	1.0	6.5	1.4	4.0
F7- 2	530	20	3	41	81	10	5	< 0.5	< 0.2	2	0.5	15.8	24.0	49.4	5.91	22.9	5.0	1.32	4.6	0.8	4.7	0.9	2.8
F7- 3	80	12	1	< 5	13	14	< 2	1.1	< 0.2	2	< 0.5	11.0	35.2	70.3	8.04	30.1	5.8	1.30	5.3	0.9	5.8	1.2	3.8
F7- 4	70	3	< 1	< 5	18	2	< 2	< 0.5	< 0.2	< 1	< 0.5	1.7	6.1	8.7	1.27	4.8	1.1	0.25	1.1	0.2	1.2	0.2	0.8
F7- 5	< 30	< 1	< 1	< 5	< 2	< 1	< 2	< 0.5	< 0.2	< 1	< 0.5	< 0.5	1.0	1.8	0.20	0.7	0.1	< 0.05	0.1	< 0.1	0.1	< 0.1	< 0.1
F7- 6	< 30	3	< 1	< 5	2	< 1	< 2	< 0.5	< 0.2	< 1	< 0.5	< 0.5	9.2	24.3	2.99	10.3	1.3	0.27	0.8	0.1	0.8	0.2	0.5
F7- 8CL	360	22	2	19	97	13	2	< 0.5	< 0.2	2	< 0.5	13.4	26.2	59.5	5.97	23.8	5.0	1.24	4.4	0.7	4.5	0.9	2.8
F7- 8B	< 30	< 1	< 1	< 5	< 2	< 1	< 2	< 0.5	< 0.2	< 1	< 0.5	< 0.5	0.7	1.3	0.15	0.5	0.1	< 0.05	< 0.1	< 0.1	0.1	< 0.1	< 0.1
F7- 11	< 30	< 1	< 1	< 5	3	< 1	< 2	< 0.5	< 0.2	< 1	< 0.5	< 0.5	1.4	2.7	0.30	1.1	0.2	0.06	0.2	< 0.1	0.2	< 0.1	0.1
F8A- 1	420	2	< 1	< 5	< 2	< 1	< 2	< 0.5	< 0.2	< 1	< 0.5	< 0.5	7.0	14.0	1.64	6.2	1.2	0.24	0.7	0.1	0.8	0.2	0.6
F8A- 5	< 30	2	< 1	< 5	< 2	1	< 2	< 0.5	< 0.2	< 1	< 0.5	< 0.5	6.0	11.7	1.35	4.8	0.9	0.23	0.6	0.1	0.7	0.1	0.4
F8A- 6	90	23	< 1	< 5	171	25	< 2	0.8	< 0.2	4	< 0.5	9.0	39.5	79.1	12.6	48.3	9.2	0.70	6.5	0.9	5.2	1.0	3.3
F8A- 8	< 30	2	< 1	< 5	< 2	< 1	< 2	< 0.5	< 0.2	< 1	< 0.5	< 0.5	7.3	14.3	1.63	6.1	1.1	0.29	0.8	0.1	0.9	0.2	0.6
F8C- 1	50	18	1	7	175	17	< 2	< 0.5	< 0.2	3	0.6	1.9	43.8	97.4	10.7	40.7	8.2	0.68	7.1	1.2	8.0	1.7	4.9
F8C- 2	50	26	1	13	127	19	< 2	0.7	< 0.2	3	< 0.5	4.0	34.3	79.1	9.57	37.0	7.9	0.67	6.8	1.0	5.6	1.1	3.5
F8C- 3	60	40	2	15	153	16	< 2	0.5	< 0.2	2	0.6	9.9	50.8	130	15.8	62.8	13.6	1.22	11.1	1.4	7.2	1.3	3.8
F8C- 4	80	57	2	15	242	20	< 2	0.6	< 0.2	3	1.7	32.0	37.5	97.5	11.7	47.4	10.9	0.93	9.4	1.3	6.9	1.2	3.5
F8C- 5	60	43	1	18	225	20	< 2	0.6	< 0.2	2	1.1	27.7	39.9	131	14.0	58.4	13.2	1.13	10.3	1.4	6.7	1.2	3.4
F8C- 7	140	19	2	6	156	13	< 2	< 0.5	< 0.2	2	< 0.5	14.3	46.7	92.0	11.6	42.4	7.8	1.26	6.2	1.0	6.3	1.3	3.8
F8C- 8	110	18	2	7	131	11	< 2	< 0.5	< 0.2	2	< 0.5	11.7	41.2	97.2	10.3	37.5	6.9	1.10	5.2	0.9	5.5	1.1	3.3
F8C- 9	50	10	1	< 5	101	2	< 2	< 0.5	< 0.2	< 1	< 0.5	3.3	15.2	30.1	3.68	14.3	2.7	0.76	2.0	0.3	1.9	0.4	1.1
F8C- 10	< 30	11	< 1	< 5	2	5	< 2	< 0.5	< 0.2	< 1	< 0.5	< 0.5	24.5	48.6	5.53	19.7	3.4	0.74	2.7	0.4	2.8	0.6	1.9
F8C- 11	30	26	1	< 5	152	25	< 2	0.9	< 0.2	5	< 0.5	3.7	53.0	190	14.6	64.1	16.2	1.14	15.6	2.2	11.7	2.2	6.1

Results

Analyte Symbol	Tm	Yb	Lu	Hf	Ta	W	Tl	Pb	Bi	Th	U
Unit Symbol	ppm	ppm	ppm	ppm	ppm	ppm	ppm	ppm	ppm	ppm	ppm
Lower Limit	0.05	0.1	0.04	0.2	0.1	1	0.1	5	0.4	0.1	0.1
Method Code	FUS-MS	FUS-MS	FUS-MS	FUS-MS	FUS-MS	FUS-MS	FUS-MS	FUS-MS	FUS-MS	FUS-MS	FUS-MS
F1- 1	0.13	0.8	0.12	0.9	0.2	6	< 0.1	< 5	< 0.4	1.6	0.6
F1- 2	0.39	2.4	0.39	3.0	0.7	2	0.3	11	< 0.4	7.0	2.5
F1- 3	0.24	1.6	0.26	2.6	0.7	2	0.3	12	< 0.4	5.7	2.4
F1- 4	0.28	1.7	0.29	2.9	0.5	2	0.4	17	< 0.4	7.0	1.2
F1- 5	0.30	1.9	0.29	1.5	0.4	3	0.1	8	< 0.4	3.8	3.0
F1- 6	0.37	2.3	0.37	3.8	0.6	2	0.2	12	< 0.4	6.4	3.4
F1- 7	0.22	1.4	0.22	2.8	0.5	2	0.3	8	< 0.4	3.2	2.2
F1- 8	< 0.05	0.2	< 0.04	0.3	0.4	< 1	1.6	13	< 0.4	0.7	0.5
F1- 9	< 0.05	0.2	< 0.04	< 0.2	1.3	2	2.2	16	< 0.4	0.3	0.4
F1- 10	0.20	1.4	0.22	4.1	0.4	1	0.9	11	1.7	2.9	0.9
F2a- 2	0.23	1.4	0.22	3.7	0.3	3	0.7	21	< 0.4	3.8	1.9
F2a- 3	0.98	6.1	0.88	9.9	1.4	2	1.2	17	< 0.4	15.9	5.3
F2a- 5	0.09	0.6	0.10	0.3	< 0.1	2	< 0.1	< 5	< 0.4	0.9	1.5
F2a- 6	< 0.05	0.3	0.04	< 0.2	< 0.1	1	< 0.1	< 5	< 0.4	0.2	0.7
F2a- 7	0.30	2.0	0.29	3.9	0.8	2	0.2	16	< 0.4	5.7	3.2
F2a- 8	0.33	2.1	0.31	4.1	0.7	3	0.2	19	< 0.4	6.2	3.3
F2a- 9	0.67	4.1	0.63	7.9	0.9	3	0.6	22	< 0.4	12.0	4.6
F2a- 10	< 0.05	0.2	< 0.04	0.6	< 0.1	1	< 0.1	< 5	< 0.4	0.3	0.8
F2b- 1	0.09	0.6	0.11	1.5	0.6	1	0.5	23	< 0.4	2.4	1.2
F2b- 2	0.17	1.3	0.20	1.5	1.6	< 1	0.5	51	< 0.4	3.7	1.9
F2b- 3	0.32	2.0	0.30	4.6	5.6	2	0.3	50	< 0.4	7.7	5.3
F2b- 4	0.23	1.3	0.20	2.8	0.7	1	0.2	49	< 0.4	2.3	5.1
F2b- 5	0.24	1.5	0.20	3.1	0.8	< 1	0.1	7	< 0.4	1.5	2.1
F2b- 6O	0.29	1.9	0.29	3.4	0.8	1	0.2	16	< 0.4	6.1	4.1
F2b- 6R	0.35	2.2	0.33	3.9	0.8	3	0.1	21	< 0.4	6.5	3.4
F2b- 8	< 0.05	0.1	< 0.04	< 0.2	< 0.1	< 1	< 0.1	< 5	< 0.4	0.2	0.3
F2b- 9	0.53	3.3	0.47	1.5	0.6	1	0.3	24	< 0.4	4.5	1.9
F3- 1	0.25	1.7	0.28	3.0	0.8	1	0.2	11	< 0.4	6.4	1.7
F3- 2	0.61	4.3	0.68	8.9	1.2	2	< 0.1	15	< 0.4	7.6	2.2
F3- 3	0.27	1.8	0.29	3.3	0.7	1	0.3	10	< 0.4	5.5	1.7
F3- 4	0.74	4.7	0.73	9.1	1.6	1	< 0.1	19	< 0.4	9.6	2.4
F3- 5	0.49	3.2	0.51	8.3	1.0	2	0.1	16	< 0.4	6.8	2.1
F3- 6	0.27	1.7	0.24	2.8	0.7	1	0.3	9	< 0.4	5.5	1.5
F3- 7	0.12	0.8	0.12	0.9	0.2	< 1	< 0.1	< 5	< 0.4	1.7	0.5
F3- 8	0.96	5.7	0.86	12.1	1.9	2	< 0.1	24	< 0.4	13.2	3.9
F3- 9	0.38	2.4	0.35	3.2	0.7	< 1	0.7	12	< 0.4	8.4	1.5
F3- 10	0.77	5.2	0.81	21.8	1.3	2	0.1	22	< 0.4	13.2	4.4
F5a- 1	0.27	1.9	0.33	18.5	0.9	1	0.4	15	< 0.4	10.4	3.4
F5a- 2	0.26	1.7	0.25	5.7	0.5	< 1	0.1	11	< 0.4	4.0	2.0
F5a- 3	0.17	1.0	0.16	4.1	0.9	< 1	0.1	7	< 0.4	10.5	2.0
F5a- 4	0.20	1.5	0.25	12.7	0.8	< 1	0.3	15	< 0.4	11.5	2.8
F5a- 5	0.43	2.6	0.35	4.3	0.6	< 1	0.1	9	< 0.4	2.0	1.1
F5a- 6	0.13	0.9	0.14	5.2	0.4	< 1	0.3	12	< 0.4	4.5	1.3
F5a- 7	0.56	3.4	0.43	4.1	0.9	2	0.9	22	< 0.4	12.1	3.8
F5a- 8	0.17	1.1	0.16	1.8	0.5	< 1	0.3	16	< 0.4	7.1	2.0
F5a- 9	0.39	2.7	0.40	3.4	1.3	1	0.2	15	< 0.4	5.1	4.0
KUH	0.08	0.5	0.09	2.1	28.4	< 1	< 0.1	13	< 0.4	6.5	6.1
KLAV	0.07	0.5	0.08	1.8	0.2	< 1	< 0.1	< 5	< 0.4	1.4	0.6
KUG	0.08	0.5	0.08	0.3	< 0.1	< 1	< 0.1	< 5	< 0.4	0.5	1.1

Analyte Symbol	Tm	Yb	Lu	Hf	Ta	W	Tl	Pb	Bi	Th	U
Unit Symbol	ppm	ppm	ppm	ppm	ppm	ppm	ppm	ppm	ppm	ppm	ppm
Lower Limit	0.05	0.1	0.04	0.2	0.1	1	0.1	5	0.4	0.1	0.1
Method Code	FUS-MS	FUS-MS	FUS-MS	FUS-MS	FUS-MS	FUS-MS	FUS-MS	FUS-MS	FUS-MS	FUS-MS	FUS-MS
TLT	0.31	1.9	0.30	1.8	0.8	< 1	< 0.1	14	< 0.4	6.9	4.1
KUO	0.30	2.1	0.32	4.1	1.1	< 1	< 0.1	7	< 0.4	5.7	1.9
KLAM	0.06	0.4	0.06	2.0	0.1	< 1	< 0.1	< 5	< 0.4	1.3	0.8
F5c- 1	0.14	0.9	0.14	3.9	0.2	< 1	< 0.1	10	< 0.4	2.5	1.5
F5c- 2	0.11	0.7	0.11	3.1	0.3	< 1	0.5	7	< 0.4	2.3	2.5
F5c- 3	0.13	0.8	0.13	7.9	3.9	< 1	0.4	10	< 0.4	2.1	3.5
15.3	0.43	2.7	0.44	5.5	0.5	< 1	< 0.1	13	< 0.4	5.9	1.9
20.2	0.20	1.3	0.21	3.2	0.2	< 1	< 0.1	10	< 0.4	11.9	0.9
20.4-2	0.22	1.2	0.18	2.6	< 0.1	< 1	< 0.1	20	< 0.4	10.1	0.9
23.12	0.94	6.0	0.94	12.1	1.4	2	1.2	23	< 0.4	16.8	9.0
23.13	0.11	0.8	0.12	1.4	0.3	< 1	0.3	20	< 0.4	3.5	1.3
23.14	0.18	1.2	0.17	3.5	0.3	< 1	< 0.1	11	< 0.4	4.5	0.8
25.1	0.06	0.3	0.05	0.7	0.1	< 1	< 0.1	17	< 0.4	8.2	0.6
25.2	0.32	2.0	0.30	3.8	0.4	< 1	< 0.1	8	< 0.4	2.1	2.1
25.3	0.21	1.3	0.18	5.6	0.3	< 1	< 0.1	20	< 0.4	4.4	1.6
25.4	0.21	1.2	0.18	4.5	0.4	< 1	0.2	28	< 0.4	4.7	1.8
25.5	0.51	3.3	0.49	4.5	0.8	< 1	0.5	17	< 0.4	10.8	3.7
25.6	0.25	1.7	0.26	4.7	0.5	< 1	0.5	11	< 0.4	6.5	1.6
Q1	0.51	3.2	0.46	6.2	1.3	< 1	0.2	28	< 0.4	13.2	5.6
Q2	0.49	3.1	0.47	8.7	0.9	< 1	0.2	20	< 0.4	11.7	4.0
Q3	0.27	1.7	0.24	5.5	0.7	1	0.1	14	< 0.4	5.6	3.5
Q4	0.27	1.6	0.26	2.6	0.6	< 1	< 0.1	18	< 0.4	5.5	4.1
F7- 1	0.61	4.0	0.63	11.1	1.3	2	< 0.1	21	< 0.4	10.3	3.2
F7- 2	0.42	2.6	0.39	4.5	0.9	< 1	0.2	15	< 0.4	7.1	6.3
F7- 3	0.60	3.8	0.59	11.5	1.4	2	< 0.1	20	< 0.4	10.0	2.9
F7- 4	0.12	0.6	0.10	0.8	0.2	< 1	< 0.1	< 5	< 0.4	1.3	1.6
F7- 5	< 0.05	< 0.1	< 0.04	< 0.2	< 0.1	< 1	< 0.1	< 5	< 0.4	0.1	1.3
F7- 6	0.07	0.5	0.07	1.0	< 0.1	< 1	< 0.1	< 5	< 0.4	1.1	0.4
F7- 8CL	0.42	2.8	0.43	5.0	1.0	< 1	0.2	18	< 0.4	8.4	4.0
F7- 8B	< 0.05	< 0.1	< 0.04	< 0.2	< 0.1	< 1	< 0.1	< 5	< 0.4	< 0.1	1.1
F7- 11	< 0.05	0.1	< 0.04	< 0.2	< 0.1	< 1	< 0.1	< 5	< 0.4	0.3	3.0
F8A- 1	0.10	0.7	0.11	2.3	0.1	1	< 0.1	< 5	< 0.4	2.3	0.7
F8A- 5	0.07	0.5	0.08	1.6	0.1	< 1	< 0.1	< 5	< 0.4	1.7	0.6
F8A- 6	0.53	3.6	0.52	10.1	2.0	1	1.2	12	< 0.4	9.8	2.3
F8A- 8	0.09	0.6	0.10	2.2	0.1	< 1	< 0.1	< 5	< 0.4	2.2	0.7
F8C- 1	0.68	4.3	0.68	9.7	1.5	< 1	0.5	15	< 0.4	9.2	3.0
F8C- 2	0.51	3.4	0.48	8.1	1.7	1	0.6	17	< 0.4	8.1	2.7
F8C- 3	0.57	3.6	0.52	6.5	1.6	2	0.7	30	< 0.4	7.4	2.7
F8C- 4	0.50	3.1	0.44	7.7	1.5	2	1.0	37	< 0.4	5.5	3.1
F8C- 5	0.47	3.1	0.44	7.6	1.6	2	0.9	30	< 0.4	6.2	2.9
F8C- 7	0.56	3.7	0.58	9.6	1.3	< 1	0.7	24	< 0.4	13.0	2.7
F8C- 8	0.49	3.2	0.49	6.6	1.1	< 1	0.7	23	< 0.4	9.1	2.3
F8C- 9	0.17	1.1	0.18	3.2	0.2	< 1	0.4	15	< 0.4	3.1	1.0
F8C- 10	0.29	1.9	0.33	10.3	0.6	1	< 0.1	15	< 0.4	11.5	2.1
F8C- 11	0.84	5.3	0.79	10.5	2.2	< 1	0.6	11	< 0.4	10.1	2.3

QC

Analyte Symbol	SiO2	Al2O3	Fe2O3(T)	MnO	MgO	CaO	Na2O	K2O	TiO2	P2O5	LOI	Total	Sc	Be	V	Ba	Sr	Y	Zr	Cr	Co	Ni	Cu
Unit Symbol	%	%	%	%	%	%	%	%	%	%	%	%	ppm	ppm	ppm	ppm	ppm	ppm	ppm	ppm	ppm	ppm	ppm
Lower Limit	0.01	0.01	0.01	0.001	0.01	0.01	0.01	0.01	0.001	0.01		0.01	1	1	5	3	2	2	4	20	1	20	10
Method Code	FUS-ICP	FUS-ICP	FUS-ICP	FUS-ICP	FUS-ICP	FUS-ICP	FUS-ICP	FUS-ICP	FUS-ICP	FUS-ICP	FUS-ICP	FUS-ICP	FUS-ICP	FUS-ICP	FUS-ICP	FUS-ICP	FUS-ICP	FUS-ICP	FUS-ICP	FUS-MS	FUS-MS	FUS-MS	FUS-MS
DNC-1 Meas	47.30	18.53	10.02	0.147	9.99	11.51	1.91	0.22	0.480	0.07			31		159	105	145	16	35	270	58	250	100
DNC-1 Cert	47.15	18.34	9.97	0.150	10.13	11.49	1.890	0.234	0.480	0.070			31		148	118	144.0	18.0	38	270	57	247	100
GBW 07113 Meas	73.25	12.82	3.20	0.143	0.15	0.62	2.46	5.38	0.281	0.05			5	4	6	496	47	48	409				
GBW 07113 Cert	72.8	13.0	3.21	0.140	0.160	0.590	2.57	5.43	0.300	0.0500			5.00	4.00	5.00	506	43.0	43.0	403				
LKSD-3 Meas																				90	31	50	30
LKSD-3 Cert																				87.0	30.0	47.0	35.0
TDB-1 Meas																				250			330
TDB-1 Cert																				251			323
W-2a Meas	52.69	15.14	10.92	0.166	6.25	11.03	2.22	0.62	1.060	0.14			35	< 1	278	173	193	18	88	100	46		110
W-2a Cert	52.4	15.4	10.7	0.163	6.37	10.9	2.14	0.626	1.06	0.130			36.0	1.30	262	182	190	24.0	94.0	92.0	43.0		110
NIST 696 Meas	3.73	52.41	8.58	0.007	0.02	0.05		< 0.01	2.560	0.06					397				1000				
NIST 696 Cert	3.79	54.5	8.70	0.00400	0.0120	0.0180		0.00900	2.64	0.0500					403.0000				1037.0000				
DTS-2b Meas	40.18	0.42			49.97	0.14							3		28	13							
DTS-2b Cert	39.4	0.450			49.4	0.120							3.00		22.0	16.0							
SY-4 Meas	49.98	20.51	6.11	0.106	0.50	8.11	6.95	1.66	0.288	0.13			1	3	9	344	1195	115	518				
SY-4 Cert	49.9	20.69	6.21	0.108	0.54	8.05	7.10	1.66	0.287	0.131			1.1	2.6	8.0	340	1191	119	517				
CTA-AC-1 Meas																							50
CTA-AC-1 Cert																							54.0
BIR-1a Meas	47.68	15.36	11.51	0.170	9.44	13.42	1.81	0.02	0.964	0.03			43	< 1	338	7	107	13	15	370	53	180	130
BIR-1a Cert	47.96	15.50	11.30	0.175	9.700	13.30	1.82	0.030	0.96	0.021			44	0.58	310	6	110	16	18	370	52	170	125
NCS DC86312 Meas																							
NCS DC86312 Cert																							
ZW-C Meas																							
ZW-C Cert																							
NCS DC70009 (GBW07241) Meas																				30			950
NCS DC70009 (GBW07241) Cert																				30			960
OREAS 100a (Fusion) Meas																					17		170
OREAS 100a (Fusion) Cert																					18.1		169
OREAS 101a (Fusion) Meas																					47		430
OREAS 101a (Fusion) Cert																					48.8		434
JR-1 Meas																						< 20	< 10
JR-1 Cert																						1.67	2.68
SARM 3 Meas																							
SARM 3 Cert																							
BCR-2 Meas	54.38	13.62	14.07	0.197	3.46	7.10	3.12	1.82	2.336	0.37			33		437	701	341	29	175				
BCR-2 Cert	54.1	13.5	13.8	0.196	3.59	7.12	3.16	1.79	2.26	0.35			33		416	683	346	37	188				
F7- 8CL Orig	54.70	17.56	7.14	0.093	2.33	1.01	0.68	2.85	1.074	0.16	11.62	99.21	18	4	148	145	104	25	201	100	154	170	20
F7- 8CL Dup	55.24	17.88	7.28	0.094	2.36	1.03	0.68	2.89	1.086	0.14	11.62	100.3	18	4	150	147	105	25	205	100	155	170	20
Method Blank																				< 20	< 1	< 20	< 10

QC

Analyte Symbol	Zn	Ga	Ge	As	Rb	Nb	Mo	Ag	In	Sn	Sb	Cs	La	Ce	Pr	Nd	Sm	Eu	Gd	Tb	Dy	Ho	Er
Unit Symbol	ppm	ppm	ppm	ppm	ppm	ppm	ppm	ppm	ppm	ppm	ppm	ppm	ppm	ppm	ppm	ppm	ppm	ppm	ppm	ppm	ppm	ppm	ppm
Lower Limit	30	1	1	5	2	1	2	0.5	0.2	1	0.5	0.5	0.1	0.1	0.05	0.1	0.1	0.05	0.1	0.1	0.1	0.1	0.1
Method Code	FUS-MS	FUS-MS	FUS-MS	FUS-MS	FUS-MS	FUS-MS	FUS-MS	FUS-MS	FUS-MS	FUS-MS	FUS-MS	FUS-MS	FUS-MS	FUS-MS	FUS-MS	FUS-MS	FUS-MS	FUS-MS	FUS-MS	FUS-MS	FUS-MS	FUS-MS	FUS-MS
DNC-1 Meas	70												3.6			5.1		0.56					
DNC-1 Cert	70												3.6			5.20		0.59					
GBW 07113 Meas																							
GBW 07113 Cert																							
LKSD-3 Meas	140			25	74		< 2	2.7				2.4	47.4	90.3		43.7	7.8	1.37		0.9	5.0		
LKSD-3 Cert	152			27.0	78.0		2.00	2.70				2.30	52.0	90.0		44.0	8.00	1.50		1.00	4.90		
TDB-1 Meas	160				21								16.5	39.1		24.6		1.95					
TDB-1 Cert	155				23								17	41		23		2.1					
W-2a Meas	80		1	< 5	21	8	< 2	0.5			0.7	1.0	10.7	23.5		13.2	3.3	1.07		0.6	3.9	0.8	2.3
W-2a Cert	80.0		1.00	1.20	21.0	7.90	0.600	0.0460			0.790	0.990	10.0	23.0		13.0	3.30	1.00		0.630	3.60	0.760	2.50
NIST 696 Meas																							
NIST 696 Cert																							
DTS-2b Meas																							
DTS-2b Cert																							
SY-4 Meas																							
SY-4 Cert																							
CTA-AC-1 Meas													> 2000	> 3000		1110	159	44.2	121	14.4			
CTA-AC-1 Cert													2176	3326		1087	162	46.7	124	13.9			
BIR-1a Meas	70	16											0.6			2.5	1.1	0.52	1.9				
BIR-1a Cert	70	16											0.63			2.5	1.1	0.55	2.0				
NCS DC86312 Meas													> 2000	177		1580			236	33.8	184	35.6	98.7
NCS DC86312 Cert													2360	190		1600			225.0	34.6	183	36	96.2
ZW-C Meas	1040	102				185						263											
ZW-C Cert	1050.000	99				198						260											
NCS DC70009 (GBW07241) Meas	90	16	11	70	503					> 1000	3.1	43.3	23.3	58.1	7.58	31.6	11.9		14.0	3.0	20.0	4.1	12.7
NCS DC70009 (GBW07241) Cert	100	16.5	11.2	69.9	500					1701	3.1	41	23.7	60.3	7.9	32.9	12.5		14.8	3.3	20.7	4.5	13.4
OREAS 100a (Fusion) Meas							25						249	455	44.9	148	23.7	3.51		3.5	22.1	4.8	14.3
OREAS 100a (Fusion) Cert							24.1						260	463	47.1	152	23.6	3.71		3.80	23.2	4.81	14.9
OREAS 101a (Fusion) Meas							22						778	1380	128	388	48.6	7.96		5.4	31.6	6.5	19.0
OREAS 101a (Fusion) Cert							21.9						816	1396	134	403	48.8	8.06		5.92	33.3	6.46	19.5
JR-1 Meas		16		16	253	16	3	< 0.5	< 0.2	3		21.0	20.0	47.1	5.87	23.4	5.9		5.4	1.0			
JR-1 Cert		16.1		16.3	257	15.2	3.25	0.031	0.028	2.86		20.8	19.7	47.2	5.58	23.3	6.03		5.06	1.01			
SARM 3 Meas						916																	
SARM 3 Cert						978																	
BCR-2 Meas																							
BCR-2 Cert																							
F7- 8CL Orig	360	21	2	19	97	12	2	< 0.5	< 0.2	2	< 0.5	13.4	26.2	59.6	6.03	23.9	5.0	1.20	4.5	0.7	4.5	0.9	2.8
F7- 8CL Dup	350	22	2	18	97	13	2	< 0.5	< 0.2	2	< 0.5	13.4	26.1	59.3	5.90	23.7	5.0	1.29	4.3	0.7	4.5	1.0	2.8
Method Blank	< 30	< 1	< 1	< 5	< 2	< 1	< 2	< 0.5	< 0.2	< 1	< 0.5	< 0.5	< 0.1	< 0.1	< 0.05	< 0.1	< 0.1	< 0.05	< 0.1	< 0.1	< 0.1	< 0.1	< 0.1

QC

Analyte Symbol	Tm	Yb	Lu	Hf	Ta	W	Tl	Pb	Bi	Th	U
Unit Symbol	ppm	ppm	ppm	ppm	ppm	ppm	ppm	ppm	ppm	ppm	ppm
Lower Limit	0.05	0.1	0.04	0.2	0.1	1	0.1	5	0.4	0.1	0.1
Method Code	FUS-MS	FUS-MS	FUS-MS	FUS-MS	FUS-MS	FUS-MS	FUS-MS	FUS-MS	FUS-MS	FUS-MS	FUS-MS
DNC-1 Meas		1.9									
DNC-1 Cert		2.0									
GBW 07113 Meas											
GBW 07113 Cert											
LKSD-3 Meas		2.8	0.38		0.7					10.6	4.4
LKSD-3 Cert		2.70	0.400		0.700					11.4	4.60
TDB-1 Meas		3.3								2.4	
TDB-1 Cert		3.4								2.7	
W-2a Meas		2.1		2.5	0.5	1	0.1	9	< 0.4		0.5
W-2a Cert		2.10		2.60	0.500	0.300	0.200	9.30	0.0300		0.530
NIST 696 Meas											
NIST 696 Cert											
DTS-2b Meas											
DTS-2b Cert											
SY-4 Meas											
SY-4 Cert											
CTA-AC-1 Meas		10.5	1.05		2.6					21.9	
CTA-AC-1 Cert		11.4	1.08		2.65					21.8	
BIR-1a Meas		1.7		0.5				< 5			
BIR-1a Cert		1.7		0.60				3			
NCS DC86312 Meas	14.2	86.5	12.3							25.0	
NCS DC86312 Cert	15.1	87.79	11.96							23.6	
ZW-C Meas					82.5	330	34.0				
ZW-C Cert					82	320	34				
NCS DC70009 (GBW07241) Meas	2.19	15.2	2.20			2170				27.1	
NCS DC70009 (GBW07241) Cert	2.2	14.9	2.4			2200				28.3	
OREAS 100a (Fusion) Meas	2.24	15.1	2.11							48.8	131
OREAS 100a (Fusion) Cert	2.31	14.9	2.26							51.6	135
OREAS 101a (Fusion) Meas	2.83	18.1	2.55							34.7	411
OREAS 101a (Fusion) Cert	2.90	17.5	2.66							36.6	422
JR-1 Meas	0.68	4.9	0.66	4.2	1.9		1.4	23	0.6	25.4	8.7
JR-1 Cert	0.67	4.55	0.71	4.51	1.86		1.56	19.3	0.56	26.7	8.88
SARM 3 Meas											
SARM 3 Cert											
BCR-2 Meas											
BCR-2 Cert											
F7- 8CL Orig	0.42	2.7	0.43	4.8	1.0	< 1	0.1	17	< 0.4	8.4	4.0
F7- 8CL Dup	0.41	2.8	0.42	5.1	1.1	2	0.2	18	< 0.4	8.4	4.0
Method Blank	< 0.05	< 0.1	< 0.04	< 0.2	< 0.1	< 1	< 0.1	< 5	< 0.4	< 0.1	< 0.1